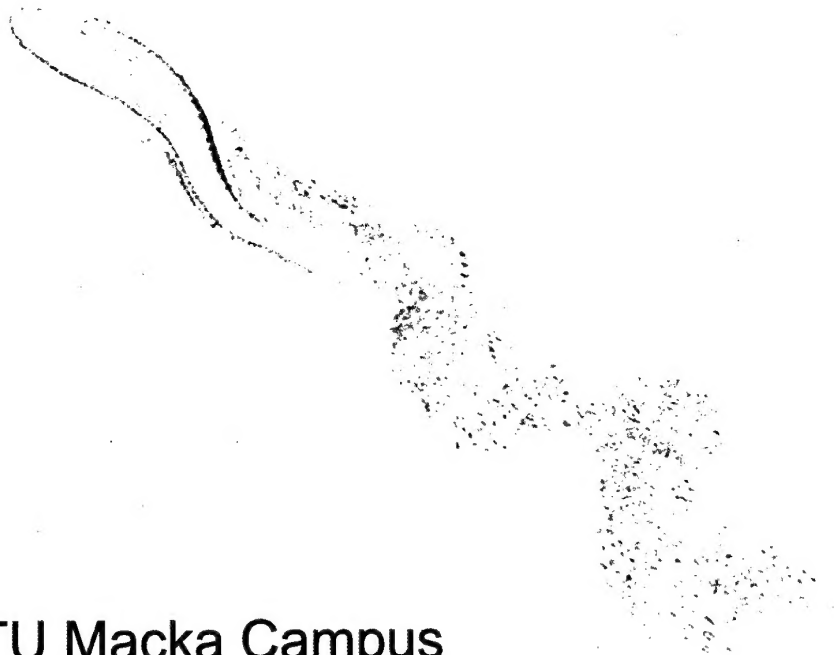


The Second International Conference on

Vortex Methods



ITU Maçka Campus
Istanbul, Turkey
September 26-28, 2001

DISTRIBUTION STATEMENT A
Approved for Public Release
Distribution Unlimited

20011113 029

ICVM / 2001

REPORT DOCUMENTATION PAGE				Form Approved OMB No. 0704-0188	
<p>Public reporting burden for this collection of information is estimated to average 1 hour per response, including the time for reviewing instructions, searching existing data sources, gathering and maintaining the data needed, and completing and reviewing the collection of information. Send comments regarding this burden estimate or any other aspect of this collection of information, including suggestions for reducing the burden, to Department of Defense, Washington Headquarters Services, Directorate for Information Operations and Reports (0704-0188), 1215 Jefferson Davis Highway, Suite 1204, Arlington, VA 22202-4302. Respondents should be aware that notwithstanding any other provision of law, no person shall be subject to any penalty for failing to comply with a collection of information if it does not display a currently valid OMB control number.</p> <p>PLEASE DO NOT RETURN YOUR FORM TO THE ABOVE ADDRESS.</p>					
1. REPORT DATE (DD-MM-YYYY) 27-10-2001		2. REPORT TYPE Conference Proceedings		3. DATES COVERED (From - To) 26 September 2001 - 28 September 2001	
4. TITLE AND SUBTITLE Second International Conference on Vortex Methods				5a. CONTRACT NUMBER F61775-01-WF035	
				5b. GRANT NUMBER	
				5c. PROGRAM ELEMENT NUMBER	
6. AUTHOR(S) Conference Committee				5d. PROJECT NUMBER	
				5d. TASK NUMBER	
				5e. WORK UNIT NUMBER	
7. PERFORMING ORGANIZATION NAME(S) AND ADDRESS(ES) Istanbul Technical University Maslak Istanbul 80626 Turkey				8. PERFORMING ORGANIZATION REPORT NUMBER N/A	
9. SPONSORING/MONITORING AGENCY NAME(S) AND ADDRESS(ES) EOARD PSC 802 BOX 14 FPO 09499-0014				10. SPONSOR/MONITOR'S ACRONYM(S)	
				11. SPONSOR/MONITOR'S REPORT NUMBER(S) CSP 01-5035	
12. DISTRIBUTION/AVAILABILITY STATEMENT Approved for public release; distribution is unlimited.					
13. SUPPLEMENTARY NOTES					
14. ABSTRACT The Final Proceedings for Second International Conference on Vortex Methods, 26 September 2001 - 28 September 2001 New Developments in mathematical and physical modeling techniques and engineering applications of vortex methods. The conference will cover topics spreading from basic theory of vortex methods to its engineering applications to unsteady flow problems such as loading of surfaces of aircraft and two phase flows with vibration, heat transfer and turbulence.					
15. SUBJECT TERMS EOARD, Vortex flows, Computational Fluid Dynamics (CFD)					
16. SECURITY CLASSIFICATION OF:			17. LIMITATION OF ABSTRACT UL	18. NUMBER OF PAGES 263	19a. NAME OF RESPONSIBLE PERSON Charbel N. Raffoul
a. REPORT UNCLAS	b. ABSTRACT UNCLAS	c. THIS PAGE UNCLAS			19b. TELEPHONE NUMBER (Include area code) +44 (0)20 7514 4299

The Second International Conference on
Vortex Methods

ITU Maçka Campus, Istanbul, Turkey
September 26-28, 2001

ICVM / 2001

AQ F02-02-0312

Cover picture: "Numerical fish", courtesy of K. Kamemoto

Library of Congress Cataloging-in-Publication Data

International Conference on Vortex Methods (2nd: 2001:Istanbul, Turkey)

The Second International Conference on Vortex Methods, Istanbul, Turkey, 26-28 September 2001-- Istanbul: Istanbul Technical University, 2001

ix, 263 p.

ISBN: 975-561-194-0

1. Vortex-motion-Congresses I. Title

QA 925 .I58 2001

This material is based upon work supported by the European Office of Aerospace Research and Development, Airforce Office of Scientific Research, Airforce Research Laboratory, Under Contract No. F61775-01-WF035

This work relates to Department of the Navy Grant N00014-01-1-1094 issued by Office of Naval Research International Field Office. The United States Government has a royalty-free license throughout the world in all copyrightable material contained herein.

Printed by Cenkler Matbaacılık, Istanbul, Turkey

FOREWORD

The creation of the Conferences on Vortex Methods results from an initiative of a committee, consisting of Prof. Kyoji Kamemoto of Yokohama National University, Prof. Masaru Kiya of Koshiro National College of Technology, Prof. Teruhiko Kida of Osaka Prefecture University and Prof. Michihisa Tsutahara of Kobe University. The initial impulse of this committee amplified after the success of the First International Conference in Kobe from 4 to 5 November, 1999, and for holding the conferences around the world on a regular basis an international organizing committee by representatives of different countries is formed.

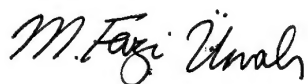
The papers contained in this book represent the content of the Second Conference that was held at Istanbul Technical University on 26-28 September, 2001. There are altogether thirty-three presentations at the conference five of which are invited lectures.

Organizing a conference requires support of organizations and considerable help from many people. On behalf of the organizing committee I wish to thank the following sponsors for their contribution to the success of this conference:

Istanbul Technical University
Istanbul Technical University Development Foundation
Istanbul Technical University Foundation
European Office of Aerospace Research and Development (EOARD), Air Force Office of Scientific Research, United States Air Force Research Laboratory, under Contract No. F61775-01-WF035
Office of Naval Research International Field Office (ONRIFO), under Grant No. N00014-01-1-1094
European Community on Computational Methods in Applied Sciences (ECCOMAS)
Turkish Scientific and Technical Research Council (TUBITAK)
Turkish National Committee on Theoretical and Applied Mechanics (TUMTMK)

My personal gratitudes are extended to Professor Kyoji Kamemoto and Professor Michihisa Tsutahara, the chairman and the co-chairman of the first conference and all the members of the organizing committee, to Dr. C. N. Raffoul of EOARD, Captain S.P. Smolinski of ONRIFO, Professor Yalçın Aköz, Professor Ülgen Gülçat of TUMTMK and to Mr. M.S. Saffet Baysal of ASSES for their invaluable help during the organization of the conference.

I would also acknowledge the support of the Rector of the Istanbul Technical University Professor Gülsün Sağlamer and the Dean of Faculty of Aeronautics and Astronautics Professor Yurdanur Tulunay towards the realization of this conference. Last but not least, the authors are thanked for providing such an interesting set of papers.



M. Fevzi Ünal
Chair of the Local Organizing Committee
Second International Conference on Vortex Methods
Professor, Istanbul Technical University

THE SECOND INTERNATIONAL CONFERENCE ON

VORTEX METHODS 2001

Local Organising Committee

M. Fevzi ÜNAL (Chair)

Professor, Istanbul Technical University

Aydın MISIRLIOĞLU (Secretariat)

Associate Professor, Istanbul Technical University

Organizing Committee

Peter W. Bearman

Professor, Imperial College, UK

Peter S. Bernard

Professor, University of Maryland, USA

Alexandre J. Chorin

Professor, University of California, Berkeley, USA

G.H. Cottet

Professor, Universite Joseph Fourier, France

J. Michael R. Graham

Professor, Imperial College, UK

Kyoji Kamemoto

Professor, Yokohama National University, Japan

Teruhiko Kida

Professor, Osaka Prefecture University, Japan

Masaru Kiya

Professor, Kushiro National College of Technology, Japan

Duck-Joo Lee

Professor, Korean Advanced Institute of Science and Technology, Korea

Anthony Leonard

Professor, CALTECH, USA

R.Ivan Lewis

Professor, Newcastle University, UK

Turgut Sarpkaya

Professor, Naval Post Graduate School, USA

Michihisa Tsutahara

Professor, Kobe University, Japan

M. Fevzi Ünal

Professor, Istanbul Technical University, Turkey

Lung-an Ying

Professor, Peking University, P.R.China

THE SECOND INTERNATIONAL CONFERENCE ON
VORTEX METHODS
ITU MAÇKA SOCIAL FACILITIES, ISTANBUL, TURKEY
SEPTEMBER 26-28, 2001

Contents

Invited Lecture	Fractional step methods for viscous incompressible flows <i>Lung-an Ying</i>	1
Session	Basic Studies on Vortices and Production of Vorticity	
	Experiment of waves on a vortex filament <i>Y. Funakubo and S. Watanabe</i>	9
	A motion of a two-dimensional vortex sheet and a doubly branched spiral <i>T. Sakajo</i>	17
	A new approach to the vortex method for determination of vorticity shedding from solid boundary <i>H. Wang and H. Tsukamoto</i>	25
	Study on higher resolution of vorticity layer over a solid boundary for vortex methods <i>S. Ota and K. Kamemoto</i>	33
Invited Lecture	Vortex method modeling of complex, turbulent, engineering flows <i>Peter. S. Bernard and Athanassios. A. Dimas</i>	41

Session	Modeling of Turbulent Flows	
	Entanglement of a co-rotating vortex pair	55
	<i>K. Ohtsuka, R. Takaki and S. Watanabe</i>	
	Numerical investigation of unsteady deformation of eddy structure by vortex methods	63
	<i>K. Fukuda, K. Kamemoto and B. Zhu</i>	
	Analysis of the homogeneous isotropic turbulence by a three dimensional vortex element method	71
	<i>Y. Totsuka and S. Obi</i>	
	Producing artificial turbulence by the vortex method	79
	<i>Y. Ogami, K. Nishiwaki and Y. Yoshihara</i>	
Session	Vortex Rings	
	Transient flow around a vortex ring by a vortex method	87
	<i>T. Kida and T. Take</i>	
	Formation of a turbulent vortex ring	93
	<i>J. Hatano and S. Watanabe</i>	
	Vortex structure of impinging round jets	99
	<i>S. Izawa and M. Kiya</i>	
Session	Flow Around Bluff Bodies	
	Velocity map and flow pattern of flow around four cylinders in a square configuration at low Reynolds number and large spacing ratio using particle image velocimetry	107
	<i>K. Lam, K.T. Chan, R.M.C. So and J.Y. Li</i>	
	Flow around four cylinders in a square configuration using surface vorticity method	115
	<i>K. Lam, R.M.C. So and J.Y. Li</i>	
	Vortex-in-cell simulation of flow around a circular cylinder downstream of a blunt based flat plate in tandem arrangement	123
	<i>H.I. Keser and M.F. Ünal</i>	

	Simulation of wake from a circular cylinder with spanwise sinusoidal waviness	131
	<i>H.İ. Keser, M.F. Ünal and P.W. Bearman</i>	
	A study of the unsteady force due to gusts of side wind on a train by the three dimensional discrete vortex method	139
	<i>K. Ogawa, M. Tsutahara, T. Nakazawa, N. Takada, T. Maeda and M. Suzuki</i>	
Invited Lecture	Application of mixed Eulerian-Lagrangian vortex methods to cross-flow past long flexible circular cylinders	147
	<i>J. Michael R. Graham and R.H.J. Willden</i>	
Session	Flows with Vibration	
	Computing the flows around a moving bluff body by a Lagrangian vortex method	157
	<i>B. Zhu and K. Kamemoto</i>	
	A discrete vortex study of streamwise oscillations of a circular cylinder: comparison with experiment	165
	<i>O. Çetiner, M.F. Ünal and D. Rockwell</i>	
Session	Applications to Turbomachinery	
	Numerical simulation of unsteady flow through a horizontal axis wind turbine by a vortex method	173
	<i>A. Ojima and K. Kamemoto</i>	
	Extension of vortex methods to the flow simulation of mixed-flow turbomachines	181
	<i>R.I. Lewis</i>	
	Numerical analysis of vortex instability in the rotor wake	189
	<i>D.J. Lee, K.H. Chung and K.W. Ryu</i>	

Invited Lecture	Engineering application of the vortex methods developed in Yokohama National University (YNU) <i>Kyoji Kamemoto</i>	197
Session	Applications to Engineering Problems	
	Prediction of aerodynamic sound spectra by using an advanced vortex method <i>A. Iida K. Kamemoto and A. Ojima</i>	211
	Application of the vortex method for investigating the behavior and potential hazard of the WIG trailing vortices <i>N. Kornev and A. Taranov</i>	219
	A study of the behavior of critical layer in density stratified shear flows by lattice vortex method <i>M. Tsutahara and X. Zhang</i>	227
	Analysis of unsteady heat transfer in the wake behind a circular cylinder in a uniform flow by a vortex and heat element method <i>H. Nakamura, K. Kamemoto and T. Igarashi</i>	235
Session	Applications to Engineering Problems	
	Vortex ring interacting with shear-layer vortices <i>H. Ishikawa, O. Mochizuki and M. Kiya</i>	243
	Effect of particle phase on vortex shedding mechanism in two phase planar jet flow <i>M. Tunç, C.R. Kaykayoglu and O. Gökçöl</i>	251
	Small scale auroral vortices <i>G. Kandemir, M.Yilmaz, B. Özüğür and Z. Kaymaz</i>	259
Index of Authors		263

FRACTIONAL STEP METHODS FOR VISCOUS INCOMPRESSIBLE FLOWS

Lung-an Ying

School of Mathematical Sciences

Peking University

Beijing, 100871

People's Republic of China

e-mail address: yingla@pku.edu.cn

ABSTRACT

The vortex method for viscous incompressible flows is a kind of fractional step method. Within each time step three different kinds of mechanism, convection, diffusion, and vorticity creation, are treated separately. The fractional step method is a general method in solving partial differential equations. In this talk we will present a survey for the fractional step method applied to the Navier-Stokes equation. We will talk about the advantage of it, and about two different approaches for viscous incompressible flows. The projection method puts emphasis on the treatment of incompressibility. On the other hand viscous splitting puts emphasis on the treatment of viscosity, especially small viscosity. we will state some mathematical results on these methods, including our recent work about the strength of vortex sheets.

1 Introduction

The vortex method for viscous incompressible flows is a kind of fractional step method. Within each time step three different kinds of mechanism, convection, diffusion, and vorticity creation, are treated separately. To the author's knowledge the fractional step method for partial differential equations can be dated back to 1955 when Peaceman and Rachford introduced the ADI (alternating direction implicit) method. Let us make a brief review of this method. For example if we consider the numerical method for the two dimensional heat equa-

tion:

$$\frac{\partial u}{\partial t} = \frac{\partial^2 u}{\partial x^2} + \frac{\partial^2 u}{\partial y^2},$$

then the implicit difference scheme reads:

$$\frac{u_{ij}^{n+1} - u_{ij}^n}{\Delta t} = \frac{u_{i+1,j}^{n+1} - 2u_{ij}^{n+1} + u_{i-1,j}^{n+1}}{\Delta x^2} + \frac{u_{i,j+1}^{n+1} - 2u_{ij}^{n+1} + u_{i,j-1}^{n+1}}{\Delta y^2},$$

where $u_{ij}^n = u(i\Delta x, j\Delta y, n\Delta t)$.

In each time step one algebraic system of equation is solved. If the scale of the domain is X in x direction and Y in y direction, then the matrix is $N \times N$, where $N = O\left(\frac{XY}{\Delta x \Delta y}\right)$, which is a large number if $\Delta x, \Delta y$ are small. For three dimensional problems the situation is even worse. To solve this problem the ADI scheme introduced by Peaceman and Rachford reads:

$$\frac{u_{ij}^{n+\frac{1}{2}} - u_{ij}^n}{\Delta t} = \frac{u_{i+1,j}^{n+\frac{1}{2}} - 2u_{ij}^{n+\frac{1}{2}} + u_{i-1,j}^{n+\frac{1}{2}}}{2\Delta x^2} + \frac{u_{i,j+1}^n - 2u_{ij}^n + u_{i,j-1}^n}{2\Delta y^2},$$

$$\frac{u_{ij}^{n+1} - u_{ij}^{n+\frac{1}{2}}}{\Delta t} = \frac{u_{i+1,j}^{n+\frac{1}{2}} - 2u_{ij}^{n+\frac{1}{2}} + u_{i-1,j}^{n+\frac{1}{2}}}{2\Delta x^2} + \frac{u_{i,j+1}^{n+1} - 2u_{ij}^{n+1} + u_{i,j-1}^{n+1}}{2\Delta y^2},$$

and the ADI scheme introduced by Douglas and Rachford reads:

$$\frac{\tilde{u}_{ij}^{n+1} - u_{ij}^n}{\Delta t} = \frac{\tilde{u}_{i+1,j}^{n+1} - 2\tilde{u}_{ij}^{n+1} + \tilde{u}_{i-1,j}^{n+1}}{\Delta x^2} + \frac{u_{i,j+1}^n - 2u_{ij}^n + u_{i,j-1}^n}{\Delta y^2},$$

$$\frac{u_{ij}^{n+1} - u_{ij}^n}{\Delta t} = \frac{\tilde{u}_{i+1j}^{n+1} - 2\tilde{u}_{ij}^{n+1} + \tilde{u}_{i-1j}^{n+1}}{\Delta x^2} + \frac{u_{ij+1}^{n+1} - 2u_{ij}^{n+1} + u_{ij-1}^{n+1}}{\Delta y^2}.$$

We see that in each step there is only one direction implicit. The scale of matrix is reduced considerably, and it is easy to be carried out by parallel computing.

Another fractional step method is the locally one dimensional method:

$$\frac{u_{ij}^{n+\frac{1}{2}} - u_{ij}^n}{\Delta t} = \frac{u_{i+1j}^{n+\frac{1}{2}} - 2u_{ij}^{n+\frac{1}{2}} + u_{i-1j}^{n+\frac{1}{2}}}{\Delta x^2},$$

$$\frac{u_{ij}^{n+1} - u_{ij}^{n+\frac{1}{2}}}{\Delta t} = \frac{u_{ij+1}^{n+1} - 2u_{ij}^{n+1} + u_{ij-1}^{n+1}}{\Delta y^2}.$$

In fact the equation is split into two equations,

$$\frac{\partial u}{\partial t} = \frac{\partial^2 u}{\partial x^2}, \quad \frac{\partial u}{\partial t} = \frac{\partial^2 u}{\partial y^2},$$

so it is called an "operator splitting". By this point of view we split a partial differential equation,

$$\frac{\partial u}{\partial t} = A_1 u + A_2 u + \dots + A_n u$$

into n equations:

$$\frac{\partial u}{\partial t} = A_1 u, \quad \frac{\partial u}{\partial t} = A_2 u, \quad \dots \quad \frac{\partial u}{\partial t} = A_n u,$$

and we solve them separately within each time step. It is supposed that the combined effort is equivalent to the original equation.

For the Navier-Stokes equation of viscous incompressible flows the fractional step method is frequently used. The advantage is not only reducing computational scale, but also overcoming the difficulty arising from different kinds of mechanisms.

At least three factors are considered simultaneously in the equation: viscosity, incompressibility, and convection. To consider the viscosity and incompressibility together, the matrix for the primary variables, velocity and pressure, is not positive definite, so many effective algorithms can not be used. To consider the viscosity and convection together, the convection term causes a considerable numerical viscosity; and if the physical viscosity is small, it will be hid by the numerical viscosity and spurious results will be produced. To overcome these difficulties, some fractional step methods were proposed. Let us consider two of them: the projection method and the viscous splitting.

2 Projection method

The projection method was designed to overcome the difficulty caused by the constraint of incompressibility. It was introduced by Chorin and Temam in the 60's. Let us consider the no-slip boundary condition on the boundary $\partial\Omega$ of a bounded domain Ω . The initial-boundary value problem for the Navier-Stokes equation is

$$\frac{\partial u}{\partial t} + (u \cdot \nabla)u + \frac{1}{\rho} \nabla p = \nu \Delta u, \quad (1)$$

$$\nabla \cdot u = 0, \quad (2)$$

$$u|_{\partial\Omega} = 0, \quad (3)$$

$$u|_{t=0} = u_0, \quad (4)$$

where u is the velocity, p is the pressure, and the constants ρ and ν are density and kinetic viscosity respectively.

With a discretization in the time direction, the backward Euler scheme reads:

$$\frac{u^{n+1} - u^n}{\Delta t} + (u^n \cdot \nabla)u^n + \frac{1}{\rho} \nabla p^{n+1} = \nu \Delta u^{n+1},$$

$$\nabla \cdot u^{n+1} = 0,$$

$$u^{n+1}|_{\partial\Omega} = 0,$$

$$u^0 = u_0,$$

where Δt is the step size. Let us neglect temporarily the constraints of incompressibility, then the problem becomes

$$\frac{u^* - u^n}{\Delta t} + (u^n \cdot \nabla)u^n = \nu \Delta u^*,$$

$$u^*|_{\partial\Omega} = 0,$$

For given u^n it is a linear elliptic boundary value problem for u^* , and many traditional methods can be applied to solve it. However the solution u^* does not satisfy (2). To set the second step, we recall the Helmholtz decomposition:

$$u = v + w,$$

where u is an arbitrary vector field, v satisfies $\nabla \cdot v = 0$, $v \cdot N|_{\partial\Omega} = 0$, where N is the unit outward normal vector along the boundary $\partial\Omega$, and $w = \nabla \varphi$, where φ is a potential. This decomposition is orthogonal in $L^2(\Omega)$,

$$\int_{\Omega} v \cdot w \, dx = 0.$$

We assume $H = \{v \in L^2(\Omega); \nabla \cdot v = 0, v \cdot N|_{\partial\Omega} = 0\}$, then v is the orthogonal projection of u on H ,

denoted by $v = Pu$. We set $u^{n+1} = Pu^*$, then $\nabla \cdot u^{n+1} = 0$, and $u^{n+1} \cdot N|_{\partial\Omega} = 0$. Following this procedure a series of approximate solutions, $u^1, u^2, \dots, u^n, \dots$ is obtained. This is a scheme with two intermediate steps.

Let

$$u^* - u^{n+1} = \Delta t \frac{1}{\rho} \nabla p^{n+1}, \quad (5)$$

then it is easy to see that

$$\begin{aligned} & \frac{u^{n+1} - u^n}{\Delta t} + (u^n \cdot \nabla) u^n + \frac{1}{\rho} \nabla p^{n+1} \\ &= \nu \Delta u^{n+1} + \nu \Delta t \frac{1}{\rho} \Delta \nabla p^{n+1}, \end{aligned} \quad (6)$$

therefore the scheme is consistent with the Navier-Stokes equation.

Convergence theorem was proved by Temam and Chorin. If $u_0 \in H$, then there exists some sequence $\Delta t \rightarrow 0$ such that the approximate solutions converge in $L^2(\Omega \times (0, T))$ to the exact solution u .

To carry out the orthogonal decomposition, we apply the operator ∇ to (5) and obtain:

$$\Delta p^{n+1} = \frac{\rho}{\Delta t} \nabla \cdot u^*.$$

The inner product of (5) with N leads to

$$\left. \frac{\partial p^{n+1}}{\partial N} \right|_{\partial\Omega} = 0.$$

Therefore the second step of this scheme is to solve a Neumann boundary value problem of a Poisson equation.

The scheme is of first order, because the truncation error of (6) is first order. Moreover u^{n+1} satisfies on the boundary that

$$u^{n+1} \cdot N|_{\partial\Omega} = 0, \quad u^{n+1} \cdot \tau|_{\partial\Omega} = -\frac{\Delta t}{\rho} \frac{\partial p^{n+1}}{\partial \tau},$$

where τ is the unit tangential vector along the boundary $\partial\Omega$. The truncation error of which is also first order. Since u^{n+1} does not satisfy the no-slip boundary condition exactly, there is a numerical boundary layer. Error estimates have been studied by Shen.

There are some second order projection schemes. First of all, the backward Euler scheme should be replaced by some higher order schemes. Using the trapezoidal rule, the equation of the Crank-Nicholson scheme for the first step is

$$\frac{u^* - u^n}{\Delta t} + (u^{n+\frac{1}{2}} \cdot \nabla) u^{n+\frac{1}{2}} = \nu \Delta \frac{u^* + u^n}{2},$$

where $u^{n+\frac{1}{2}}$ can be obtained by extrapolation.

To improve the truncation error on the boundary, Kim and Moin introduced the boundary condition for u^* ,

$$u^*|_{\partial\Omega} = \frac{\Delta t}{\rho} \nabla p^{n-\frac{1}{2}} \Big|_{\partial\Omega} - u^n|_{\partial\Omega},$$

and the second step

$$\begin{aligned} u^* &= u^{n+1} + \Delta t \nabla p^{n+\frac{1}{2}}, \\ \nabla \cdot u^{n+1} &= 0, \quad u^{n+1} \cdot N|_{\partial\Omega} = 0. \end{aligned}$$

Orszag, Israel and Deville improved the Neumann boundary condition for p^{n+1} ,

$$\left. \frac{\partial p^{n+1}}{\partial N} \right|_{\partial\Omega} = -N \cdot [\nabla \times (\nabla \times u^*)]|_{\partial\Omega}.$$

The second order scheme introduced by Bell, Colella and Glaz reads:

Step 1.

$$\frac{u^* - u^n}{\Delta t} + (u^{n+\frac{1}{2}} \cdot \nabla) u^{n+\frac{1}{2}} + \frac{1}{\rho} \nabla p^{n-\frac{1}{2}} = \nu \Delta \frac{u^* + u^n}{2},$$

$$u^*|_{\partial\Omega} = 0.$$

Step 2.

$$u^* = u^{n+1} + \Delta t (\nabla p^{n+\frac{1}{2}} - \nabla p^{n-\frac{1}{2}}),$$

$$\nabla \cdot u^{n+1} = 0, \quad u^{n+1} \cdot N|_{\partial\Omega} = 0.$$

Error estimates of higher order schemes have been studied by Shen. Using asymptotic analysis, E and Liu analyzed the structure of numerical boundary layers.

3 Viscous splitting

Viscous splitting is applied in the vortex method, which is designed to overcome the difficulty of small viscosity. Let us consider initial value problem (1)(2)(4) first. Different from the projection method, viscosity is ignored and the Euler equation is solved in the first step, which is

$$\frac{\partial u}{\partial t} + (u \cdot \nabla) u + \frac{1}{\rho} \nabla p = 0,$$

$$\nabla \cdot u = 0,$$

or in the vorticity setting let $\omega = \text{rot} u$, then

$$\frac{\partial \omega}{\partial t} + (u \cdot \nabla) \omega - (\omega \cdot \nabla) u = 0, \quad (7)$$

for three dimensional problems and

$$\frac{\partial \omega}{\partial t} + (u \cdot \nabla) \omega = 0, \quad (8)$$

for two dimensional problems. The advantage of replacing the Navier-Stokes equation by the Euler equation is that it can be solved by a characteristic method. If we introduce characteristic curves defined by

$$\frac{dx}{dt} = u(x, t),$$

then along characteristics the equation is reduced to ordinary differential equations

$$\frac{d\omega}{dt} = (\omega \cdot \nabla) u, \quad \text{or} \quad \frac{d\omega}{dt} = 0.$$

Velocity can be recovered from the vorticity using the well known Biot-Savart law. Another advantage, which might be more important, is that for high Reynold's number flows the viscosity ν is small, and in this scheme the viscosity term is separated from the convection term.

By the concept of operator splitting the second step is to solve the Stokes equation

$$\frac{\partial u}{\partial t} + \frac{1}{\rho} \nabla p = \nu \Delta u,$$

$$\nabla \cdot u = 0,$$

or in the vorticity setting

$$\frac{\partial \omega}{\partial t} = \nu \Delta \omega, \quad (9)$$

which is the heat equation, the solution of which can be expressed in terms of a Poisson integral

$$\omega(x, t) = \int K(x - \xi, t) \omega_0(\xi) d\xi,$$

where K is the heat kernel

$$K(x, t) = \frac{1}{(4\pi\nu t)^{\frac{3}{2}}} e^{-\frac{|x|^2}{4\nu t}}$$

for three dimensional problems, or

$$K(x, t) = \frac{1}{4\pi\nu t} e^{-\frac{|x|^2}{4\nu t}}$$

for two dimensional problems. Numerically the solutions may be obtained by random walk. It is noticed that there is no difference between large ν or small ν in the second step.

The previous scheme can be formulated by the following formula:

$$\omega(ik) = (H(k)E(k))^i \omega_0, \quad (10)$$

where k is the step size, $i = 1, 2, \dots$, $E(t)$ is the "Euler solver", where $E(t)\omega_0$ means the solution ω of (7) or (8) at time t with initial value ω_0 , and $H(t)$ is the solver of heat equation.

Beale and Majda studied the scheme (10) and a second order scheme

$$\omega(ik) = \left(E\left(\frac{k}{2}\right) H(k) E\left(\frac{k}{2}\right) \right)^i \omega_0.$$

First order and second order error estimates in the Sobolev spaces $H^m(\mathbf{R}^3)$ or $H^m(\mathbf{R}^2)$ are proved, where m is an arbitrary positive number, provided the initial data are sufficiently smooth.

We consider initial-boundary value problems next. The no-slip boundary condition

$$u|_{\partial\Omega} = 0 \quad (11)$$

is applied to the Stokes equation. However since the Euler equation represents an inviscid flow the condition for the first step is

$$u \cdot N|_{\partial\Omega} = 0. \quad (12)$$

The vorticity setting is difficult, because there is no local boundary condition on the vorticity. We will discuss this point later on.

After the first step u satisfies the boundary condition (12), but $u \cdot \tau|_{\partial\Omega}$ is, generally speaking, not zero. However the boundary condition (11) is imposed immediately at the second step, so the velocity u is discontinuous, and consequently there is a vortex sheet on the boundary, which is in the form of $f(\tau)\delta(N)$, where f is an ordinary function with the independent variable τ along the boundary, and δ is the Dirac δ -function with the independent variable N along the normal direction.

The solution of this scheme is very singular. However it converges. The problem has been studied by Douglis, Fabes, Alessandrini, Zheng, Huang, Zhang, and Ying. It was proved that the H^2 -norm, $s < \frac{1}{2}$, of the error of velocity at the convection step is of order 1.

Ying has studied the following problem: replacing the vortex sheet by a smooth function to prevent the solution from singularity. If the velocity after the convection step is \tilde{u} , which satisfies (12). \tilde{u} is replaced by $\phi\tilde{u}$, where ϕ is an operator such that $\phi\tilde{u}$ satisfies (11). The Stokes equation is solved with initial data $\phi\tilde{u}$. Since the initial data is modified, the equation should be modified to

$$\frac{\partial u}{\partial t} + \frac{1}{\rho} \nabla p = \nu \Delta u + \frac{1}{k} (I - \phi) \tilde{u},$$

accordingly, where I is the identity operator. The convergence result is improved. It is proved that

the H^1 -norm of the error of the velocity at both steps is of order 1. Numerical experiments confirmed this result.

Taking the boundary condition into account it is difficult to propose a mathematical formulation for the vorticity setting in the diffusion step, while it is easy in the convection step. By the boundary condition (12) the boundary $\partial\Omega \times (0, T)$ is a characteristic surface of the equations (7) (8), therefore no boundary condition is needed for the vorticity in the convection step. However the boundary condition for (9) is not local. It is proposed in [9] to replace the problem in the diffusion step by a pure initial value problem.

Let \tilde{u} be the velocity solution in Ω of the convection step and $\tilde{\omega}$ be the corresponding vorticity. \tilde{u} is extended to the exterior of Ω by an odd extension. Therefore the jump of the tangential component of the velocity is $2\tilde{u} \cdot \tau|_{\partial\Omega}$, which is also the density of the vortex sheet. The extended vorticity on the entire space is denoted by $\phi\tilde{\omega}$, where ϕ is the "vorticity creation operator". $\phi\tilde{\omega}$ consists of $\tilde{\omega}$, a vortex sheet on the boundary $\partial\Omega$, and an extension of $\tilde{\omega}$ to the exterior. The formula (10) becomes

$$\omega(ik) = (H(k) \circ \phi \circ E(k))^i \omega_0, \quad (13)$$

where $H(k)$ should be understood to solve the heat equation on the whole space. (13) is known as the Chorin-Marsden formula.

The convergence of (13) for linear equations was proved in [10].

Nonlinear problems was studied in [22] and [5]. Ω is assumed to be a convex domain. To avoid the difficulty of nonlinearity, the equation in the convection step is linearized:

$$\frac{\partial u}{\partial t} + (Pu^* \cdot \nabla)u + \frac{1}{\rho} \nabla p = 0, \quad (14)$$

where u^* is the solution of the previous diffusion step, and P is the Helmholtz projection operator. Convergence was proved.

Benfatto and Pulvirenti studied another linear scheme for nonlinear problems in two dimensional space. Let Ω be a half plane, $\Omega = \{(x_1, x_2); x_2 > 0\}$, the scheme in the convection step reads:

$$\frac{\omega - \omega^*}{k} + u^* \cdot \nabla \omega^* = 0.$$

The "vorticity creation operator" is in different form. The tangential component of velocity u is extended oddly and the normal component is extended evenly. The jump is still $2\tilde{u} \cdot \tau|_{\partial\Omega}$. It is proved that the rate of convergence is $O(k^{\frac{1}{2}})$.

Recently we studied the convergence problem of the Chorin-Marsden formula for arbitrary two dimensional bounded domains (see [23]). Our idea is to derive an expression of the vortex sheet for exact solutions, then make an approximation.

The exact solution can be expressed in terms of

$$\begin{aligned} \omega &= \int K(x - \xi, t) \omega_0(\xi) d\xi \\ &- \int_0^t \int_{\Omega} K(x - \xi, t - \tau) F(\xi, \tau) d\xi d\tau \\ &+ \int_0^t \int_{\partial\Omega} K(x - \xi, t - \tau) \rho(\xi, \tau) ds_{\xi} d\tau, \end{aligned}$$

where the first term is generated by the initial data, the second term is generated by the convection term, $F = u \cdot \nabla \omega$, and the last term is generated by the vortex sheet with density ρ .

It is proved that ρ satisfies an integral equation of Volterra type:

$$\int_0^t \int_{\partial\Omega} L(\eta, \xi, t - \tau) \rho(\xi, \tau) ds_{\xi} d\tau + f(\eta, t) = 0, \quad (15)$$

where

$$\begin{aligned} f(\eta, t) &= \int_{\Omega} M(x, \eta) \left\{ \int K(x - \xi, t) \omega_0(\xi) d\xi \right. \\ &\quad \left. - \int_0^t \int_{\Omega} K(x - \xi, t - \tau) F(\xi, \tau) d\xi d\tau \right\} dx, \end{aligned}$$

and L, M are some kernels.

Based on this formula, the following fractional step scheme is proposed: Let ω be known for $t \leq t_i$, then on $(t_i, t_{i+1}]$ ω is solved by:

Step 1. Solve the Euler equation (7) or (8) on $(t_i, t_{i+1}] \times \Omega$ with initial value $\omega(t_i)$.

Step 2. Solve the integral equation (15) on $(t_i, t_{i+1}] \times \partial\Omega$.

Step 3. Solve the heat equation on the entire space with the initial condition

$$\omega = \omega(t_i) + \omega_1 + \omega_2,$$

where

$$\omega_1 = \begin{cases} \tilde{\omega} - \omega(t_i), & x \in \Omega, \\ 0, & x \notin \Omega, \end{cases}$$

$\tilde{\omega}$ is the solution of step 1, and

$$\omega_2 = \int_{t_i}^{t_{i+1}} \rho(\xi, t) dt \delta(N).$$

Convergence was proved with a rate of $O(k^{\frac{1}{2}})$.

One may ask if $\rho = 2u \cdot \tau|_{\partial\Omega}$ holds. It is shown that if Ω is a half plane, then it is true. However for an arbitrary domain they differ from one additional term.

References

- [1] G.Alessandrini, A.Douglis, and E.Fabes, An approximate layering method for the Navier-Stokes equations in bounded cylinders, *Ann.Mat.Pura.Appl.*, 135, 329-347, 1983;
- [2] J.T.Beale, Viscous splitting of the Navier-Stokes equation with boundaries, ICIAM 91, presentation;
- [3] J.T.Beale, and A.Majda, Rate of convergence for viscous splitting of the Navier-Stokes equations, *Math.Comp.*, 37, 243-259, 1981;
- [4] J.B.Bell, P.Colella, and H.M.Glaz, A second order projection method for the incompressible Navier-Stokes equations, *J.Comput.Phys.*, 85, 257-283, 1989;
- [5] G.Benfatto, and M.Pulvirenti, Convergence of Chorin-Marsden product formula in the half-plane, *Comm.Math.Phys.*, 106, 427-458, 1986;
- [6] A.J.Chorin, The numerical solution of the Navier-Stokes equations for an incompressible fluid, *Bull.Amer.Math.Soc.*, 73, 928-931, 1967;
- [7] A.J.Chorin, Numerical solutions of the Navier-Stokes equations, *Math.Comp.*, 22, 745-762, 1968;
- [8] A.J.Chorin, On the convergence of discrete approximations to the Navier-Stokes equations, *Math.Comp.*, 23, 341-353, 1969;
- [9] A.J.Chorin, Numerical study of slightly viscous flow, *J.Fluid Mech.*, 57, 785-796, 1973;
- [10] A.J.Chorin, T.J.R.Hughes, M.F.McCracken, and J.E.Marsden, Product formulas and numerical algorithms, *Comm.Pure Appl.Math.*, 31, 205-256, 1978;
- [11] A.Douglis, and E.Fabes, A layering Method for Viscous Incompressible L_p Flows Occupying \mathbf{R}^n , *Research Notes in Mathematics*, 108, Pitman, 1984;
- [12] Weinan E, and J.-G. Liu, Projection method I: Convergence and numerical boundary layers, *SIAM J.Numer.Anal.*, 32, 1017-1057, 1995;
- [13] Weinan E, and J.-G. Liu, Projection method II: Godunov-Ryabenki analysis, *SIAM J.Numer.Anal.*, 33, 1597-1621, 1996;
- [14] J.Kim, and P.Moin, Application of a fractional step method to incompressible Navier-Stokes equations, *J.Comput.Phys.*, 59, 308-323, 1985;
- [15] S.A.Orszag, M.Israel, and M.O.Deville, Boundary conditions for incompressible flows, *J.Scientific Computing*, 1, 75-111, 1986;
- [16] J.Shen, On error estimates of projection methods for Navier-Stokes equations: first order schemes, *SIAM J.Numer.Anal.*, 29, 57-77, 1992;
- [17] J.Shen, On error estimates of some higher order projection and penalty-projection methods for Navier-Stokes equations, *Numer.Math.*, 62, 49-73, 1992;
- [18] R.Temam, *Navier-Stokes Equations, Theory and Numerical Analysis*, 3rd ed., North Holland, 1984;
- [19] L.-a.Ying, Convergence study for viscous splitting in bounded domains, *Lecture Notes in Mathematics*, Springer-Verlag, 1297, 184-202, 1987;
- [20] L.-a.Ying, Viscous splitting for the unbounded problem of the Navier-stokes equations, *Math.Comp.*, 55, 89-113, 1990;
- [21] L.-a.Ying, Optimal error estimates for a viscosity splitting formula, in *Proceedings of the Second Conference on Numerical Methods for PDE*, World Scientific, 139-147, 1991;
- [22] L.-a.Ying, Convergence of Chorin-Marsden formula for the Navier-Stokes equations on convex domains, *J.Comp.Math.*, 17, 73-88, 1999;
- [23] L.-a.Ying, Convergence study of Chorin-Marsden formula, *Math.Comp.* (to appear);
- [24] L.-a.Ying, and P.Zhang, *Vortex Methods*, Science Press, Beijing/New York, and Kluwer Academic Publishers, Dordrecht/Boston/London, 1997;
- [25] P.Zhang, A sharp estimate of simplified viscosity splitting scheme, *J.Comput.Math.*, 11, 205-210, 1993;

- [26] Q.Zheng, and M.Huang, A simplified viscosity splitting method for solving the initial boundary value problems of Navier-Stokes equation, J.Comput.Math., 10, 39-56, 1992.

EXPERIMENT OF WAVES ON A VORTEX FILAMENT

Yuko FUNAKUBO

Department of Energy Engineering Faculty of Engineering, Yokohama National University
79-5 Tokiwadai, Hodogaya, Yokohama 240-8501, Japan /Email: m00db123@ynu.ac.jp

Shinsuke WATANABE

Department of Physics Department of Energy Engineering Faculty of Engineering, Yokohama National University
79-5 Tokiwadai, Hodogaya, Yokohama 240-8501, Japan /Email: wtnb@ynu.ac.jp

ABSTRACT

A helical wave on a vortex filament is studied experimentally. A vortex filament is generated by an axial rotational flow of water in a cylindrical tank with a small hole at the center of the bottom. The motion of a filament is controlled by a solid disk inserted from top of the water tank. When the disk is flapped around a horizontal axis, a filament tends to be perpendicularly to a disk, and begins to move with the disk. Such a motion of the disk will produce perturbations on a filament. A sinusoidal motion of the disk leads to the formation of a stable helical wave on a filament. A flapping of the disk by sinusoidal motion of half period generates a wave packet which disperses during propagation. We measured a dispersion relation and group velocity from these waves, and compared with the theory. The experiment of a stable solitary wave derived by Hasimoto (1972)¹⁾ has also been carried out.

1. INTRODUCTION

The motion of a vortex filament is determined by the velocity field of its own induction. A localized induction equation which describes the motion of a thin vortex filament $\mathbf{x}=\mathbf{x}(s, t)$ has been derived²⁾ as

$$\frac{\partial \mathbf{x}}{\partial t} = A \mathbf{c} \mathbf{b}, \quad (1)$$

$$A = \frac{\Gamma}{4\pi} \ln \left(\frac{L}{\sigma} \right) \quad (2)$$

Here s is the length along the filament, t is the time, c is the curvature of filament, \mathbf{b} is a binormal unit vector, and A is proportional to the circulation Γ of filament and can be regarded to be a constant due to its slow variation compared with that of argument L/σ . This equation was derived based on the Biot-Savart law which describes the velocity field induced by the vortex, and L and σ are the upper and the lower limits of integration. The upper limit L is on the order of the radius of curvature and the lower limit σ is on the order of the radius of the vortex core. In this equation, the interaction between far distant portions along the filament is neglected.

For the helical wave with wavelength λ and amplitude a , the phase velocity U_p is obtained by using the localized induction equation as

$$U_p = \frac{A}{a^2 + (\lambda/2\pi)^2} = \frac{A}{a^2 + (1/k)^2}, \quad (3)$$

where k is a wave number. When the wavelength λ is much larger than the amplitude a , U_p may be described approximately as

$$U_p = Ak, \quad (4)$$

so that the dispersion relation of the helical wave on a vortex filament is

$$\Omega = Ak^2. \quad (5)$$

Here Ω is an angular frequency.

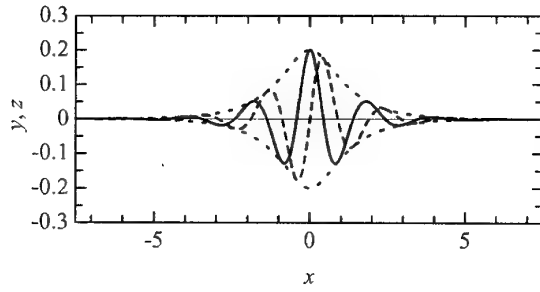


Fig. 1.1 A waveform of the soliton

The group velocity of wave is given by differencing the angular frequency with respect to the wave number. Then the group velocity U_g is

$$U_g = \frac{d\Omega}{dk} = 2Ak = 2U_p. \quad (6)$$

A solitary wave propagating stably along the filament (soliton) is derived by Hasimoto (1972). It has three-dimensional helical structure and is described following equations.

$$\begin{aligned} x &= s - \frac{2\nu}{\nu^2 + k^2} \tanh \nu s \\ y &= \frac{2\nu}{\nu^2 + k^2} \operatorname{sech} \nu s \cos ks \\ z &= \frac{2\nu}{\nu^2 + k^2} \operatorname{sech} \nu s \sin ks \end{aligned} \quad (7)$$

Here s is a variable, k is a wave number and ν is a parameter. An example of this waveform is shown in Fig. 1.1. For this figure, $k=3$ and $\nu=1$. A solid line and a broken line are the projection of x - y plane and x - z plane respectively and a dotted line is an envelope. This soliton propagates toward x -axis stably accompanied with rotational motion around x -axis.

2. EXPERIMENTAL APPARATUS AND METHOD

Our experimental apparatus is shown in Fig. 2.1. A vertical vortex filament is generated in a cylindrical tank with a small hole at the center of the bottom face. The filament is formed by the axial rotational flow, which is produced by water flow along the side face of tank. The filament is visualized by the air. To

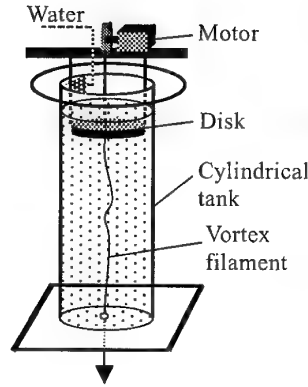


Fig. 2.1 Apparatus

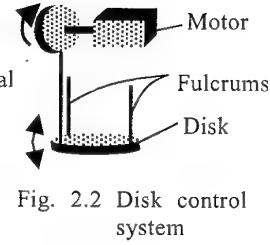


Fig. 2.2 Disk control system

control the motion of the filament, a solid disk is inserted horizontally from the top of the tank. When the disk is not horizontal (i.e., not perpendicular to rotational axis of water), the filament tends to become perpendicular to disk and to bend. As a result, perturbations associated with disk motion are brought on the filament. The disk control system is shown in Fig. 2.2. Two points hold disk as fulcrums and the third point is connected to the motor as shown in Fig. 2.2. When the motor rotates, an edge of the disk goes up and down and the disk flaps. Here, the motor is a stepping-motor that rotates in step at the same period as a pulse input from the outside, so its rotational speed can be controlled. Thus the motion of the disk can be controlled and perturbations with various frequencies can be given to the filament.

Height and inner diameter of the tank are 1[m] and 0.15[m] (or 0.3[m]), respectively, and the distance between the bottom of the tank and the disk is 0.8[m]. A diameter of the hole at the center of the bottom is 10[mm] (or 12[mm]). For the experiment of soliton, we used large size of tank diameter and bottom hole.

Rotational velocity of fluid is measured through visualization of the water flow added by fine particles (the 'diaion').

The motion of the filament is observed by the digital video camera.

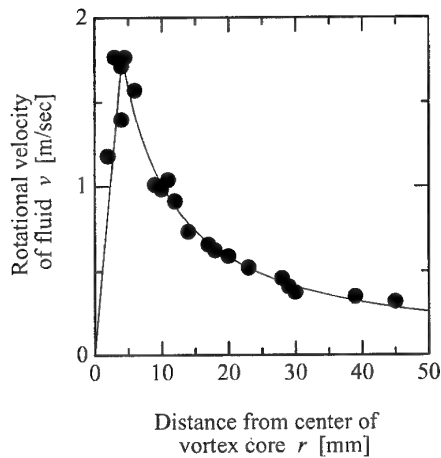


Fig. 3.1 Rotational velocity of fluid

3. EXPERIMENTAL RESULTS

3.1. Circulation of a Vortex Filament

The rotational velocity of fluid v [m/sec] is shown in Fig. 3.1 as a function of distance r [mm] from the center of vortex core. The velocity is obtained in the apparatus of small size. The diameter of air in the vortex core is about 3[mm]. Velocity profile is divided into two domains; the rigid rotation part in proportion to distance from the center and a part of potential flow in inversely proportional to that. From Fig. 3.1 rotational velocity becomes maximum 1.75[m/sec] at $r=4$ [mm]. Therefore, the diameter of the vortex core is estimated as 8[mm]. The circulation of the vortex filament is calculated from the rotational velocity around the core. The circulation Γ is found to be 0.04[m²/sec].

3.2. Control of a Filament

The motion of a filament with movement of a disk observed from two directions is shown in Fig. 3.2. The vorticity of a vortex filament in this figure is in the positive direction of Z-axis. We define X-axis as a line along two points to hold the disk as the fulcrums. Fig. 3.2 (a) is the view from negative position of Y-axis and Fig. 3.2 (b) is from positive position of X-axis. The front side of the disk is

lifted for (a) and the left side for (b). The perturbation appeared in a filament is shown for this figure for the period when one side of the disk is lifted and the disk comes back to a horizontal position again. The upper part of a filament touching at a disk moves left (negative direction of X-axis) for Fig. 3.2 (a), although it hardly moves for Fig. 3.2 (b). In other words, the upper part of a filament touching at a disk moves only in the negative direction of X-axis.

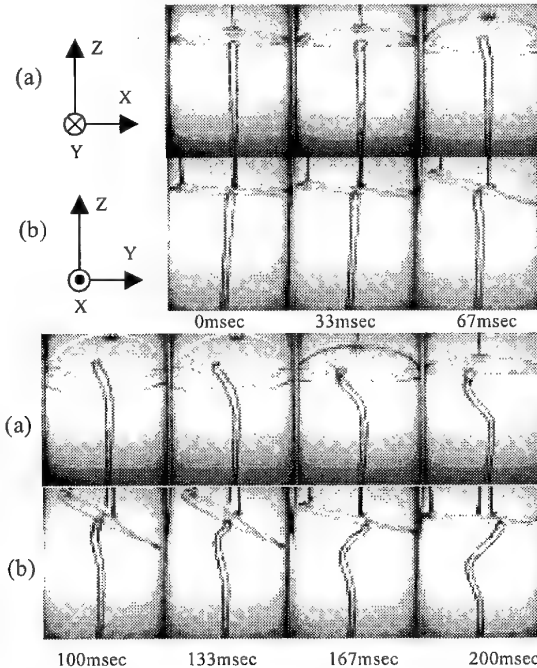


Fig. 3.2 Motion of vortex filament with disk

We consider the perturbation given to a filament. The fluid flow has only parallel component at the boundary surface, so that the filament tends to be perpendicular to the disk. Therefore, when a disk is not horizontal, the filament bends. Then, the upper part of a filament touching at a disk is moved by the velocity induced by a filament itself near that part. According to the Biot-Savart law, the direction of the velocity induced by the vortex is the same as the direction given by an outer product of a vorticity vector and a position vector. From this law, direction of velocity of fluid at the upper part of the filament is negative direction of X-axis as was

observed in Fig. 3.2. We note that the velocity induced by the mirror image against of a boundary surface is also in the same direction. From the above observation, the position of filament may be controlled and the perturbation with disk motion can be given to a filament by controlling the motion of the solid boundary surface.

3.3. The Dispersion Relation of Helical Wave on a Filament

The wave on a filament generated by sinusoidal continuous movement of a disk is shown in Fig. 3.3. The wave is characterized by three-dimensional helical structure and the direction of wave winding is counterclockwise (Fig. 3.4). It was observed that this continuous helical wave propagated stably. The waves with different wavelengths can be produced by changing frequency of disk movement, and the dispersion relation is obtained.

The phase velocity U_p , amplitude a (take $2a$ as shown in Fig. 3.3), wavelength λ (distance between tops) and angular frequency Ω of the wave are measured by photographic observation of waves. Measured values hardly vary from the upper to the lower part of the filament during propagation. In other words, it is observed that waves propagate stably. Angular frequencies obtained by the measurement are almost identical with those of the disk motion, confirming that perturbations with disk motion are given to a filament. From these measured values, the relation of phase velocity U_p and wave number $k(=2\pi/\lambda)$ is shown in Fig. 3.5. It is found that U_p is proportional to k as was expected by a theory (eq. (4)). Therefore, the dispersion relation is given by $\Omega = A'k^2$, where A' is determined as $7 \times 10^{-3} [\text{m}^2/\text{sec}]$ from Fig. 3.5.

It is assumed in the theory that the wavelength λ is much larger than the amplitude a to derive eq. (4) or eq. (5). For waves observed in this experiment eq. (5) may be applicable here, since a is about 3-6% of λ . In the theory, we note that the constant A is defined by eq. (2), where σ and L are the order of a vortex core



Fig.3.3 Wave on a vortex filament.

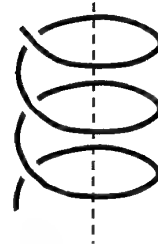


Fig.3.4 Direction of wave winding

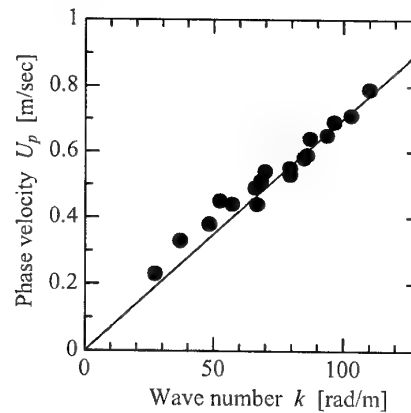


Fig. 3.5 Relation of phase velocity and wave number

radius and the radius of curvature. By setting $\sigma \approx 10^{-3} [\text{m}]$, $L \approx 10^{-2} [\text{m}]$ and $\Gamma = 0.04 [\text{m}^2/\text{sec}]$, we estimate a value of A as about $7.3 \times 10^{-3} [\text{m}^2/\text{sec}]$, which is almost equal to our measured value of A' .

3.4. The Group Velocity of Wave on a Filament

The propagation of a wave packet which is generated by flapping once of the disk is shown in Fig.3.6. This figure shows the behavior of the wave at the intervals of $2/15 [\text{sec}]$ and horizontal scale is expanded by two times compared to the vertical scale.

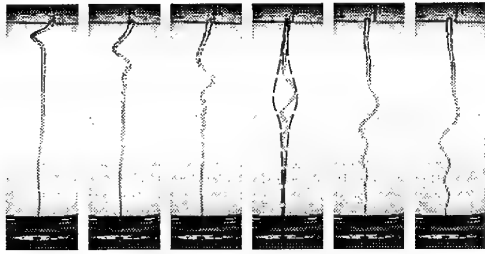


Fig. 3.6 Dispersive wave on a filament

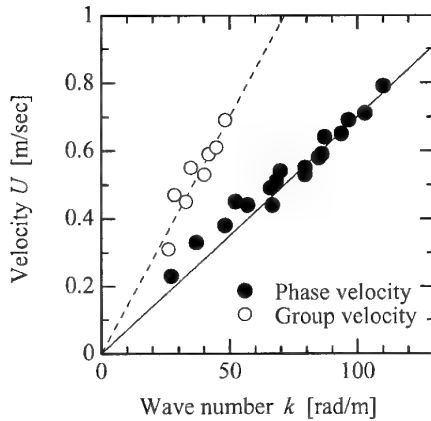


Fig. 3.7 Phase velocity and grope velocity as a function of wave number

For this filament, the perturbation is given by lifting the front side of disk and the direction of the vorticity is upward. The wave is three-dimensional helical structure and the direction of wave winding is counterclockwise (Fig. 3.4), which is same as the continuous wave. It is found that the wave disperses during propagation. The waves with short wavelength (large wave number) propagate faster than those with long wavelength. This agrees with the result of Fig. 3.5; the phase velocity is proportional to the wave number.

In this experiment, the propagation velocity of an envelope which is drawn in Fig. 3.6 is measured as a group velocity. The shape of an envelope gradually changes, so it is difficult to measure the wavelength exactly. The wavelength of a carrier wave is determined for the wave of the longest wavelength in an envelope. In this manner, the grope velocity U_g

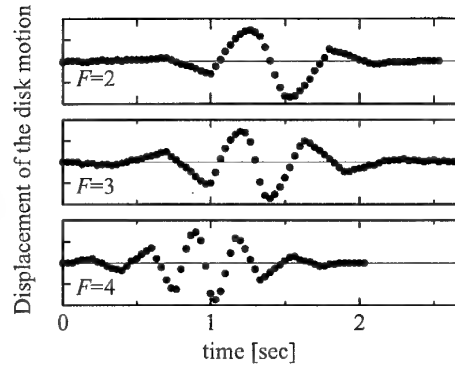


Fig. 3.8 Motion of disk as a function of a time

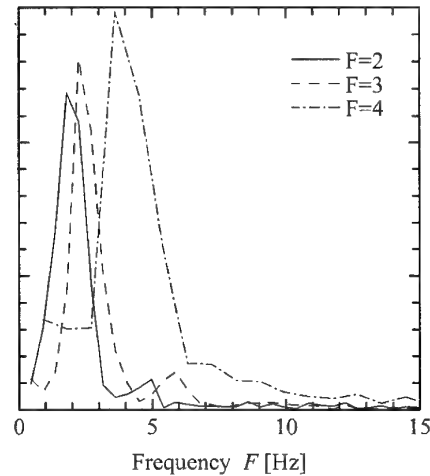


Fig. 3.9 Fourier transformation of motion of disk

and the wavelength $\lambda=2\pi/k$ are measured. The group velocity U_g is plotted for the wave number k and compared with the phase velocity in Fig. 3.7.

From the experiment for section 3.3, it is confirmed that the dispersion relation is given by $\Omega=A'k^2$. Then, the group velocity is described by eq. (6); i.e. the grope velocity is two times as large as the phase velocity. A slope of the broken line in the Fig.3.7 is $2A'$ and the observed group velocity agrees with the theory indicated for this line.

3.5. Experiment of the Solitary Wave

3.5.1. Perturbations given to filament

In this experiment, the motion of a disk is

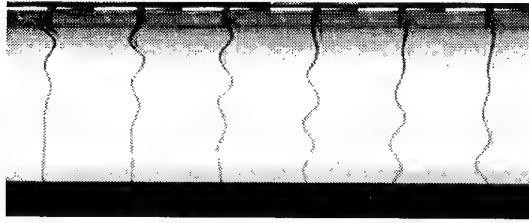
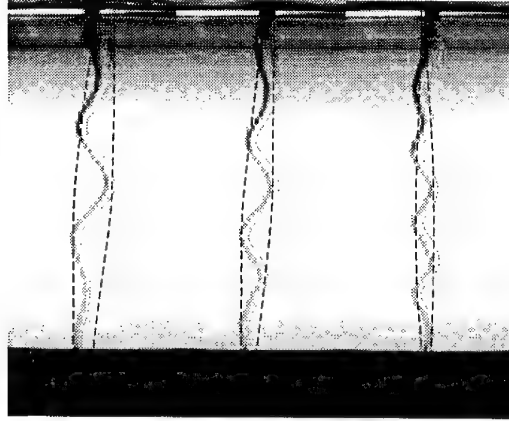


Fig. 3.10 Propagation of wave packet for $F=3$, $\theta_{\max}=10^\circ$



$F=2$ $F=3$ $F=4$

Fig. 3.11 Comparison of envelope for $\theta_{\max}=10^\circ$

determined by taking account of waveforms of soliton (like Fig. 1.1). Fig. 3.8 shows the motion of the disk. The vertical axes are displacements of disk edge which goes up and down by motor rotation. These motions are approximation of the waveforms of solitons. F is the rough frequency of the disk motion. From Fourier transformation of these motions (Fig. 3.9), it is found that their frequencies are roughly same as the values of F . For these three kinds of motion of the disk, two types of the displacement (maximum inclination of disk θ_{\max} is 10° or 5°) are employed. That is, six types of motions of the disk are employed in this experiment. These motions give perturbations to filament.

3.5.2. Comparison of produced waves and theoretical waveform

The propagation of a wave packet which is

induced by perturbation mentioned above is shown in Fig.3.10. This figure shows the behavior of wave at the intervals of 0.2[sec] and horizontal scale is expanded by three times compared to the vertical scale. For this figure, the type of the perturbation is for the case of $F=3$ and $\theta_{\max}=10^\circ$. It is noted that the total length of a wave packet is longer than the vertical scale of the apparatus.

We measured the wavelength $\lambda' (=2\pi/k')$ and maximum amplitude a' from Fig.3.10. The maximum amplitude is

$$a' = \frac{2v}{v^2 + k'^2} \quad (8)$$

from eq. (7). From this equation, the parameter v is determined by the measured values a' and k' . In this manner, the envelope over solitary wave is determined from theoretical equation. In Fig. 3.11, the observed envelope is compared with the theoretical shape. For the case of $F=2$, the envelope by broken line does not agree with the observed shape of the filament. On the other hand, for $F=3$ and $F=4$, the envelope agrees with the observation. The result is same for the case of $\theta_{\max}=5^\circ$. For $F=2$, the initial wave might not be appropriate. But for $F=3$ or $F=4$, it is concluded that a solitary wave is produced on a vortex filament in agreement with the theory.

4. CONCLUSION

We introduced a solid boundary surface to control a vortex filament. The motion of a vortex filament is successfully controlled by adding perturbations associated with the motion of the boundary surface.

It is confirmed experimentally that the dispersion relation of helical wave on a vortex filament is given by $\Omega = Ak^2$ as was predicted by the theory. And by direct measurement of the group velocity, it is verified that the group velocity is two times as large as the phase velocity.

We generated an envelope soliton on a vortex filament and confirmed that the envelope agrees with the theoretical prediction. It is, however, necessary

to verify the stability of a soliton. For this end, we have to generate a wave packet with small envelope width.

5. REFERENCES

- 1) Hashimoto, H. 1972 A soliton on a vortex filament. *J. Fluid Mech.* **51**, 477.
- 2) Batchelor, G. K. 1967 *An Introduction to Fluid Dynamics*, Cambridge University Press

A MOTION OF A TWO-DIMENSIONAL VORTEX SHEET AND A DOUBLY BRANCHED SPIRAL

Takashi Sakajo

Graduate school of mathematics, Nagoya University,
Furo-cho Chikusa-ku Nagoya Aichi 464-8602, Japan
/Email:sakajo@math.nagoya-u.ac.jp

ABSTRACT

A vortex sheet is a surface across which the velocity field of incompressible and inviscid flows has a jump discontinuity. Mathematical and numerical studies reveal that a two-dimensional vortex sheet, which is governed by the Birkhoff-Rott equation, acquires a singularity in finite time. On the other hand, a numerical computation of a regularized Birkhoff-Rott equation shows that the vortex sheet evolves into a rolling-up doubly branched spiral.

The purpose of this study is to investigate the meaning of the singularity and doubly branched spiral. An idea is to consider singular times in complex-time plane, at which solutions of the regularized Birkhoff-Rott equation lose their analyticity. We study a distribution of the complex singularity times and a limiting behavior by numerical means.

Furthermore, we propose a simple model of doubly branched spirals. Comparing the vortex sheet motion with the model, we show that the model is successful in approximating the rolling-up motion of the vortex sheet after some time. We also discuss if the doubly branched spiral is a solution of the Birkhoff-Rott equation beyond the singularity time or not.

1 INTRODUCTION

A vortex sheet is a surface across which the velocity field of incompressible and inviscid fluids has a jump discontinuity. Study of vortex sheets contributes to an understanding of turbulent shear layers, since they approximate a coherent structure of the ideal flows with high-Reynolds number. The motion of two-dimensional vortex sheets is governed by an integro-differential equation, called the Birkhoff-Rott equation[1]. While theoretical studies proved a short-time existence of

an analytic solution [2,3,4], asymptotic analyses[5,6] and numerical computations[7,8] showed strong evidences that 2-D vortex sheets lose analyticity in finite time.

Numerical computation of the equation is practically quite difficult, since not only solutions blow up in finite time but also a linearization of the equation leads an ill-posed problem in the sense of Hadamard due to Kelvin-Helmholtz instability[9]. A treatment to avoid these numerical difficulties is regularization of the equation[10,11]. Krasny regularized the Birkhoff-Rott equation by introducing an artificial parameter δ [11]. Namely, representing a vortex sheet in two-dimensional space by $(x(\Gamma, t), y(\Gamma, t))$, where Γ is a Lagrangian parameter along the sheet and t is time, he proposed the following regularized equations:

$$\begin{aligned}\frac{\partial x}{\partial t} &= -\frac{1}{2} \int_0^1 \frac{\sinh 2\pi(y-\tilde{y})}{\cosh 2\pi(y-\tilde{y}) - \cos 2\pi(x-\tilde{x}) + \delta^2} d\tilde{\Gamma} \quad (1) \\ \frac{\partial y}{\partial t} &= \frac{1}{2} \int_0^1 \frac{\sin 2\pi(x-\tilde{x})}{\cosh 2\pi(y-\tilde{y}) - \cos 2\pi(x-\tilde{x}) + \delta^2} d\tilde{\Gamma}, \quad (2)\end{aligned}$$

where $\tilde{x} = x(\tilde{\Gamma}, t)$ and $\tilde{y} = y(\tilde{\Gamma}, t)$. A periodic boundary condition is imposed on the vortex sheet: $x(\Gamma + 1, t) = x(\Gamma, t) + 1$ and $y(\Gamma + 1, t) = y(\Gamma, t)$. We call the equations the δ -equation. By computing the δ -equation for a initial condition numerically, Krasny found that the regularized vortex sheet is smooth for all the time and evolves into a rolling-up doubly branched spiral. Furthermore, investigating a limit shape of the spiral as $\delta \rightarrow 0$, he also discuss if the spiral could be a solution of the Birkhoff-Rott equation after the singularity time. His discussion motivates us greatly. However, there is a serious gap of analyticity property; While the solution of the δ -equation is smooth for all the time, that of the Birkhoff-Rott equation has been analytic only for a finite time.

In the present article, we give a clear explanation for the gap. Suppose that we regard the time variable as a complex number. Then, the

singularity time of the Birkhoff-Rott equation is referred as a point in the real-time axis. We investigate critical complex times when solutions of the δ -equation blows up by numerical means. We call these times complex singularity times. If all complex singularity times of the δ -equation are not in the real-time axis, solutions of the δ -equation is smooth for all the (real) time. Moreover, if one of the complex singularity times approaches the real singularity time of the Birkhoff-Rott equation when δ tends to zero, we can explain clearly why the solution of the Birkhoff-Rott equation blows up in finite time, although the solution of the δ -equation is smooth for all the time.

The article is organized as follows: In §2, we introduce a numerical method to search the complex singularity times. In §3, we show a distribution of complex singularity times of the δ -equation and investigate its behavior as δ goes to zero. In §4, we propose a simple model to describe a rolling-up double branched spiral. By comparing the model spiral with the regularized vortex sheet, we discuss a solution of the Birkhoff-Rott equation beyond the singularity time. Finally, we give conclusions and discussions in §5.

2 NUMERICAL METHOD

We explain a numerical method to find complex singularity times. The numerical method is originally developed by Sulem et al.[12] to detect critical times. Krasny[7] and Shelley[8] applied the method to the Birkhoff-Rott equation to investigate the singularity formation accurately. Here, we extend the method so that it can detect complex singularity times.

Assume that $x(\Gamma, t)$ and $y(\Gamma, t)$ to complex-valued functions, then we regard (1) and (2) as the equations for the four real-valued functions; $\Re x(\Gamma, t)$, $\Im x(\Gamma, t)$, $\Re y(\Gamma, t)$, $\Im y(\Gamma, t)$. Initial conditions of real parts are given by the one which Krasny [7,11] used. We set the imaginary parts to zero. Namely,

$$\begin{aligned} \Re x(\Gamma, 0) &= \Gamma + 0.01 \sin 2\pi\Gamma, & \Im x(\Gamma, 0) &= 0, \\ \Re y(\Gamma, 0) &= -0.01 \sin 2\pi\Gamma, & \Im y(\Gamma, 0) &= 0. \end{aligned} \quad (3)$$

These functions x and y are discretized by $N = 2048$ points. In order to compute the integrations of the right hand side of (1) and (2) numerically, we use a spectrally accurate method that Shelley [8] proposed.

Then, we give an integration path in complex-time plane, along which the equations (1) and (2) are integrated temporally by using forth-order Runge-Kutta method. Note

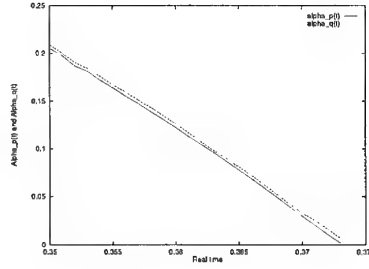


Figure 1: The fits to α_p as functions of the real time, when $\delta = 0$.

that it is unnecessary to mind how to choose the path, since the temporal integration is independent of choice of the path as long as solutions are analytic. In addition, every time step of the temporal integration, Krasny's Fourier filtering technique is implemented in order to avoid accumulation of the round-off error[7,8,13]. As for the detailed description of the filtering technique, refer to Krasny[7].

Next, we explain how to find complex singularity times. The functions $x(\Gamma, t)$ are represented by Fourier series every time step:

$$x(\Gamma, t) = \Gamma + \sum_{k=-\frac{N}{2}}^{\frac{N}{2}-1} p_k(t) e^{2\pi i k \Gamma},$$

We study behavior of the spectra $p_k(t)$; We use Ansatz for their asymptotic decay. Assume that

$$|p_k(t)| = C_p k^{-\beta_p} (1 + D_p \frac{1}{k}) \exp(-\alpha_p(t)k), \quad (4)$$

The Ansatz are the same as Shelley's, which are derived from Moore's asymptotic analysis of the vortex sheet. We compute the values of C_p , D_p , β_p and α_p by requiring that (4) holds pointwise at consecutive four points of p_i for $i = k, k+1, k+2$ and $k+3$. Note that, as is shown in Shelley[8], if the numerical computation is sufficiently accurate, these values are determined independently of k when the integration path approaches the singularity time. If α_p is getting closer to zero, we estimate a time when it vanishes by extrapolation. This is the critical time when $x(\Gamma, t)$ loses its analyticity, since the Fourier coefficient of $x(\Gamma, t)$ decays algebraically. As for the function y , we use the same procedure.

We give an examples showing that the method works well. We apply the method to the Birkhoff-Rott equation; The regularization parameter δ is zero and an integra-

tion path goes along the real-time axis. Figure 1 shows the fits to α_p as functions of the real time. The value of α_p monotonically decreases towards zero and estimated to be zero at $t \approx 0.374 + 0.00i$ by extrapolation. The critical time is equal to what Krasny estimated [7]. In the article, we specifically denote the critical time by t_c .

3 RESULTS

3.1 Complex singularity times when $\delta = 0.1$

Figure 2 shows a distribution of complex singularity times of the δ -equation in complex-time plane. We fixed the regularization parameter δ to be 0.1. We detect the complex singularity times by taking various integration paths. The complex singularity times are continuously on the boundaries between gray regions and a white region. They are symmetric with respect to the real-time axis. We can define no analytic solution inside the gray regions by the analytic continuation for any integration path starting from the origin. On the other hand, if we take an integration path along the real-time axis, an analytic solution is defined along the path by the analytic continuation, since there is no complex singularity times on the path. This is why Krasny's regularization works well to compute the δ -equation numerically.

Now, let us describe the distribution precisely; We can easily observe that there are narrow band-like white regions that exist periodically in the imaginary time direction. In Figure 3, we plot the distribution in the neighborhood of the real-time axis. The figure shows that the distribution is also periodic in the real-time direction beyond $\Re t \approx 0.85$. Since we observe the same periodic structure for another band regions, the complex singularity times are distributed doubly periodically in the region, $\Re t > 0.85$.

Now, we examine a relation between the distribution and evolution of the vortex sheet. Figure 4 shows an evolution of the vortex sheet when an integration path is taken along the real-time axis. When the path enters the band region (i.e. $\Re t > 0.75$), the vortex sheet begins rolling up in the middle. As for the other band regions, the vortex sheet is likewise rolling up when the integration path is in the band regions. Therefore, there is a close relation between the doubly periodic band structure of complex singularity times and the rolling-up motion of the vortex sheet.

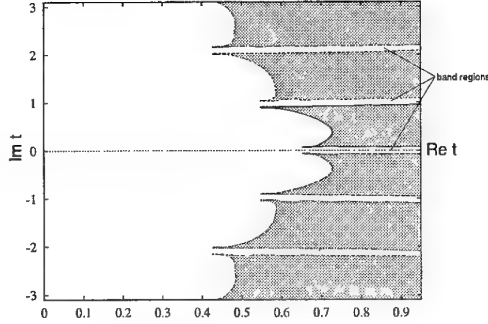


Figure 2: Distribution of the complex singularity times of the δ -equation when $\delta = 0.1$.

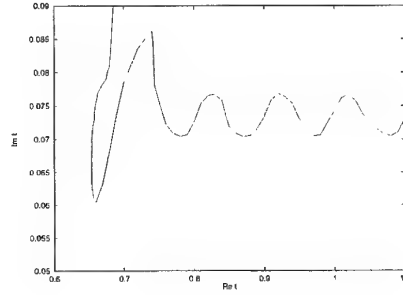


Figure 3: Distribution of the complex singularity times in the neighborhood of the real-time axis.

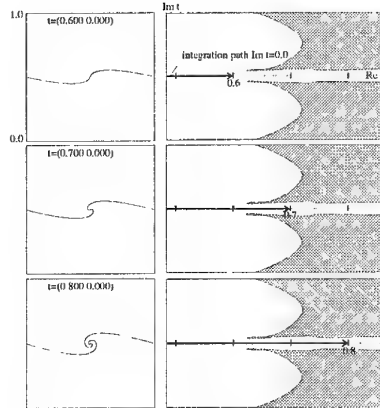


Figure 4: (Left) Numerical solution of the δ -equation when $\delta = 0.1$. (Right) Integration path, which is taken along the real-time axis.

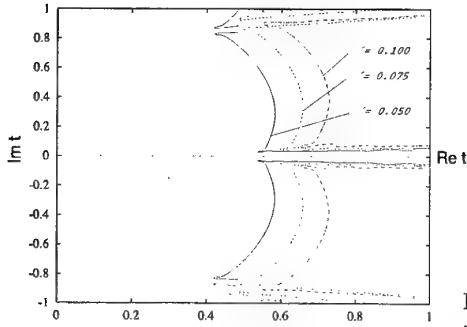


Figure 5: Distributions of complex singularity times in the neighborhood of the real-time axis for various δ .

3.2 Behavior of the distribution as $\delta \rightarrow 0$

We study how the distribution of the complex singularity times behaves when $\delta \rightarrow 0$. Figure 5 shows distributions in the neighborhood of the real-time axis for $\delta = 0.05, 0.075$ and 0.1 . While the distribution moves to the left, the width of the band regions is getting smaller as $\delta \rightarrow 0$.

In order to see how the band regions behave, we consider a complex singularity time which is the nearest to the real-time axis. In fact, there are two such times at the tips of the distribution because of symmetry of the distribution. We plot the two nearest times in Figure 6 when δ is changing from 0.0 to 0.45 . The pair of the nearest complex singularity times approach each other as δ tends zero and then collide at the singularity time t_c on the real-time axis. It means that the entrance of the band region is blocked at t_c . Hence, it is impossible to define an analytic solution of the Birkhoff-Rott equation beyond t_c by the analytic continuation along the real-time axis. This is why the solution of the Birkhoff-Rott equation blows up in finite time, although the solution of the δ -equation is smooth for all the time. Note that when we check the another band regions, the width of the band regions is getting smaller when δ tends to zero likewise when δ is exactly zero.

4 MODEL OF A ROLLING-UP SPIRAL

We propose a simple model of a rolling-up double branched spiral in order to explain the numerical results in the previous section: For a

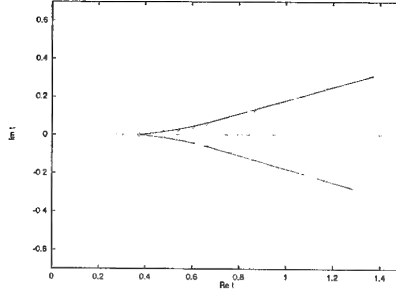


Figure 6: Positions of the pair of the complex singularity times which are the nearest to the real-time axis for $\delta = 0.00$ thorough 0.45 from the left.

given curve with the same periodic boundary condition, we assume that a point vortex is located in the middle of the curve and passive scalars are distributed uniformly in the curve except the center.

4.1 Equation and its solution

We investigate a regularized equation of the passive scalars advected by the point vortex. We assume that the point vortex is located at the origin and the passive scalars are distributed in the segment $[-0.5, 0.5]$ at the beginning. That is,

$$\begin{cases} x(\Gamma, 0) = -0.5 + \Gamma, \\ y(\Gamma, 0) = 0, \quad (0 \leq \Gamma < 1, \Gamma \neq 0.5). \end{cases}$$

Then, while the point vortex is steady for all the time, the regularized equation of the passive scalars at $(x(\Gamma, t), y(\Gamma, t))$ are described by

$$\begin{cases} \frac{dx}{dt} = -\frac{1}{2} \frac{\sinh 2\pi y}{\cosh 2\pi y - \cos 2\pi x + \delta^2}, \\ \frac{dy}{dt} = \frac{1}{2} \frac{\sin 2\pi x}{\cosh 2\pi y - \cos 2\pi x + \delta^2}, \end{cases} \quad (5)$$

whose initial conditions are given by (). We compare evolutions of the passive scalars and the vortex sheet. Figure 7 shows a numerical solution of the vortex sheet from $t = 1.2$ when $\delta = 0.3$ and that of the passive scalars from $t = 0.4$ when $\delta = 0.6$. Although the starting times of these evolutions are different, the time interval between each figures are the same and the winding number of the spirals looks similar.

The model equation is solved explicitly. The denominator of the right hand side of the equations (5) is invariant in time because $\frac{dK_\delta}{dt} = 0$. Hence, we define K_δ by

$$K_\delta(\Gamma, 0) = 2(1 + \cos 2\pi\Gamma + \delta^2) \equiv K_\delta(\Gamma).$$

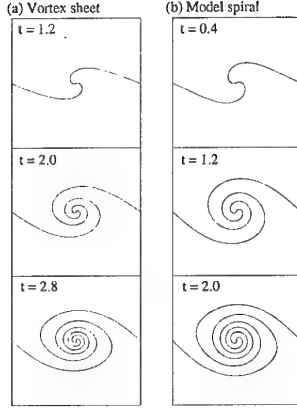


Figure 7: (a) Numerical solution of the δ -equation for $\delta = 0.3$. (b) Numerical solution of the model equation for $\delta = 0.6$.

Introducing a new time variable $\tau = \frac{t}{K_s(\Gamma)}$ and space variables $X = \sin 2\pi x$, $Y = \cos 2\pi x$, $P = \sinh 2\pi y$ and $Q = \cosh 2\pi y$, we rewrite the equation (5) as follows:

$$\frac{dY}{d\tau} = XP, \quad \frac{dQ}{d\tau} = XP. \quad (6)$$

Initial conditions of the variables are $X(\Gamma, 0) = -\sin 2\pi\Gamma$, $Y(\Gamma, 0) = -\cos 2\pi\Gamma$, $P(\Gamma, 0) = 0.0$ and $Q(\Gamma, 0) = 1.0$, respectively. It follows from (6) that $Y - Q$ is independent of τ . Accordingly, we also define an another invariant, $A(\Gamma)$, by

$$Y(\Gamma, 0) - Q(\Gamma, 0) = -(1 + \cos 2\pi\Gamma) \equiv A(\Gamma).$$

We obtain $Y(\Gamma, \tau) = Q(\Gamma, \tau) + A(\Gamma)$. We also have relations between the space variables; $X^2 + Y^2 = 1$ and $Q^2 - P^2 = 1$. Substituting them into the equation (6), we obtain the equation only for Q :

$$\left(\frac{dQ}{d\tau}\right)^2 = -(1 - (Q + A)^2)(1 - Q^2). \quad (7)$$

The solution of the equation is given by

$$Q(A, t) = 1 - \frac{6A(A+2)}{12\wp\left(\frac{t}{2(\delta^2-A)}\right) + A^2 + 6A + 4},$$

where the function $\wp(\tau)$ is Weierstrass's elliptic function.

The explicit representation of the solution Q makes it possible to consider complex singularity times of Q , which satisfy the following equation;

$$12\wp\left(\frac{t}{2(\delta^2-A)}\right) + (A^2 + 6A + 4) = 0. \quad (8)$$

According to the properties of \wp function, for given fixed $\delta \neq 0$ and $A \neq 0$, there are two solutions in a fundamental period-parallelogram of \wp function, which are symmetric with respect to the pole. Furthermore, they are distributed doubly periodically in whole complex-time plane. Hence, when solving the equation (8) for all A , we obtain doubly periodic band-like sequences of the complex singularity times of Q . This explains qualitatively the numerical results in §3 that the evolution of the rolling-up vortex sheet is closely related to the doubly periodic band structure of the complex singularity times in both the real-time and the imaginary-time directions.

4.2 Behavior of the complex singularity times as $\delta \rightarrow 0$

We are interested in a singular behavior such as collision between the complex singularity times of the model as $\delta \rightarrow 0$. When $A \neq 0$ and $\delta = 0$, the complex singularity times that satisfy (8) never collide. Hence, no singular behavior is observed in this case. Now, we consider behavior of the complex singularity times when $A = 0$. However, the function Q is undefined at $A = 0$. So, we define the function $Q(0, t)$ as the limit value of $Q(A, t)$ when $A \rightarrow 0$ for $\delta \neq 0$ keeping $\delta \neq 0$, and then observe how the complex singularity times behave as $\delta \rightarrow 0$. It is easy to show both $Q(0, t)$ and the first derivative of Q are always zero. However, the second derivative is expressed as follows.

$$\frac{d^2 Q}{d\Gamma^2}(0, t) = \frac{12\pi^2}{3\wp\left(\frac{t}{2\delta^2}\right) + 1}. \quad (9)$$

Hence, it is the second derivative of Q that can show singular behavior when $\delta \rightarrow 0$. First, we consider an equation for complex τ ;

$$\wp(\tau) = -\frac{1}{3}.$$

There are two symmetric solutions in a fundamental period-parallelogram, which are distributed doubly periodically in complex τ -plane. Then mapping these complex singularity times into complex t -plane by the scaling relation between t and τ , i.e. $\tau = \frac{t}{2\delta^2}$, we find that the complex singularity times as well as the period-parallelogram contracts to the origin in complex t -plane when δ tends to zero. Hence, when δ is exactly zero, all the complex singularity times concentrate into the origin, which is a quite singular behavior.

We verify the quadratic contracting behavior is observed in the vortex sheet motion. Figure 8 shows the second derivative of the

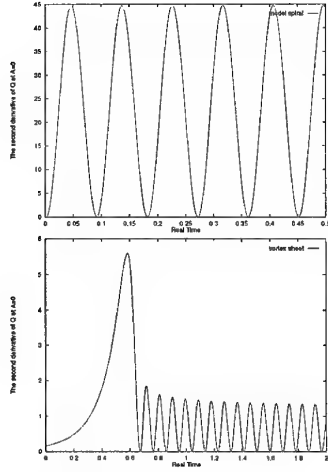


Figure 8: The second derivative of Q with respect to Γ at the center. (Upper):the model spiral ($\delta = 0.3$). (Lower):the vortex sheet ($\delta = 0.1$).

model ($\delta = 0.3$) and of the vortex sheet ($\delta = 0.1$). While the second derivative of the model changes just periodically, that of the vortex sheet begins oscillating at $t \approx 0.7$ after which the vortex sheet rolls up. These figures indicate again that the model approximates the vortex sheet after it rolls up. Here, we pay attention to the wavelength of the second derivative. This is because that the wavelength corresponds to one of the periods of the doubly periodic function (9). Figure 9 shows the periods of the second derivative of the model (\times marks) and of the vortex sheet ($+$ marks) for δ . Dotted lines in the figure are computed by the least square fit. It indicates that both of the periods decrease like quadratic function.

4.3 On a solution of the Birkhoff-Rott equation beyond the singularity time

The period of the second derivative of Q when $\delta = 0$ implies how a solution of the Birkhoff-Rott equation looks like beyond the singularity time: The second derivative of Q at $A = 0$ is equivalent to square of the first derivative of y at the center of the spiral, namely

$$\frac{d^2 Q}{d\Gamma^2}(0, t) = \left(2\pi \frac{dy}{d\Gamma}(0, t) \right)^2.$$

Therefore, the periodic behavior of the second derivative indicates that the y -component of the tangent vector to the doubly branched spiral at the center changes periodically, which

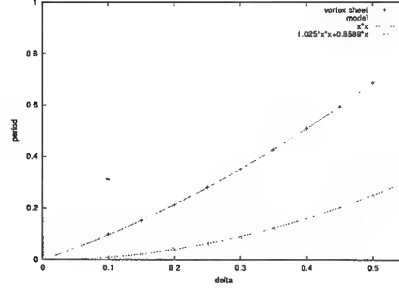


Figure 9: Periods of the second derivative of Q vs. δ . The $+$ marks represent the periods for the vortex sheet. The \times marks show the periods for the model.

represents the rotation of the spiral. Furthermore, the period corresponds to how fast the doubly branched spiral rotates. That means, the smaller the period becomes, the faster the spiral rotates. According to Figure 9, since both periods become zero when $\delta = 0$, the spiral rotates with infinite windings at the center.

5 CONCLUSIONS AND DISCUSSIONS

We investigated numerically complex singularity times when a solution of the δ -equation loses its analyticity. We indicate the complex singularity times are distributed doubly periodically in the imaginary-time and the real-time directions while the vortex sheet is rolling-up. Since the real-time axis is put between the structure, we define an analytic solution of the δ -equation by the analytic continuation. This is why numerical solutions of the δ -equation is smooth for all the time. We also pointed out relation between the doubly periodic band-like structure of the complex singularity times and the rolling-up motion of the vortex sheet.

Then, we studied behavior of the distribution as δ approaches zero and found that the entrance of the band region is closed at $t = t_c$. Therefore, we can define no analytic solution of the Birkhoff-Rott equation beyond t_c into the band region by the analytic continuation along the real-time axis. This is the reason why the solution of the Birkhoff-Rott equation blows up in finite time, while the solution of the δ -equation is smooth for all the time.

We proposed a simple model that describes a rolling-up doubly branched spiral. The model approximates the motion of the regularized vortex sheet qualitatively well after it begins rolling up. It explains the relation be-

tween the doubly periodic band structure of complex singularity times and the rolling-up doubly branched spiral. The comparison of the limiting behavior of the complex singularity times of the vortex sheet and that of the model when $\delta \rightarrow 0$ conjecture that the solution of the regularized Birkhoff-Rott equation tends to the doubly branched spiral with infinite windings.

REFERENCES

- [1] Birkhoff, G. (1962) "Helmholtz and Taylor instability", Symp. Appl. Math. XII, AMS, p.55-76.
- [2] Cafisch, R.E. & Orellana, O.F. (1986). "Long time existence for a slightly perturbed vortex sheet", Comm. Pure Appl. Math., Vol. 39, p.807-838.
- [3] Cafisch, R.E. & Orellana, O.F. (1989). "Singular solutions and ill-posedness for the evolution of vortex sheets", SIAM J. Math. Anal., Vol.20, p.293-307.
- [4] Sulem, C., Sulem, P.L., Bardos, C. & Frisch, U. (1981). "Finite time analyticity for the two and three dimensional Kelvin-Helmholtz instability", Comm. Math. Phys., Vol.80, p.485-516.
- [5] Moore, D.W. (1979). "The spontaneous appearance of a singularity in the shape of an evolving vortex sheet", Proc. R. Soc. Lond., Vol.365, p.105-119.
- [6] Mairon, D.I., Baker, G.R. & Orszag, S.A. (1982). "Analytic structure of vortex sheets dynamics. Part I. Kelvin-Helmholtz instability", J. Fluid Mech., Vol. 113, p.283-298.
- [7] Krasny, R. (1986). "A study of singularity formation in a vortex sheet by the point-vortex approximation", J. Fluid Mech., Vol.167, p.65-93.
- [8] Shelley, M.J. (1992). "A study of singularity formation in vortex-sheet motion by a spectrally accurate vortex method", J. Fluid Mech., Vol.244, p.493-526.
- [9] Saffman, P.G. (1992). Vortex Dynamics, Cambridge:Cambridge Univ. Press.
- [10] Baker, B.R. & Shelley, M.J. (1986) "Boundary integral techniques for multi-connected domains", J. Comput. Phys., Vol. 64, p.112-132.
- [11] Krasny, R. (1986) "Desingularization of periodic vortex sheet roll-up", J. Comput. Phys. Vol.65, p.292-313.
- [12] Sulem, C., Sulem, P.L. & Frisch, H. (1983). "Tracing complex singularities with spectral methods", J. Comput. Phys., Vol.50, p.138-161.
- [13] Ely, J.S. & Baker, G.R. (1993). "High-precision calculations of vortex sheet motion", J. Comput. Phys., Vol.111, p.275-281.

A NEW APPROACH TO THE VORTEX METHOD FOR DETERMINATION OF VORTICITY SHEDDING FROM SOLID BOUNDARY

Hong WANG and Hiroshi TSUKAMOTO

Department of Mechanical Engineering, Kyushu Institute of Technology
1-1 Sensui-cho, Tobata, Kitakyushu, 804-8550 Japan /E-mail: oo9902hw@tobata.isc.kyutech.ac.jp

ABSTRACT

A new approach for determination of vorticity shedding from the solid boundary was proposed in the present vortex method based on the Navier-Stokes equations. A two-dimensional unsteady flow was calculated within a diffuser pump to investigate the pressure fluctuations due to the interaction between the impeller and diffuser vanes by using the present vortex method. And a new scheme was also proposed to improve the unsteady pressure evaluation by the boundary integration method in the rotor-stator interaction problem. Moreover, Petrov-Galerkin Method was applied to yield the solutions that satisfy the boundary conditions in an integral sense, and it improved the stability and accuracy of the numerical solutions greatly. The calculated unsteady pressure fluctuations in vaned diffuser passage showed a good agreement with the experimental data and the CFD calculated ones.

1 INTRODUCTION

Shedding of the vorticity from the solid surface is one of the most important procedures in the vortex methods. It includes creation of vorticity, specification of the strength and position of the nascent vortices, and determination of the separated points. The flow separation and shedding of vorticity from the solid surface are so complicated that they are difficult to resolve essentially [1,2]. Chorin [3] proposed the vortex sheet method in random vortex method computations. Kamemoto [4] summarized the algorithms used in the deterministic vortex methods for determination of the position and rate of shedding vorticity, and classified

them into three levels. However, in the various algorithms in the existing vortex methods, the effect of the pressure gradient along the solid surface was neglected in determining the rate of the vorticity shedding from the solid boundary.

In the present study, firstly, a new approach that vortices shed from a rotating 3D solid boundary was derived theoretically based on the Navier-Stokes equations, in which the effect of the pressure gradient along the solid boundary was considered. Then, the new approach was applied to simulate the 2D unsteady flow within a whole stage of diffuser pump to investigate pressure fluctuations due to the interaction between the impeller and diffuser vanes. Finally, The calculated time-varying flow rate, total hydraulic head rise and pressure fluctuations in the diffuser passage, were compared with the measured and calculated ones by other methods.

2 NOMENCLATURE

B :	Bernoulli function $= p/\rho + V^2/2$
b :	passage width
c :	symbol of pressure traverse line
D_2 :	impeller diameter
$\Delta\psi$:	nondimensional unsteady pressure $= \Psi - \bar{\Psi}$
f :	frequency
G :	Green function
H :	total hydraulic head rise across pump
H_0 :	rated total head rise
\vec{k} :	unit vector for z direction in Cartesian system (x, y, z)
l_{eq} :	equivalent pipe length

\vec{l}, \vec{n} :	unit vector for longitudinal and normal directions on boundary L
L:	boundary of concerned domain
N:	rotational speed
Nt:	number of impeller revolutions after its start $= \int_0^t N(t) dt$
PS:	pressure side
p:	static pressure
Q:	flow rate
Q ₀ :	rated flow rate
$\vec{r}, \vec{\theta}$:	cylindrical coordinates
R_e :	Reynolds number $= D_2 V_0 / \nu$
S:	entire region of concerned domain
SS:	suction side
T ₀ :	time required for one revolution of impeller
T _i :	time required for one pitch of impeller blade
T _{na} :	nominal acceleration time
t:	time
t [*] :	nondimensional time $= t / T_i$
\vec{U} :	peripheral velocity
U ₂ :	peripheral speed of impeller
V ₀ :	meridian velocity at suction port
\vec{V} :	absolute velocity
$\vec{V}_L(\vec{r})$:	velocity induced by absolute motion of boundary L
$\vec{V}_S(\vec{r})$:	velocity induced by all vortex elements in the entire region of interest
\vec{W} :	relative velocity
Z:	number of blades
Γ :	circulation (anti-clockwise is positive)
$\vec{\Gamma}$:	sum of vorticity in a 3D domain $\vec{\Gamma} = \int_{\Pi} \vec{\omega} d\Pi = \Gamma_x \vec{i} + \Gamma_y \vec{j} + \Gamma_z \vec{k}$
$\vec{\gamma}$:	vorticity in thin layer of fluid adjoining solid boundary L
κ :	resistance coefficient of pumping system
Π :	a given 3D domain
ρ :	density
σ :	source
ν :	kinematic viscosity
Ω :	angular velocity
$\vec{\omega}$:	vorticity $\vec{\omega} = \nabla \times \vec{V} = \omega_x \vec{i} + \omega_y \vec{j} + \omega_z \vec{k}$
ψ :	pressure coefficient $= (p - \rho g H_s) / (\rho U_2^2 / 2)$
$\bar{\Psi}$:	steady value of Ψ

Subscripts

d:	diffuser
i:	impeller
1, 2:	impeller inlet and outlet
3, 4:	diffuser inlet and outlet
∞ :	infinite

3. FORMULATION AND NUMERICAL SCHEMES

3.1 Shedding of Vorticity from the Rotating Solid Boundary Surface

The basic governing equations of continuum and momentum for a 3-D incompressible flow in a relative coordinates rotating with Ω are well known as follows:

$$\nabla \cdot \vec{W} = 0 \quad (1)$$

$$\begin{aligned} \frac{\partial_R \vec{W}}{\partial t} + \frac{\partial \vec{\Omega}}{\partial t} \times \vec{r} + (\vec{W} \cdot \nabla) \vec{W} \\ = -2\vec{\Omega} \times \vec{W} - \vec{\Omega} \times (\vec{\Omega} \times \vec{r}) - \frac{\nabla p}{\rho} + \nu \nabla^2 \vec{V} \end{aligned} \quad (2)$$

The vorticity transport equations can be then derived from the above governing equations,

$$\nabla \cdot \vec{\omega} = 0 \quad (3)$$

$$\begin{aligned} \frac{\partial \vec{\omega}}{\partial t} + (\vec{U} \cdot \nabla) \vec{\omega} + (\vec{W} \cdot \nabla) \vec{\omega} \\ = (\vec{\omega} \cdot \nabla) \vec{V} + \nu \nabla^2 \vec{\omega} \end{aligned} \quad (4)$$

Consider the change of the sum of the vorticity in a given 3D domain Π rotating with Ω (see Fig. 1)

$$\begin{aligned} \frac{d_R \vec{\Gamma}}{dt} &= \int_{\Pi} \frac{d_R \vec{\omega}}{dt} d\Pi \\ &= \int_{\Pi} \left\{ \frac{\partial \vec{\omega}}{\partial t} + (\vec{U} \cdot \nabla) \vec{\omega} \right\} d\Pi \\ &= \int_{\Pi} \{ (\vec{\omega} \cdot \nabla) \vec{V} - (\vec{W} \cdot \nabla) \vec{\omega} + \nu \nabla^2 \vec{\omega} \} d\Pi \end{aligned} \quad (5)$$

The volume integral terms in the right hand of the Eq. (5) can be expressed by a surface integral as follow:

$$\begin{aligned} \frac{d_R \vec{\Gamma}}{dt} &= \nu \oint_S \left(\frac{\partial \omega_l}{\partial n} \vec{l} + \frac{\partial \omega_m}{\partial n} \vec{m} + \frac{\partial \omega_n}{\partial n} \vec{n} \right) dS \\ &+ \oint_S \{ (\omega_n U_l) \vec{l} + (\omega_n U_m) \vec{m} + (\omega_n U_n) \vec{n} \} dS \\ &+ \oint_S \{ (\omega_n W_l - W_n \omega_l) \vec{l} + (\omega_n W_m - W_n \omega_m) \vec{m} \} dS \end{aligned} \quad (6)$$

On the other hand, the Navier-Stokes equations can be re-written as describing the evolution of the velocity,

vorticity and Bernoulli function,

$$\bar{W} \times \bar{\omega} - \bar{V} \times \bar{\omega} = \frac{\partial \bar{W}}{\partial t} + \nabla B' + \frac{\partial \bar{\Omega}}{\partial t} \times \bar{r} \quad (7)$$

Then, the momentum equations in \bar{l} and \bar{m} directions can be expressed as follows:

$$\begin{aligned} \bar{l}: & \left(\frac{\partial B'}{\partial l} + \frac{\partial W_l}{\partial t} \right) + \left(\frac{\partial \bar{\Omega}}{\partial t} \times \bar{r} \right) \cdot \bar{l} \\ & = (W_m \omega_n - W_n \omega_m) - \nu \left(\frac{\partial \omega_n}{\partial m} - \frac{\partial \omega_m}{\partial n} \right) \end{aligned} \quad (8a)$$

$$\begin{aligned} \bar{m}: & \left(\frac{\partial B'}{\partial m} + \frac{\partial W_m}{\partial t} \right) + \left(\frac{\partial \bar{\Omega}}{\partial t} \times \bar{r} \right) \cdot \bar{m} \\ & = (W_n \omega_l - W_l \omega_n) - \nu \left(\frac{\partial \omega_l}{\partial n} - \frac{\partial \omega_n}{\partial l} \right) \end{aligned} \quad (8b)$$

where $B' = B - \bar{U} \cdot \bar{V}$.

By applying the above Eq. (8), the integration of Eq.(6), the change of the vorticity sum in the domain Π rotating with any speed Ω , can be obtained:

$$\bar{\Gamma}(t_{j+1}) - \bar{\Gamma}(t_j) = \int_{t_j}^{t_{j+1}} \frac{d_R \bar{\Gamma}}{dt} dt = \sum_{i=1}^{i=M} \Delta \bar{\Gamma}_i \quad (9)$$

If the panel boundary CDHG in domain ABCDEFGH (see Fig.1) is supposed to be a part of the boundary S (see Fig.2), the vorticity change $\Delta \bar{\Gamma}_i$ due to the vorticity diffusion and convection at a given period can be expressed on the panel boundary CDHG of the rotating domain Π as,

$$\begin{aligned} \Delta \bar{\Gamma}_i &= \nu \int_{t_j}^{t_{j+1}} \int_{\Delta S_i} \left(\frac{\partial \omega_n}{\partial l} \bar{l} + \frac{\partial \omega_n}{\partial m} \bar{m} + \frac{\partial \omega_n}{\partial n} \bar{n} \right) dS dt \\ &+ \int_{t_j}^{t_{j+1}} \int_{\Delta S_i} \{ (\omega_n U_l) \bar{l} + (\omega_n U_m) \bar{m} + (\omega_n U_n) \bar{n} \} dS dt \\ &+ \int_{t_j}^{t_{j+1}} \int_{\Delta S_i} \left[- \left\{ \left(\frac{\partial B'}{\partial m} + \frac{\partial W_m}{\partial t} \right) + \left(\frac{\partial \bar{\Omega}}{\partial t} \times \bar{r} \right) \cdot \bar{m} \right\} \bar{l} \right] dS dt \\ &+ \int_{t_j}^{t_{j+1}} \int_{\Delta S_i} \left[\left\{ \left(\frac{\partial B'}{\partial l} + \frac{\partial W_l}{\partial t} \right) + \left(\frac{\partial \bar{\Omega}}{\partial t} \times \bar{r} \right) \cdot \bar{l} \right\} \bar{m} \right] dS dt \end{aligned} \quad (10)$$

where $\omega_n = \bar{\omega} \cdot \bar{n} = 2\bar{\Omega} \cdot \bar{n}$.

In a 2D flow, it can be simplified as

$$\begin{aligned} \Delta \Gamma_i &= \\ & \int_{t_j}^{t_{j+1}} \int_{L_i} \left[\left\{ \left(\frac{\partial B'}{\partial l} + \frac{\partial W_l}{\partial t} \right) + \left(\frac{\partial \bar{\Omega}}{\partial t} \times \bar{r} \right) \cdot \bar{l} \right\} \bar{m} \right] dL dt \end{aligned} \quad (11)$$

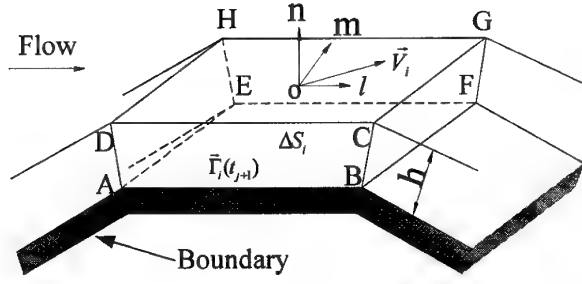


Fig. 1 Vortex panel in the 3D boundary layer

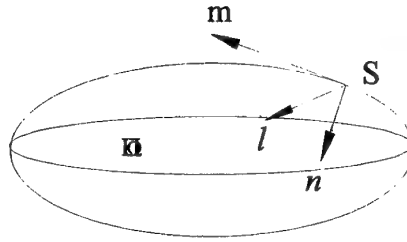
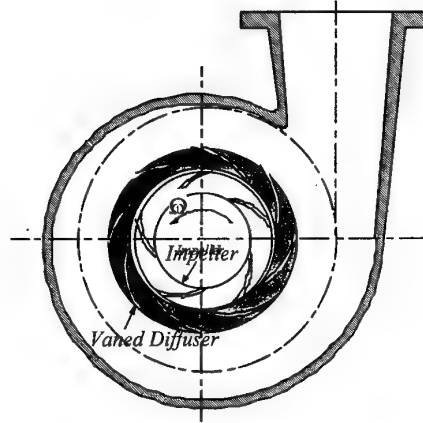
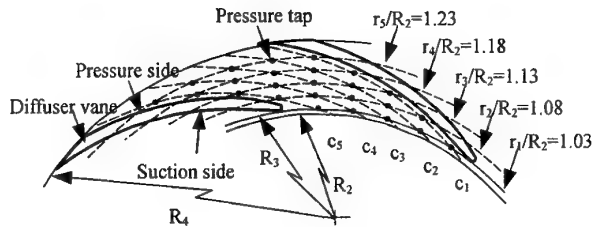


Fig. 2 Flow field Π (rotating with Ω)



(a) Test pump



(b) Pressure measurement stations in the diffuser passage

Fig. 3 Schematics of test diffuser pump

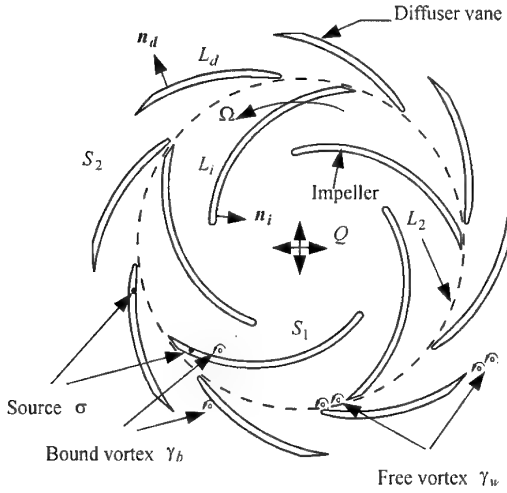


Fig. 4 Mathematical model for calculation

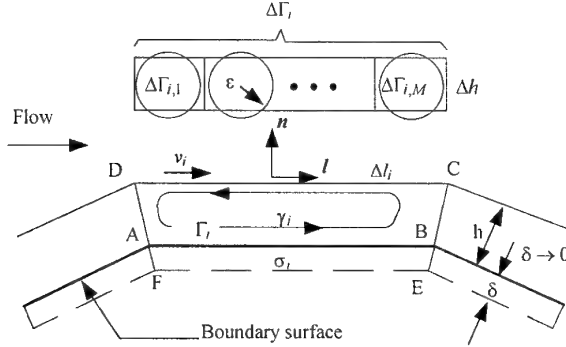


Fig. 5 Panel around solid boundary and nascent vortex elements

3.2 Shedding of Vorticity from the Stationary Solid Boundary Surface

When $\Omega = 0$ in Eq. (10), the sum of the vorticity shed from the stationary solid boundary layer can be obtained as follows:

$$\Delta\bar{\Gamma}_i = \int_{t_j}^{t_{j+1}} \int_{\Delta S_i} \left\{ -\left(\frac{\partial B}{\partial m} + \frac{\partial V_m}{\partial t}\right)\bar{l} + \left(\frac{\partial B}{\partial l} + \frac{\partial V_l}{\partial t}\right)\bar{m} \right\} dS dt \quad (12)$$

in a 2D flow, it can be simplified as [5,6],

$$\Delta\bar{\Gamma}_i = \int_{t_j}^{t_{j+1}} \int_{L_i} \left[l \left\{ \left(\frac{\partial B}{\partial l} + \frac{\partial V_l}{\partial t}\right) \right\} \right] dL dt \quad (13)$$

3.3 Flow Model

The unsteady flow in a test diffuser pump shown in Fig.3 was investigated by calculating a 2D flow field

around the impeller and diffuser vanes (see Fig.4). The 2D Unsteady viscous flow analysis was developed by using a vortex method, in which the continuous vorticity field is represented by the bound vortex elements $\bar{\gamma}_b$ adjoining the solid boundary, and the free vortices $\bar{\gamma}_w$ emanating from the trailing edges and the boundary layer. To satisfy the no flux and no-slip boundary conditions simultaneously in the present calculation, source panels σ are distributed just under the boundary surface. After the vorticity and velocity field were determined, the unsteady pressure was calculated by applying the Boundary Element Method.

3.4 Unsteady Velocity

As an extension of the well-known Biot-Savart Law [7] to a 2D unsteady viscous flow, the velocity $\vec{V}(\vec{r})$ in a domain S bounded by the boundary L can be written as the sum of velocity $\vec{V}_S(\vec{r})$ induced by all vortex elements in the domain S , and $\vec{V}_L(\vec{r})$ induced by the absolute motion of the boundary L , that is,

$$\vec{V}(\vec{r}) = \vec{V}_S(\vec{r}) + \vec{V}_L(\vec{r}) \quad (14)$$

where

$$\vec{V}_S(\vec{r}) = -\frac{1}{2\pi} \int_S \frac{\bar{\omega}_0 \times (\vec{r}_0 - \vec{r})}{|\vec{r}_0 - \vec{r}|^2} dS_0$$

and

$$\vec{V}_L(\vec{r}) = -\frac{1}{2\pi} \left[\int_L \frac{(\vec{V}_0 \cdot \bar{n}_0)(\vec{r}_0 - \vec{r})}{|\vec{r}_0 - \vec{r}|^2} dL_0 - \int_L \frac{(\vec{V}_0 \times \bar{n}_0) \times (\vec{r}_0 - \vec{r})}{|\vec{r}_0 - \vec{r}|^2} dL_0 \right]$$

where \vec{r}_0 is the position of the vortex elements or the boundary elements, and \vec{r} is the one where the velocity is being evaluated.

3.5 Satisfaction of the boundary conditions

In the present study, N vortex panels of strength $\bar{\gamma}_i$ are distributed over the solid boundary surface with a definite thickness h to represent a part of the flow boundary layer as illustrated in Fig.5. Source panels of strength σ_i are distributed just under the boundary surface so that no flux and no-slip boundary conditions can be satisfied simultaneously. Since the strength of source panels approaches zero as N increases [8], the strength of vortex panel in the domain ABCD and source

panel ABFE can be determined by the Boundary Element Method. There are $2N$ unknowns for a boundary surface discretized by N panels. Then, requiring the total velocity $\vec{V}(\vec{r})$ (Eq. (14)) to satisfy the boundary conditions produces an equivalent number of equations. However, there exist additional integral constraints to ensure a unique solution. The conservation of the circulation in the vortex panels around the solid boundary can be expressed by

$$\sum_{i=1}^N \Gamma_i(t_j) = \sum_{i=1}^N \Gamma_i(t_{j-1}) + \sum \Gamma_{in}(t_{j-1}) - \sum \Gamma_{out}(t_{j-1}) \quad (15)$$

where the second and third terms on the right-hand side of Eq. (15) are the sum of vorticity that flows into the panel ABCD, and the one of vortices shed from the panels, respectively. Similarly, the integral of source panels over the boundary surface is zero by continuity, which is,

$$\sum_{i=1}^N \sigma_i(t_j) \Delta l_i = 0 \quad (16)$$

Because of the integral constraints in Eqs. (15) and (16), this set of $2N+2$ equations is over-determined. The matrix solution for the vortex elements and source panels is formulated via Lagrange multipliers so that $2N$ boundary conditions on velocity can be satisfied in a least-squares sense and the integral constraints can be met exactly.

In order to improve the stability and accuracy of the solution, in the present study a Petrov-Galerkin Boundary Method was applied to yield a solution that satisfies the boundary conditions ($\vec{V} = 0$ on the stationary boundary whereas $\vec{W} = 0$ on the rotating boundary) in an integral sense as opposed to point-wise [6,9]. The stability and accuracy of the solution were improved, especially for the solutions at the leading and trailing edges of the blades.

3.6 Discretization of shedding vortex elements

In a short time increment Δt , the length and vorticity of the nascent vortex element were assumed to equal to those of the respective panel over which it lies. Then, the thickness can be determined by

$$\Delta h_i = h \Delta \Gamma_i / \Gamma_i(t_j) \quad (17)$$

where $\Gamma_i(t_j)$ is the circulation around panel ABCD (see Fig.5).

When the thickness Δh_i is positive and thus the vortex is shed from the panel into the flow field, a vortex element is added in the out-domain. When the thickness Δh_i is negative and the vortex elements flow into the panels, on the other hand, no vortex elements are added. The vortex elements that entered the panels were ignored in the next calculation step, but the effect of the ignored elements was calculated in the second term on the right-hand side of Eq. (15) in the next step.

As illustrated in Fig.5, in order to avoid the complicated calculation for the nascent rectangular vortex deformation and interference with the complex boundary, a rectangular vortex element was approximated by M vortex blobs with viscosity radius ϵ . By considering the viscosity diffusion with the core-spreading method in the discrete vortex blobs, in the present study, the time variation of the core radius can be calculated by

$$d\epsilon/dt = c^2 \nu / (2\epsilon); c=2.242 \quad (18)$$

3.7 Unsteady Pressure

After the vorticity and velocity field were determined by the above procedures, the unsteady pressure was directly calculated according to the calculated velocity and vorticity time to time in the present 2D flow calculation.

The Bernoulli function B can be obtained by the Boundary Element Method [10,11]:

$$\begin{aligned} & \iint_S B \cdot \nabla^2 G dS + \int_{L_i+L_d+L_\infty} B \nabla G \cdot \vec{n} dL \\ &= - \int_{L_i+L_d+L_\infty} \partial \vec{V} / \partial t \cdot \vec{n} G dL - \nu \int_{L_i+L_d+L_\infty} (\nabla G \times \omega) \cdot \vec{n} dL \\ & - \iint_S \nabla G \cdot (\vec{V} \times \vec{\omega}) dS \end{aligned} \quad (19)$$

The acceleration in the first term on the right-hand side of the above equation can be expressed in the rotational cylindrical coordinates as

$$\begin{aligned} \partial \vec{V} / \partial t &= \partial_R \vec{W} / \partial t - \nabla(\vec{U} \cdot \vec{V}) \\ &+ \vec{U} \times (\nabla \times \vec{V}) + \partial \vec{\Omega} / \partial t \times \vec{r} \end{aligned} \quad (20)$$

To avoid constructing the mesh for the evaluation of the second and third terms on the right hand side of Eq. (20), an inner boundary surface L_2 was set between the rotor

and stator as shown in Fig. 4. By applying the Gaussian divergence theorem and the flow continuum equation to Eq. (21), then the following equation was derived and employed to calculate the Bernoulli function.

$$\begin{aligned} & \beta_1 B' + \beta_2 B + \int_{L_1} B' \nabla G \cdot \vec{n} dL + \int_{L_d + L_\infty} B \nabla G \cdot \vec{n} dL \\ &= - \int_{L_1} (\partial \bar{\Omega} / \partial t \times \vec{r}) \cdot \vec{n} G dL + \bar{\Omega} \int_{L_2} (\partial \vec{V}_r / \partial \theta) G dL \\ &+ \int_{L_2} (\vec{V} \cdot \vec{U}) \nabla G \cdot \vec{n} dL - \nu \int_{L_1 + L_d + L_\infty} (\nabla G \times \vec{\omega}) \cdot \vec{n} dL \\ &- \iint_{S_1} \nabla G \cdot (\vec{W} \times \vec{\omega}) dS - \iint_{S_2} \nabla G \cdot (\vec{V} \times \vec{\omega}) dS \end{aligned} \quad (21)$$

where the values of β_1 and β_2 at $P(x_P, y_P)$ are shown in Table 1.

3.8 Instantaneous Total Head Rise and Flow Rate

The instantaneous pump operation is calculated by considering the change in the pump operating point. In the present calculation, it is assumed that the pump delivers no elevation head, so the instantaneous flow rate $Q_i(t)$ can be calculated by [12]

$$H(t) = (l_{eq} / g A_0) dQ/dt + \kappa H_0 Q^2 / Q_0^2 \quad (22)$$

where $A_0 = \pi D_0^2 / 4$ is nominal flow area. At every calculation step, the pump operating point is determined in the process of resolving iteratively the instantaneous flow rate and the total head rise in Eqs. (21) and (22).

In the present calculation, the thickness of the vortex panels adjoining the solid boundary is assumed to be $h / D_2 = 2.0 / \sqrt{Re}$; the instantaneous rotational speed $N(t)$ is assumed to be

$$N(t) = N_f (1 - e^{-t/T_{na}}) \quad (23)$$

where $T_{na} = T_0$ was assumed.

4 RESULTS AND DISCUSSION

4.1 Instantaneous Flow Rate and Total Hydraulic Head

Figures 6 show the time histories of the flow rate and the total hydraulic head after starting the pump under the rated flow condition. It can be found that the instantaneous flow rate and total hydraulic head change remarkably at the initial stage after starting the pump and reach their steady values after 6 revolutions of impeller for the pumping system described in Table 2. The mean

values of the instantaneous flow rate and the total hydraulic head in Fig. 6 are the time averaged-values after 6 revolutions of the impeller.

Table 1 Values of β_1 and β_2

Locations of P	β_1	β_2
in S_1	1	0
on L_1	0.5	0
on L_2	0.5	0.5
in S_2	0	1
on L_d	0	0.5

$$* \iint_S B \cdot \nabla^2 G dS = \beta_1 B' + \beta_2 B$$

Table 2 Specifications of the test pump

	Rating	Pump system	
Q_0	6.21 m ³ /min	D_0	0.2 m
H_0	29.2 m	κ	1
N	2066 min ⁻¹	l_{eq}	2 m
Impeller		Diffuser	
D_2	250 mm	R_3	129 mm
b_2	41.6 mm	b_3, b_4	45.8 mm
β_2	22.5 Deg.	R_4	162.5 mm
Z_1	5	Z_d	8

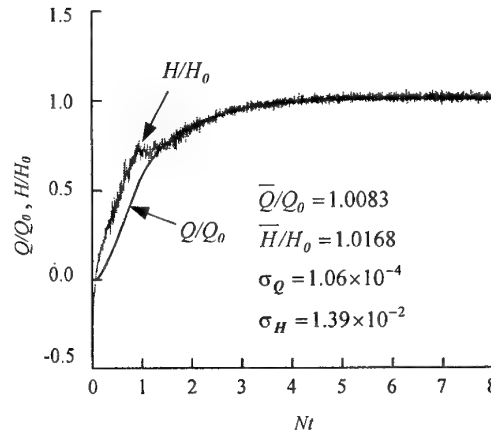


Fig. 6 Instantaneous flow rate and total hydraulic head under the rated condition

4.2 Pressure Fluctuations in the Diffuser Passage

The measured unsteady pressure data presented are phase-averaged ones in 100 revolutions of the impeller, whereas the calculated data by the present vortex method,

the singularity method and 3-D CFD code are not phase-averaged but instantaneous.

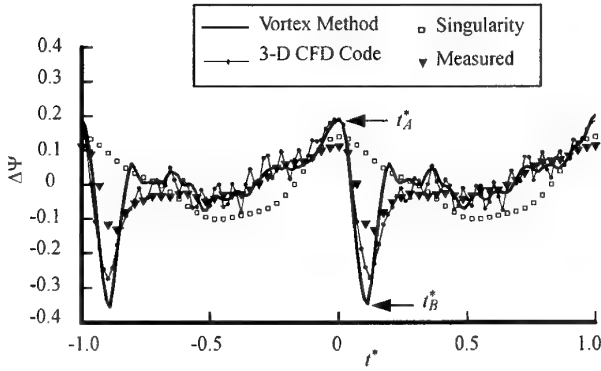
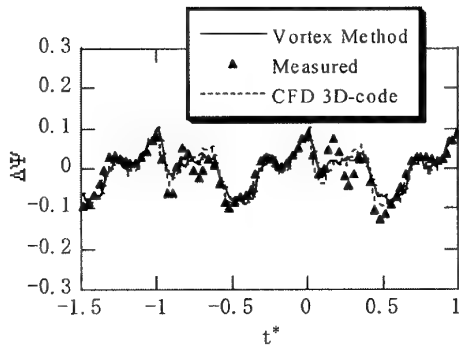
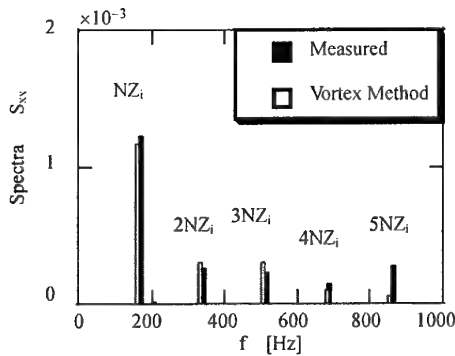


Fig. 7 Time histories of pressure fluctuations at station (r_1, c_1) at the rated condition. Experimental uncertainty in $\Delta\Psi = \pm 7.1\%$



(a) In the time domain



(b) In the frequency domain

Fig.8 Pressure fluctuations on Station (r_3, c_3) at the rated condition. Experimental uncertainty in $\Delta\Psi = \pm 7.1\%$

Figure 7 shows the comparison of the time histories of the unsteady pressure coefficient calculated by the present vortex method, the singularity method [13], and the 3-D CFD code [14] with the measured ones [15] on a representative pressure tap (r_1, c_1) (see Fig.3 (b)) under the rated condition. The waveform of unsteady pressure predicted by the present vortex method shows better agreement with the experimental result than the waveform predicted by the singularity method, which comprises only low frequency components, or the 3-D CFD code, which includes much higher frequency components. The amplitude of the pressure fluctuations predicted by the vortex method or by the 3-D CFD code, however, is bigger than the experimental result and that calculated by the singularity method. The big drop in the pressure fluctuations due to the passing of the impeller blade trailing edges is not predicted by the singularity method because the blade thickness and viscous wake-diffuser interaction are neglected in the calculation. The turbulent model and the numerical error are found to be the reasons why much higher frequency components in unsteady pressure appear in the 3-D CFD code calculation.

Figure 8 depicts the pressure fluctuations at the time domain and the frequency domain, respectively, on the representative pressure tap (r_3, c_3) in the diffuser passage (see Fig. 3 (b)) at the rated flow condition. The pressures calculated by the present vortex method show a good agreement with ones measured and predicted by 3-D CFD code (Fig. 8(a)). The power spectral density function shown in Fig. 8(b) is extracted from the corresponding data in time domain with an external FFT program. The present simulations demonstrate that the unsteady pressure in the diffuser passage fluctuates with the impeller blade passing frequency NZ_i and its higher harmonics.

The calculation by the singularity method can predict the effect of the potential interaction reasonably, but cannot predict the effect of the wake acceptably. However, the calculation by the present vortex method can predict the effect of the potential interaction as well as the effect of the wake reasonably, as can be seen in Figs. 7 and 8.

5 CONCLUSION

A new approach for vortices shedding from solid boundary was proposed theoretically based on the

Navier-Stokes equations. Then, a numerical method was developed for a more realistic prediction of the pressure fluctuations due to rotor-stator interaction in a diffuser pump by considering the change in operating point of the pump. The pressure fluctuations were predicted in a 2-D unsteady incompressible flow by using the present vortex method. The calculated pressure fluctuations in the diffuser passage were compared with the ones measured as well as calculated by the singularity method and the 3-D CFD code. From the results of the present study, the following conclusions are derived.

(1) The potential and the wake effects on the pressure fluctuations can be predicted satisfactorily by the present vortex method.

(2) The pressure in the diffuser passage fluctuates with the basic frequency of the impeller blade passing frequency NZ_i and its higher harmonics.

REFERENCES

- (1) Cottet, G.H., and Koumoutsakos, P.D., 2000, "Vortex Methods: Theory and Practice," Cambridge University Press.
- (2) Sarpkaya, T., 1989, "Computational Methods With Vortices- The 1988 Freeman Scholar Lecture," Trans. ASME, J. Fluids Engineering, Vol.111, pp.5-52.
- (3) Chorin, A.J., 1978, "Vortex Sheet Approximation of Boundary Layer," J.Comp. Phys., Vol.74, pp.283-317.
- (4) Kamemoto, K., 1995, "On Attractive Features of the Vortex Methods," *Computational Fluid Dynamic View 1995* (Ed. M.Hafez and K. Oshima), JOHN WILEY & SONS.
- (5) Wang, H. and Tsukamoto, H., 2001, "Numerical Analysis of Pressure Fluctuation due to Rotor-Stator Interaction in a Diffuser Pump by Vortex Method", Trans. JSME Ser. B, Vol. 67-654, pp.321-329. (In Japanese)
- (6) Wang, H. and Tsukamoto, H., 2001, "Fundamental Analysis on Rotor-Stator Interaction in a Diffuser Pump by Vortex Method", Trans. ASME J. Fluids Engineering. (in press)
- (7) Wu, J.C., and Thompson, J.F., 1973, "Numerical Solutions of Time-Dependent Incompressible Navier-Stokes Equations Using an Integro-Differential Formulation," Computers & Fluids, Vol. 1, pp.197-215.
- (8) Huyer, S.A., and Grant, J.R., 1996, "Computation of Unsteady Separated Flow Fields Using Anisotropic Vorticity Elements," ASME Journal of Fluids Engineering, Vol.118, pp.839-849.
- (9) Kempka, S. N., Glass, M. W., Strickland, J. H. and Ingber, M.S., 1999, "A Galerkin Boundary Element Method for Solving the Generalized Helmholtz Decomposition," Third International Workshop on Vortex Flows and Related Numerical Methods. Proceedings, Vol. 7, pp.205-214.
- (10) Uhlman, J.S., and Grant, J.R., 1993, "A New Method for the Implementation of Boundary Conditions in the Discrete Vortex Method," ASME 1993 Fluids Engineering Spring Meeting, Washington, D.C., June.
- (11) Zhu, B., 1999, "Study on Application of an Advanced Vortex Method to unsteady flow Analysis in Turbomachinery," Doctoral Thesis, Yokohama National University, Japan
- (12) Tsukamoto, H., Matsunaga, S., Yoneda, H., and Hata, S., 1986, "Transient Characteristics of a Centrifugal Pump during Stopping Period," ASME Journal of Fluids Engineering, Vol. 108, pp.392-399.
- (13) Qin, W., and Tsukamoto, H., 1997, "Theoretical Study of Pressure Fluctuation Downstream of a Diffuser Pump Impeller-Part 1: Fundamental Analysis on Rotor-Stator Interaction," ASME Journal of Fluids Engineering, Vol. 119, pp.647-652.
- (14) Shi, F., and Tsukamoto, H., 1999, "Numerical Studies of Effects of Flow Rate and Radial Gap on Pressure Fluctuations Downstream of a Diffuser Pump Impeller," Proceeding of the 3rd ASME/JSME Joint Fluids Engineering Conference, July 18-23, San Francisco, California.
- (15) Tsukamoto, H., Uno, M., Hamafuku, H., and Okamura, T., 1995, "Pressure Fluctuation Downstream of a Diffuser Pump Impeller," The 2nd Joint ASME/JSME Fluids Engineering Conference, Forum of Unsteady Flow, FED-Vol.216, pp.133-138.

STUDY ON HIGHER RESOLUTION OF VORTICITY LAYER OVER A SOLID BOUNDARY FOR VORTEX METHODS

Satomi OTA* and Kyoji KAMEMOTO

Department of Mechanical Engineering and Material Science
Yokohama National University

79-5, Tokiwadai, Hodogaya-ku, Yokohama, 240-8501, Japan / E-mail:d00ja002@ynu.ac.jp

ABSTRACT

In this paper, authors improved a scheme proposed by Zhu and Kamemoto⁽¹⁾ in order to obtain higher-resolution scheme of introduction of nascent vortex elements over a solid boundary. In this new scheme, circulation of the nascent vortex elements is calculated by considering with effects of convection and viscous diffusion, and the resolution is expressed by changing thickness of vorticity layer. The new scheme was applied to simulate unsteady flows around a two-dimensional flat plate and circular cylinder impulsively started at $Re=1000$. As results of calculations, large-scale vortices were formed not depending on the thickness of vorticity layer. Small-scale vortices were simulated when the thickness of vorticity layer was thin for the higher resolution. It was confirmed that the higher-resolution simulation could be achieved by using the new scheme.

1. INTRODUCTION

Vortex methods simulate flows by representing vorticity distributions with discrete vortex elements and calculating trajectories of these elements in a Lagrangian form. Various methods on introduction of the vortex elements into the flow fields were applied for analysis of complicated flows. In order to simulate to viscous diffusion, the random walk method by Chorin⁽²⁾ and a core spreading method by Leonard⁽³⁾ were proposed. Nakanishi and Kamemoto⁽⁴⁾ simulated flows around a sphere by using the three-dimensional core spreading method. Ohgami and Akamatsu⁽⁵⁾ presented a diffusion velocity method for two-dimensional flows. Nakajima and Kida⁽⁶⁾ mathematically confirmed the validity of the

core spreading method. Koumoutsakos and Leonard⁽⁷⁾ performed a higher-resolution of direct numerical simulations using a new numerical scheme.

On the other hand, Kamemoto⁽⁸⁾ classified procedures of vorticity layer expression into three levels, by applying to an approximation of a boundary layer depending on the accuracy required for the calculations. These schemes need much time to calculate the flows with increasing the number of the vortex elements in the flow fields. Therefore, these methods have been used properly so as to satisfy the accuracy required for the calculations. For the higher resolution of the vortex methods, Zhu and Kamemoto⁽¹⁾ proposed a procedure on the introduction of vortex elements, in which vorticity distributions over the solid surface was represented by a simple distribution of vorticity layer. This technique was applied to analysis of a two-dimensional flow through a centrifugal impeller rotating in a volute casing of a pump. Furthermore, Ojima and Kamemoto⁽⁹⁾ extended this technique to simulation of three-dimensional flows around bluff bodies.

The purpose of this study is to develop a higher-resolution scheme of the vorticity layer over the solid surface by improving the scheme proposed by Zhu and Kamemoto⁽¹⁾. In the new scheme, circulation of the nascent vortex elements is calculated by considering effects of convection and viscous diffusion of vorticity. The effects are investigated by changing the thickness of vorticity layer for the higher-resolution simulation. The new scheme is applied to simulate the unsteady flows around a two-dimensional flat plate and an impulsively started circular cylinder at Reynolds number $Re=1000$.

2. BASIC EQUATIONS

For a viscous and incompressible flow, governing equations of the vortex methods are the vorticity transport equation and pressure Poisson equation, which are obtained by taking the rotation and the divergence of the Navier-Stokes equation as follows, respectively.

$$\frac{\partial \omega}{\partial t} + (\mathbf{u} \cdot \text{grad}) \omega = (\omega \cdot \text{grad}) \mathbf{u} + \nu \nabla^2 \omega \quad (1)$$

$$\nabla^2 p = -\rho \text{div}(\mathbf{u} \cdot \text{grad} \mathbf{u}) \quad (2)$$

Here, \mathbf{u} is the velocity and the definition of the vorticity ω is written as follows.

$$\omega = \text{rot} \mathbf{u} \quad (3)$$

Velocity fields are calculated by a generalized Biot-Savart law, which is proposed by Wu and Thompson⁽¹⁰⁾. It is obtained from the definition of the vorticity as follows.

$$\mathbf{u}(\mathbf{r}) = \int_V (\omega_0 \times \nabla G_0) dv + \int_S [(\mathbf{u}_0 \cdot \mathbf{n}_0) \nabla G_0 - (\mathbf{u}_0 \times \mathbf{n}_0) \times \nabla G_0] ds \quad (4)$$

Here, G is the fundamental solution of the scalar Laplace equation, which is written for two-dimensional fields as follows.

$$G = -\frac{1}{2\pi} \ln R \quad (5)$$

Where, $R=|\mathbf{R}|=|\mathbf{r}-\mathbf{r}_0|$, subscript $[0]$ denotes the integration at a location \mathbf{r}_0 , \mathbf{r} is the arbitrary location in flow fields, and \mathbf{n} is the normal unit vector. V is the region of the flow fields and S is the boundary facing and/or surrounding region V . The inner product $\mathbf{u}_0 \cdot \mathbf{n}_0$ and the outer product $\mathbf{u}_0 \times \mathbf{n}_0$ are a normal and a tangential velocity component on the boundary surface, respectively. They respectively correspond to source and vortex distributions on the surface. Therefore, the velocity fields can be obtained from the vorticity and the velocity distributions in the flow fields and on the body surface, respectively.

On the other hand, pressure in the flow fields is calculated from an integration equation, which is proposed by Uhlman⁽¹¹⁾ as follows.

$$\beta H + \int_S H \cdot \frac{\partial G}{\partial \mathbf{n}} ds = - \left[\int_V \nabla G (\mathbf{u} \times \omega) dv + \int_S G \cdot \mathbf{n} \cdot \frac{\partial \mathbf{u}}{\partial t} ds + \nu \int_S \mathbf{n} (\nabla G \times \omega) ds \right] \quad (6)$$

Here, $\beta=1$ in the flow field V and $\beta=1/2$ on the body surface S . G is the fundamental solution given by Eq. (5) and the Bernoulli function H is written as follows.

$$H = \frac{p}{\rho} + \frac{u^2}{2}, \quad u = |\mathbf{u}| \quad (7)$$

3. INTRODUCTION OF NASCENT VORTEX ELEMENTS

In order to calculate circulation of introduction of nascent vortex elements shedding from the solid boundary, effects of convection and viscous diffusion are modeled by improving a scheme proposed by Zhu and Kamemoto⁽¹⁾.

The velocity at the distance of h_i from the solid surface on the i -th panel is calculated with the Biot-Savart law (4). If a liner distribution of velocity in the thin vorticity layer is assumed as shown in Fig. 1, a convective velocity v_c at h_i can be expressed as Eq. (8) using the relation of continuity of flow and the non-slip condition on the solid surface.

$$v_c = \frac{1}{\Delta s_i} \left(\frac{h_i u_i}{2} - \frac{h_{i+1} u_{i+1}}{2} \right) \quad (8)$$

Here, Δs_i and u_i denote the panel length and the tangential velocity at h_i , respectively. The vorticity in the vorticity layer near the solid surface convects through h_i into the flow fields with the convective velocity v_c . Using the relation between the tangential and normal velocities, the circulation of the nascent vortex elements can be calculated as follows.

$$\Delta \Gamma_C = \frac{\Delta t}{2} (u_{i+1}^2 - u_i^2) \quad (9)$$

$$A_{c2} = v_c \Delta t \Delta s_i \quad (10)$$

Here, $\Delta \Gamma_C$ and A_{c2} denote the circulation based on the convective effects and an area of the elements introduced into the flow fields.

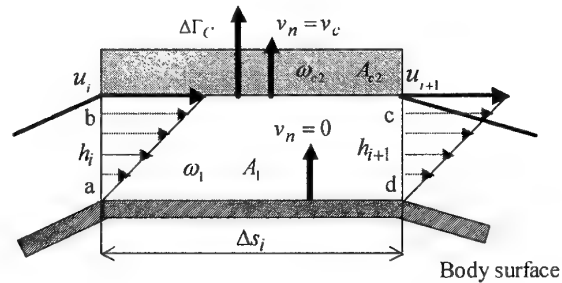


Fig. 1 Introduction of nascent vortex elements over the solid surface by considering effect of convection

On the other hand, the vorticity in the vorticity layer near the solid surface diffuses through h_i into the flow fields with a diffusion velocity v_d . In order to consider this vorticity diffusion, the diffusion method proposed by Kamemoto⁽⁸⁾ is used, which is expressed as follows.

$$v_d = \frac{1.136^2 \nu}{h_i + h_{i+1}} \quad (11)$$

The nascent vortex element is introduced in the flow fields, whose a circulation is given as follows.

$$\Delta \Gamma_D = \frac{\Gamma_1}{A_1 + A_{d2}} A_{d2} \quad (12)$$

$$A_{d2} = v_d \Delta t \Delta s_i \quad (13)$$

Here, Γ_1 is the circulation originally involved in the element of vorticity layer in Fig. 2. A_1 and A_{d2} are the area of the vorticity layer near the solid surface and the element introduced into the flow fields, respectively.

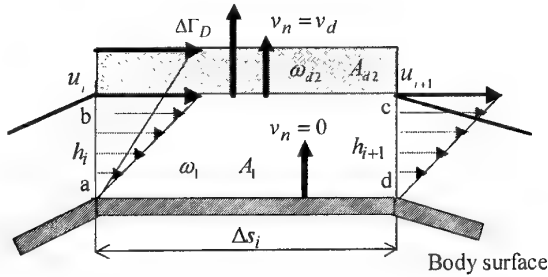


Fig. 2 Introduction of nascent vortex elements over the solid surface by considering effect of viscous diffusion

As mentioned above, the vorticity convects through the vorticity layer with the convective velocity v_c and also it diffuses with the diffusion velocity v_d as shown in Fig. 3. If $v_c + v_d$ becomes positive, the nascent vortex element is introduced into the flow fields, where the thickness and the circulation are given from the relation of convection and viscous diffusion as follows.

$$\Delta \Gamma = \Delta \Gamma_C + \Delta \Gamma_D \quad (14)$$

$$h_2 = (v_c + v_d) \Delta t \quad (15)$$

$$A_2 = (v_c + v_d) \Delta t \Delta s_i \quad (16)$$

Here, $\Delta \Gamma$ is a total circulation considering the effects of convection and viscous diffusion, and A_2 is the area of the nascent vortex element. The nascent vortex element

is introduced at the distance of a half of h_2 from a point $h = 0.5(h_i + h_{i+1})$ as a vortex of rectangular section. Furthermore, when a vortex element is convected beyond the distance of two times h from the solid surface, it is replaced with a vortex blob for convenience of treatment.

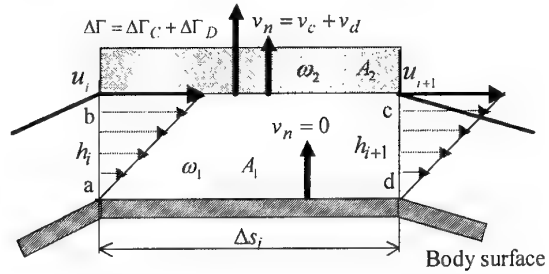


Fig. 3 Introduction of nascent vortex element over the solid surface by considering effects of convection and viscous diffusion.

The trajectory of a vortex element in the flow field is expressed as,

$$\frac{dr}{dt} = u \quad (17)$$

This equation is approximately calculated by using the second-order Adams-Bashforth scheme as follows.

$$r(t + \Delta t) \approx r(t) + \{1.5u(t) - 0.5u(t - \Delta t)\} \Delta t \quad (18)$$

Lagrangian expression for the two-dimensional vorticity transport equation is given by

$$\frac{d\omega}{dt} = \nabla^2 \omega \quad (19)$$

The vorticity is calculated with two-dimensional core spreading method proposed by Leonard⁽²⁾.

4. RESULTS AND DISCUSSION

4.1 Flat plate

To begin with, authors attempt to simulate a flow around a two-dimensional flat plate at $Re = U_\infty L / \nu = 1000$ by using a new scheme. Here, L denotes a length of the flat plate. A time interval is $\Delta t D / U_\infty = 0.02$. The flat plate is expressed as $N = 50$ panels. The thickness of vorticity layer h is $h/h^* = 0.5$, and $h^* = L/N$.

Figure 4 shows a vorticity layer structure at non-dimensional time $tL/U_\infty = 5.00$. Discrete vortex

elements can form a developing boundary layer from a leading edge. Velocity profiles at $x/L=0.9$ are in good agreement with theoretical solution as shown in Fig. 5.

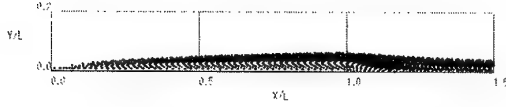


Fig. 4 Instantaneous flow pattern by discrete vortices for $h/h^* = 0.5$ ($Re = 1000$, $tL/U_\infty = 5.00$)

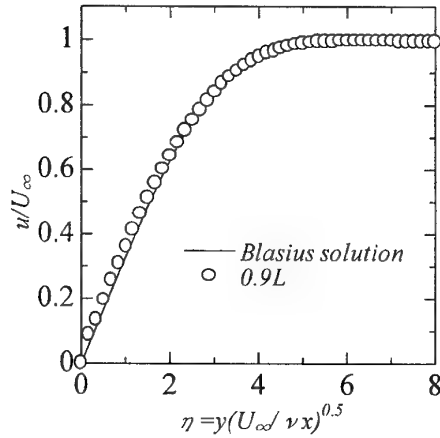


Fig. 5 Velocity profiles for $h/h^* = 0.5$ at $x/L = 0.9$ ($Re = 1000$, $tL/U_\infty = 5.00$)

4.2 Circular cylinder

For verifying effects of convection and viscous diffusion, calculations are performed for flows around an impulsively started circular cylinder in a two-dimensional flow field at $Re = U_\infty D/\nu = 1000$. Here, U_∞ , D and ν denote a uniform velocity, a diameter of the circular cylinder and kinematic viscosity, respectively. A time interval is $\Delta t D/U_\infty = 0.02$. The circular cylinder is represented by $N = 160$ panels in Fig. 6. Furthermore, each effect of convection and viscous diffusion and resolution of simulations were investigated by changing thickness of vorticity layer as follows.

$$h/h^* = 0.8, 1.0, 2.0 \quad (20)$$

Here, h is the thickness of vorticity layer and $h^* = \pi D/N$.

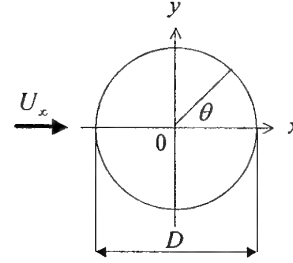
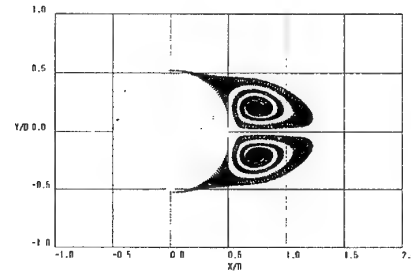


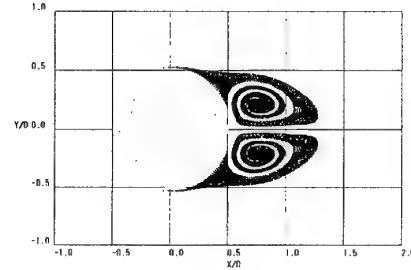
Fig. 6 Calculation model of the circular cylinder

4.1.1 Effect of convection

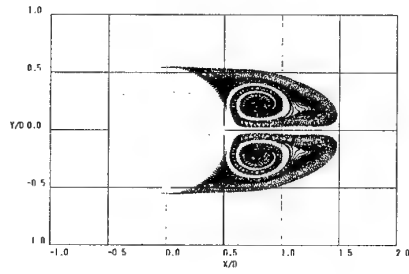
Figures 7(a) to (c) show wake structures behind a circular cylinder by considering only a convective effect at a non-dimensional time $tD/U_\infty = 4.00$ for $Re = 1000$. It is one of the most interesting points that although the value of h/h^* changes, any remarkable differences do not appear in the wake structure. Figure 8 shows a circulation of nascent vortex elements near the body surface at $tD/U_\infty = 4.00$. The circulation $\Delta\Gamma_C$ of the nascent vortex elements is generated almost the same according to Fig. 8.



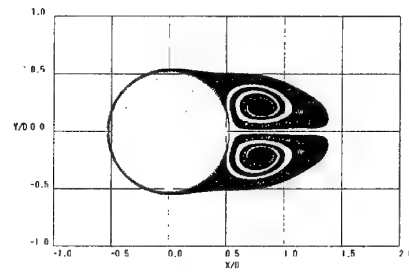
(a)



(b)



(c)



(a)

Fig. 7 Instantaneous flow patterns by discrete vortices (a) $h/h^* = 0.8$ (b) $h/h^* = 1.0$ (c) $h/h^* = 2.0$ ($Re = 1000$, $tD/U_\infty = 4.00$)

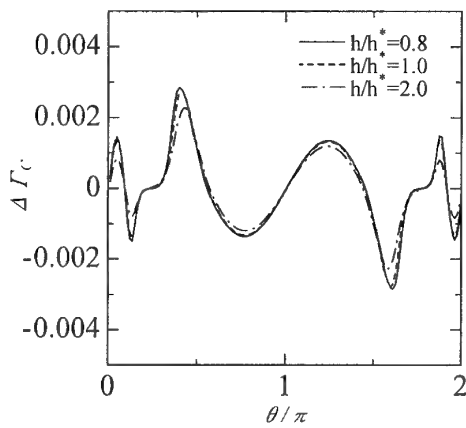
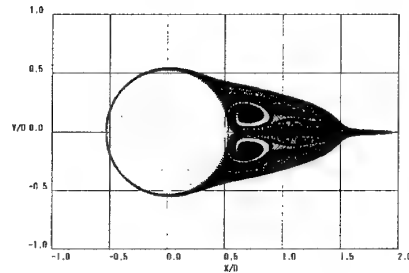
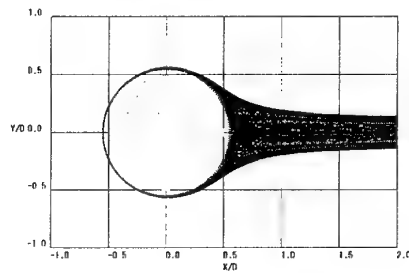


Fig. 8 Circulation distribution of nascent vortex elements by considering effect of convection ($Re = 1000$, $tD/U_\infty = 4.00$)



(b)



(c)

Fig. 9 Instantaneous flow patterns by discrete vortices (a) $h/h^* = 0.8$ (b) $h/h^* = 1.0$ (c) $h/h^* = 2.0$ ($Re = 1000$, $tD/U_\infty = 4.00$)

4.1.2. Effect of viscous diffusion

Figures 9(a) to (c) show wake structures behind a circular cylinder by considering only viscous diffusion effect at $tD/U_\infty = 4.00$ for $Re = 1000$. Twin-vortex structures formed at initial stage are confirmed behind the circular cylinder at $h/h^* = 0.8$ as shown in Fig. 9(a). However, as the value of h/h^* increases, the twin-vortex are not appeared, because the circulation $\Delta\Gamma_D$ of nascent vortex elements becomes smaller according to Fig. 10.

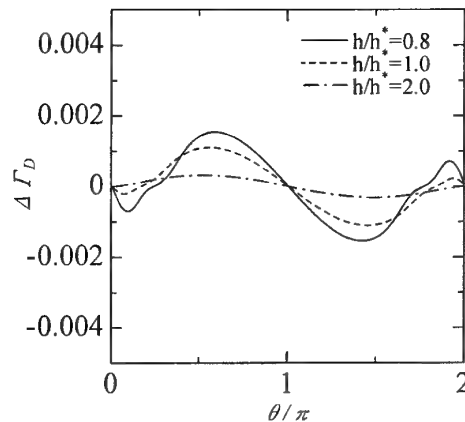
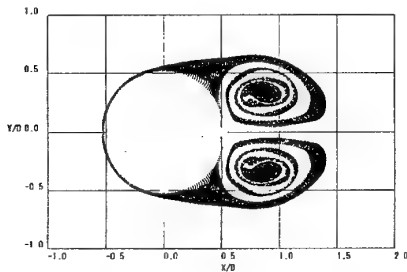


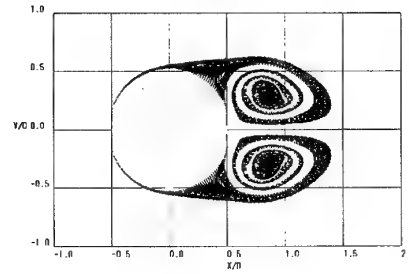
Fig. 10 Circulation distribution of nascent vortex elements by considering effect of viscous diffusion ($Re = 1000$, $tD/U_\infty = 4.00$)

4.1.3 Effects of convection and viscous diffusion

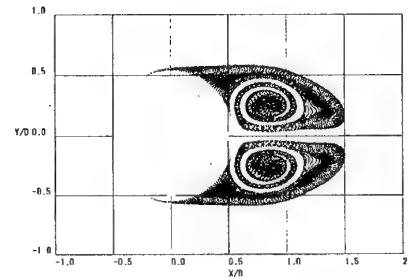
Figures 11(a) to (c) show wake structures behind a circular cylinder by considering both effects of convection and viscous diffusion at $tD/U_\infty=4.00$ for $Re=1000$. Large-scale vortices structures are formed behind the circular cylinder in Figs. 11(a) to (c), and secondary vortices appear as shown in Fig. 11(a), because of higher-resolution simulation of vorticity layer over the surface. With increasing the value of h/h^* , the effect of convection becomes larger by considering both effects of convection and viscous diffusion as shown in Fig. 12(a). On the other hand, as the value of h/h^* decreases, the effect of viscous diffusion becomes larger in Fig. 12(b). Total circulation $\Delta\Gamma_c + \Delta\Gamma_D$ of nascent vortex elements at $tD/U_\infty=4.00$ is generated almost the same in spite of changing h/h^* in Fig. 12(c). However, the circulation and the wake structure at $h/h^*=2.0$ in Fig. 11(c) are a little different compared with another structures at $h/h^*=0.8$ and 1.0 in Figs. 11(a) and (b), because the dominant effect becomes only convection at $h/h^*=2.0$. Both effects of convection and viscous diffusion have affection to create the circulation over the circular cylinder, therefore the balance of the circulation of the nascent vortex elements is maintained. Figure 13 shows time histories of drag coefficient C_D of the circular cylinder. As the value of h/h^* decreases, C_D becomes larger. However, authors can not identify whether C_D becomes stable or not after increasing of time. Further calculation of long computational time is necessary for discussion on these points. But, it is confirmed that when the higher resolution of vorticity layer can be obtained, not only the dominant wake structures of the large-scale vortices behind the circular cylinder but also secondary vortices near the circular cylinder can be simulated by using the scheme.



(a)

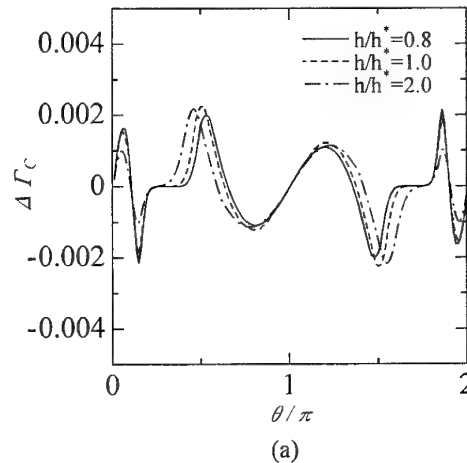


(b)



(c)

Fig. 11 Instantaneous flow pattern by discrete vortices
(a) $h/h^*=0.8$ (b) $h/h^*=1.0$ (c) $h/h^*=2.0$
($Re=1000$, $tD/U_\infty=4.00$)



(a)

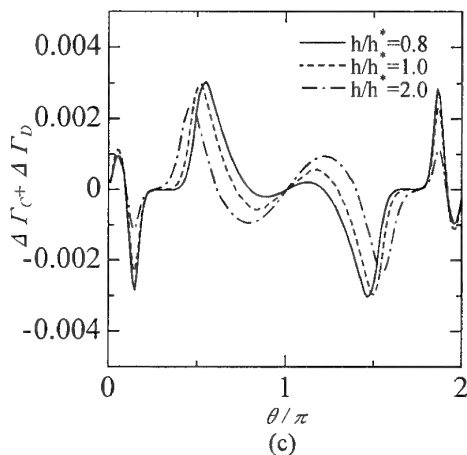
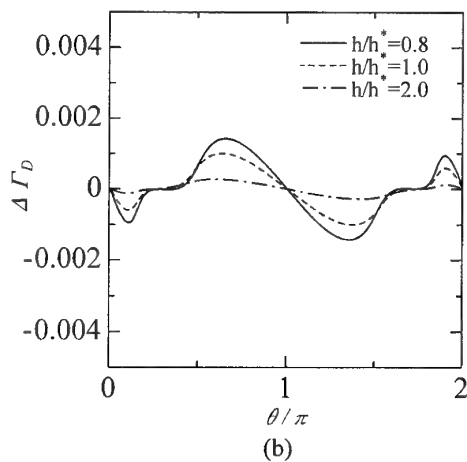


Fig. 12 Circulation distribution of nascent vortex elements (a) convection (b) viscous diffusion (c) convection and viscous diffusion ($Re=1000$, $tD/U_\infty = 4.00$)

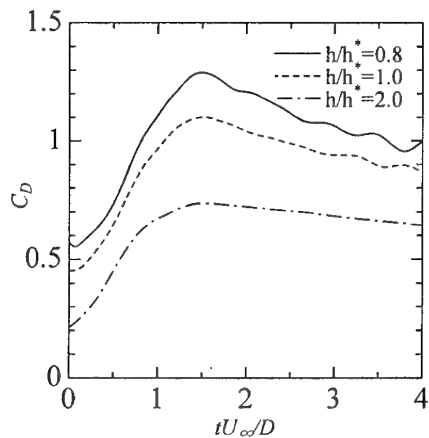


Fig. 13 Drag Coefficient ($Re=1000$)

5. CONCLUSIONS

For development of a higher-resolution scheme of vorticity layer over a solid surface, effects of convection and viscous diffusion were investigated by changing thickness of vorticity layer. By applying the new scheme to unsteady flows around a flat plate and an impulsively started circular cylinder in two-dimensional flow field, the following conclusions were obtained.

- (1) In the new scheme, with increasing of the thickness of vorticity layer, the effect of convection becomes larger. On the other hand, as the thickness of vorticity layer decreases, the effect of viscous diffusion becomes larger.
- (2) Total circulation of nascent vortex elements was generated almost the same by considering both effects of convection and viscous diffusion of vorticity in spite of changing the thickness of vorticity layer.
- (3) Any remarkable differences do not appear in the wake structure behind the body surface by considering both effects of convection and viscous diffusion in the new scheme.
- (4) When the higher resolution of the vorticity layer is obtained, not only the dominant wake structure of the large-scale vortices behind the circular cylinder but also secondary vortices near the circular cylinder can be simulated.

REFERENCES

- (1) Zhu, B. and Kamemoto, K., (1998), "Direct Simulation of Unsteady Flow through a Centrifugal Pump Impeller using Fast Vortex Method", *Computational Fluid Dynamics Journal*, Vol.7, No.1, p.15-26.
- (2) Chorin, A. J., (1973), "Numerical Study on Slightly Viscous Flow", *J. Fluid Mech.*, Vol. 57, p.785-796.
- (3) Leonard, A., (1980), "Vortex methods for flow simulations", *J. Comp. Phys.* 37, p.289-335.
- (4) Nakanishi, Y. and Kamemoto, K., (1992), "Numerical Simulation of Flow Around a Sphere with Vortex Blobs", *J. Wind Eng. And Ind Aero*, Vol. 46 & 47, p.363-369.
- (5) Ohgami, Y. and Akamatsu, T., (1991), "Viscous Flow Simulation Using the Discrete Vortex Model – The Diffusion Velocity Method", *Computers & Fluids*, Vol. 19, No.3/4, p.433-441.
- (6) Nakajima, T. and Kida, T., (1990), "A Remark of Discrete Vortex Method (Derivation from Navier-Stokes Equation)", *Trans. Jpn. Soc. Mech.*

Eng., Vol. 56, No.531, B, p.3284-3291.

- (7) P. Koumoutsakos. and A. Leonard., (1995), "High-resolution simulations of the flow around an impulsively started cylinder using vortex methods", J. Fluid Mech., Vol. 296, p.1-38.
- (8) Kamemoto, K., (1995), "On Attractive Features of the Vortex Methods", Computational Fluid Dynamics Review 1995, ed. By M. Hafez and K. Oshima, JOHN WILEY & SONS, p.334-353.
- (9) Ojima, A. and Kamemoto, K., (2000), "Numerical Simulation of Unsteady Flow around Three Dimension Bluff Bodies by an Advanced Vortex Method", JSME International Journal, Series B, Vol.43, No.2, p.127-135.
- (10) Wu, J. C. and Thompson, J. F., (1973), "Numerical Solutions of Time-Dependent Incompressible Navier-Stokes Equations Using an Integro-Differential Formulation", Computers & Fluids, Vol. 1, p.197-215.
- (11) Uhlman, J. S., (1992), "An integral equation formulation of the equation of motion of an incompressible fluid", Naval Undersea Warfare Center T.R., 10, 086.

VORTEX METHOD MODELING OF COMPLEX, TURBULENT ENGINEERING FLOWS

Peter S. Bernard

Department of Mechanical Engineering, University of Maryland
College Park, Maryland 20742, U.S.A. /Email: bernard@eng.umd.edu

Athanassios A. Dimas

Krispin Technologies, Inc.
1370 Piccard Dr., Rockville, MD 20850, U.S.A. /Email: adimas@krispintech.com

ABSTRACT

This paper presents results from several recent simulations of turbulent flows using the VorCat code. VorCat is a commercial implementation of the gridfree vortex method that is specifically designed to treat high Reynolds number, turbulent, incompressible flows of engineering interest. Computational elements consist of straight vortex tubes combined to form filaments, and finite thickness, thin, unstructured, triangular vortex sheets, several layers deep, covering solid surfaces. The sheet mesh provides an efficient vehicle for accommodating steep vorticity gradients in the near-wall region and permits accurate evaluation of viscous diffusion and surface vorticity production. To the extent that the vortex tube elements mimic the actual tube-like vortical structures of turbulence, the efficiency and physical plausibility of the algorithm is enhanced. A de facto "subgrid" model is implemented by the use of Chorin's hairpin removal algorithm to prevent the appearance of vortices of ever diminishing scale. New

vortex elements appear at the outer edge of the boundary mesh during significant ejection events. Recent applications considered here include the flow in a zero-pressure gradient boundary layer, and the flow past a multi-element airfoil at angle of attack.

1. INTRODUCTION

Vortex Methods have long been regarded as a natural approach to take for the simulation of turbulent flows: they are minimally affected by numerical diffusion; they provide an opportunity to directly model turbulent flow through vorticity dynamics, and, by being grid-free, they are more readily applied than grid-based methods to complex geometries found in industrial applications. Moreover, with the advent of the Fast Multipole Method (FMM), vortex methods are able to simulate flows with sufficient numbers of vortex elements to accommodate turbulence. While it is not necessarily realistic to expect vortex methods to find application as a tool for Direct Numerical Simulations of turbulence, they do have

sufficient resolution to qualify at the level of a Large Eddy Simulation (LES). How best to achieve this end is not self-evident; this paper considers the attributes of one particular approach toward developing a vortex method LES of turbulent flow which is the basis for the commercial VorCat code.

The form of the vortex method adopted by VorCat takes advantage of a number of special physical properties of turbulence in order to gain efficiency and accuracy. The method has been applied to several complex flows with the goal of benchmarking the level of its performance in diverse situations. Recently, computations of a zero-pressure gradient flat plate boundary layer has been undertaken for the purpose of providing stringent quantitative verification of the accuracy of the method in a standard canonical turbulent flow. Preliminary results from this study are given here including predicted mean velocity and Reynolds stresses and a qualitative analysis of the computed turbulence structure. Some results from a computation of the flow past a multi-element airfoil are also presented.

2. VORCAT ALGORITHM

The development of the VorCat code is constrained by the need to be efficient and accurate in simulating turbulent flow yet also be adaptable to the realities of commercial applications. Some guidance in how to best configure a vortex method for this end can be found by considering some of the primary physical properties of turbulence and how to best capture them numerically. In particular, the restriction to Reynolds numbers in the turbulent range suggests that viscosity will affect the flow of interest only in the near-wall region, i.e., the viscous sublayer of turbulent flow, as well as spatially intermittent regions throughout the flow where viscous energy dissipation takes place. The latter are characterized by the presence of highly stretched small-scale vorticity.

To capture these particular viscous effects, two important attributes must be imparted to the numerical

scheme. First of all, the viscous sublayer adjacent to solid surfaces needs to be resolved well enough to predict viscous diffusion of vorticity from the boundary surface. Secondly, the vortex elements in the outer flow must be able to accommodate the stretching process causing the energy cascade to dissipation scales. In addressing the first of these requirements it may be noticed that the region where significant molecular vorticity diffusion occurs is largely two-dimensional in character, consisting of the accumulated regions adjacent to solid boundaries. Clearly, high aspect ratio vortex sheet elements are a natural candidate to fill out the viscous sublayer so as to provide a platform upon which to compute vorticity diffusion. It should also be noted that it is typical of engineering design analyses to provide information about the shapes of solid bodies in the form of triangularizations of the surface. This implies that a natural and efficient representation of the near-wall region should be in the form of a fixed, thin, unstructured triangular mesh of finite thickness vortex sheets. For the VorCat code the sheets are stacked normal to the surface several layers deep, with a half-thickness sheet adjacent to the boundary, and are meant to cover the viscous sublayer of turbulent wall flows, i.e., approximately no further from the wall than $y^+ = 30$. Creating such a mesh is a simple matter for even the most complicated geometries. The half-thickness sheets at the surface are assigned that vorticity necessary to enforce the no-slip condition. In particular, an image half-sheet is introduced so the surface sheet and its image do not produce any velocity outside themselves, yet locally enforce the no-slip condition without generating a local flow normal to the solid surface.

It is not practical to have the wall vortices convect since this would unnecessarily complicate the effort at accurately computing viscous diffusion normal to the surface, e.g., extra measures would have to be taken to make sure that an adequate resolution of vortices is maintained at all times. To advance the vorticity on the mesh region, a finite volume numerical scheme for

solving the 3D vorticity equation is used. If the resolution is fine enough, then wall-normal viscous diffusion with its attendant vorticity generation at the solid surface is determined with acceptable accuracy. In particular, numerical diffusion is kept within bounds so that flow at the desired Reynolds number is indeed modeled. In a further step to enhance accuracy, the vorticity on the sheets is made to be piecewise linear. This is used when computing the contributions of sheets to the velocity field.

In regards to the second viscous effect, namely, the energy dissipation occurring intermittently in turbulent flow, a useful and generally accepted model of the process assumes that energy cascades to small scales through vortex stretching. Moreover, the fine scale structure of turbulence is tube-like (1), and stretching and folding of vortex tubes takes energy to small scales (2). With this picture in mind it is natural to choose vortex tubes as the primary grid-free element of the simulation. Moreover, unlike vortex blob representations, where the vorticity amplitude can become unbounded, a tube method is unconditionally stable since the circulation is conserved during the stretching process.

In high Reynolds number flows vortex tubes stretch and fold until they approach the fine scales where viscous dissipation becomes important. Not only is it prohibitively expensive to run a vortex method calculation until such scales are populated, but it is not obvious how to correctly accommodate viscous diffusion once the tubes arrive at these scales. Fortunately, both of these pitfalls can be avoided by adopting Chorin's hairpin removal algorithm in which folded vortex pairs - as in a kink in a filament - are removed and the ends reattached (3). A conceptual basis for this procedure lies in the observation that each folded vortex tube is primarily responsible for a contribution to local energy, since the far field velocities cancel. Removal of hairpins then mimics the local dissipation process, i.e., their energy vanishes with them. If this is done, then there is no need to expend great computational resources tracking the

vortex folding process until the energy reaches the viscous scales and is dissipated. In effect, the hairpin removal algorithm acts like a subgrid model, and a vortex method incorporating it has the character of a LES. The unresolved scales are those that fall below the smallest length allowed among the tube segments.

An additional benefit to the use of tubes is that they provide a direct means for representing the principal dynamical features of the near-wall region in bounded turbulent flows, i.e., the quasi-streamwise vortices which control the momentum exchange near boundaries associated with the Reynolds shear stress. It may be imagined that a tube method is the optimal means of representing the wall layer dynamics controlled by tubes. As will be illustrated below, tubes also show a significant tendency to combine together forming other kinds of vortical structures that are routinely observed in turbulent flows.

The dynamics of vortex tubes is contained in the movement of their end points and the application of rules such as hairpin removal and the subdivision of segments if they become too long. Other rules govern their creation at the outermost sheet level of the wall grid. Vorticity produced at the wall in satisfaction of the no-slip condition diffuses and convects through the mesh. To mimic the idea that new vorticity is produced in the outer flow primarily during significant ejection events from the near wall region, new vortex tubes are made to appear at the top mesh level only when the vorticity at this location exceeds a threshold. In practical terms, this helps limit the amount of new tubes in the calculation by restricting them to those that are the most significant in the sense of containing the most energy. A description of these and other facets of the method may be found in some earlier reports, e.g., (4,5,6).

3. BOUNDARY LAYER

As a rigorous test of the VorCat code a canonical zero-pressure-gradient flat plate boundary layer has been simulated. The plate used in the simulation has a total

length of 2 and a span length of 0.28. The surface is resolved by approximately 5000 triangles. In the simulations, 4 periodic images are used to enforce periodicity conditions in the spanwise direction. The flow is tripped by a bump placed at $x=0.1$ with height 0.003. Computed flow statistics are taken at $x=1.1$ which corresponds to a Reynolds number of 200,000 based on the distance from the trip.

3.1 Physical Properties

The boundary layer trip is observed to have an effect on the computed solution that agrees with current understanding of the physics of boundary layer transition and its subsequent development into a turbulent state. This is illustrated in Figs. 1 and 2 showing snapshots of the computed vortex element population from the top and side at a sequence of increasing times. Figures 3 and 4 give a magnified view of the flow from each of these perspectives. Besides the vorticity in the tubes, it should be remarked that there is considerable vorticity in the sheet mesh that is not depicted in these figures. Upstream of the boundary layer trip, there are a relatively small number of purely spanwise vortices which are typical of a laminar boundary layer. The flow in this region is clearly stable throughout the calculation, e.g., its character is unchanged in time, and the vortex elements have low vorticity amplitude.

Immediately downstream of the bump the flow remains laminar for a short distance, but is soon followed by strong transition into a highly perturbed state (where the elements are various shades of purple and magenta). This behavior is strongly reminiscent of transition in which 2D Tollmein-Schlichting waves first appear, followed by a focusing of their spanwise vorticity, which subsequently undergoes instability causing the appearance of streamwise vorticity and finally turbulence (7). Evidently, the effect of the bump is to inject vorticity outwards from the wall surface, and by so doing, accelerate the appearance of the transition process. A close-up view of the vortex elements in the latter part of

the transition region shown in Fig. 5, indicates that reorientation of spanwise vorticity to the streamwise direction is associated with the presence of alternating regions of faster and slower streamwise motions, i.e., the beginnings of the streaky structure which characterizes turbulent boundary layers, and which is found to underlie the fully turbulent regions of the simulation.

The side views in Figs. 2 and 4 reveal a thickening of the boundary layer in the transition region and the generation of wall-normal vorticity. Further downstream the flow develops many structural features in the form of coherent vortices. The side images show the characteristic crumpled outer edge pattern of the boundary layer formed from individual large-scale structures. A detail of one such mushroom shaped object is shown in Fig. 6. Its appearance is identical to similar objects which are sometimes described as the "typical eddies" of the turbulent boundary layer (7). It is also noteworthy that the appearance of large-scale vortical structures in the calculation is as the end result of many individual vortex filaments undergoing collective organization into larger structures, i.e., they form naturally in the calculation, not by outside intervention.

The pictures in Figs. 1 and 2 show the spread of turbulence downstream as the flow evolves. This is clear evidence that the appearance of turbulence at this Reynolds number is attributed to the boundary layer trip. Another interesting aspect of these figures is the fingering pattern at the leading edge of the turbulent front as the vortices convect downstream. Once the turbulent field passes a given point, then the flow thereafter remains in a state of local turbulence regeneration. The number of vortices in the calculation grows with time until vortex elements reach the downstream end of the domain and are eliminated from the computation. Fig. 7 shows the number of vortices in the calculation as a function of time, as well as the time history of the time step. After $t \approx 0.75$, the number of vortex elements increases more rapidly and the flow transitions from the initial laminar state to turbulent flow. The numerical

time-step reaches a quasi-equilibrium value of about 0.0004, while the number of vortex elements starts to level off after $t \approx 2$. Note that the total number of vortex elements consists of the sum of vortex sheets and vortex tubes, where the number of vortex sheets is constant. The number of vortices indicated in the figure is for just the central panel of the foil and does not include the image panels. Thus, towards the end of this calculation there are approximately 1.5 million vortex elements contributing to the velocity field in the central region.

3.2 Turbulence Statistics

A rigorous assessment of the physical correctness of the computed boundary layer depends on comparing average statistics of the predicted velocity field against measured values. For this purpose, the velocity field at the location $x = 1.1$, corresponding to $Re_x = U_\infty x / \nu = 200,000$ is considered. It is evident from the previous discussion that at any fixed x location it is necessary to wait until after the turbulent front has passed before collecting data with which to evaluate the turbulence statistics. At the time of this writing, the boundary layer simulation has been computed for approximately 4000 time steps with an elapsed time of 2 dimensionless units. The turbulent flow field reached the location $x = 1.1$ sometime after $t = 1$. Consequently, for the purpose of computing flow statistics, data in the time interval $1.5 < t < 2$ spaced at intervals of $\Delta t = .05$ is used.

The velocity data for computing statistics is obtained at 15 equally spaced spanwise locations at $x = 1.1$. The mean wall shear stress at this location can be used to calculate a friction velocity, U^* and with it convert all quantities to wall units, e.g., $y^+ = y U^* / \nu$ and $t^+ = t (U^*)^2 / \nu$. A conversion of time to t^+ units reveals that the elapsed time interval over which the averaging has been done is approximately $\Delta t^+ = 200$, which is much smaller than previous DNS studies have shown to be necessary for fully converged velocity and Reynolds stress statistics. Thus, converged statistics are not yet available for this calculation and will have to be obtained later, after an

opportunity arises to run the solution for a longer time period. Note that the simulation to time 2 has taken approximately one week of CPU time for a calculation using 64 processors.

In terms of wall units, it is also found that the typical transverse length of the sheet mesh is $\Delta z^+ \approx 80$. This is approximately 4 times larger than one would expect to be necessary to accurately represent the correct scale of the wall region structure. As a consequence, for the present simulation vortices are not placed into the flow at a fine enough scale to fully resolve the smallest scale behavior of the low speed streaks and their attendant vortices. Clearly, the results of the previous section suggest that this limitation is not enough to deprive the calculation of physical legitimacy, but it can be expected to have some effect on the mean velocity statistics. For this reason new calculations of the boundary layer will be done with a revised and improved mesh. Despite these shortcomings, it will be seen here that the predicted results give a strong signal that the physicality of the boundary layer simulation shown in the previous section is also reflected in the quantitative statistics.

First consider the mean velocity profile, U^+ displayed in Fig. 8. Also plotted is the standard log law result $U^+ = (1/41) \log(y^+) + 5$, the near wall relation $U^+ = y^+$, and the Spalart mean velocity DNS solution for $R_\theta = 670$ (8). The latter is appropriate since a calculation yields that $R_\theta \approx 575$ for the VorCat simulated boundary layer at $x = 1.1$. It may be noted from the figure that the computed U^+ field displays a log law behavior with the correct slope, and a slight overestimation of the magnitude. It is most likely (a conjecture we hope to conclusively establish in the near future) that such quantitative discrepancies are the result of the limited sheet mesh resolution of the current simulation and the lack of sufficient time averaging. It should also be pointed out that other sources of error have yet to be fully identified, e.g., parametric studies of the effect of numerical parameters such as tube length have not been completed. Moreover, a number of enhancements to the computation of the velocity from the

wall sheets are scheduled to be implemented in the near future.

A plot of the normal Reynolds stresses is shown in Figure 9. While there are some quantitative differences with the DNS solution, the degree of agreement is quite significant, particularly in view of the aforementioned resolution problem. It is clear that the magnitude of the individual stresses are well accounted for in the simulation. This means that the essential anisotropy of the turbulent boundary layer is realistically modeled. This result is all the more significant when it is realized that the Reynolds stress statistics are associated with the chaotic motion and structures in the previously described visualizations of the flow field. The most significant quantitative discrepancies in Fig. 9 are the underestimation of v_{rms} and the over-prediction of w_{rms} close to the wall surface.

The collective behavior of the normal stresses is revealed in the plot of turbulent kinetic energy shown in Fig. 10. As before, the results are suggestive of the effectiveness of the vortex method calculation. Finally, the prediction of Reynolds shear stress is also indicated in Fig. 10. The quantitative accuracy is similar to that in the normal stresses. It is significant that a definite shear stress of the correct sign and magnitude appears as part of the vortex method solution. This confirms the presence of a correct physical organization to the flow, i.e., the Reynolds stress and its attendant momentum exchange are not likely to be correctly predicted without capturing the true physical structures and their dynamics (9).

An examination of the statistics further downstream shows the development of the same trends in the data as at $x = 1.1$. For example, a negative Reynolds shear stress appears at any location once the turbulence passes that point. Of course, resolution continues to decrease with downstream distance, a property of boundary layers that will be addressed in subsequent computations. One other significant point is that the use of the Biot-Savart law in computing velocities is incompatible with imposing a simplified exit plane boundary condition. In fact, the

absence of vorticity downstream of the plate end, affects the velocity on the nearby upstream part of the plate (10). The consequence is a tendency to exaggerate the streamwise velocities. The implication of this for the present calculation is that the boundary layer beyond approximately 1.5 experiences some acceleration that distorts the statistics. The data discussed here, at $x = 1.1$ is safely buffered from this part of the flow field.

4. MULTI-ELEMENT FOIL

Another application of VorCat receiving considerable attention at the present time is that of the flow past a multi-element airfoil (30P30N). To match the conditions of experimental data (11), the Reynolds number is taken to be 9 million and flow at angles of attack $\alpha = 8^\circ$ and $\alpha = 19^\circ$ are considered. The span of the foil is 1.08 and 2 periodic images are placed on either side of the main section in order to enable satisfaction of the periodicity boundary condition in the Biot-Savart calculation of velocities. In view of the high Reynolds number, the sheet mesh is very thin and thus requires a small time step to satisfy the CFL condition. Since the vortex tubes themselves do not have a similar stability requirement, their velocities can be updated according to a larger time step than that used for advancing the vorticity field in the unstructured mesh. The resulting gain in efficiency from this technique brings the calculation of the airfoil flow to a matter of weeks instead of months. Thus, a typical foil calculation until $t = 10$ with $\Delta t = 0.001$ will take 2-3 weeks and have millions of vortices. At the present time, simulations of the multi-element foil have been carried out up to time $t \approx 2.2$ for both $\alpha = 8^\circ$ and $\alpha = 19^\circ$ angles of attack.

The time-step and the number of vortex elements that have been generated during the airfoil calculation are shown in Fig. 11 for the case with $\alpha = 19^\circ$. After about time $t \approx 1.9$, the increase in the number of vortex elements steepens and the flow transitions from the initial laminar state to a turbulent one. The vortex sheet time-

step drops to a value of approximately 0.00003, while the vortex filament time-step is set to 0.0005.

A visualization of the vortex element distribution on the 30P30N foil at time $t \approx 2$ and angle of attack $\alpha = 19^\circ$ is displayed in Fig. 12 from a perspective above and below the airfoil. Vortex filaments are colored according to their circulation strength: red being the strongest and blue the weakest. Across the top of the main airfoil section the flow appears to be going through transition from a laminar state after entering through the forward slot. It is seen that there is increasing levels of streamwise vorticity. At the time in the image, the flow developing on the top surface is just shy of reaching the high vorticity sheet that is shedding off the sharp trailing edge of the main section. The figures suggest that the flow travels above and below the rear flap in a turbulent state.

The relatively short time since the development of turbulence in the calculation completed thus far is evident in the visualizations in Fig. 12. Clearly, it is too early to make comprehensive comparisons of the predicted turbulence statistics against experimental data. Nevertheless, some idea of the trend of the VorCat solution can be gleaned by comparing its prediction of the distribution of the pressure coefficient C_p for $\alpha = 8^\circ$ vs. experimental data, as shown in Fig. 13. The qualitative agreement between curves is encouraging and suggests that the VorCat solution is on track toward capturing this complex flow field.

5. CONCLUSIONS

VorCat represents one approach toward designing a vortex method for the specific goal of simulating turbulent flow. Consideration of some of the fundamental physical processes of turbulence justifies the particular use of vortex sheets and tubes in the VorCat algorithm. Some examples of the results of recent efforts at validating VorCat have been described here. Both the boundary layer and airfoil calculations appear to be on course toward establishing the qualitative and quantitative accuracy of the VorCat scheme. Final results

of these studies should be reached in the near future. Extensions of this work to 3D wings or foils with partial flaps are anticipated.

With the recent award of a NIST ATP grant to VorCat, Inc., a major component of future work will be in gaining a further order of magnitude speedup in the FMM solver and in extending VorCat to include the effects of heat transfer, compressibility and combustion.

ACKNOWLEDGEMENTS

This work was funded through NASA SBIR Phase I contract number NAS1-01033 to Krispin Technologies, Inc. Computer time was provided in part by Cray, Inc.

REFERENCES

- (1) Vincent, A and Meneguzzi, M. (1991), "The spatial structure and statistical properties of homogeneous turbulence" *J. Fluid Mech.* Vol. 225, p.1-20.
- (2) Chorin, A. J. (1994), *Vorticity and Turbulence*, Springer-Verlag, New York.
- (3) Chorin, A. J. (1993), "Hairpin removal in vortex interactions II" *J. Comput. Phys.* Vol. 107, p. 1-9.
- (4) Bernard, P. S, Dimas, A.A. and Collins, J. P., (1999), "Turbulent flow modeling using a fast, parallel, vortex tube and sheet method" in 3rd Int'l Workshop on Vortex Flow and Related Numerical Methods, *European Series in Applied and Industrial Mathematics (ESAIM)* Vol. 7, 46-55. Editors: Giovannini, A., et al.
- (5) Bernard, P. S., Dimas, A. A., Collins, P. and Lottati, I. (2000), "Large scale vortex method simulation of turbulent flow" *Proc. High Performance Computing 2000*, Ed. A. Tentner, SCS, p. 25 - 30.
- (6) Bernard, P. S., Dimas, A. and Lottati, I. (2000), "Vortex method analysis of turbulent flows" in *Vortex Methods*, Kamemoto, K. and Tsutahara, M., Eds., World Scientific, p. 79 - 91.

- (7) Van Dyke, M. (1982), *An Album of Fluid Motion*, Parabolic Press, Stanford, CA.
- (8) Spalart, P.R. (1988), "Direct simulation of a turbulent boundary layer up to $Re_\theta = 1410$ " *J. Fluid Mech.* Vol. 187, p. 61-98.
- (9) Bernard, P. S., Thomas, J. M. and Handler, R. A. (1993), "Vortex dynamics and the production of Reynolds stress", *J. Fluid Mech.*, Vol. 253, p. 385-419.
- (10) Bernard, P. S. (1995), "A deterministic vortex sheet method for boundary layer flow" *J. Comp. Phys.*, Vol. 117, p. 132 - 145.
- (11) Chin, V. D., Peters, D. W. and Spaid, F. W. (1993), "Measurements about a multi-element airfoil at high Reynolds numbers" Boeing Report number MDC 93K0356.

FIGURES

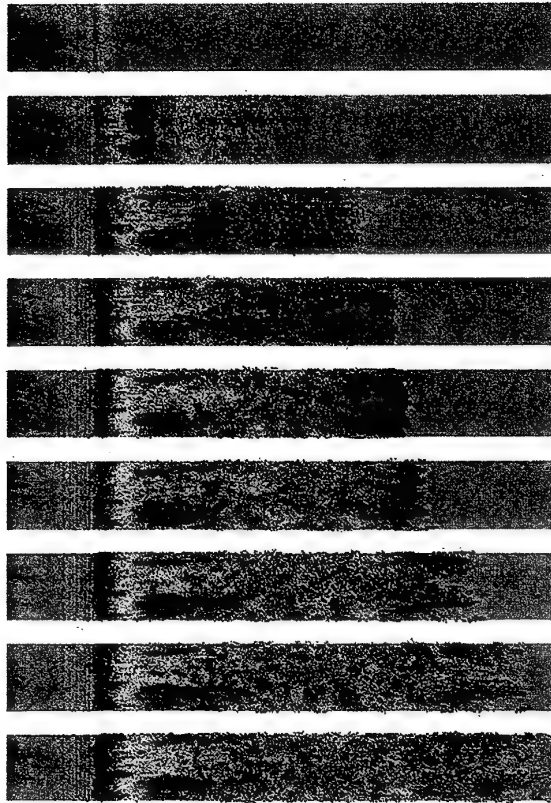


Fig. 1. Top view of the vortex filament field evolution in time (from top to bottom) for the flat-plate boundary layer at $Re = 200,000$.

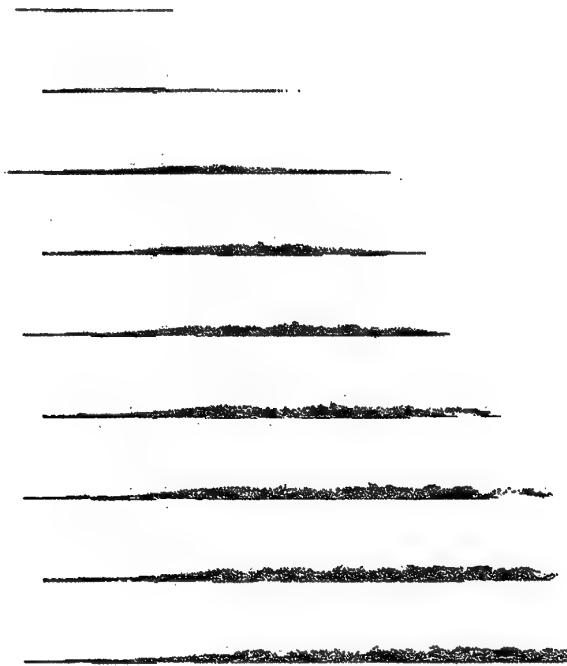


Fig. 2. Side view of the vortex filament field evolution in time (from top to bottom) for the flat-plate boundary layer at $Re = 200,000$.



Fig. 3. Top view of the vortex filament field for the flat-plate boundary layer at $Re = 200,000$



Fig. 4. Side view of the vortex filament field for the flat-plate boundary layer at $Re = 200,000$



Fig. 5. Reorientation of spanwise vorticity in regions of high and low speed fluid in late transition of the turbulent boundary layer.



Fig. 6. Detail of "typical eddy" in the form of a mushroom-shaped vortex in the turbulent boundary layer.

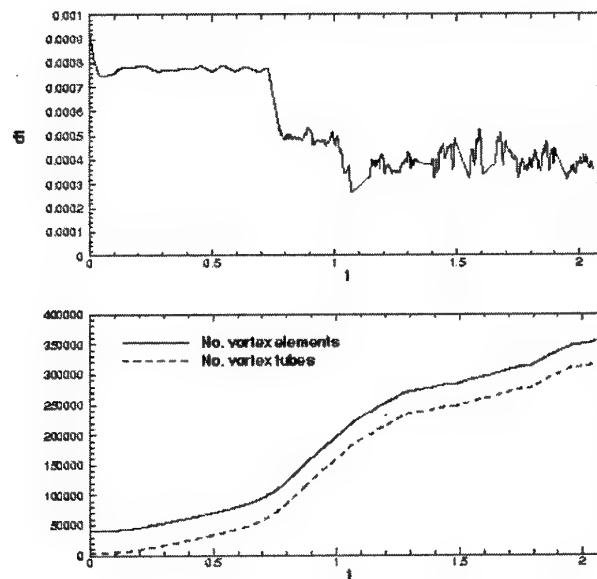


Fig. 7. Time evolution of the time-step and the number of vortex elements for the flat-plate boundary layer at $Re = 200,000$.

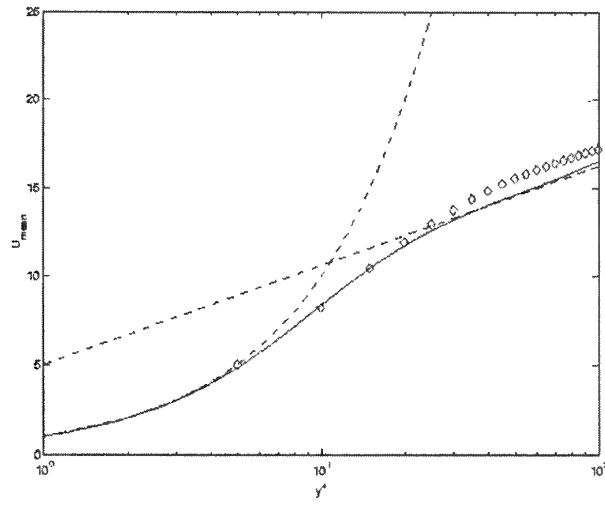


Fig. 8. Mean velocity at $x = 1.1$. Solid line is DNS (8); symbol is VorCat prediction.

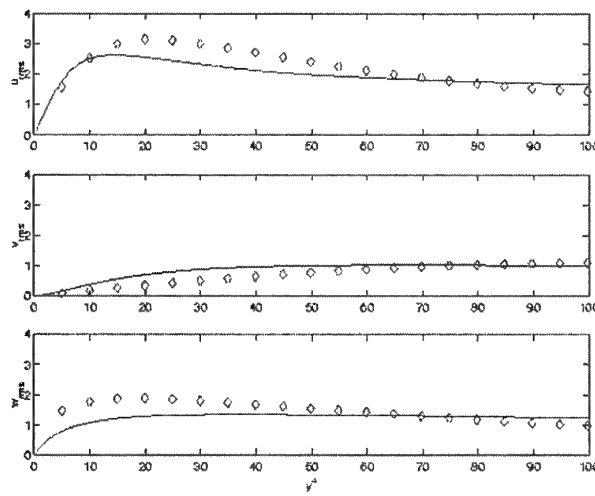


Fig. 9. Normal stresses at $x = 1.1$. Solid line is DNS (8); symbol is VorCat prediction.

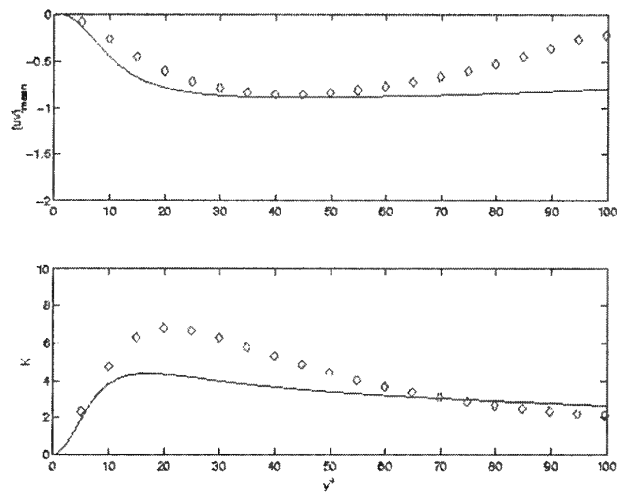


Fig. 10. Turbulent kinetic energy and Reynolds shear stress at $x = 1.1$. Solid line is DNS (8); symbol is VorCat prediction.

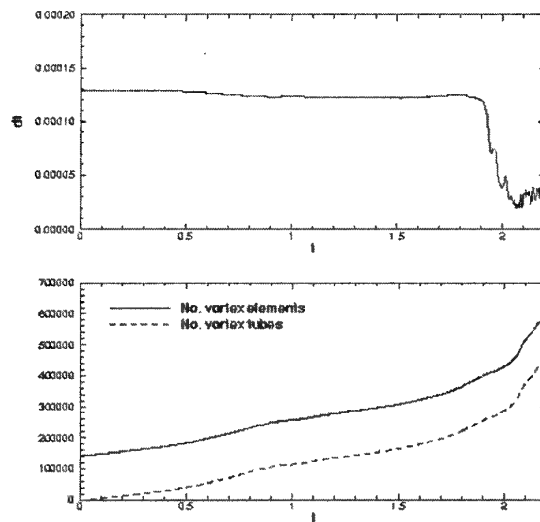


Fig. 11. Time variation of the time step and the number of vortex elements for the 30P30N foil at $Re = 9$ million and $\alpha = 19^\circ$.

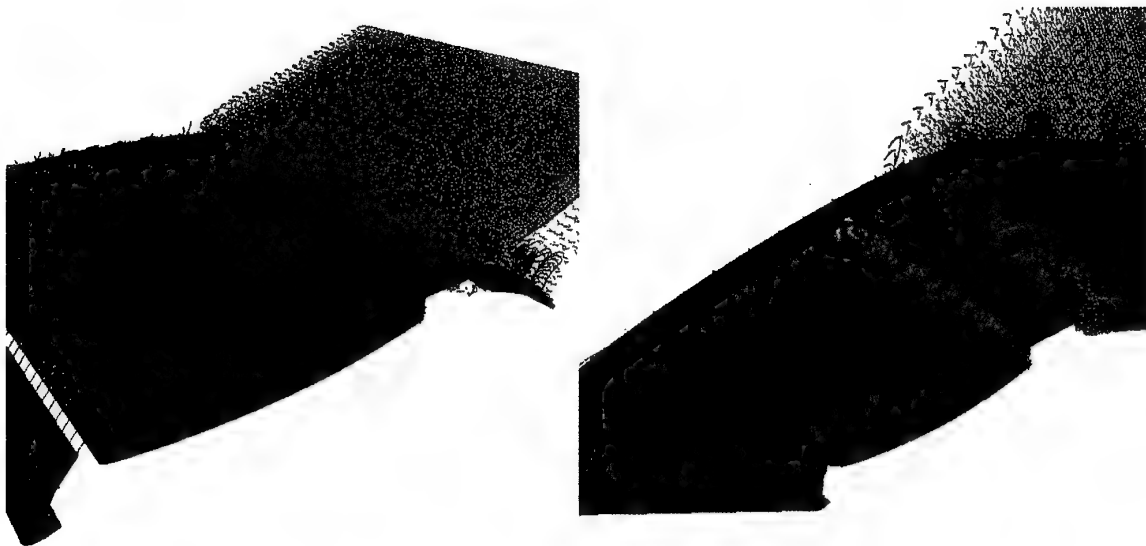


Fig. 12. Top and bottom views of the vortex filament field at $t \approx 2$ for the 30P30N foil at $Re = 9$ million and $\alpha = 19^\circ$.

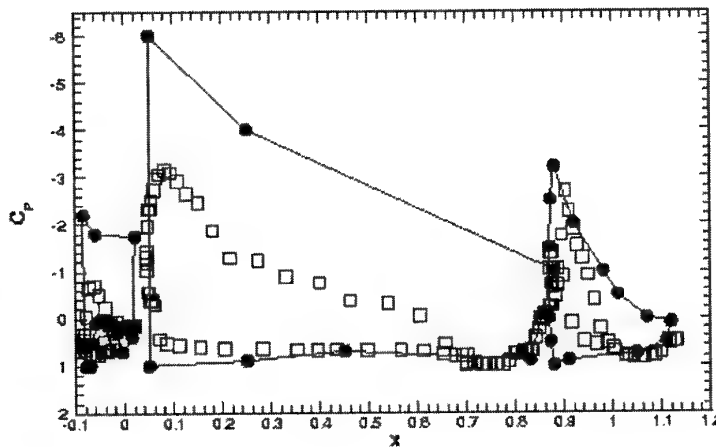


Fig. 13. The pressure coefficient distribution on the 30P30N foil at $Re = 9$ million and $\alpha = 8^\circ$. Solid circles correspond to experimental data; open squares correspond to VorCat predictions at time $t \approx 2$.

Entanglement of a co-rotating vortex pair

Kazumichi Ohtsuka

Department of Energy Engineering, Faculty of Engineering, Yokohama National University
79-5 Tokiwadai, Hodogaya, Yokohama, 240-8501, Japan/ d99jb002@ynu.ac.jp

Ryuji Takaki

Faculty of Technology, Tokyo University of Agriculture and Technology,
2-24-16 Nakamachi, Koganei, Tokyo 184-8588, Japan/ takaki@cc.tuat.ac.jp

Shinsuke Watanabe

Department of Physics, Faculty of Engineering, Yokohama National University
79-5 Tokiwadai, Hodogaya, Yokohama 240-8501, Japan/ wtnb@ynu.ac.jp

Abstract

The Biot-Savart equation or the local induction equation is the major method for analyzing the dynamics of a vortex filament. In this study, we analyze the dynamics of two co-rotating helical vortex filaments by using the entanglement equation describing the dynamics of a vortex pair. A nonlinear theoretical calculation and the physical interpretation was given about configurations and the dynamics of an entangled vortex pair. Especially, we consider the higher order nonlinear effect of this phenomenon. As a consequence, we classified the entangled direction of a vortex pair into two types by mutual distance. From theoretical solution, we found that the left-handed entanglement shortens the mutual distance of a vortex pair. In contrast the right-handed entanglement increases this distance.

1. Introduction

Analysis of the vortex motion offers a useful tool for the study of fluid turbulence. The equation governing vortex dynamics is the Biot-Savart equation and the local induction equation in inviscid fluid. Studies on single and two vortex filaments are major interest in theoretical analysis, where the propagation, evolution and stability are mainly investigated.

In the present paper, we studied the dynamics of a vortex filament and of a co-rotating vortex pair. A

theoretical framework of strong deformation of vortex filament(s) was proposed by Takaki et. al(1) and the solution of helical pairing was given. In the case of a co-rotating vortex pair, entanglement motion of the pair has been observed (2).

This phenomenon is closely related to the present study, and was theoretically analyzed. In section 2, the formulation and solution of helical pairing obtained by Takaki and Hussain was described. In the study by Takaki and Hussain, the distance between co-rotating vortex pair and the degree of entanglement(torsion) were constant. We call this type of the entanglement a global entanglement. In the present paper, we will show theoretically another type of entanglement for a co-rotating vortex pair called a local entanglement, where the distance between two vortex filaments and the degree of entanglement depend on their position. In section 3, we derived the K-dV equation which was analyzed by the present authors in previous paper(3) and higher order nonlinear equation which describe the dynamics of the entanglement vortex pair. In section 4, we visualized 3D configurations and temporally evolution of local entanglement governed by solutions of the K-dV equation and the higher order K-dV equation respectively and compared configurations of these two solutions by means of the dependence of physical parameters. In section 5, some remarks and conclusions are mentioned.

2. Theoretical analysis of helical pairing

Let us consider the motion of a vortex filament interacting with the other one. A vortex filament deforms in a complicated manner, because of the interaction with the other part of the vortex filament considered (the first filament) and also the interaction with the other vortex filament (the second filament). In the evolution of vortex deformations governed by the Biot-Savart law, the velocity of fluid, $u(\mathbf{x})$, at position $\mathbf{x} = (x, y, z)$ of the first filament is expressed by a superposition of inductions by the filament considered and by the second filament,

$$u(\mathbf{x}) = -\frac{\kappa}{4\pi} \int \frac{\mathbf{s} \times d\mathbf{l}}{s^3} - \frac{\hat{\kappa}}{4\pi} \int \frac{\hat{\mathbf{s}} \times d\hat{\mathbf{l}}}{\hat{s}^3}, \quad (1)$$

where the first and second integrals describe the inductions from the first filament and from the second one. Here, κ , $d\mathbf{l}$ and \mathbf{s} are the circulation, the tangent vector of filament and the distance between the point considered, \mathbf{x} , and the other point which induces flow to the point \mathbf{x} . The quantities with hats indicate those about the second filament. We impose here the assumption of axial symmetry, that is, the two vortex filaments are located at symmetric positions with respect to the z -axis. Then the vortex pair is described by the x - and y -coordinates of a point on one filament, $x(z, t)$ and $y(z, t)$, as functions of z and t . Introducing the following complex variable, we describe the position of a filament,

$$W(z, t) = x(z, t) + iy(z, t). \quad (2)$$

Carrying out the integration of Eq.(1) from $-L$ to $-\sigma$ and from σ to L for the first term on the right hand side of Eq.(1), and from $-L^*$ to L^* through s_0 for the second term, we have

$$\begin{aligned} \frac{\partial W}{\partial t} = & iA W'' + \frac{i}{W} \left(1 - \frac{1}{2} W' \bar{W}' \right) \\ & + \frac{(\text{Re } W \bar{W}')^2}{W \bar{W}} - \text{Re}(W \bar{W}'') \\ & + \frac{(\text{Im } W \bar{W}')}{W \bar{W}} W' + O(\epsilon^4), \end{aligned} \quad (3)$$

$$A = \ln \frac{L s_0}{L^* \sigma}. \quad (4)$$

Here ϵ , σ , s_0 and L (L^*) denote a smallness parameter, core radius, mutual distance between the filaments and cut-off lengths. The condition, $\sigma \ll s_0 \ll L, L^*$, is assumed. The prime and bar indicate the differentiation with respect to z and the complex con-

jugate. This equation is called an entanglement equation.

Eq. (3) has the solution of helical pairing:

$$W(z, t) = \exp i k(z - ct), \quad (5)$$

$$kc = -1 + k^2 \left(A + \frac{1}{2} \right). \quad (6)$$

It is interesting to note that the direction of propagation depends on the wave number k . The interaction between vortex pair modifies the direction of propagation. These are the results of global entanglement analysis.

3. Derivation of the K-dV equation expressing local entanglement

In this section, it is shown that Eq. (3) has a solution corresponding to the case of the local helical pair and pair asymptotes to parallel straight configurations in both ends. It is assumed here that the deformation of the filaments is weak and the deviation of one filament from a straight line has a magnitude with order ϵ ($\ll 1$). We now introduce the new coordinates ξ , τ through the equations

$$\xi = \epsilon^{\frac{1}{2}}(z - c_0 t), \quad (7)$$

$$\tau = \epsilon^{\frac{3}{2}} t, \quad (8)$$

g , f are expanded as power series by means of a smallness parameter ϵ ,

$$g = 1 + \epsilon G^{(1)}(\xi, \tau) + \epsilon^2 G^{(2)}(\xi, \tau) + \dots, \quad (9)$$

$$f = \epsilon F^{(1)}(\xi, \tau) + \epsilon^2 F^{(2)}(\xi, \tau) + \dots \quad (10)$$

Substitution of Eqs. (9) and (10) into Eq. (3) and separation of terms according to the first six powers of ϵ yields

$$C_0 = \sqrt{2A}, \quad (11)$$

$$F^{(1)} = \sqrt{\frac{2}{A}} G^{(1)}, \quad (12)$$

$$\begin{aligned} -C_0 G_{\xi}^{(2)} + G_{\tau}^{(1)} = & -(2A + 1) F^{(1)} G_{\xi}^{(1)} \\ & - A F_{\xi}^{(2)} - A F_{\xi}^{(1)} G^{(1)}, \end{aligned} \quad (13)$$

$$\begin{aligned} G^{(2)} - C_0 (G^{(1)} F^{(1)} + F^{(2)}) + \int F_{\tau}^{(1)} d\xi = \\ (A - 1) G_{\xi\xi}^{(1)} - (A + \frac{1}{2}) F^{(1)2} + G^{(1)2} - G^{(2)}, \end{aligned} \quad (14)$$

$$\begin{aligned} C_0 G_{\xi}^{(3)} - G_{\tau}^{(2)} = \\ (2A + 1) [G_{\xi}^{(1)} F^{(2)} + G_{\xi}^{(2)} F^{(1)}] \end{aligned}$$

$$\begin{aligned}
& +A \left[F_{\xi}^{(3)} + G^{(1)} F_{\xi}^{(2)} + G^{(2)} F_{\xi}^{(1)} \right], \\
& G^{(3)} - C_0 \left[F^{(3)} + G^{(2)} F^{(1)} + G^{(1)} F^{(2)} \right] \\
& + \int F_{\tau}^{(2)} d\xi + G^{(1)} \int F_{\tau}^{(1)} d\xi = \\
& +(A-1)G_{\xi\xi}^{(2)} - (A+\frac{1}{2}) \left[2F^{(2)}F^{(1)} + G^{(1)}F^{(1)2} \right] \\
& -G^{(3)} + \left[2G^{(2)}G^{(1)} - G^{(1)3} + \frac{1}{2}G_{\xi}^{(1)2} \right].
\end{aligned} \tag{15}$$

$$\begin{aligned}
& + (A-1)G_{\xi\xi}^{(2)} - (A+\frac{1}{2}) \left[2F^{(2)}F^{(1)} + G^{(1)}F^{(1)2} \right] \\
& -G^{(3)} + \left[2G^{(2)}G^{(1)} - G^{(1)3} + \frac{1}{2}G_{\xi}^{(1)2} \right].
\end{aligned} \tag{16}$$

Eq. (11) is phase velocity of local entanglement. From these six equations, we obtained K-dV equation about $G^{(1)}$ and $F^{(1)}$,

$$2C_0 G_{\tau}^{(1)} + 4(A+1)G^{(1)}G_{\xi}^{(1)} - A(A-1)G_{\xi\xi\xi}^{(1)} = 0, \tag{17}$$

and higher order nonlinear equation about $G^{(2)}$ and $F^{(2)}$ by using the relation

$$F^{(2)} = \frac{A}{C_0}(G^{(2)} - G^{(1)2}),$$

is

$$\begin{aligned}
& 2C_0 G_{\tau}^{(2)} + 4(A+1)\frac{\partial}{\partial \xi} G^{(1)}G^{(2)} - A(A-1)G_{\xi\xi\xi}^{(2)} \\
& = -C_0 \frac{\partial}{\partial \xi} G^{(1)} \int G_{\tau}^{(1)} d\xi + C_0 \frac{\partial G^{(1)2}}{\partial \tau} \\
& - \frac{1}{3}(A+5)\frac{\partial G^{(1)3}}{\partial \xi} + \frac{A}{2}\frac{\partial G_{\xi}^{(1)2}}{\partial \xi} + 2AG^{(1)}\frac{\partial G^{(1)2}}{\partial \xi}.
\end{aligned} \tag{18}$$

Eq. (17), the K-dV equation, has one-soliton solution, we find that

$$G^{(1)}(z, t) = -A_{m1} \text{sech}^2 \theta_1, \tag{19}$$

$$\int F^{(1)}(z, t) dz = -\epsilon^{-\frac{1}{2}} \sqrt{\frac{6A_{m1}(A-1)}{(1+A)}} \tanh \theta_1. \tag{20}$$

The solution of Eq. (18) is given by

$$G^{(2)} = A_{m1}^2 \text{sech}^2 \theta_1 \tanh \theta_1 + c_1 \text{sech}^2 \theta_1 + c_2 \text{sech}^4 \theta_1, \tag{21}$$

$$\begin{aligned}
& \int F^{(2)} dz = \epsilon^{-\frac{1}{2}} A_{m1}^{\frac{3}{2}} \sqrt{\frac{6(A-1)}{A+1}} \\
& \left(-\frac{1}{2} \text{sech} \theta_1 + \frac{1}{6} \tanh \theta_1 + c_3 \text{sech}^2 \theta_1 \tanh \theta_1 \right),
\end{aligned} \tag{22}$$

where θ_1, c_1, c_2, c_3 represents

$$\begin{aligned}
\theta_1(z, t) &= \sqrt{\frac{\epsilon A_{m1}(1+A)}{3A(A-1)}} \times \\
& \left(z - \sqrt{2A}t \left[1 - \frac{\epsilon A_{m1}}{3} \left(1 + \frac{1}{A} \right) \right] \right),
\end{aligned} \tag{23}$$

$$c_1 = A_{m1}^2 \left(\frac{5}{4} + \frac{1}{6(A-1)} \right), \tag{24}$$

$$c_2 = -A_{m1}^2 \left(\frac{5}{8} + \frac{1}{4(A-1)} \right), \tag{25}$$

$$c_3 = -\frac{1}{12} \left(\frac{13}{2} + \frac{1}{(A-1)} \right). \tag{26}$$

From Eqs. (19)-(22), we obtain the solution of Eq. (2). Exact form of the solution of $W(z, t)$ which indicates the position of the first filament is

$$\begin{aligned}
x(z, t) &= (1 + \epsilon G^{(1)} + \epsilon^2 G^{(2)}) \\
& \cos \left(\epsilon \int F^{(1)} dz + \epsilon^2 \int F^{(2)} dz + t \right),
\end{aligned} \tag{27}$$

$$\begin{aligned}
y(z, t) &= (1 + \epsilon G^{(1)} + \epsilon^2 G^{(2)}) \\
& \sin \left(\epsilon \int F^{(1)} dz + \epsilon^2 \int F^{(2)} dz + t \right).
\end{aligned} \tag{28}$$

From the assumption, vortex pair is located at symmetric positions with respect to the z -axis, so the position of second filament is represented by $-W(z, t)$. To obtain the simple representation of these solutions, we rewrite the amplitude of soliton, $\epsilon A_{m1} = A_{m1}$.

4. Visualization of the local entanglement

We'll show shapes and the temporally evolution of the local entanglement which is governed by the K-dV and the higher order K-dV solution. To visualize the propagation and the dynamics of the local entanglement explicitly, figures of vortex shapes in 3D space are shown here observed in the rotating frame of reference around ξ axis and in the wave frame of reference with phase velocity, $c_0 = \sqrt{2A}$, along a vertical axis ξ , too. In Figures 1 to 6, the mutual distance of the each vortex filament is unity of the dimensionless length in the upper and the lower limits. Dimensionless time, $t = 1$, is the same order in which the vortex makes one rotation. The propagation of the local entanglement described by one soliton solution ($G^{(1)}, F^{(1)}$) with $A = 5$, $A_{m1} = 0.9$ is shown in Fig. 1. From this Figure, we can find that a single local-entanglement

of co-rotating vortex pair propagates stably to the direction of negative ξ and makes left-handed local entanglement, where the filament rotates clockwise as ξ increases, by shortening the mutual distance of vortex filaments. In Fig. 2, we show the temporally evolution of two soliton solution of Eq. (17) that the local entanglement with the parameter $A = 5$, $A_{m1} = 0.9$ outstrips the parameter with $A_{m2} = 0.5$. They interact with each other and the same entanglements reappear after the interaction, so we can understand that two local entanglements behave like a particle. To indicate the characteristics of a local entanglement obviously, we show the dependence of 3D configurations of vortex pair with parameters A and A_{m1} in Figures. 3-6. Here Figures. 3 and 4 show lower order solution described by K-dV equation, and Figures. 5 and 6 show higher order K-dV solution described by Eqs. (27), (28). In Figures of higher order K-dV solution, we can find more complex shapes than Fig. 3 and 4. In this model, the increasing A indicates the increasing vorticity, so it makes the strongly interaction of a vortex pair. In Figures. 4, 6, The scale of the local entanglement is growing with the increasing A . To compare configurations of vortex entanglement containing the higher order nonlinear effect with nonlinear effect of K-dV solution, we consider the dependence of parameter A at Figures. 4 and 6. If vortex pair contain higher order nonlinear effect of $G^{(2)}$, $F^{(2)}$, the direction of the entanglement on vortex filaments exists left- and right- handed local entanglement respectively. In Figures 1-4, we can find only left-handed local entanglement, if amplitude g exists, but considering the higher order nonlinear effect, we can find right-handed entanglement locally in Fig. 5, 6. From physical interpretation, we find that the increasing of A_{m1} indicates not only shortening mutual distance by the generating of the left-handed local entanglement but also the increasing mutual distance by the generating of the right-handed local entanglement. This cases are shown in Figures 5, 6. From these Figures, we can find and understand that the degree of the entanglement decreases by the right- handed local entanglement of the higher nonlinear effect. However as is seen from Figures. 1-6, the instantaneous shape of filaments are left-handed helixes globally. As a result, we proof theoretically that the changing of mutual distance is classified by the direction of entanglement. This point is different from previous study

(3). These are the basic characteristics of local entanglement by the higher order nonlinear approximation. This property coincides with experimental observation (2)

5. Conclusion

In this study, we derived the higher order nonlinear equation from an entanglement equation, and showed differences between the local entanglement of vortex filaments described by the K-dV solution(lower order nonlinear solution) and higher order solution. As a consequence, we can find that lower order effect makes only left-handed entanglement, and if we considered the higher order nonlinear effect, right- handed local entanglement exist locally, however configurations of filaments are left-handed helixes globally. It should be noted here that the visualization experiments by Chandrusuda et. al (2) , R. Breidenthal (4) and Hopfinger et. al (5) were made in mixing layers or in a rotating tank. Therefore, effects of background shear or solid rotation would affect the dynamics of filaments. However the present analysis gives a basic understanding of helical pairing. Numerical analysis including the effects of these background fields is an interesting problem to be investigated. Our theoretical results should be compared with the experimental observation under more stable and controlled condition than (2, 5). This problem remains as our future work.

Reference

- (1) R. Takaki and A. K. M. F. Hussain "Dynamics of Entangled vortex filaments," Phys. Fluid **27**, 761 (1984)
- (2) C. Chandrusuda, R. D. Mehta and A. D. Weir and P. Bradshaw "Effect of free-stream turbulence on large structure in turbulent mixing layers," J. Fluid Mech. **85**, 693 (1978)
- (3) K. Ohtsuka, R. Takaki & S. Watanabe "Dynamics of the local entanglement about two vortex filaments described by K-dV equation" Preprint(2000)
- (4) R. Breidenthal "Response of plene shear layer and wakes to strong three dimensional disturbances," Phys. Fluid **23**, 1929 (1980)
- (5) E. J. Hopfinger, F. k. Browand and Y. Gagne "Turbulence and waves in a rotating tank," J. Fluid Mech. **125**, 505 (1982)

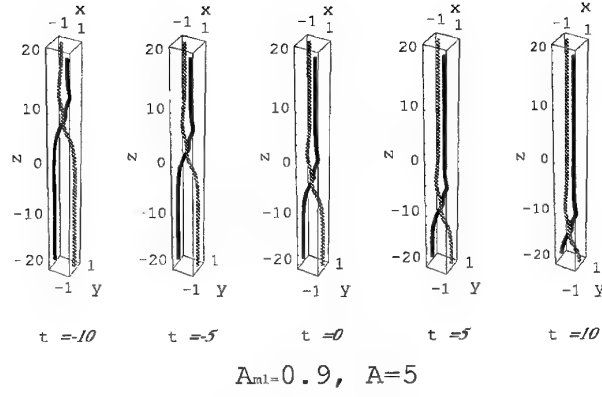


Figure 1: Dynamics of the local entanglement with the amplitude $A_{m1} = 0.9$, and the parameter $A = 5$.

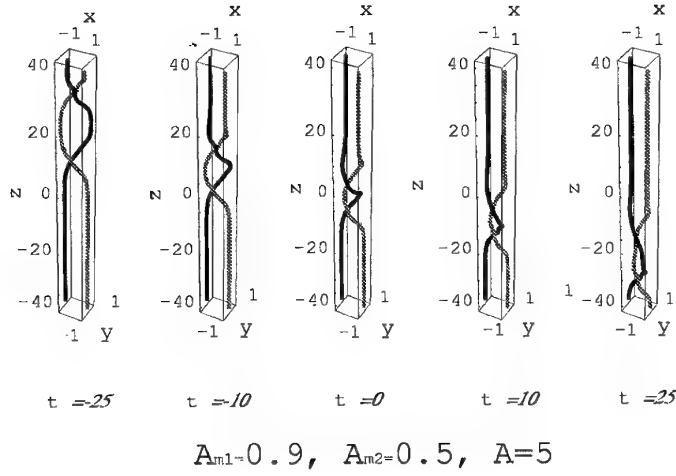


Figure 2: Dynamics of two local entanglements with the amplitude $A_{m1} = 0.9, A_{m2} = 0.5$, the parameter $A = 5$.

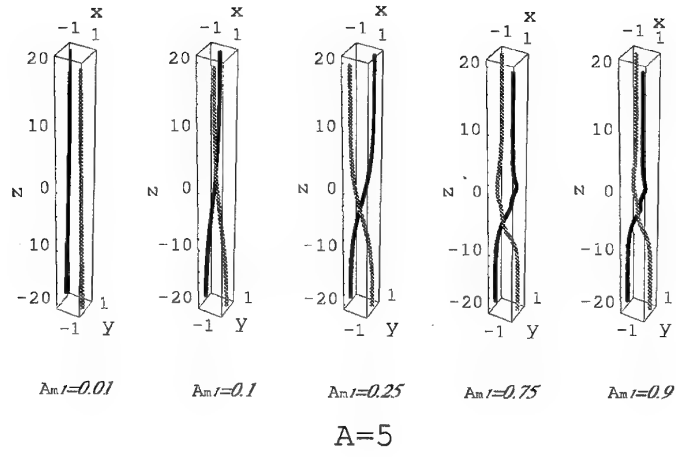


Figure 3: Transition of vortex entanglement shape by the amplitude A_{m1} where the parameter $A = 5$.

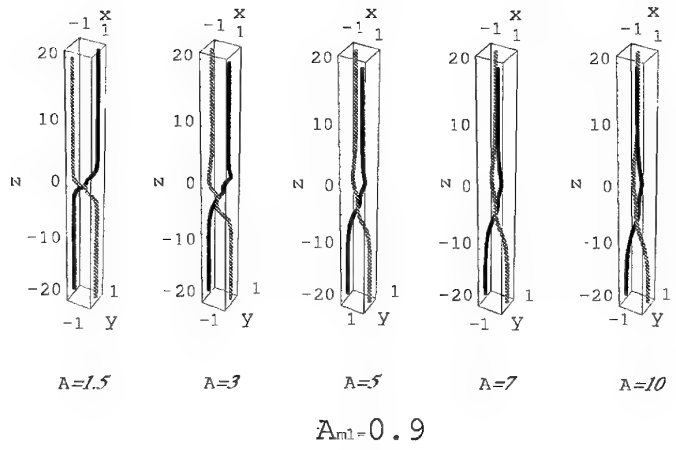


Figure 4: Transition of vortex entanglement shape by the parameter A where the amplitude $A_{m1} = 0.9$.

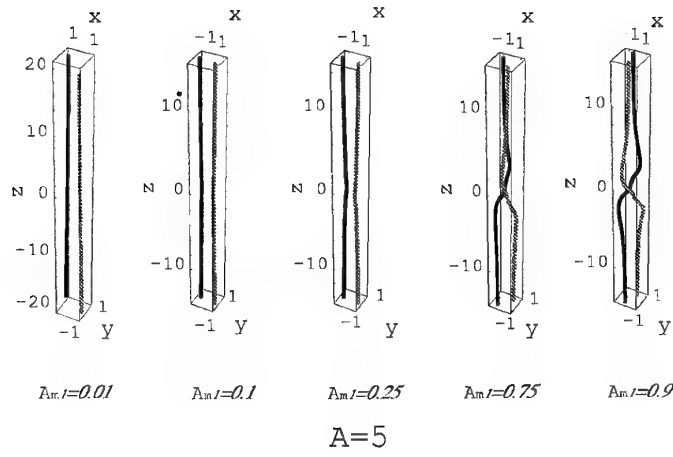


Figure 5: Transition of vortex entanglement shape by the amplitude A_{m1} where the parameter $A = 5$.

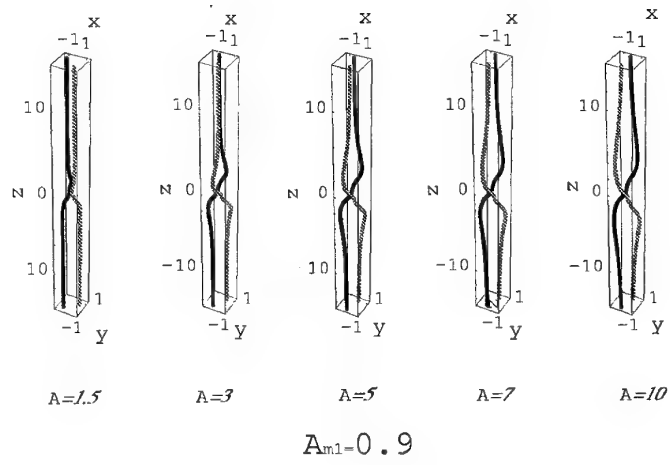


Figure 6: Transition of vortex entanglement shape by the parameter A where the amplitude $A_{m1} = 0.9$.

NUMERICAL INVESTIGATION OF UNSTEADY DEFORMATION OF EDDY STRUCTURE BY VORTEX METHODS

Kota Fukuda*, Kyoji Kamemoto and Baoshan Zhu

Department of Mechanical Engineering and Materials Science, Yokohama National University

79-5 Tokiwadai, Hodogayaku, Yokohama 240-8501, Japan / Email: m00da067@ynu.ac.jp

ABSTRACT

In this study, three-dimensional unsteady deformation of Sub-Core Scale (SCS) eddies of a vortex structure is numerically investigated by discretizing the vortex structure with discrete vortex elements, and the results are used to examine the effect of SCS eddy structures. Furthermore, the velocity energy distribution is calculated. The results indicate detail information on unsteady change of vorticity distribution of SCS eddies, which is hoped to contribute to development of turbulence models for Large Eddy Simulation (LES) by vortex methods.

1. INTRODUCTION

Although the recent progress of Computational Fluid Dynamics (CFD) is quite rapid, the numerical analysis of high Reynolds number flow seems still not easy. Direct Numerical Simulation (DNS) has to take account of all scales of vortices, from the largest scale to the smallest scale (the Kolmogorov dissipation scale). As Reynolds number increase, calculation load becomes large because the ratio of the smallest scale to the largest scale may be of the order of $1/Re_l^{3/4}$, where Re_l is Reynolds number based on the largest scale.

On the other hand, the vortex methods have been developed and applied for analysis of complicated, unsteady and vortical flows related with problems in a wide range of industry, because they consist of simple algorithm based on physics of flow. Vortex Methods simulate flows by discretizing the vorticity-containing regions with discrete vortex elements and tracking these vortex elements in a Lagrangian form.

In vortex methods, numerical resolution is dependent on the scale of discrete elements. If the size of discrete vortex elements approaches the Kolmogorov scale, the calculation could be considered as Direct numerical scheme for turbulence. However, for high Reynolds number flows, the simulation requires huge number of vortex elements, and calculation load becomes large.

Therefore, in order to simulate high Reynolds number flows with vortex methods, turbulence models are necessary to make the calculation manageable and to simulate them in reasonable computational time. Pioneering works have already been attempted by some researchers^[1-4]. In those studies, isotropic eddy-viscosity models used in finite difference LES were applied to vortex methods. In order to obtain higher resolution and develop more applicable models, the effect of unsteady motion of SCS eddies such as effect of splitting and merging of the concentrated vorticity should be considered.

On merging process of the vorticity-containing regions in two-dimensional turbulence, some works have already been attempted. Buntine and Pullin^[5] studied numerically the merging of two Burgers vortices for some Reynolds numbers, and the results were used to calculate the energy spectrum for three-dimensional, homogeneous turbulence.

In this study, as the first stage of development of turbulence models for vortex methods, three-dimensional unsteady deformations of SCS eddies of a vortex structure are numerically investigated by using discrete vortex elements. The vortex structure consists of two spherical vortices with a radially symmetric distribution of vorticity. In order to examine the dependence of the size of the discrete vortex elements, the deformations are calculated with two types of discrete vortex elements. Furthermore, the velocity energy distributions are calculated.

2. MATHEMATICAL BASIS

The governing equations of viscous and incompressible flow are described by the vorticity transport equation.

$$\frac{\partial \omega}{\partial t} + (\mathbf{u} \cdot \text{grad}) \omega = (\omega \cdot \text{grad}) \mathbf{u} + \nu \nabla^2 \omega \quad (1)$$

Where \mathbf{u} is a velocity vector and the vorticity ω is defined as

$$\omega = \text{rot } \mathbf{u} \quad (2)$$

As explained by Wu and Thompson^[6], the Biot-Savart law in an infinite free flow field, can be derived from the definition of vorticity as follows.

$$\mathbf{u} = \int_V \boldsymbol{\omega}_0 \times \nabla_0 G dV \quad (3)$$

Here, subscript "0" denotes the variable, the differentiation and the integration at a location \mathbf{r}_0 , G is the fundamental solution of the scalar Laplace equation with the delta function $\delta(\mathbf{r}-\mathbf{r}_0)$ in the right hand side, which is written for a three-dimensional field as follows.

$$G = \frac{1}{4\pi R} \quad (4)$$

Here, R is defined as,

$$R = |\mathbf{r} - \mathbf{r}_0| \quad (5)$$

It is mathematically understood that velocity fields of viscous and incompressible flows are obtained from the field integration concerning vorticity distributions in the flow field.

3. 3-D VORTEX BLOB MODEL

In the vortex methods, the evolution of vortical region is represented by discrete vortex elements. In this study, vortex blob model is employed. The vortex blob is a spherical model with a radially symmetric distribution of vorticity. The i -th vortex blob is defined by its position $\mathbf{r}_i = (r_x, r_y, r_z)$, its vorticity $\boldsymbol{\omega}_i = (\omega_x, \omega_y, \omega_z)$ and its core radius ε_i . The following equations represent the vorticity distribution around the vortex blob

$$\boldsymbol{\omega}_i(\mathbf{r}) = \boldsymbol{\omega}_i P(|\mathbf{r} - \mathbf{r}_i| / \varepsilon_i) \varepsilon_i^{-3} dV_i \quad (6)$$

$$P(\xi) = \frac{15}{8\pi} (\xi^2 + 1)^{-7/2} \quad (7)$$

Here, $P(\xi)$ is smoothing function proposed by Winckelmann & Leonard (1988)^[7]. The motion of the vortex blob at a location \mathbf{r} is represented by Lagrangian form as follows.

$$\frac{d\mathbf{r}}{dt} = \mathbf{u} \quad (8)$$

On the other hand, the evolution of vorticity is calculated by Eq. (1) with three-dimensional core spreading methods modified by Nakanishi & Kamemoto^[8].

In this method, the stretch term and diffusion term of Eq. (1) are separately considered. The change of core radius due to the stretch is calculated according to following equation.

$$\frac{d\boldsymbol{\omega}}{dt} = (\boldsymbol{\omega} \cdot \text{grad}) \mathbf{u} \quad (9)$$

$$\frac{dl}{dt} = \frac{l_i}{|\boldsymbol{\omega}_i|} \left| \frac{d\boldsymbol{\omega}}{dt} \right| \quad (10)$$

$$\left(\frac{d\varepsilon}{dt} \right)_{\text{stretch}} = \frac{\varepsilon_i}{2 \cdot l_i} \frac{dl}{dt} \quad (11)$$

Here, ε and l are the core radius and the length of the vortex blob model as shown in Fig.1. The viscous term

of Eq. (1) is expressed by the core spreading method. The core spreading method is based on the Navier-Stokes equation for viscous diffusion of an isolated two-dimensional vortex filament in a rest fluid, and the rate of the core spreading is represented as follow.

$$\left(\frac{d\varepsilon}{dt} \right)_{\text{stretch}} = \frac{c^2 \nu}{2\varepsilon_i}, \quad (c = 2.242) \quad (12)$$

Taking two factors into account, each value of a new element is obtained from following equations. In this study, the new elements are replaced into a vortex blob that has equivalent volume.

$$\varepsilon_{i+\Delta t} = \varepsilon_i + \left[\left(\frac{d\varepsilon}{dt} \right)_{\text{stretch}} + \left(\frac{d\varepsilon}{dt} \right)_{\text{diffusion}} \right] \cdot \Delta t \quad (13)$$

$$l_{i+\Delta t} = l_i + \frac{dl}{dt} \cdot \Delta t \quad (14)$$

$$|\boldsymbol{\omega}_{i+\Delta t}| = |\boldsymbol{\omega}_i| \cdot \left(\frac{\varepsilon_i}{\varepsilon_{i+\Delta t}} \right)^2 \quad (15)$$

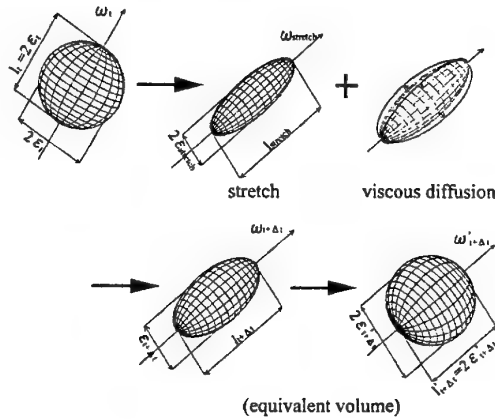


Figure 1 Mechanism of three-dimensional core spreading method for a vortex blob

4. INITIAL CONDITION

We calculated the deformation of the SCS eddies of a vortex structure by discretizing the vortex structure with discrete vortex elements. The vortex structure consists of two spherical vortices with a radially symmetric distribution of vorticity as Eq. (6), Eq. (7).

The discrete vortex elements to represent the vortex structure are based on vortex blob model. In order to examine the dependence of the size of the discrete vortex elements, the deformation of the vortex structure is calculated with discrete vortex elements of two sizes. The core radius of each discrete vortex element is $\varepsilon_i = 0.68\varepsilon$, 1.0ε , where ε_i is the core radius of the discrete vortex elements, and ε is the core radius of the spherical vortex.

The other parameters are set as: Reynolds number $Re = V_0 \varepsilon / \nu = 1.0 \times 10^4$, where V_0 and ε are induced velocity at core radius of the spherical vortex and core

radius of the spherical vortex. The time interval $\Delta t V_0 / \varepsilon$ is 0.01, respectively.

On the discrete vortex elements with the core radius $\varepsilon_i / \varepsilon = 0.68$, the discrete vortex elements are located as Fig. 2, and Fig. 3 shows vorticity distribution. On turbulence, we can consider the order of the ratio of the largest scale to the smallest scale as $Re_i^{3/4}$, where Re_i is Reynolds number based on the largest scale. If we consider core radius of the spherical vortex ε as the largest scale of the vortex structure, $\varepsilon_i / \varepsilon = K_0 / Re^{3/4} = 0.68$ ($K_0 = 680$). The factor K_0 shows relation between the core radius of the vortex blobs and the Kolmogorov dissipation scale. The number of vortex elements to discretize one spherical vortex is 1357 pieces. The core overlapping between neighboring discrete vortex element $\varepsilon_i / h = 2.71$, where ε_i is the core radius of a discrete vortex element and h is the distance between neighboring vortex.

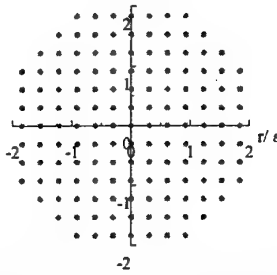


Figure 2 Initial position of discrete vortex elements

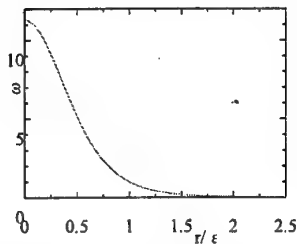


Figure 3 vorticity distribution induced by discrete vortex elements

5. CALCULATION RESULTS AND DISCUSSIONS

5.1. Merging of SCS eddies of two spherical vortices whose vorticity vectors are parallel to each other

Calculations are performed for SCS eddies of a vortex structure. The vortex structure consists of two spherical vortices. The vorticity vectors of the spherical vortex are parallel to each other. The distance of the center of the spherical vortices is 4ε . At initial condition, the position of the two spherical vortices are $r_1 = (0, 0, 0)$, $r_2 = (0, -4, 0)$, and their vortices are $\omega_1 = (20, 0, 0)$, $\omega_2 = (20, 0, 0)$, respectively.

Figure 4 shows instantaneous flow pattern represented

by vorticity vectors of discrete vortex elements at sequential times during merging events.

The merging event shows similar qualitative features as two-dimensional vortex merging considered by Buntine & Pullin^[5].

Initially, two regions of discrete vortex elements rotate around each other. As the vortices rotate, the elements with strong vorticity spiral inwards and eventually merge into a single region of strong vorticity. During this process, the cores rotate more rapidly than other regions, so regions of weaker vorticity are left behind. It is interesting that the vorticity regions with spiral arm structure left behind the strong vorticity region are merged again into the strong vorticity region at the time when the strong region rotate near the weaker vorticity region, on this condition.

5.2. Deformation of SCS eddies of two spherical vortices whose vorticity vectors cross vertically

5.2.1. Deformation of SCS eddies of two spherical vortices whose vorticity vectors cross vertically

Calculations are performed for SCS eddies of a vortex structure. The vortex structure consists of two spherical vortices. The vorticity vectors of the spherical vortices cross vertically. At initial condition, the position of the two spherical vortices are $r_1 = (0, 0, 0)$, $r_2 = (0, -4, 0)$, and their vortices are $\omega_1 = (20, 0, 0)$, $\omega_2 = (0, -20, 0)$, respectively.

On the condition of $\varepsilon_i / \varepsilon = 0.68$, Figure 5 shows instantaneous flow pattern represented by vorticity vectors of discrete vortex blobs at sequential times during deformation events. Initially, the parts of the lower region of discrete vortex elements rotate around another one. As time goes on, the strong vorticity regions of the lower vortices locate into the side of the upper vortices. By the angular velocity induced by the strong vorticity region, the weaker vorticity regions close to each strong vorticity region rotate around them. After that, the vorticity vectors of upper vortex regions rise under the influence of the strong vorticity region of lower vortex. Eventually, upper strong vorticity region and the lower one locate closely with opposing axis. Thus, they are propelled by mutual induced force. That lead to the weaker vorticity region left behind those strong vorticity regions and the region appears to separate to some extent from the strong vorticity region. It is interesting that the weaker vorticity region left behind the strong vorticity regions forms characteristic structure.

On the condition of $\varepsilon_i / \varepsilon = 1.0$, Fig. 6 shows instantaneous flow pattern represented by vorticity vectors of discrete vortex blobs over a time range of $t V_0 / \varepsilon = 0 - 160$. As shown in Fig. 6, initially the lower vortex rotates around the upper one as good as the result under the condition of $\varepsilon_i / \varepsilon = 0.68$. By the angular velocity induced by lower vortex, upper vortex rotates

around lower one. As time goes on, the axis of upper one rises. Thus, both vortexes are propelled by mutual induction process.

5.2.2. Distribution of velocity energy

Figure 7 shows instantaneous iso-surface of velocity energy induced by two spherical vortexes at sequential times under the condition of $\varepsilon_i/\varepsilon = 0.68$. Fig. 8 shows instantaneous iso-surface of velocity energy at sequential times under the condition of $\varepsilon_i/\varepsilon = 1.0$.

At earlier time in this deformation, each velocity energy distribution is similar to each other qualitatively. On the deformation of velocity energy under the condition of $\varepsilon_i/\varepsilon = 0.68$, high velocity energy region become narrow because of the cancellation of opposite vorticity regions. On the other hands, on the velocity energy under the condition of $\varepsilon_i/\varepsilon = 1.0$ keeps the high velocity energy region because the vortex elements deformed by other vorticity region are replaced into a vortex blob that has equivalent volume at every time step.

5.3. Deformation of SCS eddies of two spherical vortexes whose vorticity vectors are in skew position

5.3.1. Deformation of SCS eddies of two spherical vortexes whose vorticity vectors are in skew position

Calculations are performed for SCS eddies of a vortex structure. The vortex structure consists of two spherical vortexes. The vorticity vectors of the spherical vortexes are in skew position. At initial condition, the position of the two spherical vortexes are $r_1=(0,0,0)$, $r_2=(0, -4,0)$, and their vortices are $\omega_1=(20,0,0)$, $\omega_2=(0,0,20)$, respectively.

On the condition of $\varepsilon_i/\varepsilon = 0.68$, Fig. 9 shows instantaneous flow pattern represented by vorticity vectors of discrete vortex blobs at sequential times during deformation events. In this condition, the changes of vorticity region are similar as change of two spherical vortexes whose vorticity vectors cross vertically.

As time goes on, the strong vorticity regions of each spherical vortex locate into the side of the another one. By the angular velocity induced by these strong vorticity regions, each vorticity vector of those strong vorticity regions rise and those regions locate closely with opposing axis. Thus, they are propelled by mutual induced force. That lead to the weaker vorticity region left behind those strong vorticity regions and the region appears to separate to some extent from the strong vorticity region. The structure left behind the strong vorticity regions is little different from one of deformation of two spherical vortexes whose vorticity vectors cross vertically.

On the condition of $\varepsilon_i/\varepsilon = 1.0$, Fig. 10 shows instantaneous flow pattern represented by vorticity vectors of discrete vortex blobs over a time range of $tV_0/\varepsilon = 0-200$. As shown in Fig. 10, initially the lower vortex and the upper vortex rotate around each other as good as deformation of two spherical vortexes whose vorticity vectors cross vertically. As time goes on, the vorticity vector of each vortex rises. Thus, both vortex elements are propelled by mutual induction process.

5.3.2. Distribution of velocity energy

Figure 11 shows instantaneous iso-surface of velocity energy induced by two spherical vortexes at sequential times under the condition of $\varepsilon_i/\varepsilon = 0.68$. Fig. 12 shows instantaneous iso-surface of velocity energy induced at sequential times under the condition of $\varepsilon_i/\varepsilon = 1.0$.

At earlier time in this deformation, each velocity energy distribution is similar to each other qualitatively. On the deformation of velocity energy under the condition of $\varepsilon_i/\varepsilon = 0.68$, high velocity energy region become narrow because of the cancellation of opposite vorticity regions. On the other hands, on the velocity energy under the condition of $\varepsilon_i/\varepsilon = 1.0$ keeps the high velocity energy region because the vortex elements deformed by other vorticity region are replaced into a vortex blob that has equivalent volume at every time step.

6. CONCLUSIONS

Three-dimensional unsteady deformation of Sub-Core Scale (SCS) eddy structures is numerically investigated under various initial conditions by using discrete vortex elements, and the following conclusions were obtained.

1. The deformation of SCS eddies of two spherical vortexes from three initial conditions, are numerically investigated For the case that the vorticity vectors of two spherical vortexes are parallel to each other, the merging event are similar as one of two-dimensional turbulence.
2. For the case that the vorticity vectors of two spherical vortexes cross vertically, the strong vorticity regions and the weaker vorticity regions left behind the strong vorticity region are formed. Further, on the distribution of velocity energy, it was found that at earlier time, the result under the condition of $\varepsilon_i/\varepsilon = 0.68$ is similar as the one of the condition of $\varepsilon_i/\varepsilon = 1.0$, but as time goes on, the high velocity energy region become narrow differently from the result of the condition of $\varepsilon_i/\varepsilon = 1.0$.

3. For the case that the vorticity vectors of two spherical vortexes are in skew position, the strong vorticity regions and the weaker vorticity regions left behind the strong vorticity region are formed. But these structures are a little different from the one of two spherical vortexes whose vorticity vectors cross vertically. Furthermore, on the distribution of velocity energy, it was found that at earlier time, the result under the condition of $\varepsilon_i/\varepsilon = 0.68$ is similar as the one of the condition of $\varepsilon_i/\varepsilon = 1.0$, but as time goes on, the high velocity energy region become narrow differently from the result of the condition of $\varepsilon_i/\varepsilon = 1.0$.

REFERENCES

- (1) Leonard, A. and Chua, K. (1989). "Three-dimensional interaction of vortex tubes", *Physica D (Nonlinear Phenomena)*, 37, pp490-496.
- (2) Mansfield, J.R., Knio, O.M., and Maneveau, C. (1998). "A dynamic LES scheme for the vorticity transport equation: Formulation and a priori tests", *J. of comp. Phys.*, 145, pp.693-730
- (3) Mansfield, J.R., Knio, O.M., and Maneveau, C. (1999). "Dynamic LES of colliding vortex rings using a 3D vortex method", *J. of comp. Phys.*, 152, pp.305-345
- (4) Kiya, M., Izawa, S., and Ishikawa, H. (1999), "Vortex method simulation of forced, impulsively started round jet", *Proc. of the 3rd ASME/JSME Joint Fluids Engng. Conf. San Francisco, July 18-22, FEDSM99-6813*
- (5) Buntine, J.D. and Pullin, D.I. (1989). "Merger and cancellation of strained vortices", *J. Fluid Mech.*, Vol.205, pp.263-295
- (6) Wu, J.C. and Thompson, J.F. (1973). "Numerical Solutions of Time-Dependent Incompressible Navier-Stokes Equations Using an Integro-Differential Formulation", *Computers & Fluids*, Vol.1, pp.197-215
- (7) Winkelmann, G. and Leonard, A. (1988). "Improved vortex methods for three-dimensional flows", *Proc. Workshop on Mathematical Aspect of Vortex Dynamics*.23-35, Leeburg, Virginia.
- (8) Nakanishi, Y. and Kamemoto, K. (1992). "Numerical Simulation of Flow Around a Sphere with Vortex Blobs", *J. Wind Eng. and Ind. Aero*, Vol.46 & 47, pp.363-369.

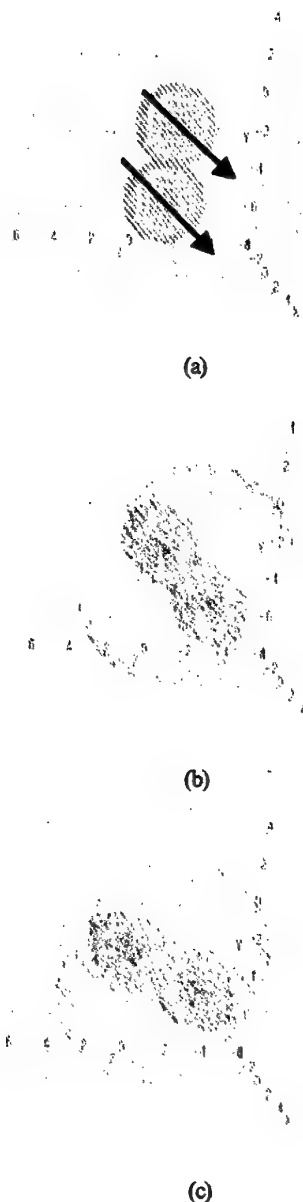
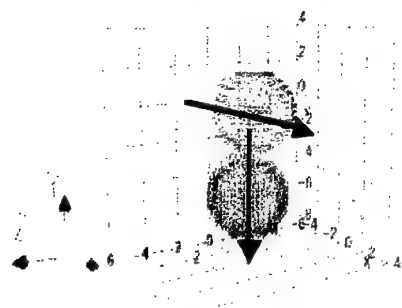
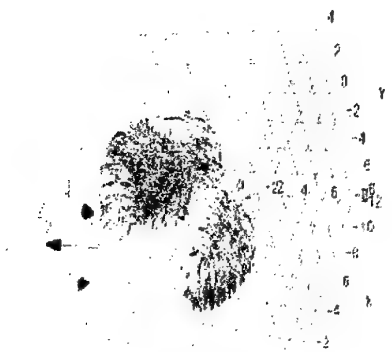


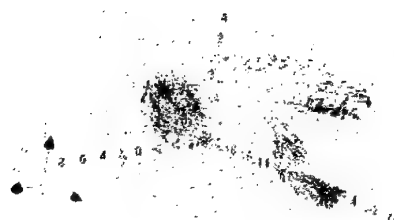
Figure 4 Instantaneous flow pattern represented by vorticity vectors of discrete vortex blobs under the condition of $\varepsilon_i/\varepsilon = 0.68$ (a) $tV_0/\varepsilon = 0$ (b) 80 (c) 280



(a)

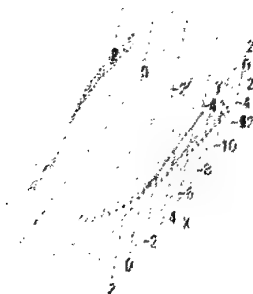


(b)



(c)

Figure 5 Instantaneous flow pattern represented by vorticity vectors of discrete vortex blobs under the condition of $\epsilon_i/\epsilon = 0.68$ (a) $tV_0/\epsilon = 0$ (b) 80 (c) 160

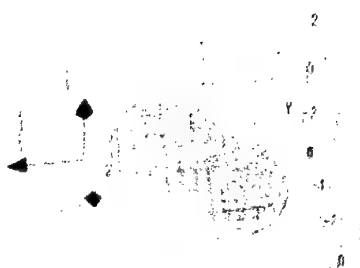


(d)

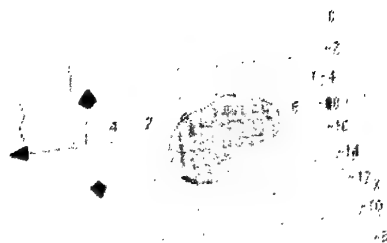
Figure 6 Instantaneous flow pattern represented by vorticity vectors of discrete vortex blobs under the condition of $\epsilon_i/\epsilon = 1.0$ over a time range of $tV_0/\epsilon = 0-160$



(a)



(b)



(c)



Figure 7 Iso-surface of velocity energy induced by discrete vortex blobs under the condition of $\epsilon_i/\epsilon = 0.68$ (a) $tV_0/\epsilon = 40$ (b) 80 (c) 120 (d) 160

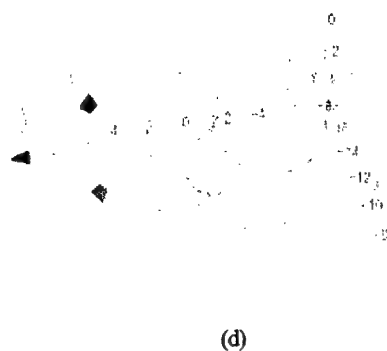
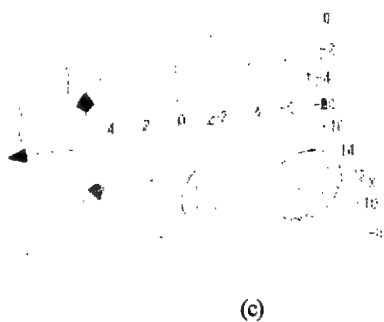
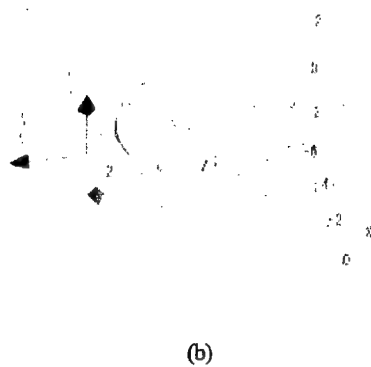
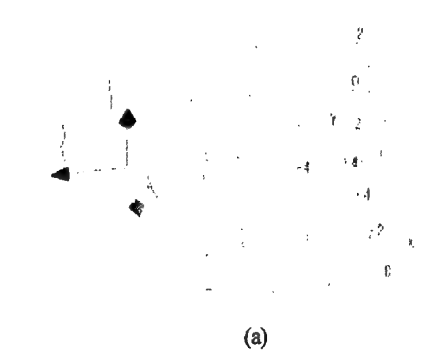


Figure 8 Iso-surface of velocity energy induced by discrete vortex blobs under the condition of $\varepsilon_i/\varepsilon = 1.0$

(a) $tV_0/\varepsilon = 40$ (b) 80 (c) 120 (d) 160

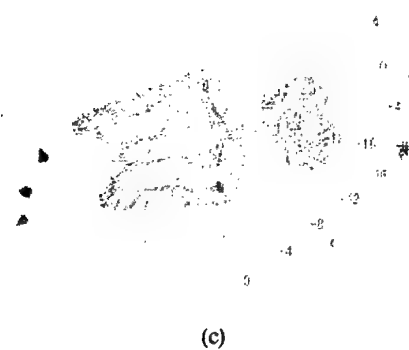
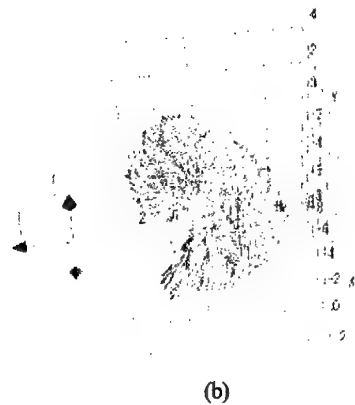
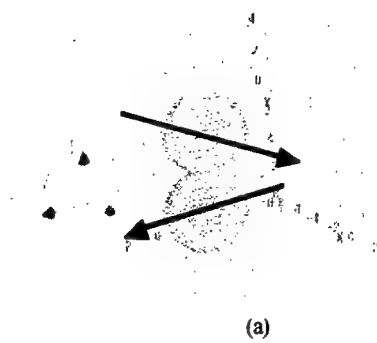


Figure 9 Instantaneous flow pattern represented by vorticity vectors of discrete vortex blobs under the condition of $\varepsilon_i/\varepsilon = 0.68$ (a) $tV_0/\varepsilon = 0$ (b) 50 (c) 70 (d) 260

Figure 11 Iso-surface of velocity energy induced by discrete vortex blobs under the condition of $\varepsilon_i/\varepsilon = 0.68$ (a) $tV_0/\varepsilon = 40$ (b) 80 (c) 160

Figure 10 shows instantaneous flow pattern represented by vorticity vectors of discrete vortex blobs under the condition of $\varepsilon_i/\varepsilon = 1.0$ over a range of $tV_0/\varepsilon = 0-200$

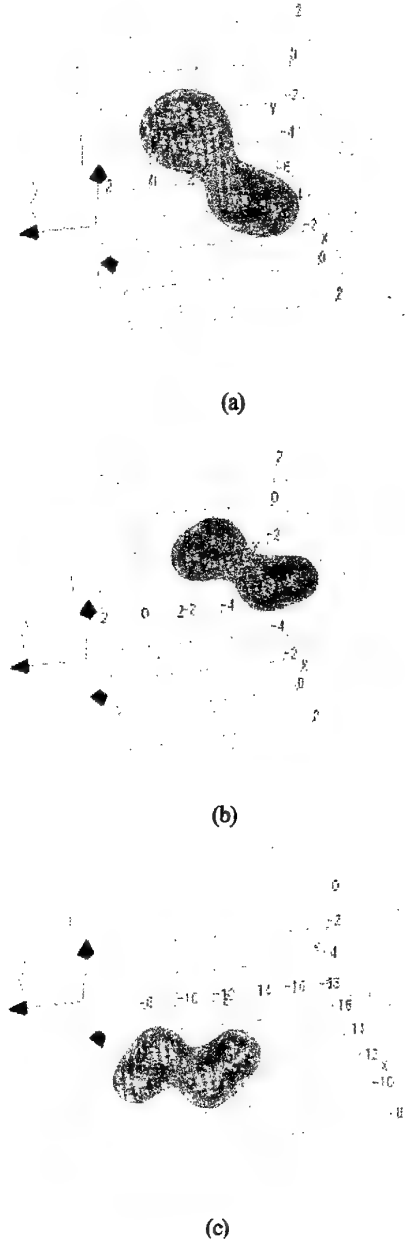
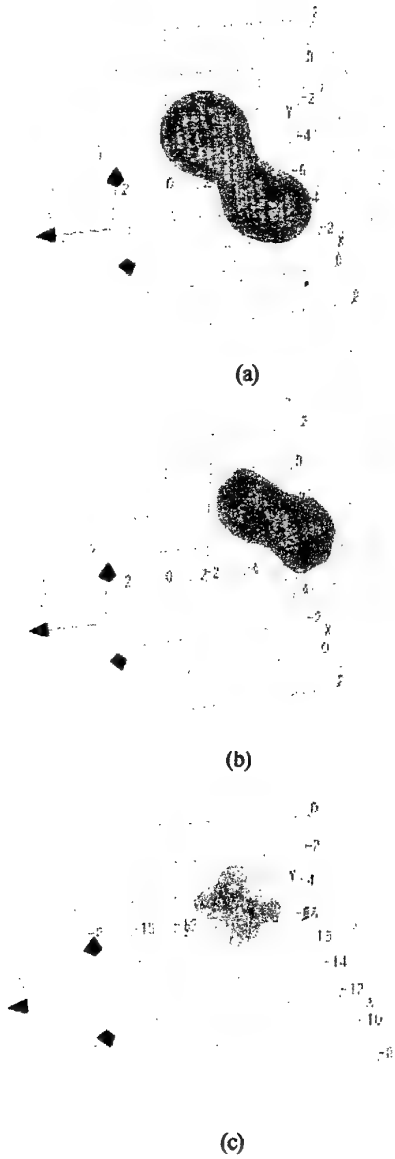


Figure 12 Iso-surface of velocity energy induced by discrete vortex blobs under the condition of $\varepsilon_i/\varepsilon = 1.0$ (a) $tV_0/\varepsilon = 40$ (b) 80 (c) 160

Analysis of the homogeneous isotropic turbulence by a three dimensional vortex element method

Yoshitaka TOTSUKA and Shinnosuke OBI

Department of Mechanical Engineering, Keio University
3-14-1 Hiyoshi, Kouhoku-ku, Yokohama 223-8522, JAPAN
E-mail: d996208@msr.st.keio.ac.jp

ABSTRACT

The performance of the vortex method in simulating turbulent flow has been investigated. Three viscous schemes, including the core spreading method, particle strength exchange method and Fishelov's method are chosen and compared with the existing DNS database of full Navier-Stokes simulation. PSE scheme provides the viscous dissipation process of turbulent kinetic energy at satisfactory level, though there are some different characteristics of the viscous schemes, while the split/merge procedure plays only a minor role. It is concluded that the correct dissipation rate can be obtained by the vortex method simulation using the element that is 4 times larger compared with the Kolmogorov scales of turbulence.

1 INTRODUCTION

There are increasing interests on the application[1] of vortex methods to engineering turbulent flows. For an engineering application, the continuum approach seems to be standstill in the viewpoint of the heavy load and the creation of grid. In contrast, the vortex method is based on the grid-free nature, that is suitable for the turbulent flow analysis with the complex geometry. In light of efficiency, the vortex method has only to represent the confined vorticity field by using the vortex elements, while the fine scale vortex is seen in the various turbulent flow field. Consequently, the vortex method has a potential to develop as a practical tool for turbulent flow simulation.

For consistent representation of turbulent flows, the vortex dynamics over the wide range in time as well as in space must be captured. The depiction of the turbulent flow phenomena is obtained as the energy production process of large scale vortex by the shear of mean flow, the energy cascade process through the nonlinear distortion or stretching of the vortices and the energy dissipation process of the small scale vortex by the viscosity. In the case of the vortex method, to capture the large scale

vortex can be expressed easily[2]. The split/merge procedure and the stretching term in the vorticity equation represents the energy cascade process of the intermediate scale vortex. While the effect of the viscous scheme on the viscous dissipation process of the small scale vortex is questionable.

The dissipation process occurs at the smallest eddies, hence viscous action of vortex elements should represent the dissipation of kinetic energy. Consequently, the resolution scale is the core radius of vortex element in the vortex method. However one question exists: What is the proper scale of vortex element that dissipates the energy?

The most probable answer is the minimum scale in the turbulent flow phenomena, i.e., the Kolmogorov scales L_k that is expressed by

$$L_k = \left(\frac{\nu^3}{\epsilon} \right)^{0.25} = \left(\frac{\nu^3}{U_0^3/L_0} \right)^{0.25},$$

where ϵ , ν , U_0 and L_0 are the energy dissipation rate, kinematic viscosity coefficient, the root mean square of the fluctuation velocity and integral scale. Assumed that the resolution scale as the Kolmogorov scales is required, the necessary number of vortex elements N in each direction is $N = \frac{L_0}{L_k}$ for high Reynolds number flows, the number of vortex elements upscales according to N^3 .

However, there are some arguments in a recent study of DNS[3] that the minimum resolution may be several times larger than the Kolmogorov scales. These results prompted us to investigate whether the vortex method can simulate the viscous dissipation process properly by the resolution of several times of the Kolmogorov scales or not. We also attempted to clarify how the vortex element method can capture the coherent structure of the fine scale vortices that is found in the spectral DNS.

The objective of the present study is to examine the existing viscous scheme in the vortex method to estimate the viscous dissipation process. To restrict our attention to the viscous

dissipation process, the decaying homogeneous isotropic turbulence was chosen and investigated. Three viscous schemes, including the core spreading method[6], particle strength exchange method[PSE][7] and Fishelov's method[8] are investigated and compared with each other and the spectral DNS database[4].

2 BASIC EQUATIONS

2.1 Vortex element method

In a three-dimensional incompressible flow, the time development of vorticity field in the Lagrangian description by

$$\frac{D\omega}{Dt} = (\omega \cdot \nabla)u + \nu \nabla^2 \omega, \quad (1)$$

where u and ω are the velocity and vorticity.

The relation between the velocity field and the vorticity field is determined by Biot-Savart equation as

$$u(x) = -\frac{1}{4\pi} \int \frac{(x-y) \times \omega(y)}{|x-y|^3} dy. \quad (2)$$

The vorticity field is discretized by the vortex elements of spherical blob model as

$$\omega(x_i) = \sum_j \alpha_j \zeta_\sigma(x_i - x_j), \quad (3)$$

where α_i and x_i denotes the vortex strength and position of the i th vortex element. The regularization function ζ_σ is represented by

$$\zeta_\sigma(x_i - x_j) = \frac{1}{\sigma^3} \zeta\left(\frac{|x_i - x_j|}{\sigma}\right). \quad (4)$$

where σ is a smoothing radius.

For the energy and enstrophy calculation, Leonard-Winkelmans' high order algebraic smoothing $\zeta(\rho)$ [5],

$$\zeta(\rho) = \frac{15}{8\pi} \frac{1}{(\rho^2 + 1)^{7/2}}, \quad (5)$$

was used in this study.

The following discretized equations based on the vortex elements update the velocity, position and the vorticity at the center of the i th vortex element in each timestep:

$$u(x_i) = \sum_j K_\sigma(x_i - x_j) \times \alpha_j, \quad (6)$$

$$\frac{d}{dt} x_i = u(x_i), \quad (7)$$

$$\frac{d}{dt} \alpha_i = (\alpha_i \cdot \nabla)u(x_i) + \nu \nabla^2 \alpha_i, \quad (8)$$

where $K_\sigma \times$ denotes the regularized Biot-Savart kernel.

2.2 Viscous schemes

On the quantitative evaluation for the viscous dissipation process, three typical viscous schemes, including the core spreading method, Fishelov's method and particle strength exchange method are chosen and investigated.

The core spreading method has a grid free nature and easily implemented. Fishelov's method and PSE represent the viscous effect due to the magnitude of ambient vorticity, and these two schemes require the remeshing of vortex elements onto a regular lattice for the stability and accuracy. To have the grid free nature in these two schemes, the split/merge procedure was substituted for the remeshing scheme.

2.2.1 Core spreading method

Proposed by Leonard[6], the core radius of the vortex blob σ spreads on the basis of the diffusion equation, that is given as

$$\frac{d\sigma^2}{dt} = 4\nu, \quad (9)$$

where ν denotes the kinematic viscosity coefficient.

Greengard[9] demonstrated that this scheme gives incorrect convection when applied to the Navier-Stokes equation. Though assumed that the timestep and the core of the vortex blob are sufficiently small, the numerical simulation is valid within the finite time. The creation of small scale vortex through the split procedure weakens this disadvantage. This scheme represents the viscous effect as an isolated vortex, thus it is easily implemented.

2.2.2 Fishelov's method

In Fishelov's method[8], the viscous term in the vorticity equation is represented by superposition of the Laplacian on each vortex blob as,

$$\nu \nabla^2 \alpha_i = \sum_j \nu \Delta(\zeta_\sigma(x_i - x_j)) \alpha_j, \quad (10)$$

where $\zeta_\sigma()$ denotes the regularized vorticity kernel in Eq.(4) and the Laplacian is approximated through the explicit differentiation of the smooth function for the vorticity.

In Fishelov's method, the viscous effect decreases the own vortex strength and redistribute the own vortex strength to the surrounding vortex element. Though the viscous effect is varied with the distance between the elements considerably. Therefore to keep the proper distance between the elements, this scheme requires the remeshing of vortex elements onto the regular lattice.

2.2.3 Particle strength exchange method(PSE)

This scheme is introduced by Degond and Mas-Gallic[7], the diffusion operator is replaced by an integral one.

The viscous term in the vorticity equation is represented by

$$\nu \nabla^2 \alpha_i = \frac{2\nu}{\sigma^2} \sum_j (\alpha_j dv_i - \alpha_i dv_j) \eta_\sigma(\mathbf{x}_i - \mathbf{x}_j), \quad (11)$$

where dv_i is the volume of the i th vortex element.

The smoothing function is defined as

$$\eta_\sigma(\mathbf{x}_i - \mathbf{x}_j) = \frac{1}{\sigma^3} \eta\left(\frac{|\mathbf{x}_i - \mathbf{x}_j|}{\sigma}\right),$$

and

$$\eta(\rho) = -\frac{1}{\rho} \frac{d}{d\rho} \zeta(\rho),$$

where $\zeta(\rho)$ denotes the smoothing function for the vorticity in Eq.(5)

This viscous scheme functions as the smoothing of the vortex strength with nearby vortex element. It has similar advantages and disadvantages with Fishelov's method owing to the requirement for the proper particle distribution. In the present study, the split/merge procedure was substituted for the remeshing scheme.

2.3 Split / Merge procedure

The time development of the vortex element's length is monitored through out the computation. When the vortex element's length exceed 1.5 times of the initial length, the split procedure is performed. In the split procedure, the old element is splitted into three elements. These new elements have equal volume, vortex strength and smoothing radius, and the vortex strength of new element is determined so that the kinetic energy in consideration of the nearby element is conserved.

On the other hand, the elements approach to each other and when the distance becomes narrower than 0.2 times of the element length, the merging procedure is performed. In the merging procedure, the position, length and smoothing radius of the merged element are determined by the weight of the element's vortex strength. Then the vortex strength is calculated in the same way as the split procedure. The results indicated that the error of the kinetic energy through the split/merge procedure is estimated to be within 1% of the total kinetic energy.

3 COMPUTATIONS

3.1 Initial condition

Calculation using the vortex blob model was performed for a cubic domain with $2\pi \times 2\pi \times 2\pi$. At the beginning of the com-

putation, $16 \times 16 \times 16$ elements were introduced in the domain and the position of the vortex elements are set at the constant distance in all directions. The vorticity at the center of i th vortex element was given by

$$\omega_1(\mathbf{x}_i) = A_0 \sin r_1(\mathbf{x}_i) \cos r_2(\mathbf{x}_i), \quad (12)$$

$$\omega_2(\mathbf{x}_i) = A_0 \sin r_1(\mathbf{x}_i) \sin r_2(\mathbf{x}_i), \quad (13)$$

$$\omega_3(\mathbf{x}_i) = A_0 \cos r_1(\mathbf{x}_i), \quad (14)$$

where r denotes the random number that is distributed in the interval $0 \leq r \leq 2\pi$.

After the each vortex strength $\omega'(\mathbf{x}_i)$ were determined to satisfy the divergence free property of the vorticity field, the kinetic energy E was calculated. After that, a coefficient C_ω for all the vortex strength is determined to correspond to the initial kinetic energy E_0 in the DNS database [4] as $C_\omega = (E_0/E)^{0.5}$. Then the initial vortex strength for each element is determined as $\omega(\mathbf{x}_i) = C_\omega \omega'(\mathbf{x}_i)$.

3.2 Boundary condition

The periodic boundary condition was applied for along the surfaces of the domain. In addition, the following mirror boundary condition was applied for the π cubic domain that is a part of Kida[10]'s high symmetry flow's concept.

Mirror symmetries with respect to a plane $x_1 = \pi$,

$$\begin{aligned} \omega_1(x_1, x_2, x_3) &= \omega_1(2\pi - x_1, x_2, x_3), \\ \omega_2(x_1, x_2, x_3) &= -\omega_2(2\pi - x_1, x_2, x_3), \\ \omega_3(x_1, x_2, x_3) &= -\omega_3(2\pi - x_1, x_2, x_3). \end{aligned} \quad (15)$$

Mirror symmetries with respect to a plane $x_2 = \pi$,

$$\begin{aligned} \omega_1(x_1, x_2, x_3) &= -\omega_1(x_1, 2\pi - x_2, x_3), \\ \omega_2(x_1, x_2, x_3) &= \omega_2(x_1, 2\pi - x_2, x_3), \\ \omega_3(x_1, x_2, x_3) &= -\omega_3(x_1, 2\pi - x_2, x_3). \end{aligned} \quad (16)$$

Mirror symmetries with respect to a plane $x_3 = \pi$,

$$\begin{aligned} \omega_1(x_1, x_2, x_3) &= -\omega_1(x_1, x_2, 2\pi - x_3), \\ \omega_2(x_1, x_2, x_3) &= -\omega_2(x_1, x_2, 2\pi - x_3), \\ \omega_3(x_1, x_2, x_3) &= \omega_3(x_1, x_2, 2\pi - x_3). \end{aligned} \quad (17)$$

3.3 Calculation condition

The simulations were undertaken for several cases summarized in Table 1. The Reynolds number based on the root mean square of velocity fluctuation and the fundamental wave length at the beginning of the calculation. As shown in the Table 1,

Table. 1 Comparison of length scale: Initial core radius $\sigma=0.5890$, k_k :Kolmogorov wave number, L_k :Kolmogorov scales, Re :Reynolds number, ν :kinematic viscosity coefficient.

σ/L_k	k_k	$L_k(\text{cm})$	Re	$\nu(\text{cm}^2/\text{s})$
2	21	0.2935	20	0.16
4	43	0.1467	80	0.04
8	86	0.0734	300	0.01

the kinematic viscosity coefficient was chosen on the condition that the ratio of initial core radius σ to the Kolmogorov scales L_k is obtained as 2, 4, 8 respectively. In the case of $\sigma/L_k=8$, the results were compared to the spectral DNS database [4].

The timestep was set to 0.005s. This corresponds to that of the spectral DNS [4]. For the time advancement, second order Adams-Bashforce scheme was used.

4 RESULTS AND DISCUSSION

4.1 Vortical structure of decaying homogeneous isotropic turbulence

The time development of the vortical structure shall be argued in the definition of vortex as a positive second invariant.

The second invariant Q is defined as

$$Q = \frac{1}{2}(\|\Omega\|^2 - \|S\|^2), \quad (18)$$

where Ω and S are the antisymmetric and symmetric components of ∇u , respectively.

Figures 1 to 3 show isosurfaces of the second invariant for 10% of Q_{max} on the 2π cubic box in three viscous schemes at $Re=20$. These results indicate that the large scale vortical structure remains with the time advance, while the small scale vortex decay rapidly.

Shown in Fig.6 are the time development of the number of elements. At $Re=20$, the number of vortex elements is approximately the same through the computation in all viscous schemes. Notice that the creation of the smaller scale vortex through the split/merge procedure is not necessary to dissipate the kinetic energy.

Figure 7 indicates the time development of the distance from a nearest element that is averaged for all elements. At $Re=20$, the average distance decreases with the time advance, although the creation of the vortex elements rarely occurred. This tendency indicates that the vortex elements concentrate of themselves to organize the larger vortical structure.

Figures 4 (a) to (c) show the time histories of the second invariant's isosurface for 10% of Q_{max} on the 2π cubic box in

PSE scheme at $Re=20, 80, 300$ and $t=1.5s$. As shown in Fig.6, at $Re=300$, the number of the vortex elements begins to increase from the time $t=0.5s$. Consequently the advent of the small scale vortical structure at $Re=300$ depends on the creation of the vortex elements through the split procedure.

The results at $Re=300$ in Fig.7 indicate that the concentration of the vortex elements were more prominent than that of $Re=20$. That means the strong trend for the self-organization by the vortex elements. The split/merge procedure scarcely effect on the average distance since the average distance decrease monotonously.

4.2 Divergence of vorticity

The consistency of the calculation was checked in the view point of the divergence free property of the vorticity field. The vorticity field obtained in Eq.(3) is not generally divergence free in a three-dimensional vortex element method. Although the divergence free vorticity field is given at the beginning of the calculation, the divergence-free property is violated with the time advance. Some relaxation schemes were proposed to satisfy the divergence free vorticity field. In this study, the relaxation scheme was not used to exclude its side effect in the viscous scheme.

Next, the error from the divergence free vorticity field is calculated. The divergence free vorticity field $\omega^{df}(x_i)$ is calculated by taking the curl of the velocity field as

$$\begin{aligned} \omega^{df}(x_i) &= \nabla \times u_i \\ &= \sum_j \left[\left(\zeta_\sigma(x_i - x_j) - \frac{q_\sigma(x_i - x_j)}{|x_i - x_j|^3} \right) \alpha_j \right. \\ &\quad \left. + \left(3 \frac{q_\sigma(x_i - x_j)}{|x_i - x_j|^3} - \zeta_\sigma(x_i - x_j) \right) \right. \\ &\quad \left. \times \frac{((x_i - x_j) \cdot \alpha_j)}{|x_i - x_j|^2} (x_i - x_j) \right], \end{aligned} \quad (19)$$

where the smoothing function $q(\rho) = -\rho^2 \frac{d}{d\rho} G(\rho)$ and $q_\sigma = q(|x|/\sigma)$. The relative error ε from the divergence free vorticity field was calculated as,

$$\varepsilon = \frac{\left(\sum_{i=1}^N \sum_{j=1}^3 (\omega_j^{df}(x_i) - \omega_j(x_i))^2 \right)^{1/2}}{\left(\sum_{i=1}^N \sum_{j=1}^3 (\omega_j^{df}(x_i))^2 \right)^{1/2}}, \quad (20)$$

where $\omega_j^{df}(x_i)$ and $\omega_j(x_i)$ represent the vorticity obtained in Eq.(3), divergence free vorticity, the direction of vorticity vector and the j th vortex element.

Figure 5 shows the comparison of the time development of relative error ϵ from the divergence free vorticity field in three viscous schemes at $Re=20$ and 300 .

About the same trend was shown in all the viscous schemes. The results at $Re=20$ show nearly 3% of the constant relative error ϵ , even though the relaxation scheme was not used. On the contrary, the results at $Re=300$ indicate that the error increased by 3 times compared to the initial error.

The results in higher Reynolds number mean that the high strain and weak dissipation increase the deviation from the divergence-free. This issue is risen to the surface to calculate the turbulent shear flow.

4.3 Kinetic energy and decay rate

4.3.1 decay of Energy spectrum

The vortex scale and the energy spectra is discussed in three viscous schemes. Figure 8 (a) to (c) show the time development of the energy spectra and the wavenumber in three viscous schemes at $Re=20$. In this case, the Kolmogorov wavenumber is 2 times of the wavenumber due to the initial core radius of vortex elements. The initial element's wavenumber was approximately 11 and that was not the peak of the energy spectrum. The peak in the initial energy spectrum was obtained at the wavenumber that correspond to the mirror symmetries of π box.

The energy spectra at high wavenumber decayed more rapidly than that at low wavenumber. This implies that the larger scale vortex tends to sustain with time development and it agrees with the results obtained from the isosurfaces of second invariant.

In the case of the core spreading method, as the time evolves, the energy spectra shift to the lower wavenumber than that in the other viscous schemes. The shift to the lower wavenumber corresponds to the increase of the core radius.

Figure 9 show the time development of the energy spectra and the wavenumber in PSE schemes at $Re=20$. As shown in Fig.9, the creation of smaller scale vortex through the split/merge procedure shifts the distribution of the energy spectra to slightly higher wavenumber.

4.3.2 decay of kinetic energy

Figure 10(a) to (c) show the time development of kinetic energy in three viscous schemes compared with each other and spectral DNS [4]. The time is nondimensionalized by k/ϵ where k and ϵ is the kinetic energy and the dissipation rate. As shown in Fig.10, PSE scheme is superior to the other viscous scheme

on the consistency with the DNS database.

At $Re=300$, all viscous schemes can't dissipate the energy properly as spectral DNS database, since the creation of smaller vortex elements can't supplement the dissipation. On the Fishelov's method, further examination is indispensable on the treatment for the concentration of vortex elements. Because the kinetic energy begin to increase, as the distance between the elements getting smaller.

The time averaged decay coefficient was estimated for $0.5s$ from the beginning in Fig.11 to compare with the various Reynolds number. For $0.5s$ from the beginning, the split/merge procedure didn't work, since the number of the vortex elements is approximately steady. The decay coefficient c is defined as

$$E = E_0 \exp(-ct), \quad (21)$$

where E_0 and t are the initial kinetic energy and time, respectively. As the Reynolds number increases, the decay rate of kinetic energy decrease in all viscous schemes. Whereas the decay rate is different significantly in each viscous schemes. The highest decay rate was the Fishelov's method and the lowest one is the core spreading method.

5 CONCLUSION

Direct numerical simulation of decaying homogeneous isotropic turbulence was investigated by using a three-dimensional vortex element method. Three viscous schemes, including core spreading method, particle strength exchange method and Fishelov's method were investigated for decay rate of kinetic energy.

Isosurface results by using second invariant exhibited that large vortical structure remains as the time evolves. Self-organization of the vortex elements acts a main role on the formation of this large vortical structure. These results correspond to that are obtained from energy spectra.

Results from energy spectra have indicated that spectra in core spreading method shift to lower wavenumber with time advance than other schemes. These were due to the increase of core scale.

Results for the decay of kinetic energy have indicated that PSE scheme is superior to other viscous scheme on the consistency with DNS database. Due to the support of the split/merge procedure, correct dissipation rate can be obtained by using PSE and core scale of element that is 4 times of Kolmogorov scales.

ACKNOWLEDGEMENTS

The authors are grateful to Prof. S.Masuda for valuable discussions. The first author thanks to Keio Leading-edge Laboratory of Science and Technology and Keio Kougakukai for providing the scholarship.

REFERENCES

- [1] Bernard, S.P., Dimas, A.A., and Lottati, I.(1999). "Vortex method analysis of turbulent flow", Proceedings of First International Conference on Vortex Methods, Kobe, Nov.4-5, p.79-91.
- [2] Sethian, A.J., and Ghoniem, F.A.(1988). "Validation study of vortex methods", Journal of Computational Physics, Vol.74, p.283-317.
- [3] Tanahashi, M., Iwase, S., Uddin, A.Md., and Miyauchi, T.(1999). "Three-dimensional features of coherent fine scale eddies in turbulence", Turbulence and Shear Flow Phenomena -1, Eds. S. Banaerjee & J.K. Eaton, p.79.
- [4] Miyauchi, T. and Ishizu, T.,(1991). "Direct numerical simulation of homogeneous isotropic turbulence, - Decay of passive scalar fluctuation", ERCOFTAC Classic DNS database C.48, <http://cfd.me.umist.ac.uk/ercoftac/>
- [5] Winckelmans, G.S. and Leonard, A.(1993). "Contributions to vortex particle methods for the computation of three-dimensional incompressible unsteady flows", Journal of Computational Physics, Vol.109, p.247-273.
- [6] Leonard, A.(1980). "Vortex methods for flow simulation", Journal of Computational Physics, Vol.37, p.289-335.
- [7] Degond, P. and Mas-Gallic, S.(1989). "The weighted particle method for convection-diffusion equations", Mathematics of Computation, vol.53, p485-507.
- [8] Fishelov, D.(1990). "A new vortex scheme for viscous flows", Journal of Computational Physics, Vol.85, p.211-224.
- [9] Greengard, C.(1985). "The core spreading vortex method approximates the wrong equation", Journal of Computational Physics, Vol.61, p.345-348.
- [10] Kida, S.(1985). "Three-dimensional periodic flows with high-symmetry", Journal of the Physical Society of Japan. Vol.54, No.6, p2132-2136.

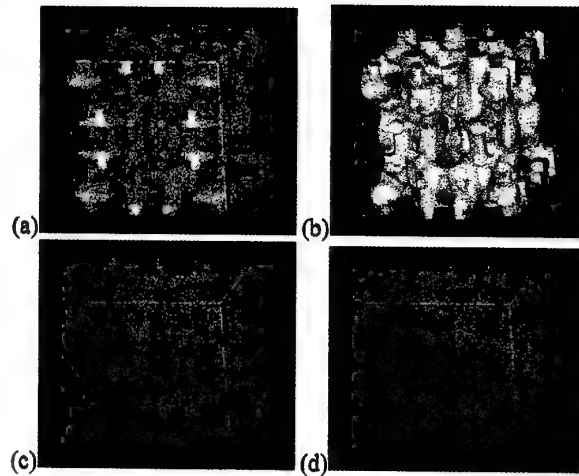


Fig. 1 The isosurfaces of Q for 10% of $|Q_{max}|$ in the core spreading method at $Re=20$ and (a) $t=0.0(s)$, (b) $t=0.5(s)$, (c) $t=1.0(s)$, (d) $t=1.5(s)$.

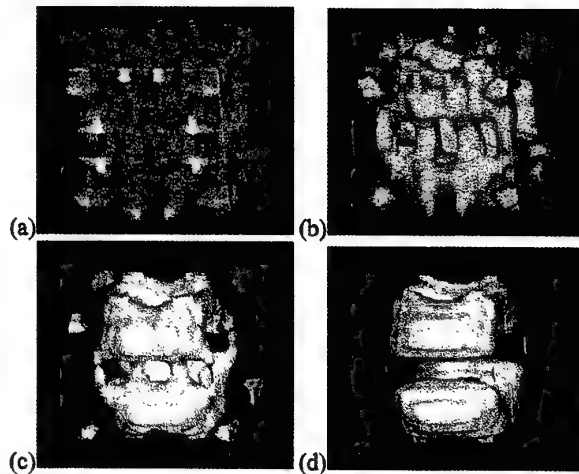


Fig. 2 The isosurfaces of Q for 10% of $|Q_{max}|$ in Fishelov's method at $Re=20$ and (a) $t=0.0(s)$, (b) $t=0.5(s)$, (c) $t=1.0(s)$, (d) $t=1.5(s)$.

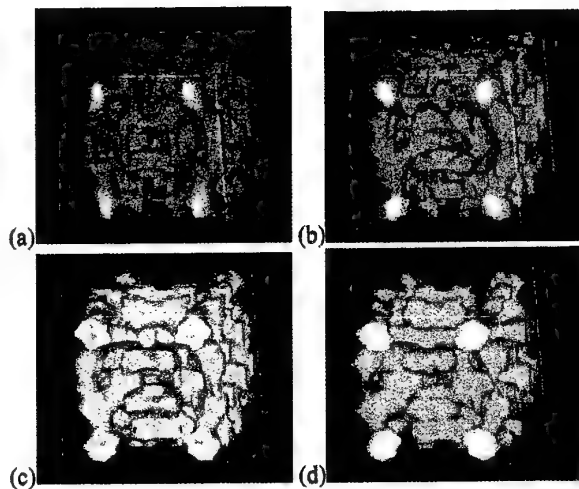


Fig. 3 The isosurfaces of Q for 10% of $|Q_{max}|$ in PSE at $Re=20$ and (a) $t=0.0(s)$, (b) $t=0.5(s)$, (c) $t=1.0(s)$, (d) $t=1.5(s)$.

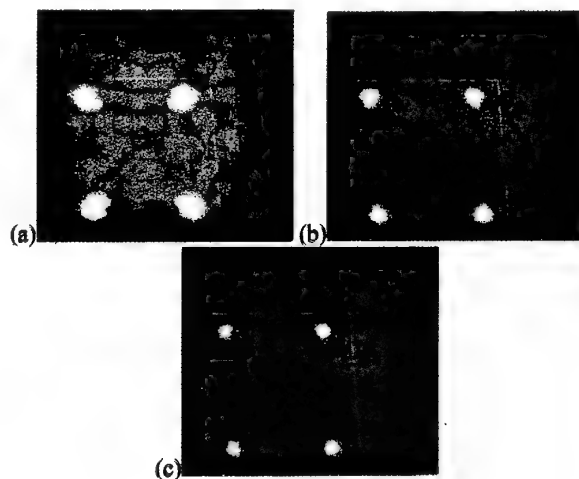


Fig. 4 The isosurfaces of Q for 10% of $|Q_{max}|$ in PSE at (a) $Re=20$, (b) $Re=80$, (c) $Re=300$ and $t=1.5(s)$.

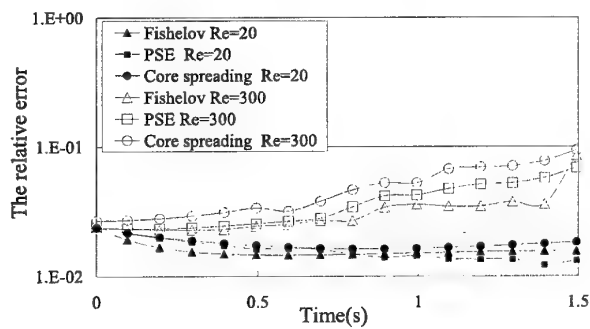


Fig. 5 The comparison for the relative error of the vorticity field in three viscous scheme.

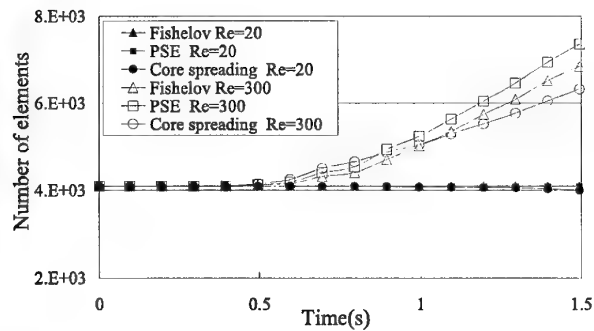


Fig. 6 The time development of the vortex elements number.

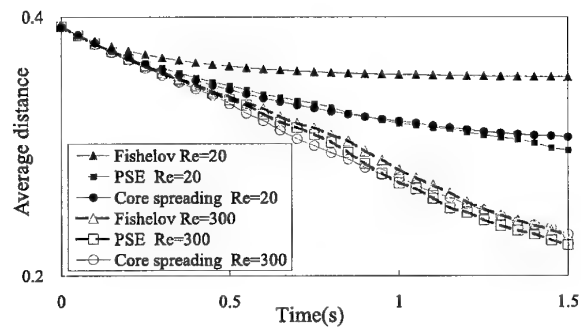


Fig. 7 The time development of the distance between the elements.

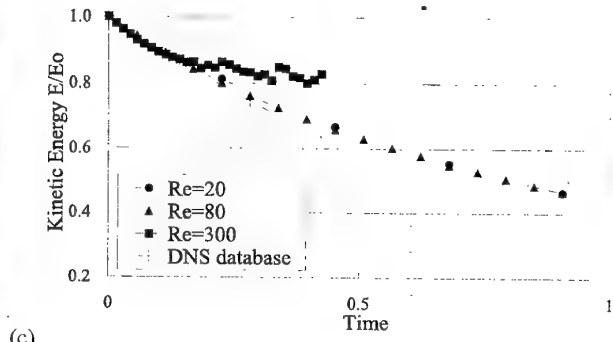
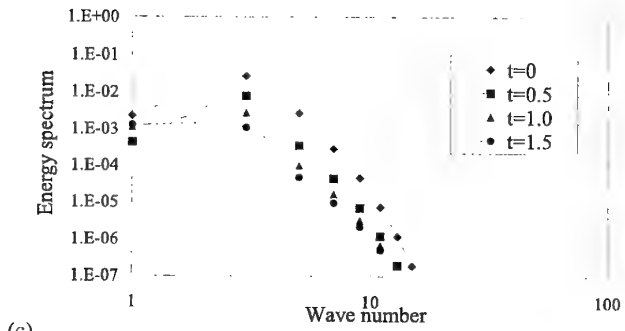
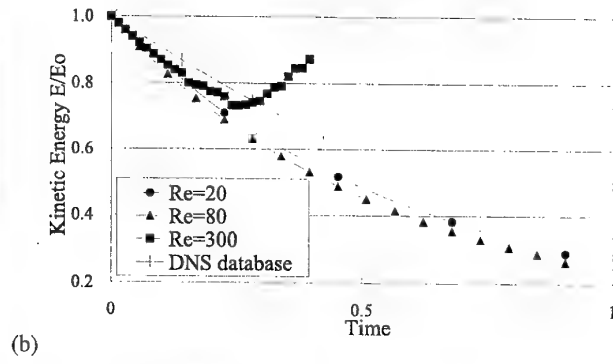
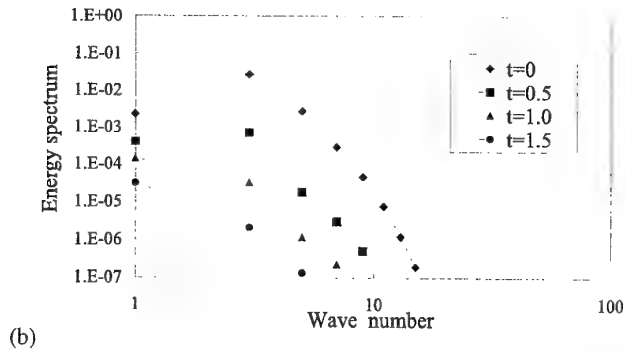
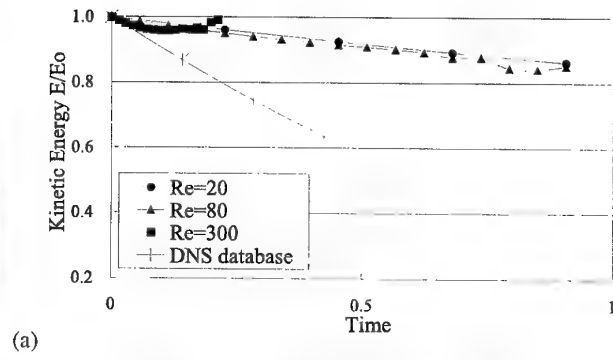
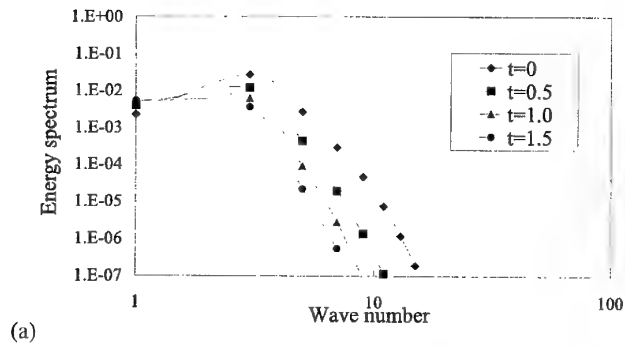


Fig. 8 The time development of the energy spectra, (a)core spreading method, (b)Fishelov's method, (C)PSE at $Re=20$.

Fig. 10 The time development of kinetic energy, (a)core spreading method, (b)Fishelov's method, (c)PSE at $Re=20, 80, 300$.

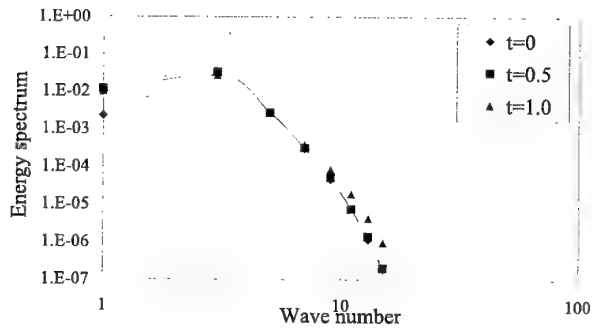


Fig. 9 The time development of the energy spectra in PSE scheme at $Re=300$.

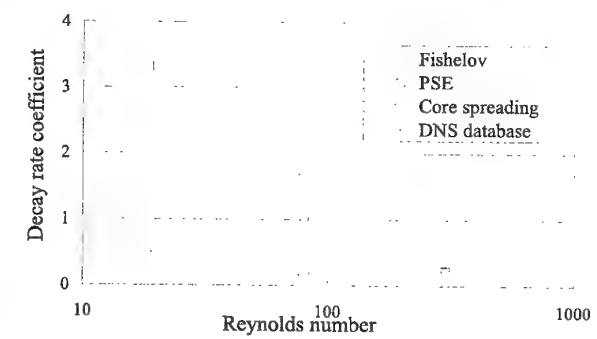


Fig. 11 The decay rate of kinetic energy as a function of the Reynolds number.

PRODUCING ARTIFICIAL TURBULENCE BY THE VORTEX METHODS

Yoshifumi Ogami, Kazuie Nishiwaki and Yoshinobu Yoshihara

Department of Mechanical Engineering, Ritsumeikan University
1-1-1 Noji-Higashi, Kusatsu 525-8577, Japan /Email: ogami@cf.d.ritsumei.ac.jp

ABSTRACT

A simple and accurate numerical method is presented to produce velocity fluctuations that are determined by the prescribed physical quantities and qualities of turbulence. The fluctuations are directly obtained by solving a system of nonlinear equations. This method requires as many computer memories and computations as one-dimensional case even for the three dimensional calculations. The solutions are quite accurate with less than 0.01% relative errors. Then these solutions are used to examine the capability of the vortex methods to produce turbulent flows with the prescribed parameters. Although the energy spectra by the vortex method scatter to some extent, they are distributed along the prescribed spectra even at the higher frequency regions. It can be said that the vortex methods are able to simulate the target turbulence qualitatively well. Also it is found that the solutions with the LES model increase and deviate from the target spectrum at the higher frequency regions.

1. INTRODUCTION

One of the crucial problems for the turbulent simulation is how to set up the inlet boundary condition that provides the physical quantities and qualities of turbulent flows as listed below.

1. Longitudinal and transverse spectra: $E_L(f)$ and $E_T(f)$
2. Root mean square of the velocity fluctuation:

$$\text{RMS} = \sqrt{\frac{\int_0^T u(t)^2 dt}{T}}$$
3. Mean velocity: U
4. Kinematic viscosity: ν
5. Longitudinal and transverse integral scale: L_{11} and L_{22}
6. Kolmogorov scale: $\eta = \left(\frac{2\nu^3 L_{11}}{u^3} \right)^{\frac{1}{4}}$

7. Gaussian frequency distribution of velocity fluctuations

Several researchers have presented numerical methods to produce velocity fluctuations for the turbulent simulation. Iwatani (1) used the multidimensional autoregressive processes to produce velocity fluctuations from the power spectra and the cross spectra of fluctuations. The velocity fluctuations are given by a linear summation of white noise and of the past fluctuations with the coefficients that are obtained by solving a system of linear equations. The simulated results are somewhat noisy and have to be modified to obtain desired RMS.

Maruyama and Morikawa (2), and Kondo et al. (3) used the method of the trigonometric series with Gaussian random coefficients, in which the velocity fluctuations are expressed by a series of cosine and sine functions. The coefficients of the functions are obtained by solving a system of linear equations. They do not consider the distant grid points to lighten computational loads. This may produce numerical errors that cannot be disregarded.

The first purpose of this paper is to present, in Section 2, a simpler and more accurate numerical method to produce series of velocity fluctuations. In this method, it is the longitudinal or transverse spectrum that is expressed by a series of cosine and sine functions. The coefficients of the functions are the velocity fluctuations themselves and these are obtained by solving a system of nonlinear (not linear) equations.

On the other hand, the vortex methods have been used for turbulent flow simulations with LES models (4, 5, 6, 7). Leonard and Chua (4), and Kiya and Izawa (5) incorporated the Smagorinsky model into the vortex methods by means of nonlinear core-spreading algorithm. Mansfield et al. (6) presented a LES scheme using a dynamic eddy diffusivity model. Kamemoto et al. (7) reviewed the recent works on LES modeling and emphasized the necessity of developing wall turbulence models. To see if these models are really working, it is necessary to examine whether the energy spectrum produced by these vortex methods are expected one because LES is to handle the energy spectrum of the lower frequency by modeling that of

the higher frequency. Before doing this examination, it should be confirmed whether the vortex methods can handle the energy spectrum or are versatile enough to produce the prescribed energy spectrum. Totsuka and Obi (8) calculated the energy spectrum using vortices and reported that the spectrum deviates from the target at the higher frequency regions when the resolution (vortex number) is insufficient.

The next purpose of this paper is to examine the capability of the vortex methods to produce flows with the prescribed physical quantities and qualities of turbulence mentioned at the beginning of this section. To do so, in Section 3 we apply the results of Section 2 to the vortex methods, and the LES model is used to see how it works. It is found that the vortex methods are able to simulate the target turbulence qualitatively well, and that the solutions with the LES model increase and deviate from the target spectrum at the higher frequency regions.

2. PRODUCING VELOCITY FLUCTUATION

2.1 One-Dimensional Case

In this subsection, we introduce a method to numerically produce a series of velocity fluctuations, which are determined by the prescribed physical quantities or parameters mentioned in Section 1.

We consider the following longitudinal spectrum $E_L(f)$ and the Eulerian time-correlation $R_E(\tau)$,

$$\begin{cases} E_L(f) = \overline{4u(t)^2} \int_0^T R_E(\tau) \cos(2\pi f \tau) d\tau \\ R_E(\tau) = \frac{u(t) \cdot u(t + \tau)}{u(t)^2} \end{cases} \quad (1.1)$$

In this case, the directions of the mean velocity U and the velocity fluctuation $u(t)$ are the same.

Equation (1.1) can be rewritten as

$$\begin{aligned} E_L(k) = & \frac{4T}{N^2} \left[\sum_{j=0}^{N-1} u_j \cos\left(2\pi j \frac{k}{N}\right) \right]^2 \\ & + \frac{4T}{N^2} \left[\sum_{j=0}^{N-1} u_j \sin\left(2\pi j \frac{k}{N}\right) \right]^2 \end{aligned} \quad (1.2)$$

where the following relations have been employed.

$$\begin{cases} \Delta t = \frac{T}{N}, \Delta f = \frac{1}{T}, t = j \Delta t = j \frac{T}{N}, \\ f = k \Delta f = \frac{k}{T} = \frac{k}{n \Delta t}, \\ f_{\max} = \frac{n}{2T} = \frac{1}{2 \Delta t} \text{ (Nyquist frequency)} \end{cases} \quad (1.3)$$

Equation (1.2) is regarded as a system of simultaneous quadratic equations with N unknowns, u_j . Since the number of the equations is $N/2$ ($k = 0 \sim N/2 - 1$), we divide Eq.(1.2) into two parts

to supply the deficit in the equations as

$$\begin{cases} \frac{T}{N} \sum_{j=0}^{N-1} u_j \cos\left(2\pi j \frac{k}{N}\right) = \text{sign}(r) \sqrt{\frac{T}{N} E_L(k) \frac{r^2}{r^2 + 1}} \\ \frac{T}{N} \sum_{j=0}^{N-1} u_j \sin\left(2\pi j \frac{k}{N}\right) = \text{sign}(r) \sqrt{\frac{T}{N} E_L(k) \frac{1}{r^2 + 1}} \end{cases} \quad (1.4)$$

where r is a random number which we introduce expecting the frequency distribution of the solutions to be Gaussian. This division makes the equation number the same as the unknowns, and also linearizes the nonlinear equations, which promotes the convergence of the solutions.

When $k = 0$ for the lower equation in Eq.(1.4), all the coefficients in the left hand side become zero, which makes no sense. We use the following equation instead in order to incorporate RMS, which is given as one of the prescribed parameters.

$$\text{RMS} = \sqrt{\frac{\sum_{j=0}^{N-1} u_j^2}{N}} \quad (1.5)$$

Equation (1.5) is nonlinear and thus the system of the simultaneous equations has to be treated as a nonlinear system. Even so, the velocity fluctuations can be obtained directly by as simple manner as just solving these equations because the unknowns are the velocity fluctuations themselves unlike the methods mentioned in Section 1 (1, 2, 3).

It should be noted that the solutions to the system of equations (1.4) and (1.5) are not unique so that various sets of the solutions depending on the initial values and the random numbers can be obtained. This is another advantage of our method because of the coincidence with the characteristics of the turbulent flows.

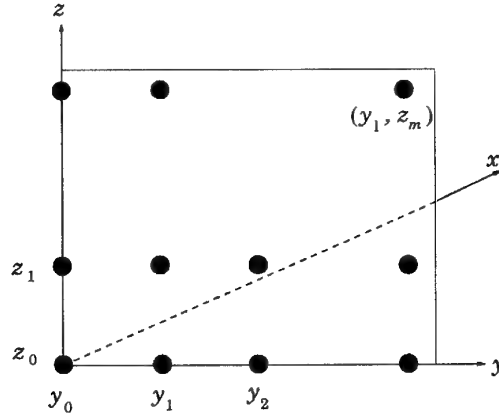


Figure 1 Three dimensional model

2.2 Three-Dimensional Case

Since the inlet boundary is usually two-dimensional,

Table 1 Longitudinal and transverse correlations to consider

	x - direction	y - direction	z - direction
u	longitudinal	transverse	transverse
v	transverse	longitudinal	transverse
w	transverse	transverse	longitudinal

Table 2 Parameters used in simulation

Mean velocity: U	2.11m/s
Kinematic viscosity: ν	$1.562 \times 10^{-5} \text{ m}^2/\text{s}$
Root mean square of velocity fluctuations: rms	0.159m/s
Time step: Δt	$1.94 \times 10^{-3} \text{ s}$
Grid spacing in flow direction: Δx	$U \Delta t$
Integral scale: L_{11}	$5 \Delta x$
Fluctuation number: N	200
Grid number in x - and y - directions: M	20

the series of velocity fluctuations passing through the boundary grids must be produced on the basis of both the longitudinal correlation and of the transverse correlation.

As shown in Fig.1, we consider that the inlet boundary is located on the y-z plane, and that the fluid flows in the x - direction.

First, we obtain the velocity fluctuations u_j^{00} that pass through the grid point (y_0, z_0) by the method explained in subsection 2.1. Then the fluctuations u_j^{10} going through the next grid point (y_1, z_0) can be also obtained by the same procedure except that the following transverse correlation has to be incorporated.

$$\sum_{j=0}^{N-1} \frac{u_j^{00} u_j^{10}}{N} = \sum_{j=0}^{M/2-1} \frac{1}{T} E_T(k) \cos\left(2\pi \frac{k}{M}\right)$$

where $E_T(k)$ is the energy spectrum of the transverse correlation, and M is the grid number on the y- and z- axes. Further, the fluctuations u_j^{20} at the next point (y_2, z_0) require the following two more equations.

$$\sum_{j=0}^{N-1} \frac{u_j^{00} u_j^{20}}{N} = \sum_{j=0}^{M/2-1} \frac{1}{T} E_T(k) \cos\left(2\pi \frac{2k}{M}\right)$$

$$\sum_{j=0}^{N-1} \frac{u_j^{10} u_j^{20}}{N} = \sum_{j=0}^{M/2-1} \frac{1}{T} E_T(k) \cos\left(2\pi \frac{k}{M}\right)$$

Generally, the fluctuations u_j^{lm} at (y_l, z_m) are calculated by Eqs.(1.4) and (1.5), and the following equations

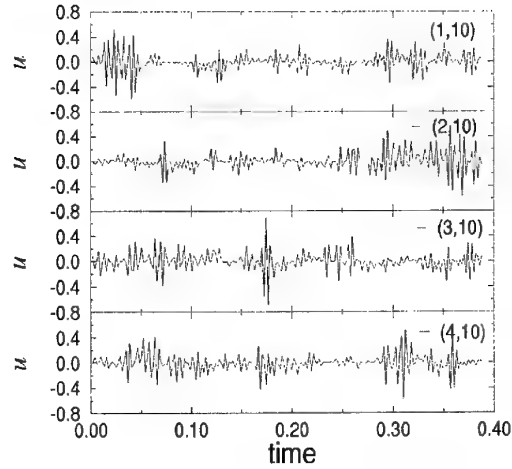


Figure 2 Calculated velocity fluctuations

$$\sum_{j=0}^{N-1} \frac{u_j^{l'm} u_j^{lm}}{N} = \sum_{j=0}^{M/2-1} \frac{1}{T} E_T(k) \cos\left(2\pi \frac{(l-l')k}{M}\right) \quad (0 \leq l' < l)$$

$$\sum_{j=0}^{N-1} \frac{u_j^{lm'} u_j^{lm}}{N} = \sum_{j=0}^{M/2-1} \frac{1}{T} E_T(k) \cos\left(2\pi \frac{(m-m')k}{M}\right) \quad (0 \leq m' < m)$$

The velocity fluctuations of the y- and z- components, v_j and w_j , can be obtained by the same procedures mentioned above except that the longitudinal correlation and the transverse correlation should be considered for each case (Table 1).

In this way, the velocity fluctuations on the inlet boundary are obtained from one grid to the next. The number of unknowns is always N regardless of the grid number M , and these are easily obtained by solving a system of nonlinear equations. This effectively saves the computer memories and loads.

2.3 Examples

For example simulations are conducted using the parameters listed in Table 2. The longitudinal and transverse spectra given in ref.(9) are used, and these spectra are illustrated in Fig.3 by the solid line (longitudinal) and by the dashed line (transverse). The system of nonlinear equations is solved by the subroutine "hybrd" provided in the free software package called minpac (downloadable at, for example, <http://www.netlib.org/minpack/>).

Figure 2 shows four examples of the simulated velocity fluctuations, which pass through the points (y_1, z_{10}) , (y_2, z_{10}) , (y_3, z_{10}) and (y_4, z_{10}) . Though these are artificially produced, they resemble well those experimentally measured. Each series of the

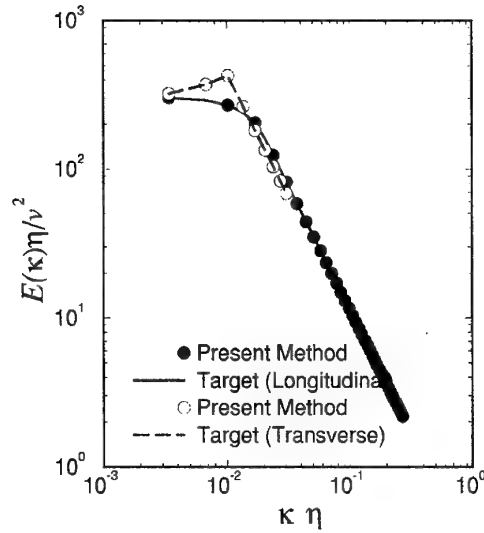


Figure 3 Target and calculated energy spectra

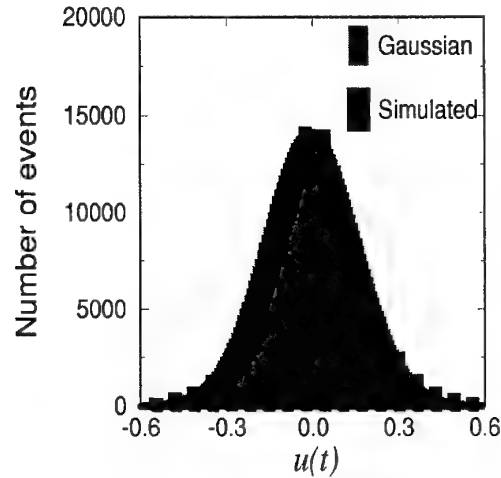


Figure 4 Frequency distribution

fluctuations is clearly different but the statistic is the same.

The spectra calculated from these fluctuations precisely agree with the target spectra as compared in Fig.3. The relative error is less than 0.01%, which can be controlled by the input parameter.

Figure 4 indicates that the velocity fluctuations are adequately random so that their frequency distribution fits the Gaussian distribution.

3. APPLICATION TO THE VORTEX METHOD

In this section, the capability of the vortex methods to produce flows with the prescribed physical quantities and qualities of turbulence is examined.

Table 3 Parameters used in simulation

Mean velocity: U	10m/s
Kinematic viscosity: ν	$1.562 \times 10^{-5} \text{ m}^2/\text{s}$
Root mean square of velocity fluctuations: rms	1.0m/s
Time step: Δt	$8.2 \times 10^{-4} \text{ s}$
Grid spacing in flow direction: Δx	$U \Delta t$
Integral scale: L_{11}	Δx and $30\Delta x$
Fluctuation number: N	1024
Grid number in y - and z - directions: M	2 and 1

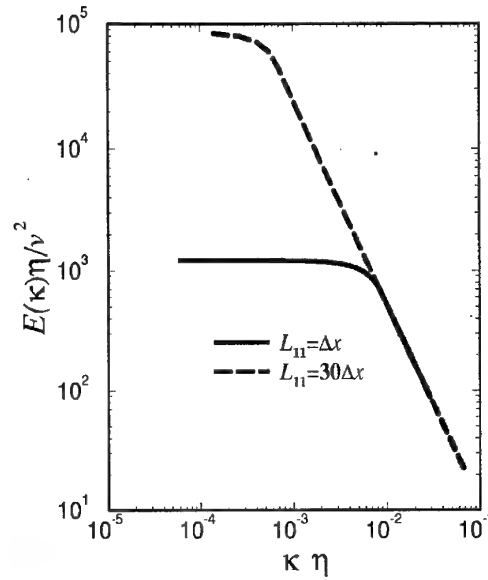


Figure 5 Target energy spectra

Concretely, we examine whether the vortex methods can produce the prescribed longitudinal spectrum and the root mean square of the velocity fluctuations, and whether the frequency distribution is Gaussian.

3.1 Vortex Strength

The velocity fluctuations produced in the previous section can be used as the boundary conditions of the finite-difference methods as well as the vortex methods as explained below.

In the two dimensional flows, the vortex strength is given by

$$\Gamma = \left(\frac{\partial v}{\partial x} - \frac{\partial u}{\partial y} \right) \Delta s \quad (1.6)$$

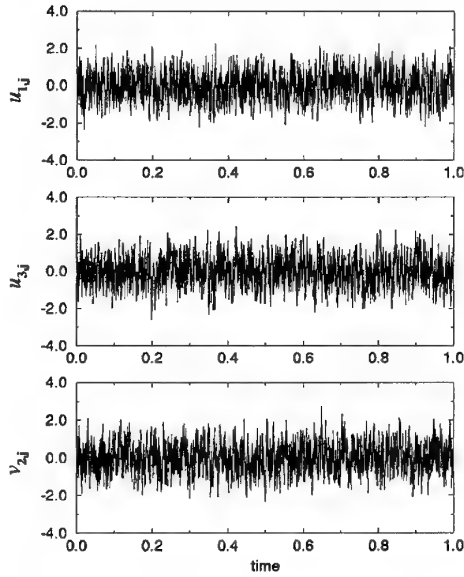


Figure 6 Velocity fluctuations at $L_{11} = \Delta x$

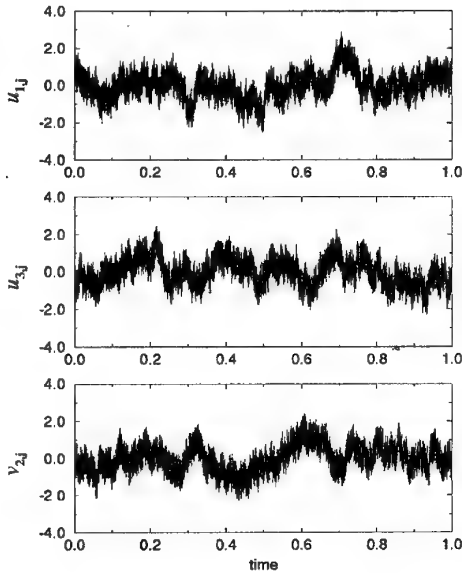


Figure 7 Velocity fluctuations at $L_{11} = 30\Delta x$

where Δs is the area the vortex occupies. Using the velocity fluctuations u_j and v_j , Equation (1.6) can be approximately rewritten as

$$\Gamma_{j,l} = \left(\frac{v_{j+1,l} - v_{j-1,l}}{2\Delta x} - \frac{u_{j,l+1} - u_{j,l-1}}{2\Delta y} \right) \Delta s \quad (1.7)$$

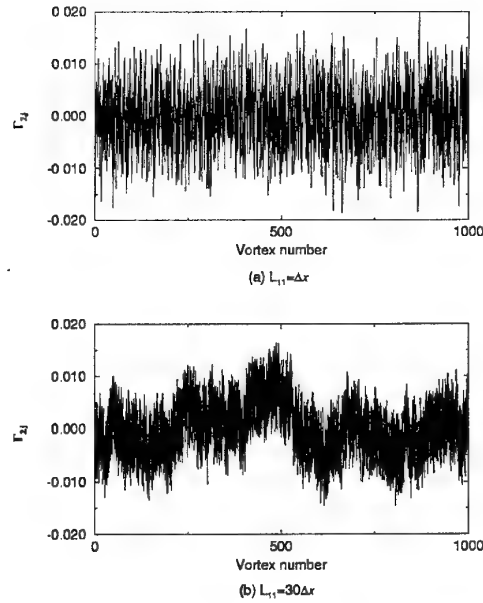


Figure 8 Vortex strength

Table 4 Parameters used in simulation

Mean velocity: U	10m/s
Kinematic viscosity: ν	$1.562 \times 10^{-5} \text{ m}^2/\text{s}$
Time step: Δt	$8.2 \times 10^{-4} \text{ s}$
Initial core radius: σ	$2U \Delta t$
Updated core radius: σ'	$2 \times (\text{distance to the nearest vortex})$

where the subscript j, l indicates the j th vortex or velocity fluctuation passing through the l th point on the y -axis.

Simulations are conducted for two different longitudinal integral scales, $L_{11} = \Delta x$ and $30\Delta x$ using the parameters listed in Table 3. The transverse spectrum is not considered for simplicity. The energy spectra obtained by these integral scales are illustrated in Fig.5 showing that the energy at smaller wave numbers increases with L_{11} .

Figures 6 and 7 show the velocity fluctuations respectively with $L_{11} = \Delta x$ and $30\Delta x$ which are calculated by the method explained in the previous section. Roughly speaking, the fluctuations of $L_{11} = \Delta x$ lie in the straight band while these of $L_{11} = 30\Delta x$ in the wavy band, which indicates that the latter fluctuations have more energy in the smaller wave number regions as the target spectrum (Fig.5).

The vortex strengths calculated using these fluctuations are shown in Fig.8. The characteristics of

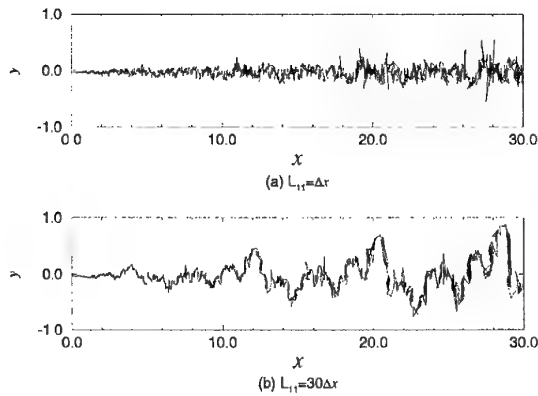


Figure 9 Vortex distributions

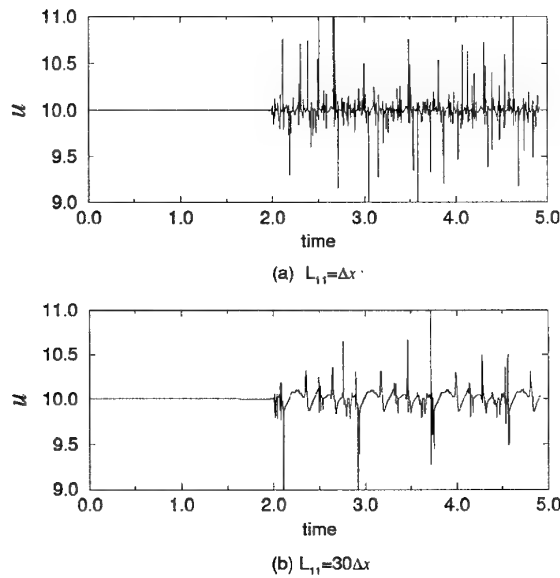


Figure 10 Velocity fluctuations produced by vortices

the vortex strength are very similar to that of the velocity fluctuations.

3.2 Vortex Methods and Turbulence

The vortices of the strengths calculated in subsection 3.1 are supplied at the origin one by one at each time step. The series of the strengths are used repeatedly until the simulations stop. We do not expect that the field of the velocity fluctuations (Figs.6, 7) can be completely reproduced by these vortices because of the use of limited number of the vortices.

The movements of the vortices are calculated by the vortex method with the diffusion velocity (10). The core radius of each vortex is updated to simulate the

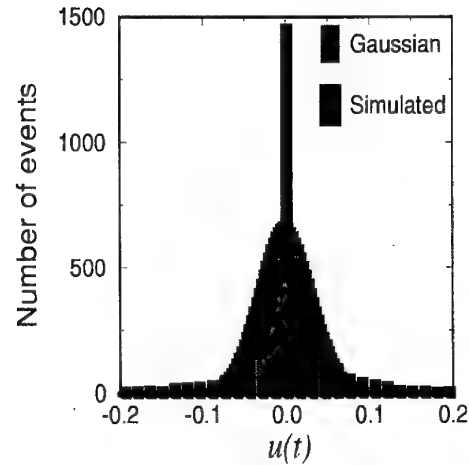


Figure 11 Frequency distribution by the vortex method $L_{11} = \Delta x$

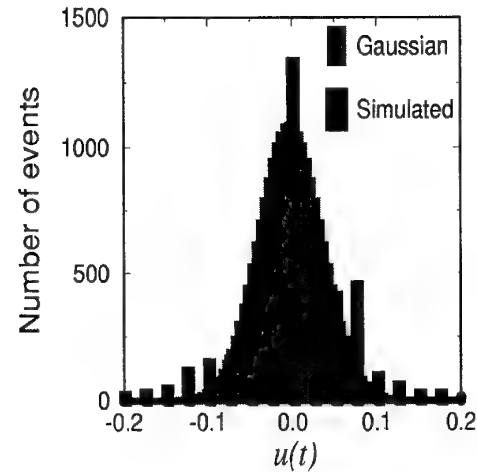


Figure 12 Frequency distribution by the vortex method $L_{11} = 30\Delta x$

vortex stretch. The new core radius is $2 \times (\text{distance to the nearest vortex})$. The parameters used for the simulations are listed in Table 4.

Figure 9 shows the vortex distributions at time 3.35872s, namely after supplying four cycles of the series of vortices. The successive vortices are connected by the straight lines. This figure is extended four times in the y -direction. It is observed that the arrangement of the vortices with $L_1 = 30\Delta x$ is much more wavy than the one with $L_1 = \Delta x$ just like the velocity fluctuations and the vortex strengths.

Figure 10 shows the velocity fluctuations at the point (20, 0) produced by the vortices. The velocity is zero until the vortices reach this point at almost time=2. The frequency distributions of these fluctuations shown in Fig.11 and 12 deviate somewhat from the Gaussian

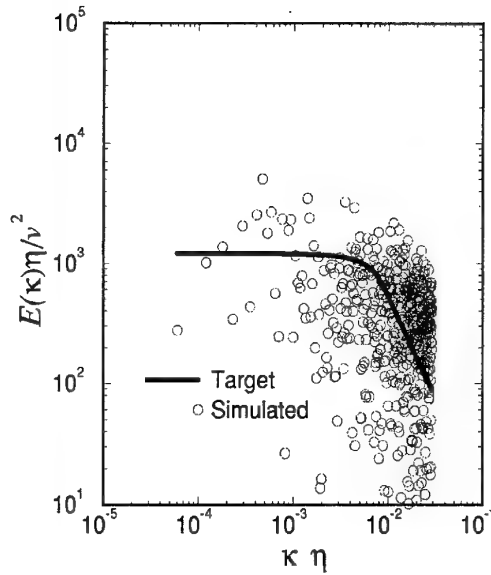


Figure 13 Target and simulated spectra with $L_{11} = \Delta x$

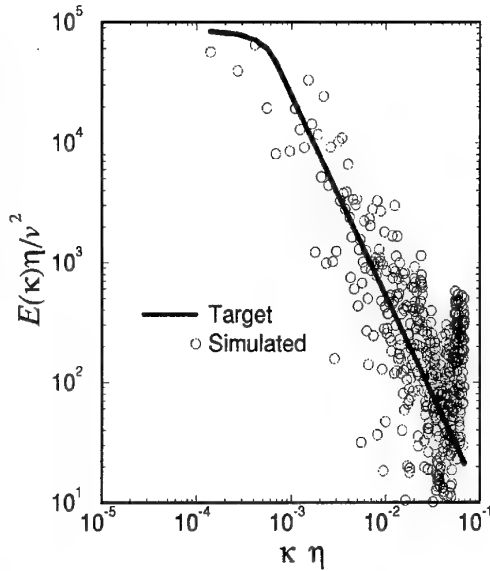


Figure 14 Target and simulated spectra with $L_{11} = 30\Delta x$

profile. The root mean square is 0.098m/s for $L_1 = \Delta x$ and 0.112m/s for $L_1 = 30\Delta x$. These values are almost ten times smaller than that in Table 3 (namely, 1.0m/s). This is because the vortex number is not large enough to reproduce the velocity fields (Figs. 6 and 7) with which the vortices are created.

The energy spectra calculated from these velocity fluctuations during $t = 4.1984 \sim 5.03808$ (namely, from 1024×5 steps to 1024×6 steps) are illustrated by the

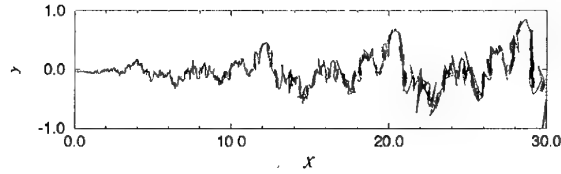


Figure 15 Vortex distribution with LES model

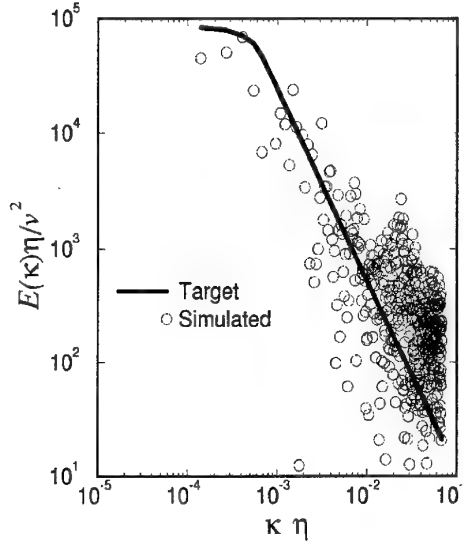


Figure 16 Energy spectrum with LES model

mark in Figs.13 and 14. The energy spectrum is multiplied by E_v / E_T where E_v is the total energy of the spectrum by the vortex method and E_T is that of the target spectrum. Though the calculated values are scattered to some extent, they are distributed surely along the target spectra even at the higher frequency regions in contrast to the results by Totsuka and Obi (8). We may say that qualitatively the vortex method can produce turbulent flows with prescribed parameters.

3.3 Vortex Methods and LES

The LES model for the vortex methods (4, 5) is used to see how it works. Simply, we add the subgrid scale viscosity

$$\nu_{\text{SGS}} = \max \left[0, C \sigma^2 \frac{1}{\omega} \frac{d\omega}{dt} \right]$$

to the diffusion velocity, where $C=0.17$ is employed. With this model, the vortex distribution in Fig.15 is almost identical to the one without the model (Fig.9b). However, the spectrum at higher frequency regions slightly increases and deviates from the target as shown in Fig.16 because the LES model is to filter out the spectrum of higher frequency that the grid spacing

cannot handle. However, in contrast to the finite-difference methods, the grid spacing (the distances between vortices) of the vortex methods can increase and decrease freely so that we can obtain better solutions at the higher frequency regions (Fig.14) than those with the LES model (Fig.16).

4. CONCLUSION

First, a simple and accurate numerical method is presented to produce velocity fluctuations that are determined by the prescribed physical quantities and qualities of turbulence. The fluctuations are easily obtained by solving a system of nonlinear equations using free software. Also this method requires as many computer memories and computations as one-dimensional case even for the three dimensional calculations. The solutions are quite accurate with less than 0.01% relative errors.

Next, these fluctuations are used to examine the capability of the vortex methods to produce turbulent flows with the prescribed parameters. The RMS obtained is smaller than that expected probably because of the use of insufficient number of vortices. Although the energy spectra by the vortex method scatter to some extent, they are distributed along the prescribed spectra even at the higher frequency regions. It can be said that the vortex methods are able to simulate the target turbulence qualitatively well. Also the solutions with the LES model deviate from the target at the higher frequency regions. Further improvement will be required for obtaining quantitative agreement.

REFERENCES

- (1) Iwatani, Y. (1982). "Simulation of multidimensional wind fluctuations having any arbitrary power spectra and cross spectra", *Journal of Wind Engineering*, No.11, p.5-18. (in Japanese)
- (2) Maruyama, T. And Morikawa, H. (1994). "Numerical simulation of wind fluctuation conditioned by experimental data in turbulent boundary layer", *Proc. 13th Symp. On Wind Eng.*, p.573-578. (in Japanese)
- (3) Kondo, K. Murakami, S. And Mochida, A. (1997). "Generation of velocity fluctuations for inflow boundary condition of LES", *Journal of Wind Engineering and Industrial Aerodynamics*, Vol.67&68, p.51-64.
- (4) Leonard, A. And Chua, K. (1989). "Three-dimensional interactions of vortex tubes", *Physica D*, Vol.37, p.490-496.
- (5) Kiya, M., Izawa, S. And Ishikawa, H. (1999). "Vortex method simulations of forced, impulsively started round jet", *Proceedings of FEDSM'99*, FEDSM99-6813.
- (6) Mansfield, J.R., Knio, O.M. And Meneveau, C. (1999). "Dynamic LES of colliding vortex rings using a 3d vortex method", *J. Comp. Phys.*, Vol.152, p.305-345.
- (7) Kamemoto, K., Zhu, B. And Ojima, A. (2000). "Attractive features of an advanced vortex method and its subjects as a tool of lagrangian LES", *Proceedings of 14th Symposium of Computational Fluid Dymanics*, B06-4.
- (8) Totsuka, Y. And Obi, S. (2000). "Turbulent flow analysis by a three dimensional vortex method (estimation of the dissipation rate)", *Proceedings of 14th Symposium of Computational Fluid Dymanics*, E09-4 (in Japanese)
- (9) Tennekes, H. And Lumley, J.L. (1999). *A First Course in Turbulence*, 17th edn., MIT Press, Cambridge, p.273.
- (10) Ogami, T. And Akamatsu, T. (1991). "Viscous flow simulation using the discrete vortex method - the diffusion velocity method", *Computers & Fluids*, Vol.19, p.433-441.

TRANSIENT FLOW AROUND A VORTEX RING BY A VORTEX METHOD

Teruhiko Kida*

Department of Energy Systems Engineering, Osaka Prefecture University,
Sakai, Osaka 599-8531, Japan / Email: kida@energy.osakafu-u.ac.jp

Tekanori Take

Department of Mechanical Systems Engineering, Shiga Prefecture University,
Hikone, Siga 522-8533, Japan

Abstract

The transient flow around a ring is simulated by a vortex blob method, which is derived from the integral equation with respect to vorticity. In this paper lengths and velocities are normalized with a typical length of the ring vortex and a typical circulation of the ring, respectively. From the normalized Navier-Stokes equations the vorticity equation is derived and the governing integral equation is constructed from it. As the discrete form of the vorticity field a vortex blob method is proposed and numerical calculations are carried out for the flow around an elliptic ring vortex. This method has an advantage that we can hold the distance between the nascent vortices within a given allowance.

INTRODUCTION

The present paper treats a transient flow around a vortex ring placed in unbounded fluid flow, in order to know the validity of the vortex blob method derived in this paper. In 3-D Euler flows, the high stretching of the vortex stick induces the divergence of the velocity field (see Maffott (2000)), thus, a tool such as reconnection of the vortex tube is used to continue the numerical calculation of the vortex method in this case.

The breakdown of smooth solutions of the 3-D Euler equations signifies the onset of the turbulent behavior and the formulation of the singularity is related to the concentration of vorticity on successively smaller sets. Beale et al. (1984) and Ponce (1985) proved that the maximum vorticity necessarily grows without bound as the critical time approaches and it is not possible for other kinds of singularities to form before the vor-

ticity becomes unbounded. Constantin & Fefferman (1993) shows that large curvatures in vortex lines are necessary if a singularity is to form. Gibbon et al. (2000) shows by using Kerr's picture (1993) that the structure of vortex stretching and compression around the singular point is very complicated and there is a strong switch from stretching to compression like a vortex jump.

Pelz (1997) studies the finite-time singularity of a high-symmetric flow with dodecapole by using a vortex filament method and shows the existence of this singularity in 3-D Euler flows. In this calculation, a cubic Gaussian core function for the vorticity distribution and a second-order Runge-Kutta scheme for time marching are used. Further remeshing algorithm and cubic splines are used and he shows the finite time singularity. However, for the viscous flow Boratav & Pelz (1994) use a Fourier pseudospectral method and show: The six vortex dipoles deform one another, their cores become more and more flattened, and the distances shrink exponentially. There is a short local equilibrium interval when the viscous force and vortex stretching forces balance each other. And viscous dissipation forces will play a role against the singularity formation as rapidly as the convective forces play toward a singularity.

The vortex method is one of powerful numerical method for knowing the mechanism of the onset of turbulent as shown by Pelz (1997). The present paper aims to construct an alternative vortex blob method based on the Navier-Stokes equations. First the Navier-Stokes equations are depicted by normalizing with a typical global length and a typical circulation, using the idea of Pelz (1997). Second the integral expression is derived by considering the expression derived by Nakajima & Kida (1997) and a vortex blob method is introduced as the discrete form of this

expression. Finally, numerical results are shown for flows around an elliptic ring with constant circulation initially.

1 Governing equations

We here consider 3-D incompressible fluid flow. The governing equations are given as Navier-Stokes equations:

$$\frac{\partial \vec{u}}{\partial t} + (\vec{u} \cdot \nabla) \vec{u} = -\nabla P + \nu \nabla^2 \vec{u}, \quad (1)$$

$$\nabla \cdot \vec{u} = 0, \quad (2)$$

where P is the pressure divided by ρ . Lengths and velocities are normalized with a typical global length of the vortex tubes $l(t)$ and a typical circulation around the tubes Γ_o . Normalized position vector and velocity vector are respectively denoted as \vec{X} and \vec{v} :

$$\vec{X} = S(t) \vec{x}, \quad (3)$$

$$\vec{v} = \frac{S(t)}{\Gamma_o} \vec{u}, \quad (4)$$

where $S(t) = 1/l(t)$, and \vec{x} and \vec{u} are the position vector and the velocity vector in the physical state, respectively. Then, Eqs.(1) and (2) become as

$$\begin{aligned} \frac{\partial \vec{v}}{\partial t} + (\vec{v} \cdot \nabla) \vec{v} + S \dot{S} \sum_{i=1}^3 \frac{\partial}{\partial X_i} \vec{v} \\ = \frac{\dot{S}}{S} \vec{v} - \frac{S^2}{\Gamma_o^2} \nabla P + \frac{S^2}{\Gamma_o} \nu \nabla^2 \vec{v}, \end{aligned} \quad (5)$$

$$\nabla \cdot \vec{v} = 0, \quad (6)$$

where $\dot{S} = \frac{dS}{dt}$.

We here consider the relative coordinate systems given by

$$\vec{X} = \vec{X} - \frac{1}{2} S^2 (\vec{e}_1 + \vec{e}_2 + \vec{e}_3), \quad (7)$$

where \vec{e}_i is the unit vector of the i direction. Furthermore, we denote \vec{X} as \vec{x} again. Then, the Navier-Stokes equations, Eqs.(5) and (6), are given as

$$\frac{\partial \vec{v}}{\partial t} + (\vec{v} \cdot \nabla) \vec{v} = \frac{\dot{S}}{S} \vec{v} - \frac{S^2}{\Gamma_o^2} \nabla P + \frac{S^2}{\Gamma_o} \nu \nabla^2 \vec{v}, \quad (8)$$

$$\nabla \cdot \vec{v} = 0. \quad (9)$$

Here, we introduce the vorticity as

$$\vec{\omega} = \text{rot} \vec{v}. \quad (10)$$

Then, we have from Eq.(8),

$$\begin{aligned} \frac{\partial \vec{\omega}}{\partial t} + (\vec{v} \cdot \nabla) \vec{\omega} &= \frac{\dot{S}}{S} \vec{\omega} + (\vec{\omega} \cdot \nabla) \vec{v} \\ &+ \frac{S^2}{\Gamma_o} \nu \nabla^2 \vec{\omega}. \end{aligned} \quad (11)$$

Furthermore, we again define the vorticity $\vec{\tilde{\omega}} = \vec{\omega}/S(t)$ and we put $\vec{\tilde{\omega}}$ as $\vec{\omega}$ again. Then, we have

$$\frac{\partial \vec{\omega}}{\partial t} + (\vec{v} \cdot \nabla) \vec{\omega} = (\vec{\omega} \cdot \nabla) \vec{v} + \frac{S^2}{\Gamma_o} \nu \nabla^2 \vec{\omega}. \quad (12)$$

We note that the relation between the original physical field and the normalized field is given by

$$\vec{\Omega} = \Gamma_o S \vec{\omega}, \quad (13)$$

$$\vec{x} = \frac{1}{S} \left(\vec{X} + \frac{1}{2} S^2 (\vec{e}_1 + \vec{e}_2 + \vec{e}_3) \right). \quad (14)$$

where $\vec{\Omega}$ is the vorticity in the physical state.

1.1 Integral Expression

The construction of an integral equation with respect to vorticity from the Navier-Stokes was carried out by Nakajima and Kida (1997). Their expression, however, is not proved rigorously.

From the approach by Nakajima and Kida (1997), the vorticity field is supposed to be expressed as the following integral form:

$$\begin{aligned} \omega_i(\vec{X}, t) &= \int_{-\infty}^{\infty} \omega_{oj}(\vec{a}) \\ &\times g(\vec{X} - \vec{X}(0), \beta(t)) a_j^i(\vec{a}, t, 0) da \\ &+ \int_0^t ds \int_{-\infty}^{\infty} g(\vec{X}(s) - \vec{X}', \beta(t-s)) \\ &\times a_j^i(\vec{a}, t, t-s) f_j(\vec{X}', a, s) da dX', \end{aligned} \quad (15)$$

where $\vec{\omega}_o$ is an initial vorticity field, $\vec{X}(s) = \vec{X} - \vec{a} - \int_s^t \vec{v}_a(\vec{a}, s) ds$, \vec{v}_a is a velocity vector, and g, β are defined as

$$\beta(t) = \frac{\Gamma_o}{4S^2 \nu t}, \quad (16)$$

$$g(\vec{X}, \sigma) = \left(\frac{\sigma}{\pi} \right)^{3/2} \exp(-\sigma |\vec{X}|^2). \quad (17)$$

In this expression Eq.(15), \vec{f} is unknown vector function. Substituting Eq.(15) into Eq.(12), we have the following relation:

$$\begin{aligned} &\int_{-\infty}^{\infty} f_j(\vec{X}, \vec{a}, t) a_j^i(\vec{a}, t, t) da \\ &= \int_{-\infty}^{\infty} \omega_{oj}(\vec{a}) \left[(\vec{v}(\vec{X}, t) - \vec{v}_a(\vec{a}, t)) \right. \\ &\quad \cdot \nabla g(\vec{X}(0), \beta(t)) a_j^i(\vec{a}, t, 0) \\ &\quad + \left(\frac{\partial}{\partial t} a_j^i(\vec{a}, t, 0) - \varepsilon_{kji}(\vec{X}, t) a_j^k(\vec{a}, t, 0) \right) \\ &\quad \left. \times g(\vec{X}(0), \beta(t)) \right] da \end{aligned}$$

$$\begin{aligned}
& + \int_0^t ds \int_{-\infty}^{\infty} f_j(\vec{X}', \vec{a}, s) \left[(\vec{v}(\vec{X}, t) - \vec{v}_a(\vec{a}, t)) \right. \\
& \cdot \nabla g(\vec{X}(s) - \vec{X}', \beta(t-s)) a_j^i(\vec{a}, t, s) \\
& + \left(\frac{\partial}{\partial t} a_j^i(\vec{a}, t, s) - \epsilon_{ki}(\vec{X}, t) a_j^k(\vec{a}, t, s) \right) \\
& \left. \times g(\vec{X}(s) - \vec{X}', \beta(t-s)) \right] dX' da \quad (18)
\end{aligned}$$

where $\epsilon_{ij} = \frac{1}{2} \left(\frac{\partial v_i}{\partial X_j} + \frac{\partial v_j}{\partial X_i} \right)$. Therefore, we have

$$\begin{aligned}
f_j(\vec{X}, \vec{a}, t) a_j^i(\vec{a}, t, t) &= \omega_{oj}(\vec{a}) \left[(\vec{v}(\vec{X}, t) - \vec{v}_a(\vec{a}, t)) \right. \\
& \cdot \nabla g(\vec{X}(0), \beta(t)) a_j^i(\vec{a}, t, 0) \\
& + \left(\frac{\partial}{\partial t} a_j^i(\vec{a}, t, 0) - \epsilon_{ki}(\vec{X}, t) a_j^k(\vec{a}, t, 0) \right) \\
& \left. \times g(\vec{X}(0), \beta(t)) \right] \\
& + \int_0^t ds \int_{-\infty}^{\infty} f_j(\vec{X}', \vec{a}, s) \left[(\vec{v}(\vec{X}, t) - \vec{v}_a(\vec{a}, t)) \right. \\
& \cdot \nabla g(\vec{X}(s) - \vec{X}', \beta(t-s)) a_j^i(\vec{a}, t, s) \\
& + \left(\frac{\partial}{\partial t} a_j^i(\vec{a}, t, s) - \epsilon_{ki}(\vec{X}, t) a_j^k(\vec{a}, t, s) \right) \\
& \left. \times g(\vec{X}(s) - \vec{X}', \beta(t-s)) \right] dX'. \quad (19)
\end{aligned}$$

Here, we suppose that a_j^i satisfies the following relation:

$$\frac{\partial}{\partial t} a_j^i(\vec{a}, t, s) = \epsilon_{ik}(\vec{a} + \vec{\Phi}(\vec{a}, t), s) a_j^k(\vec{a}, t, s), \quad (20)$$

where

$$\vec{\Phi}(\vec{a}, t) = \int_0^t \vec{v}_a(\vec{a}, s) ds.$$

From Eq.(19), we can express f_j as

$$\begin{aligned}
f_j(\vec{X}, \vec{a}, t) &= \vec{F}(\vec{X}, \vec{a}, t; j) \cdot \nabla g(\vec{X} - \vec{A}(\vec{a}, t)) \\
& + G(\vec{X}, \vec{a}, t; j) g(\vec{X} - \vec{A}(\vec{a}, t)), \quad (21)
\end{aligned}$$

where $\vec{A}(\vec{a}, t) = \vec{a} + \vec{\Phi}(\vec{a}, t)$.

Let us assume that $\beta(t) \gg 1$, that is, $\frac{\Gamma_0}{S^2 \nu t} \gg 1$. Then, we easily see

$$\begin{aligned}
\omega_i(\vec{X}, t) &\approx \int_{-\infty}^{\infty} \omega_{oj}(\vec{a}) g(\vec{X}(0), \beta(t)) a_j^i(\vec{a}, t, 0) da \\
& + \int_0^t a_j^i(\vec{a}, t, s) ds \int_{-\infty}^{\infty} f_j(\vec{X}(s), \vec{a}, s) da \\
& + \frac{1}{4} \int_0^t \frac{a_j^i(\vec{a}, t, s)}{\beta(t-s)} ds \\
& \times \int_{-\infty}^{\infty} \nabla^2 f_j(\vec{X}(s), \vec{a}, s) da. \quad (22)
\end{aligned}$$

We choose the approximate velocity field \vec{v}_a as

$$\vec{v}_a(\vec{a}, t) = \vec{v}(\vec{A}(\vec{a}, t), t). \quad (23)$$

Then, we easily see for $|\vec{X} - \vec{A}| \ll 1$:

$$\vec{F}(\vec{X}, \vec{a}, t; j) \approx (\vec{X} - \vec{A}(\vec{a}, t)) \cdot \nabla \vec{F}(\vec{A}, \vec{a}, t; j) \quad (24)$$

$$G(\vec{X}, \vec{a}, t; j) \approx (\vec{X} - \vec{A}(\vec{a}, t)) \cdot \nabla G(\vec{A}, \vec{a}, t; j). \quad (25)$$

Therefore, we have

$$\begin{aligned}
\omega_i(\vec{X}, t) &\approx \int_{-\infty}^{\infty} \omega_{oj}(\vec{a}) g(\vec{X}(0), \beta(t)) a_j^i(\vec{a}, t, 0) da \\
& + O(t/\beta). \quad (26)
\end{aligned}$$

Thus, for small time t we have the same expression as one given by Nakajima & Kida (1997):

$$\begin{aligned}
\omega_i(\vec{X}, t) &\approx \int_{-\infty}^{\infty} \omega_{oi}(\vec{a}) g(\vec{X}(0), \beta(t)) da \\
& + t \int_{-\infty}^{\infty} \omega_{oj}(\vec{a}) \epsilon_{ij}(\vec{a}) g(\vec{X}(0), \beta(t)) da, \quad (27)
\end{aligned}$$

where $\vec{X}(0) = \vec{X} - \vec{a} - \vec{\Phi}(\vec{a}, t)$ and $\vec{\Phi}(\vec{a}, t) \approx \vec{v}_a(\vec{a})t$.

1.2 Vortex Blob Method

Let us derive a vortex blob method from Eq.(27). We here assume that the vorticity field is approximately expressed as the following discrete form:

$$\omega_i(\vec{X}, t) = \sum_{k=1}^N \Gamma_k^i(t) g(\vec{X} - \vec{X}_k, \sigma). \quad (28)$$

Multiplying $g(\vec{X} - \vec{X}_m, \sigma)$ to Eq.(28) and integrating with respect to \vec{X} , we have from using Eq.(27):

$$\begin{aligned}
& \int_{-\infty}^{\infty} \omega_i(\vec{X}, t) g(\vec{X} - \vec{X}_m(t), \sigma) dX \\
& \approx \sum_{k=1}^N \Gamma_k^i(0) \int_{-\infty}^{\infty} \int_{-\infty}^{\infty} g(\vec{a} - \vec{a}_k, \sigma) \\
& \times g(\vec{X} - \vec{X}_m(t), \sigma) g(\vec{X} - \vec{A}(\vec{a}, t), \beta) da dX \\
& + t \sum_{k=1}^N \Gamma_k^j(0) \int_{-\infty}^{\infty} \int_{-\infty}^{\infty} g(\vec{a} - \vec{a}_k, \sigma) \\
& \times g(\vec{X} - \vec{X}_m(t), \sigma) g(\vec{X} - \vec{A}(\vec{a}, t), \beta) \\
& \times \epsilon_{ij}(\vec{a}) da dX. \quad (29)
\end{aligned}$$

Here, we use the following relation:

$$\begin{aligned}
& \int_{-\infty}^{\infty} g(\vec{a}, \sigma) g(\vec{x} - \vec{a}, \beta) da = g(\vec{x}, \sigma\beta), \\
& \sigma\beta = \frac{\sigma\beta}{\sigma + \beta}. \quad (30)
\end{aligned}$$

Then, we have the relation with respect to $\vec{\Gamma}_k$:

$$\begin{aligned} \sum_{k=1} \Gamma_k^i(t) g(\vec{X} - \vec{X}_k(t), \sigma/2) &= \sum_{k=1} \Gamma_k^i(0) \\ &\times g(\vec{X} - \vec{X}_k(t), \sigma_{2\beta}) \\ &+ t \sum_{k=1} \Gamma_k^j(0) E_{ij}(\vec{X}, k), \end{aligned} \quad (31)$$

where $\sigma_{2\beta} = \frac{\sigma\beta}{\sigma+2\beta}$ and E_{ij} is defined as

$$\begin{aligned} E_{ij}(\vec{x}, k) &= \int_{-\infty}^{\infty} g(\vec{x} - \vec{A}, \sigma_\beta) \\ &\times g(\vec{a} - \vec{a}_k, \sigma) \epsilon_{ij}(\vec{a}) d\vec{a}. \end{aligned} \quad (32)$$

The velocity field is obtained by using the Biot-Savart formula. Substituting Eq.(28) into the Biot-Savart formula, we can obtain the velocity field as

$$v_l = -\frac{1}{4\pi} \sum_{k=1} \Gamma_k^i \frac{\partial}{\partial X_j} \hat{I}_o(\vec{X} - \vec{X}_k, \sigma) \epsilon_{ijl}, \quad (33)$$

where ϵ_{ijk} is the Eddington tensor and \hat{I}_o is defined as

$$\hat{I}_o(\vec{x}, \sigma) = \frac{2\pi}{\sigma^{3/2}} \frac{1}{|\vec{x}|} \text{Erf}(\sigma^{1/2} |\vec{x}|), \quad (34)$$

$$\text{Erf}(x) = \int_0^x \exp(-x^2) dx. \quad (35)$$

Using Eq.(33), we can easily obtain the strain rate ϵ_{ij} as

$$\begin{aligned} \epsilon_{ij} &= -\frac{1}{8\pi} \sum_{k=1} \Gamma_k^p \left[\frac{\partial^2}{\partial X_j \partial X_q} \hat{I}_o(\vec{X} - \vec{X}_k, \sigma) \epsilon_{pqj} \right. \\ &\quad \left. + \frac{\partial^2}{\partial X_i \partial X_q} \hat{I}_o(\vec{X} - \vec{X}_k, \sigma) \epsilon_{pqj} \right]. \end{aligned} \quad (36)$$

We substitute Eq.(36) into Eq.(32), then we have

$$\begin{aligned} E_{ij}(\vec{X}, k) &= -\frac{1}{8\pi} \sum_{s=1} \Gamma_s^p \\ &\times \left[\frac{\partial^2}{\partial X_{sj} \partial X_{sq}} \hat{J}(\vec{X} - \vec{X}_k, \vec{X}_s - \vec{X}_k) \epsilon_{pqj} \right. \\ &\quad \left. + \frac{\partial^2}{\partial X_{si} \partial X_{sq}} \hat{J}(\vec{X} - \vec{X}_k, \vec{X}_s - \vec{X}_k) \epsilon_{pqj} \right], \end{aligned} \quad (37)$$

where \hat{J} is defined as

$$\begin{aligned} \hat{J}(\vec{x}, \vec{y}) &= \int_{-\infty}^{\infty} g(\vec{x} - \vec{a}, \sigma_\beta) g(\vec{a}, \sigma) \\ &\times \hat{I}_o(\vec{a} - \vec{y}, \sigma) d\vec{a}. \end{aligned} \quad (38)$$

In order to obtain $\hat{J}(\vec{x}, \vec{y})$, we define the following function $K(\vec{x}, \vec{y}, \gamma)$:

$$\begin{aligned} K(\vec{x}, \vec{y}, \gamma) &= \int_{-\infty}^{\infty} g(\vec{a} - \vec{x}, \sigma) g(\vec{a} - \vec{y}, \sigma_\beta) \\ &\times \hat{I}_o(\vec{a}, \gamma^2) d\vec{a}. \end{aligned} \quad (39)$$

Here, we consider $\frac{\partial K}{\partial \gamma}$:

$$\begin{aligned} \frac{\partial}{\partial \gamma} K(\vec{x}, \vec{y}, \gamma) &= \frac{2}{\pi^{1/2}} \int_{-\infty}^{\infty} g(\vec{a} - \vec{x}, \sigma) g(\vec{a} - \vec{y}, \sigma_\beta) \\ &\times \exp(-\gamma^2 |\vec{a}|^2) d\vec{a}. \end{aligned} \quad (40)$$

Then, we have

$$\begin{aligned} \frac{\partial}{\partial \gamma} K &= \frac{2}{\pi^{1/2}} \left(\frac{\sigma \sigma_\beta}{\pi(\sigma + \sigma_\beta + \gamma^2)} \right)^{3/2} \\ &\times \exp \left[\frac{|\sigma \vec{x} + \sigma_\beta \vec{y}|^2}{\sigma + \sigma_\beta + \gamma^2} - \sigma |\vec{x}|^2 - \sigma_\beta |\vec{y}|^2 \right]. \end{aligned} \quad (41)$$

Since $K(\vec{x}, \vec{y}, 0) = 0$ and $\beta \gg 1$, that is, $\frac{\sigma\beta}{\sigma+\beta} \approx \sigma$, we have

$$\begin{aligned} \hat{J}(\vec{x}, \vec{y}) &\approx \frac{2}{\pi^{1/2}} \int_0^{\sigma^{1/2}} \left(\frac{\sigma^2}{\pi(2\sigma + \gamma^2)} \right)^{3/2} \\ &\times \exp \left[\frac{|\sigma \vec{x} - 2\sigma \vec{y}|^2}{2\sigma + \gamma^2} \right] d\gamma \\ &\times \exp(-\sigma(|\vec{y}|^2 + |\vec{x} - \vec{y}|^2)). \end{aligned} \quad (42)$$

Performing the above integration, we finally arrive at

$$\begin{aligned} \hat{J}(\vec{x}, \vec{y}) &\approx \left(\frac{\sigma}{\pi} \right)^2 \left(\frac{2}{\sigma} \right)^{1/2} \frac{1}{|\vec{x} - 2\vec{y}|} \\ &\times \exp \left(-\frac{\sigma}{2} |\vec{x}|^2 \right) \text{Erf} \left(\left(\frac{\sigma}{2} \right)^{1/2} |\vec{x} - 2\vec{y}| \right). \end{aligned} \quad (43)$$

Thus, we can obtain E_{ij} by substituting Eq.(43) into Eq.(37). Therefore, we can construct the linear equation with respect to $\vec{\Gamma}_k(t)$. In the present vortex blob method, the global length of the vortex tubes is kept to be constant, so that we can choose the length between control points of Eq.(31) within a given allowance.

2 Numerical Results

The present paper treats the transient flow around an elliptic vortex ring. The initial physical state is shown in Fig.1. In the present calculation, the vortex ring is constructed by M vortex tubes:

$$x = r \cos \theta, \quad y = br \sin \theta, \quad z = r_m \sin \delta_k, \quad (44)$$

where $r = 1 + r_m \cos \delta_k$; ($k = 1, 2, \dots, M$). The typical length and the typical circulation are taken as the initial total length of the vortex tubes constructing the ring and the initial circulation of the tubes, respectively.

The total length of the vortex ring is given as

$$l = \frac{l_o}{S} = \sum_{i=1}^N |\vec{X}_{i+1} - \vec{X}_i|, \quad (45)$$

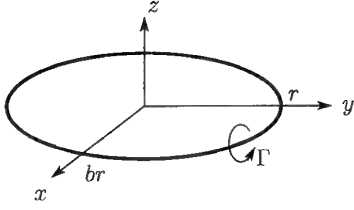


Figure 1: Physical model of an elliptic vortex ring

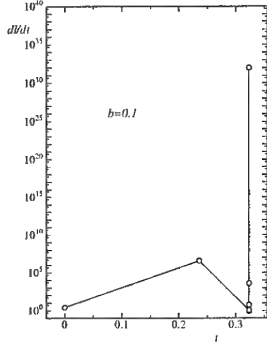


Figure 2: Global stretching.

where l_0 is the initial total length of the vortex tubes and N is the total number of the vortex blobs, $N = nM$, where n is the number of vortex blobs of a vortex ring tube. The rate of the total length of the vortex ring is given by

$$\begin{aligned} \frac{dl}{dt} &= -l_0 \frac{\dot{S}}{S^2} \\ &= \sum_{i=1}^N \frac{(\vec{X}_{i+1} - \vec{X}_i) \cdot (\vec{v}_{i+1} - \vec{v}_i)}{|\vec{X}_{i+1} - \vec{X}_i|}. \end{aligned} \quad (46)$$

This rate, $\frac{dl}{dt}$, is the global stretching rate of the vortex ring. Figure 2 shows the numerical result of the elliptic ring with ratio $b = 0.1$ in the case where $\nu = 1$, $n = 20$, $M = 2$, $r_m = \epsilon/n$, $\epsilon = 1.5\pi/n$, and $\delta_0 = 0$ and $\delta_1 = \pi$.

Figure 3 shows the vortex blob distribution of the circular vortex ring. Within the present calculated time, the configuration of the ring is circular, which is moved downward. Figure 4(a) and (b) are the vortex blob distribution in the case of the elliptic ring with ratio $b = 0.1$. The vortex blobs near the largest curvature are moved rapidly at early stage of motion and the elliptic configuration is changed remarkably with lapse of time.

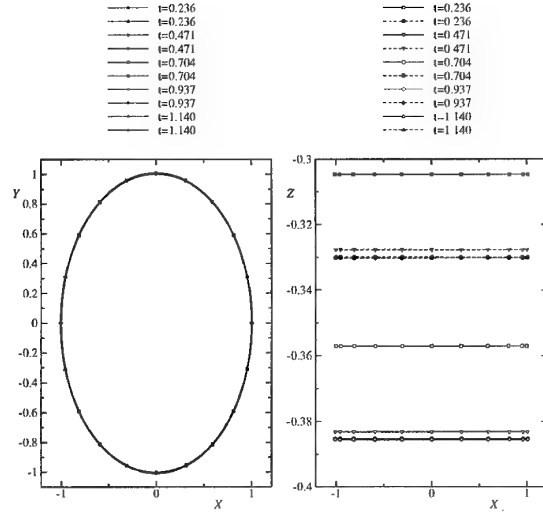


Figure 3: Vortex blob distribution in the case of the circular ring.

From Eq.(12), we have

$$\begin{aligned} \frac{D|\vec{\omega}|^2}{Dt} &= 2\vec{\omega} \cdot \vec{e} \cdot \vec{\omega} + \frac{S^2\nu}{\Gamma_o} \nabla^2 |\vec{\omega}|^2 \\ &\quad - \frac{S^2\nu}{\Gamma_o} \frac{\partial \omega_j}{\partial x_i} \frac{\partial \omega_j}{\partial x_i}, \end{aligned} \quad (47)$$

where \vec{e} is the strain rate, $\{\epsilon_{ij}\}$, calculated by Eq.(36). Thus, the local stretching rate α is defined as

$$\alpha = \frac{\vec{\omega} \cdot \vec{e} \cdot \vec{\omega}}{|\vec{\omega}|^2}. \quad (48)$$

Figure 5 shows the numerical result, $\vec{\omega} \cdot \vec{e} \cdot \vec{\omega}$, at $t = 0.323406588$. We see that the stretching and compression of vorticity field are calculated.

The total kinematic energy $T = \int_{-\infty}^{\infty} \frac{1}{2} |\vec{v}|^2 dX$ is given by

$$\begin{aligned} T &= \frac{1}{4\pi^{3/2}} \sum_{k=1} \sum_{m=1} \Gamma_k^i \Gamma_m^i \frac{1}{|\vec{X}_k - \vec{X}_m|} \\ &\quad \times \text{Erf} \left(\left(\frac{\sigma}{2} \right)^{1/2} |\vec{X}_k - \vec{X}_m| \right). \end{aligned} \quad (49)$$

The enstrophy Ω is also give as

$$\Omega = \frac{1}{2} \sum_{k=1} \sum_{m=1} \Gamma_k^i \Gamma_m^i g(\vec{X}_k - \vec{X}_m, \sigma/2). \quad (50)$$

Figure 6 shows the total kinematic energy and the enstrophy calculated by the present method.

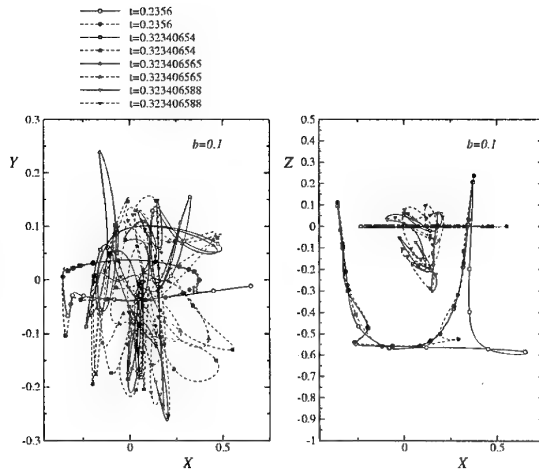


Figure 4: Vortex blob distribution.

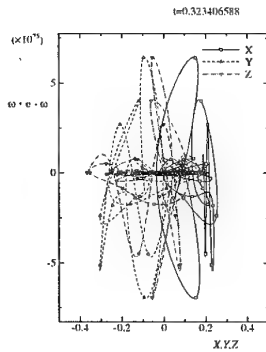


Figure 5: Global stretching.

3 Conclusions

The present paper introduces an alternative vortex blob method derived from the Navier-Stokes equations normalized with the typical length of the vortex tubes and the circulation of the tubes. The numerical calculation is carried out for an elliptic vortex ring and the stretching and compression of vorticity field are simulated.

This work was supported by Grant-in-Aid for Scientific Research (No.12650178) from the Ministry of Education, Science and Culture of Japan.

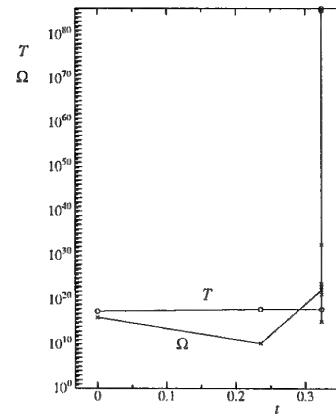


Figure 6: Total kinematic energy and enstrophy.

References

- [1] Moffatt, H.K. (2000), "The interaction of skewed vortex pairs; a model for blown-up of the Navier-Stokes equations", J. Fluid Mech., 409, p51-68.
- [2] Boratov, O.N. & Pelz, R.B. (1994), "Direct numerical simulation of transition to turbulence from a high-symmetry initial condition", Phys. Fluids, 6, p2757-2784.
- [3] Gibbon, J.T., Galanti, B. & Kerr, R.M. (2000), Stretching and compression of vorticity in the 3D Euler equations, "Turbulence structure and vortex dynamics", ed. Hunt, J.C.R. & Vassilicos, J.C., Cambridge Univ. Press, p23-34.
- [4] Constantin, P. & Fefferman, C. (1993), "Direction of vorticity and problem of global regularity for the Navier-Stokes equations", Indian Univ. Math. J., 42, p775-789.
- [5] Pelz, R.B. (1997), "Locally self-similar, finite-time collapse in a high-symmetry vortex filament model", Physical Review E, 55, p1617-1626.
- [6] Kerr, R.M. (1997), "Evidence for a singularity of the three-dimensional, incompressible Euler equations", Phys. Fluids A-5, p1725-1746.
- [7] Beale, J.T., Kato, T. & Majda, A. (1984), "Remarks on the breakdown of smooth solutions for the 3-D Euler equations", Commun. Math. Phys., 94, p61-66.
- [8] Ponce, G. (1985), "Remarks on a paper by J.T. Beale, T. Kato, and A. Majda", Commun. Math. Phys., 98, p349-353.
- [9] Nakajima, T. & Kida, T. (1997), "Three-dimensional vortex methods derived from the Navier-Stokes equations", JSME International J., B, 40, p191-199.

FORMATION OF A TURBULENT VORTEX RING

Junichi Hatano

Department of Energy Engineering, Faculty of Engineering, Yokohama National University
79-5 Tokiwadai, Hodogaya, Yokohama 240-8501, Japan /Email: m00db111@ynu.ac.jp

Shinsuke Watanabe

Department of Physics, Faculty of Engineering, Yokohama National University
79-5 Tokiwadai, Hodogaya, Yokohama 240-8501, Japan /Email: wtnb@ynu.ac.jp

ABSTRACT

The laminar and turbulent vortex ring has been observed experimentally. In the previous study, we employed an exploding wire method to generate the vortex ring in water and observed the laminar vortex ring in spite of the high Reynolds number in the order of 10^5 .

In this study, we observe the turbulent vortex ring does not depend on Reynolds number but the interaction of vortex rings. After the interaction, the only one vortex ring remains and the other one collapses. The remained vortex ring has a wavy shape with a turbulent trailing wake. This turbulent vortex ring does not return to the stable circular shape.

We also observe the elliptic vortex ring to study whether a deformed vortex ring returns to a stable circular vortex ring. An elliptic vortex ring propagates with periodic oscillation, which does not decay for a long distance.

1. INTRODUCTION

A vortex ring is one of the fundamental motions of fluid with vorticity. Laminar and turbulent vortex rings have been observed experimentally. In the experiments on vortex ring in water, mechanical methods such as piston are employed traditionally, which enables us to generate a vortex ring with Reynolds number in the order

of $\sim 10^4$ at maximum. However, the vortex ring in the Reynolds number of 10^4 has a turbulent structure which presumably comes from the method for producing a vortex ring. In the previous paper, we have presented a new method for producing a vortex ring in water and observed a laminar vortex ring with the Reynolds number even in the order of 10^5 . The method made use of an explosion of molten metal produced from wire by Joule heating of a fine tungsten wire in water, which is called an exploding wire method. The formation of vortex ring depends on the applied voltage (input energy) to a metallic wire.

We have observed that a vortex ring propagates stably in water when an applied voltage is relatively low, ~ 1 kV. By increasing the applied voltage, a vortex ring disintegrates into multiple vortex rings and a mutual slip-through of vortex rings are observed.

In this paper, we study formation process of a turbulent vortex ring. The formation of a turbulent vortex ring is closely related to the interaction of vortex rings. A turbulent vortex ring is characterized by a wavy structure of a vortex core and by a turbulent trailing wake. Once a vortex ring become turbulent, it seems that the vortex ring never recover a circular shape. So we also study the propagation of an elliptic vortex ring to observe whether a deformed vortex ring returns to a circular vortex ring.

2. EXPERIMENTAL APPARATUS AND METHOD

The experimental setup composed of a water tank and a vortex driver is shown in Fig.1. An acrylic water tank of 0.5 m in length, 0.5 m in width and 1.35 m in height is employed. The depth of water is 1.3 m. At the top of water tank, a vortex driver is installed. In a cylindrical vortex driver shown in Fig.2, a tungsten wire of 0.2 mm in diameter and 12 mm in length is connected between a pair of stainless electrodes. A high voltage is applied to the tungsten wire through the electrodes from a capacitor bank of 100 μF which can be charged up to 5 kV. At the outlet of vortex driver, an orifice of 0.03 m in diameter is fixed.

The method for generating a vortex ring is as follows. When a high voltage is applied to a tungsten wire, a molten metal is created in water. Due to a rapid heat exchange between the molten metal and the surrounding water, a vapor bubble grows around the molten metal, which induces a high speed flow of water from the surrounding pipe and generate a vortex ring.¹⁾

A vortex ring formed in this method has high-speed rotation of fluid in the vortex core. The rotational velocity at the edge of the core reaches to ~ 10 m/s. Because of cavitation due to high-speed rotation, the center of vortex core consists of air, which visualizes the motion of vortex ring. To visualize motion of fluid associated to a vortex motion, we employ dye. A vortex ring is observed by means of image converter camera (Ultrac FS501, NAC Inc.).

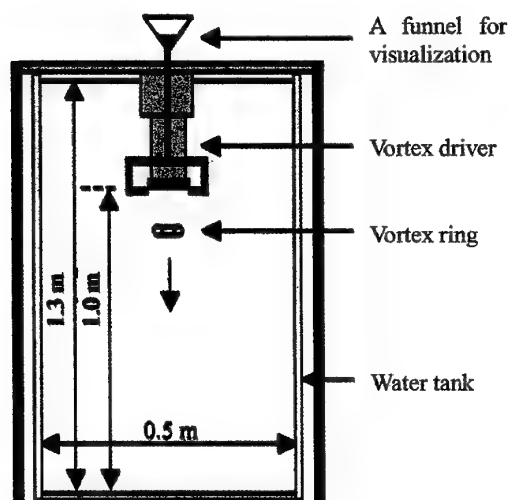


Fig.1 Experimental Setup

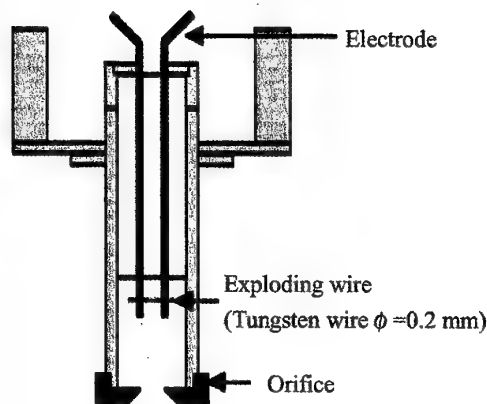


Fig.2 Vortex driver

3. EXPERIMENTAL RESULT

3.1 Single vortex ring

The evolution of a vortex ring generated by the exploding wire is shown in Fig.3, where an applied voltage is 0.875 kV. A vortex ring and a trailing wake are observed by flow visualization. In this case, the initial translational velocity u of a vortex ring is 3.78 m/s, and the Reynolds number is calculated to be 1.27×10^5 , where the orifice diameter $D (=0.03 \text{ m})$ and the kinematic viscosity $\nu (=0.893 \times 10^{-6} \text{ m}^2/\text{s}, \text{ at } 298 \text{ K})$ are employed in the definition of the Reynolds number, $Re = uD/\nu$. We notice that a vortex ring is laminar even in the Reynolds number of 10^5 .

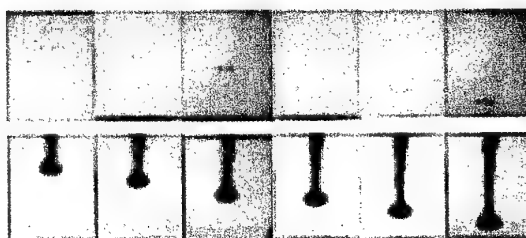


Fig.3 The temporal evolution of vortex ring with and without visualization

Applied voltage: 0.875 kV
Diameter of orifice: 30 mm

It is interesting to compare this result with the previous one obtained by Glezer.²⁾ A laminar vortex ring with $Re = 7.5 \times 10^3$ and a turbulent vortex ring with

$Re=2.7 \times 10^4$ are shown in Fig.4 (a) and (b). In the experiment by Glezer, a mechanical method has been employed to launch a vortex ring. Although the Reynolds number is different by about 20 times, a laminar vortex ring of our experiment is similar to that in Fig.4 (a). In the case of mechanical method, however, a vortex ring becomes turbulent even for lower Reynolds number compared to our method. The result indicates that the transition to a turbulent vortex motion does not depend on the Reynolds number, but on the method for generating a vortex ring.



Fig.4 Laminar and turbulent vortex rings photographed by Glezer (1988)

- (a) Laminar vortex ring ($Re=7.5 \times 10^3$)
- (b) Turbulent vortex ring ($Re=2.7 \times 10^4$)

3.2 Vortex tube

The temporal evolution of vortex tube is shown in Fig.5. If an applied voltage to an exploding wire is increased higher than that in Fig.3, the amount of water ejected from a pipe is larger than the amount that is needed for producing single vortex ring. Then a vortex ring of which the length in the direction of propagation is larger than that of single vortex ring is generated. We define it a vortex tube. We formed the vortex tube with the applied voltage 1.050 kV in this study. The initial translational velocity is 5.63 m/s and the Reynolds number is 1.67×10^5 . The upper and the lower pictures in Fig.5 are taken by UltranaC and CCD camera

respectively. The vortex tube propagates with oscillating the diameter and length periodically. The trailing edge of a tube decreases its diameter, goes inside of the tube and appears again in the leading edge. When the trailing edge is just inside of the tube, the length is at its minimum and the diameter is also at its minimum. That is, the diameter of a tube and the length in the direction of propagation oscillate in phase. The lower pictures clearly show this motion. The oscillatory motion looks like turning of a circular gum belt inside out. The vortex tube propagates repeating this motion and is gradually reduced to a vortex ring.

The visualization of flow by a vortex tube is shown in Fig.6. Whenever the trailing edge of a vortex tube shrinks its diameter during its propagation, a part of the vortex is left behind indicated by arrows, leading to the dissipation of vorticity. Because of the dissipation of vorticity, a vortex tube evolves to a vortex ring.

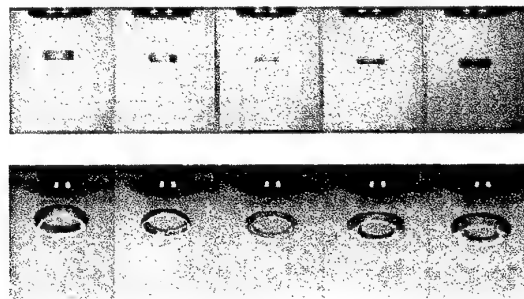


Fig.5 The temporal evolution of vortex tube.
Upper picture: Side view (UltranaC)
Lower picture: Diagonal under view (CCD).

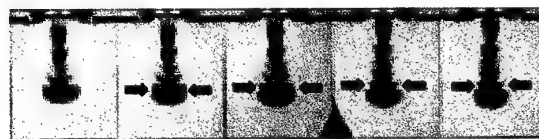


Fig.6 The visualization of the vortex tube.
Applied voltage: 1.050 kV.

3.3 Two vortex rings

If an applied voltage to an exploding wire is increased higher than that in Fig.5, the amount of water ejected from a pipe is larger than the amount that is

needed for producing a vortex tube. Then a vortex tube splits into two vortex rings in the course of propagation, where an applied voltage is 1.475 kV. The initial translational velocity is 7.13 m/s and Reynolds number is 2.12×10^5 . The temporal evolution of two vortex rings is shown in Fig.7.

In Fig.7, a vortex tube splits into two vortex rings at first. The rear vortex ring shrinks its diameter and the forerunner expands its diameter. Then rear vortex ring goes inside the front one and reappears in the front. After that, the role of two vortex rings is exchanged and the mutual slip-through restarts for the second time. In the second interaction, however, the rear vortex ring collapses. The visualized pictures of interaction of two vortex rings are shown in Fig.8. When the rear vortex ring shrinks its diameter, a part of the vortex is left behind (indicated by arrows). In the second interaction, a part of the vortex ring is also left behind. The flow leads to the dissipation of vorticity³⁾.

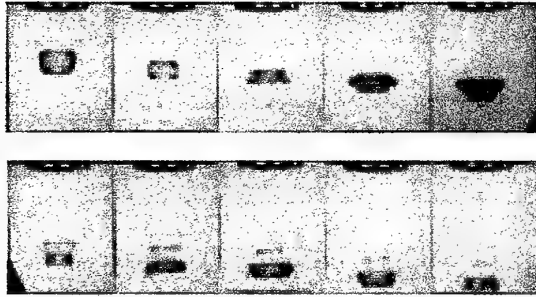


Fig.7 The temporal evolution of two vortex rings.
Applied voltage: 1.475 kV.

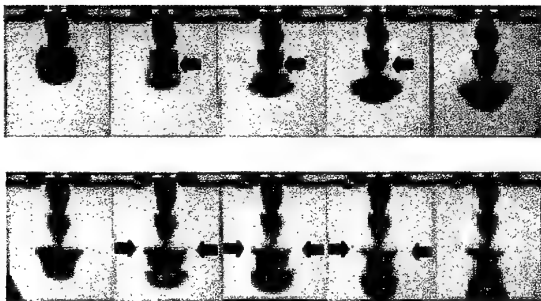


Fig.8 The visualization of two vortex rings.

After the second interaction between two vortex rings, only one vortex ring is remained. The structure of

the remainder is shown in Fig. 9 together with the trailing flow associated with the vortex ring. The left picture was taken from below and the other two pictures, horizontally. The left two pictures show that a vortex ring after the interaction has wavy structure and looks like a turbulent vortex ring. In fact, the rightmost picture visualized by dye represents a turbulent trailing wake, indicating that a turbulent vortex ring is generated through the interaction between vortex rings. The undulation of a vortex ring never disappears and hence a stable circular structure does not recover in the present experiment.

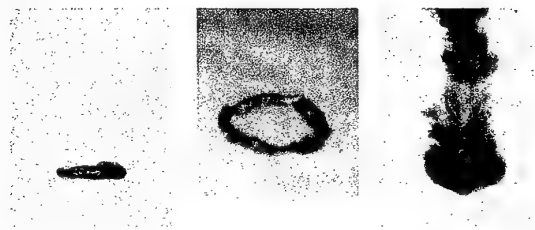


Fig.9 The turbulent vortex ring which is seen after interaction of two vortex rings.
Applied voltage: 1.475 kV.
33 ms passed from the orifice.

3.4 Elliptic vortex ring

In the previous section, we have observed that a turbulent vortex ring induced by the interaction between vortex rings has undulation of vortex core and does not recover a stable circular structure. To verify if the undulation of a vortex ring disappears in the course of propagation, we generate an elliptic vortex ring and observe the behavior of a perturbed vortex ring. For this end, we use an elliptic orifice to excite a perturbed vortex. It is well known that an elliptic vortex ring changes the diameter periodically while propagating⁴⁾. So far, a long distance evolution of an elliptic vortex ring has not been investigated, and thus we try to observe the evolution for a long distance to verify if a perturbed vortex ring returns to a circular one.

The elliptic vortex is excited in the voltage of 0.875 kV. The initial velocity is 3.15 m/s and Reynolds number is 8.93×10^4 . Here, we employed the average diameter of an elliptic vortex ring to calculate the

Reynolds number in terms of D . The major and minor radii are 40 mm and 34 mm respectively and the aspect ratio is 1.18. The temporal evolution of an elliptic vortex ring is shown in Fig.10. In the leftmost picture in the upper rank, the major radius of an elliptic vortex ring is seen. The radius gradually decreases and the minor radius appears in the rightmost picture in the upper rank or the leftmost picture in the lower rank. In the meantime of decreasing the radius, the velocity depends on the position of an elliptic ring and a vortex ring becomes convex. Then, the radius increases and the major radius reappears in the rightmost picture in the lower rank. In the meanwhile of increasing the radius, a vortex ring becomes concave.

The evolution of an elliptic vortex ring observed from below is shown in Fig.11. The change of the radius is clearly seen.

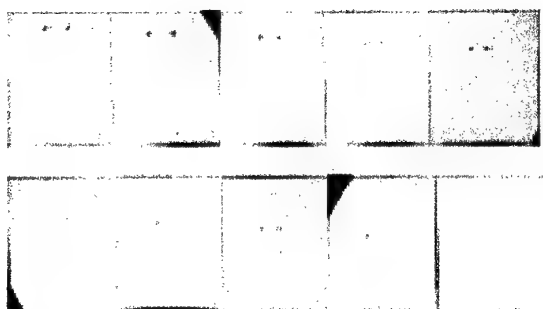


Fig.10 The elliptic vortex ring which formed by elliptic orifice, where aspect ratio is 1.18.

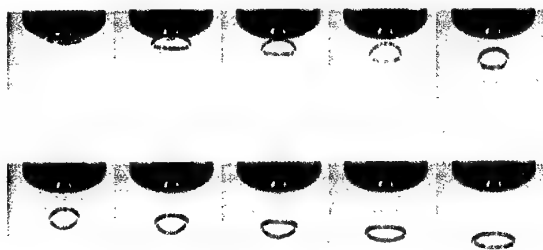


Fig.11 The elliptic vortex ring.
(Diagonal under view of Fig.10)

These geometrical changes are caused by the induced velocity. The local induction equation is given by $d\mathbf{X}/dt = A c \mathbf{b}$, where $A = (\Gamma/4\pi) \ln(R/\epsilon)$, c is the curvature and \mathbf{b} is a binormal unit vector. Here, Γ , R and ϵ denote a circulation, a diameter of a vortex ring and a diameter

of the vortex core respectively. Because of the velocity of the vortex filament is proportional to the curvature, the part of an ellipse with a large curvature travels faster than the part with a small curvature. Thus an elliptic vortex ring deformed periodically during its propagating.

The detailed form of an elliptic vortex ring is shown in Fig.12, where the ring is observed at a position perpendicular to the direction of propagation. At 31 msec and 48 msec, the major radius is seen and at 40 msec, the minor radius is observed. Except for these three cases, a vortex ring is not straight, but is bended.

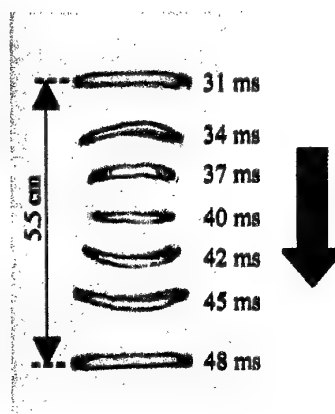


Fig.12 The detailed form of an elliptic vortex ring.

The visualized pictures of an elliptic vortex ring are shown in Fig.13. The backward trailing flow is almost straight contrary to the turbulent trailing flow of a perturbed vortex ring after the interaction shown in Fig.9. So, the dissipation of vorticity is not expected in the propagation of an elliptic vortex ring and the oscillation of a vortex ring would continue periodically.

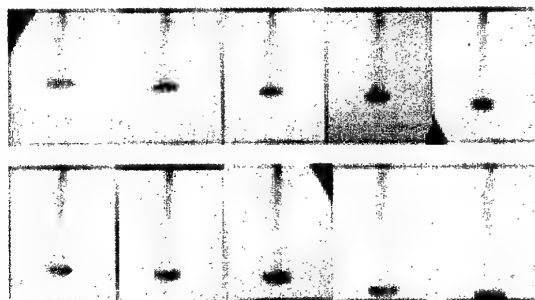


Fig.13 The visualized elliptic vortex ring of forth period.

The temporal evolution of diameter of an elliptic vortex ring is shown in Fig.14. The oscillation of the diameter is evidently periodic. In this figure, the ratio of the minor radius to the major is 66.3 % for the first period and is 66.7 % for the seventh period. That is, an elliptic vortex ring does not transform to a circular vortex.

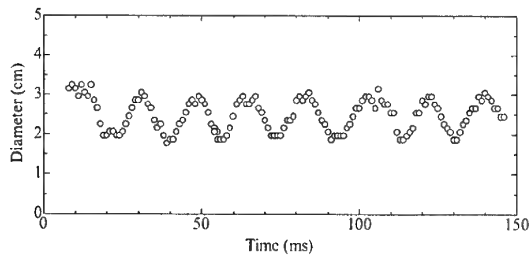


Fig. 14 The temporal evolution of diameter of an elliptic vortex ring.

4. CONCLUSIONS

We have experimentally investigated the formation of a turbulent vortex ring in high Reynolds number region, $Re \sim 10^5$.

Single vortex ring keeps on propagating as a laminar vortex ring even in the Reynolds number of 10^5 . In case of exciting two vortex rings, a vortex ring becomes turbulent after the collapse of another vortex ring by the interaction. So it is concluded that the interaction and collapse of vortex rings lead to the formation of a turbulent vortex ring.

We have also experimentally investigated the propagation of an elliptic vortex ring to verify whether a perturbed vortex ring evolves to a circular vortex ring. The elliptic vortex ring propagates with periodic oscillation. The oscillation does not decay. So it is concluded that an elliptic vortex ring does not transform to a circular vortex ring.

In order to verify if a perturbed vortex ring recovers a circular vortex ring, further investigations might be necessary in such cases as an elliptic vortex ring with different aspect ratio and also of an elliptic vortex ring with perturbation of different wave number.

REFERENCES

- 1) S. Watanabe, K. Nakamichi, I. S. Jang, K. Kazama, S. Hasegawa and S. Ishiwata 1995 "Generation of a Vortex Ring with High Reynolds Number by an Exploding Wire in Water" *J. Phys. Soc. Jpn.* **64** 3748-3757
- 2) A. Glezer 1988 "The formation of vortex rings" *Phys. Fluids*, **31** 3532-3542
- 3) S. Watanabe and K. Domon 1999 "Motion of a vortex tube in water in high Reynolds number region" FEDSM99-6819 Proceeding of the 1999 ASME/JASME Fluids Engineering Division Summer Meeting. July 18-22 1999, San Francisco, California.
- 4) T. Kambe and T. Takao 1971 "Motion of Distorted Vortex rings" *J. Phys. Soc. Jpn.* **31** No.2 591-599

VORTEX STRUCTURE OF IMPINGING ROUND JETS

S. Izawa

Machine Intelligence and System Engineering, Tohoku University
Sendai, 980-8579, Japan / Email: izawa@fluid.mech.tohoku.ac.jp

M. Kiya

Kushiro National College of Technology
Kushiro, 084-0916, Japan / Email: kiya@office.kushiro-ct.ac.jp

ABSTRACT

This paper presents results of three-dimensional vortex blob method simulations of two impinging round jets issuing from nozzles of the same diameter. When the jets face each other, the circular shear layers roll-up into vortex rings that impinge continuously in the following manner: As the two rings from each jet approach each other, they are stretched in the radial direction by the velocity induced by the other ring. Some distinct clumps are generated in the circumferential direction, growing into azimuthal waves by a symmetrical instability. This phenomenon is in good agreement with the experimental observation [1]. On the other hand, when the jets impinge obliquely, a new vortex ring is generated in the average direction of motion of the jets after the impingement. Thus, the vortex structure grows rapidly in this direction. The energy dissipation takes place actively in these vortex-reconnecting regions.

1. INTRODUCTION

Impinging jets have been used in many industrial applications, such as in chemical and biochemical industries, semiconductor manufacturing process, and combustion. These applications mainly focus on the mixing and

heat transfer behaviors of jets impinging onto solid surfaces. On the other hand, this paper studies the jet-to-jet impingement phenomena from a fluid dynamics perspective. There are a few researches in this area compared with those of the wall-impinging flows; these studies discuss only the shape of the spray or flame by flow visualization experiments.

The subject of this paper is to promote our understanding on the mechanism of the round jets impinging at an angle, focusing on the dynamics of vortex motions, using a three-dimensional vortex blob method. The results should yield useful pieces of information, for example, on flow inside internal combustion engines, especially a direct injection type engines, where mixing of fuel and oxidant is crucial.

In our previous study, the evolution of vortical structure in an impulsively started round jet forced by sinusoidal disturbances was clarified by the visualization of compact and highly organized, coherent structures within the jet [2]. In the present paper, we discuss the relation between the vortical structure in impinging jets and the mixing of jets with the surrounding fluid. We also discuss the energy dissipation caused by the jet impingement.

2. VORTEX METHOD

2.1. Formulation and Numerical Schemes

Vortex method calculates the evolution of a vorticity field represented by a collection of vortex particles, namely vortex blobs. A vortex blob α is defined by the position \mathbf{x}^α , vorticity ω^α , volume $d^3\mathbf{x}^\alpha$. Each blob has a spherically symmetric core-structure with a regulating function f_δ characterized by a smoothing radius (that is, a cutoff radius) σ_α ,

$$f_\delta(\mathbf{x}) = \frac{1}{\sigma_\alpha^3} f\left(\frac{|\mathbf{x}|}{\sigma_\alpha}\right) \quad (1)$$

with the normalization

$$4\pi \int_0^\infty f(\xi) \xi^2 d\xi = 1. \quad (2)$$

For the regulating function, the high-order algebraic smoothing [3] is used.

$$f(\xi) = \frac{15}{8\pi} \frac{1}{(\xi^2 + 1)^{7/2}}. \quad (3)$$

Thus, the entire vorticity field ω is obtained as a sum of these distributions,

$$\omega(\mathbf{x}, t) = \sum_\alpha \omega^\alpha(t) d^3\mathbf{x}^\alpha f_\delta(\mathbf{x} - \mathbf{x}^\alpha(t)). \quad (4)$$

The evolution of position \mathbf{x}^α and vorticity ω^α is described by the Biot-Savart law and the vorticity equation in a Lagrangian form, as follows

$$\frac{d\mathbf{x}^\alpha}{dt} = -\frac{1}{4\pi} \sum_\beta \frac{(r_{\alpha\beta}^2 + (5/2)\sigma_\beta^2)}{(r_{\alpha\beta}^2 + \sigma_\beta^2)^{5/2}} \mathbf{r}^{\alpha\beta} \times \boldsymbol{\gamma}^\beta, \quad (5)$$

$$\frac{d\omega^\alpha}{dt} = (\omega^\alpha \cdot \nabla) \mathbf{u}^\alpha, \quad (6)$$

where $\mathbf{r}^{\alpha\beta} = \mathbf{x}^\alpha - \mathbf{x}^\beta$, $|r_{\alpha\beta}| = |\mathbf{r}^{\alpha\beta}|$, and $\boldsymbol{\gamma}^\beta = \omega^\beta d^3\mathbf{x}^\beta$ is the strength. The vorticity equation (6) is solved by the transpose scheme [3]

$$\frac{d\omega^\alpha}{dt} = (\omega^\alpha \cdot \nabla^T) \mathbf{u}^\alpha. \quad (7)$$

The viscous diffusion is approximated by the particle exchange method. Thus, we obtain

$$\begin{aligned} \frac{d\omega^\alpha}{dt} = & \frac{1}{4\pi} \sum_\beta \left\{ \frac{(r_{\alpha\beta}^2 + (5/2)\sigma_\beta^2)}{(r_{\alpha\beta}^2 + \sigma_\beta^2)^{5/2}} (\omega^\alpha \times \boldsymbol{\gamma}^\beta) \right. \\ & + 3 \frac{(r_{\alpha\beta}^2 + (7/2)\sigma_\beta^2)}{(r_{\alpha\beta}^2 + \sigma_\beta^2)^{7/2}} (\omega^\alpha \cdot (\mathbf{r}^{\alpha\beta} \times \boldsymbol{\gamma}^\beta)) \mathbf{r}^{\alpha\beta} \\ & \left. - \frac{105\nu}{\sigma_\alpha^2} \frac{\sigma_\beta^6}{(r_{\alpha\beta}^2 + \sigma_\beta^2)^{9/2}} (\boldsymbol{\gamma}^\beta d^3\mathbf{x}^\alpha - \boldsymbol{\gamma}^\alpha d^3\mathbf{x}^\beta) \right\}. \quad (8) \end{aligned}$$

Note that the cut-off radius σ is constant for the particle exchange method; that is, $\sigma_\alpha = \sigma_\beta$.

Fluid motion is described by only the vorticity transport equation (8); this implies that pressure is not the essence of fluid motion. Pressure field can be obtained as a Poisson equation by taking the divergence of Navier-Stokes equations,

$$\frac{\nabla^2 p}{\rho} = -\nabla \cdot (\mathbf{u} \cdot \nabla \mathbf{u}), \quad (9)$$

where ρ is the density. Instead of using the iteration method such as SOR (successive over-relaxation) in the finite difference method, we solve the pressure Poisson equation as follows:

$$H = \frac{1}{4\pi} \sum_\beta \frac{(r_{\alpha\beta}^2 + (5/2)\sigma_\beta^2)}{(r_{\alpha\beta}^2 + \sigma_\beta^2)^{5/2}} (\mathbf{r}^{\alpha\beta} \cdot (\mathbf{u}^\beta \times \boldsymbol{\gamma}^\beta)) \quad (10)$$

where H is the Bernoulli function,

$$H = \frac{p}{\rho} + \frac{|\mathbf{u}|^2}{2}. \quad (11)$$

Total energy dissipation is defined by

$$\varepsilon(t) \equiv 2\nu \int s^2(\mathbf{x}, t) d^3\mathbf{x} \quad (12)$$

where s is a rate-of-strain tensor,

$$s^2(\mathbf{x}, t) = \sum_{i,j} \left(\frac{1}{2} \left(\frac{\partial u_i}{\partial x_j} + \frac{\partial u_j}{\partial x_i} \right) \right)^2. \quad (13)$$

Vorticity of the vortex blobs generally increases with time owing to the vortex stretching. Thus, to maintain the spatial resolution, a vortex blob α of length l_α is divided into two vortex blobs of the same vorticity ω^α , cut-off radius σ_α , and length $l_\alpha/2$, located at $\mathbf{x}^\alpha \pm (l_\alpha/2)\omega^\alpha/|\omega^\alpha|$, when the length l_α becomes greater than twice its initial value.

2.2. Flow Configuration

Calculations are performed for impulsively started round jets issuing with velocity U into the same fluid at rest from a straight nozzle of radius R . The xyz -coordinate system is defined such that the x -axis is along the axis of the nozzles when the jets impinge head-on, the y - and z -axes normal to the x -axis, and the origin is at the center

of both nozzles. Two nozzles are horizontally placed $40R$ apart facing each other when the jets impinge exactly head-on. The axes of both jets can also rotate around the y axis in the xz -plane with an arbitrary impinging angle θ . In this study, we simulate the head-on collision ($\theta = 180^\circ$) and the impingement at the right angle ($\theta = 90^\circ$).

The surface of the nozzle is constructed by 48 vortex blob panels. Vorticity of the vortex blobs is determined so as to satisfy the zero cross-flow velocity at the center of gravity of the panels. The nozzles are $1.048R$ long. The jet flow is produced by a source disk located in the yz -plane, which consists of 289 sources arranged in 8 circular shells of the same thickness. The image nozzle is placed on the opposite side of the above-mentioned yz -plane. The image flow issuing from this nozzle is ignored to save the calculation time because it has been found that whether the image flow is considered or not has little influence to the flow.

2.3. Numerical Procedure

Nascent vortex blobs are introduced into the flow at $0.061R$ downstream of the edge of the nozzle. To satisfy Kelvin's Law of conservation of circulation, the circulation of the nascent vortex blob $\Gamma_{nj}(t)$ at time t after its introduction is determined by

$$\Gamma_{nj}(t) = \Gamma_{pj}(t) - \Gamma_{pj}(t - \Delta t_n) \quad (14)$$

with $\Gamma_{nj}(0) = \Gamma_{pj}(0)$, where Γ_{pj} is the circulation of the vortex blobs which belong to the j -th panel at the edge of the nozzle, and Δt_n is the time interval of introducing the nascent vortex blobs. The nascent vortex blobs are advanced by the velocity induced at their center to simulate the shedding of vorticity from the edge.

The time interval of advancing the vortex blob Δt is $0.03R/U$, while the time interval of introducing the vortex blobs is $\Delta t_n = 2\Delta t$. The cut-off radius of the nascent vortex blobs is chosen as $0.785R$ which is 1.5 times the distance between neighboring panel blobs. The same cut-off radius is also used for the vortex blobs of the panels. The time advancement is made by the forth-order Adams-

Bashforth scheme.

Numerical simulations are performed at a Reynolds number $Re (= 2RU/\nu)$ of 2,000.

3. RESULTS AND DISCUSSION

3.1. Head-on Collision

Figure 1 shows the evolution and deformation of vortical structures in the impulsively started jets that face each other. The level of vorticity is represented with reference to the average vorticity of the nascent vortex blobs ω_0 . Initial shear layer rolls up into vortex rings continuously owing to the Kelvin-Helmholtz instability. As the rings approach each other, they are stretched in the radial direction by the velocity induced by the other rings. This behavior is consistent with the prediction of the inviscid theory. After the impingement at $x=0.0$, the rings expand outwards rapidly, and the vortex cores become shorter to maintain their volume while the vorticity increase to keep the circulation constant (frame (b)). Therefore, the vorticity gradient becomes larger, which leads to the enhanced vorticity diffusion and its cancellation.

The generation of distinct clumps in the circumferential direction and their growth into the azimuthal waves are results of the symmetrical instability. The number of the unstable waves is twelve in this case. In order to find out why the rings deform into the twelve circumferential waves, we carried out simulations under different conditions. That is, the number of vortex blobs around the perimeter of the nozzle N_c was changed from twelve to ten to find out that the wave number shifted to ten. This means that a numerical error was introduced from the position of connection of vortex blobs. In fact, by the thin vortex-tube simulation in which the cross section of the ring with core radius σ_R is represented by one blobs with cut-off radius $\sigma = \sigma_R$, we confirmed that, for a fixed core size, the number of blobs required for accurate discretization grows with the curvature of the ring [4, 5]. For example, when $\sigma/R = 0.3$, $N_c \geq 20 \sim 30$ is needed. This discussion is based on the assumption that $\sigma/R \ll 1.0$ since the analytical solution [6]

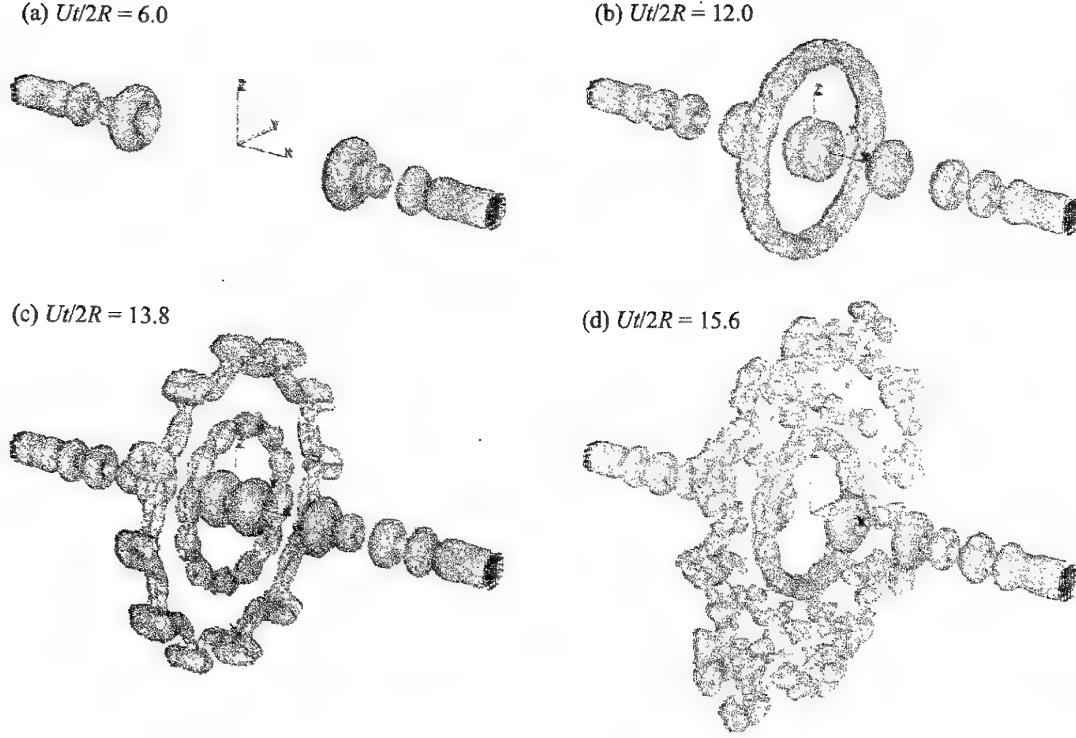


Fig.1: Impingement of round jets facing each other. Vorticity strength isosurface $\omega/\omega_0 = 14.3$.

which yields the self-induced velocity of a thin vortex ring was derived within this range. Thus, the present simulation is a crest-to-crest type collision in which the seed of azimuthal sinusoidal wave perturbation is sowed into both rings in phase.

When the radius of the impinging ring has increased to about four times its diameter, the symmetric instability in the form of azimuthal waves becomes distinct. Figure 2 shows the details of process of the vortex reconnection caused by impingement. The wave on the ring grows rapidly when its diameter is more than $4D$, $D (= 2R)$ being the diameter of the nozzle. After this instant, they reconnect to form a train of vortex rings since their cores are locally anti-parallel. Thus, the small-scale ringlets in Fig.2 (b) and (c) were generated by the cancellation and reconnection of the impinging ring vortices. Using an inviscid model, Crow [7] analyzed the same instability related to the waves on the trailing produced by the wing tips of an aircraft. This is also consistent vortices

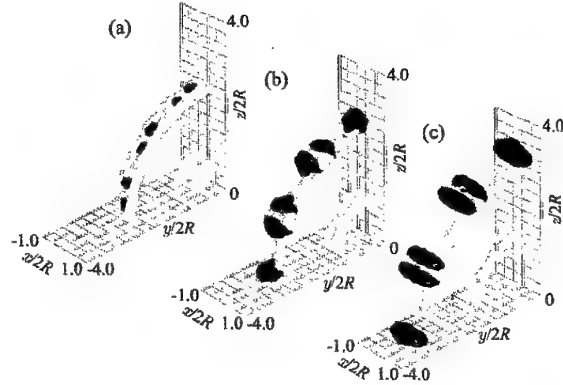


Fig.2: Ringlets generation by impinging jets at $Ut/2R = 12.0$ (a), 12.6 (b) and 13.2 (c). Vorticity strength isosurface $\omega/\omega_0 = 28.6$ (pale blue regions) and $\omega_x/\omega_0 = \pm 20.0$ (blue regions for positive ω_x and red regions for negative ω_x).

with an experimental result [1].

Figure 3 illustrates the relation between the energy dissipation and the vortex interaction. The energy is dissipated where the velocity gradient changes drastically, in partic-

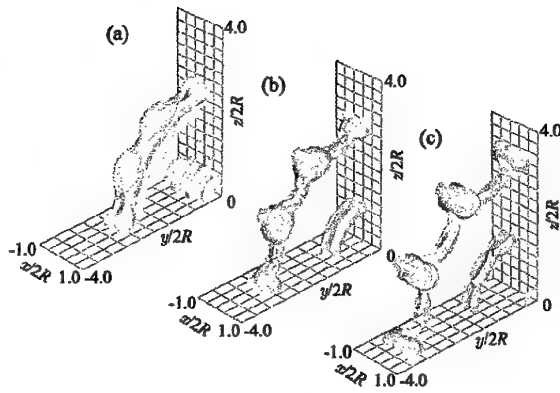


Fig.3: Energy dissipation and vortex interaction at $Ut/2R = 12.0$ (a), 12.6 (b), 13.2 (c). Vorticity strength isosurface $\omega/\omega_0 = 28.6$ (pale blue regions) and $s^2/s_{max}^2 = 0.3$ (orange regions).

ular in the impingement plane. On top of this, the energy dissipation is also caused by the ringlets because they produce a high additional velocity gradient in the radial direction.

The pressure distribution in the impingement plane is plotted in Fig.4. At the time $Ut/2R = 13.2$, the large "lead-off" vortex rings break up into the ringlets, while the following rings just impinge with each other. Thus, the high-pressure region is distributed concentrated within the impinging rings while the pressure decreases outward. It can be also found that the pressure in the area between the ringlets becomes low since the ringlets induce the velocity opposite to the direction of travel.

3.2. Oblique Collision

When the angle between the jet axes becomes smaller, a particular direction begins to appear in the vortex movement after the impingement. Figure 5 shows a series of vortical structure of the impinging jets at an angle of $\theta = 90^\circ$. As the vortex rings from the two jet approach each other, their closest parts start to collide and then, they move together in the $\theta/2$ direction. Thus, the rings are enlarged in this direction during reconnection, because each part of the rings of opposite-sign vorticity that is locally in close proximity experiences mutual cancellation (frame (b)). As

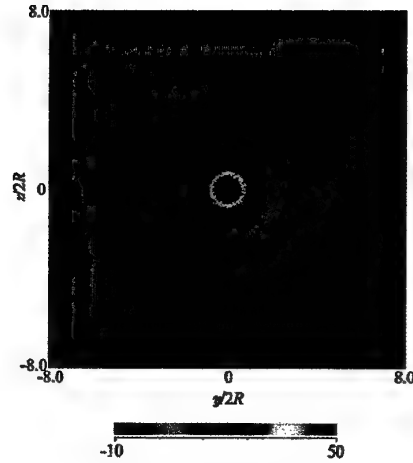


Fig.4: Pressure distribution $p/\rho U^2$ at $x/2R = 0.0$ and $Ut/2R = 13.2$.

a result, a new vortex ring in the form of an arc is generated. This arc ring slightly changes in shape as if a bag is closed by zipping since the induced velocity of the reconnection part is larger than that of the center (frame (c)). The rest of original rings interacts with the following ring (frame (c), (d)). These phenomena take place almost entirely in the impingement plane.

3.3. Further Discussions

The number of vortex blobs N_v in the simulated jets increases with time as presented in Fig.6. The rate of increase is linear up to a particular time $Ut/2R = 10.0$. This is due to the introduction of elemental vortex rings consisting of nascent vortex blobs with interval Δt_n . Beyond this time, the increase in N_v is enormously accelerated because the longitudinal vortices emerge by the vortex stretching during the impingement. This exponential increase in the number of vortex blobs requires the manipulation of blob merging or deleting in order to maintain spatial resolution. Although Rossi [8] analyzed the process of merging groups of many Gaussian basis functions into a single basis function in the two-dimensional vortex simulation, the quantitative discussions for the three-dimensional vortex method has been insufficient yet.

Furthermore, for N_v computational elements, $O(N^2)$

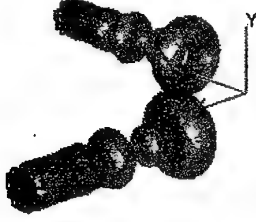
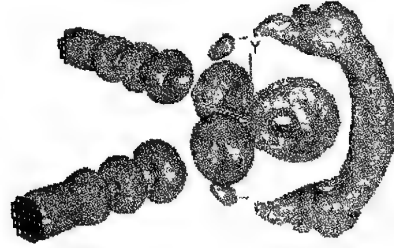
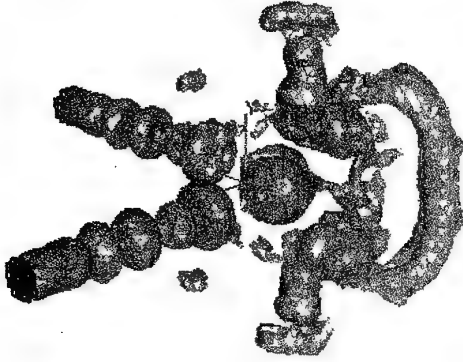
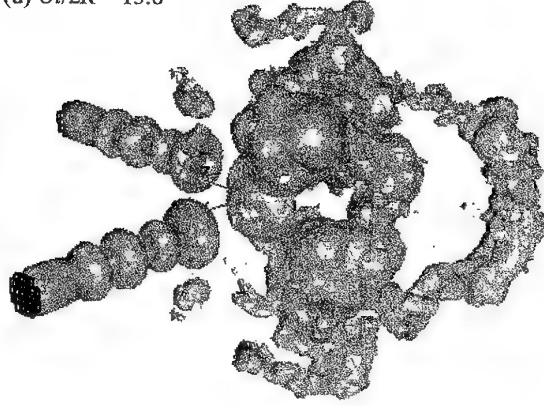
(a) $Ut/2R = 6.0$ (b) $Ut/2R = 12.0$ (c) $Ut/2R = 13.8$ (d) $Ut/2R = 15.6$ 

Fig.5: Impingement of round jets in flank at $Re = 2,000$. Vorticity strength isosurface $\omega/\omega_0 = 14.3$.

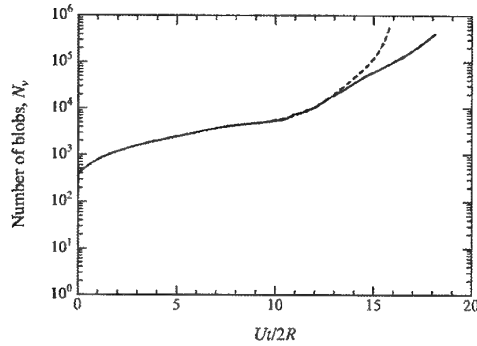


Fig.6: Number of vortex blobs N_v as a function of time at different impinging angle. Thick solid line is for $\theta = 180^\circ$ and short-dashed line for 90° .

operations are required to solve Eqs.(5) and (8). There are two approaches to avoid these problems so far; one is a Vortex-in-Cell (VIC) method which is based on the idea to retain the Lagrangian treatment of the vorticity field but to solve the Poisson equation for the velocity field

on a fixed Eulerian mesh [9]. The other is a method in which positions of blobs or filaments are redistributed every some time steps. Fernandez et al. [10] apply a filament "surgery" algorithm based on the energy density as regulation for the vortex collapse in addition to hierarchical methods (tree code), introducing a time extrapolation framework for each element. These are challenging issues in the three-dimensional vortex methods.

4. CONCLUSIONS

In this paper, the evolution of vortical structures at the jet-to-jet impingement has been simulated by the use of the three-dimensional vortex blob method. The process of generation of the ringlets in the head-on collision at moderate Reynolds number is demonstrated by the visualization of vortex motions. The energy dissipation occurs actively at the moment of impingement within the ringlets. The transformation of vortical structures in the oblique im-

pingement was demonstrated.

5. ACKNOWLEDGEMENTS

The authors would like to thank Prof. Yu Fukunishi of Tohoku University for his helpful discussions and encouragement during the preparation of this paper.

REFERENCES

- [1] Lim, T. T. & Nickels, T. B. (1992), Instability and Reconnection in the Head-on Collision of Two Vortex Rings, *Nature*, Vol. 357, pp. 225-227.
- [2] Izawa, S. & M. Kiya (2000), A Turbulence Model for Three-Dimensional Vortex Blob Method, *JSME International Journal*, Vol.43, No.3, pp. 434-442.
- [3] Winckelmans, G. S. & Leonard, A. (1993), Contributions to Vortex Particle Methods for Computation of Three-dimensional Incompressible Unsteady Flows, *Journal of Computational Physics*, Vol. 109, pp. 247-273.
- [4] Izawa, S. (2001), Vortex Method Simulations of Unsteady Vortical Flows, *Ph.D. thesis*, Hokkaido University.
- [5] Knio, O. M. & Ghoniem, F. (1990), Numerical Study of a Three-Dimensional Vortex Method, *Journal of Computational Physics*, Vol. 86, pp. 75-106 .
- [6] Saffman, P. G. (1992), *Vortex Dynamics*, Cambridge University Press.
- [7] Crow, S. C. (1970), Stability of Theory for a Pair of Trailing Vortices, *AIAA J.*, Vol. 8, pp. 2172-2179.
- [8] Rosshi, L. F. (1996), Resurrecting Core Spreading Vortex Methods: A New Scheme that is both Deterministic and Convergent, *J. Sci. Comput*, Vol. 17, No. 2, pp. 370-397.
- [9] Leonard, A. (1980), Vortex Methods for Flow Simulation, *Journal of Computational Physics*, Vol. 37, pp. 289-335.
- [10] Fernandez, V. M., Zabusky, J., Liu, P., Bhatt, S. & Gerasoulis, A. (1996), Filament Surgery and Tem-

poral Grid Adaptivity Extensions to a Parallel Tree Code for Simulation and Diagnosis in 3D Vortex Dynamics, *Vortex Flows and Related Numerical Methods II, ESAIM: Proceedings*, Vol. 1, pp. 197-211, <http://www.emath.fr/proc/Vol.1/>.

VELOCITY MAP AND FLOW PATTERN OF FLOW AROUND FOUR CYLINDERS IN A SQUARE CONFIGURATION AT LOW REYNOLDS NUMBER AND LARGE SPACING RATIO USING PARTICLE IMAGE VELOCIMETRY

K. Lam, K. T. Chan, R. M. C. So

Department of Mechanical Engineering, The Hong Kong Polytechnic University
Hung Hom, Kowloon, Hong Kong, PRC, E-mail: mmklam@polyu.edu.hk

and

J. Y. Li

Department of Fluid Engineering, Xi'an Jiaotong University, PRC, E-mail: jyli@xjtu.edu.cn

ABSTRACT

The velocity fields of the flow around four cylinders in a square configuration at Reynolds number, $Re = 200$ were investigated using particle image velocimetry (PIV) for a spacing ratio of $L/D = 4.0$ and an angle of incidence $\alpha = 0^\circ$ to 45° at 5° interval in a water tunnel. A range of sensitive α was observed. Within this range, a small change of α can cause a great difference in the flow pattern. At $\alpha < 15^\circ$, a jet flow pattern was observed. Such a phenomenon is a distinctive feature of this particular configuration and should be noted and be aware of in practical engineering applications. Moreover, three basic flow patterns, an anti-phase flow pattern, an in-phase flow pattern and a complex flow pattern, were observed in this experiment. The processes of shear layer reattachment, induced separation, vortex synchronisation and vortex impingement were involved in the above mentioned flow patterns. Furthermore, the experimental results could be used to validate numerical simulation methods developed specifically for flows around cylinder arrays.

1. INTRODUCTION

A four-cylinder array in a square configuration is a common arrangement in many engineering applications, such as off shore platforms, overhead cables and heat-exchanger tube banks. The flow pattern, including main flow direction, vortex shedding, near-wake flow patterns, the position of boundary layer separation, the stagnation regions, and the local velocity distributions around a four-cylinder array could have significant effects on the instantaneous pressure field, and hence the fluctuating lift and drag characteristics of the cylinders. Therefore, a detailed investigation of the

instantaneous velocity field using particle image velocimetry to highlight the flow pattern around a four-cylinder array with different spacing ratios and orientation to the main flow direction could provide important information and understanding of the fluctuating forces acting on the cylinders. Such information could be used to prevent and predict flow-induced vibrations on engineering structures. It could also contribute to the understanding of how local high velocities could give rise to severe flow-induced vibrations of the structures. Furthermore, an in-depth understanding of the regions of high local velocities coupled with the regions of wide stagnant wake resulting from flow/structural interference could also give insight to the physics of heat transfer to and from cylindrical tubes in heat exchanger tube banks.

Cross flow around multi-cylinders may exhibit many interesting and unexpected phenomena different from that of a single cylinder because of the mutual interference among the cylinders. However, due to the complexity of the wake flow behind cylinder arrays, previous experimental investigations were mainly concentrated on one or two cylinders [1-6]. Investigations on the flow around four cylinders by Lam & Lo [7] and Lam & Fang [8] showed that the wake of the array was far more complicated than that found in two cylinders as a result of the complex wake-structure interference. Even then, the velocity field around the four cylinders had not been measured. Such data is not available in the literature either. With the advent of laser techniques for flow visualisation and full-field velocity measurement, it is now possible to carry out a detailed investigation of the flow around four-cylinder arrays with different configurations, different α and different Re .

Up to now, only investigations on two- and three-cylinder arrays have been extensively carried out because they are the simplest of cylinder arrays. For example, Price & Paidoussis [1] measured the aerodynamic forces acting on groups of two and three circular cylinders. Sumner *et al.* [9] investigated the flow field around two and three circular cylinders of equal diameter arranged in a side-by-side configuration using flow visualisation, hot-film anemometry and particle image velocimetry (PIV). Furthermore, Sumner *et al.* [10] investigated the flow around two cylinders of equal diameter arranged in a staggered configuration using flow visualisation and PIV and identified nine different flow patterns. Numerical studies on two-cylinder arrays have also been carried out by Ng and Ko [11], while three-cylinder arrays have been investigated by Lam and Cheung [12]. The latter investigation examined the flow pattern and vortex shedding in different equilateral arrangements using flow visualisation and numerical method and was able to identify some prominent features that are quite different from those seen in two-cylinder arrays.

Although the equi-spaced square arrangement of four cylinders is frequently encountered in practical engineering applications, few studies have been carried out to study the interference effects in this particular arrangement. Sayer [13-14] conducted experiments on four cylinders in a square configuration and measured the base pressure, vortex shedding, lift and drag coefficients acting on one cylinder. Lam and Lo [7] carried out a visualisation study on the flow around four cylinders in a square configuration and their results showed that the wake of the array was far more complicated than that found in a two-cylinder array. On the other hand, Lam and Fang [8] measured the pressure distribution caused by the interference of the four equi-spaced cylinders and found great variations in the mean lift and drag coefficients of the cylinders as a result of the complex flow interference. On the other hand, numerical studies on four cylinders in square and other configurations using cell boundary element method have been carried out by Farrant *et al.* [15].

Until now, no full field measurements of the velocity distribution around four cylinders in a square configuration have been made. In the present study, as a preliminary attempt, the flow fields around four cylinders arranged in a square configuration at $Re = 200$ and $L/D = 4$ but with different α were investigated. The objective of the investigation is to carefully examine the effect of cylinder wake interference on the velocity distribution and flow patterns around the cylinders arranged as shown in Figure 1. The flow fields were measured using PIV in a water tunnel, and the fluid-structure interference effects were studied carefully by analysing the vortex distribution and the streamline patterns derived from the PIV measurements. The choice of $Re = 200$ is essentially dictated by the need to resolve the flow correctly and does not compromise the

value of the present investigation. After all, a need does exist on the understanding of the fluid-structure interference effects of multiple cylinders in a cross flow.

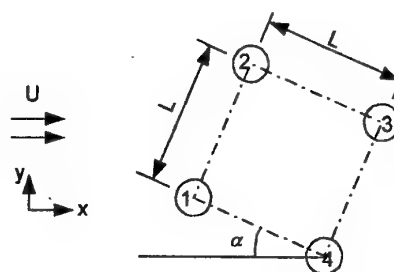


Figure 1. General configuration of the model

The experimental results could be used to validate numerical simulation methods developed for the flow around cylinder arrays at the same or higher Re range, different L/D ratios and different α .

2. EXPERIMENTAL DETAILS

Experimental Set Up The experiments were carried out in a low speed closed-loop water tunnel with a working section that has a $150\text{mm} \times 150\text{mm}$ cross-section. The walls of the test section were made of acrylic and glass plates to facilitate laser transmission and flow visualisation. The velocity in the test section was kept at 20 mm/s , thus giving a $Re = 200$, based on the diameter of a single cylinder and the free-stream velocity. The flow in the test section was laminar as observed by flow visualisation and its velocity was determined from the PIV measurements. The volume flow rate was also monitored by an orifice flow meter.

All four cylinders were installed on a circular plate in a cantilever manner. A schematic of the array configuration is shown in Figure 1. Note the numbering of the cylinders and α is measured with respect to the line joining cylinders 1 and 4. The clearance between the end of the cylinders and the test section side walls was about 1mm . Mounting facilities were provided in one of the vertical walls at the measuring station so that the plate could be flush mounted with the surface of the wall and can be rotated to any desired α . The cylinder cluster was positioned in the middle of the working section to prevent the possibility of near-wall effects. The angle α was varied from 0 to 45° at 5° interval.

The cylinders were made of hollow glass tubes filled with water. This was done to minimise the shadow created by the cylinders when illuminated by the laser sheet so that the velocity field around the cylinders can be measured. One end of each cylinder was sealed with a cap to prevent leakage while the other end was fitted with an adapter cap. The adapter cap was designed so that one of its ends could be fitted securely

into the remaining open end of the cylinder while the other end went through the plate and was tightened up by nuts from the other side. The outer diameter of the cylinder is 10mm. This gave an aspect ratio of about 15 and a blockage ratio (per cylinder) of ~6.7%. No attempt has been made to account for blockage effect in this investigation.

the optical flow system software, VidPIV, once the digital image of the flow field has been acquired from the CCD camera. In the analysis, the image is divided into small "interrogation regions". The interrogation region is 32×32 pixels, corresponding to a flow area of $3.75\text{mm} \times 3.75\text{mm}$. The image magnification is of the order of 0.117mm/pixel , so in the 40ms time difference

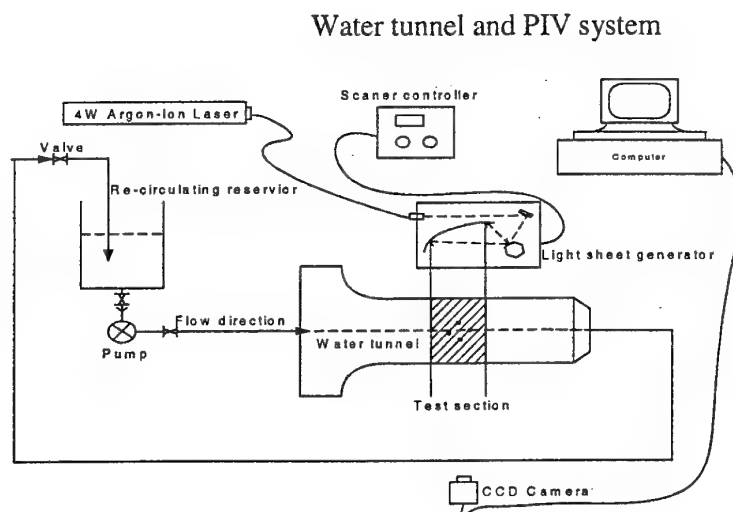


Figure 2. Schematic diagram of experimental apparatus

In order to facilitate the use of the PIV technique, nearly neutrally buoyant reflective particles of diameters 100 to 300 μm in size were added to the re-circulating reservoir as shown in Figure 2. The mid-section of the cylinder array was illuminated with a scanning light sheet generated by a Spectra-Physics Stabilite 2017 4W Argon-ion laser. A scanner controller was used to control the scanning frequency of the light sheet with a range from 1.5ms to 12.5ms. The digital images were recorded using an Adimec MX12P CCD camera and a Matrox Pulsar frame grabber. The resolution of the camera is 1024×1024 pixels while the integration time could be varied from 2 ms to 38ms so that the speed was high enough to provide a single frame/multi-exposed image. A maximum frame rate of about 25 images/s could be taken so that the cross-correlation technique of the multi-frame/single exposure method can be performed. The size of the imaging area covered about $120\text{mm} \times 120\text{mm}$ of the flow region. The camera data transfer interface was installed in a Pentium III 600MHz computer with a high-resolution monitor of the same order as the pixel density, a 256 Mbytes RAM and a 10G-byte hard disk.

Data Reduction The velocity vectors, the streamlines and the vorticity map are determined using

(25 frames/s) between the images comprising a pair, a particle moving at a mainstream velocity of 20mm/s ($Re = 200$) would cover a distance of 0.8mm , i.e. 6.8 pixels or 0.08 diameters. Of course, the size of the interrogation region effectively limits the minimum size of the vortex structures. After the image fields have been digitised, the particle displacements are extracted using a cross-correlation algorithm. In evaluating the cross-correlation, the initial positions of the seeding particle images are recorded on the first frame and the final positions are recorded on the second frame. The displacements of the seeding particles between the first frame and the second frame over the time interval are used to determine the velocity vectors. From the velocity plot, the software will also give the streamline pattern and the vorticity map.

3. RESULTS AND DISCUSSION

In the following, the results deduced from the PIV measurements are shown in three different panels, arranged from left to right. The panel on the left gives the velocity vector plot of the flow around the four cylinders, the centre panel gives the streamline pattern and the panel on the right shows the vorticity map thus

deduced. The results for $\alpha = 0^\circ$ to 45° in 5° interval are shown in Figures 3 to 12, respectively. All results are for the case where the free stream velocity is 20mm/s, corresponding to $Re = 200$. A velocity vector corresponding to 100 mm/s is inserted for comparison.

be about the same as that for a single cylinder. On the other hand, vortices are shed immediately downstream of cylinders 3 and 4. The vector plot clearly shows that the velocity of the gap flow is slightly higher than elsewhere, and the anti-phase flow pattern behind

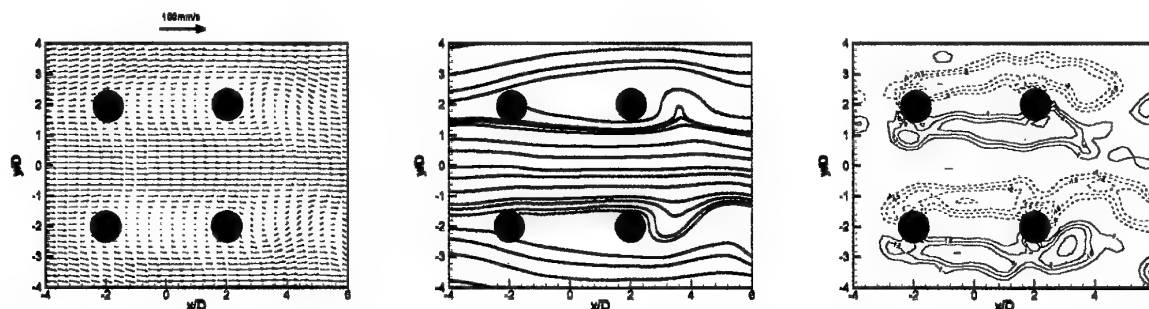


Figure 3. Flow field at 0° incident angle

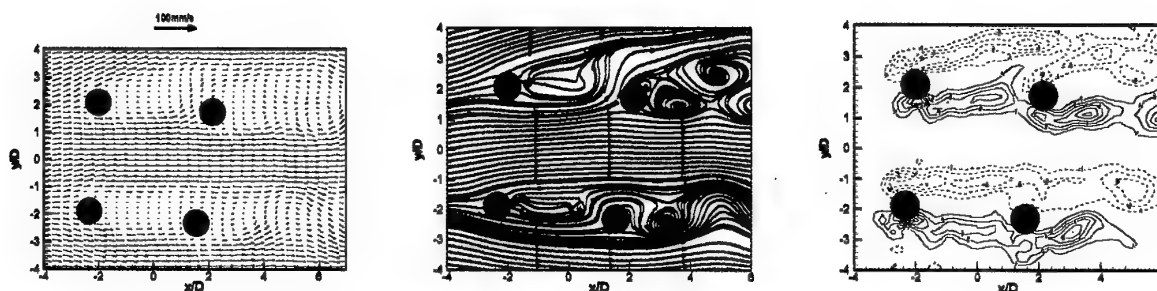


Figure 4. Flow field at 5° incident angle

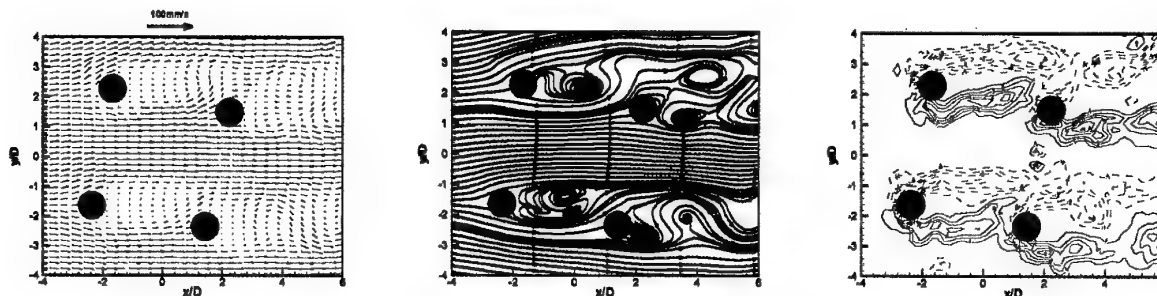


Figure 5. Flow field at 10° incident angle

At $\alpha = 0^\circ$, the cylinder array can be regarded as two rows of two-cylinder array in tandem (Figure 3). At this Re and L/D , the downstream cylinder is almost 'shielded' by the upstream cylinder, a result similar to that observed for two cylinders in tandem. No vortex shedding occurs for the upstream cylinder and the position of its boundary layer separation is observed to

cylinders 3 and 4 is easily recognised from the streamline plot. Even at $L/D = 4$, fluid-structure interference is discernible. From the vorticity map, it can be seen that the vortex strength is weak with the presence of the second cylinder. The overall effect of the cylinder is attributed to proximity interference.

The velocity vectors, streamline pattern and vorticity map at $\alpha = 5^\circ$ are shown in Figure 4. At this α , the cylinders take on a slightly staggered arrangement. Although α changes slightly, the flow pattern was completely different from the $\alpha = 0^\circ$ case. The flow behind cylinders 3 and 4 is not anti-phase, however, the flow is biased towards the top side of the downstream cylinders. It can be seen that the wake flow of every cylinder is different. Vortex shedding from cylinders 1 and 2 are suppressed and there is no obvious vortex shedding formed behind them. However, due to the effect of the high jet stream velocity in the gap, the wake of cylinders 1 and 2 are only slightly biased towards the gap flow. For cylinder 3, the jet stream impinges on the cylinder thus causing a shear layer induced separation. As a result, the wake formed behind the cylinder 3 is wide and the vortex strength is also strong. The jet stream does not impinge on cylinder 4, hence there is no shear induced separation. It follows that the wake formed is narrow and the vorticity in the wake is weak. Consequently, the lift force acting on cylinders 2, 3 and 4 is positive while that on cylinder 1 is negative according to Lam & Fang [8].

separations occur for cylinders 3 and 4. For cylinder 3, there is a jet flow with high momentum through the gap between cylinders 2 and 3. On the other hand, the jet flow through cylinders 1 and 4 is not so strong. As a result, the wake and vortex shedding from cylinder 4 is not as wide and strong as that of cylinder 3. However, the width of the wake behind cylinder 4 has increased compared with that for the $\alpha = 5^\circ$ case. Moreover, there are weak vortex shedding from cylinders 1 and 2 due to the presence of cylinders 3 and 4.

As α increases to 15° , noticeable changes occur for cylinder 3 and 4 (Figure 6). The jet stream that impinges on cylinder 3 has an even higher momentum. Under the influence of the wake of cylinder 2, a rather strong jet flow was formed and pointed at an oblique angle outward. From the vorticity plot, it is obvious that even though the jet is very narrow, its vortex strength is rather strong. Consequently, the width of the wake of cylinder 3 becomes wider. Such a spectacular flow pattern should be noted because the flow pattern will give rise to a strong lift force on cylinder 3 as measured by Lam & Fang [8]. These results show that a change of lift will occur with a change of α . For cylinder 4, a similar jet is formed. However, due to the

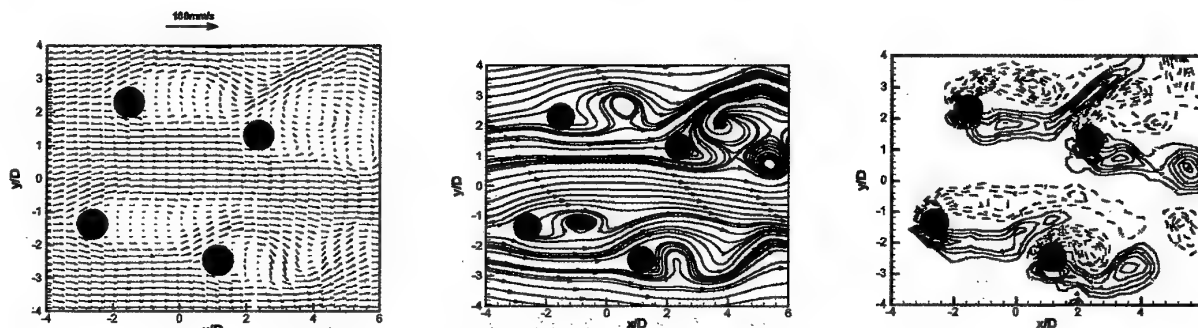


Figure 6. Flow field at 15° incident angle

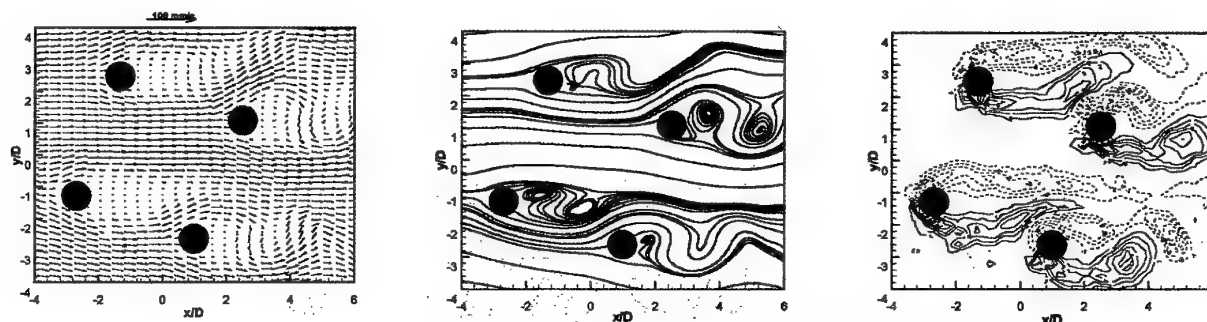


Figure 7. Flow field at 20° incident angle

Similar plots for the $\alpha = 10^\circ$ case are shown in Figure 5. At this α , cylinders 3 and 4 are not completely shielded by cylinders 1 and 2 as in the previous two cases. Unlike the $\alpha = 5^\circ$ case, shear layer induced

obstruction of the high momentum gap flow, the jet is suppressed. The wake becomes narrow and short compared with that of cylinder 3. It is interesting to note that the wake formation length of cylinder 4

becomes shorter compared with the $\alpha = 10^\circ$ case. Contrast to cylinders 1 and 2, the wakes of cylinders 3 and 4 are quite asymmetrical.

Figure 7 shows the plots at $\alpha = 20^\circ$. The flow patterns of the four cylinders are all different. For cylinder 1, the wake and vortex shedding is like that of a single cylinder. Due to the influence of cylinder 4, the wake behind cylinder 1 cannot develop fully. As a result, the wake is weak and short. For cylinder 2, its wake vortex is wider compared with cylinder 1. The jet flow through cylinders 2 and 3 still exists and is again stronger than that through cylinders 1 and 4. Consequently, the vortex distributions for the $\alpha = 15^\circ$

and $\alpha = 20^\circ$ case are similar, except the width of the jet flow before cylinders 3 and 4 becomes much wider and stronger.

At $\alpha = 25^\circ$, the two rows of cylinders form an approximate diamond configuration (Figure 8). As a result, the flow pattern is quite different from that at $\alpha = 15^\circ$ and 20° . The wake behind cylinder 1 is completely surrounded by the mainstream. Due to the existence of the gap formed by cylinders 3 and 4, the length of the wake could only reach the location of cylinder 4. There is little change in the shape of the wake. The wake behind cylinder 2 cannot fully develop either because of the presence of cylinder 3, but the vortices in the wake

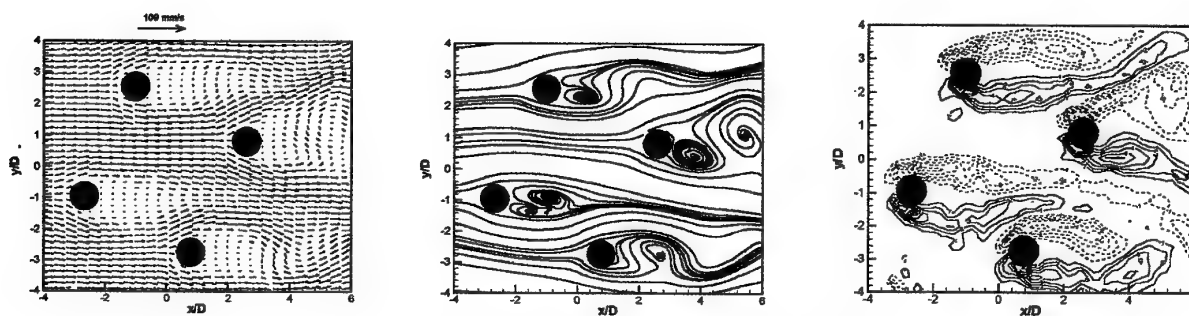


Figure 8. Flow field at 25° incident angle

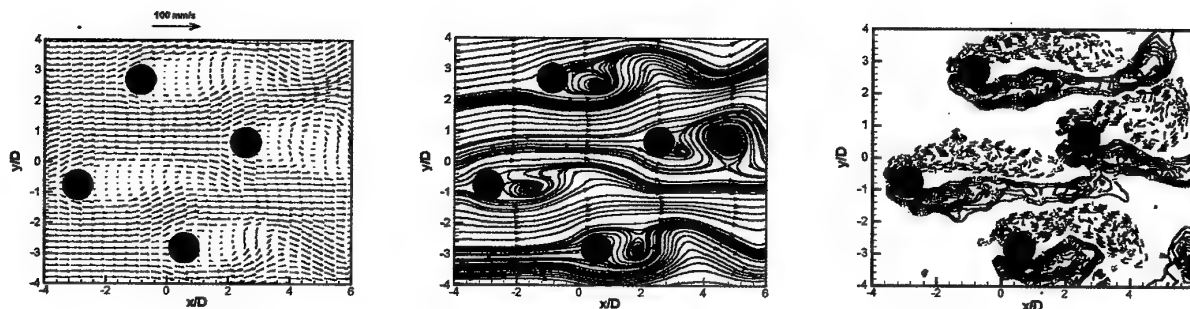


Figure 9. Flow field at 30° angle

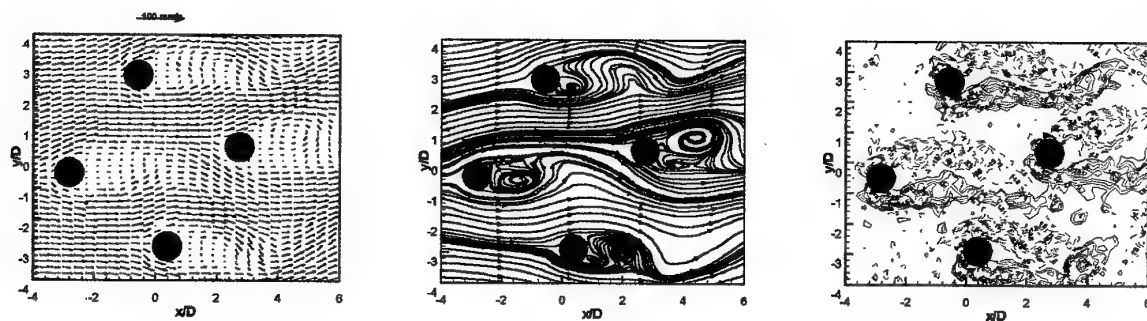


Figure 10. Flow field at 35° incident angle

quickly move down with the mainstream flow. For cylinder 3, the jet flow is not so strong and obvious as before, the mainstream impinges on it almost directly. However, due to the interference of the wake of cylinders 1 and 2, separation from the cylinder moves upstream. As the vertical position of cylinder 3 is closer to cylinder 2 than to cylinder 1, the separation angle appears to be smaller at the top than at the bottom side. Therefore, the flow around cylinder 3 is not symmetric. The gap flow and the main flow surround the wake behind cylinder 4. Consequently, its wake width is smaller compared with that of cylinder 3 and its vortex shedding moved rapidly to the mainstream.

Figure 9 shows the representative flow field at $\alpha = 30^\circ$. At this α , the shear layer from cylinder 1 begins to impinge on cylinder 3, and its vortex shedding are influenced by cylinders 3 and 4 also. For other cylinders, no obvious changes are observed. The interference is mainly caused by the proximity effect of the cylinders. From the force measurement of Lam & Fang [8], it was known that the lift force acting on cylinders 1 and 2 are close to zero, while that of cylinder 3 is slightly negative and cylinder 4 is slightly positive. Therefore, it can be deduced that the pressure field in the area bounded by cylinders 1, 3 and 4 is low, while the fluctuating lift force on cylinder 3 would be

larger than those on other cylinders.

The flow field at $\alpha = 35^\circ$ is shown in Figure 10. At this angle, the shear layer from cylinder 1 impinges directly on cylinder 3. Moreover, it is interesting to note that vortex shedding from cylinders 2 and 4 are more likely in phase even though the eddies from cylinder 2 are larger than those shed from cylinder 4. It appears that the effect of mutual interference is the least at α between 30° and 35° .

Figure 11 shows the flow field at $\alpha = 40^\circ$. At this α , the vortices shed from cylinder 1 impinge on cylinder 3 directly (vortex impingement phenomena) and then separates from the cylinder. The vortex formation length is shortened as well. Meanwhile, the vortex shedding from cylinder 2 and 4 are almost in-phase, and their vortex formation length are shortened also due to the presence of cylinder 3. As for cylinder 3, vortex shedding from the cylinder interacts rapidly with the vortices from cylinders 2 and 4. It can be seen that cylinder 3 is subjected to a wake interference from cylinder 1. As α increases to give a pure diamond configuration ($\alpha = 45^\circ$), the flow patterns of cylinders 2 and 4 are nearly in-phase (Figure 12). Contrast this to the flow pattern at $\alpha = 0^\circ$ (Figure 3), the free shear layers of cylinder 1 do not develop long enough to cover the downstream cylinder 3. Only the vortex shed

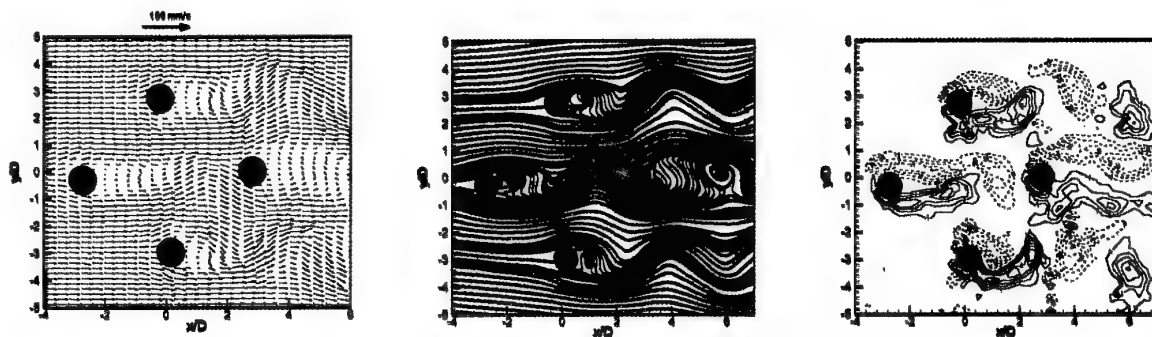


Figure 11. Flow field at 40° incident angle

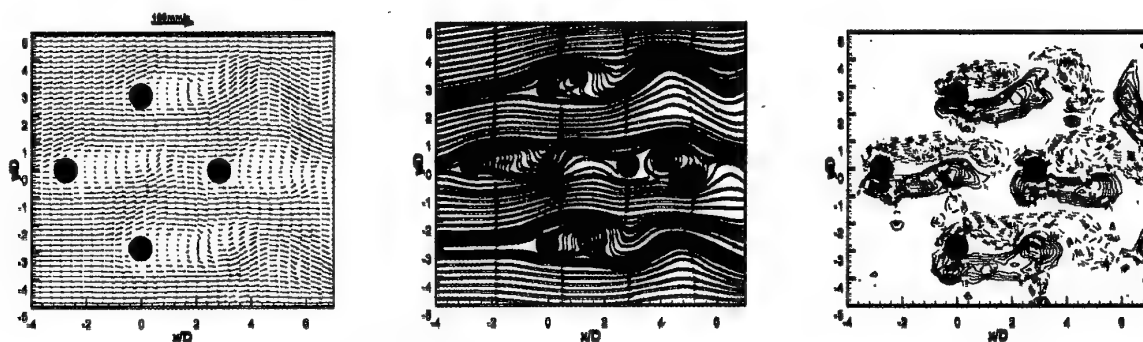


Figure 12. Flow field at 45° incident angle

from cylinder 1 impinges on cylinder 3 alternatively. Unlike the flow patterns of the cylinders at a side by side arrangement, the vortex shedding from cylinders 2 and 4 are nearly in phase, but the vortex shedding from cylinder 1 appears to be anti-phased. Cylinders 1 and 3 are in tandem arrangement with cylinder 3 being impinged by the turbulent eddies of cylinder 1, while cylinders 2 and 4 are in a side-by-side configuration with little interference on each other. In general, the flow fields around cylinder 1, 2 and 4 are close to that of a single cylinder.

4. CONCLUSION

In this study, the flow field around four cylinders arranged in a square configuration was investigated using PIV to measure the flow field and to deduce the streamline pattern and the vorticity map. The free stream was set at 20mm/s, thus corresponding to $Re = 200$, and the spacing ratio was fixed at $L/D = 4$. On the other hand, α was varied from 0° to 45° at 5° interval. Some interesting observations on the flow and certain conclusion can be made.

- (1) There exists a range of sensitive α where even a small variation can cause a drastic change in the flow pattern. This sensitive α range varies from 0° to 15° .
- (2) A jet flow pattern was observed in the α range from 5° to 15° . Such a phenomenon is very noticeable in the present arrangement and should be mentioned and made aware of in practical engineering applications.
- (3) Three basic flow patterns were observed in the present experiment. The first is an anti-phase flow pattern at $\alpha = 0^\circ$. The second is an in-phase flow pattern at α ranging from 35° to 45° . The third is that every cylinder has its own flow pattern and it is different from each cylinder to the next.
- (4) The results could be used to validate numerical codes developed to calculate flow around cylinder arrays. These codes are needed for the calculation of flow around structural arrays at much higher Re , different L/D and a wide range of α , so that offshore pilings and other structures can be designed properly.

ACKNOWLEDGEMENTS

Funding support from the Research Grants Council of the Hong Kong Special Administrative Region, China under Project No. PolyU5147/99E is gratefully acknowledged.

REFERENCES

- [1] Price, S. J. & Paidoussis, M. P. (1984) The aerodynamic forces acting on groups of two and three

circular cylinders when subjected to a cross flow, *Journal of Wind Engineering and Industrial Aerodynamics*, Vol. 17, pp. 329-347.

- [2] Zdravkovich, M. M. (1987) The effects of interference between circular cylinders in cross flow, *Journal of Fluids and Structures*, Vol. 1, pp. 235-261.

[3] So, R. M. C. & Savkar, S. D. (1981) Buffeting forces on rigid circular cylinders in cross flows, *Journal of Fluid Mechanics*, Vol. 105, pp. 397-425.

- [4] Sin, V. K. & So, R. M. C. (1987) Local force measurement on finite-span cylinders in a cross-flow. *ASME Journal of Fluids Engineering*, Vol. 109, pp. 136-143.

[5] Baban, F. & So, R. M. C. (1991) Aspect ratio effect on flow-induced forces on circular cylinders in a cross-flow, *Experiments in Fluids*, Vol. 10, pp. 313-321.

- [6] Baban, F. & So, R. M. C. (1991) Recirculating flow behind and unsteady forces on finite-span circular cylinders in a cross-flow, *Journal of Fluids and Structures*, Vol. 5, pp. 185-206.

[7] Lam, K. & Lo, S. C. (1992) A visualization study of cross-flow around four cylinders in a square configuration, *Journal of Fluids and Structures*, Vol. 6, pp. 109-131.

- [8] Lam, K. & Fang, X. (1995) The effect of interference of four equi-spaced cylinders in cross flow on pressure and force coefficients, *Journal of Fluids and Structures*, Vol. 9, pp. 195-214

[9] Sumner, D., Wong, S. S. T., Price, S. J. & Paidoussis, M. P. (1999) Fluid behaviour of side-by-side circular cylinder in steady cross-flow, *Journal of Fluids and Structures*, Vol. 13, pp.309-338.

- [10] Sumner, D., Price, S. J. & Paidoussis, M. P. (2000) Flow-pattern identification for two staggered circular cylinders in cross-flow, *Journal of Fluid Mechanics*, Vol. 411, pp. 263-303.

[11] Ng, C. W. & Ko, N. W. M. (1995) Flow interaction behind two circular cylinders of equal diameter - a numerical study, *Journal of Wind Engineering and Industrial Aerodynamics*, Vol. 54/55, pp. 277-287.

- [12] Lam, K. & Cheung, W. C. (1988) Phenomena of vortex shedding and flow interference of three cylinders in different equilateral arrangements, *Journal of Fluid Mechanics*, Vol. 196, pp. 1-26.

[13] Sayers, A. T. (1988) Flow interference between four equispaced cylinders when subjected to a cross flow, *Journal of Wind Engineering and Industrial Aerodynamics*, Vol. 31, pp. 9-28.

- [14] Sayers, A. T. (1990) Vortex shedding from groups of three and four equi-spaced cylinders situated in a cross flow, *Journal of Wind Engineering and Industrial Aerodynamics*, Vol. 34, pp. 213-221.

[15] Farrant, T., Tan, M. & Price, W. G. (2000) A cell boundary element method applied to laminar vortex shedding from arrays of cylinders in various arrangements, *Journal of Fluids and Structures*, Vol. 14, pp. 375-402.

FLOW AROUND FOUR CYLINDERS IN A SQUARE CONFIGURATION USING SURFACE VORTICITY METHOD

K. Lam, R. M. C. So

Department of Mechanical Engineering, The Hong Kong Polytechnic University
Hung Hom, Kowloon, Hong Kong, PRC, e-mail: mmklam@polyu.edu.hk

and

J. Y. Li

Department of Fluid Engineering, Xi'an Jiaotong University, PRC, e-mail: jyli@xjtu.edu.cn

ABSTRACT

With an increased in popularity of PC and Windows95, a user-friendly Visual C++ software is developed specifically for the simulation of the flow around four cylinders. The Surface Vorticity Method (SVM) is used to simulate this two-dimensional (2-D) flow. With the grid-free SVM package, four cylinders at different incident angles and spacing ratios can be placed in the flow for simulation easily so that large numbers of numerical experiments can be performed. During the simulation, full cloud vortices were shed into the flow initially. A 'Velocity Direction Scheme' was used to correct the positions of shedding of the free vortices. Extensive simulations have been carried out at sub-critical Reynolds number ($Re = 1.3 \times 10^4$) and several spacing ratios. However, typical results for four equal size cylinders at spacing ratios of 1.5 and 4, and with flow incident angles that vary from 0° (normal square configuration) to 45° (rotated square configuration) are presented. Spectacular change of vortex cloud flow patterns and velocity field maps was obtained with changing incident flow angle and spacing ratio. Comparison of the computed results with experimental measurements showed that SVM is able to replicate most of the salient features observed in cylinder array experiments. Thus, SVM a reasonably accurate and convenient simulation method for the study of 2-D flows around cylinders at sub-critical Reynolds numbers.

1. INTRODUCTION

Understanding the flow around four equi-spaced cylinders in a cross-flow has important impact in many practical engineering applications, such as offshore structures, chimneys, overhead cables and heat exchanger tube bundles. The near-wake flow patterns, and the local velocity distributions around a four-

cylinder array could directly affect the instantaneous pressure field and hence the fluctuating lift and drag characteristics of the cylinders. Investigation of the instantaneous velocity field around a four-cylinder array at different flow incident angles, α , and with different spacing ratios, L/D , could provide insight to the causes of flow-induced vibrations of engineering structures and the heat transfer characteristics in heat exchangers. Here, L is the spacing between cylinders, and D is the cylinder diameter. Some experimental investigations on the flow around four equal size cylinders at different L/D and α [1-2] have shown that the flow around four cylinders is far more complex than that found in one or two cylinders as a result of wake-structure interference. Since there are numerous possible arrangements and configurations for four cylinders, experimental studies would be rather time consuming and costly. Therefore, it would be desirable to develop a simulation package to study the flow around 2-D cylinder arrays so that extensive numerical experiments can be performed easily. It is hoped that the availability of such computer software could save a lot of laborious and costly experimental investigations.

Most computational approaches used for flow simulations can be divided into two broad categories; namely the grid methods and the grid-free methods. For the grid methods, such as finite difference method and finite element method, the governing Navier-Stokes equations are solved directly. However, the flow around cylinder arrays are usually computed at Reynolds number (Re) up to a few hundred [3-4] while the Re for flows around cylinders in many engineering applications are of much higher order $O(10^6)$. In such circumstance, the conventional grid methods will not give a satisfactory prediction within a reasonable computational cost. In addition, the pre-processing and mesh-generation are time-consuming for the grid

method in numerical experiments. Instead of the above approach, the vortex methods, such as those discussed in Sarpkaya [5], Slaouti & Stansby [6] and Tsutsui *et al.* [7], represent an attractive alternative. Attempts have also been made to predict the vortex patterns and the velocity distributions around cylinders using a numerical surface vorticity modelling approach [8]. With such a method, the 2-D vorticity distribution, the instantaneous full-field velocity distribution map and the force characteristics can be computed conveniently using a Pentium PC. In view of this convenience, the grid-free surface vorticity method originated by Martensen [9] and further developed by Lewis [10] is employed in the present investigation. However, it should be noted that, at the present investigation, the method is restricted to 2-D flows only. In spite of this limitation, it might be regarded as an engineering approach to flow simulation because it could be used to seek understanding of the fundamental flow physics embedded in the complex flow around cylinder arrays.

In this method, the thin boundary layer is simplified to a simple surface vorticity sheet. Martensen's surface vorticity model was found to be very simple for the simulation of potential flow around any arbitrary shaped body in a 2-D flow. The method was originally applied to flows around bluff bodies assuming fixed separation points [10, 11]. In the present simulation, instead of fixed separations, full cloud vortices are shed into the flows initially. Thus, one of the method's restrictions is relaxed in the present approach. A 'Velocity Direction Scheme' (VDS) is adopted to correct the positions of free vortex shedding. The vortices shed are free to convect under mutual induction by the Biot-Savart induction theorem.

Extensive simulations have been carried out at $Re = 1.3 \times 10^4$ for small and large L/D at different α . However, for illustration purposes, typical results for the flow around four equi-spaced cylinders at $L/D = 1.5$ and 4 and different α are presented. A comparison of the calculated results with some visualisation studies and velocity maps measured using PIV is attempted. The ability of the SVM and the viability of the VDS to predict separation and the subsequent flow behaviour in the flow around cylinder arrays are assessed. Particular attention is paid to the method's ability to replicate the salient features observed in the cylinder array experiments.

2. THEORY AND NUMERICAL MODELLING

The fluid motion is governed by the Navier-Stokes equations. The momentum equation can be transformed to a vorticity transport equation which, for incompressible viscous flow, is given by

$$\frac{\partial \bar{\omega}}{\partial t} + \bar{U} \cdot \nabla \bar{\omega} - \bar{\omega} \cdot \nabla \bar{U} = \nu \nabla^2 \bar{\omega} \quad (1)$$

For 2-D flows, the vorticity transport equation can be further simplified to

$$\frac{\partial \omega}{\partial t} + \bar{U} \cdot \nabla \omega = \nu \nabla^2 \omega \quad (2)$$

From (2), instead of the transport of momentum, flow development can be regarded as the results of vorticity generation, $\partial \omega / \partial t$, vorticity convection, $(\bar{U} \cdot \nabla) \omega$, and the diffusion of vorticity, $\nu \nabla^2 \omega$. In the present numerical model, these physical processes are simulated step by step as follows:

- (i) Martensen's potential flow calculation,
- (ii) Free vortex production and shedding, and separation point determination,
- (iii) Free vortex convection and viscous diffusion.

These steps are briefly described below.

2.1 Martensen's Potential Flow Method for Calculating Surface Vortices

Potential flow around an arbitrary body In the case of attached flow past a bluff body, a very thin boundary layer is formed on the body surface. According to boundary layer theory, only the flow inside the boundary layer is viscous. Outside the flow could be considered as inviscid and irrotational. In Martensen's surface vorticity method, the boundary layer is simplified to a vortex sheet of strength $\gamma(s)$ parallel to the surface of the body. Thus, the vorticity sheet creates a flow discontinuity parallel to the body surface. Equating the vortex sheet of length ds and the circulation around it, the velocity immediately outside the boundary layer can be shown to be given by $v_s(s) = v_e(s) = \gamma(s)$ and the convection velocity of the vorticity sheet is $v_s(s)/2$. Therefore, the potential flow problem is reduced to the calculation of the surface vorticity distribution such that the resulting flow is parallel to the body surface at all points. Using this condition, Martensen [9] developed a well-known integral equation

$$\int \gamma(S_n) K(S_n, S_m) dS_n - \frac{1}{2} \gamma(S_m) = -W_\infty (\cos \beta_m \cos \alpha_\infty + \sin \beta_m \sin \alpha_\infty) \quad (3)$$

where

$$\cos \beta_m = \frac{dx_m}{ds} \quad \& \quad \sin \beta_m = \frac{dy_m}{ds} \quad (4)$$

α_∞ is the inclination of the mainstream W_∞ to the x axis and $K(S_n, S_m)$ are the coupling coefficients, whose values are that of the velocity at S_m parallel to the body surface, induced by a unit surface vortex located at S_n . A detailed calculation of the above coupling coefficient is given by Lam [12] as

$$K(S_n, S_m) = \frac{1}{2\pi} \frac{-(x_m - x_n) \sin \beta_m + (y_m - y_n) \cos \beta_m}{(x_m - x_n)^2 + (y_m - y_n)^2} \quad (5)$$

In the case of separated flow, free vortices are present in the computational flow domain. These vortices affect the potential flow calculation as illustrated in Figure 1. Taking these vortices into account, Martensen's Integral Equation can be modified to

$$\oint \gamma(S_n) K(S_n, S_m) dS_n - \frac{1}{2} \gamma(S_m) = -W_\infty (\cos \beta_m \cos \alpha_\infty + \sin \beta_m \sin \alpha_\infty) - \sum_{N=1}^Z \Gamma_N L(N, m) \quad (6)$$

where $L(N, m)$ is the coupling coefficient which gives the velocity at S_m parallel to the surface due to a unit Rankine vortex at position N .

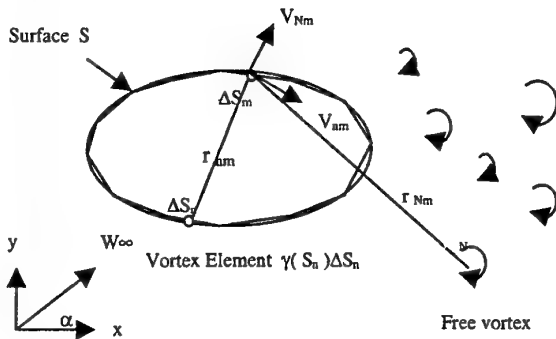


Figure 1 Induction of surface element m by vorticity element n with N free vortices

The induced velocity at m due to a free vortex at S_N is calculated from

$$V_\theta = \frac{\Gamma}{2\pi r} \quad (r \geq r_c)$$

$$= \frac{\Gamma r}{2\pi r_c^2} \quad (r \leq r_c) \quad (7)$$

For unit vortex strength, the x and y components of the velocity are given by

$$u_\Gamma(s_m, s_N) = \frac{(y_m - y_N)}{2\pi [(x_m - x_N)^2 + (y_m - y_N)^2]} \quad \text{for } (r_{mN} > r_c)$$

$$= \frac{(y_m - y_N)}{2\pi r_c^2} \quad \text{for } (r_{mN} \leq r_c) \quad (8)$$

$$v_\Gamma(s_m, s_N) = -\frac{(x_m - x_N)}{2\pi [(x_m - x_N)^2 + (y_m - y_N)^2]} \quad \text{for } (r_{mN} > r_c)$$

$$= -\frac{(x_m - x_N)}{2\pi r_c^2} \quad \text{for } (r_{mN} \leq r_c) \quad (9)$$

and

$$L(N, m) = u_\Gamma(s_m, s_N) \cos \beta_m + v_\Gamma(s_m, s_N) \sin \beta_m \quad (10)$$

Here, r_c is the core radius of the vortex defined as $2\nu\Delta t$ [13].

2.2 Production of Free Vortices

Separation point estimate For flow around an arbitrary shaped body, the vortex sheet drift along the surface until separation occurs. After reaching the separation point, the vortex sheet is detached from the surface to form a free shear layer. Regarding the role of the separation point, it is extremely important to determine the correct location of separation. In the case of bodies with sharp edges, it is reasonable to fix separation at the sharp corner specified by Lewis [10]. However, for circular cylinders, the flow accelerates up to an angle of 90° from the front stagnation point based on potential flow theory. In reality, the laminar boundary layer separates at an angle smaller than 90° in a region where the pressure gradient is favourable for potential flow. This could be due to the influence of the previously shed vortices resulting in the separation points moving upstream. Moreover, for flows around multiple cylinders, due to cylinder-cylinder interference effects, the separation positions are not known in advance. They move along the surface when periodic mature vortices are formed behind the cylinder. Since the application of boundary layer theory to determine the separation point is unrealistic for flow around cylinders at sub-critical Re , a VDS algorithm is used to determine the locations of flow separation. The procedure used in the algorithm to determine separation is as follows:

- (i) The whole cylinder is divided into two equal semi-circles (upper and lower part) and the line of division is the same as the main stream direction. The angle θ is measured from this line, positive upwards and negative downwards.
- (ii) In determining the upper separation point, the upper semi-circle is examined. Starting from $\theta = 0$, calculate the velocity vectors at one shedding distance, ϵ , and at two shedding distances, 2ϵ , from the surface. If the two velocity vectors converge to a point, no separation occurs at that point. The process is repeated by scanning in the clockwise direction until the two velocity vectors are parallel or diverge

from each other. The first occurrence of parallel or divergence velocity vectors is defined as the primary separation point.

- (iii) The same calculation in (ii) is also used to determine the lower separation point. However, when the lower semi-circle is used and the scanning process is in the anti-clockwise direction. For flows around multiple cylinders, the procedure (i), (ii) and (iii) are used repeatedly for each cylinder.

Besides the primary separation location, when a surface is embedded in the wake region, local induced surface velocity occurs within the wake region and causes secondary flow separation. The cause of this is due to the localised effect of the previously shed vortices. To take this effect into account, secondary vortices are also shed wherever the surfaces are embedded in the wake region.

The above algorithm is found to be a practical approach to estimate the locations of separation. First of all, if the two velocity vectors converge, the flow is accelerating near that point. Thus, a favourable pressure gradient occurs. In this situation, the velocity component normal to the surface is towards the surface. The effect of convection, therefore, is to oppose the diffusion of vorticity away from the wall and prevent the boundary layer from thickening in the flow direction. Consequently, the boundary layer remains attached on the surface. On the other hand, for divergent velocity vectors, the opposite is true. The flow moves away from the surface. The vorticity produced on the surface is carried away from the wall and the boundary layer is thickened at that location. According to boundary layer theory, the laminar boundary layer has less energy to overcome this momentum deficit, thus, is more liable to the thickening process and might cause separation.

Adopting the above algorithm, it was found that when a separated shear layer was formed behind a cylinder the direction of the velocity vectors would change even on the front side of the cylinder. Divergent velocity vectors were found depending on the development of the free shear layer. Hence, separations might occur at locations less than 90°.

Vortex shedding During a time increment, a new vortex is shed at each separation point. In the present model, separation can be classified as primary separation and secondary separation. Consider the primary separation, from the potential flow calculations, $\gamma(sp)$ for the vorticity on the body element just before the previously determined primary separation points have been computed. Since the convection velocity of vorticity at the separation point is $v_{sp} = \gamma(sp)/2$, it follows that during a time increment Δt , a vortex is shed into the fluid and its strength is

$$\Gamma_n = \gamma(sp) V_{sp} \Delta t = \frac{1}{2} \xi V_{sp} V_{sp} \Delta t \quad (11)$$

As adopted by Tsutsui *et al.* [7], the relaxation factor ξ is introduced to simulate the decay of the shed vortex. Since secondary vortices could also shed in the wake region as explained above, (11) should be modified to take this phenomenon into account. The calculation of the strength of the secondary vortices is the same as that used to evaluate the primary vortices. The local velocity within the wake is very small, therefore, the strength of the secondary vortices is also very small. During shedding, all nascent vortices are assigned a distance normal to the surface, called the shedding distance ϵ .

2.3 Transport of Free Vortices

Vorticity Transport After the vortices are shed from the surface, each of them moves under the influence of the mainstream, the surface vorticity and other free vortices. Also, each vortex moves by viscous diffusion. In the computation, a first order time scheme is used, ie,

$$x_{new} = x_{old} + u_r \Delta t$$

$$y_{new} = y_{old} + v_r \Delta t, \quad (12a, b)$$

where u_r and v_r are the resultant velocity components in x and y direction, respectively. To find u_r and v_r , it is necessary to superimpose the individual influence of the mainstream, the surface vorticity and the free vortices together.

To calculate the induced velocity due to the surface vortices, a similar formulation is used as in the derivation of the coupling coefficients for free vortices. The result is

$$u_\gamma(m, n) = \frac{(y_m - y_n)}{2\pi[(x_m - x_n)^2 + (y_m - y_n)^2]} \quad \text{for } (r_{mn} > r_i)$$

$$= \frac{(y_m - y_n)}{2\pi r_i^2} \quad \text{for } (r_{mn} \leq r_i), \quad (13)$$

$$v_\gamma(m, n) = -\frac{(x_m - x_n)}{2\pi[(x_m - x_n)^2 + (y_m - y_n)^2]} \quad \text{for } (r_{mn} > r_i)$$

$$= -\frac{(x_m - x_n)}{2\pi r_i^2} \quad \text{for } (r_{mn} \leq r_i), \quad (14)$$

and

$$U_\gamma = \sum_{m=1}^M \gamma(m) \Delta S_m u_\gamma(m, n)$$

$$V_\gamma = \sum_{m=1}^M \gamma(m) \Delta S_m v_\gamma(m, n), \quad (15a, b)$$

The summation is taken over all surface vortices around the cylinders and r_i is the cut-off length of the vortex

sheet. A reasonable choice of the value r_i is equal to $\Delta S_m/2\pi$ as suggested by Chorin [14] in order that the induced velocity field exactly annihilates the tangential velocity at the boundary.

To calculate the induced velocity due to other free vortices, the same $U_\Gamma(S_m, S_n)$ and $V_\Gamma(S_m, S_n)$ are used and the summation is taken over all other free vortices. Consequently,

$$U_\Gamma = \sum_{m=1}^Z \Gamma_m u_\Gamma(S_m, S_n)$$

$$V_\Gamma = \sum_{m=1}^Z \Gamma_m v_\Gamma(S_m, S_n) \quad (16a, b)$$

where Γ_m is the strength of the vortex at m .

For a symmetric body subjected to the above numerical scheme, symmetrical twin vortex flow pattern is obtained initially and would last for some time before alternate vortex shedding occurs. In real flows, symmetrical twin vortex pattern only occurs at low Re. For sub-critical Re flow, alternate vortex shedding occurs almost instantaneously. In order to achieve the desired flow pattern in a shorter computation time, it is necessary to artificially insert certain perturbation, which, on the other hand, would not affect the global feature of the flow field. Therefore, free stream turbulence is introduced and is implemented by the random walk method, such that

$$\frac{u_{turb}}{U_\infty} = I_{turb} * \eta \quad \text{and} \quad \frac{v_{turb}}{U_\infty} = I_{turb} * \zeta \quad (17a, b)$$

where u_{turb} and v_{turb} are the turbulence velocity components, I_{turb} is the turbulent intensity, η and ζ are random numbers that vary from 0 to 1. These random numbers are generated automatically by the random walk method. Therefore, the resultant velocity is the sum of all the contributing velocity vectors,

$$u_r = U_{main} + U_\Gamma + U_\gamma + u_{turb}$$

$$v_r = V_{main} + V_\Gamma + V_\gamma + v_{turb} \quad (18a, b)$$

Using the same formulation, velocity at any position in the flow field can be calculated. In the Results and Discussion section, plots of velocity vectors are used to illustrate the behaviour of the velocity field.

Free vortices in a viscous fluid In a real fluid, it is necessary to take into account the effect of viscosity. There are several ways to implement viscous effect into the numerical model. The first one is called "the core spreading vortex method". In this method, each vortex blob has a vortex core whose size increases with time. The second one is called "the random vortex method". This method is based on the fact that the probability of existence of a particle moving at random, like Brownian motion, is determined by the diffusion equation. The random walk added to the motion of the vortices reproduces the viscous diffusion in a statistical sense. In the present study, "the diffusion velocity method" [13], is

employed to simulate the effect of viscous diffusion. From the diffusion velocities, (U_{di}, V_{di}) are calculated. Summing up the convection and diffusion velocities, the resultant transport velocities of free vortices in a viscous fluid can be expressed as

$$U_r = u_r + U_{di}$$

$$V_r = v_r + V_{di} \quad (19a, b)$$

and the transport of free vortices can be calculated by replacing (u_r, v_r) by (U_r, V_r) .

Velocity vector calculations The resultant velocity vectors in the flow field can then be calculated with magnitude of the vector equal by

$$\sqrt{U_r^2 + V_r^2} \quad (20)$$

at a direction α to the mainstream direction, where

$$\alpha = \tan^{-1}\left(\frac{V_r}{U_r}\right) \quad (21)$$

2.4 Coalescence of the Free Vortices

To account for the coalescence of vortices when they are too close to each other as well as to reduce computation time, a vortex-combining scheme is introduced. Consider two vortices labeled 1 and 2 which will merge to form a single vortex. The strength of the resultant vortex is

$$\Gamma_{comb} = \Gamma_1 + \Gamma_2 \quad (22)$$

The resultant vortex position is at (x, y) such that

$$x = \frac{|\Gamma_1| x_1 + |\Gamma_2| x_2}{|\Gamma_1| + |\Gamma_2|} \quad (23a)$$

$$y = \frac{|\Gamma_1| y_1 + |\Gamma_2| y_2}{|\Gamma_1| + |\Gamma_2|} \quad (23b)$$

and the core radius is given by,

$$r_{comb} = \frac{|\Gamma_1| r_1 + |\Gamma_2| r_2}{|\Gamma_1| + |\Gamma_2|} \quad (24)$$

The induction effect of vortices may cause some vortices to drift into the cylinder. This is impossible in reality and may cause a large leakage flux through the cylinder. It will lead to numerical error in calculation and may cause unpredictable effect to the flow regime. Thus, these vortices need to be cancelled out once they are found inside the cylinder. Finally, to save computer memory, when the free vortices move far downstream, they are deleted since their influence on the near wake will be insignificant.

2.5 Pressure and Force Coefficients

The pressure distribution around the cylinders can be calculated using the Bernoulli equation derived from

potential flow theory and by accounting for the loss of dynamics pressure across the free shear layer as suggested by Lewis [10] when flow separations occurred. After the pressure distribution has been calculated, the lift and drag coefficients can be obtained by integrating the pressure coefficients around the cylinder. The Strouhal number can be determined once the variations of the lift coefficient with time are known.

3. RESULTS AND DISCUSSION

Calculations have been carried out at $Re = 1.3 \times 10^4$ and $L/D = 1.5 - 4$ for different α . The reason for this choice of parameters is because experimental data obtained at sub-critical Reynolds numbers ($2 \times 10^2 - 1.3 \times 10^4$) can be found in Lam & Lo [1], Lam & Fang [2] and Lam *et al.* [15]. Thus, the data can be used to validate the SVM and the present approach to model 2-D flow around multiple cylinders. Typical results are discussed under three separate headings because of the different flow behaviour observed for different α values. These three categories are (i) in-line square arrangement where $\alpha = 0^\circ$, (ii) a slightly staggered arrangement where $10^\circ < \alpha < 20^\circ$, and (iii) a large angle staggered arrangement where $30^\circ < \alpha < 45^\circ$.

3.1 In-line Square Arrangement

The development of the vorticity and velocity field for $\alpha = 0^\circ$ are shown in Figure 2. At $L/D = 1.5$, the upper free shear layer of cylinder 1 and the lower free shear layer of cylinder 2 re-attached on the surface of their respective downstream cylinder. Thus, cylinders 3 and 4

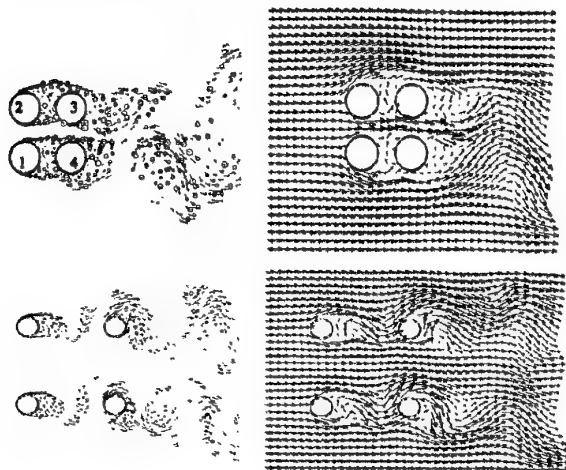


Figure 2 Vorticity and velocity map at 0° incident angle for $L/D = 1.5$ & 4

are 'shielded' by their upstream cylinders 2 and 1. From the velocity diagram, a high gap flow velocity is formed between the two rows of cylinders. Alternate vortex shedding only occurs behind cylinders 3 and 4. As a result, the high gap flow appears as a jet oscillating

upward and downward, forming a 'bi-stable' narrow wake and wide wake behind cylinders 3 and 4.

At $L/D = 4$, alternate vortex shedding occurs behind cylinders 1 and 2. Cylinders 3 and 4 were exposed to an impingement of wake vortices from cylinder 2 and 1, respectively. Experiments showed that the occurrence of critical spacing for re-attachment of upstream free shear layer is Reynolds number dependent. The experiments of Lam *et al.* [15], on the other hand, showed that the phenomena of free shear layer re-attachment of the upstream cylinders might occur for $Re = 200$ and $L/D = 4$. This drastic difference in the velocity field for the $L/D = 1.5$ and 4 cases has important implications on the force field and the heat transfer characteristics of the downstream cylinders. Experimental results further indicated that the above simulations match with the flow patterns at Re ranging from 2×10^3 to 1.3×10^4 (Lam & Lo [1]).

3.2 Slightly Staggered Arrangement

For $\alpha = 10^\circ - 20^\circ$, the two rows of cylinders are at slightly staggered arrangement. Typical flow patterns are shown in Figure 3.

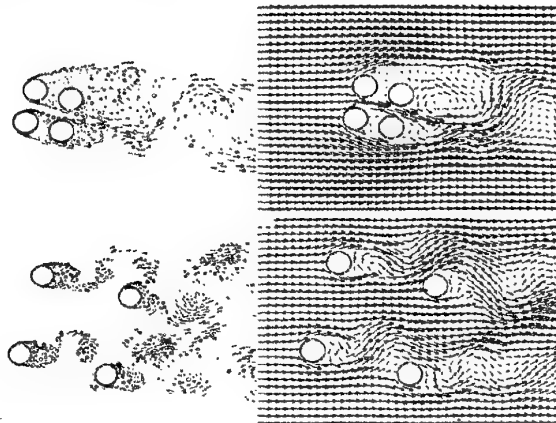


Figure 3 Vorticity and velocity map at 15° incident angle and $L/D = 1.5$ & 4.0

At $L/D = 1.5$, the free shear layers of cylinder 1 and the lower free shear layer of cylinder 2 touch the surfaces of the downstream cylinders forming a gap flow at 15° downward. No vortex shedding occurs behind cylinders 1 and 2. Cylinders 3 and 4 are under the umbrella of cylinders 2 and 1, respectively. A wide wake is formed behind cylinders 2 and 3, while a narrow wake is formed behind cylinders 1 and 4. Such a flow pattern is quite stable. At $L/D = 4$, alternate vortex shedding occurs behind all the cylinders. Due to the wake vortex of the upstream cylinders 1 and 2, a high velocity regime often occurs on the upper side of cylinders 4 and 3. This could explain the reason why cylinders 3 and 4 have a positive mean lift coefficient as obtained experimentally by Lam & Fang [2].

3.3 Large Angle Staggered Arrangement

As α increases to 30° - 45° , the two rows of cylinders are at a large angle staggered arrangement and a rotated square arrangement. Typical flow patterns at $\alpha = 30^\circ$ and 45° are shown in Figure 4 and Figure 5, respectively.

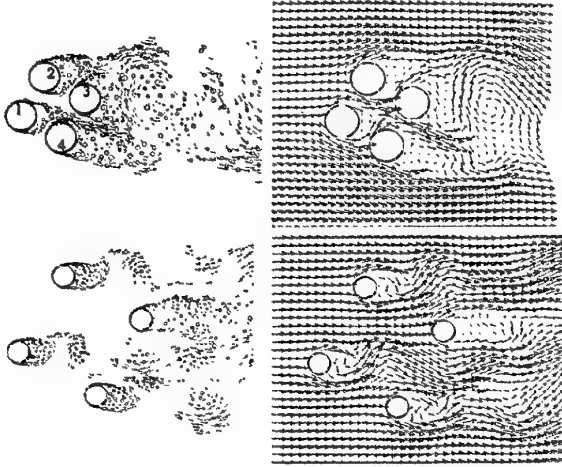


Figure 4 Vorticity and velocity map at 30° incident angle and $L/D = 1.5$ & 4.0

At large α , even when $L/D = 1.5$, the lower free shear layer of cylinder 2 does not impinge on the surface of cylinder 3. Rather the shear layer bends upward through a spectacular angle (Figure 4). The same is also true of the shear layer from cylinder 1. A wide wake is formed behind cylinder 3 but not behind cylinder 4. The wake size and shape vary greatly from cylinder 1 to 4. However, as L/D increases to 4, the wakes behaviour changes to that of a single cylinder for all four cylinders. It is observed that at $L/D > 4$ and $\alpha = 30^\circ$ - 40° , the interference among cylinders is a minimum.

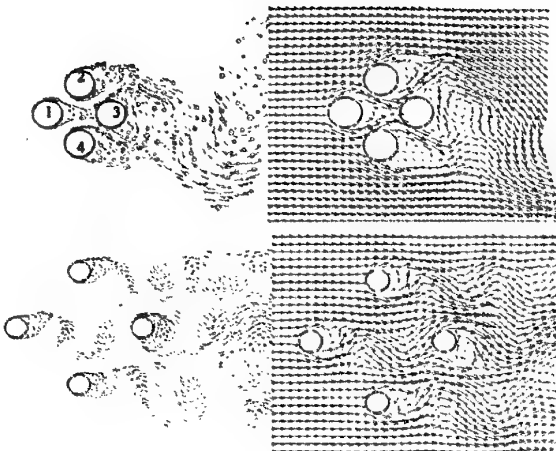


Figure 5 Vorticity and velocity map at 45° incident angle at $L/D = 1.5$ & 4.0

For $\alpha = 45^\circ$ (Figure 5), a symmetrical flow pattern is observed. At $L/D = 1.5$, cylinder 1 has an extremely

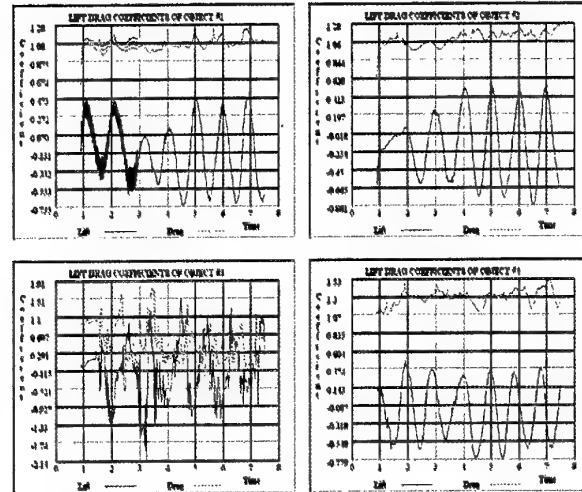


Figure 6 Variation of Lift coefficient and drag coefficient with time for 45° incident angle and $L/D = 4.0$

narrow wake while cylinder 3 has the largest wake observed. As a result, cylinders 1 and 3 have a smaller drag coefficient as observed by Lam & Fang [2]. When L/D increases to 4 (Figure 6), the variations of lift and drag coefficient of cylinders 1, 2 and 4 are quite periodic and are similar to the behaviour shown for a single cylinder. On the other hand, as a result of the turbulent wake interference of cylinder 1, the fluctuating lift and drag characteristics of cylinder 3 are no longer periodic and show the behaviour typical of that of a single cylinder exposed to a turbulent stream [16]. However, due to the wake interference of cylinder 2, the mean drag coefficient of cylinder 3 is reduced significantly from 1.2 to 0.5. A comparison of the mean drag coefficient and mean lift coefficient for $L/D = 4$ at $\alpha = 45^\circ$ obtained in the present simulation and experimental results by Lam & Fang [2] is shown in table 1. A better agreement between the calculated values and the experimental values was obtained in the drag direction while large discrepancy was obtained in the lift direction. A more sophisticated scheme is required to obtain better prediction on pressure and force characteristics.

L/D	Cylinder 1	Cylinder 2	Cylinder 3	Cylinder 4
$C_{D,cal.}$	1.06	1.1	0.5	1.29
$C_{D,expt.}$	1.02	1.3	0.62	1.3
$C_{L,cal.}$	-0.14	-0.15	-0.13	-0.16
$C_{L,expt.}$	-0.01	-0.02	-0.02	-0.03

Table 1 Comparison of mean drag coefficient and lift coefficient for $L/D = 4$ and $\alpha = 45^\circ$

4. CONCLUSIONS

The Surface Vorticity Method (SVM) has been used to simulate flows around four equi-spaced cylinders. With this grid-free SVM package, multiple cylinders can be placed in the flow so that large numbers of numerical experiments on flow around cylinder arrays are carried out easily. Extensive simulations have been carried out at small and large L/D . Only typical flow patterns and velocity fields for four cylinders at $L/D = 1.5$ and 4 with different α , ranging from $\alpha = 0^\circ$ (normal square configuration) to $\alpha = 45^\circ$ (rotated square configuration) were examined and discussed. It is observed that a spectacular change of vortex cloud flow patterns and velocity field maps occurred when L/D and α are varied. Comparison of the calculated results with experimental studies showed that the SVM provides a reasonably accurate and convenient method for the simulation of 2-D flows around cylinder arrays at sub-critical Reynolds numbers. Furthermore, the SVM simulation using VDS to account for vortex shedding in separated flows is able to replicate most, if not all, of the salient features observed in the cylinder array experiments.

ACKNOWLEDGEMENTS

Research support from the Research Grants Council of the Hong Kong Special Administrative Region, China under Project No. PolyU5147/99E is gratefully acknowledged. Thanks are also due to Mr. Y. F. Chan and Mr. Y. N. Lo for their contributions in the computer programming.

REFERENCES

- [1] Lam, K. & Lo, S. C. (1992) A visualization study of cross-flow around four cylinders in a square configuration, *Journal of Fluids and Structures* Vol. 6, pp. 109-131.
- [2] Lam, K & Fang, X. (1995) The effect of interference of four equal-distance cylinders in cross flow on pressure and force coefficients, *Journal of Fluids and Structures*, Vol. 9, pp. 195-214.
- [3] Fornberg, B. (1985) Steady viscous flow past a circular cylinder up to Reynolds number 600, *Journal of Fluid Mechanics*, Vol. 61, pp. 297-320.
- [4] Jackson, C. P. (1987) A finite-element study of the onset of vortex shedding in flow past variously shaped bodies, *Journal of Fluid Mechanics*, Vol. 182, pp. 23-45.
- [5] Sarpkaya, T (1989) Computational methods with vortices-The 1988 Freeman Scholar Lecture, *Journal of Fluids Engineering*, Vol. 111, pp. 5-51.
- [6] Slaouti, A. & Stansby, P. K. (1992) Flow around two circular cylinders by the random-vortex method, *Journal of Fluids and Structures*, Vol. 6, pp. 641-670.
- [7] Tsutsui T, Igarashi T. & Kamemoto K (1997) Interactive flow around two circular cylinders of different diameters at close proximity: Experiment and numerical analysis by vortex method, *Journal of Wind Engineering and Industrial Aerodynamics*, Vol. 69-71, pp. 279-291.
- [8] Lam K. & Chan Y. F. (1998) A refined surface vorticity modelling method for separated flow around a circular cylinder, *Proceedings of the 1998 ASME Fluids Engineering Division Summer Meeting*, FED-Vol. 245, Session 191-03, FEDSM98-5199, Washington D.C., 21-23 June 1998.
- [9] Martensen, E. (1959) Die Berechnung der Druckverteilung an Dicken Gitterprofilen mit Hilfe. Art, *Arch-Ret. Mech. Anel.*, Vol. 3, pp. 235-237.
- [10] Lewis, R. I. (1981) Surface vorticity modelling of separated flows from two-dimensional bluff bodies of arbitrary shape, *Journal of Mechanical Engineering Science*, Vol. 23, pp. 1-12.
- [11] Lam, K. (1987) Potential flow calculation by surface vorticity method and computer graphics, *Computers & Graphics*, Vol. 11, pp. 35-47.
- [12] K. Lam (1989) Application of surface vorticity method to flow around two cylinders arranged in tandem, *Proceedings of the Fourth Asian Congress of Fluid Mechanics*, Hong Kong, Vol. 1, pp. c23-26, August.
- [13] Ogami, Y. & Akamatsu, T. (1991) Viscous flow simulation using the discrete vortex model-the diffusion velocity method, *Computers & Fluids*, Vol. 19, pp. 433-441.
- [14] Chorin, A. J. (1973) Numerical study of slightly viscous flow, *Journal of Fluid Mechanics*, Vol. 57, pp. 785-796.
- [15] Lam, K., Chan, K. T., So, R. M. C. & Li, J. Y. (2001) Velocity map and flow pattern of flow around four cylinders in a square configuration at low Reynolds number and large spacing ratio using particle image velocimetry, *Proceedings of the Second International Conference on Vortex Methods*, 26-28 September 2001, Istanbul, Turkey.
- [16] So, R. M. C. & Savkar, S. D. (1981) Buffeting forces on rigid circular cylinders in cross flows, *Journal of Fluid Mechanics*, Vol. 105, pp. 397-425.

VORTEX-IN-CELL SIMULATION OF FLOW AROUND A CIRCULAR CYLINDER DOWNSTREAM OF A BLUNT BASED FLAT PLATE IN TANDEM ARRANGEMENT

H. İbrahim Keser and M. Fevzi Ünal

Faculty of Aeronautics and Astronautics, Istanbul Technical University

80626 Maslak, İstanbul, Turkey / Email: munal@itu.edu.tr

ABSTRACT

The two dimensional vortex-in-cell method (VIC) is used to investigate the flow around a circular cylinder placed downstream of a blunt-based flat plate in tandem arrangement. Variation of flow pattern and the drag coefficient as function of the longitudinal spacing between the bodies are in agreement with those indicated by the mean pressure distributions obtained experimentally.

1. INTRODUCTION

Owing to its practical importance in many areas of engineering, flow interference between bodies of various arrangements has received considerable attention in the past. Interfering wakes of two bluff bodies placed in a uniform flow lead to vortex shedding and aerodynamic characteristics that are drastically different from those found in the case of a single body. Considerable insight into variations of these characteristics depending on the arrangements of bodies has been provided mainly by experimental studies. Extensive review articles by Zdravkovich (1, 2) summarize important research contributions and recent studies of Sumner et al. (3) and Gu & Sun (4) provide more insight into the interference between circular cylinders of the same diameter, which, among various body shapes, has received most research attention.

However, relatively little has been done for the case of bluff bodies of different cross-stream length scales. According to an experimental study of tandem circular cylinders of different diameters ($D_2/D_1=0.68$; D_2 and D_1 are diameters of downstream and upstream cylinders respectively), for small spacing (i.e. $L/D_1 \leq 1$; L is distance between centres of the cylinders), the separated layers from the upstream cylinder do not reattach onto the downstream one (5). However, as the spacing increases, different flow patterns extending from reattachment in synchronization with vortex shedding from the downstream cylinder to quasi-steady vortex formation in front of the cylinder are observed. Further increase to a critical spacing result in roll-up of separated boundary layers in front of the cylinder. However, the appearance of these flow patterns depends not only on the spacing but also on Reynolds number (6) and the diameter ratio of two cylinders (7).

On the other hand, the Lagrangian and Lagrangian-Eulerian hybrid discrete vortex methods have provided basis for a large number of studies on simulation of separated flow from bluff bodies (8). However, the discrete vortex applications for interfering wakes of a group of bluff bodies have received less attention and thus are rather limited. Stansby (9) studied the flow around two cylinders in the side-by-side arrangement, using the image vortex technique for the boundary

condition, and basically an inviscid, Lagrangian discrete vortex method for separated flow simulation. Slaouti & Stansby (10) and Stansby et al. (11) used random walk method in combination with the vortex-in-cell technique (12) to predict flow around two circular cylinders in various arrangements.

To the numerical simulation presented herein, an experimental study provides a basis for comparison. In the experimental study, wake of a long blunt-end plate interacting with a downstream circular cylinder has been investigated (13). This case differs from that of pair of circular cylinders, in that, the boundary layers developing on upper and lower surfaces of the plate become relatively thicker before they reach to the blunt-end. The objective of the present study is to develop a code to predict the flow features implied by the experimentally found mean pressure distributions around a circular cylinder as function of its longitudinal spacing from a blunt-based flat plate in tandem arrangement (Figure 1).

2. NUMERICAL METHOD

The basis for the study of flow is the equation for the transport of vortices, which for the vorticity scalar $\omega = \nabla \times \vec{U}$ in two-dimensional flow, $\vec{U} = (u, v, 0)$, reduces to,

$$\frac{D\omega}{DT} = \frac{\partial \omega}{\partial T} + (\vec{U} \cdot \nabla) \omega = \frac{2}{Re} \Delta^2 \omega \quad (1)$$

where Re is based on the free stream velocity U_0 and H (Figure 1); rest of the quantities are non-dimensionalized with respect to $H/2$. The term $(\vec{U} \cdot \nabla) \omega$ represents the rate of change due to convection of fluid, whereas the one on the right represents the rate of change due to molecular diffusion of vorticity.

With the surface vorticity modeling, calculation of flow before the start of separation, i.e. the potential flow, reduces to selection of a strength distribution such that the resulting flow is parallel to the body surface at a number of points along the boundary. In doing this, the surfaces of the plate and the cylinder are divided into

discrete segments and the strengths of the corresponding segments of vortex sheet are given by the tangential velocity at their mid-points before the sheet is in position and an influence matrix. The segments or panels are chosen to be straight and of uniform strength along their lengths. The number of panels for the plate and the cylinder are 160 and 120 respectively. To calculate the time evolution of flow around bodies, the sheet segments are reduced to discrete vortices at their midpoints. Then, they are diffused by random walk and convected through the vortex-in-cell calculation.

The viscous effect is simulated by treating the convection,

$$\frac{\partial \omega}{\partial T} + (\vec{U} \cdot \nabla) \omega = 0 \quad (2)$$

and viscous diffusion phenomena,

$$\frac{\partial \omega}{\partial T} = \frac{2}{Re} \nabla^2 \omega \quad (3)$$

in separate, sequential rather than simultaneous numerical procedures (14). To approximate the diffusion equation, at the end of each convection stage each vortex undergoes a random walk η_x and η_y sampled from a Gaussian variable with zero mean and standard deviation $\sigma = \sqrt{4\delta T/Re}$, in two orthogonal directions x and y respectively. The non-dimensional standard deviation of random walk for non-dimensional integration time step of $\delta T=0.15$ and $Re=U_0 H/\nu=600$ is 3.16×10^{-2} . The geometry of the plate used in the calculations is chosen to be a semi-ellipse the length ratio of major to minor axes of which is 2 to 1.

Selection of a plate geometry much closer to that of the experiment increased the computer time greatly simply because enlargement of the computational mesh around the plate. However, with the chosen plate geometry, relatively lower Reynolds number of the calculation allowed a ratio of thickness of the separated boundary layers from the plate to the thickness of the plate similar to that in the experiment. Rather than the exact shape of the plate, this ratio is

expected to play a major role in obtaining similar flow patterns to the experiment.

In addition to the displacements due to diffusion, each vortex experiences a displacement in x and y directions due to the convection process. The definition in relation with the velocity components, u and v of stream function, ψ , leads to an expression for the vorticity scalar ω ,

$$\frac{\partial^2 \psi}{\partial x^2} + \frac{\partial^2 \psi}{\partial y^2} = -\omega \quad (4)$$

which allows one to determine ψ from a known vorticity distribution. In order to allow formulation of the Poisson's equation in terms of the differentiable function the right hand side of the equation is considered as the "mesh vorticity" deduced from the circulations of the discrete vortices (12). In doing this, by assuming a uniform distribution of vorticity for each cell, circulation of a vortex contributes according to an area-weighting scheme to the vorticity at the four mesh points of the cell in which it is situated. The Poisson's equation is solved on a rectangular grid with square cells. A small mesh size is required for the boundary layer on surfaces, while a large dimension is adequate to transport large vortex structures (clouds of vortices) which have been convected far away from the body. To achieve this, overlapping meshes are used (Figure 1). An inner mesh, with a non-dimensional size of $\Delta x = \Delta y = 0.05$, and just large enough to cover the body, is used to provide sufficient definition for the boundary. The middle mesh with a non-dimensional size of 0.2 covers the formation regions, where the vorticity shed from the surfaces form large scale vortices which are eventually convected downstream on the outer mesh. Since the outer mesh is used to convect the vortices far from the boundaries, a cell size of 0.8 is considered sufficient. On the outer mesh, the Poisson's equation is solved using the discrete Fourier transform. Whereas, for the middle and inner meshes, the Simultaneous Over-Relaxation is used. The stream function values calculated on the outer mesh determine the values on the boundaries of the middle

mesh through linear interpolation, and the discrete vortices determine the vorticity distribution. The process is repeated for the inner meshes with boundary conditions

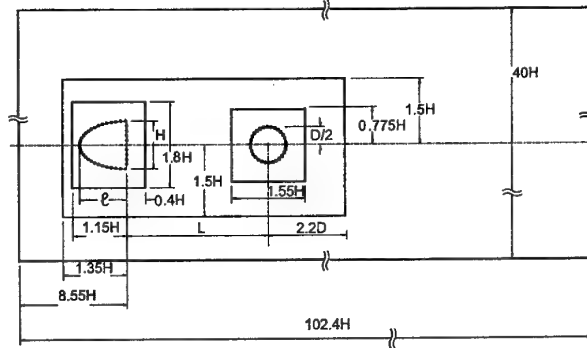


Figure 1: Dimensions of the overlapping meshes.

obtained from the middle mesh. With this procedure, the Poisson's equation is solved four times at each time step, and the velocity of a vortex is calculated from the stream function distribution of the mesh with the smallest possible cell size. The streamfunction computed on the mesh from the Poisson's equation leads to the mesh velocities and thus, through the use of an area weighting scheme, to the velocity components of each discrete vortex. Having calculated the velocities at the discrete vortex locations, the vortices are convected with the fluid. In doing this, the first order Euler scheme is used, and the new locations of vortices after a time step are found as,

$$x(T + \delta T) = x(T) + u(T)\delta(T) \quad (5)$$

$$y(T + \delta T) = y(T) + v(T)\delta(T)$$

During advancement of vortices to their new locations, some of the vortices cross the boundaries. These vortices are given an additional radial displacement to reflect them back to the flow field. It should also be noted that, after the random walks are added to the orthogonal coordinates of vortices, the Poisson's equation solved again for all meshes beginning with the outer mesh. Therefore, the stream function calculations are carried out for the four meshes twice per time step. The numerical parameters chosen produce results in good agreement with experiments. For a circular cylinder at $Re=450$, the mean value of the drag force reaches a constant value at

approximately 1.2 and lift oscillation with an amplitude of approximately 0.6. The Strouhal number is predicted to be 0.21.

The pressure distributions are calculated via the following formula by Spalart and Leonard (15) for the pressure increment between any two consecutive points around the cylinder,

$$\Delta P_j = -\rho \Gamma_j / \Delta T \quad (6)$$

where, ΔT is equal to $2\delta T$, ρ is the density and Γ_j is equal to the difference between the newly created circulation at j th bound vortex location and the circulation lost by vortices crossing the j th surface segment.

3. RESULTS

Using the to-dimensional VIC method, variation with longitudinal spacing L/H of flow patterns around the plate and the circular cylinder and the mean pressure distributions around the cylinder are computed. Computations are carried out at values of spacing $L/H = 0.65, 1.5, 2.5, 2.85, 3, 5, 8$ and 10 . For values of $L/H = 2.5, 2.85$ and 5 the discrete vortex distributions at five consecutive instants with a constant time interval between them demonstrate the evolution of flow within a period of lift fluctuation of the circular cylinder (Figure 3). Up to the value of $L/H = 2.5$, the separated boundary layers from the plate can not roll-up into vortices in front of the downstream of the cylinder. For a further increase to $L/H = 2.85$, a "jumped" flow pattern is encountered. That is, in contrast to the case for $L/H \leq 2.5$, at the critical spacing of $L/H = 2.85$ the separated boundary layers originating from the plate roll-up and form vortices in front of the cylinder. The predicted critical spacing is in agreement with that implied by variation with L/H of the experimentally found mean pressure distributions around the base region of the plate and the cylinder (13).

This critical spacing is also evidenced by the variation with L/H of the profiles of the longitudinal and vertical components of the fluctuation velocity as well as the mean velocity within the gap region between the plate and the cylinder (Figure 3). Both the fluctuation and the mean

velocity profiles at three stations before and a single station after the cylinder give clear indication of a stagnant gap region before the critical spacing. For values of spacing larger than the critical, however, the profiles are typical of a developed vortex street wake approaching the downstream cylinder.

For values of $L/H = 0.65$ and 1 , the viscous VIC method used in this the study also allowed realistic prediction of the mean pressure distributions on the cylinder surface (Figure 4). The distributions of the mean pressure as well as the mean velocities are obtained by averaging over an integer number of periods of C_L variation after the quasi-steady oscillations are obtained. For comparison with the experiment, the calculated mean pressure value at the back stagnation point is set to the measured value at the corresponding L/H . In agreement with the experiment (13), for $L/H = 0.65$, the drag force acting on the cylinder is towards the base of the plate, i.e. negative (Figure 5). From that value of the spacing on, the experimentally determined drag coefficient increases with increasing L/H . However, as exemplified for $L/H = 2$ in Figure 4, the VIC computation results in larger suction on the front face of the cylinder with respect that at the back and thus leads to negative drag coefficient values for all L/H up to 2.5 (Figure 5).

At these L/H values before the critical spacing, e.g. $L/H = 2.5$, within a period of the lift fluctuation, the instantaneous pressure distribution indicated by the envelopes around the cylinder does not vary appreciably with time (Figure 2). Only the pressure on the backside of the cylinder experiences a small variation from one instant to another. In Figure 2, an outward radial distance from the envelope to the surface is proportional to the magnitude of suction. Since the pressure distributions could be calculated within an arbitrary constant, the pressure coefficient at the front stagnation point of the cylinder is arbitrarily set to -1 , so the distributions do not reflect absolute values. However, the arbitrary value has no effect on the integral outcome of the distributions, i.e. the drag and lift coefficients, which are shown by arrows at the centre of the cylinder.

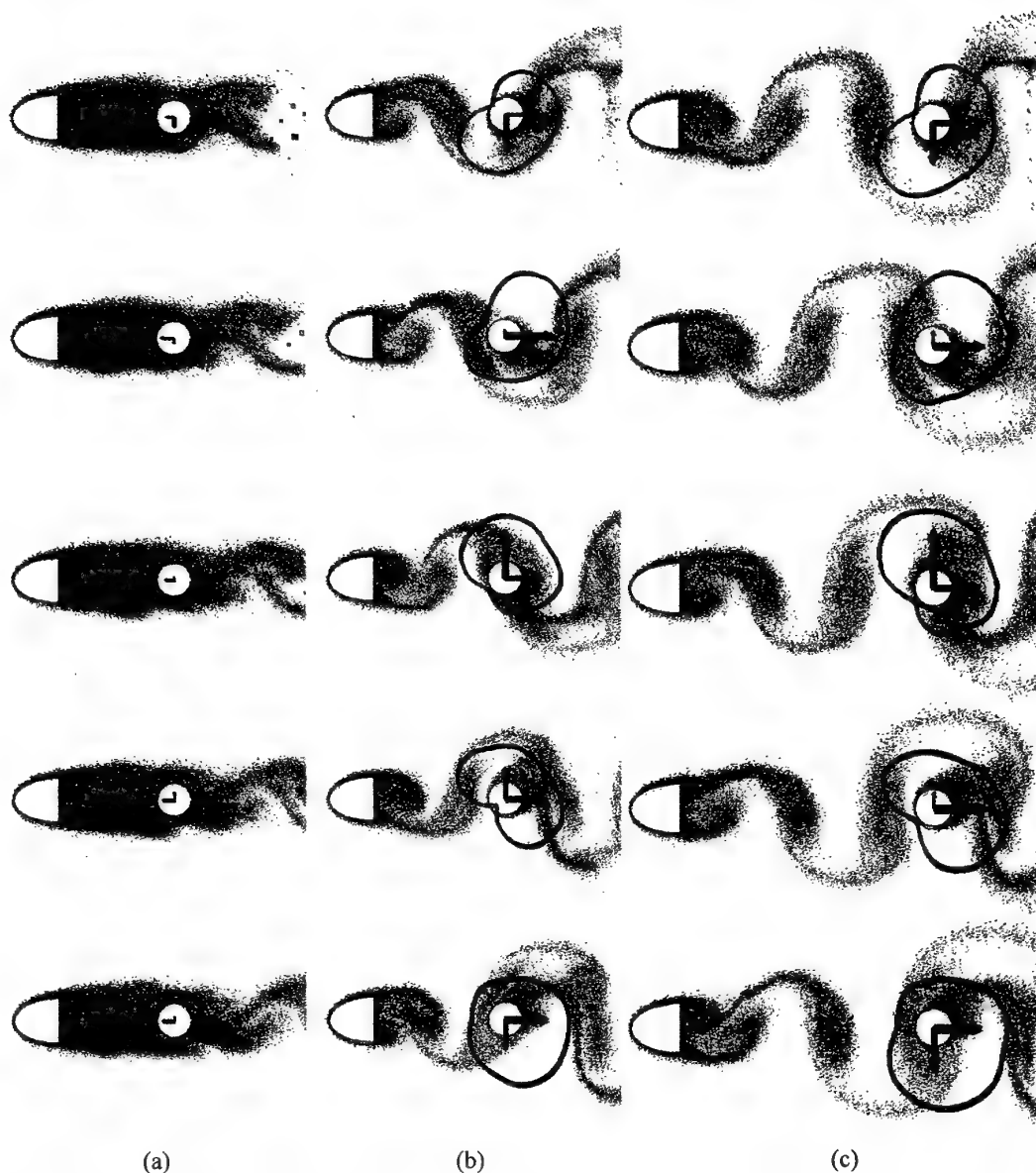


Figure 2: Variation in time (T) of flow structure and associated pressure distribution, C_D , C_L of cylinder for $L/H=2.5$ (a), $L/H=2.85$ (b) and $L/H=5.0$ (c)

With the appearance of the “jumped” flow at $L/H=2.85$, the computed mean drag coefficient experiences a sudden increase to a large positive value instead of the gradual increase found in the experiment (Figure 5). For larger L/H , the computed drag coefficient continues to increase with L/H , but at a much smaller rate and provides a better qualitative agreement with its experimental counterpart. However, parallel to the appreciable deviations between the measured and calculated mean pressure distributions as exemplified for $L/H=3$ and 5 in Figure 4, the values of the

drag coefficient in the interval $2.85 \leq L/H < 8$ are over-predicted. For $L/H=8$, a better agreement in terms of the pressure difference between the front and the back stagnation points of the cylinder is found. However, the suction maximums of the experiment are absent for not only for $L/H=8$ but also for $L/H=3$ and 5. It is clear that, rather than the differences between the measured and calculated pressure distributions as a whole the pressure difference between the front and the back faces of the cylinder affects the comparison of the measured and

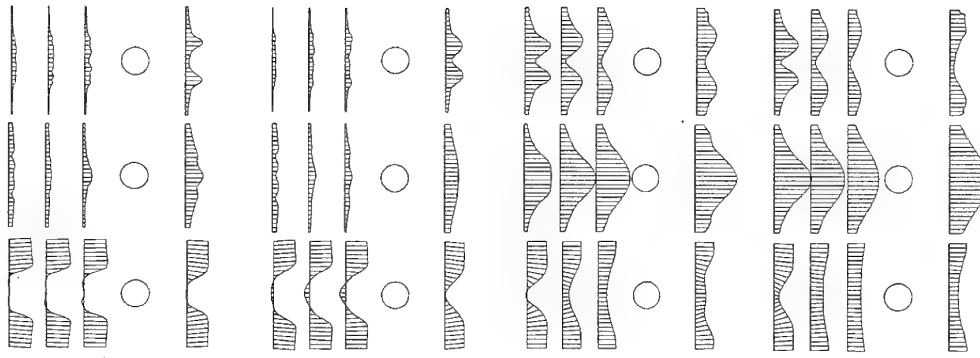


Figure 3: Variation with respect to $L/H=1, 2, 3$ and 5 (from left to right) of mean velocity profiles (u, v and U , from top to bottom) for 3 upstream ($x/H=-0.75(L-D/2)/H, -0.50(L-D/2)/H, -0.25(L-D/2)/H$) and 1 downstream ($x/H=0.25(L-D/2)/H$) location from the center of cylinder .

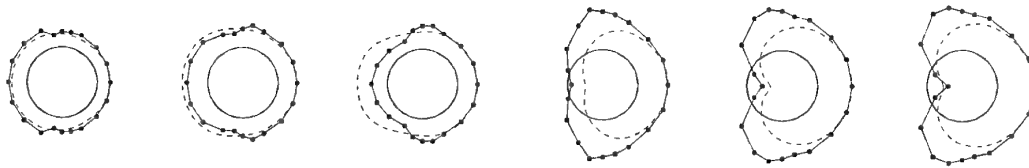


Figure 4: Comparison calculated (dashed line) and measured (symbols connected by lines) mean pressure coefficient (C_p) distributions around the cylinder for various values of $L/H=0.65, 1, 2, 3, 5, 8$ (from left to right).

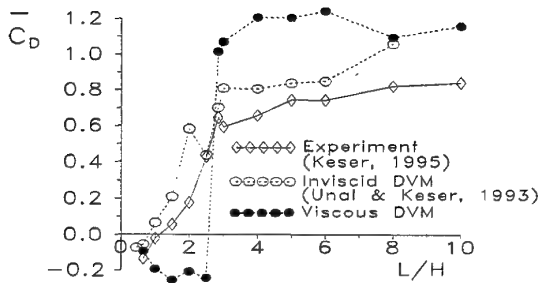


Figure 5: Comparison of measured and calculated mean drag coefficients (C_D) of the cylinder with respect to L/H .

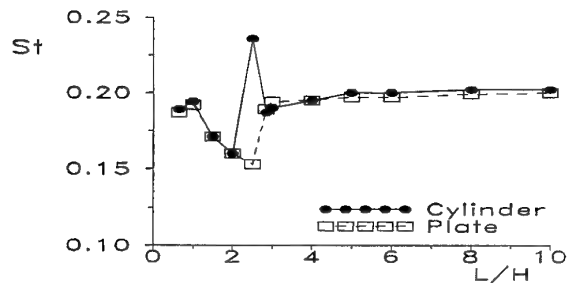


Figure 6: Variation of Strouhal number (St) with respect to L/H for cylinder and plate

the calculated drag coefficient variations (Figure 5).

The tandem arrangement of the plate and the cylinder has been previously studied using an inviscid discrete vortex method in which the finite thickness separated boundary layers from the plate are represented by practically zero thickness discrete vortex rows (16). It is interesting to note that, although the inviscid simulation is not able to predict the critical spacing it provides a better agreement with the experiment in the drag coefficient variation (Figure 5).

The simulated flow patterns provide insight into the interaction of the vortices from the plate with the downstream circular cylinder and the resulting instantaneous pressure distribution around it. The large scale vortices originating from the plate transport downstream and pass mainly on the side of the cylinder shedding vorticity of the same rotation (Figure 2(b) and (c)). While passing, they travel along and interact with the cylinder surface. As the vortex shed from the upper corner of the plate with a clockwise circulation approaches the upper part of the leading portion of the cylinder, it induces an instantaneous maximum pressure there (top pictures in Figures 2(b) and (c)). With a π phase difference, an approaching vortex with counter-clockwise circulation from the lower corner of the plate results in, again a positive peak at the lower part of the leading portion of the cylinder (3rd pictures from the top in Figures 2(b) and (c)). On the other hand, impinging vortices are split by the cylinder and a small portions of them pass on the side of the cylinder shedding vorticity of the opposite rotation. As they pass by, these small split-vortices cause minimum pressure peaks in the instantaneous pressure distribution on the leading portion of the cylinder (3rd and 5th pictures in Figure 2(c) for clockwise and counter-clockwise split-vortices on the lower and upper portion of the leading end of the cylinder respectively). However, as shown in 3rd and 5th pictures of Figure 2(c), while interacting with the surface, the small portions of the split-vortices are highly distorted and lose their coherence. This is in contrast to the larger portions of the split-vortices which preserve their identity. As the

impinging vortices pass the leading portion of the cylinder and travel along the rest of the surface, they induce suction peaks in the instantaneous pressure distributions regardless of their sense of rotation, i.e. the vortex centres approximately correspond to pressure minimums. Similar pressure variations are observed in an experimental study of vortex street impinging on a practically semi-infinite plate with an elliptical leading edge (17).

The above described evolution of the instantaneous pressure distribution provides an explanation of the discrepancy between the measured and the calculated mean pressure distributions (Figure 4). The over predicted pressures on the front side of the cylinder for $L/H=3, 5$ and 8 may be due to the fact that the highly coherent, two-dimensional vortices of this numerical study overemphasizes the induced pressure maximums by the approaching vortices, while leading to an over prediction of pressure minimums induced by the passage of vortices. The coherent vortices is highly dominant over the shedding of vorticity from the cylinder: vortices shed from the cylinder are always nested in the vortices originally shed from the plate. Diffuse vortices, in contrast to the highly coherent ones of this study are expected to improve the pressure distribution comparison, and allow prediction of the experimentally-observed suction peaks corresponding to flow separation from the cylinder.

The variation with respect to L/H of the Strouhal number deduced from the spectral analysis of the lift fluctuations of the plate and the cylinder are shown in Figure 6. Passing from $L/H=0.65$ to 1 , the Strouhal number of both the plate and the cylinder slightly increase. Then, with increasing L/H up to the critical spacing $L/H=2.85$, they both experience parallel reductions. For further increase of L/H , they increase and finally reach to their values of 0.20 in the corresponding free-wake cases. The Strouhal number variation with longitudinal spacing described herein for the downstream cylinder is in agreement with that found in an experimental study by Igarashi (5).

ACKNOWLEDGMENTS

The authors would like to thank Professor J. M. R. Graham for making an early version of his hybrid vortex code available at the beginning of the present research. Supports of the Istanbul Technical University Research Fund through grant no 978 and the NATO Scientific Affairs Division through grant no.CRG972960 are acknowledged.

REFERENCES

- (1) Zdravkovich, M.M. (1977), "Review of flow interference between two circular cylinders in various arrangements", ASME J. Fluids Eng., Vol.99, p. 618-631.
- (2) Zdravkovich, M. M. (1987), "The effects of interference between circular cylinders in cross flow", J. Fluids and Structures, Vol. 1, p. 239-261.
- (3) Sumner D., Price, S. J. and Paidoussis, M. P. (2000), "Flow-pattern identification for two staggered circular cylinders in cross-flow", J. Fluid Mechanics, Vol. 411, p.263-303.
- (4) Gu, Z. F. and Sun, T. F. (1999), "On interference between two circular cylinders in staggered arrangement at high subcritical Reynolds number", J. Wind Engineering and Industrial Engineering, Vol.80, p. 287-309.
- (5) Igarashi, T. (1982), "Characteristics of a flow around two circular cylinders of different diameters arranged in tandem", Bulletin of the JSME, Vol. 25, No. 201, p. 349-357.
- (6) Okajima, A. (1979), "Flows around two tandem circular cylinders at very high Reynolds numbers", Bulletin of the JSME, Vol. 22, p. 504-511.
- (7) Hiwada, M., Taguchi, T., Mabuchi, I. And Kumada, M. (1979), "Fluid flow and heat transfer around circular cylinders of different diameters in cross flow", Bulletin of the JSME, Vol. 22, p. 715-723.
- (8) Sarpkaya, T. (1988), "Computational methods with vortices-The 1988 Freeman scholar lecture", ASME J. Fluids Eng., Vol. 111, pp. 5-52.
- (9) Stansby, P.K. (1981), "A numerical study of vortex shedding from one and two circular cylinders", J. Aeronautical Quarterly, Vol. 32, p.48-71.
- (10) Slaouti, A. and Stansby, P. K. (1992), "Flow around two circular cylinders by the random vortex method", J. Fluids and Structures, Vol. 6, p. 641-670.
- (11) Stansby, P.K., Smith, P.A. and Penoyre, R. (1987), "Flow around multiple cylinders by the vortex method", In Proceedings International Conference on Flow Induced Vibrations, Bowness-on-Windermere, England, pp. 41-50.
- (12) Graham, J. M. R. (1988), "Computation of viscous separated flow using a particle method", In Numerical Methods in Fluid Mechanics (ed K.W. Morton), vol.3, p. 310-317. Oxford University Press.
- (13) Keser, H. I. (1995), "Flow around two bluff bodies in tandem and staggered arrangements by the discrete vortex method and experiment", Ph.D. Dissertation, Department of Aeronautics and Astronautics, Istanbul Technical University, Istanbul, Turkey.
- (14) Chorin, A. J. (1973), "Numerical study of slightly viscous flow", J. Fluid Mechanics, Vol. 57, p. 785-796.
- (15) Spalart, P.R. and Leonard, A. (1981), "Computation of separated flows by a vortex tracing algorithm", AIAA 14th Fluid and Plasma Dynamics Conference, Paper No. 81-1246.
- (16) Unal, M. F. and Keser, H. I. (1993), "Flow around and mean pressure field on a circular cylinder placed downstream of a blunt-based flat plate", In Proceedings Numerical Methods in Laminar and Turbulent Flow, Vol. VIII, p. 839-850. Swansea, U.K.: Pineridge Press.
- (17) Gursul, I. and Rockwell, D. (1990), "Vortex street impinging upon a leading edge", J. Fluid Mechanics, Vol. 211, p. 211-242.

SIMULATION OF WAKE FROM A CIRCULAR CYLINDER WITH SPANWISE SINUSOIDAL WAVINESS

H. İbrahim Keser, M. Fevzi Ünal

Faculty of Aeronautics and Astronautics, Istanbul Technical University
80626 Maslak, İstanbul, Turkey / Email: munal@itu.edu.tr

P. W. Bearman

Department of Aeronautics, Imperial College of Science, Technology and Medicine
London SW7 2BY, U.K. / Email: p.bearman@ic.ac.uk

ABSTRACT

Using a three-dimensional discrete vortex method, separated flow around a circular cylinder having sinusoidal waviness along its span is simulated. The simulation method is fully Lagrangian and thus does not require a grid around the cylinder. Two different sinusoidal forms are considered: a constant diameter cylinder with a wavy axis and a circular cylinder having a sinusoidal waviness in its diameter along the span. The numerical simulation is successful in predicting the experimentally found characteristic features of the flow such as the three dimensional structures behind and the associated periodic variation of wake width across the span of the cylinder with wavy axis.

1. INTRODUCTION

Owing to its importance in many engineering applications, including heat exchangers, risers in marine technology, road vehicles, building and bridges, flow around bluff bodies has been subject to numerous experimental and computational studies (1).

In contrast to the view expressed in many computational studies of flow around bluff bodies, even the fundamental flow case of a nominally two-dimensional body, e.g. a circular cylinder in a uniform stream exhibits several three-dimensional features (2) and at low Reynolds numbers, maintaining parallel vortex

shedding to the cylinder axis requires very carefully controlled end conditions by means of suitably angled end plates (3) or with other types of end constraint (4). At high Reynolds numbers, two-dimensional shedding is possible only with a strong external influence such as body or flow oscillation in synchronisation with shedding (5). Strictly, two-dimensional geometries and two-dimensional flows can only exist in theoretical models, since in reality, all bodies have finite lateral extents and, above some critical Reynolds number, all flows generate instabilities with some spanwise wavelength.

Consequently, in recent years increasing experimental and numerical research effort is being directed towards three-dimensional features of nominally two dimensional, mildly or strongly three-dimensional bluff bodies. Since key three-dimensional features of the wake of a nominally two-dimensional body, such as vortex dislocations, appear apparently randomly in time and space, Tombazis and Bearman (6) attempted to control their locations by applying a mild geometric disturbance in the form of a wavy trailing edge. They made interesting observations about a number of distinct vortex shedding patterns. Several other authors (e.g. 7) have reported results of investigations of bluff body flows influenced by geometric disturbances that might also be described as mild.

More recently, Owen et al (8) have shown that above a certain value of wave height to length ratio of the waviness the regular vortex shedding can no longer be detected behind a circular cylinder with a wavy axis and associated with this, sizeable reductions in drag can be achieved.

Increasing appreciation of the importance of three-dimensional effects aroused interest also in numerical studies. Several researchers have developed finite difference (e.g. 11), finite element and spectral element codes (12) to simulate three-dimensional bluff body flows.

In the present study, a fully Lagrangian discrete vortex method is employed to simulate separated flow around a three-dimensional circular cylinder. The three-dimensionality is introduced into the cylinder by having a sinusoidal waviness along its span. In addition to a sinuous axis circular cylinder of constant diameter, a circular cylinder with its diameter having sinusoidal variation along its span is considered. Surface representation of the bodies is performed by means of source panels allowing satisfaction of the normal velocity condition at the surface of the cylinder. As previously applied by Nakanishi and Kamemoto (9) the vorticity field around bodies is represented by a number of vortex panels shed into the flow field from the surface. These are transformed into discrete vortices with a spherically symmetric distribution of vorticity, i.e. vortons.

2. NUMERICAL METHOD

In the discrete vortex method, the basic equation is that for vorticity transport,

$$\frac{D\vec{\omega}}{Dt} = \frac{\partial \vec{\omega}}{\partial t} + (\vec{U} \cdot \nabla) \vec{\omega} = (\vec{\omega} \cdot \nabla) \vec{U} + \nu \nabla^2 \vec{\omega} \quad (1)$$

with the vorticity definition given by,

$$\vec{\omega} = \nabla \wedge \vec{U} \quad (2)$$

Using the vorticity definition equation, the Biot-Savart law can be determined (13) as,

$$\vec{U}(r) = \frac{1}{4\pi} \int_V \frac{\vec{\omega}_O \wedge \vec{R}}{|\vec{R}|^3} dV_O - \frac{1}{4\pi} \int_S \left(\frac{\sigma_O \vec{R}}{|\vec{R}|^3} + \frac{\vec{\gamma}_O \wedge \vec{R}}{|\vec{R}|^3} \right) dS_O \quad (3)$$

Once the vorticity distribution $\vec{\omega}_O$ in a flow field (V) is approximated by a number of discrete vortices, source, σ_O and/or vortex, $\vec{\gamma}_O$ distribution on a body surface can be calculated so as to satisfy the normal or tangential velocity conditions at a finite number of control points on it. This is done by solving a set of equations, in the form of,

$$[K]\{\beta\} = \{b\} \quad (4)$$

where, [K] is a coefficient matrix depending on surface geometry, {b} is induced velocities at the control points and, {β} is the unknown source and/or vortex strengths around the surface.

In the representation of bodies (Figure 1) with rectangular panels, the number of divisions along the azimuthal and spanwise directions is 36. The parallel walls at both ends of the bodies extend from -2.5D to 27.5D and from -5D to 5D in x and y directions respectively. Each wall has 12 equal divisions in the y direction. In the x direction the part extending from -5D to 7.5D is equally divided into 12 whereas the rest has 6 divisions.

Zero normal velocity condition is satisfied at the panel corners by considering only a single image with respect to the walls of the body along with those of the vortex panels and the vortons representing the separated flow. At the start of the motion there are no vortex elements in the flow field. By means of Equation 4, source strengths at panel corners are determined. This potential flow calculation is followed by calculation of surface velocities at the panel corners on the body and

then by virtue of the vorticity definition Equation 2 the vorticity components are calculated there. To simulate evolution of the flow field, the surface panels with known

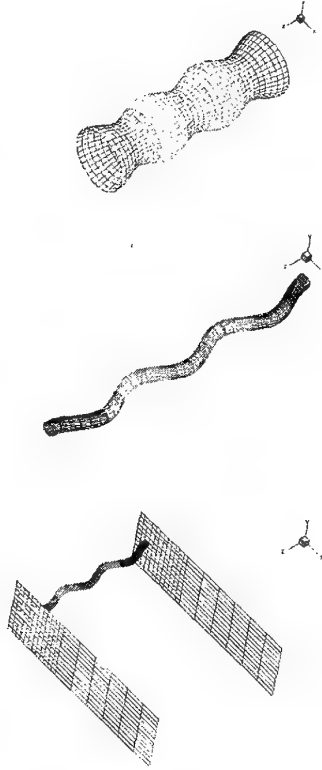


Figure 1: Perspective views of the bluff-bodies and sidewalls of the experimental investigation.

vorticities at their corners are introduced into the flow from a small distance $0.0254D$ away from the cylinder boundary and are convected to their new locations by induced velocities from the vorticity in the field and the basic, potential flow around the cylinder. Changing right hand side of Equation 4 by newly introduced vortex panels is recalculated, and an updated source strength distribution around the body surface and the walls is determined. After the previously introduced ones are displaced to their new locations, those vortex panels with updated strengths are introduced into the flow field. Then the calculation procedure returns to the first step in which an updated source strength distribution at the body surface and the walls is determined again

In order to cut down on the computational time, vortex panels convected outside of an envelope during evolution of the separated flow are converted into vortons of equivalent strengths. The envelope is in the form of a 2D diameter cylinder having its axis coincident with the centrelines of the bodies. Trajectories of vortex panels and vortons are calculated by means of the induced velocities resulting from the Biot-Savart law and, from,

$$\frac{d\vec{r}_O}{dt} = \vec{U}_O \quad (5)$$

equation with the Euler method, i.e.

$$\vec{r}_O(t + \Delta t) = \vec{r}_O(t) + \vec{U}_O \Delta t \quad (6)$$

The non-dimensional time step of the calculation based on the free stream velocity U_∞ and the cylinder diameter D is $\Delta t = U_\infty t / D = 0.1$.

On the other hand, the distribution function and the resultant induced velocity of i^{th} vorton having a spherically symmetric vorticity distribution are given (14) as,

$$\vec{\omega}_{oi} = \frac{\vec{\alpha}_i}{\varepsilon_i^3} f(\chi) \quad , \quad \vec{U}_i = \frac{\vec{\alpha}_i \wedge \vec{R}}{4\pi|\vec{R}|^3} g(\chi) \quad (7)$$

where, ε_i and α_i represent radius and strength of the vorton, and

$$f(\chi) = \frac{15}{8\pi} \frac{1}{(\chi^2 + 1)^{7/2}} \quad ; \quad g(\chi) = \frac{5\chi^3 + 2\chi^5}{2(\chi^2 + 1)^{5/2}} ;$$

$$\chi = \frac{|\vec{R}|}{\varepsilon_i} ; \quad \vec{\alpha}_i = \frac{4}{3} \pi \varepsilon_i^3 \vec{\omega}_i \quad (8)$$

The variation of vorticity with time due to stretching is represented by the first term on the rhs of Equation 1. This is calculated with a method proposed by Nakanishi

and Kamemoto (9). According to this model, a spherical vortex blob is tentatively replaced by an equivalent cylindrical vortex stick in order to calculate the longitudinal elongation. The stick is elongated during the time interval Δt under the influence of the local velocity field and replaced again by a new equivalent spherical blob with a different core radius. A detailed explanation of the method can be found in (15). The variation of vorticity due to viscous diffusion is not considered in this study.

As explained above, the bodies used in the investigation are represented with 1728 rectangular panels. For simulation of flow around a bluff body and its wake about 250,000 vortex elements are used. Parallel computing using MPI (Message Passing Interface) routines has been performed with a computer having 8x400 Mhz IP35 processors and a memory size of 5120 Mbytes. A typical computational time is on the order of a week.

3. RESULTS

Three-dimensional separated inviscid flows around two different sets of circular cylinders with spanwise waviness (Figure 1) have been calculated using a source panel method in combination with the Lagrangian discrete vortex method. The first set consists of circular cylinders having sinusoidal variation of diameter along their span with values of $W/\lambda=0, 0.125$ and 0.14 , where W is the peak to peak wave height and λ is the wave length of the variation. For these cases, the ratio of the wave height to maximum diameter is kept constant at $W/D=0.15$ which along with the W/λ values above leads to λ/D values of around unity. In the second set, with $W/\lambda=0.167$ and 0.334 at a constant value of $\lambda/D=7.5$, the diameter of circular cylinder is kept constant along its sinuous axis.

Side and perspective views of the simulated wake patterns are demonstrated in Figure 2. The circular cylinder without waviness leads to vortices with a relatively shorter formation length with respect to the

wavy cylinders. The longitudinal spacing between the vortices in the wake is similarly shorter. Although the vortices immediately behind the cylinder are apparently well correlated along the span, evolution of three-dimensionality further downstream is clearly visible. On the other hand, the vortical structures originating from the wavy cylinders mimic this waviness and attain an undulated shape and thus a periodically varying formation length along the span. In an experimental study of the wake from a wavy cylinder similar to the one considered here, Ahmed et al (16) observed that at Reynolds number of 10,000 and $W/\lambda=0.139$; $\lambda/D=1.2$ the vortices in the immediate wake maintain the same degree of spanwise coherence as behind the right circular cylinder. However, it should be indicated that in their experiment, the shear layers emanating from the cylinder show a transitional character and achieve a turbulent state before spiralling into vortices. Consequently, as stated by Ahmed et al, it is natural to have similar mean velocity profiles (in the x-y plane) along the span, which lead to similar instability characteristics. This may not be the case for the laminar simulation herein. Additionally, as demonstrated by Bearman (1), the physical mechanism behind the two-dimensional vortices observed at certain instants immediately downstream of a wavy trailing end is in fact three-dimensional.

The numerical simulation indicates a certain effect of increased waviness on the wake evolution. With the increase of the wave steepness W/λ from 0.125 to 0.14 , the shedding is not suppressed. However, evolution of the separated boundary layers from the cylinder into large-scale vortices is delayed for a relatively longer time. While the wake structure exhibits a double shear layer formation with small undulation in the downstream direction for non-dimensional time $T=19$, eventual enhancement of transverse motion of the undulated wake leads to Karman type shedding of vortices at $T=26$.

For the sinuous axis cylinder the numerical simulation produces some of the experimentally observed features of flow by Owen et al (8). Although for $W/\lambda=0.167$ the

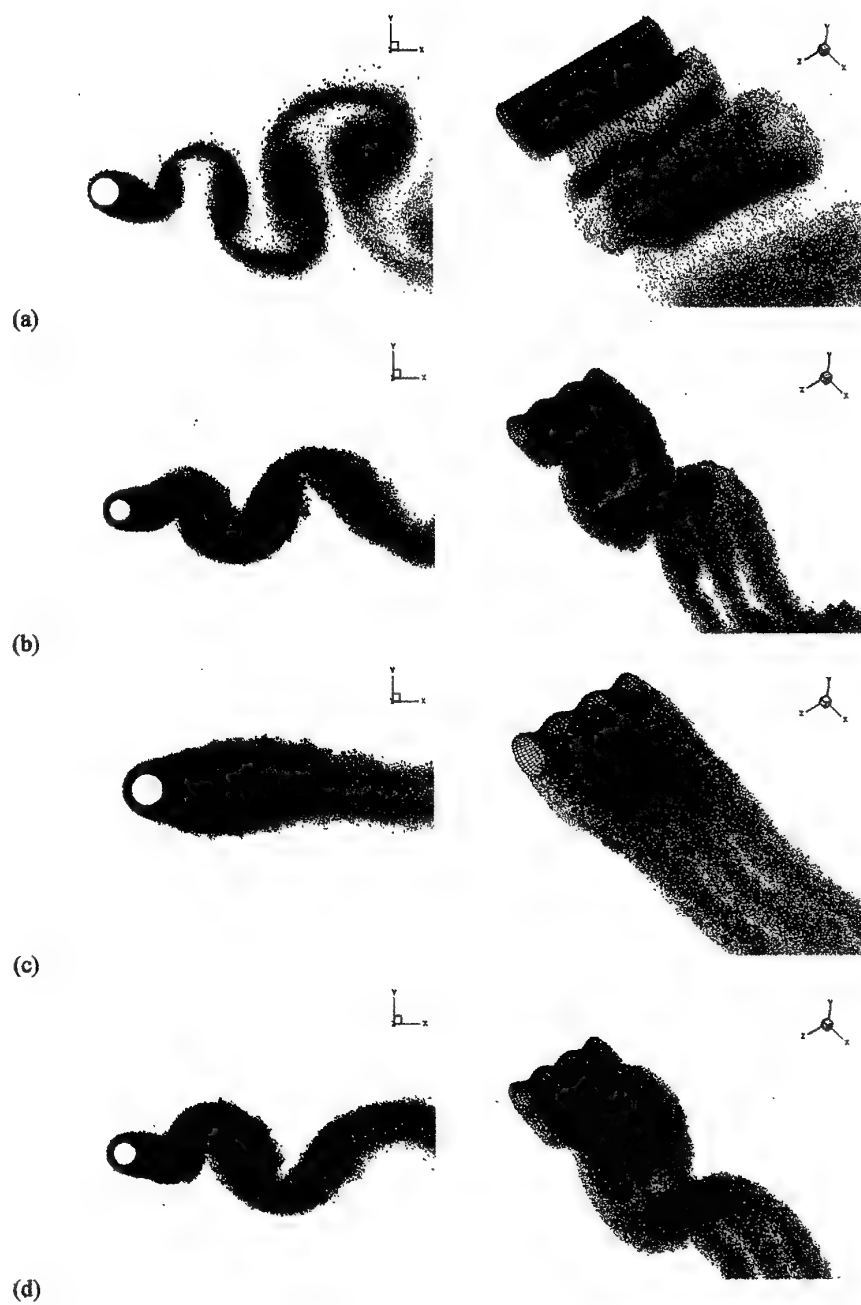


Figure 2: Wake structures of right circular cylinder at $T=26$ (a) and cylinders with $W/\lambda=0.125$ at $T=26$ (b); $W/\lambda=0.14$ at $T=19$ (c); $W/\lambda=0.14$ at $T=26$ (d)



Figure 3: Instantaneous wake structures behind valley (left) and peak (right) at $T=30$, $W/\lambda=0.167$

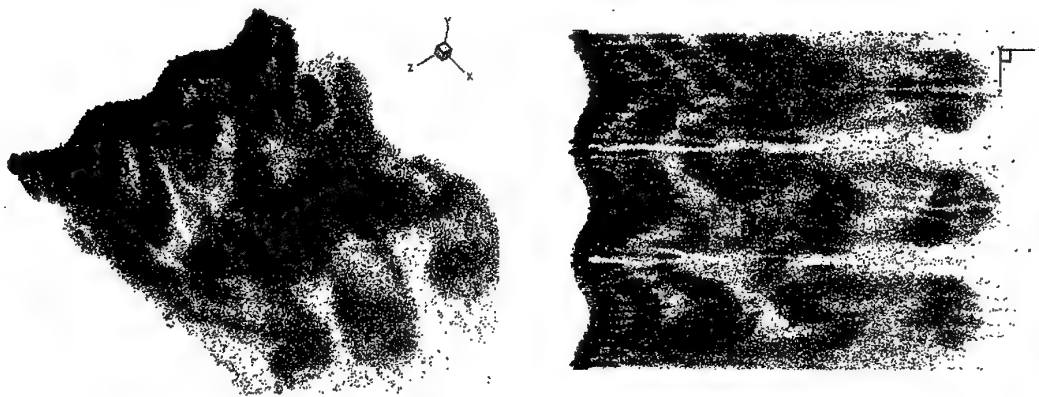


Figure 4: Perspective and plan views of wake structure for $W/\lambda=0.167$ at $T=30$.

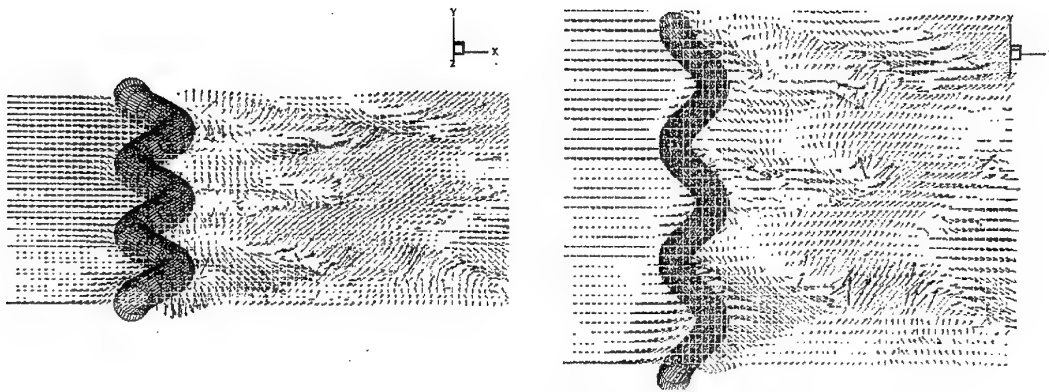


Figure 5: Instantaneous velocity vectors at $y=0$ and $y=0.6D$ for $W/\lambda=0.167$; $T=30$.

shedding is not suppressed as opposed to their experimental findings, the periodic variation of wake width along the span is well predicted. As shown in Figure 3, a narrow wake is present where the cylinder extends furthest upstream (geometric peak) and a wide wake is observed behind a valley. Also in agreement with the experiment (8), is that vorticity accumulates more behind the valleys to leave more of a wake than behind the peaks. This is evident both from the perspective and plan views of the simulated wake structure (Figure 4) and the velocity vector fields at the centre plane $y=0$ and $y=0.6D$ (Figure 5).

ACKNOWLEDGMENTS

The authors would like to thank Professor Kyoji Kamemoto for making an early version of his vortex code available at the beginning of the present research. This study has been supported by NATO under Research Grant no CRG972960 and the Istanbul Technical University research fund.

REFERENCES

- (1) Bearman, P.W. (1997), "Near wake flows behind two- and three-dimensional bluff bodies", *J. Wind Engng. & Ind. Aero.*, Vol. 69-71, p. 33-54.
- (2) Gerrard, J.H. (1966), "The three-dimensional structure of the wake of a circular cylinder", *J. Fluid Mech.*, Vol.25, p.143-164.
- (3) Williamson, C.H.K. (1989), "Oblique and parallel modes of vortex shedding of a circular cylinder", *J. Fluid Mech.*, Vol. 206, p.579-627.
- (4) Eisenlohr, H. and Eckelmann, H. (1989), "Vortex splitting and its consequences in the vortex street wake of cylinders at low Reynolds numbers", *Phys. Fluid A1*: p.189-192.
- (5) Bearman, P.W. (1984), "Vortex shedding from oscillating bluff bodies", *Ann. Rev. Fluid Mech.*, Vol.16, p.195-222.
- (6) Tombazis, N. and Bearman, P.W. (1997), "The effects of three-dimensional imposed disturbances on Bluff Body Near Wake Flows", *J. Fluid Mech.*, Vol. 330, p. 85-112.
- (7) Nuzzi, F., Magnes, C. and Rockwell, D. (1992), "Three-dimensional vortex formation from an oscillating non-uniform cylinder", *J. Fluid Mech.*, Vol.238, p. 31-54.
- (8) Owen, J.C., Bearman, P.W. and Szewczyk A.A. (2001), "Passive control of VIV with drag reduction", *J. Fluids and Structures*, Vol. 15, p. 597-605.
- (9) Nakanishi, Y., Kamemoto, K. (1992), "Numerical simulation of flow around sphere with vortex blobs", *J. Wind Eng. & Ind. Aero.*, Vol.46, p.363-369.
- (10) Graham, J.M.R. and Arkell, R.H. (1999), "A Hybrid Vortex Method", *Proc. First Int. Conf. On Vortex Methods*, Maiko Villa, Kobe, Japan, p. 47-58.
- (11) Dallmann, U., Herberg, Th., Gebing, H., Su, W.H., Zhang, H.Q. (1995), "Flow field diagnostics: topological flow changes and spatio-temporal flow structure", *AIAA Paper 95-0791*.
- (12) Darekar R. and Sherwin, S.J. (2001), "Flow past a square section cylinder with a wavy stagnation face", *J. Fluid Mech.* Vol. 426, 9. 263-294.
- (13) Kamemoto, K. (1995), "On attractive features of the vortex methods", *Computational Fluid Dynamics Review* (Editors Hafez, M. and Oshima, K.), John Wiley & Sons.
- (14) Winckelmans, G. and Leonard, A. (1988), "Improved vortex methods for three-dimensional flows", *Proc. Workshop on Mathematical Aspects of Vortex Dynamics*, Leeburg, Virginia, p. 25-35.
- (15) Ojima, A. and Kamemoto, K. (1999), "Numerical simulation of unsteady flow around a sphere by a vortex method for Re number from 300 to 1000", *Proc. First Int. Conf. On Vortex Methods*, Maiko Villa, Kobe, Japan, p. 83-91.
- (16) Ahmed, A., Khan, M.J. and Bays-Muchmore, B. (1993), "Experimental Investigation of a three-dimensional bluff-body wake", *AIAA Journal*, Vol.31, No. 3, p. 559-563.

A Study of the Unsteady Force due to Gusts of Side Wind on a Train by the Three-dimensional Discrete Vortex Method

Kazuhiko Ogawa, Michihisa Tsutahara *

Takaaki Nakazawa* and Naoki Takada

Department of Mechanical Engineering, Kobe University

Rokko, Nada, Kobe 657-8501 Japan / Email:ogawa@mech.kobe-u.ac.jp

*Also with the Graduate School of Science and Technology

Tatsuo Maeda and Minoru Suzuki

Railway Technical Research Institute

2-8-38 Hikarimati, Kokubunji, Tokyo, 185-8540 Japan

ABSTRACT

Lateral forces on a train due to gusts of large-scale side wind and local-scale side wind are investigated by using the three-dimensional vortex method. In case that the scale of gust is sufficiently large compared with the size of the train, the lateral force coefficient increases only at the beginning of the acceleration of the side wind but that the lateral force coefficient after the acceleration is not so different from that without the acceleration. Local acceleration of the side wind is simulated by a vortex ring of which the shape is square in the initial condition and the vortex ring is assumed to approach the train by the side wind. The condition that the direction of induced velocity is upwards in the vortex ring is called "Blowing up" and the condition that the direction of induced velocity is downwards in the vortex ring is called "Blowing down" in our study. In case of "Blowing down", the numerical results of the lateral force coefficients show large fluctuations and some peaks. On the other hand, in case of "Blowing up", the results of lateral force coefficients show relatively small

fluctuations and that the effect of the vortex ring seems to be small. The unsteady fluctuation of the lateral force coefficient by the local acceleration of the side wind is important and must be considered in the investigation of the countermeasure for the derailment especially in case of blowing down.

1. INTRODUCTION

Lateral force is one of the causes of the derailment of trains and some countermeasures like windbreak walls or the improvement of structures are often done in bridges. However, in case of running on level ground, effective countermeasures against the side wind are not always done because the prediction of the side wind is difficult. In general, the natural wind is unsteady and the force acts on trains complicatedly. Therefore, the analysis of the effect of the side wind is important. Authors have been studying on the side wind and the reduction of the lateral force by rotating cylinders setting on the roof of trains^{(1)~}⁽³⁾. Moreover, the three-dimensional flow around a train has also been investigated by the vortex method taking

into account the gust of the side wind.

In this study, lateral forces on a train due to gusts of large-scale side wind and local-scale side wind are investigated by using the three-dimensional discrete vortex method. In case of the large-scale gust, the scale of the side wind is assumed to be sufficiently larger than the length of the train. In case of the local-scale gust, the scale of the side wind is assumed to be about the same as the length of the train. By using the discrete vortex method, the grid generation is not needed and the load of the calculation is relatively smaller than that of other numerical methods. Moreover, in the discrete vortex method, the local-scale gust is easily expressed as a vortex ring with a large circulation that approaches to the train.

2. NUMERICAL ANALYSIS BY THREE-DIMENSIONAL DISCRETE VORTEX METHOD

2.1 Calculation method of velocities

In our analysis, the surface of the train is expressed by source panels and the strength of each source is determined by the condition that the normal velocity is zero at the centroid. The separation of the flow is expressed by introducing vortex sticks to the flow field and diffusion of vorticity is calculated by core-spreading method. The discrete vortex method does not need to generate a grid because the body shape and the separation of the flow are expressed by the vortex sticks and the source panels. The calculation load of the vortex discrete method in an early stage of the calculation is smaller than that of other methods. Therefore, the discrete vortex method is very advantageous for three-dimensional flow analysis.

The position releasing the vortex sticks to express the flow separation is the corner of the roof and the sidewall of the train. Figure 1 shows the condition of free vortices released from the boundary layer and bound vortices on

the body surface observed from the top and cross-sectional direction. The strength of the circulation $\Delta\Gamma$ of the vortex stick released into the flow field at each time step is given by the following equation,

$$\Delta\Gamma = \frac{1}{2} U_s^2 \Delta t \quad (1)$$

where U_s is the velocity component of which direction is perpendicular to the vortex sticks, $\Delta\Gamma_e$ and $\Delta\Gamma_d$, and parallel to the panels. The circulations of free vortices at the beginning of the simulation are given by equation (1) and those in following steps are obtained in the same way. However, one of the parts of the circulation of the vortex sticks of the former steps remains on the panels of the body surface. The translation of vortex sticks is calculated by the vorticity equation and the continuity equation under the assumption that the circulations of vortex sticks are constant. As for the discretization of time, Adams-Bashforth scheme of second order accuracy is used.

The effect of the ground is taking into account by using images of the source panels and vortex sticks. When the images of vortices are arranged to the calculation field, the sign of the circulations of the images are reversed. If

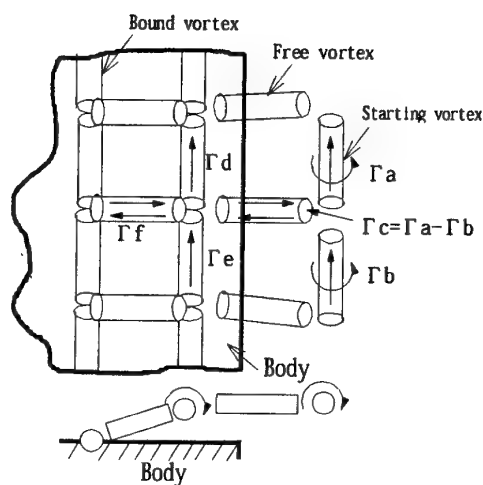


Fig.1 Shed Vortices and vortex sticks

the vortices penetrate into the body surface of the train or the ground, the vortices are rearranged to the position of the images.

2.2 Calculation method of pressure

The calculation of the pressures is performed with the following equation by Shintani et al⁽⁴⁾.

$$\begin{aligned} & -C_i H_i + \int_{A_s + A_w} H \nabla G_i \cdot \mathbf{n} dA \\ & = -2 \left[\int_V \nabla G_i \cdot (\mathbf{u} \times \boldsymbol{\omega}) dV - \frac{1}{\text{Re}} \int_{A_s + A_w} G_i \mathbf{n} \cdot \nabla^2 \mathbf{u} dA \right. \\ & \quad \left. + \int_{A_s + A_w} G_i \mathbf{n} \cdot \frac{\partial \mathbf{u}}{\partial t} dA \right] \end{aligned} \quad (2)$$

)

The above equation is the boundary integral equation transformed from the Poisson equation by the boundary element method. In the above equation, H is Bernoulli's function and G_i is Green's function of the Poisson equation as follows.

$$H = 2 \left(\frac{P}{\rho} + \Omega \right) + u_\alpha u_\alpha = C_p + u^2 \quad (3)$$

$$G_i = \frac{1}{4\pi r} = \frac{1}{4\pi} \frac{1}{\sqrt{(x-x_i)^2 + (y-y_i)^2 + (z-z_i)^2}} \quad (4)$$

In equation (2), C_i is the shape function. The value of C_i depends on the position of the source points and

those are as follows in three-dimensional flow:

$$\begin{aligned} C_i &= 1 \quad \text{for a source point in the domain} \\ C_i &= \theta / (4\pi) \quad \text{for a source point on the boundary} \\ & \quad (\theta : \text{solid angle}) \\ C_i &= 0 \quad \text{for a source point out of the domain} \end{aligned}$$

The calculation procedure has been reported in the reference⁽³⁾ and the detail is omitted in this paper. Roughly speaking, when the body surface is divided into N regions and M discrete vortices are arranged in the

flow field, the pressures can be obtained by solving the simultaneous equations for Bernoulli's function H_i .

3. CALCULATION CONDITION

3.1 Calculation Model

Figure 2 shows a calculation model of the train. The roof of the train is a convex surface and the surface of the train is covered by 332 source panels. It is assumed that the train is fixed on the ground and that the side wind blows perpendicularly to the train. The flow separation is assumed to be occurred from the edge of the sidewall of the train and the vortex sticks are released from the edge.

3.2 Calculation Condition and Lateral force coefficient

Table 1 shows the parameters of the calculation. The width of the train is the reference length and the height is the same as the width. The lateral force is assumed to be determined by only the pressure distribution and the lateral force coefficient is defined as follows,

$$C_{Fy} = \frac{F_y}{\rho U^2 A} \quad (5)$$

where y shows the direction perpendicular to the train, U is the uniform velocity, and A is the area of the sidewall of the train.

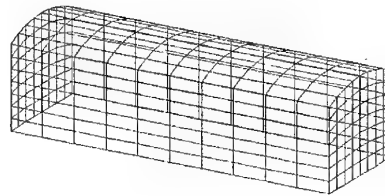


Fig.2 The shape of the car and the panel

Table 1. Initial Parameter

Reynolds Number	Re	10,000
Time Step	Δt	0.1
Panel Number	N	332
Initial Core Radius	σ_0	0.05

4. LARGE SCALE GUST OF SIDE WIND

4.1 Acceleration of flow filed by large-scale gust

Even in potential flow, a body is subjected to the force by virtual mass effect in case of acceleration and this effect is taken into account in numerical simulation.

When the acceleration is \dot{U}_∞ , the pressure gradient occurs in the flow field as follows.

$$-\frac{dp}{dy} = \rho \dot{U}_\infty \quad (6)$$

It is assumed that the uniform velocity is accelerated during the dimensionless time $T = tU/L = 1$ and $T = 2$ and that the uniform velocity becomes 1.5 times after the acceleration. The parameter in Fig.3 shows the magnitude of the acceleration.

4.2 Lateral force coefficient

Figure 4 shows the lateral force coefficients and the reference velocity is the instantaneous uniform velocity. The parameter in the figure shows the acceleration. In each case, the lateral coefficients increases at the beginning of the acceleration, about $t=10$. However, as shown in Fig.5, when the uniform velocity before the acceleration is taken as the reference velocity, the lateral force coefficient shows some increase of the drag by the increase of the velocity and the effect of the acceleration is not clear in this result. Moreover, on the calculation

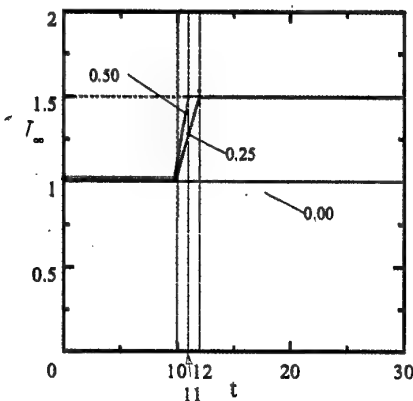


Fig.3 Acceleration of Uniform Flow

result that was obtained by omitting the effect of the virtual mass, the lateral force coefficient tend to decrease

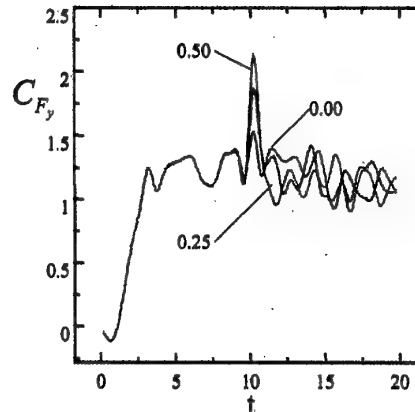


Fig.4 Lateral force coefficient based on $U(t)$

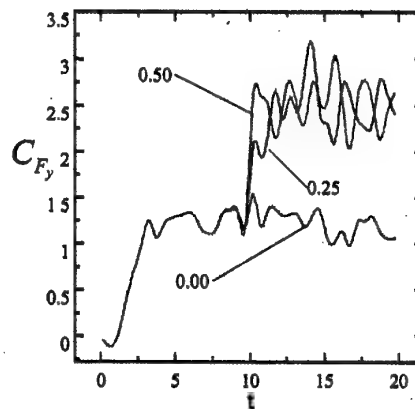


Fig.5 Lateral force coefficient based on $U=1$

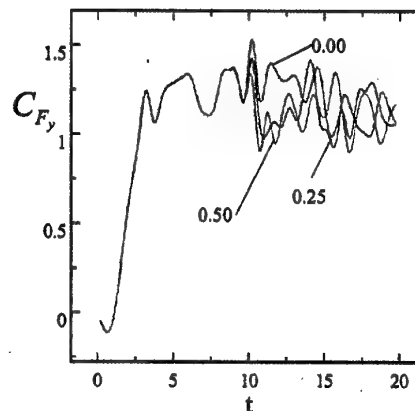


Fig.6 Lateral force without virtual mass effect

at the beginning of the acceleration as shown in Fig.6.

This reason is as follows. Figure 7 shows the velocity vectors between $t=10$ and $t=11$. In this time period, the change of the lateral force coefficient is large and it can be seen that the separation point above the roof moves downstream. In the calculation without taking into account the effect of virtual mass, the drag decreases by the effect of moving the separation point downstream. This effect seemed to cancel the increase of the drag by the effect of virtual mass. Accordingly, in case of the large-scale gust of the side wind, the train will not be subjected to the large effect of acceleration.

5. LOCAL SCALE GUST OF SIDE WIND

5.1 Local acceleration flow field by local scale gust

By the use of the discrete vortex method, the local-scale gust of the side wind was easily expressed by a square of vortex ring as shown in Fig.8. This vortex ring is assumed to be translated by the uniform velocity and the induced velocities of vortex sticks. The position of the vortex ring at the initial stage of the calculation is at $L=10$ (the width of the train=1) and at about the same height of the roof of the train. In this paper, the case that the gust blows to the ground inside the vortex ring is called "Blowing down" and the case that the gust blows

upward inside the vortex ring is called "Blowing up".

5.2 The case of "Blowing down"

In Fig.9, the solid line signed "none" shows the result without the vortex ring. In this case, the lateral force coefficient shows a slight fluctuation with time and the average value is about 1.25. The thin solid line and the broken line show the results that the strength of the circulation of the vortex ring is -0.3, -0.5 and -1.0. The minus sign of the circulation expresses that the gust blows to the ground inside the vortex ring (Blowing down). The lateral force coefficient shows peaks at about $t=10$ and $t=16$ and decreases between $t=10$ and $t=16$. The fluctuation of the lateral force coefficients becomes large as the strength of circulations increases.

As shown in Fig.10, the lateral velocity (the velocity of the gust to the side wall) decreases at about $t=10$ and increases again after $t=10$. When the lateral force coefficient shows the peak again (at about $t=16$), the lateral velocity becomes almost constant. In case of the local-scale gust, the increase of the lateral force coefficient seems to have the correlation with the velocity fluctuation at each time rather than the magnitude of the velocity.

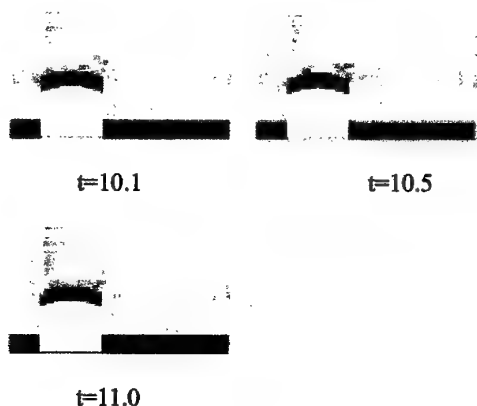


Fig.7 Velocity vector field on center cross section when the flow accelerates globally

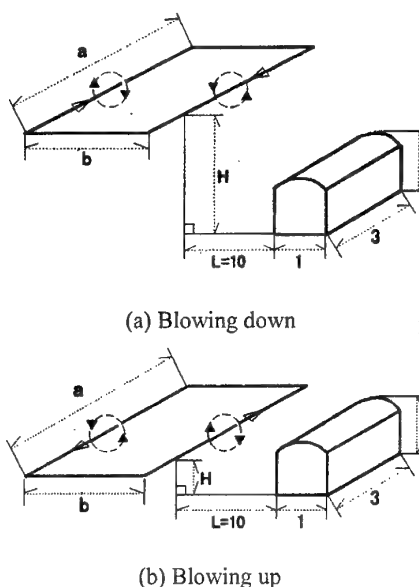


Fig.8 A vortex ring approaching the train

Figure 11 shows the distribution of the vortex sticks. The vortex ring breaks up soon after the start of the calculation. Comparing Fig.9 with Fig.11, it can be seen from the result of $t=10$ and $t=12$ in Fig.11 that the decrease of the lateral force coefficient after $t=10$ in Fig.9 concerns with that the vortex sticks begin to be taken in the wake of the train. It is presumed that the vortex sticks having the direction opposite to the vorticity vector of the wake are taken in the wake when the vortex ring begins to cross over the train and that those vortex sticks cancels the induced velocities of the wake region. Moreover, as shown in the result of $t=14$ and $t=16$ in Fig.11, it can be seen that the next peak of the lateral coefficient at about

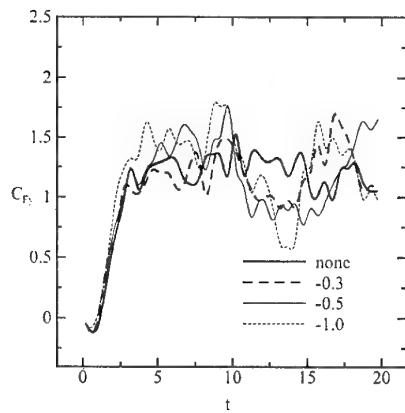


Fig.9 Lateral Force Coefficient
(Blowing Down, $a=3, b=3$)

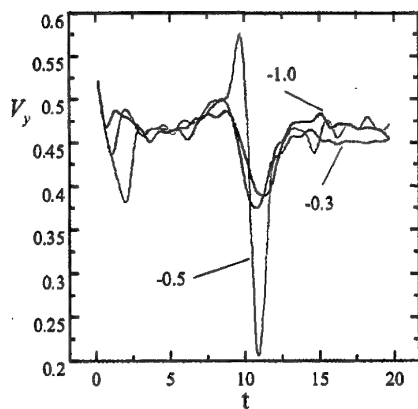


Fig.10 Lateral Velocity at a Point just ahead the car

$t=16$ in Fig.9 corresponds to the time when the vortex sticks of which the direction is the same as the vorticity vectors of the wake begin to be taken in the wake when the vortex ring almost finishes crossing over the train.

Figure 12 shows the velocity vectors at the central

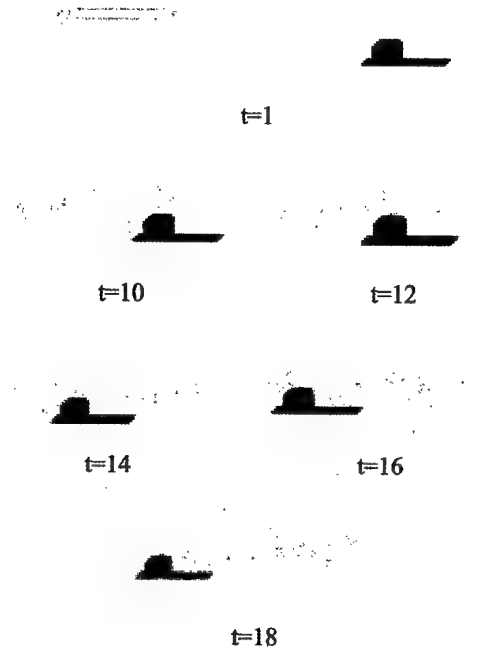


Fig.11 Distribution of Vortex Sticks
(Blowing down, $\Gamma=-0.3, a=5, b=5$)

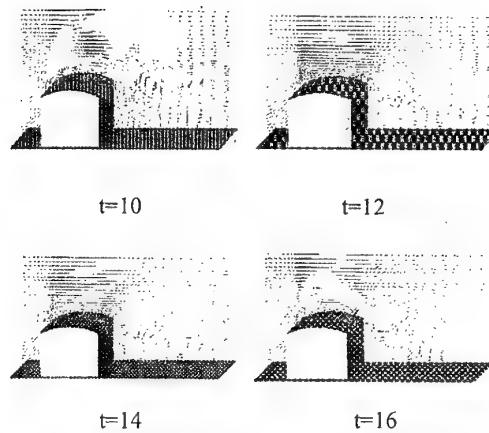


Fig.12 Velocity vectors at the central cross section
(Blowing down, $\Gamma=-0.3, a=5, b=5$)

cross section. The condition of the separation and the wake changes greatly between $t=10$ and $t=16$ and this is related to that the lateral force coefficient decreases once and increases between $t=10$ and $t=16$.

Figure 13 shows the distributions of the vortex sticks observed from the top. The black square indicates ground for the reference and the scale varies in each figure. The shape of the vortex ring varies from a square to a ring and it keeps the ring shape after crossing over the train. This tendency is characteristic in the case of blowing down and ensured what is mentioned about Fig.11. As the shape of the vortex ring is kept even in crossing over the train, the vortex sticks having the direction opposite to the vorticity vectors of the wake are easy to be taken in the wake at about $t=12$ and this causes the decrease of the lateral force coefficient.

5.3 The case of "Blowing up"

Figure 14 shows the lateral force coefficient in case of blowing up and it can be seen that there is not large difference from the case without the gust shown as "none" in Fig.14. Comparing the results with that of blowing down (Fig.9), the fluctuations are smaller than that of blowing down.

Figure 15 shows the velocity vectors at the central cross section. Even between $t=12$ and $t=18$, a large change cannot be seen in the separation and the wake. Figure16 shows the distribution of the vortex sticks. The vortex ring keeps the rectangular shape to $t=10$ but the vortex sticks tend to concentrate to the corners of the front and the rear of the train. This tendency seems to have the relation with that the flow does not show large change as mentioned above. The distribution of the vortex sticks of blowing up is clearly different from that of blowing down and it seems that the effect of blowing up is small because vortex sticks tends to scatter more randomly comparing with the case of blowing down. Accordingly, the induced velocities of the vortex sticks

are canceled and the fluctuation of the lateral force coefficient becomes small. As for the movement of the vortex sticks, in case of blowing up, the shape of the vortex ring keeps square or rectangular before passing the train and the vortex sticks tend to concentrate to the

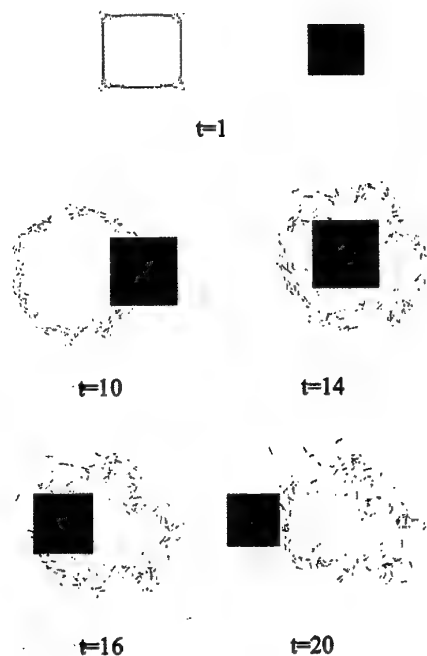


Fig.13 Distributions of Vortex sticks
(Blowing down, $\Gamma = -0.3$, $a=5$, $b=5$)

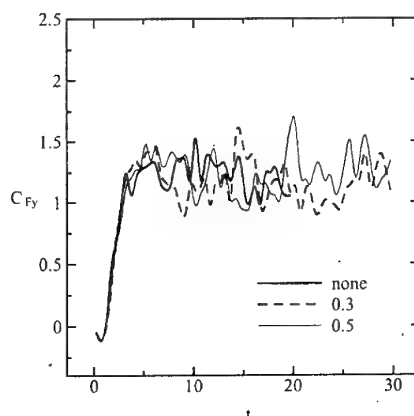


Fig.14 Lateral Force Coefficient
(Blowing Up, $a=5$, $b=5$)

corners of the front and the rear of the train when the vortex ring crossed over the train. It seems that the difference of the movement of vortex sticks between "Blowing down" and "Blowing up" affects the change of lateral force coefficients.

6. Concluding Remarks

In case of large-scale gust, it is found that the lateral force increases only by the magnitude of the velocity of the side wind and that a train is not subjected to the effect of acceleration of the side wind.

In case of local-scale gust, it is found that the unsteady fluctuation of the lateral force coefficient by the local acceleration of the side wind is important and must be considered in the investigation of the countermeasure for the derailment. Especially, the case of "Blowing down" is important because the lateral force coefficient shows large fluctuations and peaks.

REFERENCES

- (1) Tsutahara, M., Maeda, T. et al. (1999) "A study Reduction of Lateral Force on Railway Car due to Side Wind", Transactions of The Japan Society of Mechanical Engineers, Ser. B Vol. 65, No. 630, p. (in Japanese)
- (2) Tsutahara, M., Nagahisa, N. et al. (1999) "Study of

- Reducing of Fluid Force due to Side Wind on a Running Train", Transactions of The Japan Society of Mechanical Engineers, Ser. B, Vol. 65, No. 636, p. 2595-2603. (in Japanese)
- (3) Tsutahara, M., Tatsumi, Y. et al. (2000) "A study of the Fluid Force due to Side Wind on a Railroad Car by Three-Dimensional Discrete Vortex Method", Transactions of The Japan Society of Mechanical Engineers, Ser. B, Vol. 66, No. 644, p. 1021-1028. (in Japanese)
- (4) Shintani M. and Akamatsu H (1994) "Investigation of Two Dimensional Discrete Vortex Method with Viscous Diffusion Model", Computational Fluid Dynamics Journal, Vol. 3, No. 2, p. 237-254.
- (5) Christiansen, J. P. (1973) "Numerical simulation of hydrodynamics by the method of point vortices", Journal Computational Physics, Vol. 13, p. 363-379.
- (6) Leonard, A. (1980) "Vortex Methods for Flow Simulation", Journal of Computational Physics, Vol. 37, No. 3, p. 289-335.
- (7) R. I. Lewis, (1991) "Vortex Element Methods for Fluid Dynamic Analysis of Engineering Systems", Cambridge University Press

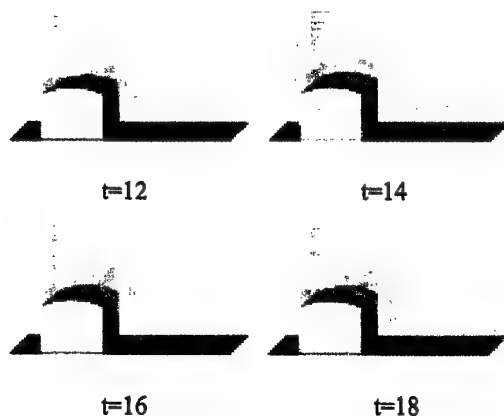


Fig. 15 Velocity vectors

(Blowing up, $\Gamma = 0.3$, $a=5$, $b=5$)

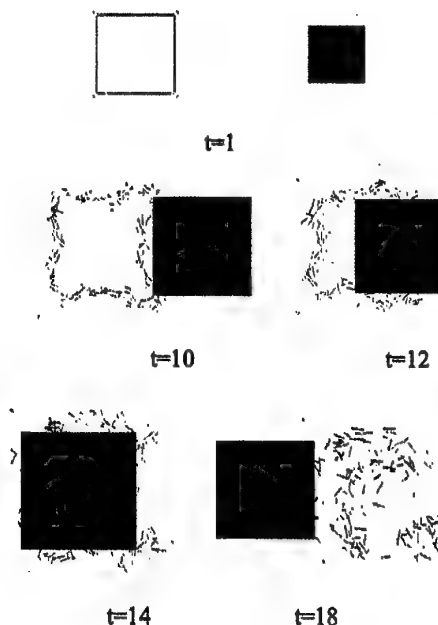


Fig. 16 Distribution of Vortex sticks

(Blowing up, $\Gamma = 0.3$, $a=5$, $b=5$)

APPLICATION OF MIXED EULERIAN-LAGRANGIAN VORTEX METHODS TO CROSS-FLOW PAST LONG FLEXIBLE CIRCULAR CYLINDERS

By J.M.R. Graham and R.H.J. Willden

Department of Aeronautics, Imperial College, London SW7 2BY, UK.

ABSTRACT

A quasi-three-dimensional numerical method for simulating incompressible, viscous flows and its application to the problem of vortex shedding from long flexible cylinders in cross-flow is described. The method is based on a hybrid Lagrangian vortex method in which the velocity and diffusion fields are computed on a mesh through which the vortex elements are advected. In the present paper the application of this method to numerical simulation of vortex shedding and dynamic response from long flexible cylinders of circular cross-section is considered. First transverse vortex-induced-vibration (VIV) of rigid, elastically mounted, cylinders is simulated for a range of cases, particularly including low mass ratio. Then long flexible cylinders, permitting bending in two directions but not torsion, are studied. These are a good representation of offshore riser pipes, which, in currents, are often subject to VIV. A quasi-three-dimensional method has been developed to incorporate some effects of three-dimensionality from variations of vortex shedding along the length of the cylinder due to shear in the incident flow and to modal response of the structure. In order to permit useful flow evolution times to be computed for practical cases on a workstation level of computing resource the method utilises sectional flow computations which are linked via the motion of the cylinder and also through a three-dimensional vortex lattice model of its wake at large scale. Turbulence is modelled through a simple implementation of a sub-grid viscosity. Results are compared with experimental tests of flexible pipes at Reynolds numbers up to the order of 10^5 .

Key Words: Vortex-Induced-Vibration, Vortex Methods

1. INTRODUCTION

Lagrangian vortex methods are less widely used for industrial Computational Fluid Dynamics than their flux based counterparts which solve the Navier-Stokes equations in primitive variable (velocity and pressure)

form on an Eulerian mesh. One of the main reasons for this is the perception that they are limited to incompressible two-dimensional flows. There have been attempts to use vortex methods for compressible flows but the additional terms, which arise in the vorticity, transport and vorticity-velocity equations make their application to compressible flows more difficult. There has been more application of vortex methods to three-dimensional incompressible flows, see eg. Arkell (1). A major issue here is the enforcement of a divergence-free field which cannot be automatically satisfied as it can in two-dimensional flow. In principle the problem is not significantly different from the enforcement of this condition in velocity-pressure codes, but in addition the relative advantage of solution efficiency is lost in three dimensions since now 6 velocity and vorticity variables must be solved for at each time step as against 4 in the primitive variable formulations. The advantage of Discrete Vortex (particle based) Methods is that the Lagrangian procedure of carrying the flow field on convected particles considerably reduces the numerical diffusion which is required to stabilise flux based representations of convection at high Reynolds number. For this reason and also because of the direct simulation of the vortex structures provided by the methods, discrete vortex methods have been quite widely used for separated flows. These are generally more prevalent in Civil rather than other areas of Engineering and discrete vortex methods have been considered at least equal to commercial velocity-pressure codes for many of these cases.

The Discrete Vortex Method originated as an inviscid method, which was attractive as an inexpensive way of simulating two-dimensional separated flows at high Reynolds number for which the separation points could be specified independently. Later developments of the method introduced viscous diffusion through various approaches, the Random Walk method which uses the Einstein simulation of diffusion, Smith and Stansby (2), the 'diffusion velocity' method, Ogami and Akamatsu (3), the use of growing vortex cores simulating discrete vortex diffusion but requiring continual subdivision to retain accuracy and direct particle-particle interaction (4, 5). The vortex-in-cell method was introduced,

Christiansen (6), as was later the fast multi-pole method, Greengard and Rokhlin (7), as a way of getting round the problem of the quadratic growth in time required to compute the velocity field at each time step as the numbers of vortex particles present in the flow increased. In the vortex-in-cell method direct computation of the velocity field by the Biot-Savart law is replaced by much faster solution of a Poisson equation on a mesh. This mesh introduces a minimum resolution of the flow field, which may be greater than the discrete vortex separation and has been criticised as introducing the disadvantages of a mesh. However it does also permit the viscous diffusion to be carried out by standard Eulerian flux methods on the mesh. Diffusion is effectively a smoothing process implying a relationship between vorticity gradients, mesh resolution and Reynolds number and therefore a flux-based mesh simulation seems appropriate. This approach has led to the development of a viscous vortex based method which has now been extensively validated against other (primitive variable) methods and against experimental results for low Reynolds number flow around rigid circular cylinders for which the flow field is laminar and two-dimensional.

A major separated flow category of engineering relevance consists of the flows in which vorticity shed into the wake rolls up into concentrated structures and generates a strong periodicity in the wake. For long bluff cylindrical bodies in cross flow a von-Karman alternating vortex street is formed with a spectrum (of, say, velocity) dominated by a single natural frequency and its harmonics. This type of wake has a narrow spectrum of forcing on the cylindrical body generating it. As a result flexible or flexibly supported cylinders are often subject to vortex-induced-vibrations (VIV) with the vortex shedding frequency from the wake exciting a structural frequency of vibration of the body. The amplitude of this vibration can be large (of order one diameter) if the structural damping is low and the structural and natural frequencies are sufficiently close for the two to become 'locked'. The range over which lock-in occurs depends on the vibration amplitude and on the mass and damping ratios. Flow induced vibrations of this sort can be a multiple degree of freedom problem, in which coupling exists between motions in-line with and transverse to the stream. The large amplitude of the oscillations can present a potent source of fatigue as well as the possibility of clashing in multiple body assemblies.

Designers of pipework which is exposed to high winds or significant (water) currents always have to take account of the possibility of VIV and calculate the critical velocity range over which it might occur. In particular the phenomenon has become a major issue in the design of deep water riser pipes which convey fluids between the sea bed and the surface in the production of hydrocarbons offshore. The deep water fields which are

now beginning to be exploited involve depths of order 2000m and currents of as much as 2m/s, with a significant shear profile over the whole or part of the total depth. Under these conditions the riser is subject to different frequencies of vortex shedding and hence VIV along its length and the higher modes of vibration of long flexible risers which fall into possible structural excitation ranges can often be relatively close in frequency to each other. Each section of the riser can be subject to a number of modes of vibration occurring simultaneously, having been excited by the current at different depths.

Because of the great length of these riser pipes, three-dimensional flow simulations at realistic Reynolds numbers ($10^5 - 10^6$) are computationally impractical at present. A few cases with either limited length or Reynolds number have been computed (eg. Lucor et al. (8) and Newman and Karniadakis (9)). More usually approximate techniques such as strip theory (eg. Dalheim et al. (10) and Herfjord et al. (11)) have been

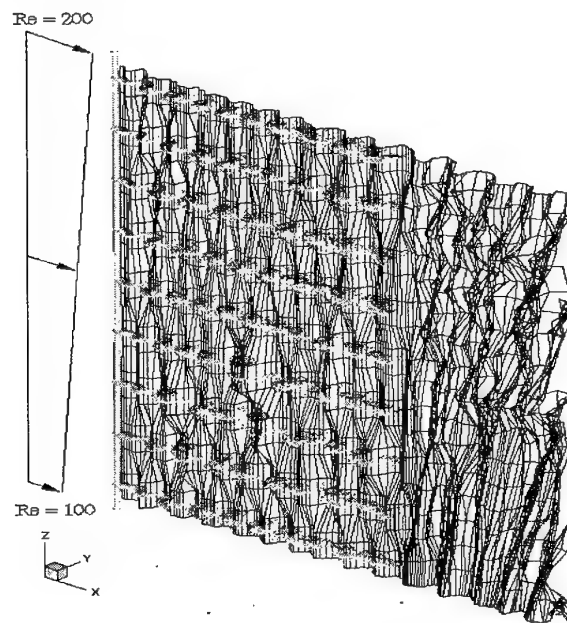


Figure 1. Vortex Wake of Rigid Cylinder in Shear Flow

used to simulate riser response. This is the basis of the technique employed in the present work but with the addition of a quasi-three-dimensional extension. Two-dimensional computations using a vortex in cell Navier-Stokes code, Graham (12), are linked hydrodynamically through a three-dimensional large scale vortex lattice representation of the wake, Giannakidis and Graham (13) and Willden (14). The response of the riser is computed using a finite (beam) element model of the three-dimensional structural dynamics coupled to the CFD.

2. COMPUTATIONAL METHOD

The vortex-in-cell method is used to solve the incompressible Navier-Stokes equations in velocity-vorticity form. For the cases of two-dimensional flow first examined (rigid circular cylinders, elastically mounted, at low Reynolds numbers) the two-dimensional solver described below is used. In the later cases of flow (low and high Reynolds numbers) around long flexible cylindrical bodies across the incident stream the major component of the wake vorticity is still assumed to be aligned with the cylinder and spanwise gradients of all flow variables are assumed to be much less than gradients in other directions. A first approximation therefore is still to use the same two dimensional flow solver for each cross-section along the cylinder. The two-dimensional vorticity transport equation:

$$\partial\omega/\partial t + (\mathbf{u} \cdot \nabla)\omega = \nu \nabla^2 \omega \quad (1)$$

is solved using a split time-step approach for the convection and diffusion parts, evaluating diffusion by an Eulerian finite element method for the Poisson equation on a fixed, body-fitted, unstructured mesh and projecting the change back onto the vortex particles which in turn are used to convect the vorticity field taking a Lagrangian approach:

$$\omega = \omega^n + \nu \Delta t \nabla^2 \omega \quad (2)$$

$$\omega^{n+1} = \omega - \Delta t (\hat{\mathbf{u}} \cdot \nabla) \omega \quad (3)$$

The velocity field is evaluated from the vorticity field through a finite element solution of the two-dimensional Poisson equation:

$$\nabla^2 \mathbf{u} = - \nabla \times \omega \quad (4)$$

The pressure field is computed when required from the Poisson equation with velocity gradient source terms using the mesh and finite element method at the time intervals when the forces on the body are to be linked to the structural response equations. In the cases of flexible cylinders examined here these intervals had to be similar to the flow field time steps and were therefore taken as such, but in other cases depending on the spanwise wave speed along the structure they might be less frequent. The skin friction contribution to the body force was computed directly from the body surface value of the vorticity.

The two-dimensional computational planes were placed at equi-spaced intervals along the cylinder's length. They are linked hydrodynamically using an inviscid unsteady three-dimensional vortex lattice. The lattice is constructed so as to represent the three-dimensional vorticity field. This is done by updating its spanwise vorticity content from the underlying and much higher

resolution two-dimensional, sectional, vorticity fields (the vortex particles). A coarse mesh is used to amalgamate this vorticity so that typically there are the order of ten spanwise elements in each rolled up vortex wake structure (figure 1). The remaining vorticity components are derived by constructing the lattice so as to give continuity of circulation which provides a divergence free vorticity field. The point vortices in the cross-sectional planes and the lattice joining them are convected over each time-step by the whole of the velocity field. Those parts of the lattice which intersect the two-dimensional computation planes are updated from the vorticity fields in the planes (ie. from the point vortex distributions). Those parts of the lattice which have been convected beyond the computational planes are convected by the velocity field in the far wake. Distortion by velocity gradients is included in this region but viscous diffusion is not included on the assumption that its effect on the distant body is negligible. The velocity field for convection of the lattice and as a boundary condition for the cross-sectional planes is computed directly from the lattice using the Biot-Savart law. Different methods of constructing the three-dimensional vortex lattice and of applying the boundary conditions to the cross-sectional planes have been tried with some effects on the results. In the present case amalgamation into the lattice combines all point vortices within narrow transverse strips crossing the wake thus giving a single vortex lattice sheet shed per body with significant cancellation of vorticity. Combining vortices according to sign which results in two lattice sheets per body has also been implemented in other calculations. In the present case the velocity boundary condition from the three-dimensional lattice wake onto each two-dimensional plane has been computed at one point only per plane (the centre of the body cross-section) which gives a process similar to classical lifting line theory. Again other variations have also been implemented.

The elastically mounted rigid cylinder is modelled structurally as a simple one-degree of freedom spring-mass-damper equation which is solved explicitly. In the second case the flexible pipe is modelled as a bending beam under pretension using a linear finite element implementation of the Bernoulli-Euler beam equations.

$$EI \partial^4 \eta / \partial z^4 - T \partial^2 \eta / \partial z^2 + \rho A \partial^2 \eta / \partial t^2 = F_\eta \quad (5)$$

where η is the component in the x or y direction.

This model permits five degrees of freedom at each of the finite element nodes, axial and two transverse displacements and two rotations about axes normal to the planes of the displacements. The model incorporates tension, buoyancy and gravity but assumes zero structural damping. The response of the cylinder to the fluid loading is also calculated explicitly by this structural model. In both cases the explicit structural

solution is interleaved at each time step with the implicit CFD.

For lower Reynolds numbers than about 140 or perhaps 200 if end conditions are carefully controlled, the wake of a circular cylinder can be treated as two-dimensional. At higher Reynolds numbers the present method assumes that a sub-grid turbulence model can be used to represent the increasing turbulence and smaller scales of three-dimensionality which cannot be represented by the vortex lattice model of the wake. This involves the major assumption which cannot be completely justified that the usual process of Large Eddy Simulation can incorporate both the small scale turbulence which is not resolvable on the scale of the mesh and that *all* three-dimensional effects not represented by the coarse three-dimensional vortex lattice may be accounted for by the sub-grid eddy viscosity. If in the case of a rigid cylinder at high Reynolds number only one section is used to capture the large scale flow field (ie. the flow is assumed to be two-dimensional at large scale) the effective mesh scale in the non-resolved (spanwise) direction becomes strictly infinite. A Smagorinsky sub-grid eddy viscosity v_{sg} is evaluated using the resolved rate of strain tensor and a length scale based on the length scale l of the grid. In a 3-dimensional simulation:

$$v_{sg} = (C_s l)^2 \sqrt{\{ S_{ij} S_{ij} \}}$$

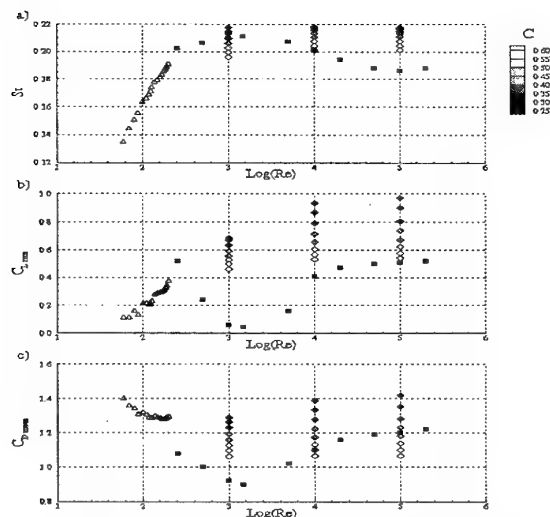


Figure 2 Effect of Sub-Grid Eddy Viscosity Coefficient on Strouhal Number, Lift and Drag.
■ Experimental Data, Norberg (16)

where $S_{ij} = \partial u_i / \partial x_j$ and C_s is the Smagorinsky coefficient which is usually given a value in the region of 0.15 for these types of separated flows, Arakawa et al. (15). But since the mesh resolved flow is two-dimensional only two grid scales (δx and δy) are available to construct the sub-grid length scale. Two

ways of doing this have been considered: (1) using just these two and ignoring the third direction, thus $l = (\delta x \cdot \delta y)^{1/2}$ or equivalently for an unstructured mesh with cell area δA , $(\delta A)^{1/2}$; (2) using for the third (lengthwise) dimension the spanwise correlation length L_z of the vortex shedding, so that $l = (\delta A \cdot L_z)^{1/3}$. A possibly more justifiable third length scale to use (3) would be the spacing between the cross-sections on which the resolved flow is computed, ie. the spanwise scale of the vortex lattice which carries the large scale three-dimensionality. This third alternative has not so far been tried. Because of the low exponent involved in the expression for eddy viscosity there is not in practice much difference between these three once the average magnitude has been adjusted by the sub-grid eddy-viscosity coefficient C , except that the second alternative includes directly some effect of increased correlation length in the lock-in region which the first and third relationships do not.

3. RIGID CIRCULAR CYLINDER IN UNIFORM FLOW

Figure 2 shows values of Strouhal number, mean drag coefficient and transverse force (lift) coefficient for a rigid circular cylinder over a range of Reynolds numbers up to 10^5 , computed by the method without structural dynamics using a single two-dimensional plane to represent a spanwise average of the large scale flow and the sub-grid eddy viscosity using the first formula for length scale and different values of C . The results are compared with the experimental values given by Norberg (16). In the present case a value of $C = 0.416$ has been selected as most generally appropriate and used for the subsequent three-dimensional riser computations. This value is equivalent to the value often used in fully three-dimensional large eddy simulations. But it should be noted that although it may be a reasonably optimum choice for some of the comparisons shown in figure 2 it is clearly very unrepresentative at Reynolds numbers around 10^3 where vortex shedding is known to have a very small spanwise length scale and many of the assumptions made are invalid. The rigid case is likely to be a more severe test case than the elastically mounted cylinder since outside the lock-in region the flow about the latter has many similarities to the former, but inside the lock-in region the large scale vortex shedding becomes correlated and three-dimensionality is only present within the small scale turbulence.

4. ELASTICALLY MOUNTED, RIGID, CIRCULAR CYLINDER IN LOW REYNOLDS NUMBER FLOW

A first set of computations were carried out using the two-dimensional solver (ie. one plane representing the whole flow, assumed to be two-dimensional) for a rigid

circular cylinder mounted elastically at either end and free to move in one degree of freedom transverse motion. It is well known that under these conditions a plot of Strouhal number against reduced velocity V_r (free stream velocity non-dimensionalised by cylinder diameter and structural frequency of the system measured in vacuo) shows a region in which the Strouhal number is approximately inversely proportional to the reduced velocity (ie natural frequency remains constant equal to the structural frequency). This lock-in region, which is associated with a transverse oscillation amplitude response of the order of one half to one diameter, lies between regions showing small response and the usual relationship between Strouhal number and Reynolds number for a fixed cylinder. However this well known result is most often obtained for the high mass ratios associated with relatively heavy cylinders in light fluids (such as air). Mass ratio m^* is defined here as $\pi m/2m_f$ where m is the mass of the body and m_f the mass of the displaced fluid. In the case of steel riser pipes conveying a gas/oil mixture in sea water much lower mass ratios of the order of 4 are usual. In these cases the added mass of the water associated with the pipe oscillations can be significant compared with the mass of the body and hence effect changes in the natural frequency from its value in vacuo. In addition the coefficient of added mass is not constant but varies through the lock-in region as the vortex shedding changes phase relative to the motion, becoming increasingly negative with increasing reduced velocity. The result of this is that if the mass ratio is small enough it is possible for the effective mass of cylinder plus added mass to approach zero and the lock-in region to extend indefinitely with increasing reduced velocity. This occurs because the

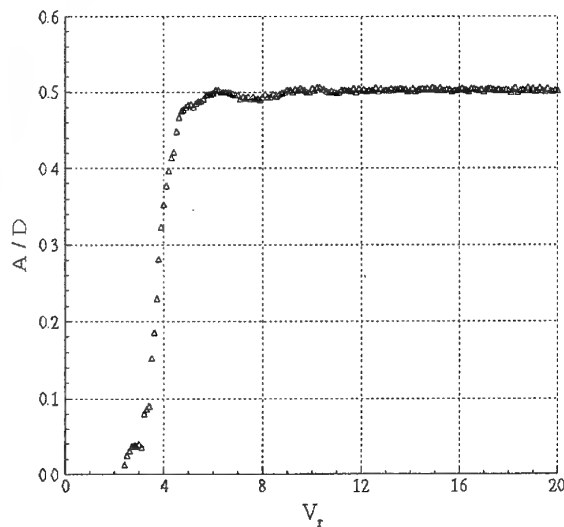


Figure 3. Non-dimensional amplitude of oscillation plotted against reduced velocity.

effective mass adjusts sufficiently increasing the structural frequency so that it remains locked to the natural shedding frequency as the velocity is increased, rather than the more limited entrainment of the shedding frequency by the structural frequency associated with high mass ratios.

Computations have been carried out to study the single degree of freedom (transverse) response of a spring mounted circular cylinder under conditions of zero structural damping in a low Reynolds number flow (~ 100) and with mass ratio $m^* = 1.0$. Figure 3 shows a plot of the non-dimensional amplitude y/D (y = amplitude of transverse oscillation, D = cylinder diameter) against reduced velocity and figure 4 a similar plot of the added mass to body mass ratio (defined from the transverse force on the cylinder in phase with its acceleration).

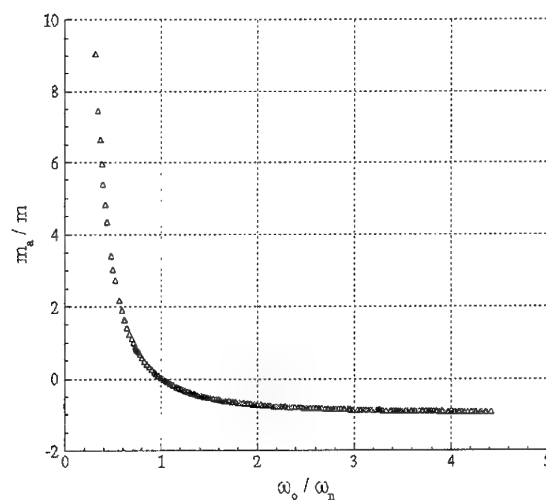


Figure 4. Ratio of transverse motion added mass to body mass plotted against frequency ratio.

5. FLEXIBLE PIPE IN LOW REYNOLDS NUMBER SHEARED FLOW

The simulation of flow past transversely oscillating cylinders at low Reynolds number has been extended to cases of forced three-dimensionality by considering sheared incident flow (sheared along the length of the cylinder). Results for a 25m length L of rigid cylinder with diameter $D = 0.25m$ and aspect ratio $L/D = 100$, subject to a sheared inflow were computed using the quasi-three-dimensional flow solver. The inflow Reynolds number was made to vary linearly from 200 at the top end to 100 at the bottom end. In the first case the cylinder was kept rigid and fixed. A particle and lattice image of the wake is shown in Figure 1. Although this figure yields limited insight into the structure of the wake, it demonstrates how the computational method works. Nine equally spaced

computational planes are depicted in this figure, each separated by 10D. The variation of spanwise Strouhal number and the time evolution of the lift coefficient acting on the cylinder are shown in figure 5. The Strouhal number varies from 0.156 at the low Reynolds

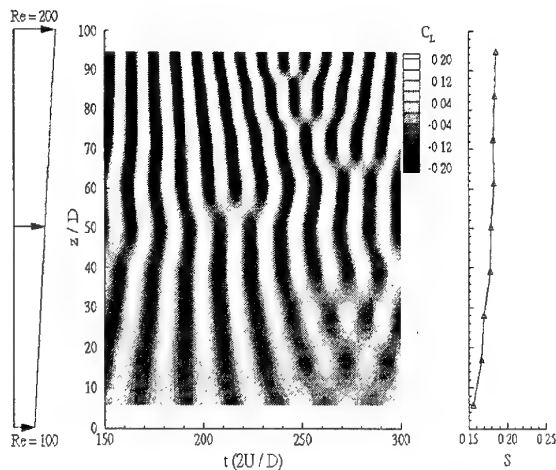


Figure 5. Transverse Force and Strouhal Number for a Rigid Cylinder in Shear Flow

number end to 0.185 at the upper end. The lift force coefficient shows signs of cellular shedding, as has been widely reported for sheared flow, but this result may also be dependent here on the spanwise resolution.

The cylinder was then made flexible and allowed to oscillate freely in the transverse direction, with its ends pinned. The stiffness and applied axial tension are 19.8 MNm^2 and 14.8 MN respectively. The tension was set deliberately high in order that the fundamental mode would be excited. Buoyancy and gravity forces are ignored, structural damping is set to zero and $m^* = 4.26$.

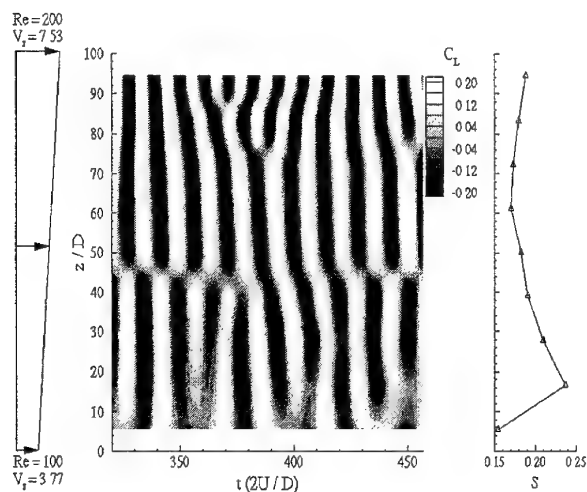


Figure 6. Transverse Force and Strouhal Number for Flexible Cylinder in Shear Flow.

In contrast with lower mass ratio cases around 1, the structural mass is dominant and as a result in the lock-in region the shedding frequency is moved towards the natural frequency. Figure 6 shows that the shedding frequencies at the end points remain relatively unperturbed by the oscillation, the amplitude of response being very small there, whereas those in between are significantly modified. The lift coefficient evolution, Figure 6, shows significant lengthwise correlation between $z/L = 0.25$ and 0.75 , over which the shedding and oscillatory frequencies remain locked. At the location of the peak response, $z/L = 0.44$, the lift evolution shows an abrupt phase change. On the lower velocity side, $z/L < 0.44$, lift and response remain in phase but towards the higher end, $z/L > 0.44$, they are in anti-phase. This phase change is not altogether unsurprising as to some degree it mimics the changes one would expect as the reduced velocity is increased from below to above the critical value. By comparing this result with the lock-in range of a spring mounted rigid cylinder undergoing single degree of freedom transverse VIV it can be seen that a substantial length of the cylinder on the lower (velocity) end of the model riser is well below the onset of lock-in and it is clear from the phase change of the lift that for $z/L < 0.44$ the riser response is hydrodynamically damped whereas for $z/L > 0.44$ it is being excited. Thus power flows in this case down the riser from the upper to the lower part. In this particular case it appears that the lift phase is such as to generate excitation over an upper segment $0.44 < z/L < 0.75$, but above this segment, $z/L > 0.75$ a combination of reduced amplitude towards the pinned end and increasing values of reduced velocity due to the shear lead to a region not locked-in where the response is again hydrodynamically damped for at least some of the time.

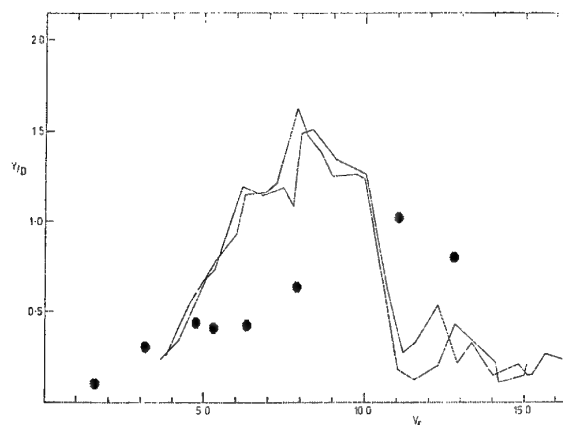


Figure 7 First Mode Transverse Response of Cylinder: — Experiment, Lamb (1988) • Computation

6. RESULTS FOR SIMULATED MODEL RISER EXPERIMENT.

The next stage of the work has been to carry out computations to predict the response of a flexible model riser, similar to one tested in a large scale laboratory flume with uniform and sheared incident flow. This circular section flexible pipe had a diameter of 0.076m and length 6m, the lower end pinned at the bottom of the flume and the upper end just above the water surface. Appropriate structural and mass properties of the model were used in the computations. The structural damping, which was very low in the experiment, was taken to be zero for the computations. Figure 7 shows results computed using the quasi-3-dimensional method at a mean flow Reynolds number of order 10^5 (depending on the value of the reduced velocity V_r). Measurements taken in the corresponding flume experiment (Lamb, 1988) gave a peak transverse response of approximately 1.5D at a reduced velocity of about 8 with the response falling sharply for reduced velocities above 10. The numerically predicted responses of the fundamental modes in both transverse and in-line directions are predicted to rise through the lock-in region with the largest response occurring at the highest reduced velocity reached, $V_r = 11$, but the amplitudes are somewhat underpredicted compared with the experiment. The higher structural modes were also predicted to respond as in the experiments but again the amplitudes were somewhat lower than measured. The mean deflection of the model riser in the downstream direction due to the mean drag is given fairly accurately.

7. RESPONSE OF TWO INDEPENDANT ELASTICALLY MOUNTED CYLINDERS.

A major problem of practical interest concerns the interactive motion of arrays of cylinders which are close enough to interfere and may even clash as a result of flow induced motion. This phenomenon can occur for transmission lines in the natural wind and of present interest for riser arrays subject to currents. Prediction of the resulting flows necessitates the use of an unstructured mesh which is able to accommodate the relative motion of the risers to one another. Hence mesh deformation must be implemented, efficiently, at every time step. In the present case two different methods have been investigated to do this. In the first a linear trans-finite interpolation was used to stretch the mesh proportionately between the moving boundaries, retaining its topology. This method is fast but leads eventually to unacceptable distortion of the elements. In the second separate overlapping sets of mesh node points have been constructed for each cylinder separately. Each set is fixed to its own cylinder as it moves. The full computation mesh is reconstructed at each time step from a Delaunay triangulation on the

union of these sets. This is a lengthier but still efficient process. In the end it was found most efficient if the computations used a combination of the two procedures.

Tests were carried out for a pair of rigid cylinders of the same diameter placed with one downstream of the other either in line or staggered. The cylinders were simulated as if spring mounted allowing independent motion with two degrees of freedom each. Zero structural damping was assumed. The results are compared with the experiments of Bryndum and Andersen, (18), who measured forces and responses on a pair of towed, spring mounted cylinders free to move similarly. Figure 8 shows an example of the vorticity field predicted for a case in which both cylinders were free to move under the induced hydrodynamic forces. Comparisons were made of the mean forces predicted and measured on the two cylinders for similar Reynolds numbers ($\sim 10^5$) and a range of relative positions. Initially both cylinders were held fixed. Figure 9 shows the lift when the rear cylinder was offset and is typical. There are significant differences although the trends are similar.

The cylinders were then released and Figure 10 shows a plot of the time history of the in-line (x) and transverse (y) responses. For the case shown the cylinders were initially at rest in-line, separated by 4 diameters, and then subjected to a uniform flow with a reduced velocity $V_r = 3$. These computations have only been carried out for a small number of flow cycles (much less than in the experiments) and it is probable that the predicted maximum amplitudes should be increased.

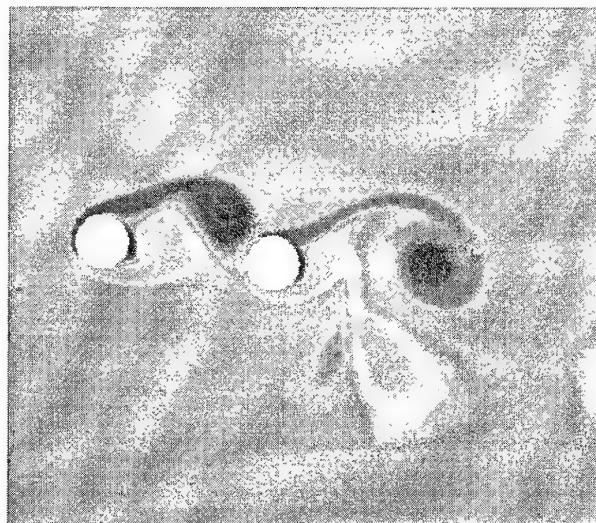


Figure 8 Vorticity Computed in the Wakes of a Pair of Independently Flexibly Mounted Cylinders.

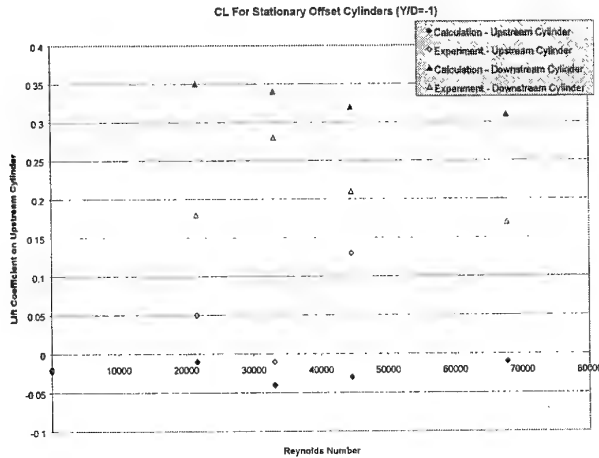


Figure 9. Mean lift coefficients on a pair of offset cylinders.

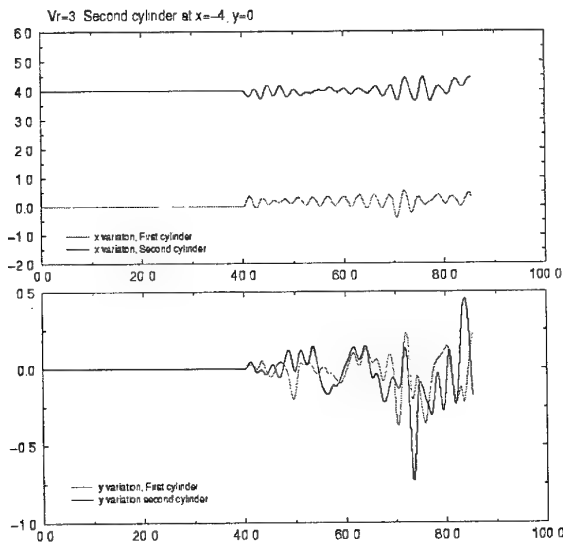


Figure 10 In-Line (x/D) and Transverse (y/D) Responses of a Pair of Flexibly Mounted Cylinders

8. CONCLUSIONS

The paper has presented a quasi-three-dimensional method based on discrete vortices to predict the response of long flexible cylinders in shear flows. Lock-in regions extending indefinitely have been predicted for cylinders at low mass ratio in agreement with the observations of others. However at low Reynolds numbers maximum transverse response amplitudes were limited to just over half a diameter, which is equivalent to the lower branch response but considerably less than the upper branch response observed at higher Reynolds numbers.

Cellular shedding in the three-dimensional wake of a fixed circular cylinder subject to a sheared onset flow, was observed. However the transverse vibrations of a flexible cylinder responding in the same shear flow were seen to correlate the vortex shedding over a substantial proportion of the cylinder's length. Comparison of the predictions with the results of a laboratory experiment on a model of a flexible riser pipe at Reynolds numbers around 10^5 showed representative excitation of structural modes but some underprediction of the amplitudes. Sectional computations have also been carried out for a pair of riser pipes in tandem in a current and the results have been compared with a laboratory experiment on pairs of towed, flexibly mounted, rigid cylinders performing (two-dimensional) transverse and in-line oscillations. Qualitative agreement has been found for the responses of the cylinders.

9. ACKNOWLEDGEMENTS

The financial support of BP Ltd and of the UK EPSRC is acknowledged for this work.

REFERENCES

1. Arkell R.H. (1995) Wake dynamics of cylinders encountering free surface gravity waves. PhD thesis, Univ. London, U.K.
2. Smith P.A. & Stansby P.K. (1988) Impulsively started flow around a circular cylinder by the vortex method. *J. Fluid Mech.*, 194, p45.
3. Ogami Y. and Akamatsu T. (1991) Viscous flow simulation using the discrete vortex model - the diffusion velocity method. *Computers and Fluids*, 19, p443.
4. Raviart P.A. (1986) Particle numerical models in fluid dynamics. *Numer. Meth. Fluid Dyn. II*, (IMIA Conf. Series. No. 7), p231.
5. Leonard A. (1980) Vortex methods for flow simulation. *J. Comp. Phys.*, 37, p289.
6. Christiansen J.P. (1973) Numerical simulation of hydrodynamics by the method of point vortices. *J. Comp. Phys.*, 13, p363.
7. Greengard C. and Rokhlin V. (1987) A fast algorithm for particle simulation. *J. Comp. Phys.*, 73, p325.
8. Lucor, D., Evangelinos, C. and Karniadakis, G. E. (2000) DNS-derived force distribution on flexible cylinders subject to VIV with shear flow. In *Flow-Induced Vibration* (eds S. Ziada & T. Staubli), p.281-287, Lucerne: A. A. Balkema.

9. Newman, D. and Karniadakis, G. E. (1995) Direct numerical simulations of flow over a flexible cable. In *Flow-Induced Vibration* (ed. P. W. Bearman), p.193-203, London: A. A. Balkema.
10. Dalheim, J. (1999) Numerical Prediction of VIV on Deepwater Risers Subjected to Shear Currents and Waves. In *Offshore Technology Conference*, Houston.
11. Herfjord, K., Larsen, C. M., Furnes, G., Holmas, T. and Randa, K. (1999) FSI-simulation of vortex-induced vibrations of offshore structures. In *Computational Methods for Fluid-Structure Interaction* (ed. T. Kvamsdal et al.), p.283-303, Trondheim: Tapir.
12. Graham, J. M. R. (1988) Computation of viscous separated flow using a particle method. In *{Numerical Methods for Fluid Dynamics III}*, IMA Conf. Series {17}, p.310-317.
13. Giannakidis, G. and Graham, J. M. R. (1997) Prediction of the loading on a HAWT rotor including effects of stall. In *EWEC97* (ed. R. Watson), p.434-439, Dublin: IWEA.
14. Willden, R. H. J. (1999) Computation of the flow past deep water risers. Technical Report AERO TN 99-101, Dept. of Aeronautics, Imperial College, London, U.K.
15. Arakawa, C., Saito, K. and Shimano, K. (2000) Massively Parallel Computing with Coupled Algorithm for Introduction of Large Eddy Simulation. Proc. 1st. Int. Conf. on Computational Fluid Dynamics, Kyoto, Japan.
16. Norberg, C. (2000) Private Communication, to be published.
17. Lamb, W. S. (1988) Collaborative Research Programme for Vortex Induced Vibration in Sheared Velocity Profiles. Report CR 2897, British Hydraulic Research Association, Cranfield, U.K.
18. Bryndum, M. B. and Andersen, H. (1999) 2-D Model Testing of Risers. Report on Project No. 99-50399, Danish Hydraulic Institute, Hoersholm, Denmark.

COMPUTING THE FLOW AROUND A MOVING BLUFF BODY BY A LAGRANGIAN VORTEX METHOD

Baoshan Zhu* and Kyoji Kamemoto

Department of Mechanical Engineering and Materials Science, Yokohama National University
79-5 Tokiwadai, Hodogaya, Yokohama 240-8501, Japan/Email: zhu@post.me.ynu.ac.jp*

ABSTRACT

In the present paper, a computational method facilitating long-time, high-resolution flow simulation is developed with the advantages of the discrete vortex methods. A generalized Biot-Savart law is used to calculate the velocity of the flow field. Lagrangian representation of the evolving vorticity field is well suited to moving boundaries. An adaptive grid-free splitting and merging algorithm is added to core spreading model. An integral pressure equation shows the pressure distribution can be estimated directly from the instantaneous velocity and vorticity field. The method was applied to simulate the two-dimensional viscous incompressible flows over a circular cylinder. The results show that not only the global characteristic of the separation flow but also the evolution of the fine structure of the flow field can be calculated. Comparison with results obtained by experiments and other simulations shows that the present method is well adapted to calculate flows over the moving bluff body.

1. INTRODUCTION

Bluff bodies are utilized in almost branches of engineering. Flow separation is one of the most important hydrodynamics problems investigated intensively for bluff bodies. The generation and shedding of large coherent vortex structures due to flow separation made the bluff body flows complex and very difficult to predict. Traditionally bluff body flows have been studied experimentally with relatively simple models. As computer power increases, more and more CFD studies of bluff body flows are becoming available. As pointed by Bearman⁽¹⁾, from the viewpoint of basic research, one of the most attractive features of CFD is that it can provide insight into bluff body flow mechanisms that are

either very difficult to obtain from experiment or perhaps even impossible. However, bluff bodies present a particular challenge to CFD. One of the reasons for this is that the flow in the near wake of a bluff body is dominated by the presence of large coherent structures whose effects on the flow are not well predicted by using codes based on the Reynolds-Averaged Navier-Stokes equations and standard turbulence models.

A variety of numerical methods have been applied to simulate bluff body flows. Since the introduction of the vortex methods by Rosenhead⁽²⁾, vortex methods have become a distinct alternative to establish computational techniques (such as, finite difference, finite element, and spectral element) for incompressible flow and are widely used to simulate bluff body flows. In unsteady bluff body flows, the vorticity-containing regions move about and deform with time and it is much more difficult to resolve the ever-changing vorticity support using a fixed grid. As one of the vorticity-based methods, the Lagrangian vorticity methods, which place the computational points within the vorticity-containing regions of the flow and move these points with local velocity, has been developed and applied, notably by Chorin⁽³⁾, Leonard⁽⁴⁾⁽⁵⁾, Sarpkaya⁽⁶⁾, and more recently among others by Kamemoto⁽⁷⁾ and Koumoutsakos et al⁽⁸⁾.

The purpose of the present paper is to develop a computational method facilitating long-time, high-resolution vortex simulation with the advantages of discrete vortex methods. Both velocity and pressure are calculated according to the integral equations which reduce the need to grid large portions of the flow field and concentrates the calculation points in the regions where vorticity is present. An adaptive grid-free splitting and merging algorithm is added to core spreading model in order to simulate the viscous diffusion. The grid-free nature of the present method makes it suitable for moving profiles and extensive to complex geometries. In

order to illustrate the usefulness and accuracy of the present method, we consider three cases of flow past a circular cylinder. Although the flow around a fixed circular cylinder may remain highly two-dimensional only up to a Reynolds number of 200 due to the perturbation in real flow, in the present investigation of the flow past a rotating cylinder and rotationally oscillating cylinder, two-dimensional, unsteady, viscous simulations are utilized to illustrate the physical phenomenon. Some comparisons with experiments and other numerical simulations are performed.

2. EQUATIONS OF MOTION

Two-dimensional incompressible viscous flow past a solid body can be described by vorticity equation

$$\frac{D\omega}{dt} = \frac{\partial\omega}{\partial t} + (\mathbf{u} \cdot \nabla)\omega = \nu \nabla^2 \omega, \quad (1)$$

where \mathbf{u} is the velocity and ν the kinematic viscosity. Vorticity ω is defined as

$$\omega = \nabla \times \mathbf{u}. \quad (2)$$

Let the flow domain be V with boundary ∂V moving with velocity \mathbf{U}_b . The initial and boundary conditions are

$$\mathbf{u} = \mathbf{U}_\infty \quad \text{at } t=0 \quad \text{in } V, \quad (3)$$

$$\mathbf{u} = \mathbf{U}_b \quad \text{on } \partial V. \quad (4)$$

The boundary ∂V may consist of a solid surface B and an infinite bound ∂V_∞ . At infinity, we have

$$\mathbf{u} \rightarrow \mathbf{U}_\infty \quad \text{as } |\mathbf{r}| \rightarrow \infty, \quad (5)$$

with \mathbf{U}_∞ the freestream velocity. On the boundary surface, with the body translating with velocity $\mathbf{U}_c(t)$ and rotating around its center of mass (\mathbf{r}_c) with angular velocity $\Omega(t)$, the fluid velocity on the boundary surface (\mathbf{r}_b), is equal to the velocity of the body \mathbf{U}_b :

$$\mathbf{u}(\mathbf{r}_b) = \mathbf{U}_b = \mathbf{U}_c(t) + \Omega(t) \times (\mathbf{r}_b - \mathbf{r}_c) \quad \text{as } \mathbf{r} = \mathbf{r}_b. \quad (6)$$

The definition of the vorticity allows determination of the vorticity field from a known velocity field. Conversely, one can determine the velocity field from a known vorticity field. The following Poisson equation shows that \mathbf{u} is related to ω

$$\nabla^2 \mathbf{u} = -\nabla \times \omega. \quad (7)$$

The velocity-vorticity formulation avoids solving for the pressure and keeping the velocity solution

divergence-free. However, it introduces additional constraints in the kinematics of the flow field and requires the transformation from the velocity adherence to vorticity form.

3. INTEGRAL FORMULATIONS

Following the work of Wu and his coworkers⁽⁹⁾, we can use an integral formula to compute velocities in the region of interest.

$$\begin{aligned} \mathbf{u}(\mathbf{r}, t) = & \frac{1}{2\pi} \int_V \frac{\omega(\mathbf{r}_0, t) \times (\mathbf{r} - \mathbf{r}_0)}{|\mathbf{r} - \mathbf{r}_0|^2} dV + \\ & \frac{1}{2\pi} \int_{\partial V} \frac{(\mathbf{n}_b \times \mathbf{U}_b) \times (\mathbf{r} - \mathbf{r}_0)}{|\mathbf{r} - \mathbf{r}_0|^2} dS - \\ & \frac{1}{2\pi} \int_{\partial V} \frac{(\mathbf{n}_b \times \mathbf{U}_b) \cdot (\mathbf{r} - \mathbf{r}_0)}{|\mathbf{r} - \mathbf{r}_0|^2} dS \end{aligned} \quad (8)$$

where the subscript '0' indicates that the variables and the integrations are performed in the \mathbf{r}_0 space, \mathbf{n}_b is the inward normal unit vector. The above equation serves two purposes in this study. First, if the vorticity $\omega(\mathbf{r}_0, t)$ is known and the domain D is large enough to contain all of the vorticity generated at the solid boundary prior to time t , then the velocity distribution in the flow field V can be evaluated directly. Second, it links the velocity and vorticity on the solid boundary.

By taking divergence of the Navier-Stokes equation and introducing a Bernoulli-type variable H , a Poisson equation for body surface pressure can be obtained as

$$\nabla^2 H = \nabla \cdot (\mathbf{u} \times \omega), \quad (9)$$

where

$$H = \frac{p}{\rho} + \frac{u^2}{2}, \quad (10)$$

as $\mathbf{r} \rightarrow \infty$, assume $H = p/\rho + U_\infty^2/2 \rightarrow \text{const.}$ (for external flow with uniform velocity at infinity). The Green's function solution of Equation (10) is

$$\begin{aligned} \int_D H \nabla^2 G dV + \int_S H \nabla G \cdot \mathbf{n} dS = \\ \int_S \nabla H \cdot \mathbf{n} G dS + \int_D \nabla G \cdot (\mathbf{u} \times \omega) dV, \end{aligned} \quad (11)$$

where $G = 1/(2\pi) \ln(1/R)$ for two-dimensional flows. Taking the inner product of the Navier-Stokes equation with \mathbf{n} , yields an expression of $\nabla H \cdot \mathbf{n}$ as

$$\nabla H \cdot \mathbf{n} = \mathbf{n} \cdot \left(-\frac{\partial \mathbf{u}}{\partial t} + \mathbf{u} \cdot \nabla \mathbf{u} + \nu \nabla \times \omega \right). \quad (12)$$

Submitting Equation (12) into Equation (11) and using the divergence theorem yields a boundary-integral equation for H as

$$\beta H + \frac{1}{2\pi} \int_S H \frac{\partial \ln(1/R)}{\partial \mathbf{n}} dS = -\frac{1}{2\pi} \int_S \frac{\partial \mathbf{u}}{\partial t} \cdot \mathbf{n} \ln(1/R) dS - \frac{1}{2\pi} \int_V \frac{\mathbf{R} \cdot (\mathbf{n} \times \boldsymbol{\omega})}{R^2} dS - \frac{1}{2\pi} \int_D \frac{\mathbf{R} \cdot (\mathbf{u} \times \boldsymbol{\omega})}{R^2} dV \quad (13)$$

where β is $\beta=1$ inside the flow field and $\beta=1/2$ on the boundary S . When the surface pressure is computed according to Eq.(13), the left-hand side of the equation represents a matrix formulation which must be decomposed on the first time when there is no relative movement among the flow boundaries. The right-hand side accounts for the motion of the bodies and the volume vorticity in the flow field.

4. A LAGRANGIAN VORTEX METHOD

4.1 The velocity Field Induced by Vorticity

The evolution of a vorticity distribution covering a relevant domain is described by Equation (1). In a Lagrangian vortex method, the vorticity is approximated by

$$\boldsymbol{\omega}(\mathbf{r}, t) = \sum_{i=1}^N \Gamma_i(t) f_\varepsilon(|\mathbf{r} - \mathbf{r}_i|, t). \quad (14)$$

Therefore, the continuous vorticity field is replaced by a discrete sum of the individual vortex particles with a core radius ε , strength $\Gamma_i(t)$ and an individual distribution of vorticity determined by the function f_ε . If we use a Gaussian distribution for the vortex particle as

$$f_\varepsilon = \frac{1}{\pi \varepsilon^2} \exp\left(-\frac{|\mathbf{r}|^2}{\varepsilon^2}\right). \quad (15)$$

A contribution for the velocity field based on a vorticity field (the first integral in Equation (8)) represented by particles of Gaussian distribution is thus given by

$$\mathbf{u}(\mathbf{r}, t) = \frac{1}{2\pi} \sum_{i=1}^N \Gamma_i \frac{((\mathbf{r}_i - \mathbf{r}) \times \mathbf{k})}{(|\mathbf{r}_i - \mathbf{r}|)^2} \left(1 - \exp\left(-\frac{(|\mathbf{r}_i - \mathbf{r}|)^2}{\varepsilon_i^2}\right)\right). \quad (16)$$

The vorticity transport equation (1) may be expressed by an operator splitting scheme as

$$\frac{\partial \boldsymbol{\omega}}{\partial t} + \mathbf{u} \cdot \nabla \boldsymbol{\omega} = 0, \quad (17)$$

and

$$\frac{\partial \boldsymbol{\omega}}{\partial t} = \nu \nabla^2 \boldsymbol{\omega}. \quad (18)$$

According to Equation (17), the discrete vortex elements can be traced by the Lagrangian approach with the local flow velocity and the circulation of these vortices remain constant. Velocity field can be determined by Equation (8). The trajectory of the particles over a time step Δt can be approximately computed from the second order Adams-Bathforth method as

$$\mathbf{r}_i^{n+1} = \mathbf{r}_i^n + \Delta t \left(\frac{3}{2} \mathbf{u}_i(\mathbf{r}_i^n, t) - \frac{1}{2} \mathbf{u}_i(\mathbf{r}_i^{n-1}, t - \Delta t) \right). \quad (19)$$

Equations (8), (17) describe the evolution of an inviscid flow. Therefore, these equations are for the solution of Euler equations using discrete vortices. The solution of the Navier-Stokes equations requires in addition a model for the diffusion of vorticity, which is explained next.

4.2 A Deterministic Core-Spreading Method

The splitting operator involves separating the convective and diffusive portions of the vorticity equation. Core-spreading method is used to treat the viscous diffusion. The core-spreading approach uses a variable core size to solve the heat equation (18) of the viscous step exactly according to Leonard⁽⁴⁾. For solving the heat equation (18), the following equation arises

$$\frac{d\varepsilon}{dt} = \frac{c^2 \nu}{2\varepsilon} \quad c=2.242. \quad (20)$$

The core expansion model was objected to by Greengard⁽¹⁰⁾ based on a lack of convergence in the limit of infinitesimal parameters. Rossi⁽¹¹⁾ showed that the core expansion with splitting was convergent. However, splitting leads to excessive number computational particles. This difficulty can be alleviated by allowing a merger of multiple particles into a single new element. Splitting and merging are made by enforcing the original and split or merged particles share the same total circulation, linear impulse, angular impulse. Namely, for a particle of index i centered at location \mathbf{r}_i being split into multiple particles of index j centered at location \mathbf{r}_j ,

$$\Gamma_i = \sum_{j=1}^N \Gamma_j, \quad (21)$$

$$\Gamma_i \mathbf{r}_i = \sum_{j=1}^N \Gamma_j \mathbf{r}_j, \quad (22)$$

$$\Gamma_i(|\mathbf{r}_i|^2 + \delta_i^2) = \sum_{j=1}^N \Gamma_j(|\mathbf{r}_j|^2 + \delta_j^2). \quad (23)$$

Without loss of generality, one can assume the original vortex is located at the origin. If we split vortex element i into N identical vortices, each with a radius of $\alpha^2 \varepsilon_j^2$, here α is the splitting ratio and is assumed to lie between 0 and 1. Rossi⁽¹¹⁾ shows the error in the splitting behaves as $O(1-\alpha^2)$. Conservation of the zeroth moment indicates the obvious: the new vortices must have the same circulation as the original. Conservation of the first moment along with rotational symmetry of the system requires that each vortex have circulation Γ_i/N and be centered uniformly along a circle of radius r_j . Conservation of the second moment constraints the last variable

$$r_i = \delta_i \sqrt{1 - \alpha^2}. \quad (24)$$

As with the splitting, equations (21~23) can also applied to merge $j=1 \sim N$ particles into a particle i . Strength Γ_i and location \mathbf{r}_i of the merged particle i can be defined through conservation of circulation and first moment of vorticity. The second moment constraint results in the core of the merged vortex.

The core expansion technique allows for variable spatial resolution through control of the size ε with the splitting and merging processes. On the other hand, fine resolution is usually necessary near the solid surface, to resolve the boundary layer, while the relevant length scales are much coarser away from the body. Therefore, near the solid surface, the fine particles are necessary. In order to effectively and accurately solve the problem, the blob size is scaled by the distance to center of the bluff body. In the calculation, the entire flow field is divided into two regions. Region 1 is the 'layer' with the thickness of δ near the solid surface, where δ is in scale of the boundary layer thickness on the surface of the bluff body. Region 2 is the flow region outside the 'layer' and extends from the boundary of 'layer' to infinity. Corresponding to above two regions, the core size informally defined as

$$\varepsilon(r) = c_1 \sqrt{\nu \Delta t}, \quad (\text{Region 1}) \quad (25)$$

$$\varepsilon(r) = (c_2 \sqrt{r^2 - \delta^2} + c_1) \sqrt{\nu \Delta t} \quad (\text{Region 2}), \quad (26)$$

here c_1 and c_2 are the constant defined according to the accuracy and efficiency required.

4.3 Vortex Boundary Condition

After we convect the particles with the local velocity and change their cores according to the core-spreading model, there is a slip velocity at the wall. The vortex sheet $\gamma = \mathbf{n} \times (\mathbf{u} - \mathbf{U}_b)$ necessary on the body surface to cancel this slip velocity is then computed equation (8). Generally, in equation (8), we cannot impose both $\mathbf{n} \cdot \mathbf{u} = \mathbf{n}_b \cdot \mathbf{U}_b$ and $\mathbf{n} \times \mathbf{u} = \mathbf{n}_b \times \mathbf{U}_b$ as the vortex sheet is decided. The freestream velocity \mathbf{U}_∞ and the body velocity \mathbf{U}_b are usually known and the vorticity is known everywhere except on the solid boundary. If we suppose $\mathbf{n} \cdot \mathbf{u} = \mathbf{n}_b \cdot \mathbf{U}_b$, the strength of the vortex sheets can be decided by the following Fredholm integral equation:

$$\begin{aligned} \frac{\gamma(\mathbf{s})}{2} + \frac{1}{2\pi} \int_B \frac{\gamma(\mathbf{s}) \times (\mathbf{r}_b - \mathbf{r}_0)}{|\mathbf{r}_b - \mathbf{r}_0|} = \\ \frac{1}{2\pi} \iint_{V'} \frac{\omega(\mathbf{r}_0, t) \times (\mathbf{r}_b - \mathbf{r}_0)}{|\mathbf{r}_b - \mathbf{r}_0|^2} dV \cdot \mathbf{s} + \\ \frac{1}{2\pi} \int_B \frac{(\mathbf{n}_b \times \mathbf{u}) \times (\mathbf{r}_b - \mathbf{r}_0)}{|\mathbf{r} - \mathbf{r}_0|^2} dS \cdot \mathbf{s} + \mathbf{U}_\infty(\mathbf{s}) \end{aligned} \quad (27)$$

An integral constraint for vorticity should be imposed on the strength of the vortex sheet. In a similar way as the introduction of Equation (12), we can derive a relation for the tangential derivative of Bernoulli function H around the boundary surface B . We suppose that H is continuous along the boundary surface including the trailing edge. By integration with applying the Stokes theorem, following equation can be obtained

$$\frac{d}{dt} \int_B \gamma dB + 2 \frac{d\Omega(t)}{dt} \big|_{V'} + \nu \int_B \frac{\partial \omega}{\partial \mathbf{n}} dB = C. \quad (28)$$

In above equation, V' is the domain occupied by the solid body. The term $\nu(\partial \omega / \partial t)_B$ is considered as the boundary vorticity flux on a solid wall. Equation (28) shows the sum of the total vorticity of the fluid and of the solid is always constant. This principle of total vorticity conservation is adaptable for any arbitrary rotational and transnational motion of a solid in a fluid, which is freestream at infinity.

In a viscous flow, computation of the vortex sheets is only the first step in properly handling a boundary. The Neumann condition is usually adopted by utilizing γ to determine the circulation of the discrete vortices newly created from the boundary surface (such as Koumoutsakos et al.⁽¹²⁾, Huang and Kinney⁽¹³⁾).

$$\nu \frac{\partial \omega}{\partial t} \big|_B = \frac{\gamma}{\Delta t}. \quad (29)$$

Consider a single segment of the discretized vortex sheet γ with a length as shown in Fig.1. A thin 'Euler layer' is employed above each body panel to ensure resolution of the boundary layer for all times. The amount circulation Γ_i received by an area A is

$$\Gamma_i = \iint_A \omega dA, \quad (30)$$

where ω can be approximately expressed as shown by Kamoutsakos et al. ⁽¹²⁾ as

$$\omega(x, y) = \frac{\gamma}{2\sqrt{\pi\nu\Delta t}} \exp\left(-\frac{y^2}{4\nu\Delta t}\right) \left[\operatorname{erf}\left(\frac{\frac{L}{2}-x}{\sqrt{4\nu\Delta t}}\right) + \operatorname{erf}\left(\frac{\frac{L}{2}+x}{\sqrt{4\nu\Delta t}}\right) \right] \quad (31)$$

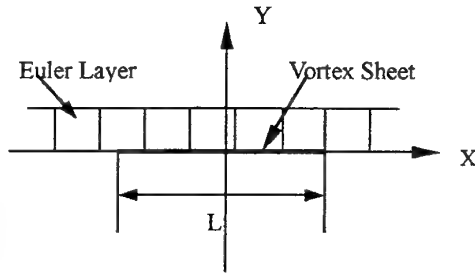


Figure1: Schematic of vortex sheet to surface flux

5. EXAMPLES AND RESULTS

5.1 Flow around an Impulsively Started Circular Cylinder

To show the accuracy and efficiency of the proposed method, flow around an impulsively started circular cylinder has been carried out. This flow problem has been extensively used as a prototype of unsteady separated flows and a number of numerical and experimental results are available. In the following, early stage development of the flow for a Reynolds number $Re=2UR/\nu=1000$ are presented.

When the discrete vortices are used to simulate the flow field, the core size ϵ dominantly determines the convective error with scale as $O(\epsilon^2)$. In this study, the variable spatial core size ϵ was used according to Equation (25) and (26), where c_1 and c_2 are informal decided as $c_1=2.0$ and $c_2=0.25$, and region 1 is the domain with thickness $5.0(1/R_c)^{0.5}$ near the circular cylinder surface. In order to evaluate the influence of

core size on the solution, two cases are shown for different core size at $Re=1000$. For the finer core, we have timestep $dt=0.02$ and the core size ϵ in region 1 is about $\epsilon=0.90$; and when the timestep increases to $dt=0.04$, the core size in region 1 has been changed to $\epsilon=0.125$. In Fig.2, the drag coefficients calculated from the different core sizes are compared. The small discrepancy indicates the core sizes are fine enough to capture all the flow structures for the Reynolds number considered. In Fig.3, the streamline patterns at $T=5.0$ are also shown for two cases, from which it can be seen that, although a slight difference in the size of the secondary vortex is noticeable, the global structures of the flow are the same.

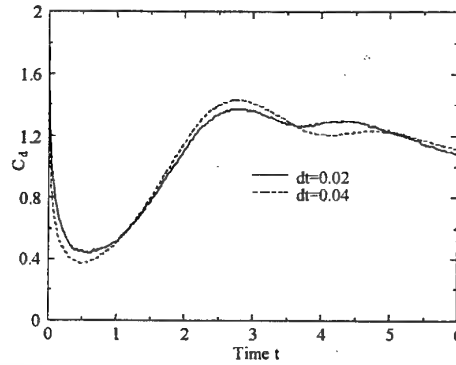


Figure 2: Effect of timestep (core size) on the drag coefficient

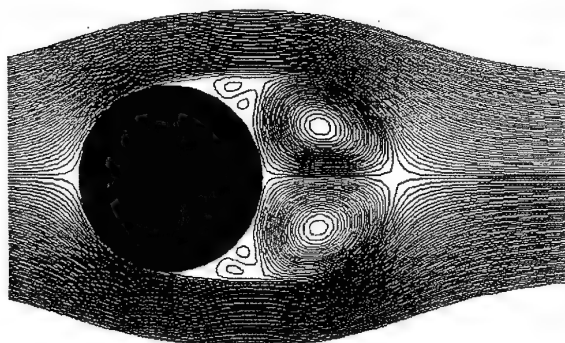
Figure 4 compares the drag coefficient evolution from the present study with other numerical results. From this figure, it can be seen that the present result agrees well with the result from references ⁽⁸⁾⁽¹⁴⁾, although an order of magnitude more vortex elements were reportedly used by Kamoutsakos and Leonard ⁽⁸⁾. We have calculated the long time evolution of the flow around the impulsively started cylinder at $Re=1000$. No artificial perturbation was applied to the flow to initiate the alternate vortex shedding; instead, it is triggered solely by numerical errors (truncation and roundoff errors) during the calculation. After a long time, about 30, the vortex shedding process begins to collapse.

5.2 Flow Past a Rotating Circular Cylinder

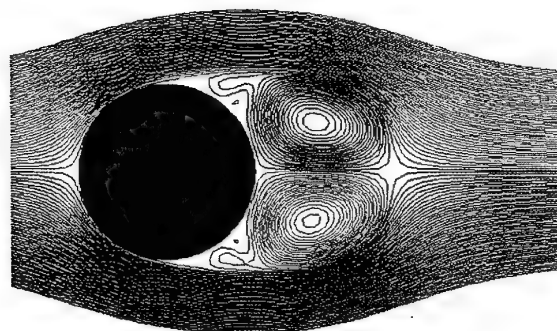
The flow associated with a circular cylinder which begins its rotational and translation motion impulsively in a stationary fluid is a rather complex one. Using the computational scheme presented in this paper, we have

conducted the calculation of the flow past a rotating circular cylinder for $R_c=1000$. The rotational to translational speed ratio α is $\alpha=\omega r/U=0.5$. Owing to the rotation of the cylinder, not only the formation and shedding of the large vortices but also the microscale flow characteristics are changed. In Fig.5, at $T=3$, a secondary vortex appears near the cylinder in the neighborhood of the bottom right vortex and this secondary vortex still exists at $T=4.0$. It is known that the

secondary vortices are generated during the transient stage and are of opposite vortices to the main vortices. With the anticlockwise rotation of the cylinder, the relative velocity between the moving cylinder surface and the flow in these secondary vortices tends to decrease the strength of the secondary vortex on the upper side and increase it on the lower side. Badr et al.⁽¹⁵⁾ reported many secondary vortices were formed adjacent to the large (main) ones on the lower side.



(a) Streamline, $T=5.0$, $dt=0.02$



(b) Streamline, $T=5.0$, $dt=0.04$

Figure 3: Effect of timestep (core size) on the streamline for flow around impulsively started cylinder.

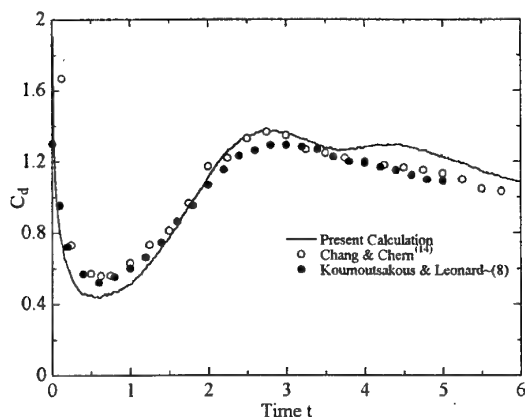
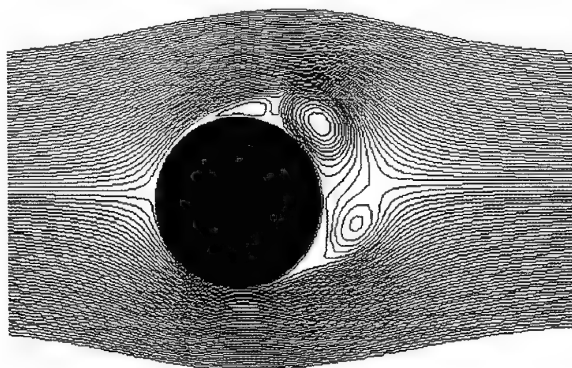
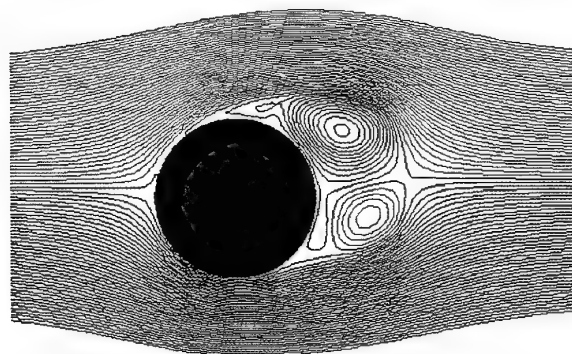


Figure 4: Comparison of drag coefficient.



(a) Streamline, $T=3.0$



(b) Streamline, $T=4.0$

Figure 5: Streamline patterns for $\alpha=\omega r/U=0.5$

Figure 6 shows the vorticity contours at different time. The rotation creates asymmetry in the formation of the wake behind the cylinder. When $T=8.0$, the first vortex (a negative or clockwise vortex) is shed from the upper side of the cylinder. The second vortex (a positive or anticlockwise vortex) is shed from the lower side of the cylinder at $T=12$. In Fig.7, we show the variation of the calculated lift coefficient C_l and drag coefficient C_d . For the lower rotation $\alpha=0.5$, according to Fig.7., both the present calculations and the results of Badr et al.⁽¹⁵⁾ show a periodic variation associated with vortex shedding soon develops and continues indefinitely.

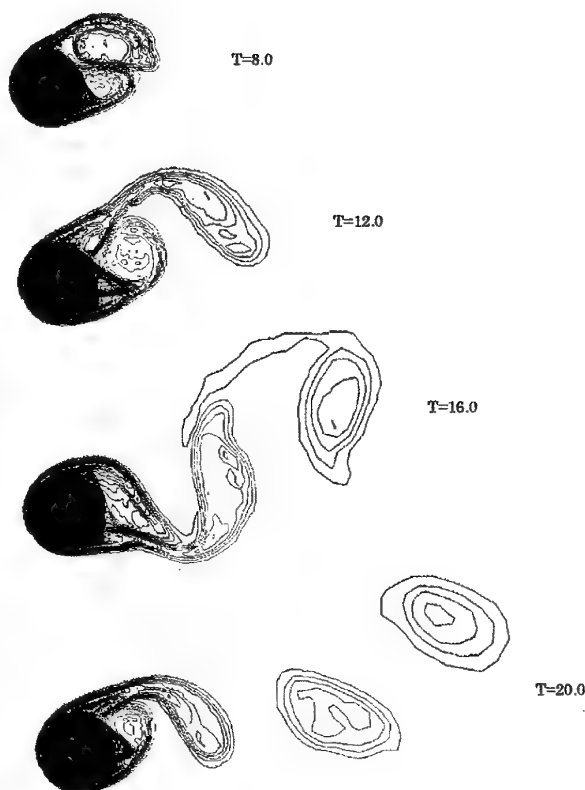


Figure 6: Vorticity contours at several time instants for $\alpha = \omega r / U = 0.5$

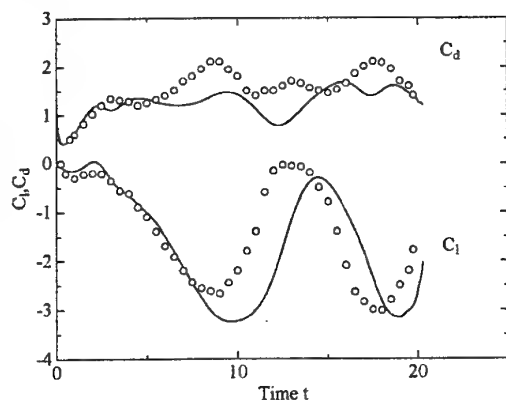


Figure 7: Variation in lift and drag coefficient with time for $\alpha = \omega r / U = 0.5$.

5.3 Flow around a Circular with Rotational Oscillations

Finally, using the computational advantages provided by the present grid-free vortex method, we have conducted the calculations of a cylinder undergoing

rotatory $\omega r / U_\infty = \Omega(t) = 3 \sin(\pi t)$ for $R_e = 1000$. Tokumaru and Dimotakis⁽¹⁶⁾ studied flow over a circular cylinder undergoing rotational oscillation and revealed drag reduction caused by the rotational oscillation. The results in Fig.9 show a drastic drag reduction for the certain rotation frequency calculated in this case. The drag reduction is attributed to the modification of the shedding mechanisms from the surface of the cylinder. As shown in Fig.8, after some time, bipolar vortex structures are formed downstream the rotating cylinder. These bipolar vortex structures results in high drag reduction.

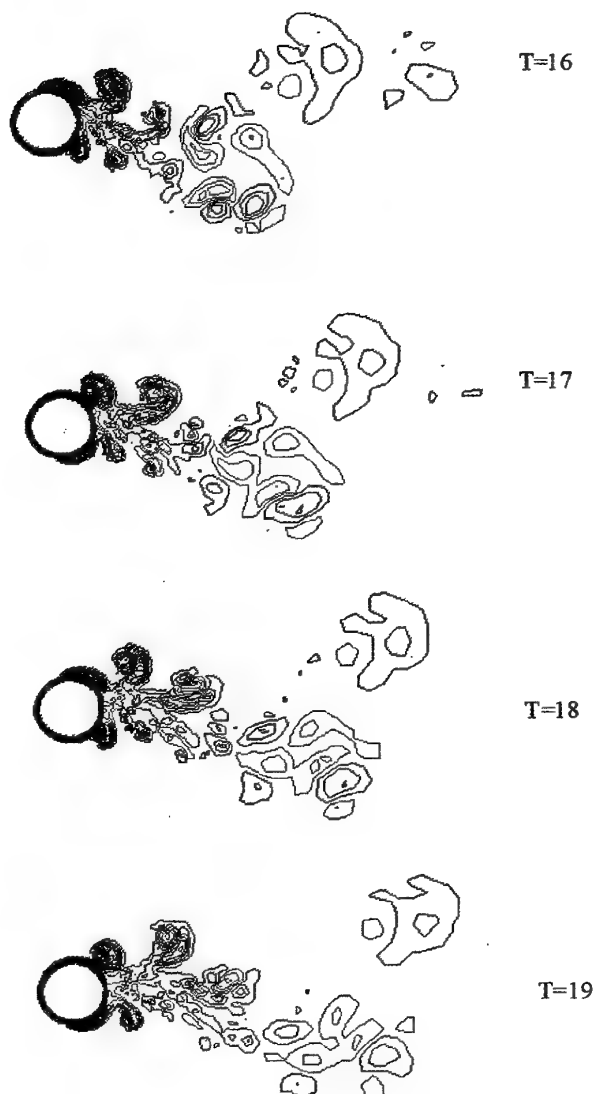


Figure 8: Vorticity contours at several time instants for $\omega r / U_\infty = \Omega(t) = 3 \sin(\pi t)$.

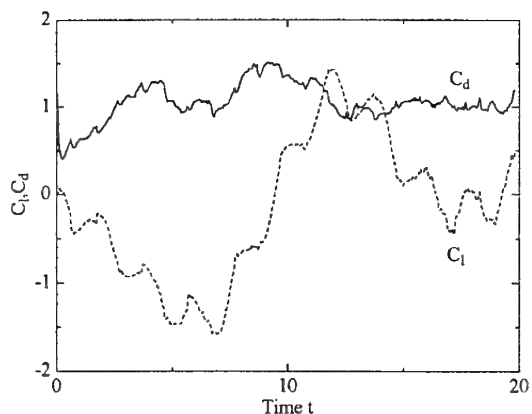


Figure 8: Variation in lift and drag coefficient with time for rotatory circular cylinder

6. CONCLUDING REMARKS

A computational method facilitating long-time, high-resolution vortex simulation is developed with the advantages of the discrete vortex methods. A generalized Biot-Savart law is used to calculate the velocity of the flow field. An integral pressure equation shows the pressure distribution can be estimated directly from the instantaneous velocity and vorticity field. An adaptive grid-free splitting and merging algorithm is added to core spreading model. The numerical results show the present method is capable of satisfactorily predicating the flow characteristics in the vicinity of a circular cylinder as well as the global flow features. Some comparisons show that the results of the present computations are in good agreement with the experimental and numerical results obtained by other investigators.

REFERENCES

- (1) Bearman, P.W. (1998). "Developments in the understanding of bluff body flow", *JSME International Journal, Series B*, Vol.41, No.1, p14-25.
- (2) Rosenhead, L. (1931), "The formation of vortices from a surface of discontinuity", *Proceeding of Royal Society, A*, Vol.134, p.170-192.
- (3) Chorin, A.J. (1973). "Numerical study of slightly viscous flow", *Journal of Fluid Mechanics*, Vol.57, p785-798.
- (4) Leonard, A. (1980), "Vortex methods for flow simulation", *Journal of Computational Physics*, Vol.37, p289-335.
- (5) Leonard, A. (1985). "Computing three-dimensional incompressible flows with vortex elements", *Annual Review of Fluid Mechanics*, Vol.17, p.523-549.
- (6) Sarpkaya, T. (1989). "Computational methods with vortices-the 1988 freeman scholar lecture", *Journal of Fluid Engineering*, Vol.111, p5-52.
- (7) Kamemoto, K. (1995). "On attractive features of the vortex methods", *Computational Fluid Dynamics Review 1995*, Ed. H.Hafez & K.Oshima, p.334-353.
- (8) Koumoutsakos, T. and Lenoard, A. (1995). "High-resolution simulations of the flow around an impulsively started cylinder using vortex methods", *Journal Fluid Mechanics*, Vol.296, p1-38.
- (9) Wu, J.C. and Thompson, J.F. (1973) "Numerical solution of time-dependent incompressible Navier-Stokes equations using an integro-differential formulation", *Computers & Fluids*, Vol. 1, p197-215.
- (10) Greengard, C. (1985). "The core spreading vortex method approximated the wrong equation", *Journal of Computational Physics*, Vol. 61, p.345-347.
- (11) Rossi, L.F. (1996). "Resurrecting core spreading vortex methods: a new scheme that is both deterministic and convergent", *SIAM Journal of Scientific Computation*, Vol.17, p370-397.
- (12) Koumoutsakos, P., Leonard, A. and Pepin, F. (1994). "Boundary conditions for viscous vortex methods", *Journal of Computational Physics*, Vol.113, p.52-61.
- (13) Huang, S.C. and Kinney, R.B. (1988). "Unsteady viscous flow over a grooved wall: a comparison of two numerical methods". *International Journal of Numerical Methods in Fluids*, Vol.8, p.1403-1437.
- (14) Chang, C.C. and Chern, R.L. (1991). "A numerical study of flow around an impulsively started circular cylinder by a deterministic vortex method", *Journal of Fluid Mechanics*, Vol.233, p.243-263.
- (15) Badr, H.M., Coutanceau, M., Dennis, S.C.R. and Meneard, C. (1990). "Unsteady flow past a rotating cylinder at Reynolds number 10^3 and 10^4 ", *Journal of Fluid Mechanics*, Vol.220, p.459-484.
- (16) Tokumaru, P.T. and Dimotakis, P.E. (1991). "Rotary oscillation control of a cylinder wake", *Journal of Fluid Mechanics*, Vol.224, p.77-90.

A DISCRETE VORTEX STUDY OF STREAMWISE OSCILLATIONS OF A CIRCULAR CYLINDER: COMPARISON WITH EXPERIMENT

O. Cetiner and M. F. Unal

Faculty of Aeronautics and Astronautics, Istanbul Technical University
80626 Maslak, Istanbul, Turkey / Email: cetiner@itu.edu.tr

D. Rockwell

Department of Mechanical Engineering and Mechanics, Lehigh University
19 Memorial Dr. West, Bethlehem, PA 18015, U.S.A. / E-mail: dor0@lehigh.edu

ABSTRACT

Instantaneous patterns of vorticity in the near-wake and associated unsteady loading arising from streamwise oscillations of a cylinder in a steady current have been investigated numerically using a two-dimensional vortex-in-cell (VIC) method incorporating viscous diffusion. This simulation captures the key features of the distinctive force modulations that were observed experimentally and, furthermore, relates them to the structure of the near- and intermediate-wake.

1. INTRODUCTION

Studies of streamwise oscillations of a cylinder in a steady current are related to the practical applications of towing cables in the ocean environment or components of offshore structures subjected to wave motion, steady flow, or a combination of them. In the limiting case of infinitely long wavelength, the wave motion can be simulated either by unidirectional oscillatory flow, or conversely, unidirectional oscillations of the cylinder in quiescent fluid. A steady flow component is superposed on the oscillatory component of the flow or on the oscillations of the cylinder; thereby, the effects of current can be taken into account.

For the case of cylinder subjected to controlled oscillations in the streamwise direction, in presence of a steady inflow (current), a number of investigations have visualized the patterns of vortex formation, relative to the limiting case of oscillations in quiescent fluid. Griffin and Ramberg (1) studied patterns of vortex formation for small-amplitude, in-line oscillations of the cylinder in a steady uniform flow. Oengören and Rockwell (2) defined patterns of vortex formation over a wider range of excitation frequency. Sarpkaya and Storm (3), among other findings, demonstrated experimentally the importance of considering both the Keulegan-Carpenter number and the relative velocity of the flow. Cetiner and Rockwell (4) recently established the relationship between instantaneous, quantitative patterns of vortex formation in the near wake, and distinctive classes of modulations of the transverse force coefficient. A wide variety of numerical investigations also have provided a valuable framework for interpreting the features of in-line oscillations in presence of a steady flow component. Numerical simulations of Sarpkaya et al. (5) and Graham et al. (6) demonstrated complex and interesting patterns of vortices in the intermediate wake region and corresponding ordered modulations of transverse force.

In recent years, experimental qualitative, and especially quantitative, flow imaging has been used to aid in the development and verification of numerical techniques. Such numerical simulations can provide an effective means of understanding complex, separated flows over a wide range of parametric variations. This study investigates numerically the conditions of an experimental study on streamwise oscillations of a circular cylinder in steady current and aims to give further insight into the experimentally observed features of the near-wake vortex formation and related instantaneous loading.

2. NUMERICAL METHOD

For the solution of the laminar pulsatile flow (oscillatory plus mean flow) around a circular cylinder, the governing equations are two-dimensional unsteady Navier-Stokes equations in vorticity (ω) and stream function (ψ) form, i.e.,

Vorticity Transport equation,

$$\frac{D\omega}{DT} = \frac{\partial\omega}{\partial T} + (\vec{U} \cdot \nabla)\omega = \nu \nabla^2 \omega \quad (1)$$

Poisson's equation,

$$\nabla^2 \psi = -\omega \quad (2)$$

Using the operator-splitting technique (7), the convection and diffusion of vorticity are treated separately and sequentially, i.e.,

$$\frac{\partial\omega}{\partial T} = -(\vec{U} \cdot \nabla)\omega \quad \text{and} \quad \frac{\partial\omega}{\partial T} = \nu \nabla^2 \omega \quad (3)$$

When modelling convection, a mixed Eulerian-Lagrangian scheme known as Vortex-in-Cell (VIC) method is used while the diffusion of vorticity is calculated on a mesh using the finite difference technique (8). With respect to a Lagrangian discrete vortex method, the key to the VIC method is to by-pass the Bio-Savart law and use sequentially the Eulerian frame to calculate the velocities at discrete vortex locations through the use of the Poisson's equation for stream function and Lagrangian frame to track vortices.

The present study uses a conformal transformation $z(x, y) \rightarrow \zeta(\xi, \eta)$ with logarithmically spaced cells which provide a fine grid scale near the cylinder wall and a coarse grid in the far field. The cylinder wall is specified by a line $\eta = 0$ in the transformed plane.

Although equivalent experimental results will be used in verifying the numerical technique and establishing its limits, the calculations have been first tested for the well-known case of a circular cylinder fixed in a uniform flow at $Re=200$ as reported in (9). The results are in agreement with both numerical and experimental studies (10). The average drag coefficient is approximately 1.24, the rms value of lift coefficient is 0.60 and the Fourier analysis of the fluctuating lift yields a Stouhal number ($f_s D/U$) of about 0.193. All of the present simulations were carried out at a value of Reynolds number $Re = 200$

3. EXPERIMENTAL SYSTEM

Experimental investigations have been carried out in the Fluid Mechanics Laboratories at Lehigh University, using a laser scanning version of high-image-density particle image velocimetry (PIV) and measuring simultaneously the instantaneous forces. Detailed description of the experimental system can be found in the recent study of Cetiner and Rockwell (4).

For all experiments in which space-time images of the velocity and vorticity fields were obtained, the amplitude and the frequency of the cylinder motion was kept constant so that $KC = 6$ and $f_c = 0.28\text{Hz}$. The effect of amplitude variations on force signatures and spectra was also investigated by varying the oscillation amplitude over the range $1 \leq KC \leq 10$. Variations in the dimensionless frequency f_c/f_0 were attained by changing the free-stream velocity, U ; f_0 represents inherent Kármán shedding from the stationary cylinder. Correspondingly, values of the ratio of the free-stream velocity U to the velocity amplitude of the cylinder oscillation $2\pi f_c A$ were varied over the range $0 \leq U/2\pi f_c A \leq 2.25$. The range of flow velocities considered was $0 \leq U \leq 95 \text{ mm/sec}$,

corresponding to values of Reynolds number $405 \leq Re \leq 2,482$. These values of Re are clearly higher than the value of $Re = 200$ employed in the numerical simulation. From a physical standpoint, it is well known that over a range of Re employed in the experiments, small-scale shear layer or Kelvin-Helmholtz vortices can arise, and influence the magnitude of the Reynolds stress in the separating shear layer. It is therefore expected that certain details of the experiments will not be evident in the numerical simulation. Nevertheless, it is anticipated that the major, large-scale features of the near-wake vortex formation process will persist over a range of Reynolds number.

4. RESULTS

Numerical experiments were performed for two sets of f_c , A and U values which give the same non-dimensional parameters, namely KC , f_c/f_0 and $U/2\pi f_c A$. One of the sets matches the experimental conditions, hereinafter referred as Case 1, the other differs mainly by the excitation frequency which is set to be $f_c = 0.1\text{Hz}$, hereinafter referred as Case 2. For all of the runs, the Reynolds number is fixed at 200; as the free-stream velocity changes in order to vary the frequency ratio f_c/f_0 , the kinematic viscosity is also varied. In parallel with the experimental study, forces were normalized by the maximum cylinder oscillation frequency which is equal to $KC \times D/T$.

Figure 1 shows the time traces and the spectra of transverse force coefficient for the experimental results, focusing on the oscillations of the cylinder at subharmonic and oscillations of the cylinder below, at, and above the fundamental of the inherent Kármán shedding frequency (4). The spectrum for oscillations at $f_c/f_0 = 0.65$ has been also added to show the existence of a non-locked-on region in between fundamental and subharmonic oscillations. Numerical results in the form of time traces of the transverse force coefficient for both cases are given in Figure 2 and 3.

As can be seen in Figures 1 and 2, oscillations of the cylinder at the fundamental of the inherent Kármán shedding frequency give rise to persistent, repetitive signatures of $C_y(t)$. In physical experiments, these persistent patterns in the transverse force traces last until $f_c/f_0 = 0.74$, except for the occurrence of a second mode of the oscillations at the fundamental. However for numerical experiments, in both cases, $f_c/f_0 = 0.74$ exhibits non-locked-on oscillations. Meanwhile, a frequency ratio outside the locked-on region around the oscillations at the fundamental in Figure 1, $f_c/f_0 = 0.65$, generates persistent and repetitive signatures of $C_y(t)$ in numerical simulations for both excitation frequencies. The resemblance of the time trace at $f_c/f_0 = 0.65$ for Case 2 to the experimentally obtained time trace at $f_c/f_0 = 0.74$ is obvious and interesting.

Changing the excitation frequency slightly affects the persistence of the transverse force traces; Case 1 and Case 2 differ in the same manner from the experimental results.

Even though experimentally and numerically obtained time traces of transverse force coefficient are not identical, a characteristic modulation can be identified, especially for oscillations at subharmonic and fundamental frequencies. A large positive peak followed by a smaller positive peak, and then, a large negative peak followed by a smaller negative peak are present in the experimental results and in both cases of the numerical results for oscillations of the cylinder at the fundamental of the inherent Kármán shedding frequency. Subharmonic oscillations exhibit a different characteristic modulation with a small positive peak followed by a large negative and then a large positive peak. These identified modulations of the transverse force coefficient have been studied on the images of vortex formation in Figures 4 and 5. For the case of subharmonic oscillations, images designated as A and B represent the maximum negative and maximum positive peaks respectively. The images have been selected from a cinema sequence of experimentally resolved vorticity contours and numerically obtained positions of positive and negative

discrete vortices. The near-wake vorticity patterns dictate the behaviour of the transverse force; for images A, the upper large-scale region of negative (gray dots and lines) vorticity leads the positive vorticity formed from the bottom surface of the cylinder. In contrast, for images B, the lower large-scale positive (white dots and lines) vorticity leads the negative vorticity shed from the upper surface of the cylinder. These basic features of the near-wake and the occurrence of negative and positive peaks in the $C_y(t)$ trace are in accord with the reasoning of Maull and Milliner (11). A similar process of vortex formation and associated loading on the cylinder is evident for oscillations at the fundamental. Images A and B of Figure 5 illustrate two similar sequential stages of Kármán-like shedding. However, they are interrupted in this case by the vortex formation shown in images C. The vortices sweep back onto the cylinder due to very small values of the relative velocity of the free-stream ($U-U_C$). The induced transverse force is nearly equal to zero.

Figure 6 shows instantaneous patterns of vorticity for oscillations at $f_c/f_0=0.67$. Eleven excerpts have been selected from a cinema sequence to illustrate the designated points on the time trace of C_y . Images 1 through 3 represent the first sequential stage of Kármán-like shedding and images 9 through 11 the second. In between, for images 4 through 6, the relative velocity of the free-stream decreases and the pair of vortices approach the lower surface of the cylinder inducing a small negative peak on $C_y(t)$. When the relative free-stream velocity starts to increase, the pair of vortices move away from the cylinder and induce a small positive peak on $C_y(t)$. As the numerical results allow visualizing far wake of the cylinder, image 11 is also presented covering approximately 30 diameters downstream. The evolution of the vortex pair and its amalgamation with positive vorticity concentration formed from the upper surface of the cylinder are evident.

5. CONCLUDING REMARKS

Although the numerical approach assumes a two-dimensional laminar flow, the results are generally in agreement with experiments. As the numerical procedure allows higher time resolution and can cover the far wake of the cylinder, it gives further insight into the direct correlation between instantaneous patterns of vorticity in the near-wake and the unsteady loading on the cylinder.

REFERENCES

- (1) Griffin, O. M. and Ramberg, S. E. (1976), "Vortex Shedding from a Cylinder Vibrating in Line with an Incident Uniform Flow", *Journal of Fluid Mechanics*, Vol. 75, Part 2, pp. 257-271.
- (2) Öngören, A. and Rockwell, D. (1988), "Flow Structure from an Oscillating Cylinder. Part 2: Mode Competition in the Near-Wake." *Journal of fluid Mechanics*, Vol. 197, pp. 225-246.
- (3) Sarpkaya, T. and Storm, M. (1985), "In-line Force on a Cylinder Translating in an Oscillatory Flow", *applied Ocean Research*, Vol. 7, No. 4, pp. 188-196.
- (4) Cetiner, O. and Rockwell, D. (2001), "Streamwise Oscillations of a Cylinder in a Steady Current. Part I: Locked-On States of Vortex Formation", *Journal of Fluid Mechanics*, Vol. 427, pp. 1-28.
- (5) Sarpkaya, T., Putzig, C., Gordon, D., Wang, X and Dalton, C. (1992), "Vortex Trajectories around a circular cylinder in Oscillatory Plus Mean Flow", *Journal of Offshore Mechanics and Arctic Engineering*, Vol. 114, pp. 291-298.
- (6) Graham, J. M. R., Arkell, R. H. and Zhou, C. -Y. (1993), "The Effect of Combinations of Mean Current and Oscillatory Flow on the Forces Induced on a Bluff Body", *Journal of Wind Engineering and Industrial Aerodynamics*, Vol. 50, pp. 85-96.
- (7) Chorin, A. J. (1973), "Numerical study of slightly viscous flow", *J. of Fluid Mechanics*, Vol. 57, p. 785-796.

- (8) Graham, J. M. R. and Cozens, P. D. (1988), "Vortex shedding from Edges Including Viscous Effects", Fluid Dynamic Research, Vol. 3, pp. 111-114.
- (9) Cetiner, O. and Unal, M. F. (1995), "A Discrete vortex Study of Vortex-Induced Oscillations of a Circular Cylinder", Numerical Methods in Laminar and Turbulent Flow, Volume IX, Part 2, pp. 1567-1479.
- (10) Braza, M., Chassing, P. and H. H. Minh (1986), "Numerical Study and Physical Analysis of the Pressure and Velocity Fields in the Near-Wake of a Circular cylinder", Journal of Fluid Mechanics, Vol. 173, pp. 667-681.
- (11) Maull, D. J. and Milliner, M. C. (1978), "Sinusoidal Flow Past a Circular Cylinder, Costal Engineering, Vol. 2, pp. 149-168.

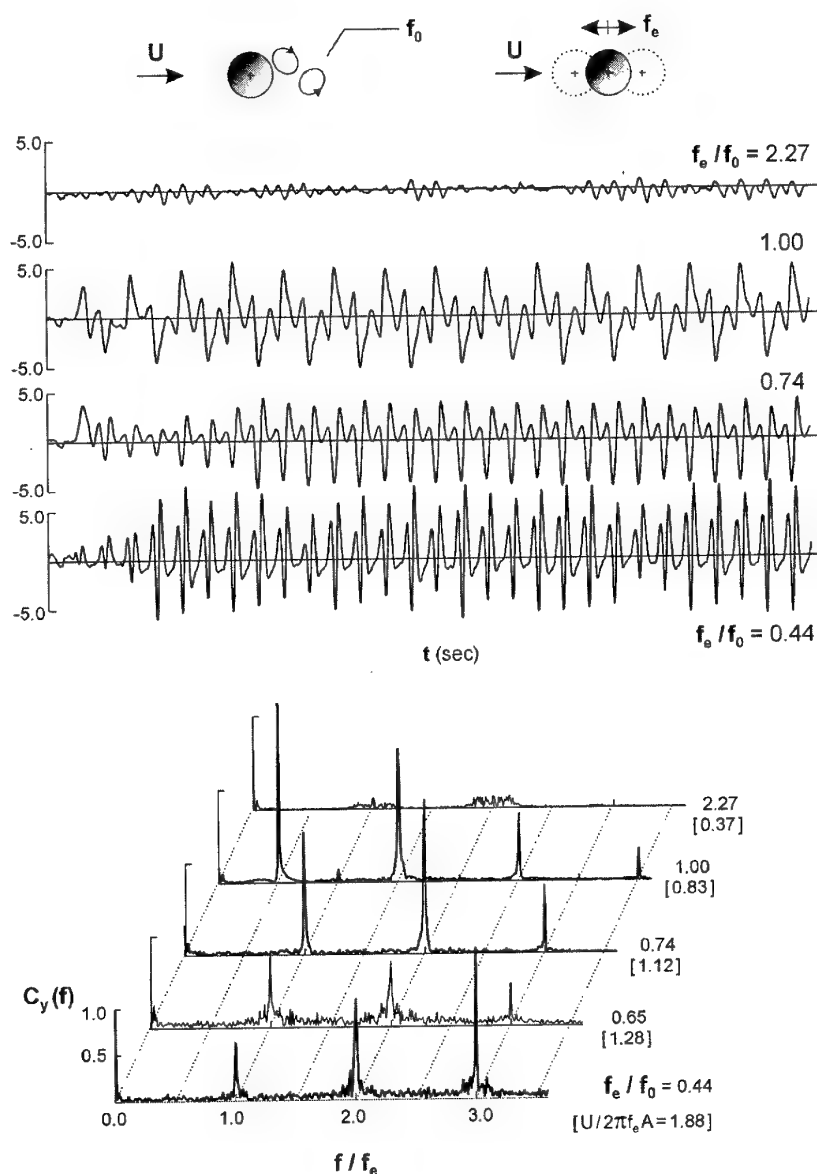


Figure 1: Experimentally obtained time traces and spectra of transverse force coefficient over a range of excitation frequency f_e relative to inherent frequency f_0 of Kármán vortex formation from the corresponding stationary cylinder.

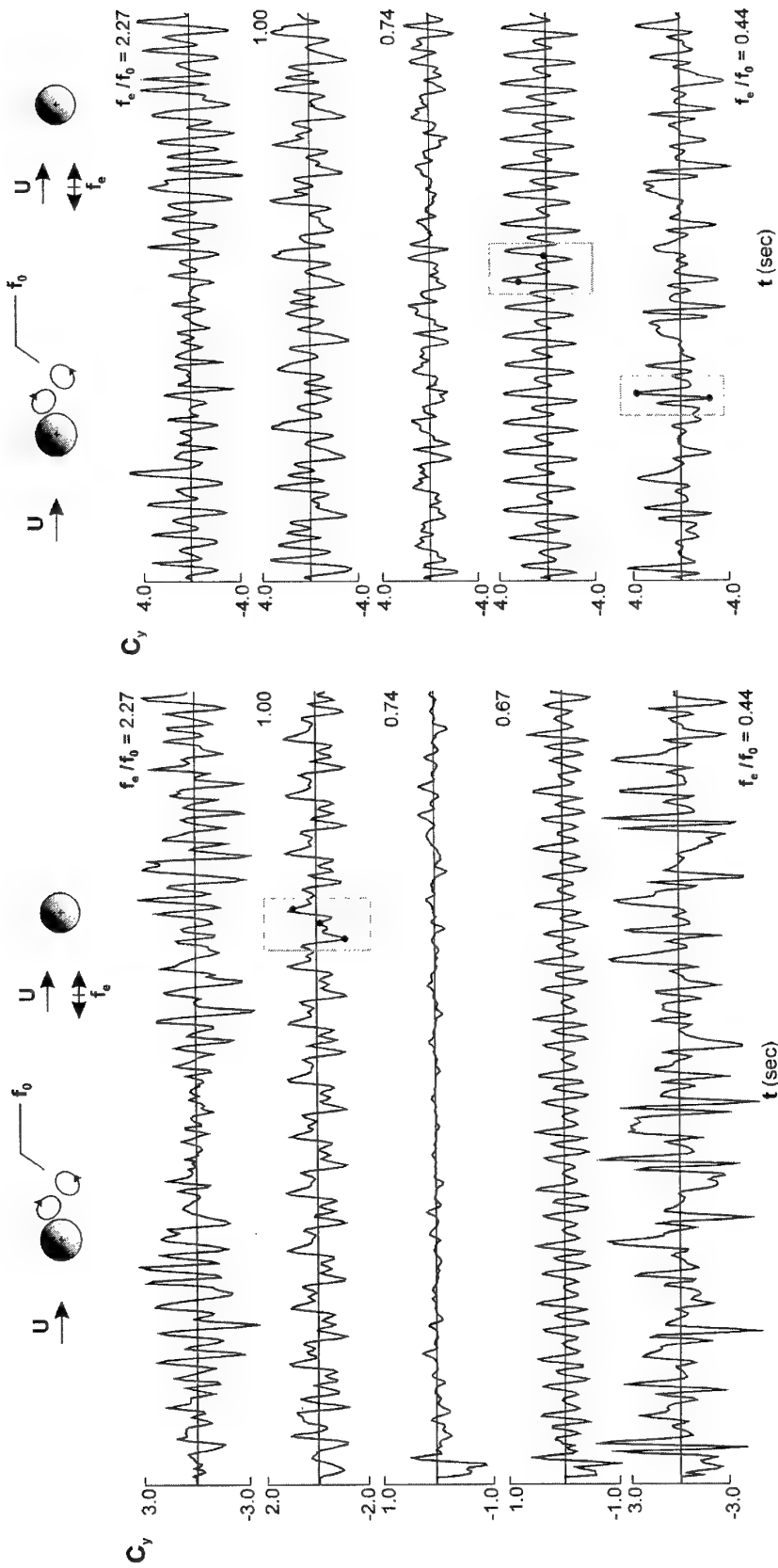


Figure 2: Time traces of transverse force coefficients obtained from numerical results for $f_e = 0.28$ Hz.

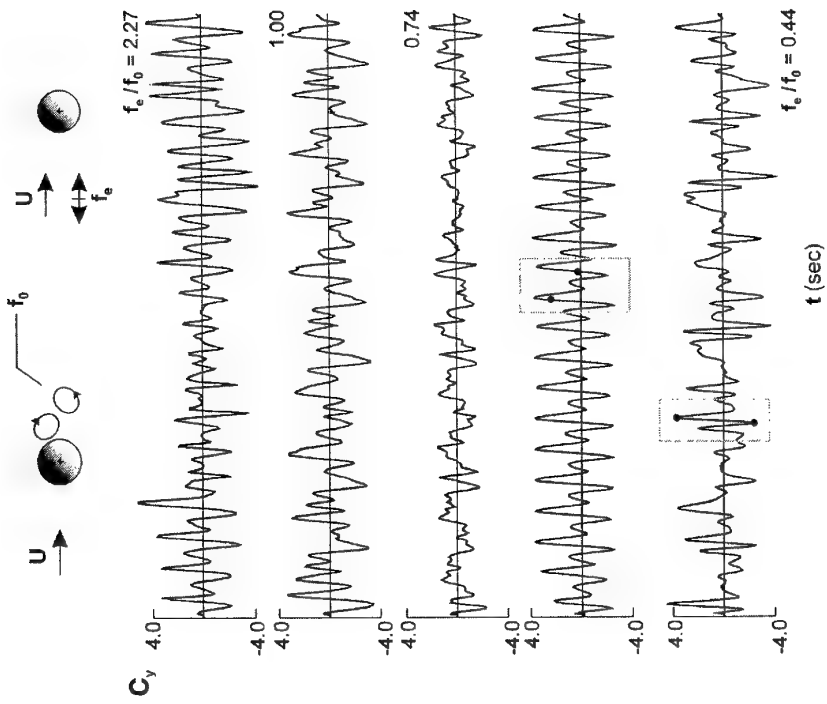


Figure 3: Time traces of transverse force coefficients obtained from numerical results for $f_e = 0.1$ Hz.

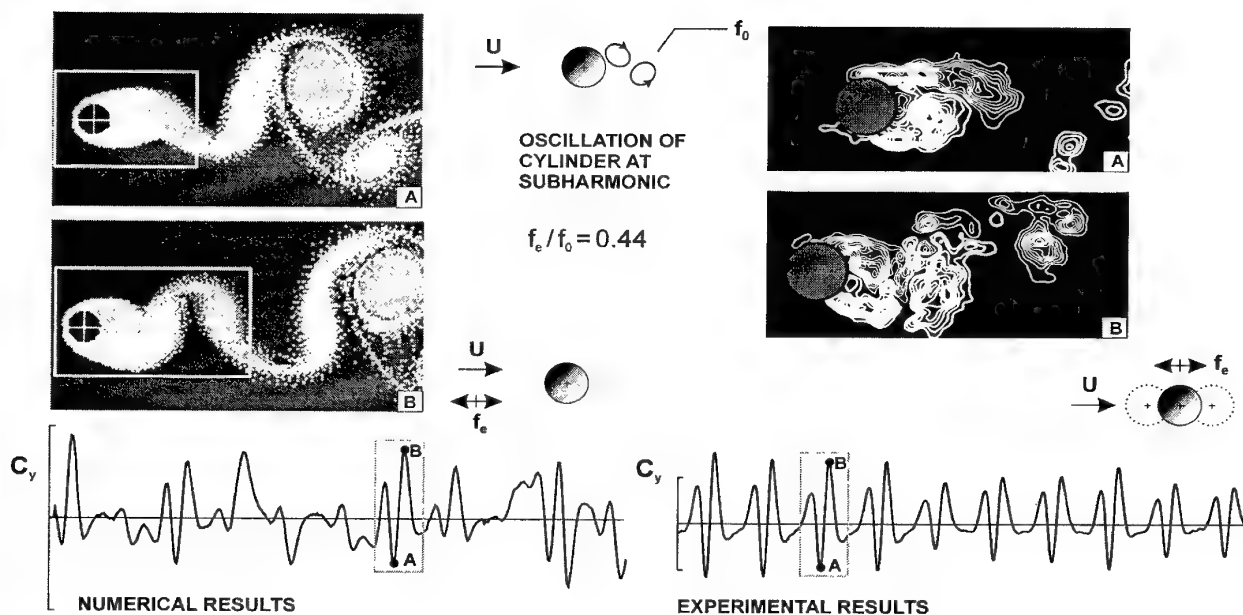
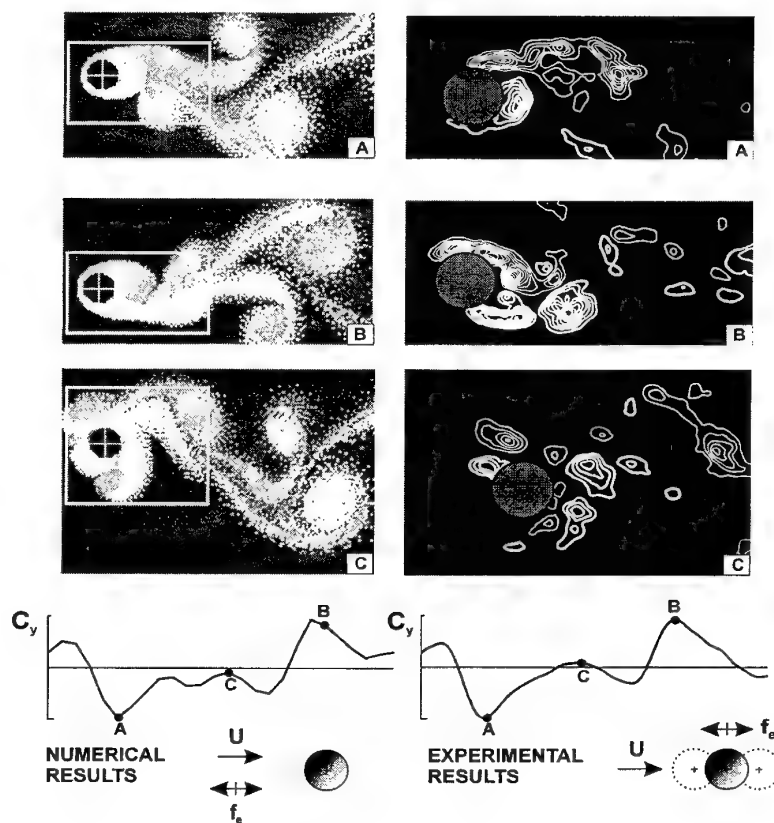


Figure 4: Instantaneous patterns of vorticity and corresponding time history of transverse force for oscillations at subharmonic frequency of Kármán shedding from the corresponding stationary cylinder: numerical and experimental results

OSCILLATION OF
CYLINDER AT
FUNDAMENTAL
 $f_e/f_0 = 1.00$



Figure 5: Instantaneous patterns of vorticity and corresponding time history of transverse force for oscillations at fundamental frequency of Kármán shedding from the corresponding stationary cylinder: numerical and experimental results



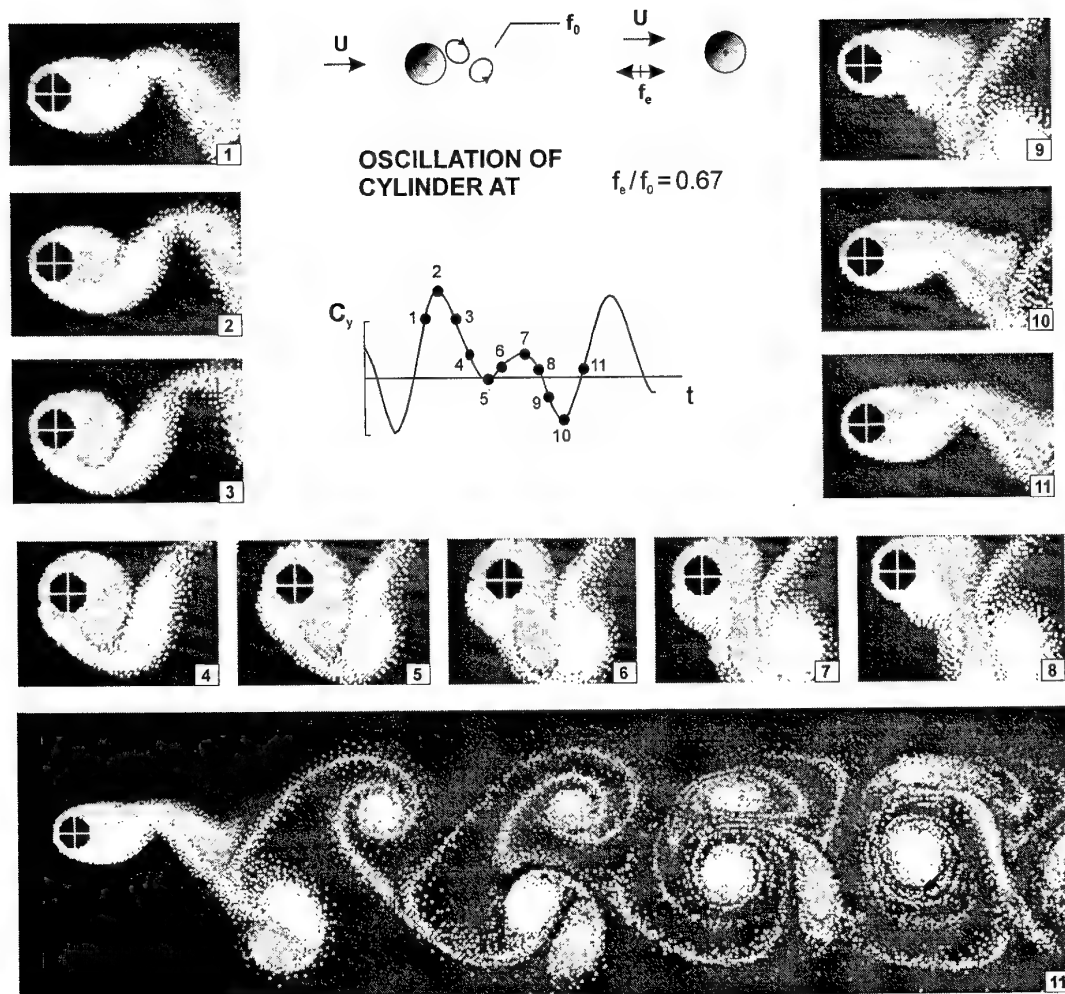


Figure 6: Instantaneous patterns of vorticity for oscillation of cylinder at $f_c/f_0=0.67$.

NUMERICAL SIMULATION OF UNSTEADY FLOW THROUGH A HORIZONTAL AXIS WIND TURBINE BY A VORTEX METHOD

Akira OJIMA and Kyoji KAMEMOTO

Department of Mechanical Engineering and Materials Science, Yokohama National University
79-5 Tokiwadai, Hodogaya-ku, Yokohama 240-8501, Japan /Email: a-ojima@ynu.ac.jp

ABSTRACT

The purpose of this study is to develop the reasonable and easy-to-handle numerical technique in order to predict the unsteady performance of a horizontal-axis wind turbine (HAWT). The vortex method has been applied to the numerical simulation of unsteady and three-dimensional flow through a HAWT. From the calculation results, it was confirmed that vortex crowds are formed in a trailing vortex, which is shed from a blade tip seemingly due to the instability of vortex. Aerodynamic characteristics of two shapes of the blade, i.e. MEL012 developed only for wind turbine and NACA0012 for the conventional airfoil, were investigated and the applicability of MEL012 was confirmed. The comparison of the calculation results of power and axial drag coefficients with and the experimental ones showed reasonable agreement.

1. INTRODUCTION

Wind energy is widely recognized as one of the most promising clean and reproducible energy resources for solving global environmental problems. Wind energy has small energy density compared with hydraulic one, and is supplied irregularly. In order to compensate these problems, it is asked for development of the wind power system to obtain energy efficiently. Wind turbine blades are usually designed as optimum shape at the rated operation. In practice, the flow around a turbine blade has the unsteady phenomena such as the flow separation, fluctuation of wind velocity and so on. For conditions out of the conventional design, it is necessary to predict complex vortical flow features to design suitable operational procedure. In order to simulate these phenomena, development of reasonable and easy-to-handle numerical technique is required.

In order to predict the performance of a wind turbine, the means based on the inviscid flow such as the momentum theory, the blade element theory, the local momentum theory⁽¹⁾, the vortex theory and the asymptotic acceleration potential method⁽²⁾ were employed before. These methods correctly provide a wealth of information when unsteady phenomena such as

the flow separation do not occur. Recently, Iida et al.⁽³⁾ applied three-dimensional flow analysis through a HAWT by using the pseudo-compressively method combined with overset grid method. Duque et al.⁽⁴⁾ calculated the complicated flow around a HAWT including boundary layer transition, unsteady tower wakes and rotor-tower interaction by a Reynolds-averaged Navier-Stokes (RaNS) method.

Although the recent progress of computational fluid dynamics is quite radical, the numerical analysis of a complicated separated flow around a moving or oscillating boundary and a higher Reynolds number flow still is not so easy to solve from the view of engineering applications. With a finite difference method or a finite element method, it is complicated to proceed the computation requiring treatment of moving grids, generation of fine grids according to the magnitude of Reynolds number, tuning up of turbulence model and so on. On the other hand, the vortex methods have been developed and applied to the analysis of complicated vortical flow and to the simulation of unsteady separated flow problems in a wide range of industries, because the vortex methods consist of simple algorithm based on physics of flow and are grid-free Lagrangian methods. Therefore, the vortex methods may be the means to provide one of the most suitable techniques for the prediction and solution of the present problems. Many researches, related to the two-dimensional analysis with vortex methods, have been done. However, only a few studies related to the three-dimensional analysis for the turbomachinery with vortex methods have been reported. Tsutahara et al.⁽⁵⁾ applied a three-dimensional vortex stick method to the simulation of the flow around helicopter rotors. Lee⁽⁶⁾ calculated the wake geometries of two-bladed helicopter rotor in axial flights by using a time-marching free-wake method. Imamura et al.⁽⁷⁾ calculated the potential flow around HAWT rotor blades with winglets by a vortex lattice method (VLM) with a free-wake model.

The purpose of this paper is to develop the reasonable and easy-to-handle numerical technique in order to predict the unsteady performance of a HAWT. This paper described the initial approach of the simulation of unsteady flow through a HAWT rotor by using a three-dimensional vortex method. This

calculation is performed in the assumption that the flow adheres to the blade surface and separates from the portion of the edge such as the trailing edge and the tip of the blade. From the results of this calculation, the unsteady behavior of the vortex shed from the edge is described in detail. The validity of the method using this study is confirmed in comparison with the performance of a HAWT from this calculation and the experiment.

2. VORTEX METHOD

2.1. Mathematical basis

The governing equations of viscous and incompressible flow are described by the vorticity transport equation and the pressure Poisson equation which can be derived by taking the rotation and the divergence of Navier-Stokes equations, respectively

$$\frac{\partial \omega}{\partial t} + (\mathbf{u} \cdot \text{grad}) \omega = (\omega \cdot \text{grad}) \mathbf{u} + \nu \nabla^2 \omega \quad (1)$$

$$\nabla^2 p = -\rho \text{div}(\mathbf{u} \cdot \text{grad} \mathbf{u}) \quad (2)$$

Where \mathbf{u} is a velocity vector and a vorticity ω is defined as follows.

$$\omega = \text{rot } \mathbf{u} \quad (3)$$

As explained by Wu and Thompson⁽⁸⁾, the Biot-Savart law can be derived from the definition equation of vorticity as follows.

$$\mathbf{u} = \int_V \omega_0 \times \nabla_0 G dv + \int_S [(\mathbf{n}_0 \cdot \mathbf{u}_0) \cdot \nabla_0 G - (\mathbf{n}_0 \times \mathbf{u}_0) \times \nabla_0 G] ds \quad (4)$$

Here, subscript "0" denotes variable, differentiation and integration at a location \mathbf{r}_0 , and \mathbf{n}_0 denotes the normal unit vector at a point on a boundary surface S . And G is the fundamental solution of the scalar Laplace equation with the delta function $\delta(\mathbf{r} - \mathbf{r}_0)$ in the right hand side, which is written for a three-dimensional field as follows.

$$G = \frac{1}{4\pi R} \quad (5)$$

Here, $R = |\mathbf{r} - \mathbf{r}_0|$, $R = |\mathbf{R}| = |\mathbf{r} - \mathbf{r}_0|$. In Eq.(4), the inner product, $\mathbf{n}_0 \cdot \mathbf{u}_0$ and the outer product $\mathbf{n}_0 \times \mathbf{u}_0$ stand for normal and tangential velocity components on the boundary surface, and they correspond to the source distribution on the surface and the vortex distribution that has the rotating axis in parallel to the surface, respectively. Therefore, it is mathematically understood that velocity fields of viscous and incompressible flow are obtained from the field integration concerning vorticity distributions in the flow field and the surface integration concerning source and vortex distributions around the boundary surface.

The pressure in the field is obtained from the integration equation formulated by Uhlman⁽⁹⁾, instead of the finite difference calculation of the Eq.(2) as follows.

$$\beta H + \int_S H \frac{\partial G}{\partial n} ds = -[\int_V \nabla G (\mathbf{u} \times \omega) dv + \int_S G \cdot \mathbf{n} \cdot \frac{\partial \mathbf{u}}{\partial t} ds + \nu \int_S \mathbf{n} \cdot (\nabla G \times \omega) ds] \quad (6)$$

Here, $\beta = 1$ in the flow field and $\beta = 1/2$ on the boundary S . G is the fundamental solution given by Eq.(5). H is the Bernoulli function defined as follows.

$$H = \frac{p}{\rho} + \frac{u^2}{2} \quad (7)$$

2.2. Panel method

In this present study, boundary surface is represented by the panel method. The source and vortex corresponding to the first and second terms of Eq.(4) are distributed on the boundary surface. The strengths of source and vortex are obtained by using the following two conditions; zero normal component of relative velocity to the boundary surface $\mathbf{u} \cdot \mathbf{n} = 0$ and the relation of the conservation of the vortex strength, respectively.

In the pressure calculation, the value of H on the boundary surface is solved from Eq.(6) by using the panel method. After the pressure distribution around the boundary surface is calculated from Eqs.(6) and (7), the integration of the pressure acting on the body surface yields the force acting on the body.

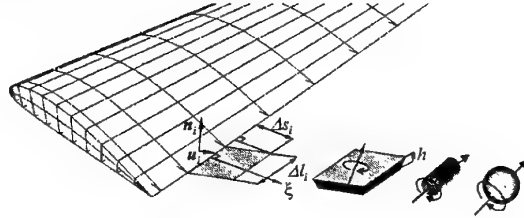


Fig.1 Introduction of vortex elements.

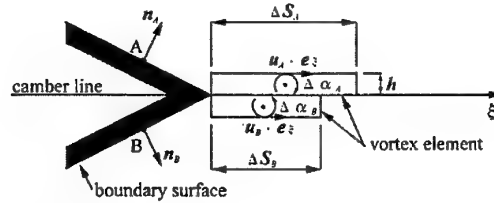


Fig.2 Introduction of vortex elements from the trailing edge.

2.3. Vortex shedding from the solid surface

The simulation of the flow past a body must involve a vorticity creation around its surface accompanied by the processes of the viscous diffusion and the convection. However, much simpler simulations may be attempted for bodies with known separation points such as edged bodies. In this study, discrete vortex elements are introduced from the portions of edge such as the trailing edge and the blade tip and root, on the assumption that the flow adheres to the blade surface and separates from the portion of the edge such as the trailing edge and the tip of the blade.

At the trailing edge, the vorticity created within the boundary layers is shed parallel to the camber line into the wake, as shown in Figs.1 and 2. When the intensity of the vortex $\alpha = (\alpha_x, \alpha_y, \alpha_z)$ is defined as $\alpha = \int_V \omega dv$, the values of intensity of the vortex per unit area just

upstream of the trailing edge (points A and B as shown in Fig.2 are defined as $\Delta\alpha_A = n_A \times u_A$ and $\Delta\alpha_B = n_B \times u_B$. Here, n , u and dv are normal unit vector, velocity vector at each point on the boundary and volume, respectively. The convective velocities of vortex sheets at each point are $u_A/2$ and $u_B/2$, respectively. If the perpendicular component to the trailing edge of convective velocity at each point are $u_A/2 \cdot e_\xi$ and $u_B/2 \cdot e_\xi$, the total amount of the vortex strength shed into the wake during the time interval Δt are calculated as follows.

$$\alpha_A = \Delta\alpha_A \cdot \Delta S_A \cdot \Delta l_A \quad (8)$$

$$\alpha_B = \Delta\alpha_B \cdot \Delta S_B \cdot \Delta l_B \quad (9)$$

Here, ΔS , Δl and e_ξ are the convective length of $\Delta S = u/2 \cdot e_\xi \cdot \Delta t$, the spanwise panel length of the trailing edge and the unit vector along the camber line at a blade section, respectively. The vortex element is introduced as the vortex plate, which has the convective length of ΔS , the spanwise length Δl and the thickness of $h = 1.136(\nu \Delta t)^{1/2}$. Here, ν is kinematic viscosity. In the assumption that the boundary layer without the thickness is developed near the wall, this thickness of the nascent vortex element was employed in this calculation, because of the decision in the same manner as the viscous diffusion of the vorticity in the shear layer developing over a suddenly accelerated plate wall. In the same way, at the blade tip and root, nascent vortex plates are shed parallel to the surface with angle ϕ into the wake as shown in Fig.3. Here, ϕ is defined as follows.

$$\tan \phi = \frac{u_B \cdot e_\xi}{u_A \cdot e_\xi} \quad (10)$$

Here, e_ξ is unit vector parallel to the blade surface toward the blade tip and root. In this study, every vortex plate element, which moves beyond a boundary at the distance of 5% of chord length from the solid surface, is replaced with a vortex stick element with a viscous core ε .

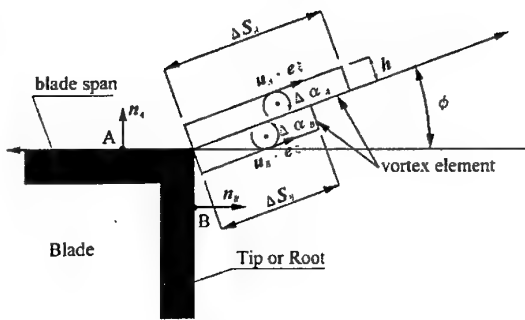


Fig.3 Introduction of vortex elements of the blade tip and root.

2.4. Three-dimensional vortex models

In this study, vortex blob and stick models are employed. A vortex blob is a spherical model with a radially symmetric distribution of vorticity and vortex stick is a cylindrical model. The i -th vortex blob is defined by the position $r_i = (r_x, r_y, r_z)$, its vorticity $\omega_i = (\omega_x,$

$\omega_y, \omega_z)$ and its core radius ε_i . The vorticity distribution around the vortex blob is represented by the following equations.

$$\omega_i(r) = \omega_i p(|r - r_i|/\varepsilon_i) \varepsilon_i^{-3} dv_i \quad (11)$$

$$p(\xi) = 15/8\pi (\xi^2 + 1)^{-7/2}$$

$p(\xi)$ is smoothing function proposed by Winckelmans & Leonard⁽¹⁰⁾. The i -th vortex stick is defined by the coordinates of the center of the stick $r_i = (r_x, r_y, r_z)$, its vorticity $\omega_i = (\omega_x, \omega_y, \omega_z)$, its core radius ε_i and its length l_i . Here, the vortex stick has a constant distribution of vorticity within the core radius.

The motion of the discrete vortex element at a location r is represented by Lagrangian form of a simple differential equation.

$$\frac{dr}{dt} = u \quad (12)$$

Then, the trajectory of the discrete vortex element over a time step dt is approximately computed from the Adams-Bashforth method.

On the other hand, the evolution of vorticity is calculated by Eq.(1) with the three-dimensional core spreading method^{(11),(12)} modified by Nakanishi & Kamemoto. In this study, stretch and diffusion terms in Eq.(1) are separately considered. The change of core radius due to the stretch is calculated from the following equations.

$$\frac{d\omega}{dt} = (\omega \cdot \text{grad})u \quad (13)$$

$$\frac{dl}{dt} = \frac{l_i}{|\omega_i|} \cdot \left| \frac{d\omega}{dt} \right| \quad (14)$$

$$\left(\frac{d\varepsilon}{dt} \right)_{\text{stretch}} = -\frac{\varepsilon_i}{2l_i} \cdot \frac{dl}{dt} \quad (15)$$

Here, ε and l are the core radius and the length of the vortex blob model, respectively. The viscous term in Eq.(1) is expressed by the core spreading method. The core spreading method is based on Navier-Stokes equation for the viscous diffusion of an isolated two-dimensional vortex filament in a rest fluid, and the rate of core spread is represented as follows.

$$\left(\frac{d\varepsilon}{dt} \right)_{\text{diffusion}} = \frac{c^2 \nu}{2\varepsilon_i}, \quad (c=2.242) \quad (16)$$

Taking two factors into account, each value of a new element is obtained from the following equations.

$$\varepsilon_{i+\Delta t} = \varepsilon_i + \left[\left(\frac{d\varepsilon}{dt} \right)_{\text{stretch}} + \left(\frac{d\varepsilon}{dt} \right)_{\text{diffusion}} \right] \cdot \Delta t \quad (17)$$

$$l_{i+\Delta t} = l_i + \frac{dl}{dt} \cdot \Delta t \quad (18)$$

$$|\omega_{i+\Delta t}| = |\omega_i| \cdot \left(\frac{\varepsilon_i}{\varepsilon_{i+\Delta t}} \right)^2 \quad (19)$$

In this calculation, the new element is replaced into a vortex blob that has equivalent volume. Calculation accuracy in the vortex method will be maintained if the core radius of an adjacent vortex element is enough larger than the distance between centers of these elements.

The vortex stick element changes into a new element, which has the core radius $\varepsilon_{t+\Delta t}$ and the length $l_{t+\Delta t}$, after a time interval Δt obtained from Eqs.(17)-(19). If the diameter of a vortex stick element 2ε becomes larger than the length of it l , every vortex stick element is replaced with an equivalent vortex blob.

3. CALCULATION CONDITIONS

Calculations have been performed for an impulsively rotated HAWT blade, which is constructed by one blade and rotates about y-axis with constant angular speed Ω in the uniform flow U_∞ as shown in Fig.4. The blades are connected by a hub at the rotating axis but the hub is not considered in this calculation. The turbine nacelle and the tower are not considered either.

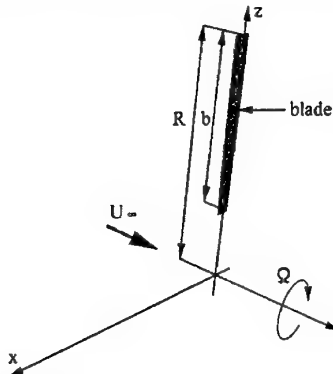


Fig.4 Coordinate system of wind turbine rotor.

Two types of the blade shape are investigated in this study. As the first type of the blade, the airfoil section NACA0012, which is not common for HAWT, has been chosen for the rotor blades, because the performances of this Wind Turbine model have been measured in open jet wind tunnel at Delft University of Technology by Vermeer⁽¹³⁾. The optimum tip speed ratio for this model is approximately $\lambda=8.0$. Here, tip speed ratio is defined as $\lambda=V/U_\infty$ ($V=R\Omega$: tip velocity, R : rotating radius). The second type of the blade is employed the one based on MEL012⁽¹⁴⁾, which designed as the optimum tip speed ratio $\lambda=8.0$ at Mechanical Engineering Laboratory in Japan and shown in Fig.5. Specifications of each blade are shown in Table 1. Here, c is the chord length.

Each blade is divided into 572 source and vortex panels [22(span wise) \times 26(sectional blade element)].

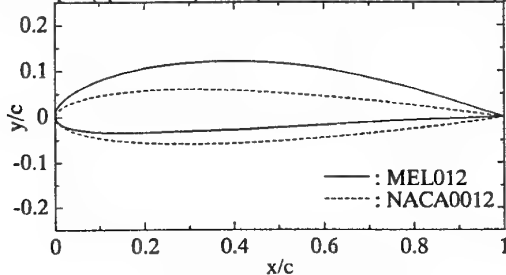


Fig.5 Shape of blade section.

Profile	MEL012 (no-taper)
Blade number	N=1
Span length	$b/R=0.7$
Cut-off radius	$R_{cut}/R=0.3$
Aspect ratio	$Ar=b/c=8.0$
Twist angle	$\theta=4.8\sim 15.2[\text{deg}]$

(a) MEL012

Profile	NACA0012 (no-taper)
Blade number	N=1 or 2
Span length	$b/R=0.7$
Cut-off radius	$R_{cut}/R=0.3$
Aspect ratio	$Ar=b/c=5.25$
Twist angle	$\theta=(\theta_{tip}+6.0)-6.67\times(r/R)[\text{deg}]$ ($0.3<r/R<0.9$) $\theta_{tip}=0.0[\text{deg}]$ ($0.9<r/R<1.0$)

(b) NACA0012

Table.1 Specification for wind turbine blade.

The calculations have been performed for each blade based on MEL012 and NACA0012 and the calculation results for each blade are compared for the vortex distribution behind the rotor disk, pressure distribution on the blade surface and the performance, respectively. In order to compare with the experimental results by Vermeer⁽¹³⁾, calculations have been performed for a HAWT with two blades, which have NACA0012 as the sectional shape of the blade. The parameters for calculations are shown as follows: Reynolds number based on the tip velocity and the rotating radius $Re=VR/\nu=1.0\times 10^6$ and the time interval $\Delta t/R=T_0/200$. Here, ν is kinematic viscosity and the period of one rotor revolution T_0 is defined as $T_0=2\pi R/(R\Omega)$.

To examine the performance for HAWT, a power coefficient C_{power} and an axial force coefficient C_{Daxis} are defined as follows.

$$C_{power} = \frac{T \cdot \Omega}{1/2 \cdot \rho U_\infty^3 \pi R^2} \quad (20)$$

$$C_{Daxis} = \frac{D_{axis}}{1/2 \cdot \rho U_\infty^2 \pi R^2} \quad (21)$$

Here, T and D_{axis} are the torque and the axial force acting on the blade. After the pressure distribution around the blade surface is calculated from Eqs.(6) and (7), the integration of unsteady pressure and moment of pressure force acting on the blade surface yields the unsteady axial force D_{axis} and the torque T on the blade. It is convenient to represent the aerodynamic force acting on the sectional element of the blade by its circumferential and axial components. The circumferential force coefficient C_{LT} and the axial force coefficient C_{DT} at a blade section shown in Fig.6 are defined as follows.

$$C_{LT} = \frac{dL_T}{1/2 \cdot \rho V^2 \cdot c} \quad (22)$$

$$C_{DT} = \frac{dD_T}{1/2 \cdot \rho V^2 \cdot c} \quad (23)$$

Here, C_a and C_b are the induced factors of circumferential and axial directions, respectively. α_{eff} is an effective angle of attack. In this study, a circumference force dL_T and an axial force dD_T acting on a blade element are evaluated from the integration of circumferential and axial components of unsteady force acting on the blade.

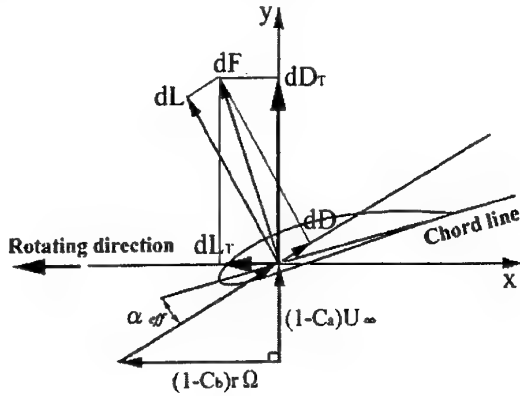
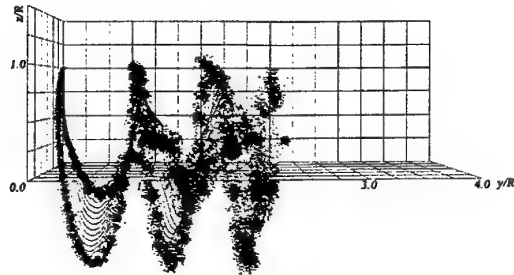


Fig.6 Aerodynamic forces acting on a blade section.

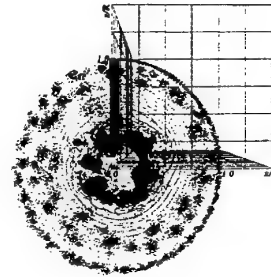
4. CALCULATION RESULTS

The evolution of vortical wake behind a rotor blade, which impulsively rotated, is explained by using the distribution of discrete vortices. For each blade based on MEL012 and NACA0012, Fig.7 shows instantaneous flow patterns represented by discrete vortices after three rotor revolutions at the tip speed ratio $\lambda = V/U_\infty = 8.0$, where U_∞ is a wind velocity. For both blades, helical vortex structure, which consists of the trailing vortices shed from the blade tip and root, is formed behind the rotor disk. As time goes on, the starting vortices flow downstream and the trailing vortices tend to have dominant effects in the flow field. It is confirmed that the vortex crowds is periodically formed in vortex structures shed from the tip and root. These vortex crowds are generated by the growth of the vortex instability in the trailing vortex. The trailing vortex shed from the root of the blade forms vortex crowds larger than the one shed from the blade tip. This occurs because the blockage associated with the turbine nacelle is not represented in this calculation. If the vortex crowds flow downstream and interact with another wind turbine blade, it seems that the behavior of the vortex crowds is deeply concerned with the noise. It is interesting to investigate about the influence of the vortex crowds to the rotor blade.

Figure 8 shows an instantaneous pressure distributions on the blade surface of suction side at the tip speed ratio $\lambda = 8$ after three rotor revolutions. For both blades, the lower pressure region is formed on the suction side of the blade near the leading edge close to the blade tip. From Fig.8, it is confirmed that the lower pressure region for the blade based on NACA0012 is formed on the suction side nearer the leading edge than that for MEL012.

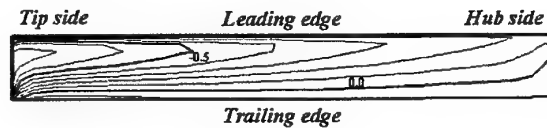


(a) y-z plane

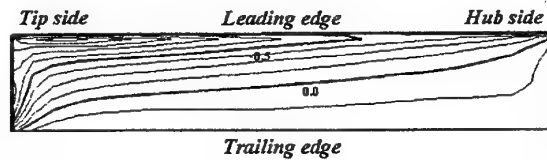


(b) x-z plane

Fig.7 Instantaneous flow pattern presented by discrete vortices (MEL012, $\lambda = 8.0$, $T/T_0 = 3.0$).



(a) MEL012



(b) NACA0012

Fig.8 Instantaneous pressure distributions on the blade surface of the suction side ($\lambda = 8.0$, $T/T_0 = 3.0$).

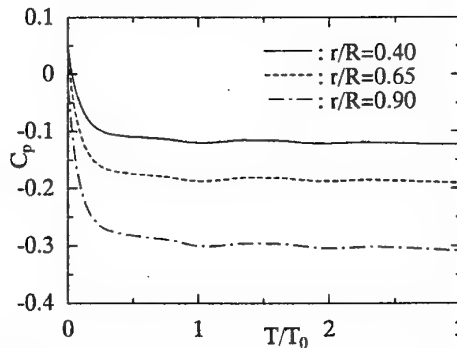
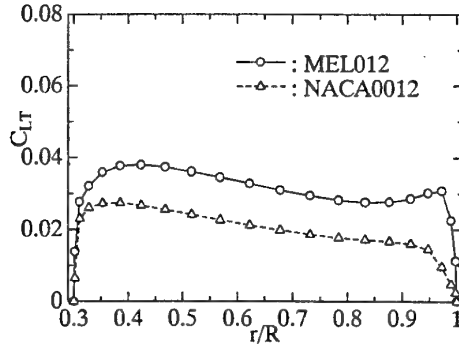
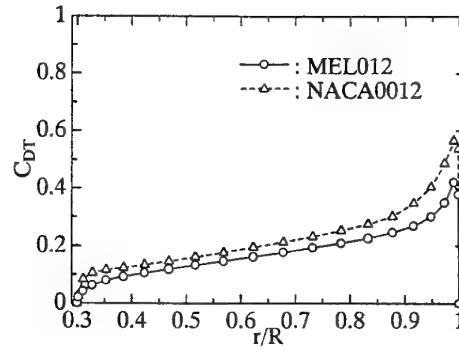


Fig.9 Time histories of pressure coefficient C_p on the surface for the blade based on MEL012 ($\lambda = 8.0$).

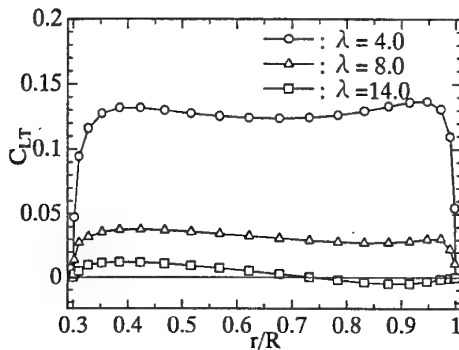


(a) Circumferential force coefficient C_{LT}

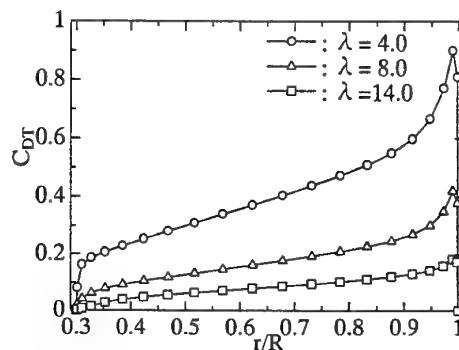


(b) Axial force coefficient C_{DT}

Fig.10 Spanwise distributions of the aerodynamic forces.



(a) Circumferential force coefficient C_{LT}



(b) Axial force coefficient C_{DT}

Fig.11 Spanwise distributions of the aerodynamic forces.

Figure 9 shows time histories of the pressure coefficient C_p at the quarter chord length from the leading edge on the suction side of the blade and various spanwise positions ($r/R=0.90, 0.65, 0.40$) at the tip speed ratio $\lambda=8$ for the blade based on MEL012. Here, a pressure coefficient C_p is defined as $C_p=(p-p_\infty)/(\rho V^2/2)$. According to Fig.9, the pressure coefficient C_p at each spanwise position is still decreasing at three rotor revolutions, but the rate of this decreasing is slightly smaller than that for the initial stage of rotation.

Then, Fig.10 shows spanwise distributions of the circumferential force C_{LT} and the axial force coefficient C_{DT} , which have averaged at the second and third rotor revolutions, respectively. To predict the spanwise distribution of the circumferential force coefficient, which produces the rotational torque and was defined as Eq.(22), is one of the most important factors to design the blades. In Fig.10(a), the circumferential force coefficient C_{LT} for the blade based on MEL012 is larger throughout the spanwise than that for NACA0012. It is important to predict the spanwise distribution of the axial force coefficient C_{DT} , because the axially bending moment is caused by axial force acting on the blade. As shown in Fig.10(b), the axial force coefficient C_{DT} for the blade

based on MEL012 is smaller than that for NACA0012 at the anywhere of spanwise. Therefore, it can be easily understood that the blade based on MEL012 is suitable for Wind Turbine in comparison of the one based on NACA0012.

Then, it is explained about the difference in the aerodynamic forces acting on the sectional element of the blade by the tip speed ratio. Figure 11 shows the spanwise distributions of the circumferential force coefficient C_{LT} and the axial force coefficient C_{DT} for the blade based on MEL012 at the tip speed ratio $\lambda=4, 8$ and 14 . As shown in Fig.11(a), the value of C_{LT} for $\lambda=14$ becomes negative in the range of $0.7 < r/R < 1.0$. This leads to the reduction of the total efficiency, because the decreasing of C_{LT} means the reduction of the torque. In Fig.11(b), the axial force coefficient C_{DT} becomes larger as the tip speed ratio decreases. The axial force coefficient C_{DT} gradually increases with the spanwise position r/R being close to the blade tip, but it suddenly decreases near the blade tip. It seems that these distributions of the axial force coefficient C_{DT} near the blade tip are caused by the shape of the blade tip, which have right-angled edge.

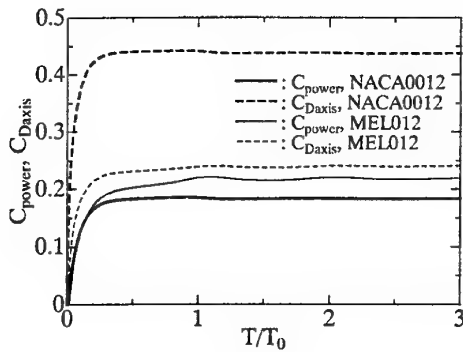


Fig.12 Time histories of power coefficient C_{power} and axial drag force coefficient C_{Daxis} ($\lambda=8.0$).

Figure 12 shows time histories of a power coefficient C_{power} and an axial force coefficient C_{Daxis} defined as Eqs.(20) and (21) at the tip speed ratio $\lambda=8$ for each blade. Here, C_{power} and C_{Daxis} are calculated by integrating the unsteady pressure and moment caused by the pressure around the blade surface. It is identified that C_{power} and C_{Daxis} periodically fluctuate with the starting vortices passing behind the blade. Figure 13 shows the power coefficient C_{power} and the axial force coefficient C_{Daxis} as a function of tip speed ratio λ . For the blade based on MEL012, it is understood that the maximum output power is obtained at the tip speed ratio $\lambda=10$ from the results shown in Fig.13. Then, it seems that this tip speed ratio on the maximum power is larger than the value of the design point of the blade ($\lambda=8$), because the blade used in this study has no taper. It is confirmed from Fig.13 that the higher power coefficient and the lower axial drag coefficient are acted on the blade of MEL012 in comparison with NACA0012. Therefore, it can be easily understood that the blade based on MEL012 is suitable for the Wind Turbine blade in comparison with NACA0012.

In order to compare with the experimental results by Vermeer, calculations have been performed for a HAWT with two blades, which have NACA0012 as the sectional shape of the blade. It is explained about the results calculated the unsteady flow through a HAWT with two blades which have NACA0012 as the sectional shape of the blade in accordance with the experiment by Vermeer⁽¹³⁾. Figure 14 shows the instantaneous flow pattern represented by discrete vortices after three rotor revolutions at tip speed ratio $\lambda=7.5$. It is confirmed from Fig.14 that the helical vortex structures shed from each blade are formed behind the rotor disk. For a HAWT with two blades, each blade is strongly affected from the helical vortex structures that have been made by itself and another one. The time histories of the power and axial drag coefficients are shown in Fig.15. In the initial stages of rotation, C_{power} and C_{Daxis} increase abruptly up to $T/T_0=0.5$ and to $T/T_0=1$ after a little decreasing. This fluctuation occurs by the starting vortex shed from the first blade passing behind the second blade. Figure 16

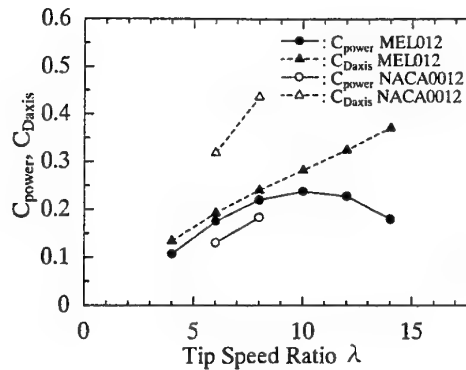


Fig.13 Comparison of the performance for the blade based on MEL012 with the one for NACA0012.

shows the results in comparison with the power and the axial drag force coefficients obtained from the experiment and the present calculation. It is confirmed that the power and the axial drag coefficients, which were obtained from this calculations, are reasonably agreement with experimental results.

5. CONCLUSION

A three-dimensional simpler vortex method was applied to the simulation of unsteady flows around a Horizontal Axis Wind Turbine and the following conclusions were obtained.

- (1) It was confirmed that the vortex crowds was formed in the trailing vortex shed from the blade tip.
- (2) As the result of the comparison with two types of the blade, it was confirmed that the performance of the blade developed for wind turbines was superior to the one for conventional airfoil.
- (3) The comparison between the calculation results and the experimental ones showed reasonable agreement for the power and the axial drag coefficients acting on the wind turbine.

It is confirmed that the method used in the present study is useful for the investigation of the unsteady and complicated vortical flow and the performance around the optimum-operation point of HAWT.

REFERENCES

- (1) Azuma, A. and Kawachi, K., (1979), "Local Momentum Theory and its Application to the Rotary Wing", Journal of Aircraft, Vol. 16, No. 1, pp. 6-13.
- (2) Hasegawa, Y., Kikuyama, K., Karikomi, K., Sumi, T. and G.J.W. van Bussel, (1999), "Numerical Analysis of Yawed Inflow Effects on a HAWT", Proc. ASME FEDSM99-7820.
- (3) Iida, M., Araki, K., Arakawa, C. and Matsumiya, H., (1999), "Numerical Simulation of Horizontal Windturbine using Overgrid Method", 13th CFD Symposium (in Japanese), C09-3.

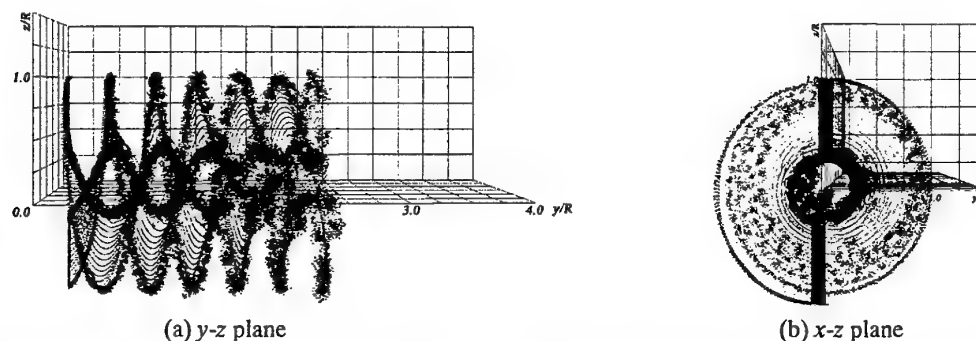


Fig.14 Instantaneous flow pattern presented by discrete vortices for two blades wind turbine ($\lambda=7.5$, $T/T_0=3.0$).

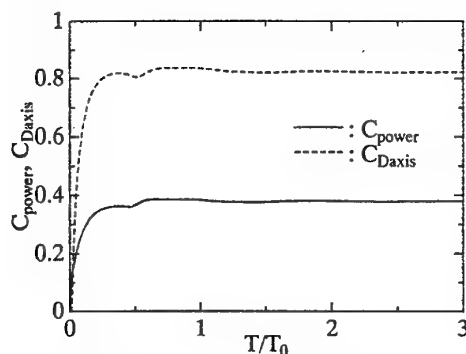


Fig.15 Time histories of power coefficient C_{power} and axial drag force coefficient C_{Daxis} for two blades wind turbine ($\lambda=7.5$).

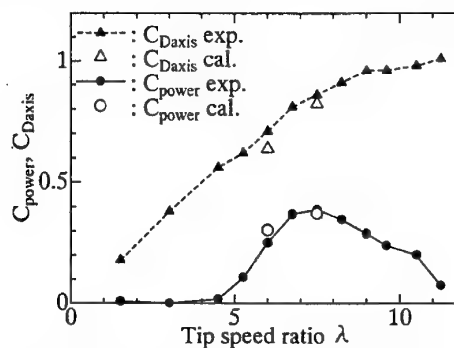


Fig.16 Comparison of calculated wind turbine performance with experimental results.

- (4) Duque, E.P.N, Dam, C.P., Brodeur, R.R. and Chao, D.D., (1999), "Navier-Stokes Analysis of Time-Dependent Flows about Wind Turbines", Proc. ASME FEDSM99-7814.
- (5) Tsutahara, M., Shima, E., Kitayama, Y. and Utsumi, H., (1999), "A Study of Flow around Helicopter Rotors by the Three Dimensional Vortex Method", Proc. ASME FEDSM99-6814.
- (6) Lee, D.J., (1999), "Numerical Prediction of Rotor Tip-Vortex Roll-Up in Axial Flights by Using a Time-Marching Free-Wake Method", Proc. 1st Int. Conf. Vortex Method, pp.243-253.
- (7) Imamura, H., Hasegawa, Y. and Kikuyama, K., (1998), "Numerical Analysis of the Horizontal Axis Wind Turbine with Winglets", JSME Int. Journal, Vol. 41, No. 1, B, pp. 192-198.
- (8) Wu, J.C. and Thompson, J.F., (1973), "Numerical Solutions of Time-Dependent Incompressible Navier-Stokes Equations using an Integro-Differential Formulation", Computers & Fluids, Vol. 1, pp. 197-215.
- (9) Uhlman, J.S., (1992), "An Integral Equation Formulation of the Equation of Motion of an Incompressible Fluid", Naval Undersea Warfare Center T.R., 10, 086.
- (10) Winkelmann, G. and Leonard, A., (1988), "Improved Vortex Methods for Three-Dimensional Flows, Proc. Workshop on Mathematical Aspects of Vortex Dynamics", pp. 25-35, Leeburg, Virginia.
- (11) Nakanishi, Y. and Kamemoto, K., (1992), "Numerical Simulation of Flow around a Sphere with Vortex Blobs", Journal Wind Eng. and Ind. Aero, Vol. 46 & 47, pp. 363-369.
- (12) Ojima, A. and Kamemoto, K., (2000), "Numerical Simulation of Unsteady Flows around Three Dimensional Bluff Bodies by an Advanced Vortex Method", JSME Int. Journal, Vol. 43, No. 2, B, pp. 127-135.
- (13) N-J Vermeer, (1991), "Performance measurements on a rotor model with Mie-vanes in the Delft open jet tunnel", IW-91048R, Delft University of Technology Faculty of Civil Engineering Institute for Wind Energy.
- (14) Matsumiya, H., "Performance of New 'MEL-Wing Sections' for Wind Turbines", (1992), 14th Wind Power Energy Symposium (in Japanese), pp.7-19.

EXTENSION OF VORTEX METHODS TO THE FLOW SIMULATION OF MIXED-FLOW TURBOMACHINES

R. Ivan Lewis

Department of M.M.M.Eng., Newcastle University,
2-16 Bruce Building, Newcastle upon Tyne, NE1 7RU, UK, /Email: r.i.lewis@ncl.ac.uk

Abstract

The main objective of this paper is the extension of vortex methods to the simulation of the flow through general mixed-flow (radial/axial) turbo-machines. Vortex methods in this context are twofold. The first category of analyses involves surface vorticity modelling of inviscid flows, numerical techniques which are extremely important as basic fluid dynamic design tools for the whole range of axial, mixed-flow and radial turbo-machines. The second category involves completely new developments of the vortex dynamics or vortex cloud Lagrangian method for modelling viscous flows in order to deal with the whole range of turbo-machinery blade-to-blade flows. The present paper introduces the basic numerical models for handling these problems and the relevant equations for vortex cloud simulation of the flow through mixed-flow turbomachines. Applications are given for fluid dynamic design and analysis of mixed-flow fans, radial fans or pumps and Francis turbines, including designs for which the Coriolis loading is so great that flow reversal occurs within the rotor due to the relative eddy and its associated "slip flow". Vortex dynamics is shown to be an extremely powerful form of Computational Fluid Dynamics (CFD) to simulate such flows within a practical design context.

1. Introduction

A detailed analytical introduction into the author's surface and cloud vorticity methodology has been given elsewhere, Lewis (1) and its extension to vortex cloud modelling of turbo-machinery blade rows was outlined in the previous conference, Lewis (2). Further extensions of this to radial fans were given by Lewis (3), in which use was made of a conformal transformation to relate the radial cascade to an equivalent axial cascade as illustrated in Figure 1 below. This was the first step of extending vortex dynamics modelling to completely general mixed-flow cascades that is the subject of the present paper. Closely related work involving the impact of a radial pump rotor wake on the downstream diffuser was completed by Zhu and Kamemoto (4).

An outline of the cascade transformation process will be given in Section 2 including treatment of the relative eddy effects, followed in Section 3 by a brief overview of the numerical process adopted for the vortex cloud simulation. Applications to mixed-flow and radial fans will be presented in Sections 4 & 5 followed by analysis of a Francis turbine rotor in Section 6.

2. Transformation of a mixed-flow cascade

Figure 1(a) illustrates the intersection of a surface of revolution, or so-called meridional surface, with the blades of a mixed-flow fan in the x, r, θ plane and its transformation into a geometrically equivalent infinite straight cascade in the $\zeta(\xi, \eta)$ plane. For conformality this must obey the following transformation relationship.

$$\frac{d\xi}{d\eta} = \frac{ds}{r d\theta} = \frac{1}{\sin \gamma} \frac{dr}{r d\theta} \quad (1)$$

where γ is the local cone angle and s is measured along the meridional surface. This may be achieved by the separate coordinate transformations

$$d\xi = \frac{ds}{r} = \frac{1}{r \sin \gamma} dr, \quad d\eta = d\theta \quad (2)$$

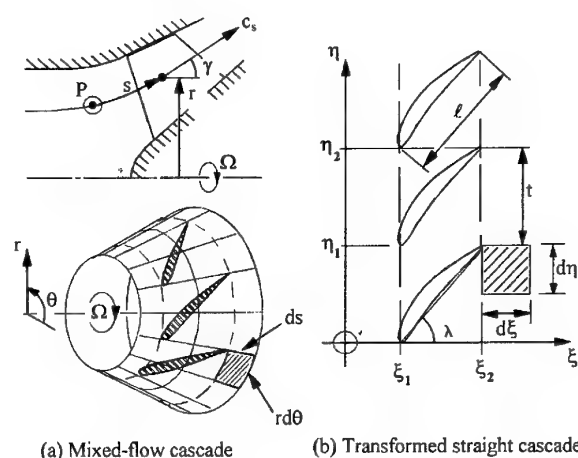


Figure 1 Transformation a mixed-flow fan blade section into an equivalent straight cascade in the ζ plane.

These equations may be integrated to yield the direct coordinate relationships linking the actual blade profile on the surface of revolution to its equivalent rectilinear cascade.

$$\left. \begin{aligned} \xi - \xi_1 &= \int_{s_1}^s \frac{1}{r} ds = \int_{s_1}^s \frac{1}{r \sin \gamma} dr \\ \eta - \eta_1 &= \theta - \theta_1 \end{aligned} \right\} \quad (3)$$

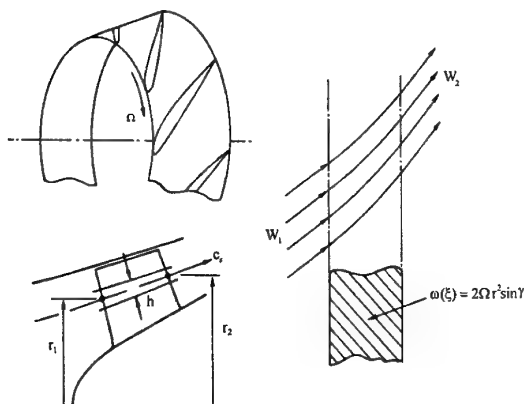


Figure 2 Transformation of the "relative eddy" for a mixed-flow fan into its equivalent in the cascade plane.

If however the blade row is rotating with angular velocity Ω , for example the mixed-flow fan illustrated in Figure 1, then the flow viewed relative to the rotor will have a "relative eddy", that is a distributed vorticity, of magnitude 2Ω throughout the domain. If we wish to model the two-dimensional flow on the surface of revolution as illustrated above in Figure 2, we must therefore account for the component of this $2\Omega \sin \gamma$ normal to the conical surface. This vorticity component must be transformed across to the equivalent vorticity $\omega(\xi)$ in the rectilinear cascade plane. Applying the circulation theorem to the two equivalent elements of area $ds r d\theta$ and $d\xi d\eta$ shown in Figures 1(a) and 1(b) respectively, we then have,

$$\omega(\xi) \cdot d\xi d\eta = 2\Omega \sin \gamma \cdot ds r d\theta$$

or finally, making use of equation (1),

$$\omega(\xi) = 2\Omega r^2 \sin \gamma \quad (4)$$

If we consider first the undisturbed flow as seen by an observer relative to the rotor, in the cascade plane this will comprise the curved flow illustrated in Figure 2. The mainstream velocity rotates from the vector W_1 at inlet to W_2 at exit due to the presence of the vorticity $\omega(\xi)$ within the blade region. In fact the observer would note that the curvature as perceived does in fact curve both upstream and downstream of the blade region due to the presence of the relative eddy throughout the domain. However for

cascade analysis we are only concerned with the blade surface interactions with the mainstream flow within the confines of the blade row. The component of velocity v_Ω in the η direction follows from the definition of vorticity, namely,

$$\omega(\xi) = \frac{dv_\Omega}{d\xi} = \frac{dv_\Omega}{dr} r \sin \gamma \quad (5)$$

Combining this result with equation (4) then yields a direct transformation for the velocity v_Ω in the ξ plane.

$$v_\Omega = \Omega r^2 + \text{constant}$$

By arguments of symmetry we can show that the components at inlet and exit, $v_{\Omega 1}$ and $v_{\Omega 2}$ are equal and opposite in sign, namely,

$$v_{\Omega 1} = -v_{\Omega 2}$$

so that finally the undisturbed mainstream flow in the ξ plane is given by

$$\left. \begin{aligned} U &= U_\infty \\ V &= V_\infty + \Omega \left\{ r^2 - \frac{1}{2} (r_1^2 + r_2^2) \right\} \end{aligned} \right\} \quad (6)$$

where U_∞ and V_∞ are components of the uniform stream \hat{W}_∞ . Now for the arbitrary mixed-flow machine the slope angle γ of the meridional surface will not normally be constant but may vary between leading and trailing edge locations (as for example in a Francis turbine). However, quite remarkably, we observe that the final expression for the mainstream velocity component V , equation (6)b, is totally independent of γ and depends only on the local radius r of the meridional surface. We observe also that the relative eddy of the blade-to-blade flow is zero for the special case of cylindrical meridional flow as obtained in axial turbomachines.

3. Governing equations for vortex dynamic analysis

The governing equation for surface vorticity modelling of the flow through the blade row, (Martensen's equation), is then

$$\begin{aligned} & -\frac{1}{2} \gamma(s_m) + \oint k(s_m, s_n) \gamma(s_n) ds_n \\ & + U_\infty \cos \beta_m + \{V_\infty + \Omega[r^2 - \frac{1}{2}(r_1^2 + r_2^2)]\} \sin \beta_m \\ & + \sum_{j=1}^Z L(m, j) \Delta \Gamma_j = 0 \end{aligned} \quad (7)$$

which states the surface boundary condition that the velocity on and parallel to the blade surface at any point m due to all the available disturbances is to be zero. This is the appropriate boundary condition for the surface vorticity method in which the slip flow at the body surface is represented by the vorticity sheet $\gamma(s_n)$. The first line accounts for the velocity at s_m due to the surface vorticity sheet itself. The second line accounts for the mainstream flow. The last line accounts for all the vortex elements $\Delta \Gamma_j$ which have been shed from the body surface into the fluid since the motion began.

The general approach to solution of equation (7) involves discretisation of the body surface into say M

surface elements Δs_n , whereupon the contour integral is replaced by a summation, resulting in a set of M linear equations as follows.

$$\sum_{n=1}^M K_{mn} \gamma(s_n) = -U_\infty \cos \beta_m - \{V_\infty + \Omega[r^2 - \frac{1}{2}(r_1^2 + r_2^2)]\} \sin \beta_m \quad (8)$$

$$- \sum_{j=1}^Z L(m, j) \Delta \Gamma_j$$

The computation continues over a sequence of time steps of duration Δt , during each of which the surface vorticity due to the new slip flow is shed in the form of M new discrete vortices $\Delta \Gamma_n$ which for element n are of strength

$$\Delta \Gamma_n = \gamma(s_n) \Delta s_n \quad (9)$$

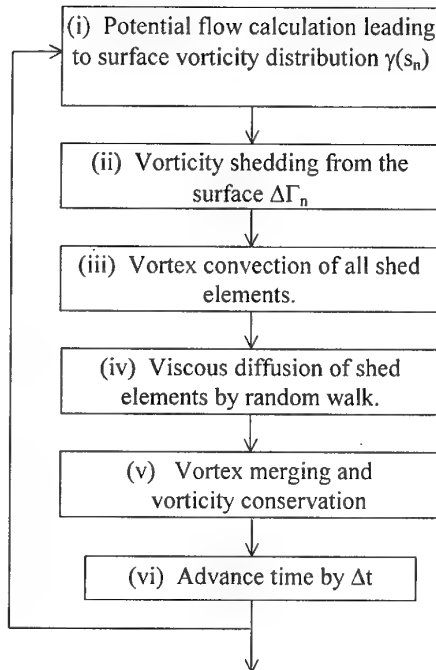


Figure 3 Flow diagram for Vortex Cloud simulation process.

As illustrated by the above simple flow diagram, at each time step a potential flow analysis is completed by the surface vorticity method outlined above. This is followed by the shedding of M discrete vortices resulting from the new slip flow at the body surface. All free vortices are then given a convection under their mutual influence and that of the mainstream for the time step Δt . (We note here that this must be a thermodynamically and thus physically reversible process). The irreversible effects of viscous diffusion are then accounted for by giving each discrete vortex element $\Delta \Gamma_j$ a random walk, Chorin (5), Porthouse (6). Vortices in close proximity are then merged (which avoids excessive convection velocities and helps to control the scale of computation).

Vortices which stray into the body domain during the random walk are eliminated and a total vorticity conservation routine ensures that they are compensated for at the next surface vorticity shedding process.

4. Sample flow analysis for a mixed-flow fan.

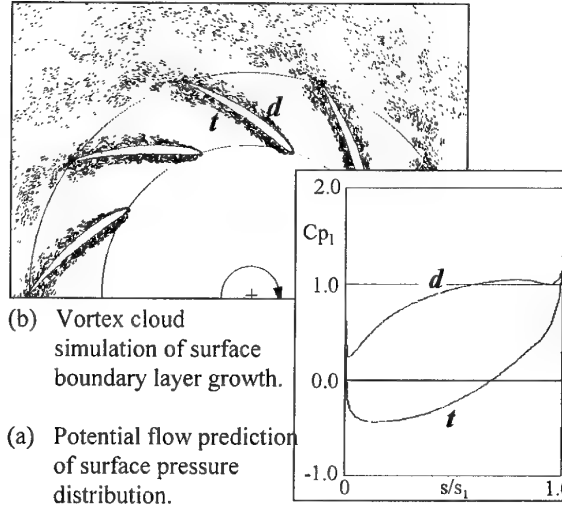


Figure 4 Predicted flow through a mixed-flow fan rotor.

Presented in Figure 4 are predictions of the flow through a mixed-flow fan by the above method, including (a) an inviscid potential flow prediction of the blade surface pressure distribution C_{p1} used for guidance during the design stage of this rotor and (b) a full vortex cloud analysis of the viscous flow taken over 200 time steps $\Delta t = 0.002\text{sec}$. As may be observed from Figure 4(a), the rotor has been designed for shock-free inflow, resulting in attachment of the stagnation point precisely on the blade leading edge and smooth flow on both surfaces. The pressure coefficient C_{p1} appropriate for fans is defined

$$C_{p1} = \frac{p - p_1}{\frac{1}{2} \rho W_1^2} \quad (10)$$

where W_1 is the relative inlet velocity and p_1 the inlet pressure. Thus the pressure rises on both surfaces from a mean value of $C_{p1} = 0.0$ at the leading edge to an outlet value for this design of $C_{p1} \approx 1.0$.

Pressure levels are generally higher on the driving surface d as expected and lower on the trailing surface t and the vortex cloud simulation shows that this diffusing blade row is generally stable on both surfaces, with a tendency towards flow separation in regions of high diffusion close to the trailing edge trailing surface. One also observes a rapid growth of the boundary layer on the driving surface just downstream of the leading edge due to the rapid diffusion in that region too. We note also the tendency of the wake downstream to tend towards formation of a periodic vortex street and to exhibit slip

flow, namely inclination towards the tangential or θ direction.

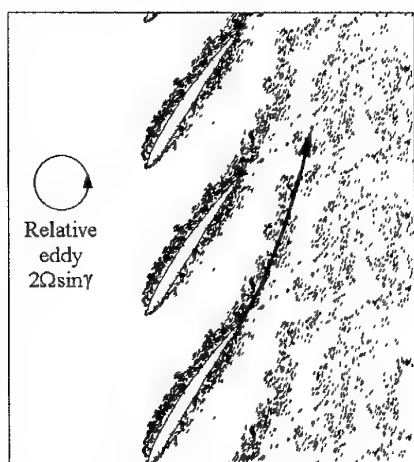


Figure 5 Vortex cloud simulation of mixed-flow fan shown in the equivalent cascade plane.

“Slip” is better illustrated if the vortex cloud simulation is transformed onto the equivalent straight cascade plane as shown in Figure 5. Here the centre-line of the wake has been indicated by an arrow which reveals distinct slip flow curvature downstream due to the presence of the relative eddy $2\Omega\sin\gamma$.

As illustrated by this example, the author’s recommendation for turbomachinery design philosophy is to use frictionless flow calculations when developing the basic blading geometry and then to use CFD, in this case vortex dynamics simulation, to check out the general fluid-dynamic behaviour of the fully viscous flow.

5. Sample flow analyses for radial fans.

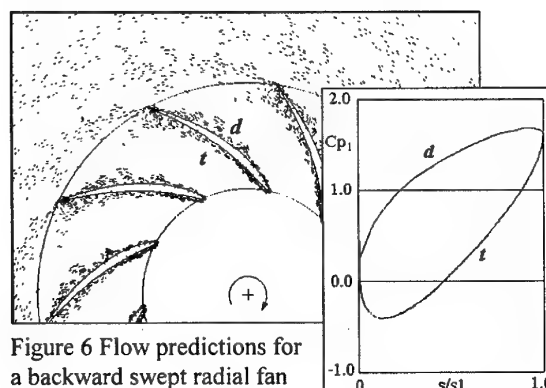


Figure 6 Flow predictions for a backward swept radial fan

Shown in Figure 6 is the predicted flow through a backward swept centrifugal (radial) fan with 8 log-spiral (i.e. uncambered) blades set at a stagger (log-spiral angle) of 45° and with zero pre-whirl. The speed of rotation of 15.055 revs/min. has been chosen to provide shock-free

inflow as may be seen from the predicted inviscid surface pressure distribution Cp_1 . The inlet radius is 0.5m and the radius ratio $r_2/r_1=2.0$. The meridional inlet velocity was set at 1.0m/s. The predicted viscous flow is shown in Figure 6(b) after 200 time steps of magnitude 0.005141s, demonstrating fairly stable flow on both the driving and trailing surfaces of the blades. As may be seen from the Cp_1 plot, the overall pressure rise for this purely radial-flow fan is roughly 1.6 times the relative inlet dynamic head at the rotor inlet radius r_1 , which is well in excess of that for the previous mixed-flow fan example. The reason for this is the increased influence of Coriolis accelerations in the radial rotor. Despite this extra blade loading and thus pumping power, stable flow is still possible as revealed by the vortex cloud analysis.

Fan type	ϕ	ψ
Mixed-flow Fan	0.400	0.361
Backward swept Radial Fan	0.318	0.496

Table 1 - Comparison of the design duty coefficients for the two fan cases.

In this respect it is of some interest to compare the design duty coefficients for these two fans as shown in Table 1 above, where we define ϕ and ψ as follows:

$$\left. \begin{aligned} \phi &= \frac{c_{m2}}{U_2} \text{ Flow coefficient} \\ \psi &= \frac{\Delta p_0}{\rho U_2^2} \text{ Work coefficient} \end{aligned} \right\} \quad (11)$$

where c_{m2} is the exit meridional velocity, $U_2=r_2\Omega$ is the exit blade speed and Δp_0 is the stagnation pressure rise. Thus ϕ represents the flow passing capability of the fan and ψ the energy input capability. It is of interest to note from Table 1 that the work coefficient available from the radial fan is much greater than that for the mixed-flow machine. The flow coefficients however are the other way round. Thus although we may adopt a radial fan where pressure rise is the priority, we will have to accept a lower flow passing performance. The work coefficients for these two fans are in fact very demanding compared with an axial fan for which ψ would not normally exceed a value of 0.3, whereas ϕ values as high as 0.6 may not be uncommon. Many of these aspects of overall turbomachinery performance analysis have been considered by the present author in relation to detailed flow performance analysis for a wide range of turbomachines including axial, mixed-flow and radial pumps and fans, Lewis (7).

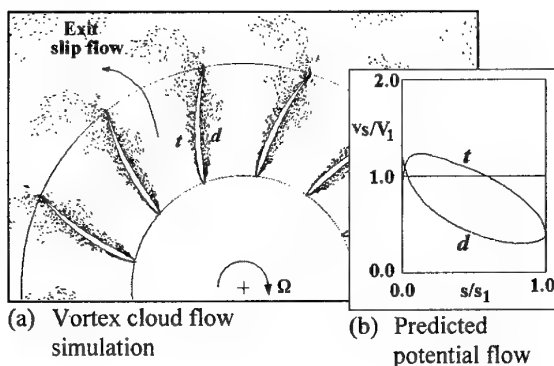


Figure 7 Predicted of the flow through a forward sloping radial fan.

A second example is illustrated in Figure 7 for the case of a forward swept radial fan. The design aim here is raise the work coefficient even further by reversing the sign of the stagger in order to obtain a blade which actually leans forward into the direction of rotation. In this case a stagger angle of $\lambda = -15^\circ$ has been combined with a camber angle of $\theta = 15^\circ$ to generate the blade shape shown in Figure 7(a). As can be seen, there is considerable slip flow at exit contrary to the direction of rotation as expected and a general build up of boundary layer on the driving surface d . The flow is generally stable although there is some evidence of flow separation towards the trailing edge of the trailing surface t . It must be mentioned that with such a design it is essential to introduce substantial pre-whirl at inlet in order to establish smooth entry flow and avoid leading edge separation. In this case the pre-whirl inflow angle was set at $\alpha_2 = 40^\circ$ in the direction of rotation, resulting in the predicted potential flow velocity distribution shown in Figure 7(b) where the surface velocity v_s is expressed as a fraction of the relative inflow velocity V_1 at the rotor inlet edge. We observe here very low velocities on the driving surface but with modest diffusion required over the second half of the blade profile. Conversely on the trailing surface the surface velocity at first rises above the inflow value V_1 and then undergoes rapidly increasing diffusion downstream of the 15% chord location. A summary of the performance data is given below in Table 2 for this radial fan.

Design data	Predicted fan duty
Stagger $\lambda = -15^\circ$	$\phi = 0.50913$
Camber $\theta = 15^\circ$	$\psi = 0.63613$
$\alpha_1 = 45^\circ$	$\alpha_2 = 64.42^\circ$ (predicted)
Number of blades = 13	
$r_1/r_2 = 0.5$	

Table 2 - Design and predicted performance data for the forward swept radial fan.

We note from Table 2 that both the flow and work coefficients are considerably higher than those for the backward swept fan design recorded in Table 1. The effect of forward sweep is to increase the exit swirl generated by the rotor and thus the pressure rise and work coefficient ψ . To ease this it was found necessary by trial and error to raise the meridional velocity level by 80% and thus the flow coefficient ϕ . To accommodate the additional loading the number of blades was also increased from 8 to 13.

In radial and mixed-flow turbomachines the influence of the relative eddy 2Ω can be so dominant, notably for reduced flow rates, that a standing eddy is found on the driving surface of the blades. The first CFD prediction of this using finite difference analysis was given by Stanitz (8) for radially bladed centrifugal compressors and we will conclude this section, on radial machines, with one final example of this shown in Figures 8 and 9.

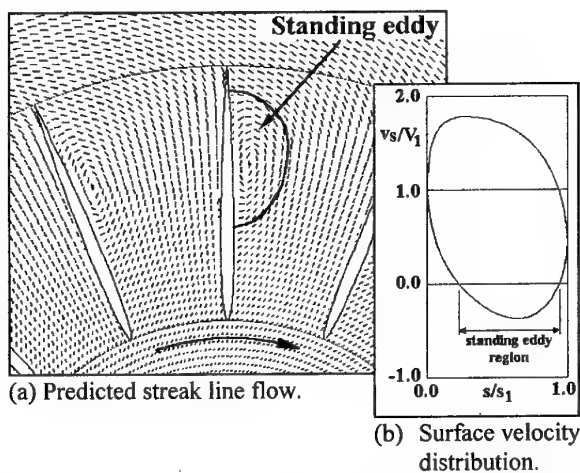


Figure 8 Predicted flow of an inviscid fluid through a radially bladed centrifugal compressor at reduced flow.

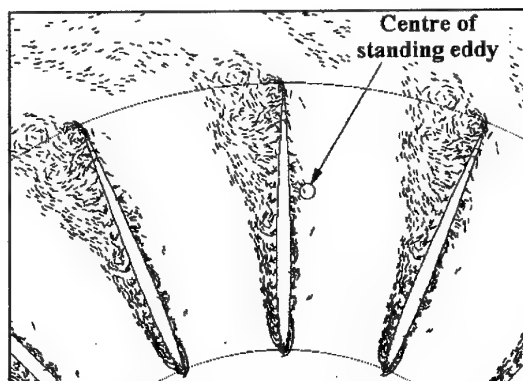


Figure 9 Vortex cloud prediction of the flow of a real fluid through the radial compressor depicted in Figure 8.

To begin with, the flow of an inviscid fluid is considered in Figure 8, which shows the resulting streakline pattern and the predicted surface velocity distribution v_s/V_1 where V_1 is the relative inlet velocity and sufficient pre-whirl has been introduced to provide shock-free inflow. As may be seen from Figure 8(b), the velocity on the driving surface becomes negative over much of the blade surface due to the presence of a large anti-clockwise standing eddy as revealed by Figure 8(a). The slip flow at exit in the direction opposite to rotation is enormous due to the induced effect of this relative eddy. This slip flow combined with the blockage effect of the standing eddy, results in demand for a rapid diffusion over most of the trailing surface from v_s/V_1 values of roughly 1.8 at the quarter chord position to 0.4 at exit.

As seen from Figure 9, this diffusion over the trailing surface for a real fluid results in unstable flow with an extensive separation zone from roughly the mid chord position to the trailing edge, with enormous thickening of the trailing surface boundary layer downstream of the quarter chord position as expected. There is some evidence of the presence of the standing eddy on the driving surface. However, as already pointed out, this is essentially an inviscid eddy due to the relative rotation 2Ω . Since the velocities are low in this region, there is consequently very little penetration of viscous diffusion into this eddy, although there is a general build up of low velocity fluid at its centre. Furthermore, one or two vortex elements have escaped into the outer flow (due to the scatter effect of the random walk procedure), and these indicate that the general local flow pattern is close to that of the predicted inviscid flow of Figure 8(a). Thus it is very clear from this study that inviscid flow calculations remain very powerful tools for the basic design/analysis process of a turbomachine and should never be discarded in favour of pure CFD simulation. The subsequent CFD fluid prediction then adds essential further insights which highlight the predominating additional effects of viscous diffusion. This particular test case can be regarded as an extreme example and perhaps the hardest test of any CFD procedures. In more practical and realistic turbomachines much more modest flow situations are likely to be found, thus increasing our confidence in the recommended combination of both inviscid and full CFD procedures for design/analysis. The final case of a Francis turbine to be presented in the next section illustrates this point of view.

6. Flow through a Francis Turbine rotor.

Figure 10 shows the meridional view of a model Francis turbine comprising typically three blade rows, namely fixed pitch stay vanes, variable pitch guide vanes and the rotor or "runner". For the purpose of meridional flow computations, the annulus is fitted with a grid which is aligned with the annulus walls and the blade leading and trailing edge sections. Furthermore the longitudinal grid lines roughly demarcate the meridional stream

surfaces which interact with the blading to form mixed-flow or radial cascades. We will concern ourselves here with just the runner which comprises a series of blade sections ranging from almost radial cascades at the hub with radial in-flow, to almost axial cascades at the casing.

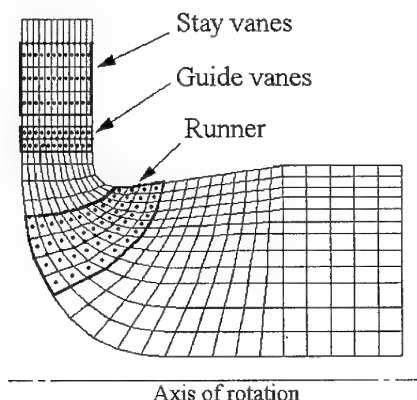


Figure 10 Meridional view of a Francis turbine.

Focusing on the hub section, the dominantly radial meridional flow introduces strong relative eddy and Coriolis accelerations in a region where, due to the convex curvature of the meridional streamlines, meridional velocities would tend to be low. The outcome of this combination of effects could be the presence of a standing eddy on the runner blade driving surface, a condition which has just been avoided in this design as may be seen from the predicted surface velocity distribution shown in Figure 11 below.

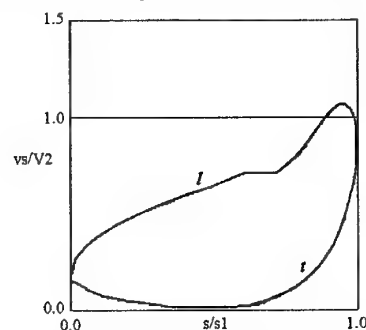


Figure 11 Predicted surface velocity distribution on Francis turbine runner hub section.

We note that the surface velocity is extremely low over the centre section of the high pressure trailing surface t of the blade due to the relative eddy and with slightly higher loading would result in the generation of a standing eddy. Thus with the same head but reduced flow, obtained by increasing the stagger of the inlet guide vanes, a standing eddy would result. Conversely with increased flow rate at the same head, the velocity on the trailing surface would be increased. This turbine is thus operating here at one extreme of its available flow range, namely reduced flow rate. We note also that suitable setting of the guide vane angle has enabled us to retain

smooth entry flow and this condition is confirmed by the vortex cloud simulation shown in Figure 12 below.

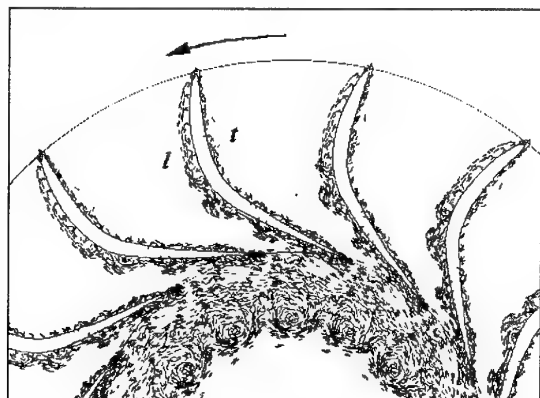


Figure 12 Vortex cloud simulation of the Francis turbine runner hub section flow at reduced flow rate.

Figure 12 shows the flow through the hub section viewed normal to the meridional stream surface. The technique used here is first to transform the predicted flow into the straight cascade plane through equations 2 as illustrated in Figures 1 and 5, and from there into an equivalent conical surface with the same average cone angle as the actual meridional streamline. This conical surface is finally unwrapped onto a flat plane for visualisation as seen above in Figure 12. From this presentation we observe as expected that the flow on both blade surfaces is stable. On the heavily loaded leading surface *l*, where the surface velocity rises fairly steadily from about $v_s/V_2 = 0.2$ at the leading edge to the value 1.0 at exit (see Figure 11), the boundary layer grows progressively with some thinning towards the high velocity throat region. On the trailing surface *t* on the other hand, as might be anticipated, there is limited boundary layer growth over most of the blade surface due to the very low mainstream velocities. This flow computation represents the starting motion taken over a period sufficiently long for the flow to have approached the steady state and the starting vortices may be seen downstream of the trailing edges.

Conclusions

To conclude, a vortex element CFD methodology has been presented comprising the use of both inviscid quasi-three-dimensional analysis for design of turbomachines and full vortex cloud modelling of the cascade or blade-to-blade elements.

Inviscid modelling involves the superposition of a series of mixed-flow blade sections (typically six from hub to casing) upon a circumferentially averaged meridional flow. This inviscid analysis is recommended for basic design purposes and involves iterative

alternating computations of the meridional and blade-to-blade flows including mutual interactions.

The main purpose of this paper has been to introduce an extension of full vortex cloud simulation of the real viscous flow to mixed-flow cascades and its adaption to the complete Computational Fluid Dynamic Vortex Analysis of axial, radial or mixed-flow turbomachines including its use for design/analysis of Francis turbines.

References

- (1) Lewis, R.I. (1991) "Vortex Element Methods for Fluid Dynamic Analysis of Engineering Systems.", Engine Technology Series, Cambridge University Press.
- (2) Lewis, R.I. (1999). "Vortex element methods, the most natural approach to flow simulation - A review of methodology with applications." Vortex Methods, Selected Papers of the First International Conference On Vortex Methods, Kobe.
- (3) Lewis, R.I. (2000) "Development of vortex dynamics for simulation of turbomachine cascades and blade rows.", Journal of Computational and Applied Mechanics, Vol. 1, No. 2, pp 1-13, Miskolc, Hungary.
- (4) Zhu, Baoshan, Kamemoto, Kyoji (1999) "Simulation of the unsteady interaction of a centrifugal impeller with its diffuser by an advanced vortex method.", Proc. of the First International Conference on Vortex Methods, Kobe, pp 263-275.
- (5) Chorin, A.J. (1973) "Numerical study of slightly viscous flow.", J. Fluid Mech., **57**, pp 785-796.
- (6) Porthouse, D.T.C. & Lewis, R.I. (1981) "Simulation of viscous diffusion for extension of the surface vorticity method to boundary layers and separated flows.", J. Mech. Eng. Sci., I. Mech. E., **23**, No. 3, pp 157-167.
- (7) Lewis, R.I. (1996) "Turbomachinery Performance Analysis.", Butterworth-Heinemann (Formerly co-published by W. Arnold with John Wiley & Sons Inc.).
- (8) Stanitz, J.D. (1952) "Some theoretical investigations of impellers in radial and mixed-flow centrifugal compressors.", Trans. ASME, **74**, No. 4.

NUMERICAL ANALYSIS OF VORTEX INSTABILITY IN THE ROTOR WAKE

Duck Joo Lee and Ki Hoon Chung

Department of Mechanical Engineering, Division of Aerospace Engineering,
Korean Advanced Institute of Science and Technology,
Kusong-Dong, YuSong-Gu, Taejon, 305-701, Korea /Email: djlee@mail.kaist.ac.kr

Ki Wahn Ryu

Department of Aerospace Engineering, Chonbuk National University,
Duckjin-Dong, Duckjin-Gu, Chonju, Chonbuk, 561-756, Korea /Email: kwryu@moak.chonbuk.ac.kr

ABSTRACT

Wake instability is indirectly analyzed by calculating the vortex-induced noise spectrum, because the sound source term at low Mach number is linearly dependent on the third-order derivatives of the vorticity distributions and their position vectors. Wake geometries of a two-bladed rotor in axial flights are calculated by using a time-marching free-wake method without a non-physical model of the far wake. The acoustic field can be obtained by using acoustic analogy. To obtain the sound pressure accurately, detailed descriptions of the vortex motion are required.

To show the accuracy of the vortex-motion calculation, the tip-vortex geometries of the present calculation are compared with those done in small-scaled rotor experiment. The accuracy of the vortex sound calculation is validated by comparing the numerical solution with the analytic one of circular vortex ring interaction.

From the noise calculation of tip-vortex pairing phenomenon, it can be known that the tip-vortex pairing amplifies the noise amplitude and generates new dominant frequencies. And from these new dominant peak components of noise spectrum, the pairing period and an instability mode can be numerically analyzed.

1. INTRODUCTION

An improved understanding of the physical nature of the vortical wake is the most important key in accurately predicting the aerodynamics, noise, and stability of the helicopter rotor. The inability to fully understand and model the tip

vortices and the rotor wake limits the ability to design newer helicopter with better efficiency, low vibration, and reduced rotor noise levels. One problem that adversely influences rotor wake understanding is the inability to faithfully analyze the various types of wake disturbances and instabilities that have been observed in rotor experiments.

Wake instabilities often have their source in 'pairing' or localized roll-up between two adjacent tip-vortex filaments. Landgrebe (1) and Tangler et al. (2) first observed that the tip vortices shed from a two-bladed rotor could interact with each other significantly. Widnall (3) and Gupta & Loewy (4) tried to analyze this pairing phenomenon using linear stability theory. Recent experiments (5 & 6) showed more detailed procedures of the tip-vortex pairings.

In the present work, the vortex sound is linearly dependent on the third-order derivatives of the vorticity distributions along the wake and their position vectors (7-10). Therefore, detailed motions of the vortex due to instability are reflected on the far-field vortex acoustic field. The acoustic field can be obtained by using acoustic analogy. To obtain the sound pressure accurately, detailed descriptions of the vortex motion are required. To show the accuracy of the vortex-motion calculation, the tip-vortex geometries of the present calculation are compared with those done in small-scaled rotor experiment. The accuracy of the vortex sound calculation is validated by comparing the numerical solution with the analytic one of circular vortex ring interaction. From the noise calculation of tip-vortex pairing phenomenon, the dominant instability mode that occurs pairing is analyzed.

2. TIP-VORTEX PAIRING

Figure 1 shows a sequence of images of the tip vortex development at the rotor collective angle of 9° and the climb rate of 3.5 fps. The vortices from the two blades are identified by their numbers, i.e. an odd numbered vortex belongs to one blade and an even numbered to the other. The time spacing between each successive frame is not constant, but it was chosen to show the progress of the pairing phenomena. The first frame shows two clear vortices, marked '3' and '4'. In the next frame, the vortex '3' has begins to roll up with '4'. This process continues through the next two frames, until '3' and '4' have essentially interchanged their positions while moving downstream (left direction in figure 1).

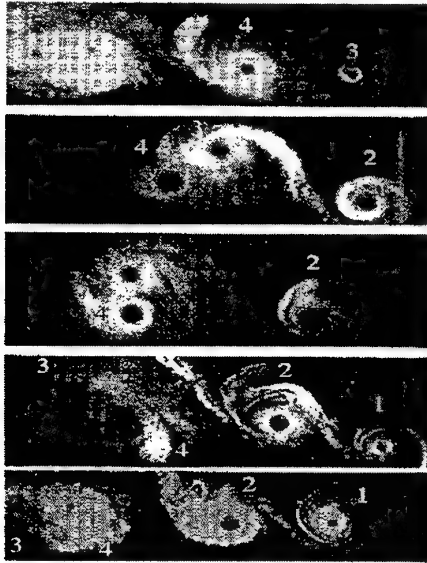


Figure 1. Sequence of tip-vortex pairing from the individual blade, 9° collective, 3.5 fps climb rate (Caradonna et al and Komerath et al. (6))

3. FLOW FIELDS

3.1 Basic Concept

The fluid surrounding a body is assumed to be inviscid, irrotational, and incompressible over the entire flow field, excluding the body's solid boundaries and its wakes. Therefore, a velocity potential $\Phi(\vec{x}, t)$ can be defined and the continuity equation in the inertial frame becomes:

$$\nabla^2 \Phi = 0 \quad (1)$$

The boundary condition requiring zero normal velocity across the body's solid boundaries is:

$$(\nabla \Phi + \vec{V}_{\text{wake}} - \vec{V}) \cdot \vec{n} = 0 \quad (2)$$

where $\vec{V}_{\text{wake}}(\vec{x}, t)$ is the induced velocity due to the vorticity field in the wake, $\vec{V}(\vec{x}, t)$ is the body surface's velocity, and $\vec{n}(\vec{x}, t)$ is the vector normal to the moving surface, as viewed from the blade.

Using the Green's second identity, the general solution of the equation (1) can be constructed by integrating the contribution of the basic solution of source (σ) and doublet (μ) distributions over the body's surface:

$$\Phi(\vec{x}, t) = \frac{1}{4\pi} \int_{\text{body} + \text{wake}} \mu \vec{n} \cdot \nabla \left(\frac{1}{r} \right) ds - \frac{1}{4\pi} \int_{\text{body}} \sigma \left(\frac{1}{r} \right) ds \quad (3)$$

Inserting equation (3) into equation (2) becomes:

$$\left\{ \frac{1}{4\pi} \int_{\text{body} + \text{wake}} \mu \nabla \left[\frac{\partial}{\partial n} \left(\frac{1}{r} \right) \right] ds - \frac{1}{4\pi} \int_{\text{body}} \sigma \nabla \left(\frac{1}{r} \right) ds - \vec{V} \right\} \cdot \vec{n} = 0 \quad (4)$$

The source term is neglected in the case of the thin blade. Thus, only the first part of the equation (3) is used to represent the lifting surface. The constant-strength doublet panel is equivalent to a closed vortex lattice with the same strength of circulation, ($\Gamma = \mu$). Then the induced velocity of the vortex lattice in the equation (4), representing the blade, can be obtained by using the Biot-Savart's law:

$$\vec{V}_{\text{wake}} = - \frac{1}{4\pi} \int \frac{\vec{r} \times \Gamma d\vec{l}}{|\vec{r}|^3} \quad (5)$$

The collocation point is at the mid-span and three-quarter chord of each. The boundary condition of no-flow penetration is satisfied at the collocation point of each lattice. The application of the flow tangency condition (equation 4) to the vortex lattice distribution yields the following linear matrix equation that is to be solved:

$$A_{ij} \Gamma_j = R_i \quad (i, j = 1, n) \quad (6)$$

where A_{ij} is the coefficient matrix of the normal induced velocity on the i -th element of the blade due to the j -th vortex lattice with the unit circulation and Γ_j is the unknown circulation value of the blade vortex lattice. R_i is the normal induced velocity at each control point due to the free stream velocity, the blade-moving velocity, and the wake-induced velocity.

A three-dimensional wing trails the bound circulation (Γ) into the wake. The radial variation of the bound circulation produces the trailed vorticity in the wake, where its direction is parallel to the local free stream direction at each instant it leaves the blade. The azimuthal variation of the bound circulation produces the shed vorticity, oriented radially in the wake. The strengths of the trailed and shed vorticity are determined by the radial and azimuthal derivatives of the bound circulation at the time the wake element leaves the blade. The bound circulation has a peak near the tip, and quickly drops to zero. The trailed sheet therefore has a high strength (proportional to the radial derivative of Γ) at the outer wake, and quickly rolls up into a concentrated tip vortex. The strength of the trailed shed wake vortex is set equal

to the one of the vortex lattice elements, which is located at the trailing edge of the blade. This condition is forced to satisfy the Kutta condition.

Since the wake surface is force-free, each vortex wake element moves with the local stream velocity, which is induced by the other wake element and the blade. The convection velocity of the wake is calculated in the inertial frame. The vortex wakes are generated at each time step. Therefore, the number of wake-elements increases as the blade is rotating. It is clear that a large number of the line elements for the highly curved and distorted wake region like the tip vortex are necessary to describe the vortex filament distortions accurately. In general, the computational time for the calculation of the wake distortion is proportional to the square of the vortex element number.

3.2 Numerical Implementation

A curved element is used to reduce the number of elements. There are many mathematical expressions to represent the three dimensional curves. Generally, the cubic spline used to describe the curves. However, the cubic spline has some disadvantages; the cubic spline requires a large tri-diagonal matrix inversion, and the numerical disturbance of position in any one segment affects all the global curve segments. Therefore, the curve is not adequate to represent the vortex filament motion in strong interaction problems. The parabolic blending, employed here, maintains the continuity of the first derivative in space, which is critical to the self-induced vortex interactions and the interactions with the wakes and blade. The parabolic blending curve, $C(\xi)$, is given by

$$C(\xi) = (1 - \xi)p(r) + \xi q(s) \quad (7)$$

The function of $p(r)$ and $q(s)$ are parametric parabolas through P_1, P_2, P_3 and P_2, P_3, P_4 as shown in figure 2, respectively.

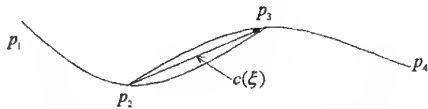


Figure 2. Parabolic blending method

A generalized parametric blending curve is developed from the assumption of the normalized chord length approximation for the position parameters, r at P_2 and s at P_3 , which are linearly related with the parameter ξ in the range of $0 \leq r, s, \xi \leq 1$. Then this blending curve is applied to the equation (5).

The induced velocity by a vortex filament with circulation Γ is given by the usual cut-off approach,

which was formulated by Moore-Rosenhead (12 & 13). It is defined as

$$\vec{v}_{wake} = \frac{1}{4\pi} \int \frac{\vec{r}}{(|\vec{r}|^2 + \mu^2)^{3/2}} \times \Gamma \frac{\partial \vec{y}(\xi, t)}{\partial \xi} d\xi \quad (8)$$

Here $\vec{y}(\xi, t)$ is the position vector of a material point denoted by the Lagrangian variable ξ at an instance, which describes a vortex filament with circulation Γ . The Rosenhead cut-off parameter μ is used to remove the singularity problem in the Biot-Savart's law at the region very close to the vortex filaments.

In this approach, there is not any non-physical assumption about the inner wake roll-up. It is theorized that the computation of the lattice convection is able to correctly predict the inner wake roll-up and the tip vortex concentration. No distinction is made between the inner and the outer filaments that are thus considered to be potential interacting vortices. The trajectory of tip vortex is re-calculated based on the results of the time-marching free-wake analysis. The tip-vortex is represented as the centroid of all the vortex filaments outboard of the maximum circulation filament.

The impulsive rotation method of the free wake calculation causes non-physical strong instability of the initial wake. One of the key points to overcome these non-physical phenomena is that the rotation speed is increased slowly from zero to the required speed. The rotational speed can be assumed to slowly increase from zero following the hyperbolic tangent function. The hyperbolic function is employed to model a slowly starting rotor.

4. ACOUSTIC FIELDS

The acoustic field due to the flow fluctuations can be described as follows:

$$\frac{1}{a_0^2} \frac{\partial^2 p}{\partial t^2} - \nabla^2 p = q \quad (9)$$

where p is the acoustic pressure, a_0 is the ambient acoustic velocity, and q is the acoustic source term. At low Mach number, Lighthill proposed the acoustic source term as $q \approx \rho_0 \partial^2 v_i v_j / \partial x_i \partial x_j$, where \vec{v} is the velocity vector of an incompressible flow and ρ_0 is the density of the ambient fluid. By using the free space Green function $G(\vec{x}, \vec{y}, t - \tau)$, the solution of the equation (9) in the integral form can be obtained as

$$p(\vec{x}, t) = \int G(\vec{x}, \vec{y}, t - \tau) q(\vec{y}, \tau) d^3 \vec{y} d\tau \quad (10)$$

where $\tau = t - |\vec{x} - \vec{y}|/a_0$ is the retarded time, \vec{x} is the observation position vector and \vec{y} is the acoustic source position vector, as shown in figure 3.

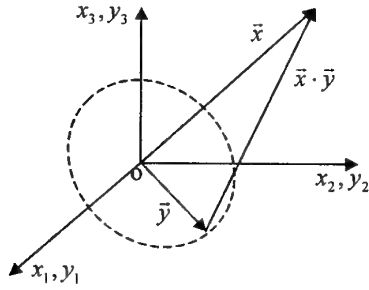


Figure 3. A schematic view of the co-ordinate system

Möhring (9) introduced the Green function vector $\vec{G}(\vec{x}, \vec{y}, t - \tau)$, satisfying the relation $\nabla_y G = \nabla_y \times \vec{G}$ and obtained the final form of the equation (10) for low Mach number flows in the far field:

$$p(\vec{x}, t) = \frac{\rho_0}{12\pi a_0^2 x^3} \frac{\partial^3}{\partial t^3} \int (\vec{x} \cdot \vec{y}) \vec{y} \cdot (\vec{\omega} \times \vec{x}) d^3 \vec{y} \quad (11)$$

where $x = |\vec{x}|$ and $\vec{\omega}$ is the vorticity in the flow field. The equation (11) can be expressed in compact form for the vortex filament as

$$p(\vec{x}, t) = \frac{\rho}{12\pi a_0^2} \sum_{i,k} \frac{\ddot{Q}_{ik}(t - x/a_0) x_i x_k}{x^3} \quad (12)$$

with

$$Q_{ik} = \int y_i (\vec{y} \times \vec{\omega})_k d^3 \vec{y} = \Gamma \int y_i (\vec{y} \times d\vec{y})_k \quad (13)$$

$(i, k = 1, 2, 3)$

where Γ denotes the circulation of the vortex filaments, and $d\vec{y}$ a curve element in the tangential direction of the vortex filament. \ddot{Q}_{ik} denotes the third-order derivative of Q_{ik} . The only non-vanishing components of Q_{ik} are its diagonal elements Q_{11} , Q_{22} and Q_{33} , which additionally satisfy the relation $Q_{11} + Q_{22} + Q_{33} = 0$ of vanishing trace. The three components of Q_{ii} are related to the acoustic pressure in the three axis directions respectively.

5. VALIDATION

5.1 Tip-Vortex Pairing Prediction by Using a Time-Marching Free-Wake Method

The rotor used in this wake calculation is a sub-scale AH-1G model with a 41-inch radius rotating at 1800 rpm. The blade is modeled using 5 chordwise panels and 10 spanwise panels. The distribution of the spanwise panels is modeled by a quarter of sine function that is clustered at the tip of the rotor. This rotor is the same as that used in the experiments of Caradonna et al. and Komerath et al. Twenty-four time-steps are taken per blade revolution and the vortex core radius is 10 % of the

chord length that is commonly used in rotor wake simulations (14).

The tip-vortex pairing process is quantified by using the trajectory tracking method. The trajectories of the tip vortices for the collective angle of 11° at a climb rate of 3.5 ft/s are shown in figure 4. The tip vortex trajectories from the two blades are offset by 180° and it is clear that they are influencing each other. The first crossing of the z/R (axial direction) curves of the two vortices indicates the beginning of the vortex pairing process. The subsequent crossings indicate the rotation of the two vortices about each other. In this case, the results of the time-marching free-wake method show good agreements with the experimental data (6), and it is validated that the tip-vortex pairing occurs at $\zeta = 720^\circ$. These trajectories clearly show that the local radial expansion is the result of adjacent tip vortices beginning to pair together and rotate about each other.

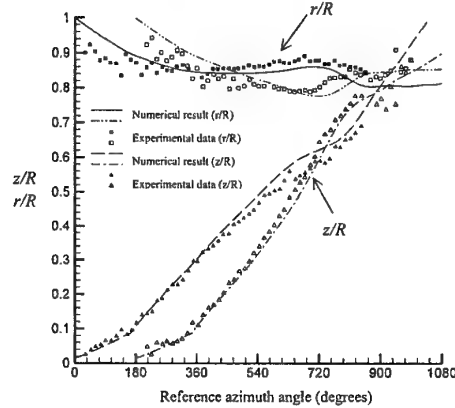


Figure 4. Wake geometries at 11° collective angle, 3.5 ft/s climb rate (Experimental data from (6))

5.2 Sound Radiation from Mutual Threading of Two Circular Vortex Rings

The previous flow and acoustic numerical schemes are used to compare the numerical and the existing analytic solutions (8) of the radiated sound owing to the interaction between two circular vortex rings as shown in figure 5. Two circular vortex rings induce velocities to each other and move to x_3 direction while interchange their positions.

Kambe and Minota (8) calculated the acoustic field due to the mutual threading and head-on collision of the two circular vortex rings analytically by using the Dyson's formula (15). To verify the present numerical method, the mutual threading problem is calculated. Two identical vortex rings are initially chosen to have the same values of the strength $\Gamma = \Gamma_1 = \Gamma_2$, the radius

$R_0 = R_1 = R_2$, the core radius $c_0 = c_1 = c_2$ and the initial separation $z_1 - z_2 = \Delta z_0$.

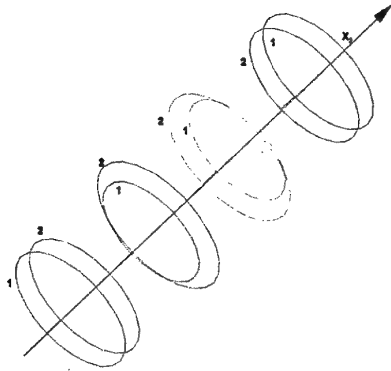


Figure 5. Mutual threading motion of two circular vortex rings.

The numerical results of the acoustic pressure at far fields for the mutual threading case are compared with the analytical results (8) in figure 6. The numerical results show good agreements with the analytic results (10).

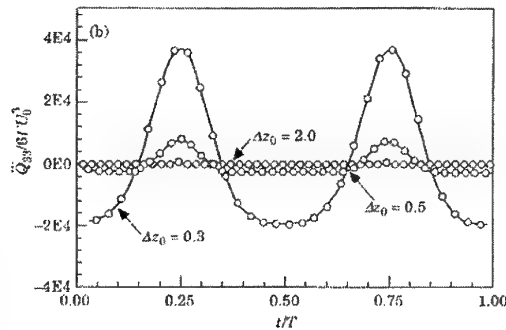


Figure 6. Comparison of the acoustic signals by mutual threading motion. —, Analytic; O, Present

The acoustic pressures \ddot{Q}_{23} in the equation (12) are scaled by $6\Gamma U_0^3$ for different initial distances of $\Delta z_0/R_0 = 0.3, 0.5$ and 2.0 respectively. Here, $U_0 = \Gamma/4\pi R_0$. The periods of the corresponding $\Delta z_0/R_0$ and $T/(R_0/U_0)$ are $0.130, 0.328$ and 3.860 respectively (8).

The acoustic field is closely related to the vortex position at each time-step, as indicated in the equations (12) and (13). The velocity at a vortex filament with circulation Γ is given by the equation (8). The Rosenhead cut-off parameter $\mu(t) = 2\delta_R c(t)$ is proportional to the core radius $c(t)$. The coefficient δ_R depends on the vorticity distribution across the core of the vortex filament. The authors choose $\delta_R = (1/2)\exp(-A-1/2)$ with $A=1$. As indicated in the equation (8), the dynamics of the filament are very dependent on the

core size $c(t)$ and the initial configuration of the filament $\bar{y}(\xi, t=0)$. The initial core radius c_0 is 0.05 for the analytic solution (8). The corresponding core radius used in the Moore-Rosenhead formula is 0.10542 . The vortex strength, time step and number of the vortex elements are the same with those of the rotor wake calculations.

In figure 7, the directivity of acoustic signal due to the mutual threading motion is shown. The noise due to the mutual threading motion has quadruple characteristics and is mainly radiated to the moving direction x_3 .

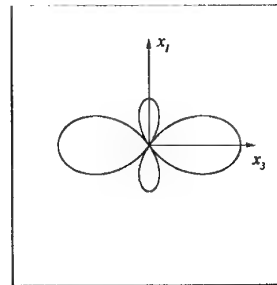
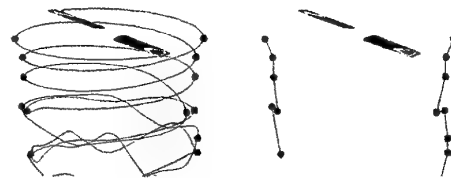


Figure 7. Directivity of acoustic signal by mutual threading motion

6. RESULTS

6.1 Mechanism of Tip-Vortex Pairing

The computed trajectories of the tip-vortices are shown in figure 8. Figure 8 (a) shows the three-dimensional view of the tip vortex trajectories and the right one shows the cross section view of it.



(a) 3D overall view (b) Cross section view

Figure 8. 3D view and cross sectional view of predicted wake geometries at 11° collective angle, 9.6 ft/s climb rate

Figure 9 shows the tip-vortex pairing process obtained at the collective angle of 11° and at the climb rate of 9.6 ft/s. In this figure, vortex '3' begins to pair with '4'. This process continues until '3' and '4' interchange their positions while moving downstream. The tip-vortex pairing consists of a turn of the tip-vortex from one blade rolling around the tip-vortex from the other blade, as shown in the figure 1 even though the different operation conditions are employed in this case.

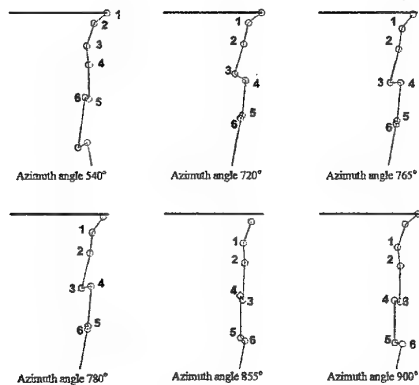


Figure 9. Predictions of Tip-vortex pairing process at 11° collective angle, 9.6 ft/s climb rate

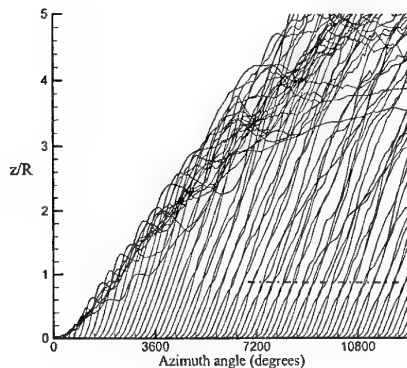
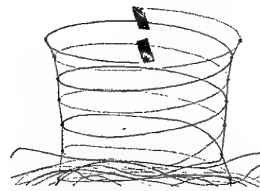


Figure 10. Detailed tip vortex geometry during 35 revolutions at 11° collective angle, 3.5 ft/s climb rate

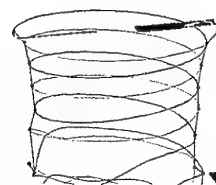
Figure 10 shows the time history of the tip-vortex locations in a fixed cross-section during 35 revolutions from the start-up. The dashed line in the figure 10 indicates the upper boundary of converged geometries of the tip vortices. It appears that, at the beginning of the solution process, the initial vortices merge together into a bundle of starting vortices. Then these starting vortices roll about one another and convect away from the rotor at a speed (the inverse of the curve slope in the figure 10) fairly lower than the individual vortex convection speed and their motions become increasingly chaotic as time passes. Thus the initial wakes in the downstream ultimately become unstable, unsteady or chaotic at a certain distance from the rotor (16).

Figure 11 shows the tip-vortex shape at various revolutions. Figure 11 (a) shows contracted fine tip-vortex geometries at 12 revolutions, that is same as the traditional tip-vortex concept. Figure 11 (b) shows vortex instability period tip-vortex shape at 14 revolutions. The Pairing occurs at far wake

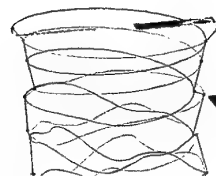
region near the initial wake bundles. And the pairing point moves toward rotor and converged to some position as shown in figure 11 (c). It is the evidence that the initial wakes perturb the tip-vortex and the tip-vortex pairing occurs.



(a) At 12 revolutions



(b) At 14 revolutions



(c) At 30 revolutions

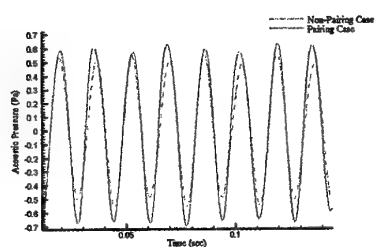
Figure 11. Tip-vortex geometries at various revolutions

6.2 Tip-Vortex Noise & Wake Instability

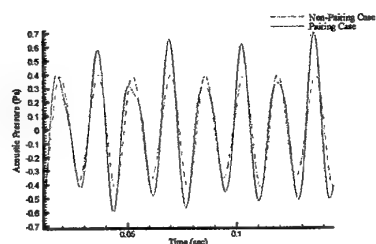
The noises generated by the tip-vortices are calculated by using the equation (11). The strength and geometries of the tip-vortex are obtained from the results of the time-marching free-wake analysis. Figure 12 shows the noise signals at various positions in time domain.

The noises of non-pairing case are calculated by using the unsteady wake geometries during 8~12 revolution. During these revolutions, there is no pairing and the tip-vortex is moving downward with the contraction as shown in figure 10 and figure 11 (a). The noises of pairing case are calculated by using the wake geometries during 30~35 revolution. As shown in figure 10 and figure 11 (b), pairing occurs always and the pairing point is converged to some point. Therefore, the noises of non-pairing case are generated by the downward moving and contracting tip-vortex. Those of pairing case include tip-vortex pairing phenomena additionally. From figure 12, we can know that tip-vortex pairing amplifies the noise amplitude and

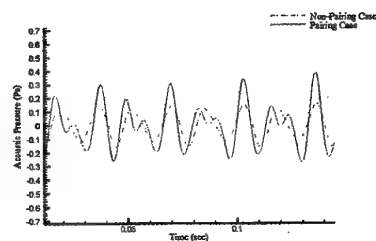
generates new dominant frequencies (See figure 12 (c)).



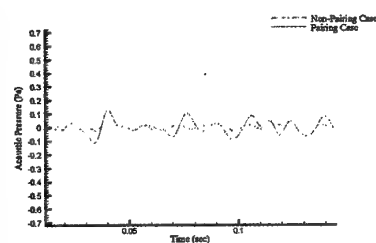
(a) Noise signal at $r=50m$, $\phi = 0^\circ$



(b) Noise signal at $r=50m$, $\phi = 30^\circ$



(c) Noise signal at $r=50m$, $\phi = 60^\circ$



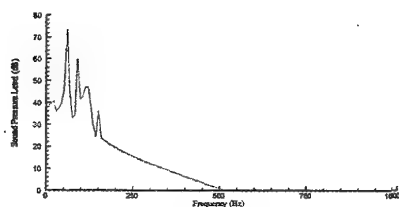
(d) Noise signal at $r=50m$, $\phi = 90^\circ$

Figure 12. Noise generated by Tip-Vortex (in time-domain)

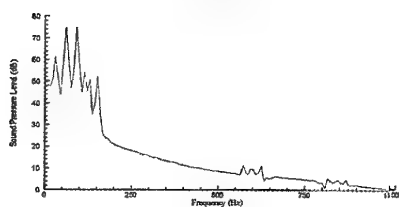
The noise signals of figure 12 (c) in frequency domain are shown in figure 13. Under the non-pairing condition, dominant frequency is 60 Hz as shown in figure 13 (a). In figure 13 (b), under the pairing condition, 30 Hz and 90 Hz frequencies increase significantly with respect to the spectrum in figure 12 (a).

From figure 9, we can know that the period of tip-vortex pairing is one revolution (30 Hz). So the tip-vortex pairing increases the 30 Hz frequency component in the noise. 90 Hz frequency component comes from the perturbation that occurs

the tip-vortex pairing. Gupta & Loewy (4) showed analytically that the two helical vortex filaments could be diverged at the artificially perturbed wave number 1, 3, and 5, etc. The wave number is defined as the numbers of waves per revolution. Before Gupta & Loewy's work (4), Widnall (3) showed that the pairing modes occur due to the perturbations that have the $3/2$ and $5/2$ wave numbers for a single helical vortex filament as shown in figure 14. It can be inferred that, for the case of two helical vortices, pairing modes occur due to 3 and 5 wave numbers. The frequencies of these wave numbers are 90 Hz and 150 Hz.



(a) Non-Pairing Condition



(b) Pairing Condition

Figure 13. Noise signal at $r=50m$, $\phi = 60^\circ$ (in frequency domain)

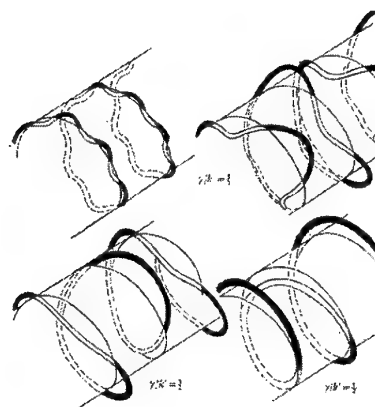


Figure 14. Instability mode shapes in single helical vortex filament (3).

Figure 15 shows the directivities of 30 Hz and 90 Hz components in wake noises. When pairing occurs, directivities of 30 Hz and 90 Hz show quadrupole characteristics. 30 Hz noise component that is increased by pairing period radiates to the direction of rotation axis (90° , 270°) and rotation plane (0° , 180°) as like figure 7. 90 Hz noise component that is increased by the instability

perturbations radiates to 45° , 135° , 225° , 315° directions.

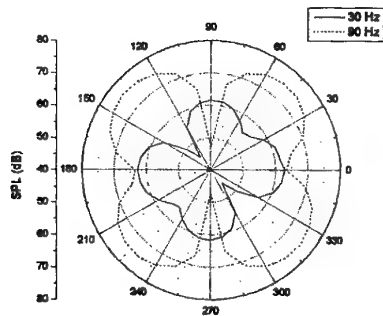


Figure 15. Directivity patterns of 30 Hz and 90 Hz in pairing case

7. CONCLUSION

In this paper, by using the vortex sound calculation that is linearly dependent on the third-order derivatives of the vorticity distributions and their position vectors, the wake instability mode is analyzed. The wake geometries of a two-bladed rotor in axial flights are calculated by using a time-marching free-wake method without a non-physical model of the far wake. The acoustic field can be obtained by using acoustic analogy. To show the accuracy of the flow calculation scheme, the tip-vortex geometries of small-scaled rotor experiment are compared with those of the calculated results. The accuracy of the vortex sound calculation scheme is validated by comparison with analytic solution of circular vortex ring interaction and numerical results.

From the noise calculation of tip-vortex pairing phenomenon, it can be known that the tip-vortex pairing amplifies the noise amplitude and generates new dominant frequencies. And from these new dominant peak components of noise spectrum, the pairing period and an instability mode can be numerically analyzed.

REFERENCES

- (1) Landgrebe, A. J. (1972), "The Wake Geometry of a Hovering Helicopter Rotor and Its Influence on Rotor Performance", *J. American Helicopter Soc.*, 17, (4), Oct., 1972, pp. 3-15.
- (2) Tangler, J. L., Wohlfed, R. M., and Miley, S. J. (1973), "An Experimental Investigation of Vortex Stability, Tip Shapes, Compressibility, and Noise for Hovering Model Rotor", NASA CR-2305
- (3) Widnall, S. E. (1972), "The Stability of a Helical Vortex Filament", *Journal of Fluid Mechanics*, Vol. 54, No. 4, pp. 641-663.
- (4) Gupta, B. P., and Loewy, R. G. (1974), "Theoretical Analysis of the Aerodynamic Stability of Multiple, Interdigitated Helical Vortices," *AIAA Journal*, Vol. 12, No. 10, pp. 1381-1387.
- (5) Martin, P. B., Bhagwat, M. J., and Leishman, J. G. (1999), "Strobed Laser-Sheet Visualization of a Helicopter Rotor Wake," Paper PF118, Proceedings of PSFVIP-2, Honolulu, HI, May 1999.
- (6) Caradonna, F., Hendley, E., Silva, M., Huang, S., Komerath, N., Reddy, U., Mahalingam, R., Funk, R., Ames R., Darden, L., Villareal, L., Gregory, and Wong, O. (1997), "An Experimental Study of a Rotor In Axial Flight", AHS Specialists' Meeting on Aerodynamics and Aeroacoustics, Williamsburg, VA, Oct. 1997.
- (7) Powell, A. (1964), "Theory of vortex sound", *Journal of Acoustical Society of America*, Vol. 36, pp. 177-195
- (8) Kambe, T. and Minota, T. (1981), "Sound radiation from vortex system", *Journal of sound and vibration*, Vol. 74, pp. 61-72
- (9) Möhring, W. (1990), "Sound radiation by two elliptic vortex rings", *Journal of sound and vibration*, Vol. 140, pp. 307-314
- (10) Ryu, K. W. and Lee, D. J. (1997), "Sound radiation from elliptic vortex rings: evolution and interaction", *Journal of sound and vibration*, Vol. 200, pp. 281-301
- (11) Na, S. U. and Lee, D. J. (1999), "Numerical Simulations of Wake Structure Generated by Rotating Blades Using a Time-Marching Free-Vortex-Blob Method", *European Journal of Mechanics*, 18, (1), pp. 147-159.
- (12) Moore, D. W. (1972), "Finite Amplitude Waves on Aircraft Trailing Vortices", *Aeronautical Quarterly*, 23, 1972, pp. 307-314.
- (13) Rosenhead, L. (1930), "The Spread of Vorticity in The Wake behind a Cylinder," *Proc. Roy. Soc.*, A127, 1930, pp. 590-612.
- (14) Leishman, J. G., Baker, A., Coyne, A. (1996), "Measurements of Rotor Tip vortices Using Three-Component Laser Doppler Velocimetry", *J. American Helicopter Society*, 41, (4), pp. 342-353.
- (15) Dyson, F. W. (1893), "The potential of an anchor ring," *Philosophical Transactions of the Royal Society of London*, A 184, 1893, pp. 1041-1101
- (16) Chung, K. H., Na, S. U., Jeon, W. H., Lee, D. J. (2000), "A Study on Rotor Tip-Vortex Pairing Phenomena by using Time-Marching Free-Wake Method," *American Helicopter Society 56th Annual Forum*, Virginia Beach, Virginia, May 2-4, 2000.

ENGINEERING APPLICATION OF THE VORTEX METHODS DEVELOPED IN YOKOHAMA NATIONAL UNIVERSITY (YNU)

Kyoji Kamemoto

Department of Mechanical Engineering, Graduate School of Engineering, Yokohama National University
79-5 Tokiwadai, Hodogaya-ku, Yokohama, Kanagawa 240-8501, Japan /Email: kame@post.me.ynu.ac.jp

ABSTRACT

This paper introduces the mathematical treatment and recent engineering application of the advanced vortex methods of Biot-Savart law, developed by the group of the present author. From consideration of mathematical basis of the methods, it becomes encouragingly clear that the vortex methods have so much interesting features that they consist of simple algorithm based on physics of flow and provide easy-to-handle and completely grid-free Lagrangian calculation of unsteady and vortical flows without use of any RANS type turbulent models. Reviewing recent attractive studies on development of large eddy simulation models for the vortex methods, the subjects to be solved for practical engineering application of the Lagrangian large eddy simulation are shortly discussed. As examples of application of the latest vortex methods developed in Yokohama National University, numerical results of investigations of the unsteady flows around an airfoil oscillating in a uniform flow, complex flows through a centrifugal impeller rotating in a volute casing are briefly explained and a few topics of numerical investigation of unsteady flows through a wind turbine and others are introduced.

1. INTRODUCTION

Although the recent progress of computational fluid dynamics is quite rapid, the numerical analysis of a higher Reynolds number flow seems still not so easy, from the viewpoint of engineering applications. The applicability of the conventional turbulence models of time-mean type seems questionable as far as unsteady separated flows are concerned. And the Large Eddy Simulation of Eulerian type inevitably meets crucial difficulties in its application to flows of higher Reynolds number, because the scheme essentially needs reasonably fine grids according to the magnitude of Reynolds number.

On the other hand, the vortex methods have been developed and applied for analysis of complex, unsteady and vortical flows in relation to problems in a wide range

of industries, because they consist of simple algorithm based on physics of flow. Leonard (1980)⁽¹⁾ summarized the basic algorithm and examples of its applications. Sarpkaya (1989)⁽²⁾ presented a comprehensive review of various vortex methods based on Lagrangian or mixed Lagrangian-Eulerian schemes, the Biot-Savart law or the Vortex in Cell methods. Kamemoto (1995)⁽³⁾ summarized the mathematical basis of the Biot-Savart law methods.

Recently, the first International Conference on Vortex Methods has been held in 1999, in Kobe, Japan, in which a review of vortex element methods by Lewis⁽⁴⁾, a proposal of a hybrid vortex method by Graham et al.⁽⁵⁾, 3D simulation of separated flow around an ellipsoid by Unal et al.⁽⁶⁾, a report on vortex method analysis of turbulent flows by Bernard⁽⁷⁾, simulation of particulate flows using a Vortex in Cell method by Walther et al.⁽⁸⁾, a convergence study for the vortex method with boundaries by Ying⁽⁹⁾, numerical prediction of rotor tip-vortex roll-up in axial flight by a time marching free-wake method by Lee⁽¹⁰⁾, achievements and challenges by a 3D Vortex in Cell Method by Cottet⁽¹¹⁾, and other interesting works related with different kinds of vortex methods were presented. In this conference, Kamemoto and Miyasaka (1999)⁽¹²⁾ proposed a vortex and heat elements method and showed application results of analysis of unsteady and forced-convective heat transfer around a circular cylinder in a uniform flow. After the conference, an interesting book consisting of selected papers of the conference has been published in 2000⁽¹³⁾.

As well as many finite difference methods, it is a crucial point in vortex methods that the number of vortex elements should be increased when higher resolution of turbulence structures is required, and then the computational time increases rapidly. Recently, in order to overcome the crucial point, some of leading researchers examined spatial averaging models of turbulence in high Reynolds number flows for Lagrangian large eddy simulation. Leonard and Chua (1989)⁽¹⁴⁾ proposed application of the Smagorinsky model in simulations of interaction between interlocked vortex rings and interaction between two colliding vortex rings. Mansfield et al. (1998)⁽¹⁵⁾ (1999)⁽¹⁶⁾ proposed a dynamic eddy viscosity model of subfilter-scale stresses for

Lagrangian vortex element methods and applied it to simulation of collision of coaxial vortex rings. Kiya et al. (1999)⁽¹⁷⁾ carried out simulation of an impulsively started round jets by a 3-d vortex method using the Smagorinsky model. Saltara et al. (1998)⁽¹⁸⁾ simulated vortex shedding from an oscillating circular cylinder with use of turbulence modeling of Smagorinsky type in a Vortex in Cell method.

In this paper, attractive characteristics of the Biot-Savart law vortex methods developed and examined up to this time in Yokohama National University are described, explaining the mathematical background. And, introducing the new movement of turbulence modeling for Lagrangian vortex methods, the subjects of the vortex methods which should be solved as a tool of the Lagrangian large eddy simulation are shortly discussed. Then, some of typical results of numerical simulation of two and three-dimensional unsteady separated flows are introduced.

2 ALGORITHMS OF VORTEX METHODS BASED ON BIOT-SAVART LAW

2.1 Mathematical Basis

Since the vortex methods have been developed for numerical analysis of incompressible and unsteady flow, their governing equations are thought to be based on the Navier-Stokes equation and the continuity equation for incompressible flow which are written in vector form as follows.

$$\frac{\partial \mathbf{u}}{\partial t} + (\mathbf{u} \cdot \text{grad}) \mathbf{u} = -\frac{1}{\rho} \text{grad } p + \nu \nabla^2 \mathbf{u} \quad (1)$$

$$\text{div } \mathbf{u} = 0 \quad (2)$$

Alternative expression of the governing equations of viscous and incompressible flow gives the vorticity transport equation and pressure Poisson equation which are derived from the rotation and divergence of Navier-Stokes equations, respectively

$$\frac{\partial \boldsymbol{\omega}}{\partial t} + (\mathbf{u} \cdot \text{grad}) \boldsymbol{\omega} = (\boldsymbol{\omega} \cdot \text{grad}) \mathbf{u} + \nu \nabla^2 \boldsymbol{\omega} \quad (3)$$

$$\nabla^2 p = -\rho \text{div}(\mathbf{u} \cdot \text{grad } \mathbf{u}) \quad (4)$$

where \mathbf{u} is a velocity vector. The vorticity $\boldsymbol{\omega}$ is defined as

$$\boldsymbol{\omega} = \text{rot } \mathbf{u} \quad (5)$$

Lagrangian expression for the vorticity transport equation (3) is given by

$$\frac{d\boldsymbol{\omega}}{dt} = (\boldsymbol{\omega} \cdot \text{grad}) \mathbf{u} + \nu \nabla^2 \boldsymbol{\omega} \quad (6)$$

When a two-dimensional flow is dealt with, the first term of the right hand side in equation (6) disappears and so the two-dimensional vorticity transport equation is simply expressed as

$$\frac{d\omega}{dt} = \nu \nabla^2 \omega \quad (7)$$

In the Biot-Savart law methods, the vorticity transport equation (6) is numerically solved by the operator-splitting scheme of Chorin (1973)⁽¹⁹⁾⁽²⁰⁾. If the vorticity of a fluid particle at time t is written as $\omega(t)$, we obtain an approximate expression of the change of vorticity through convection and diffusion during a small time interval dt as follows.

$$\boldsymbol{\omega}(t+dt) = \boldsymbol{\omega}(t) + (\boldsymbol{\omega} \cdot \text{grad}) \mathbf{u} \cdot dt + \nu \nabla^2 \boldsymbol{\omega} \cdot dt \quad (8)$$

In equation (8), the second term in the right hand side is based on the three-dimensional stretching of vorticity, which always becomes zero for two-dimensional flow, and the third term is the rate of viscous diffusion of vorticity. If the Reynolds number of the flow is sufficiently large, the convection term is considered much larger than the diffusion term, and thus, the third term in equation (8) may be neglected in the computation. Furthermore, if the high Reynolds number flow is two-dimensional, equation (8) is approximated by a simple equation like $\boldsymbol{\omega}(t+dt) = \boldsymbol{\omega}(t) = \text{constant}$. Therefore, if we take a small sectional area ds for the fluid particle and the vorticity is assumed constant in this area, the two-dimensional fluid particle is thought a free vortex element which transports a constant circulation $\Gamma = \omega ds$.

On the other hand, the motion of the fluid particle at a location \mathbf{r} is represented by a Lagrangian form of a simple differential equation.

$$\frac{d\mathbf{r}}{dt} = \mathbf{u} \quad (9)$$

Then, the trajectory of the fluid particle over a time step dt is approximately computed from the Adams-Bashforth method as follows.

$$\mathbf{r}(t+dt) = \mathbf{r}(t) + \{1.5\mathbf{u}(t) - 0.5\mathbf{u}(t-dt)\}dt \quad (10)$$

2.2 Generalized Biot-Savart Law

As explained by Wu and Thompson (1973)⁽²¹⁾, the Biot-Savart law can be derived from integration of the vorticity definition equation (5) as

$$\mathbf{u} = \int_V \boldsymbol{\omega}_0 \times \nabla_0 G dv + \int_S \{(\mathbf{n}_0 \cdot \mathbf{u}_0) \cdot \nabla_0 G - (\mathbf{n}_0 \times \mathbf{u}_0) \times \nabla_0 G\} ds \quad (11)$$

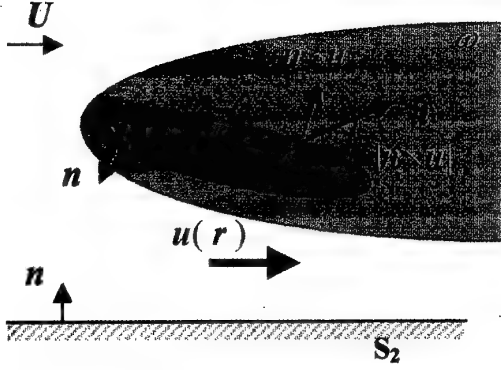


Figure 1: Flow field involving vorticity region.

Here, subscript "0" denotes variable, differentiation and integration at a location r_0 , and n_0 denotes the normal unit vector at a point on a boundary surface S . And G is the fundamental solution of the scalar Laplace equation with the delta function $\delta(r-r_0)$ in the right hand side, which is written as

$$G = \frac{1}{2\pi} \log\left(\frac{1}{R}\right) \quad (2-D) \quad (12)$$

$$\text{or} \quad G = \frac{1}{4\pi R} \quad (3-D) \quad (13)$$

here, $R = r - r_0$, $R = |R| = |r - r_0|$.

In equation (11), the inner product, $n_0 \cdot u_0$ and the outer product $n_0 \times u_0$ stand for respectively normal and tangential velocity components on the boundary surface, and they respectively correspond to source and vortex distributions on the surface.

Therefore, it is mathematically understood that a velocity field of viscous and incompressible flow is arrived at the field integration concerning vorticity distributions in the flow field and the surface integration concerning source and vortex distributions around the boundary surface as shown in Figure 1.

2.3 Calculation of Pressure

Instead of the finite difference calculation of the pressure Poisson equation represented by equation (4), the pressure in the flow field is calculated from the integration equation formulated by Uhlman (1992)⁽²²⁾ as follows.

$$\beta H + \int_S H \frac{\partial G}{\partial n} ds = - \int_V \nabla G (u \times \omega) dv - \int_S \left\{ G \cdot n \cdot \frac{\partial u}{\partial t} + \nu \cdot n \cdot (\nabla G \times \omega) \right\} ds \quad (14)$$

Here, β is $\beta = 1$ inside the flow and $\beta = 1/2$ on the boundary S . G is the fundamental solution given by

equation (12) or (13), and H is the Bernoulli function defined as

$$H = \frac{p}{\rho} + \frac{u^2}{2} \quad (15)$$

here, $u = |u|$.

2.4 Introduction of Nascent Vortex Elements

The vorticity field near the solid surface must be represented by proper distributions of vorticity layers and discrete vortex elements so as to satisfy the non-slip condition on the surface. In the advanced method developed by the group of the present authors, a thin vorticity layer with thickness h_i is considered along the body surface, and the surface of outer boundary of the thin vorticity layer is discretized by a number of vortex sheet panels as shown in Figure 2.

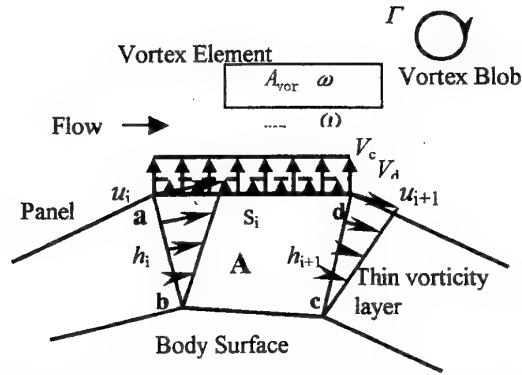


Figure 2: Thin vorticity layer and nascent vortex element.

If the flow is considered to be two-dimensional for convenience, and a linear distribution of velocity in the thin vorticity layer is assumed, the normal convective velocity V_c on a panel can be expressed using the relation of continuity of flow and the non-slip condition on the solid surface for the element of the vorticity layer [abcd] as

$$V_c = \frac{1}{s_i} \left(\frac{h_i u_i}{2} - \frac{h_{i+1} u_{i+1}}{2} \right) \quad (16)$$

here, s_i , h_i and u_i respectively denote the panel length, vorticity layer thickness and tangential velocity at a panel edge. Using the normal velocity for each panel expressed by equation (16), the strength of the vortex sheet of the panel for the next step of calculation can be evaluated numerically from equation (11).

On the other hand, the vorticity of the thin shear layer diffuses through the panel into the flow field. In order to consider this vorticity diffusion, a diffusion velocity is employed in the same manner as the vorticity layer spreading method proposed by Kamemoto (1995)⁽³⁾. The

vorticity layer spreading method is based on the viscous diffusion of the vorticity in the shear layer developing over a suddenly accelerated plate wall. In this case, the displacement thickness of the vorticity layer (δ) diffuses with the progress of time as $\delta = 1.136(\nu T)^{1/2}$ from the solid surface at a time T . Differentiating δ by T and substituting the distance of a panel from the solid surface h_i into δ , we obtain the diffusion velocity V_d at the panel as follows.

$$V_d = \frac{1.136^2 \nu}{h_i + h_{i+1}} \quad (17)$$

here, ν is kinematic viscosity of the fluid. If the value of $(V_c + V_d)$ becomes positive, a nascent vortex element is introduced in the flow field, where the thickness and vorticity of the element are given as follows

$$h_{vor} = (V_c + V_d) \cdot dt \quad (18)$$

$$\omega_{vor} = \frac{\Gamma}{A + A_{vor}} \quad (19)$$

Here, Γ is the circulation originally involved in the element of the vorticity layer [abcd], and A and A_{vor} are the areas of the vorticity layer element and the nascent vortex element.

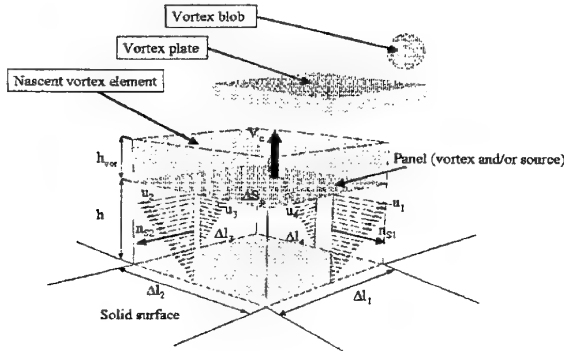


Figure 3: Introduction of three-dimensional nascent vortex element.

In case of three-dimensional flow calculation, a three-dimensional nascent vortex element of a rectangular parallelepiped is introduced in the same manner as the two-dimensional case, through each vortex sheet panel of the outer boundary of a thin vorticity layer. The details of treatments have been explained in the paper by Ojima and Kamemoto (2000)⁽²³⁾. As shown in Figure 3, if a linear distribution of velocity in the thin vorticity layer is assumed, the normal convective velocity V_c on a panel can be expressed by using the relation of continuity of

flow and non-slip condition on the solid surface for the element of the vorticity layer

$$V_c = \frac{1}{\Delta S_p} \sum_{i=1}^4 \int_{\Delta S_i} u_{si} ds \quad (20)$$

here, $u_{si} = \mathbf{u}_i \cdot \mathbf{n}_{si}$ and $\Delta S_i = h \cdot \Delta l_i$.

Where, ΔS_p , \mathbf{u}_i and \mathbf{n}_{si} respectively denote the panel area, the velocity vector and the normal vector on the side sectional planes of the element of the vorticity layer. Using the normal velocity for each panel expressed by equation (20), the intensity of the vortex sheet for the following step can be calculated numerically from equation (11).

In the same manner as the two-dimensional case, the viscous diffusion velocity at the panel is given as

$$V_d = \frac{c^2 \nu}{2h}, \quad (c=1.136) \quad (21)$$

here, ν is kinematic viscosity of the fluid. If $V_c + V_d$ becomes positive, a nascent vortex element is introduced into the flow field, where the thickness and vorticity of the element are given from the relation of the vortex strength conservation as follows.

$$\omega_{vor} = \frac{\int_V \omega dv}{V + V_{vor}} \quad (22)$$

$$h_{vor} = (V_c + V_d) \cdot dt \quad (23)$$

$$V_{vor} = \Delta S_p \cdot h_{vor} \quad (24)$$

Here, ω is the vorticity originally involved in the element of the vorticity layer, V and V_{vor} are the volume of the vorticity element and the nascent vortex element. Every vortex element is introduced at the distance of $0.5h_{vor}$ from the panel as a vortex plate.

It will be noteworthy that as a linear distribution of velocity is assumed in the thin vorticity layer, the shearing stress on the wall surface is evaluated approximately from the following equation as far as the thickness of the vorticity layer is sufficiently thin.

$$\tau_w = \mu \frac{\partial u}{\partial y} = -\mu \omega \quad (25)$$

2.5 Replacement with Equivalent Vortex Blobs

For simplification of numerical treatments, every nascent vortex element which is far from the solid surface, can be replaced with an equivalent discrete vortex. Either in a two-dimensional flow or in a three dimensional flow, the discrete vortex element is modelled by a vortex blob

which has its own smoothed vorticity distribution and a core radius, which spreads according to the viscous diffusion expressed by the third term in the right hand side of equation (8) as explained by Kamemoto (1995)⁽³⁾. In the vortex method used by the group of the present author, every nascent vortex element which moves beyond a boundary at the distance of four times h_i from the solid surface, is replaced with an equivalent, circular (2-D) or spherical (3-D) vortex blob of the core spreading model.

When a two-dimensional flow is dealt with, the total circulation and the sectional area of the blob core are determined to be the same as those of the rectangular nascent vortex element. As explained by Leonard (1980)⁽¹⁾, if a vortex blob has a core of radius ε_i and total circulation Γ_i , a Gaussian distribution of vorticity around the center of the blob is given as

$$\omega(r) = \frac{\Gamma_i}{\pi \varepsilon_i^2} \exp \left\{ - \left(\frac{r - r_i}{\varepsilon_i} \right)^2 \right\} \quad (26)$$

here r_i denotes a position of the center of the blob. As explained by Kamemoto (1995)⁽³⁾, the spreading of the core radius ε_i according to the viscous diffusion expressed by equation (7) is represented as

$$\frac{d\varepsilon_i}{dt} = \frac{2.242^2 \nu}{2\varepsilon_i} \quad (27)$$

When a three-dimensional flow is treated, a nascent vortex element of a rectangular parallelepiped is replaced by an equivalent vortex blob with a spherically symmetric distribution of vorticity which was proposed by Winckelmans and Leonard (1988)⁽²⁴⁾ and modified by Nakanishi and Kamemoto (1992)⁽²⁵⁾. The details of treatments are explained in the paper by Ojima and Kamemoto (2000)⁽²³⁾. A vortex blob is a spherical model with a radially symmetric distribution of vorticity. Once the i -th vortex blob is given in a flow field by the position $r_i = (r_x, r_y, r_z)$, its vorticity $\omega_i = (\omega_x, \omega_y, \omega_z)$ and its core radius ε_i , the vorticity distribution around the vortex blob is represented by following equations.

$$\omega_i(r) = \omega_i p(|r - r_i| / \varepsilon_i) \varepsilon_i^{-3} dv_i \quad (28)$$

$$p(\xi) = 15/8\pi(\xi^2 + 1)^{-7/2} \quad (29)$$

Here, $p(\xi)$ is smoothing function proposed by Winckelmans & Leonard (1988)⁽²⁴⁾.

On the other hand, the evolution of vorticity is calculated by equation (8) with three-dimensional core spreading method modified by Nakanishi & Kamemoto (1992)⁽²⁵⁾. In this method, the stretch term and diffusion term of equation (8) are separately considered. The change of core radius due to the stretching is calculated from following equations.

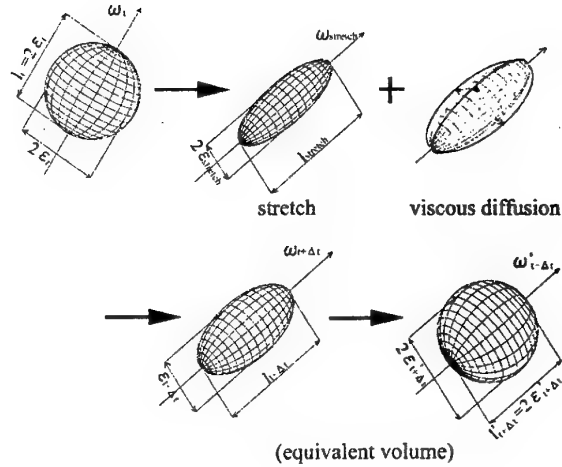


Figure 4: Mechanism of three-dimensional core spreading method for a vortex blob.

$$\frac{d\omega}{dt} = (\omega \cdot \text{grad}) u \quad (30)$$

$$\frac{dl}{dt} = \frac{l_i}{|\omega_i|} \left| \frac{d\omega}{dt} \right| \quad (31)$$

$$\left(\frac{d\varepsilon}{dt} \right)_{\text{stretch}} = - \frac{\varepsilon_i}{2 \cdot l_i} \frac{dl}{dt} \quad (32)$$

Here, ε and l are the core radius and the length of the vortex blob model as shown in Figure 4. The viscous term of equation (8) is expressed by the core spreading method. The core spreading method is based on the Navier-Stokes equation for viscous diffusion of an isolated two-dimensional vortex filament in a rest fluid, and as well as equation (27), the rate of core spreading is represented as follows

$$\left(\frac{d\varepsilon}{dt} \right)_{\text{diffusion}} = \frac{c^2 \nu}{2\varepsilon_i}, \quad (c=2.242) \quad (33)$$

Taking account of two factors expressed as equations (32) and (33), characteristic values of the elongated blob element are obtained from the following equations.

$$\varepsilon_{i+\Delta t} = \varepsilon_i + \left[\left(\frac{d\varepsilon}{dt} \right)_{\text{stretch}} + \left(\frac{d\varepsilon}{dt} \right)_{\text{diffusion}} \right] \cdot \Delta t \quad (34)$$

$$l_{i+\Delta t} = l_i + \frac{dl}{dt} \cdot \Delta t \quad (35)$$

$$|\omega_{t+\Delta t}| = |\omega_t| \cdot \left(\frac{\varepsilon_t}{\varepsilon_{t+\Delta t}} \right)^2 \quad (36)$$

And then, the elongated element is replaced into a new and spherical vortex blob which has the volume equivalent to the elongated one.

2.6 Numerical Procedure.

Once all of the vorticity layers existing in the flow field at any time are represented with discrete vortex distributions, the strengths of the vortex panels distributed along the boundary surface are numerically calculated so as to satisfy the boundary conditions of normal velocity component on it, by applying the popular scheme of the panel method to the integration equation (11). Once the vortex distributions are determined in the right hand side of equation (11), not only a flow velocity at an arbitrary position in the flow field but also the convective velocity of each discrete vortex can be calculated. Substituting the velocities into equations (8) and (10), the vorticity transport and trajectory of each discrete vortex over the time step are numerically investigated, which provide new distributions of discrete vortices corresponding to the vorticity layers transported during the time step.

Consequently, the iteration of the above procedure provides the basic scheme of the grid-free Lagrangian simulation of unsteady, incompressible and viscous flow, making use of the Biot-Savart law vortex methods.

2.7 Application to Forced Convective Heat Transfer

When a forced heat convection in a flow of a high Reynolds number and a not-so-small Prandtl number is assumed, we can ignore the effects of natural heat convection. Then, the energy equation for forced convective heat transfer is expressed as

$$\frac{\partial T}{\partial t} + (\mathbf{u} \cdot \text{grad}) T = \alpha \nabla^2 T \quad (37)$$

where T is temperature and α is the thermal diffusivity. Lagrangian expression for the energy equation (37) are given by

$$\frac{dT}{dt} = \alpha \nabla^2 T \quad (38)$$

As firstly pointed out in the study on random-particle simulation of vorticity and heat transport by Smith and Stansby (1989)⁽²⁶⁾, it is clear that the energy equation (38) is of the similar form to the vorticity transport equation (6). When a two-dimensional flow is dealt with, the vorticity transport equation is simply expressed by equation (7). Therefore, the form of equation (38) becomes completely the same as equation (7). This fact seems to suggest that the energy equation (38) can be

solved in an analogous way, with nascent temperature elements, in place of vortex elements using a time splitting scheme.

In the vortex element method developed by the group of the present author, the viscous diffusion expressed by equation (7) is approximately taken into account by the core spreading method. Therefore, in the present method, the thermal diffusion expressed by equation (38) is similarly considered by introducing a thermal core to a discrete heat element which spreads with the increase of time, and as same as that of a vortex element, the trajectory of each heat element in flow is represented by equation (9).

The details of treatments in the calculation of forced convective heat transfer are explained in the paper by Kamemoto and Miyasaka (1999)⁽¹²⁾.

3. THE WAY TO LAGRANGIAN LARGE EDDY SIMULATION

3.1 Turbulence Models for the Vortex Methods

When treating high Reynolds number flows, one can perform a large eddy simulation by modeling the effect of the small or subgrid-scale eddies on the larger scales. In their study on three-dimensional interactions of vortex tubes, Leonard and Chua (1989)⁽¹⁴⁾ proposed and used a nonlinear core-spreading algorithm, which is a pioneering work of modeling turbulence for a vortex method in the spirit of large eddy simulation. To accomplish this in a vortex method, they introduced a subgrid-scale viscosity ν_{SGS} and implemented the following nonlinear core-spreading algorithm for expression of changing rate of core radius ε_i ,

$$\frac{d\varepsilon_i^2}{dt} = 4\nu_{SGS} - \varepsilon_i^2 \frac{1}{\omega} \frac{d\omega}{dt} \quad (39)$$

where $\omega = |\omega|$, and the second term on the right-hand side is the inviscid change in core size due to stretching of vorticity and the subgrid-scale viscosity depends on the local vorticity stretching rate $(1/\omega)(d\omega/dt)$, as follows.

$$\nu_{SGS} = \max \left[0, C\varepsilon_i^2 \frac{1}{\omega} \frac{d\omega}{dt} \right] \quad (40)$$

where C is a constant. They have pointed out that the expression (40) for ν_{SGS} is very similar in form to the so-called Smagorinsky model used in large eddy simulation with finite difference methods and given by

$$\nu_{SGS} = C' \Delta^2 \left(\frac{\partial u_i}{\partial x_k} \frac{\partial u_k}{\partial x_i} \right)^{1/2} \quad (41)$$

where C' is a constant and Δ is the scale of grid. Using the nonlinear core-spreading scheme in simulations of interaction between two interlocked vortex rings and interaction between two colliding vortex rings, Leonard and Chua succeeded in observing the dynamics of the space curves of the vortex tubes, the development of complex internal structure in the vortex cores and the reconnection of vortex lines.

Mansfield et al. (1998)⁽¹⁵⁾ (1999)⁽¹⁶⁾ developed a dynamic eddy viscosity model of the subfilter-scale stresses for Lagrangian vortex element methods. Their LES scheme is based on the filtered vorticity transport equation which is expressed as

$$\frac{\partial \bar{\omega}_i}{\partial t} + \bar{u}_j \frac{\partial \bar{\omega}_i}{\partial x_j} = \bar{\omega}_j \frac{\partial \bar{u}_i}{\partial x_j} + \nu \nabla^2 \bar{\omega}_i - \frac{\partial R_{ij}}{\partial x_j} \quad (42)$$

In this equation, R_{ij} is the subfilter-scale (SFS) vorticity stress, which accounts for the effect of unresolved velocity and vorticity fluctuations and is expressed as

$$R_{ij} = (\bar{\omega}_j \bar{u}_i - \bar{\omega}_i \bar{u}_j) - (\bar{u}_j \bar{\omega}_i - \bar{u}_i \bar{\omega}_j) \quad (43)$$

where bars are used to denote spatially filtered quantities. In order to close the filtered vorticity transport equation (42), they provided a model for the vorticity stress R based on the eddy diffusivity model

$$\nabla \cdot R = -\nabla \cdot (\nu_T \nabla \bar{\omega}) \quad (44)$$

where the eddy diffusivity is expressed as

$$\nu_T = C_r \Delta^2 |S| \quad (45)$$

here, the modulus of the filtered strain-rate tensor is defined as $|S| = (2S_{mn}S_{mn})^{1/2}$. In equation (45), Δ is the filter size which is related to the core size of the vortex elements used to represent the vorticity field, and C_r is a model constant which is determined locally in the calculations according to filtering operations. Applying the LES model to simulation of the collision of coaxial vortex rings, Mansfield et al (1999)⁽¹⁶⁾ showed that the Lagrangian LES scheme captures several experimentally observed features of the ring collisions, including turbulent breakdown into small-scale structures and the generation of small-scale radially propagating vortex rings.

Recently, Kiya et al (1999)⁽¹⁷⁾ modified the nonlinear core-spreading algorithm proposed by Leonard and Chua and examined the effect of the subgrid-scale eddies on the flow of larger scales. In the original model of Leonard and Chua, as shown in equation (40), if $d\omega/dt < 0$, the subgrid-scale viscosity ν_{SGS} becomes $\nu_{SGS} = 0$. Kiya et al., however, did not use this procedure, but they simply applied the sub-grid scale viscosity based on the Smagorinsky sub-grid scale viscosity, which is expressed

$$\nu_{SGS} = c^2 \Delta^2 \left| \frac{d\omega}{dt} \right| \quad (46)$$

where Δ is replaced by the core radius ϵ_i of a vortex element and the value of the model constant $c = 0.17$, which is recommended for free turbulent shear flows in the Smagorinsky model, was employed in their study. They examined three models of core spreading based on viscous diffusion, turbulent eddies and both effects, which are respectively expressed as

$$\frac{d\epsilon_i^2}{dt} = 4\nu \quad (47)$$

$$\frac{d\epsilon_i^2}{dt} = 4\nu_{SGS} \quad (48)$$

$$\frac{d\epsilon_i^2}{dt} = 4(\nu + \nu_{SGS}) \quad (49)$$

Applying each models to an impulsively started round jet forced by two helical disturbance rotating in the counter directions, Kiya et al. compared vortical structures in the jet among the models, and concluded that the simulation of the forced round jet by the turbulence model seems to generate turbulent vortical structures although its validation based on DNS or experiments is left as a study in the future.

3.2 On Challenge to Modeling of Wall Turbulence.

So far, all of the turbulence models described above have been applied only for free turbulence. Saltara et al. (1998)⁽¹⁸⁾ simulated vortex shedding from an oscillating circular cylinder with use of turbulence modeling in a vortex in cell method. However, any challenging works on modeling of wall turbulence for the Lagrangian vortex methods have not been reported, yet.

As the algorithms of the advanced vortex method explained in the section 2 are very simple, it seems not so difficult to take account of the effects of subcore (subfilter) eddies on the flow represented with discrete vortices. Therefore, as the first step of modeling of wall turbulence, it will be very interesting to test the SGS models proposed for free turbulence in simulation of a high Reynolds number flow around a bluff body.

4. APPLICATION EXAMPLES

For investigation of unsteady and vortical flows, the Biot-Savart law vortex methods have so attractive advantages that grid generation in a flow field is not necessary and any conventional turbulence models of time-mean type are not used. Therefore, the vortex methods have been applied for analyses of unsteady separated flows related with various problems in engineering fields. The followings are typical examples of application of the advanced vortex method by the group of the present author.



(a) Pitching down at $\alpha = 15.0^\circ$ ($T = 11.0$)



(b) Pitching up at $\alpha = 15.0^\circ$ ($T = 14.1$)

Figure 5: Instantaneous flow patterns around an oscillating airfoil NACA 0012 ($\alpha = 15.0^\circ + 5.0^\circ \sin \Omega T$, $Re = 5.0 \times 10^5$)

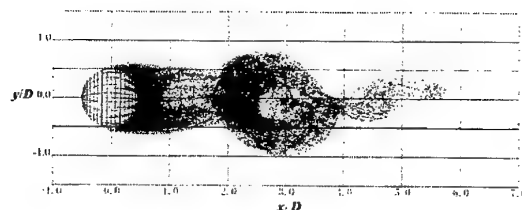
4.1 Unsteady Flow past an Oscillating Airfoil

In order to examine the effectiveness of the present method, the two-dimensional unsteady separated flow past an oscillating NACA 0012 airfoil was computed by Etoh et al. (1997)⁽²⁷⁾. Figure 5 shows instantaneous flow patterns at the mean angle of attack $\alpha = 15.0^\circ$ during pitching up and down motion, when the airfoil was oscillated in pitch angle about the quarter chord point as $\alpha = 15.0^\circ + 5.0^\circ \sin \Omega T$ at Reynolds number $Re = 5.0 \times 10^5$, where T is the non-dimensional time based on the cord length and the velocity of uniform flow, and the non-dimensional time step was $dt = 0.026$ and Ω was given as $\Omega = 1.0$. It is clearly shown that in the case of pitching down motion, the large dynamic stall vortex and trailing edge vortex still exit around the airfoil, whereas in the case of pitching up motion, the dynamic stall is developing but the both vortices are not so large, yet.

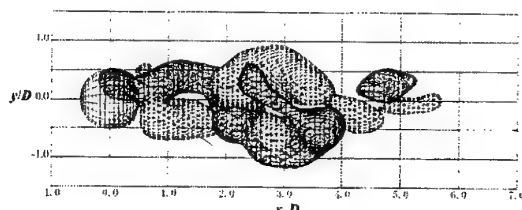
4.2 Unsteady Flows around Three-dimensional Bluff Bodies

In order to confirm the applicability of an advanced vortex method to a three-dimensional unsteady separated flow, the developments of vortical wakes behind a sphere and a prolate spheroid after their impulsive start at a constant speed in a rest fluid were simulated by Ojima and Kamemoto (2000)⁽²³⁾. In their calculation, both a sphere and the prolate spheroid were represented by 360 source and vortex panels.

Figure 6 shows calculated instantaneous flow patterns represented by discrete vortices and isosurfaces of streamwise vorticity behind the sphere at a non-dimensional time $tU/D = 10.25$ elapsed after the start at a

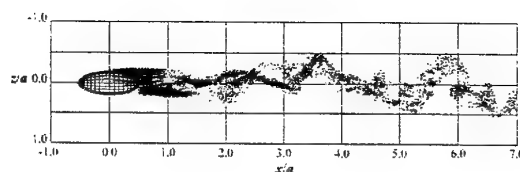


(a) Flow pattern.

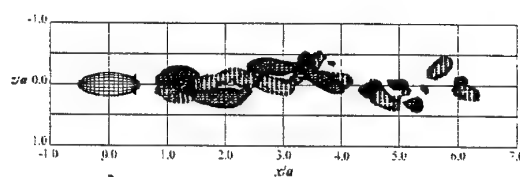


(b) Isosurfaces of streamwise vorticity.

Figure 6: Instantaneous flow patterns represented by discrete vortices and isosurfaces of streamwise vorticity behind a sphere ($tU/D = 10.25$, $Re = 300$).



(a) Flow pattern.



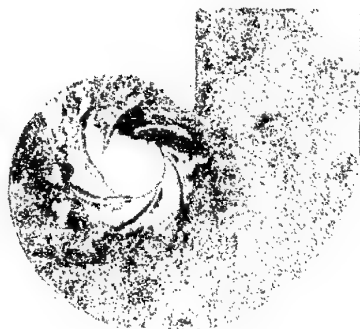
(b) Isosurfaces of streamwise vorticity.

Figure 7: Instantaneous flow patterns represented by discrete vortices and isosurfaces of streamwise vorticity behind a prolate spheroid ($tU/D = 10.25$, $\alpha = 0.0^\circ$, $Re = 1,000$).

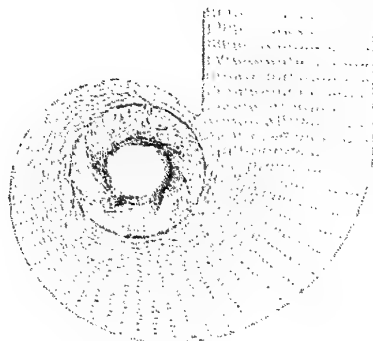
Reynolds number $Re = 300$, where U and D denote the speed and the diameter of the sphere respectively, and the time step size was $dtU/D = 0.05$. In this figure, three-dimensional vortex structures are clearly shown in the separated flow, and the development of spiral structure of wake and the interesting phenomenon like the breakdown of hair pin vortices into turbulence vortices of small scale can be observed in the wake.

Figure 7 shows instantaneous flow patterns behind the prolate spheroid of the axis ratio $b/a = 1/3$ represented

by discrete vortices and isosurface of the streamwise vorticity for $tU/D=10.25$, attack-angle $\alpha=0.0^\circ$ and $Re=Ua/\nu=1,000$, where a and b denote the length of major and minor axes respectively, and the time step size was $dtU/D=0.075$. It is seen that the typical hairpin-shaped structure begins to be periodically formed behind the spheroid in the similar manner to the wake of a sphere as shown in Figure 6.



(a) Flow pattern represented by discrete vortices.

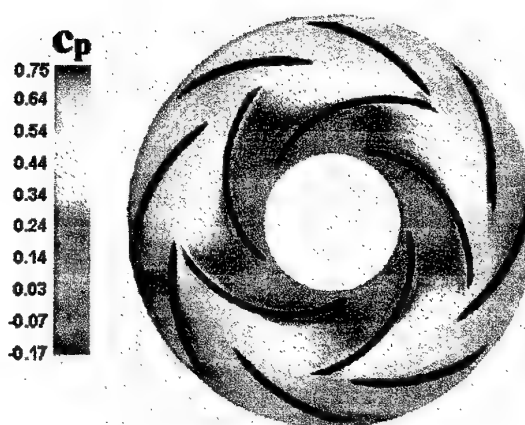


(b) Velocity vectors.

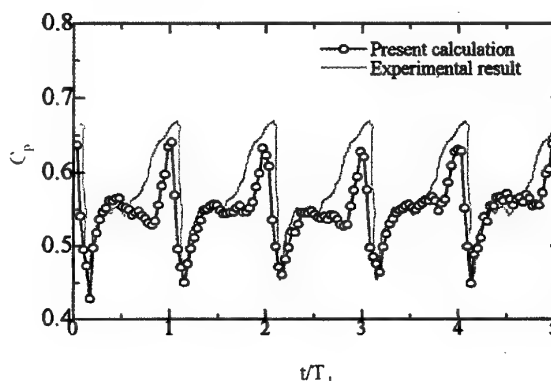
Figure 8: Two-dimensional unsteady flow in a centrifugal pump at 60% of the design flow rate.

4.3 Unsteady Flow in a Centrifugal Pump

The advanced vortex method has been applied to such an engineering purpose as simulation of unsteady and complex flow through a two-dimensional centrifugal impeller by Zhu et al. (1998)⁽²⁸⁾. Figure 8 shows an instantaneous pattern of flow through the impeller in the case of partial discharge (60% of the design flow rate) at a non-dimensional time $T=2.0$ after the start of rotation at a constant speed at the Reynolds number $Re=10^5$, where the time step size was $dt=0.01$ and the non-dimensional value were based on the inlet meridian velocity at the design condition and the outer diameter of the impeller. It is clearly demonstrated that the flow becomes completely



(a) Instantaneous pressure distribution



(b) Variation of static pressure with time at a point close to the suction-side of leading edge of a diffuser vane.

Figure 9: Interactive pressure distribution around rotor and stator vanes in a diffuser pump (100%).

non-axi-symmetrical and some of blade-to-blade passages seem to be blocked with separation bubbles.

4.4 Rotor-Stator Interaction in a Diffuser Pump

As the flow-unsteadiness generated by rotor-stator interaction in turbomachinery usually causes serious problems concerning vibration and noise, development of easy-to-handle methods have been expected to simulate the real unsteady-interaction without introducing either a sliding-surface between the rotating and stationary frames or turbulence models of time-mean type. In order to examine the applicability of the advanced vortex method for those purposes, the unsteady and interactive flows between a two-dimensional centrifugal impeller and a surrounding vaned diffuser were simulated by Zhu and Kamemoto (1999)⁽²⁹⁾. In the calculation, each vane of the impeller and diffuser was represented 50 vortex panels, and the time step size and Reynolds number were taken

as $dt=T/150$ and $Re=10^5$ respectively, here T is the period of impeller revolution. Figure 9 shows examples of calculated instantaneous pressure distribution at a time and variation of static pressure with time at a point close to the suction-side of leading edge of a diffuser vane compared with experimental data.⁽³⁰⁾ It is found that there exist considerable differences of static pressure in the flow field around the diffuser inlet corresponding to the relative position between impeller and diffuser vanes. And it is one of the most interesting points that variation of the calculated pressure coefficient C_p is in very good agreement with experimental one in its absolute value.

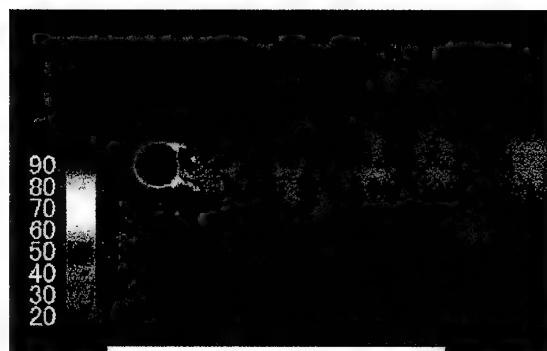
4.5 Simulation of Forced Convective Heat Transfer around a Circular Cylinder

Kamemoto and Miyasaka (1999)⁽¹²⁾ proposed a vortex and heat elements method and showed application results of analysis of unsteady and forced-convective heat transfer around a circular cylinder in a uniform flow.

Figure 10 shows an instantaneous temperature distribution and the corresponding flow pattern at a non-dimensional time $T=25.0$ after the impulsive start of flow, where $Re=10^4$ and $Pr=0.71$. It is clarified that thermal crowds are formed behind the cylinder and periodically shed in the wake, corresponding to the periodical shedding of Vortices. The time-averaged local Nusselt number distribution in the same flow is shown in Figure 11, compared with experimental results by Igarashi (1984)⁽³¹⁾ and Schmidt & Wenner (1941)⁽³²⁾. It is known that the calculated result reasonably coincides with the experiments.

4.6 Simulation of Three-dimensional Unsteady Flows through a Wind Turbine

In relation with further development of promising clean energy resources, investigations of unsteady and three-dimensional characteristics of flows around wind turbines are required. Especially, for conditions out of the conventional design, it is necessary to predict the features of complex vortical flows to design suitable operation procedures. Corresponding to those requirements, simulation of three-dimensional and unsteady flows through a horizontal-axis wind turbine (HAWT) of single blade was performed applying the advanced vortex method by Ojima and Kamemoto (2000)⁽³³⁾. In the calculation, the blade was divided into 572 source and vortex panels (span wise: 22, sectional blade element: 26), and the time step size and Reynolds number were taken as $dV/R=2\pi/(200\Omega)$ and $Re=VR/\nu=1.0\times 10^6$, where V , R and Ω denote the blade tip velocity, the rotational radius of the blade tip and angular velocity. Figure 12 shows calculated instantaneous flow pattern represented by discrete vortices at tip speed ratio $\lambda=V/U=8.0$ after three times of rotor revolution, where U is a wind velocity. At the initial stage of the flow, complex wake structure is formed behind the rotor blade due to



(a) Temperature distribution



(b) Flow Pattern

Figure 10: Instantaneous temperature distribution and flow pattern. ($Re=10^4$, $Pr=0.71$, Time=25.0)

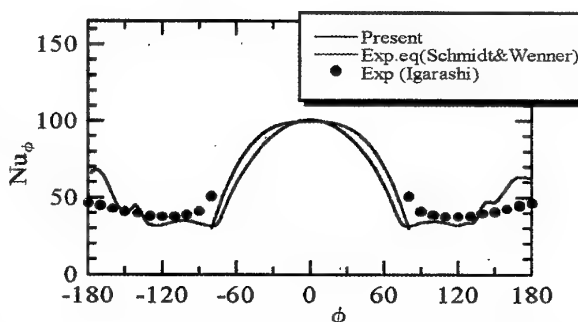


Figure 11: Time-averaged local Nusselt number distribution. ($Re=10^4$, $Pr=0.71$)

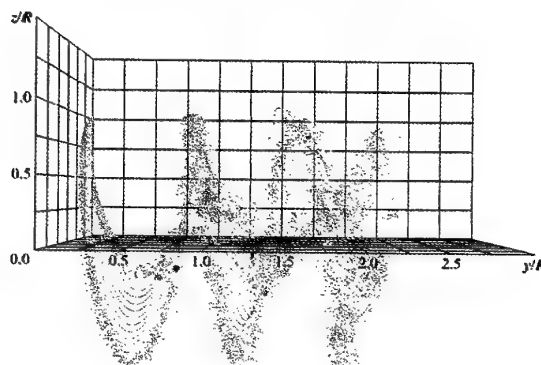


Figure 12: Instantaneous flow pattern behind a wind turbine after three times of rotor revolution at tip speed ratio $\lambda=8.0$

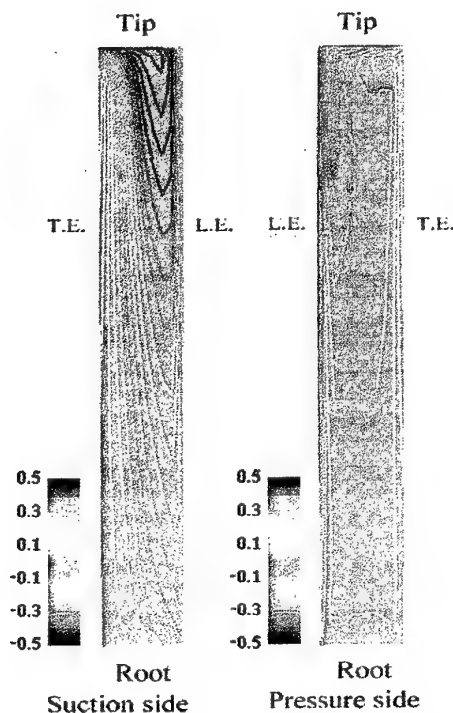


Figure 13: Instantaneous pressure distributions on the blade surfaces after three rotor revolutions for $\lambda = 8.0$

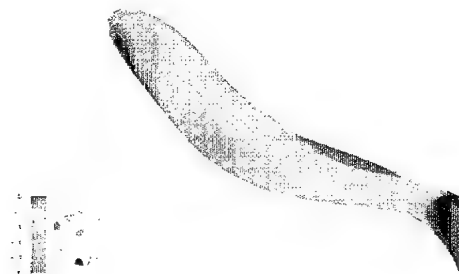
interaction among starting vortices shed from the trailing edge and the longitudinal vortices shed from the tip and root of the blade. And it is observed that as time goes on, the starting vortices flow downstream and the longitudinal vortices tend to have dominant role in the flow field. Figure 13 shows instantaneous pressure distributions on the blade surfaces after three rotor revolutions for $\lambda = 8.0$. It is seen that a lower pressure region develops near the tip and leading edges on the suction side of the blade.

4.7 Numerical Fish

Recently, in relation to conservation of fish resources, development of numerical prediction technique for confirmation of safe swimming of fishes through a hydraulic turbine of a power station. For this purpose, the group of the present author⁽³⁴⁾ have started to apply their vortex methods to numerical simulation of fish swimming. Figure 14 (a) shows the aspect of swimming of a two-dimensional trout obtained from a 2-D calculation. We can find that there is no separation region around the fish and alternative vortex rows are formed like a Karman vortex street behind the fish. However, the upper vortex row is consisting of vortices of counter-clockwise rotation and the lower is consisting of clockwise vortices. Figure 14 (b) shows the instantaneous pressure distribution on the skin of a trout obtained from



(a) Flow around a swimming trout (2-D).



(b) Instantaneous pressure distribution around a trout (3-D).



(c) 3-D and complex vortex structures in the flow behind a trout

Figure 14: Flow around a numerical fish (trout).

3-D calculation, here, the convex part shows a higher pressure region and the concave part is a lower pressure region. Figure 14 (c) shows the 3-D and complex vortex structures in the flow around the trout swimming at the best efficiency condition.

5 CONCLUSIONS

In this paper, the mathematical basis and calculation algorithms of the advanced vortex methods developed by the group of the present author were explained, and recent pioneering works on LES modeling by leading researchers were reviewed, and a short comment on necessity of development of wall turbulence models was described.

From the examples of recent application, it has been confirmed that the vortex methods standing on the Biot-Savart law are consisting of simple algorithms based on physics of flow and they provide completely grid-free Lagrangian calculation which is available and useful for research and development in various engineering fields.

Finally, the present author would like to state that the advanced vortex methods are to yield a promising way to a grid-free Lagrangian large eddy simulation of unsteady and complex flows of higher Reynolds numbers.

REFERENCES

- (1) Leonard, A., : Vortex methods for flow simulations, *J. Comp. Phys.* 37, (1980), pp. 289-335.
- (2) Sarpkaya, T. : Computational methods with vortices - the 1988 Freeman scholar lecture, *J. Fluids Engng.*, 111, (1989), pp.5-52.
- (3) Kamemoto, K. : On attractive features of the vortex methods, *Computational Fluid Dynamics Review* 1995, ed. M.Hafez and K.Oshima, JOHN WILEY & SONS, (1995), pp.334-353.
- (4) Lewis R.I. : Vortex element methods, the most natural approach to flow simulation - a review of methodology with applications, *Proc. of 1st Int. Conf. on Vortex Methods*, Kobe, Nov.4-5, (1999), pp.1-15.
- (5) Graham J.M.R. and Arkell R.H. : A hybrid vortex method, *Proc. of 1st Int. Conf. on Vortex Methods*, Kobe, Nov.4-5, (1999), pp.47-58.
- (6) Unal M. F. and Kamemoto K. : Simulation of three dimensional separated flow around an ellipsoid by discrete vortex method, *Proc. of 1st Int. Conf. on Vortex Methods*, Kobe, Nov.4-5, (1999), pp.107-112.
- (7) Bernard P.S., Dimas A.A. and Lottati I. : Vortex method analysis of turbulent flow, *Proc. of 1st Int. Conf. on Vortex Methods*, Kobe, Nov.4-5, (1999), pp.137-155.
- (8) Walther J.H. and Sagredo J.T. and Koumoutsakos P. : Simulation of particulate flow using vortex methods, *Proc. of 1st Int. Conf. on Vortex Methods*, Kobe, Nov.4-5, (1999), pp.221-231.
- (9) Ying L. : Convergence study for the vortex method with boundaries, *Proc. of 1st Int. Conf. on Vortex Methods*, Kobe, Nov. 4-5, (1999), pp.235-242.
- (10) Lee D. : Numerical prediction of rotor tip-vortex roll-up in axial flight by using a time-marching free-wake method, *Proc. of 1st Int. Conf. on Vortex Methods*, Kobe, Nov.4-5, (1999), pp.243-253.
- (11) Cottet G.H. : 3D vortex methods: achievements and challenges, *Proc. of 1st Int. Conf. on Vortex Methods*, Kobe, Nov.4-5, (1999), pp.315-329.
- (12) Kamemoto K. and Miyasaka T. : Development of a vortex and heat elements method and its application to analysis of unsteady heat transfer around a circular cylinder in a uniform flow, *Proc. of 1st Int. Conf. on Vortex Methods*, Kobe, Nov.4-5, (1999), pp.191-203, or *VORTEX METHODS*, edited by K. Kamemoto & M. Tsutahara, *World Scientific*, (2000), pp.135-144.
- (13) *VORTEX METHODS*, edited by K. Kamemoto & M. Tsutahara, *World Scientific*, (2000).
- (14) Leonard A. and Chua K. : Three-dimensional interaction of vortex tubes, *Physica D (Nonlinear Phenomena)*, 37, (1989), pp.490-496.
- (15) Mansfield J.R., Knio O.M. and Meneveau C. : A dynamic LES scheme for the vorticity transport equation :Formulation and a priori tests, *J. of Comp. Phys.*, 145, (1998), pp.693-730.
- (16) Mansfield J.R., Knio O.M. and Meneveau C. : Dynamic LES of colliding vortex rings using a 3D vortex method, *J. of Comp. Phys.*, 152, (1999), pp.305-345.
- (17) Kiya M., Izawa S. and Ishikawa H. : Vortex method simulation of forced, impulsively started round jet, *Proc. of the 3rd ASME/JSME Joint Fluids Engng. Conf.* San Francisco, July 18-22, (1999), FEDSM99-6813.
- (18) Saltara F., Meneghini J.R., Siqueira C.R. and Bearman P.W. : The simulation of vortex shedding from an oscillating circular cylinder with turbulence modelling, 1998 ASME FEDSM, *Proc. of 1998 Conf. on Bluff Body Wakes and Vortex-Induced Vibration*, (1998), Paper No. 13.
- (19) Chorin, A.J. : Numerical study of slightly viscous flow, *J. Fluid Mech.* 57, (1973), pp.785-796.
- (20) Chorin, A.J. : Vortex sheet approximation of boundary layers. *J. Comp. Phys.* 74, (1978), pp.283-317.
- (21) Wu, J.C. and Thompson, J.E., : Numerical solutions of time-dependent incompressible Navier-Stokes Equations using an integro-differential formulation. *Computers & Fluids* 1, (1973), pp.197-215.
- (22) Uhlman, J.S., : An integral equation formulation of the equation of motion of an incompressible fluid. *Naval Undersea Warfare Center T.R.* 10-086. (1992).
- (23) Ojima A. and Kamemoto K. : Numerical simulation of unsteady flow around three dimensional bluff bodies by an advanced vortex method, *JSME Int. Journal*, B, 43-2, (2000), pp.127-135.
- (24) Winkelmans, G. and Leonard, A. : Improved vortex methods for three-dimensional flows, *Proc. Workshop on Mathematical Aspects of Vortex Dynamics*. 25-35. (1988), Leeburg. Virginia.

- (25) Nakanishi, Y. and Kamemoto, K. : Numerical simulation of flow around a sphere with vortex blobs, *J. Wind Engng and Ind. Aero.*, 46 and 47, (1992), pp.363-369.
- (26) Smith P.A. and Stansby, P.K. : An efficient surface algorithm for random-particle simulation of vorticity and heat transport, *J. Comp. Phys.* 81, (1989), pp.349-371.
- (27) Etoh, F., Kamemoto, K., Matsumoto, H. and Yokoi, Y. : Numerical simulation of flow around a rotary oscillating foil with constant amplitude angle by use of the vortex method, *Proc. 11th Symp. on CFD, Tokyo*, (1997), pp.385-386.
- (28) Zhu, B., Kamemoto, K. and Matsumoto, H., Computation of unsteady viscous flow through centrifugal impeller rotating in volute casing by direct vortex method, *Comp. Fluid Dynamics J.* 7-3, (1998), pp.313-323.
- (29) Zhu, B. and Kamemoto, K., : Simulation of the unsteady interaction of a centrifugal impeller with its diffuser by an advanced vortex method. *Proc. of the 3rd ASME/JSME Joint Fluids Engng. Conf. San Francisco*, July 18-22, (1999), FEDSM99-6821.
- (30) Tsukamoto H., Uno M., Hamafuku H. and Okamura T. : Pressure fluctuation downstream of a diffuser pump impeller. *Proc. of 2nd Joint ASME/JSME Fluid Engng. Conf., FED-vol. 216*, (1995), pp.133.
- (31) Igarashi, T., : Flow and heat transfer in the separated region around a circular cylinder. *Trans. JSME. B* 50-460, (1984), pp.3008-3014. (in Japanese).
- (32) Schmidt, E. and Wenner, K. : Warmeabgabe uber den Umfang eines angeblasenen geheizten Zylinders, *Forsch. Ing.-Wes.* 12, (1941), pp.65-73.
- (33) Ojima A. and Kamemoto K. : Numerical simulation of unsteady flow around three-dimensional blades of a wind turbine by a vortex method, *Proc. of 2000 ASME FEDSM, Boston*, (2000), FEDSM2000-11078.
- (34) Iso, Y. ; Study on development of numerical fish, Master Thesis at Department of Mechanical Engineering,, Yokohama National University , (2000-3).

PREDICTION OF AERODYNAMIC SOUND SPECTRA BY USING AN ADVANCED VORTEX METHOD

Akiyoshi Iida*

Department of Mechanical Engineering, Kogakuin University,
Nakano-machi 2665, Hachioji-shi, Tokyo, 192-0015 Japan
Email: iida@fluid.mech.Kogakuin.ac.jp

Kyoji Kamemoto and Akira Ojima

Department of Mechanical Engineering and Materials Science, Yokohama National University,
79-5, Tokiwadai, Hodogaya-ku, Yokohama, 240-8501 Japan

ABSTRACT

The objective of this investigation is to develop a computational methodology for aeroacoustic simulation based on vortex methods. The simulation makes use of the Lighthill acoustic analogy, so it is based on the decomposition of the flow field and the resulting acoustic field. Simulation of an unsteady turbulent flow field requires a powerful computer and much computational time. In order to reduce this computational time, we utilize an advanced vortex method to obtain the unsteady flow field. Aerodynamic sound generated from a circular cylinder at Reynolds numbers between 10^3 to 10^5 was predicted by this method. The predicted sound pressure levels agree reasonably well with the measured ones. The developed computational methodology will thus enable aeroacoustic sound to be predicted by using a standard, desktop PC.

1. INTRODUCTION

In industries, aerodynamic noise becomes one of the most common types of noise problem. For example, the aerodynamic noise from pantographs is the dominant wayside noise source from high-speed trains. Much research has been attempted to predict aerodynamic sound by using *mesh-based* computational fluid dynamics and the Lighthill-Curle's acoustic analogy (1,2,3). As a result, aerodynamic sound can now be numerically calculated. However, this type of aeroacoustic simulation is limited to basic problems because of limited computer resources. That is, aeroacoustic simulation requires a powerful computer

and much computational time, even in the simulation of aerodynamic sound radiated from a turbulent wake of a circular cylinder. According to estimates by Kato et al (2), over 10 million grids are required, if aeroacoustic simulation, *based on conventional grid based CFD*, is applied to more complicated problems such as the industrial problems. Therefore, researchers and engineers in industrial field would like to reduce the computational time and resources.

Since vortex methods have a mesh free and simple algorithm, vortex methods are suitable for simulation of unsteady flow fields around industrial applications. In this paper, we attempted to develop the aeroacoustic simulation based on the Lighthill-Curle's theory with the Advanced Vortex Method developed by Prof. Kamemoto. The far-field sound generated from turbulent wake of a circular cylinder at Reynolds numbers between 10^3 to 10^5 have been computed by decomposing the flow field and resulting acoustic field by using low-Mach number assumption. Furthermore, in order to take into account three-dimensionality of the wake structure, we introduce the correlation length of the surface pressure fluctuation. Since the correlation length depends on the frequency of the surface pressure fluctuation or scale of turbulent eddies, aerodynamic sound spectra also depend on the scale of turbulent eddies.

The predicted sound spectra and flow structure are compared with that of the experimental and conventional numerical simulations.

2. GOVERNING EQUATIONS

2.1 VORTEX METHODS

Most current computation methods for aeroacoustic simulations use the Lighthill-Curle's acoustic analogy. Large Eddy Simulation (LES) is, therefore, used for solving the unsteady turbulent flow fields. LES-based aeroacoustic computations are successful to predict aerodynamic sound radiated from simple object, such as the circular cylinder (1). However, LES is required much computational resources. Then, this method is limited for basic problems. Conventional, LES-based, aeroacoustic simulation shows that the Lighthill-Curle's equation is useful for the aeroacoustic simulation at low Mach number turbulent wakes. It revealed that the aerodynamic sound could be predicted by using small-scale computers, if the computer resources of simulation for the unsteady flow fields can be reduced. Since the vortex methods are based on the discretization of the vorticity field and the Lagrangian description of the governing equation, computational elements only in the nonzero vorticity region. Vortex methods are initially conceived as a tool to simulate unsteady flow fields. In this paper, we propose the numerical method for aerodynamic sound by using vortex methods, which are directly simulate unsteady vortex motion with a small-scale computer or desktop PC.

The governing equations of viscous and incompressible flows have been solved by the vorticity transport equation.

$$\frac{\partial \omega}{\partial t} + (\mathbf{u} \cdot \text{grad}) \omega = (\omega \cdot \text{grad}) \mathbf{u} - (\mathbf{u} \cdot \text{grad}) \mathbf{u} + \nu \nabla^2 \omega \quad (1)$$

$$\omega = \text{rot} \mathbf{u} \quad (2)$$

where \mathbf{u} and ω denote velocity and vorticity vector, respectively.

The vorticity field ω is modeled by using a large number of discrete vorticity elements. The Biot-Savart law can be written as

$$\mathbf{u}(\mathbf{r}) = \frac{1}{\alpha} \int_V \frac{\omega_o \times \mathbf{R}}{R^\beta} dV_o - \frac{1}{\alpha} \int_{S_1+S_2} \frac{(\mathbf{u}_o \cdot \mathbf{n}_o) \mathbf{R}}{R^\beta} + \frac{(\mathbf{n}_o \times \mathbf{u}_o) \times \mathbf{R}}{R^\beta} dS_o, \quad (3)$$

where $\alpha=2\pi$, $\beta=2$ for two-dimensional flow and $\alpha=4\pi$, $\beta=3$ for three-dimensional flow. Subscript 'o' denotes variable, differentiation and integration at a location \mathbf{r}_o ,

and \mathbf{n}_o denotes the normal unit vector at a point on a boundary surface S .

In equation (3), the first term of right hand side denotes induced velocity of vortices, and the second term of the right hand side denotes normal and tangential velocity component on the boundary surface.

The pressure field can be calculated by using the integral equation derived from the Poisson equation, which is defined by Uhlman (4).

$$\beta H + \int_S H \frac{\partial G}{\partial n} = - \int_V \nabla G \cdot (\mathbf{u} \times \omega) dV - \frac{1}{\text{Re}} \int_S (\nabla G \times \mathbf{u}) \cdot \mathbf{n} dS \quad (4)$$

where $\beta=1$ in the flow field and $\beta=0.5$ on the boundary surface. G is the fundamental solution of Laplace equation. H is the Bernoulli function defined as

$$H = \frac{p}{\rho} + \frac{u^2}{2} \quad (5)$$

Since the unsteady vortex motion generates aerodynamic sound, accuracy of the aeroacoustic simulation depends on the resolution of flow separations. Model of the nascent vortex element and flow separation is important for the aeroacoustic simulation based on vortex methods.

Professor Kamemoto (5) and his colleagues (6) have been developed the new scheme of the nascent vortex elements that satisfy the non-slip condition on the body surface. They introduced a thin vorticity layer with thickness of h . This thin layer corresponds to outer boundary of the nascent vortex film along the solid surface as shown in Figure 1. The thin layer is partitioned by a number of source panels. The velocity distribution in the fluid between the body surface and upper part of the thin layer is linear, that is, the velocity is proportional to the thickness of h . Considering the continuity of flow and non-slip condition of each element on the body surface, the normal velocity v_n is defined as follows,

$$v_n = \frac{1}{\Delta s} \left(\frac{h u_i}{2} - \frac{h_{i+1} u_{i+1}}{2} \right), \quad (6)$$

where Δs is the length of the thin layer element and u_i denotes tangential velocity at edge of the element. The positive normal velocity transports vorticity element to the outer region of the thin layer. Moreover, the diffusion velocity v_d , which is generated by vorticity itself, also transports the vorticity element. The diffusion velocity can be written as follows,

$$v_d = \frac{1.136^2 v}{h_n + h_{i+1}}, \quad (7)$$

where v is the kinematics viscosity of the fluid. When the transport velocity, $v_n + v_d$, has positive value, a nascent vortex element is introduced into the outer flow field. The nascent vorticity element has vorticity strength of ω_{vor}

$$\omega_{vor} = \omega \frac{A_1}{A_1 + A_2}, \quad (8)$$

$$A_2 = \Delta s (V_n + V_d) \Delta t, \quad (9)$$

where Δs is the length of the element and A_1 is the are of the element. Every nascent vortex element is replaced with an equivalent two-dimensional vortex blob at the outer flow field. The total circulation and sectional area of the blob core are determined to be the same as those of initial nascent vortex element.

To simulate the viscous diffusion, we utilize the core spreading method. The core spreading method is based on Gaussians blobs which are explicit solutions of the heat equation. Gaussian blobs carried constant circulation of the vortex particles. The rate of core radius of ε can be written as follows;

$$\frac{D\varepsilon}{Dt} = \frac{c}{2} \sqrt{\frac{v}{t}} = \frac{c^2 v}{2\varepsilon}, \quad (10)$$

where $c=2.242$. The core radius of vortex blob is expanded by the diffusion process. After time step Δt , the core radius can be written as,

$$\varepsilon(t + \Delta t) = \sqrt{\varepsilon_0^2 + c^2 v \Delta t}. \quad (11)$$

Finally, the vorticity distribution of the i -th blob can be written as follows;

$$\omega(\mathbf{R}) = \frac{\Gamma_i}{\pi \varepsilon} \exp \left[-\left(\frac{\mathbf{R}}{\varepsilon_i} \right)^2 \right]. \quad (12)$$

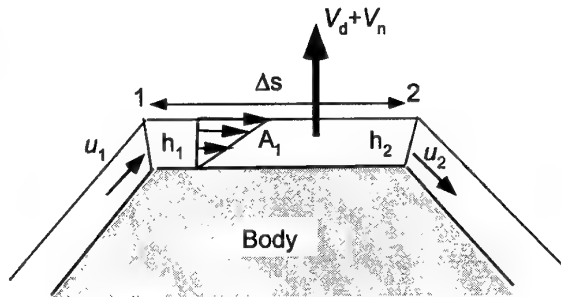


Fig.1 Nascent vortex element

2.2 FAR-FIELD SOUND CALCULATION

The far field sound pressure radiated from a low-Mach number flow can be calculated from Lighthill-Curle's equation (7)(8).

$$P_a = \frac{1}{4\pi} \frac{\partial^2}{\partial x_i \partial x_j} \int_V \frac{T_{ij}(y, t - \frac{r}{a})}{r} d^3 y + \frac{1}{4\pi} \frac{\partial}{\partial x_i} \int_S \frac{n_i p(y, t - \frac{r}{a})}{r} dS, \quad (13)$$

where a denotes the speed of sound, P_a is the far field sound pressure, P denotes the surface pressure. x_i and y denote the location of the observation point and coordinates at the noise source, respectively. r denotes the distance between the sound source and the observation point, n_i denotes the outward unit vector normal to the boundary surface. T_{ij} denotes the Lighthill's acoustic tensor, which contribution is negligibly small compared to that from the second term of equation (13) at low Mach number flow. Moreover, if the body size is much smaller than the wave length of the resulting sound, equation (13) can be written as follows;

$$P_a = \frac{1}{4\pi} \frac{x_i}{r^2} \frac{\partial}{\partial t} \int_S n_i p(y, t - \frac{r}{a}) dS. \quad (14)$$

2.3 SOUND PRESSURE LEVEL

Equation (14) shows that the aerodynamic sound can be calculated from the surface pressure fluctuation, moreover, the total aerodynamic force of the body can be calculated as

$$F_i = \int_S n_i p dS. \quad (15)$$

Therefore, the aerodynamic sound can be calculated from the instantaneous aerodynamic force obtained by the vortex methods. To reduce the computational time, two-dimensional simulation is carried out, therefore, we have to estimate the instantaneous total aerodynamic force with considering the three-dimensionality of the vortex shedding which is occurred as the result of small instability of any kind. Phillips (9) showed the radiated sound intensity level P^2 from a cylinder of length L , using the correlation length L_c , which indicates the spanwise phase difference of fluctuating force.

$$\begin{aligned} \overline{p^2(x)} &= \frac{x_i x_i}{16\pi^2 a^2 r^4} L \int_{-\infty}^{\infty} \overline{\frac{\partial f_i(z)}{\partial t} \frac{\partial f_i(z+\xi)}{\partial t}} d\xi \\ &= \frac{x_i^2}{16\pi^2 a^2 r^4} L L_c \left(\overline{\frac{\partial f_i}{\partial t}} \right)^2 \end{aligned} \quad (16)$$

where f_i denotes fluctuating force upon unit length.

Correlation length L_c is equivalent to a spanwise length along which pressure fluctuations are significantly correlated and indicates a three-dimensional structure in the wake of the circular cylinder. In this study, we estimated the three-dimensional vorticity distribution by using the spanwise correlation length previously defined by one of the authors (10)(11). That is, the correlation length of a fundamental frequency can be calculated as a function of the Reynolds number,

$$\frac{L_c}{D} = \frac{511}{\sqrt{Re}} \quad (17)$$

Moreover, the correlation length of another kind of vortex is (such as turbulent eddies) about 0.5 times the cylinder diameter. For the simulation of two-dimensional wake sounds, Kato et al (1). have proposed the following method with the correlation length of L_c . In this method, a flow field corresponding to only the unit span of the body and the sound pressure level (SPL) for the entire span is estimated with the equations as shown below:

$$\begin{aligned} \text{If } L_c \leq L_s; \\ SPL &= SPL_s + 10 \log \frac{L}{L_s} \\ \text{If } L_s \leq L_c \leq L; \\ SPL &= SPL_s + 20 \log \frac{L_c}{L_s} + 10 \log \frac{L}{L_c} \\ \text{If } L \leq L_c; \\ SPL &= SPL_s + 20 \log \frac{L}{L_s} \end{aligned} \quad (18)$$

where SPL_s and SPL denote the sound pressure level corresponding to the computational domain and the entire span, respectively. L_s is the length of the computational domain. In the case of two-dimensional calculation, we assumed L_s is equivalent to the diameter of the cylinder.

3. RESULTS AND DISCUSSIONS

Figure 2 shows the vorticity distribution near the circular cylinder obtained by the vortex method, the alternating vortices come from both sides of the cylinder, and flow is separated boundary surface. The separated

shear layer is stretched behind the cylinder and it rolls up at the formation region of the Karman vortices. The numerical result is captured this phenomena. The formation region of the Karman vortices lies between $X/D=1.5$ and 2.0. Furthermore, figure 2 shows the velocity vector field which is measured by using a conditional sampling method. This velocity vector visualized as an observer moving downstream at $0.75U_0$, show the separated shear layer rolls up at $X/D=1.5$ to 2.0. Moreover, the large-scale structure of Karman vortex is clearly observed. The general tendency of the numerical result is similar to the experimental result. We can therefore conclude that the advanced vortex method can be captured the flow separation and vorticity transportation.

Since the LES-based flow simulation requires the large number of the computational elements, unsteady flow field could not calculate a personal computer. However, the advanced vortex method simulates the unsteady flow separation by a small-scale computer with reasonable computational time.

Figure 3 shows the time averaged pressure distribution on the cylinder surface obtained from the vortex method and compared with the results of the LES (12) and experimental results (13).

The result of the vortex method is reasonably agreement with the LES and experimental ones. The base pressure is a slight difference compared with that of the three-dimensional LES and the experiment. The base pressure obtained from the vortex method is similar to the result of the two-dimensional LES. Therefore, this discrepancy is occurred by the flow structure after the separation point which has three dimensional eddy structure. However, The overall agreement with the experiment is fairly good in the vortex method.

Table 1 shows the Reynolds number dependence of the fluid forces and Strouhal number. Furthermore, the fluid forces are also compared with the measured values (14)(15) as shown in figures 4 and 5. The predicted drag is agreement with the experimental ones at the Reynolds number is smaller than 10^5 . This results shows the base pressure difference is small contribution of the drag coefficient at the sub critical Reynolds number. On the other hand, fluctuating lift coefficient, C_{Lrms} is larger than that of the measurement. Kato et al (12). shows that this is attributed to the faster separation velocity in the two dimensional simulation. In order to improve this problem, we have to utilize the three-dimensional vortex method.

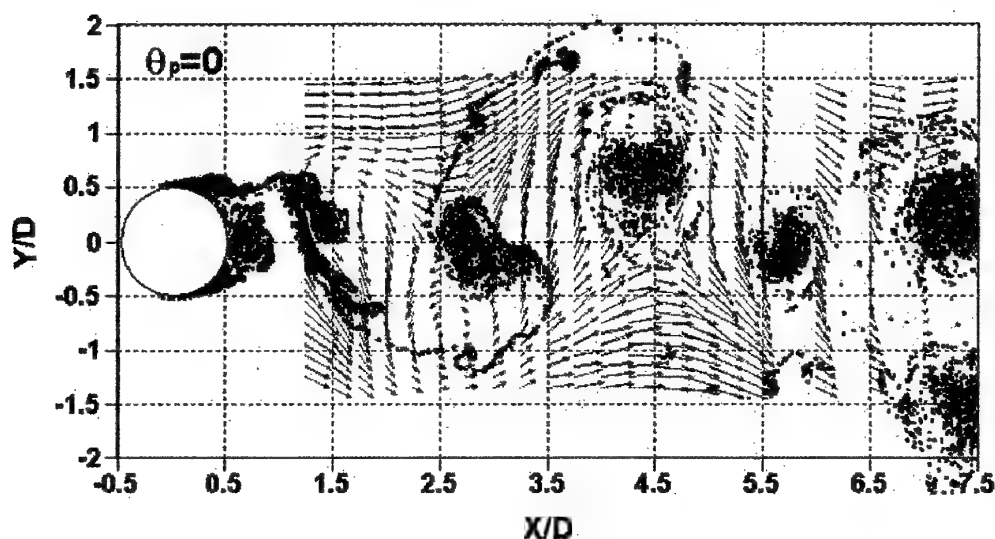


Fig. 2 Flow pattern around a circular cylinder at $Re = 4 \times 10^4$
 →: Velocity vectors measured by a conditional sampling method
 •: Vorticity distribution calculated by the advanced vortex method

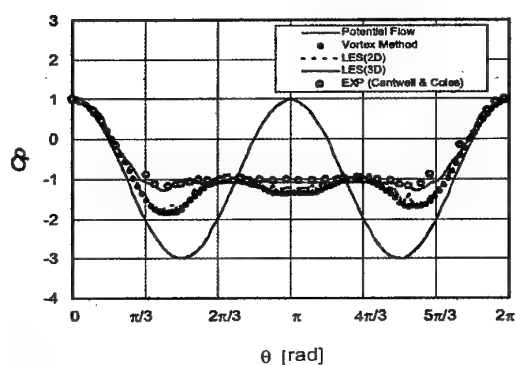


Fig.3 Time averaged surface pressure distribution

Table 1. Computed fluid forces and the Strouhal number

	Re	C_D	C_{Lrms}	S_f
Case 1	2×10^2	1.31	0.47	0.19
Case 2	1×10^3	0.79	0.63	0.21
Case 3	1×10^4	1.13	0.98	0.23
Case 4	4×10^4	1.12	1.02	0.22
Case 5	1×10^5	1.18	1.09	0.22
Case 6	5×10^5	1.01	0.96	0.21
Case 7	4×10^6	0.55	1.19	0.23

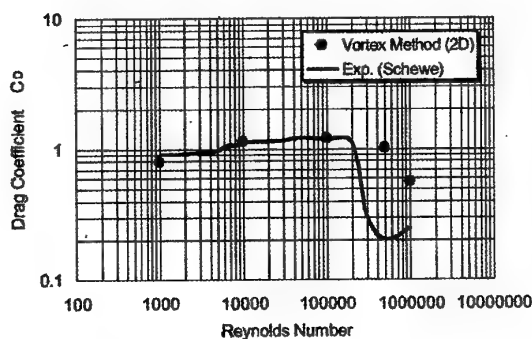


Fig.4 Reynolds number dependence of mean drag coefficient

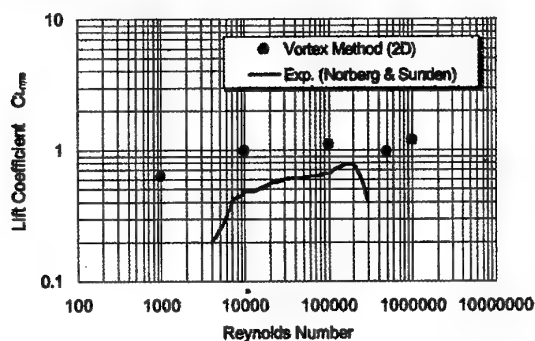


Fig.5 Reynolds number dependence of fluctuating lift coefficient

We attempt to predict aerodynamic sound spectra radiated from a circular cylinder, in Figure 6, by using the advanced vortex method with correlation length assumption. The peak level of the predicted sound obtained from the vortex method is good agreement with the measured ones at the fundamental frequency. However, The predicted spectra has wide-based shape near the fundamental frequency compared with the experimental ones. This results shows that the simulation over estimates the fluctuation of the separation points. In this simulation, 100 vortex sources are used, which means the separation points moves at least 3.6 degree. In order to capture the fine detail of the aerodynamic sound spectra, large number of vortex sources are required. Moreover, the predicted spectrum over estimated at high frequency region, which corresponds to small scale eddies. In two dimensional simulation, vortex stretching is neglected, therefore, the small-scale eddy motion can not simulate.

Aerodynamic sound obtained from the LES-based aeroacoustic simulation is also shown in figure 6. The LES-based simulation agrees fairly well with the measurement. Flow separation and evolution can be captured with the LES. The computation of the LES was performed on parallel computer using up to 32 processing node. The theoretical peak performance of each processing node is 300 MFLOPS. On the other hand, the vortex method use a personal computer or engineering workstation. The advanced vortex method is therefore suitable to simulate unsteady flow fields for industrial applications.

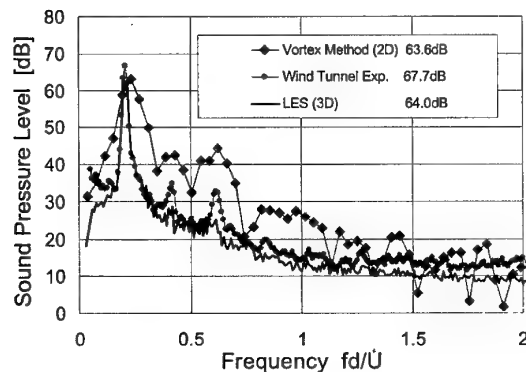


Fig.6 Sound pressure spectra radiated from cylinder wake at Reynolds number of 10^4

Table 2 shows the overall sound pressure levels simulated by the vortex methods. The overall sound pressure levels are 2.4 dB to 4.1 dB smaller than that of wind-tunnel experiments, except for lower Reynolds number. The accuracy is almost the same as the results from the LES-based aeroacoustic simulation.

Table.2 Comparison of sound pressure levels

Re	U [m/s]	Exp.	Vortex method	Error
5.0×10^3	1.8	26.2	20.4	-5.8
1.0×10^4	15	67.7	63.6	-4.1
	3.75	38.4	34.3	-4.1
2.0×10^4	7.5	51.7	49.1	-2.6
4.0×10^4	15	66.6	63.4	-3.2
1.0×10^5	37.5	89	86.6	-2.4

4. CONCLUSIONS

A computational methodology for aeroacoustic simulation based on vortex methods has been developed. The simulation makes use of the Lighthill acoustic analogy, so it based on the decomposition of the flow field and the resulting acoustic field. In order to reduce the computational time and resources, an advanced vortex method is utilized for aeroacoustic simulation.

Aerodynamic sound generated from a circular cylinder at Reynolds numbers between 10^3 to 10^5 are presented. The predicted sound pressure spectra reasonably agree with the one measured in a low-noise wind tunnel, except for the aerodynamic sound is attributed to turbulent eddies. Vortex stretching is not considered in the two-dimensional vortex methods. Therefore, they cannot be captured fine scale turbulent eddy structure and its decay process. To simulate aerodynamic sound from turbulent eddies, three-dimensional vortex methods are required.

The sound pressure levels are 2.4 dB to 4.1 dB smaller than that of the wind-tunnel experiments, which is almost the same as the result of the LES based aeroacoustic simulation. It is concluded that aeroacoustic simulation with vortex methods are sufficiently satisfied by using a standard, desktop PC.

ACKNOWLEDGEMENTS

The authors would like to thank Prof. C. Kato, University of Tokyo, for his fruitful discussions about the aeroacoustic simulation.

REFERENCES

- (1) Kato, C., et al., (1993) "Numerical Prediction of Aerodynamic Noise Radiated from Low Mach Number Turbulent Wake", AIAA Paper 93-0145
- (2) Kato, C., et al. (2000) "Numerical Simulation of Aerodynamic Sound Source in the Wake of a Complex Object", AIAA 2000-1942
- (3) Adachi, S., et al., (1992) "Computation of Aerodynamic Sound Radiation from Flows Past a Wing", DGLR/AIAA Paper 92-02-157
- (4) Uhlman, J. S., (1992) "An Integral Equation Formulation of the Equation of Motion of an Incompressible Fluid", Naval Undersea Warfare Center T.R., 10-086.
- (5) Kamemoto, K., (1995) "On Attractive Features of the Vortex Methods", Computational Fluid Dynamics Review 1995. ed. M. Hafez and K. Oshiuma, p.334-317
- (6) Ojima, A., and Kamemoto, K. (2000), "Numerical Simulation of Unsteady Flow Around Three Dimensional Bluff Bodies by an Advanced Vortex Method", JSME International Journal, (B) 43 (2), 127-135
- (7) Lighthill, M. J., (1952) "On Sound Generated Aerodynamically I. General Theory", Proc. Roy. Soc. London, A211, p.568-587
- (8) Curle, N., (1955) "The Influence of Solid Boundaries upon Aerodynamic Sound", Proc. Roy. Soc. London, A231, p.505-514.
- (9) Philips, O. M., (1956) "The Intensity of Aeolian Tones", J. Fluid Mech. 1-6, p.607-624.
- (10) Iida, A., et al., (1997) "Prediction of Aerodynamic Sound Spectra from a Circular Cylinder", Proc. FLUCOME'97 Vol. 1, p.126-131
- (11) Iida, A., et. al., (1999) "Analysis of Aerodynamic Sound Source with Measurement of Static-pressure Fluctuation", JSME International Journal, (B) 42(2), p.596-605
- (12) Kato, C., and Ikegawa, M., (1991) "Large Eddy Simulation of Unsteady Turbulent Wake of a Circular Cylinder using the Finite Element Method", ASME FED, 117, p.49-56.
- (13) Cantwell, B. and Coles, D., (1983) "An Experimental Study of Entrainment and Transport in the Turbulent near Wake of a Circular Cylinder", J. Fluid Mech., 136, p.321-374.
- (14) Schewe, G., (1983) "On the Force Fluctuation acting on a Circular Cylinder in Cross-flow Sub-critical Reynolds Numbers", J. Fluid Mech., Vol. 133, p.265
- (15) Nøberg B.C. and Sundén, (1987) "Turbulence and Reynolds Number Effects on the Flow and Fluid Forces on a Single Cylinder in Cross Flow, J. Fluids and Structures 1, p. 337

APPLICATION OF THE VORTEX METHOD FOR INVESTIGATING THE BEHAVIOUR AND POTENTIAL HAZARD OF THE WIG TRAILING VORTICES

Nikolai Kornev and Andrei Taranov

Department of Hydromechanics, Marine Technical University St.Petersburg,
Lotsmanskaya 3, St.Petersburg 190008, Russia /Email: kornev@spb.citilyne.ru

ABSTRACT

Numerical simulations based on the computational vortex viscous method are used to investigate behaviour of trailing vortices behind WIG craft. The trailing vortices of WIG craft move in a corridor of limited width. The estimation of the width is given depending on the height of the vortex generation. Characteristics of the vortex wake obtained from the viscous simulation are used for definition of a wake vortex encounter hazard boundary for the WIG craft Hydrowing.

1. INTRODUCTION

Wake vortices of large aircraft are a potential hazard to closely following smaller aircraft. An aircraft encountering the tip vortex of a preceding large aircraft could be mildly disturbed or catastrophically upset. The magnitude of the disturbance experienced depends mainly on the relative size of the vortex generating and vortex penetrating airplane. To reduce the hazard of the trailing vortices the pilot of small aircraft is required to maintain a safe separation distance with the preceding airplane according to the wake vortex separation standards recommended by the Federal Aviation Administration (FAA). The corresponding problem for WIG craft (Fig. 1) can become more important because they operate in a two-dimensional plane without the opportunity for a saving vertical maneuver. Here two questions are considered: What is the configuration of the trailing vortices shed from a WIG craft? How do the trailing vortices affect the motion of a WIG craft penetrating the vortex wake of a preceding WIG craft.

2. BEHAVIOUR OF THE TRAILING VORTICES BEHIND A WIG CRAFT

2.1 Estimates From Potential Theory And Contradiction With Experience

According to potential theory, the tip vortices of WIG craft will continue moving laterally outward until they vanish due to viscous diffusion, Fig.2. Neglecting the

influence of the tip vortex on the opposite side of the craft, the lateral speed of the vortex core is

$$W = \Gamma / (4\pi h_g) \quad (1)$$

where Γ is the vortex circulation and h_g is the height of the vortex centre above the ground.

The following simple estimates show that, if potential theory is applicable, the tip vortex shed from a WIG would produce significant air perturbations and, moving laterally, can damage small ships and coastal objects and hurt people located close to the WIG flight path. For estimating the maximum azimuth velocity induced by a tip vortex we use the Rankine model

$$V_{\max}(t) = \Gamma(t) / [2\pi r_v(t)] \quad (2)$$

where r_v is the vortex core radius. Time dependencies for $\Gamma(t)$ and $r_v(t)$ can be taken from empirical data. For the small WIG Hydrowing VT01 (1), the initial radius of the tip vortex just after roll-up is estimated by using the empirical formula proposed by McCormick et al. (2)

$$r_v(0) = L(0.024 + 0.042C_l) [8 \cdot 10^5 / (LU_0/\nu)]^n \sim 0.14 \text{ m} \quad (3)$$

where L is the mean aerodynamic chord, C_l the lift coefficient, U_0 the speed of the WIG motion, ν the coefficient of kinematic viscosity, and $0.18 < n < 0.21$. Recent investigations show, that the tip vortex radius grows at a very slow laminar rate, in spite of the fact that it is turbulent (3)

$$dr_v/dt = q/2 [\Gamma(0)/t]^{1/2} \quad (4)$$

where q is the vortex core growth rate, which value is about 0.005 for $Re = \Gamma/\nu \approx 3 \cdot 10^6$. From (4) follows

$$r_v(t) = r_v(0) + 0.005 [\Gamma(0)t]^{1/2} \quad (5)$$

As to the dependence $\Gamma(t)$, there is no consensus among researchers about the mechanism of disappearance of tip vortices (4). Two radically different concepts have been held for years. The first concept, named the predictable way (PD), describes the vortex decay as a gradual process. The decrease of vortex circulation occurs gradually under the effect of various dissipation mechanisms. The second called the stochastic collapse concept, is based on the scenario of vortex breakdown resulting from different mechanisms of vortex instability. The tip vortices are stochastically deformed, reconnected and split to small eddies which then dissipate. This concept, rooted mostly in the academic community, is

still unable to provide concrete data for the vortex decay. The PD concept, on the other hand, is based mostly on measurements and is in wide use for practical purposes. In the present work we use the model of Teske et al. (5), which is related to the PD concept. According to this model the decrease of circulation near the ground is

$$\Gamma(t) = \Gamma(0) \exp[-bqt/s] \quad (6)$$

The decay coefficient b is given by Teske et al. (5), depending on $\Gamma(0)$, U_0 , the ambient turbulence level q and the aircraft semispan s . For the craft Hydrowing VT01 we find $0.3 < bq < 0.75$. Strictly speaking, the heights of test flights used for specification of parameters of the model are too large to implement in the model for WIG craft. Unfortunately, analogous investigations for extreme ground effect have not yet been made. Having no alternative, model (6) will be used for further investigations. One can suppose that the complicated interaction of tip vortices with secondary vortices shed from the ground will lead to a much short lifespan of vortices than that predicted by model (6). At least the typical time of the Crow instability is shorter in the ground effect, see (6). Therefore, our further study of the influence of tip vortices on closely following small WIG craft corresponds to simulating the worst case. The maximum azimuth velocity is then obtained combining (2), (4) and (5)

$$V_{\max}(t) = \Gamma(0) \exp[-bqt/s] / \{2\pi(r_v(0) + 0.005[\Gamma(0)t]^{1/2})\} \quad (7)$$

The circulation $\Gamma(0)$ can be obtained by using the panel method and the software Autowing 3 (7).

Usually the open boat escorting the test flights of the Hydrowing was located at the distance of about 30 meters from the runway. If the above estimates are correct the tip vortex generated by the Hydrowing would reach the boat in the time T for which:

$$1/(4\pi h_g) \int_0^T \Gamma(t) dt = 30m \quad (8)$$

The solution of (8) gives times $T=5.35$ sec for $bq=0.3$ and $T=9.68$ sec for $bq=0.75$. At these times the tip vortex induces velocities V_{\max} of 20 m/sec and 4.5 m/sec respectively. It is clear that the perturbations of the air produced by the tip vortex are enough to be felt by a man caught in the path of the passing tip vortex. Surprisingly, the specialists have never registered any significant air perturbations when observing the flight tests of WIGs in closely following escort boats. Moreover, the serious problems with tip vortex perturbations have not been documented when testing the large Russian ekranoplans like KM weighing about 500 ton and generating strong tip vortices.

Obviously, our estimates based on potential theory are not correct. Two mechanisms, both of a viscous nature, could explain the contradiction between potential theory and observations. Either the tip vortex interacting with secondary vortices disappears more quickly than predicted by the predictable decay concept (6), or the secondary vortices generated on the ground strongly affect the motion of the tip vortex, causing it to follow a

trajectory different from potential analysis. Unfortunately, we cannot test the first explanation: present statement of numerical methods and available computer resources don't allow us to investigate the stochastic mechanism of the vortex decay in ground effect. However, the second reason is sufficient to explain the contradiction between potential theory and observations.

2.2 Formulation of Problem

Large efforts have been devoted in recent years to study the interaction of trailing vortices with the ground (8). Commonly, these works are related to the problem of interaction between a two-dimensional vortex dipole generated at a large height of flight $h_g > 2s$ with the ground. The vortex dipole descends generating secondary vortices on the ground. The left and right tip vortices then separate and interact with the secondary vortices which cause the primary vortices to follow a complicated trajectory with multiple rebounding. A usual time of simulation covers two to three loops of the primary tip vortex.

A WIG tip vortex generated in close proximity to the ground $h_g \ll s$ undergoes more intensive looping motions than that of a vortex dipole within the same time. The most advanced results with respect to the time of simulation were obtained by Türk et al. (8). Because the time of simulations published in the literature is limited it is difficult to conclude, using these, whether the rebounding process drastically changes the trajectory of the tip vortices in the ground effect or if it is a secondary effect influencing the lateral motion predicted by potential theory (see Fig.2). Our objective here is to clarify this question.

Our model assumes, that the vortex sheet has completely rolled-up, and that there is only one two-dimensional vortex. This can be assumed because the mutual influence of counter-rotating tip vortices is negligible compared with the strong ground effect. In reality, WIG and aircraft wake vortices are three-dimensional, turbulent flows with high Reynolds numbers. Unfortunately, a three-dimensional method simulating the long wave vortex instability in ground effect requires excessive computational efforts which are absolutely impossible, even with today's supercomputers (8). Below we first describe the method and results for laminar flows. Generalization on turbulent flows and preliminary results of investigations of the influence of turbulence on the vortex dynamics will be given at the end of this section.

The problem is formulated as a problem of two dimensional unsteady motion of an initial vorticity distribution

$$\alpha(x, y, z, t=0) = \begin{cases} \Gamma / (\pi r_v(0)^2), & \text{if } \sqrt{z^2 + (y - h_g)^2} < r_v(0), \\ 0 & \text{otherwise} \end{cases} \quad (9)$$

which yields a Rankine vortex of a strength Γ in a viscous flow. The core radius $r_v(0)$ can be taken from (3). The

two-dimensional Navier-Stokes equation is written in the form

$$\frac{\partial \omega}{\partial t} + \vec{u} \nabla \omega = \nu \Delta \omega \quad (10)$$

The velocity \vec{u} is obtained by solving the Poisson equation:

$$\frac{\partial^2 \psi}{\partial y^2} + \frac{\partial^2 \psi}{\partial z^2} = -\omega \quad (11)$$

for the stream function ψ , and

$$u_z = \frac{\partial \psi}{\partial y}, \quad u_y = -\frac{\partial \psi}{\partial z} \quad (12)$$

The boundary conditions required to solve the Poisson equation are obtained by

$$\psi(y, z, t) = -\frac{1}{2\pi} \iint_{-\infty}^{\infty} \omega(\eta, \xi, t) \ln r d\eta d\xi \quad (13)$$

with $r = [(y-\eta)^2 + (z-\xi)^2]^{1/2}$. The boundary condition on the ground $\vec{u}(y=0, z, t)=0$ includes the no-penetration

$$u_y(y=0, z, t)=0 \quad (14)$$

and the no-slip

$$u_z(y=0, z, t)=0 \quad (15)$$

conditions. (14), which is necessary for solving (10) and (11), can be satisfied automatically by continuously mirroring the vorticity with respect to the ground

$$\omega(-y, z, t) = -\omega(y, z, t) \quad (16)$$

2.3 Numerical Method

Difficulties arise when the problem (10-15) is solved numerically: simulation of the vortex dynamics for a few seconds real time requires, typically, 40000 steps of nondimensional time. The most significant complicating factor is the artificial diffusion which drastically increases in long-time calculations.

For numerical solutions to have a bearing on vortex-ground interaction problems as discussed, the solution procedure should ideally have the following characteristics: (i) it should be free from artificial viscosity errors- the errors implicit to the numerical approximation should be independent of Reynolds number; (ii) it should be able to perform long-time calculation with little diffusion, (iii) it should be capable of solving for impulsive phenomena. The computational vortex method is hold to satisfy these requirements. A salient feature of the method is that the computational domain includes only regions where there is vorticity. For higher Reynolds numbers this domain is increasingly reduced, since vorticity occupies a smaller and smaller fraction of the fluid volume.

It can be shown that the initial boundary value problem for the Navier-Stokes equation (10), (9) and (15) can be written in the form of a non-linear integral equation which can be expanded in a Taylor series for a small time interval (see, for example, (9)). The asymptotic approximation in powers of a small time

interval Δt allows one to define a first order numerical scheme for Δt

$$\omega(y, z, t + \Delta t) = \iint_{-\infty}^{\infty} \omega(\eta, \xi, t) G(y, z, t + \Delta t; \eta, \xi, t) d\eta d\xi + \int_{-\infty}^{\infty} \int_t^{t+\Delta t} \frac{2\gamma(\xi, \tau)}{\tau - t} G(y, z, t; \eta, \xi, \tau) d\tau d\xi + O(\Delta t^2); \quad (17)$$

$$\vec{X}(t + \Delta t) = \vec{X}(t) + \vec{u}(\vec{X}, t) \Delta t \quad (18)$$

where γ is the strength of a spurious vortex sheet generated at the boundary in the interval $[t, t+\Delta t]$ due to the no-slip condition (15) and \vec{X} is the Lagrangian coordinate of a vortex fluid particle. Thus, the initial boundary value problem for the NS equation at every time step can be reduced by splitting it into vortex diffusion (the first integral in (17)), vortex convection (18) and vortex generation at the boundary (the second integral in (17)). Usually, the strength γ is obtained from the no-penetration condition (14). For the simplest geometry, the flow above a flat wall, γ is twice the velocity induced by all vortices located above the ground. The second integral in (17) illustrates the fact that the boundary acts as a source of vorticity which enters the flow domain by mechanism of the vorticity flux (10).

Assume the solution is known at time t and the task is to find the solution at the time $t+\Delta t$. The vortex field is represented by a set of M point vortices located at the nodes of a uniform grid with dimensions $D_x = 7.5 h_g$ and $D_y = 6.5 h_g$ and a spacing of $\Delta = 0.01 h_g$. The time interval Δt was set at $0.009 h_g^2 / \Gamma$. The computational domain moves horizontally such that the primary vortex is nearly in the middle between the left and right domain borders.

In accordance with (17) the computational cycle at each time step consists of three procedures:

Diffusion. It is simulated using a modified version of the particle-strength exchange model. Distributing each point vortex within a related mesh and assuming the vorticity strength γ to be piecewise linear along the ground, both integrals in (17) can be calculated analytically. The first integral taken analytically over a i^{th} cell gives a function of vorticity distribution within the computational domain appearing after diffusion of the i^{th} cell during the time interval Δt . Integrating this vorticity over the j^{th} cell, we obtain the diffusion contribution $\delta\Gamma_{ji}$ of the i^{th} cell to the j^{th} one:

$$\delta\Gamma_{ji} = \frac{\Gamma_i}{4} \{ \text{erf}[(z_j - z_i + \Delta z/2)/\alpha] - \text{erf}[(z_j - z_i - \Delta z/2)/\alpha] \} \cdot \{ \text{erf}[(y_j - y_i + \Delta y/2)/\alpha] - \text{erf}[(y_j - y_i - \Delta y/2)/\alpha] \} \quad (19)$$

with $\alpha = \sqrt{4\nu\Delta t}$. The change in circulation of the i^{th} point vortex related to the i^{th} cell is given by formula

$$\Gamma_i(t + \Delta t) = \Gamma_i(t) + \sum_j^M (\delta\Gamma_{ji} - \delta\Gamma_{ji}) \quad (20)$$

Apparently, the total vorticity of the flow is conserved. The diffusion leads to the redistribution of the vorticity between neighbouring point vortices of the grid. The

similar algorithm is used when calculating the diffusion of a vortex panel on the ground.

Convection. Each cell node is moved by a $\vec{u} \Delta t$ (18). The total circulation within each grid cell is held constant. To calculate \vec{u} we apply a fast algorithm consisting of three steps: calculation of boundary values (13) for ψ using the fast method proposed by Greengard and Rokhlin (11), solving (11) using a fast Poisson solver based on the Hodie finite-difference scheme and numerical differentiation of the stream function (12).

Remeshing. The vorticity field is mapped back onto the original mesh using the third-order Everett's formula (12). By the end of this step we have the initial grid of M point vortices with alternating circulations. A remarkable feature of the remeshing is that the number of vortex elements remains constant and that it avoids instabilities caused by irregularity of the point vortex population. In our experience remeshing is an inevitable procedure of vortex methods. Otherwise, the population of the point vortices, and the necessary computer resources would grow intensively due to generation of new vorticity on flow boundaries.

2.4 Results and Discussion

Good success has been achieved comparing this vortex method with measurements and also with different analytical and numerical results obtained for unsteady, high Reynolds number flows over various engineering devices (see, for example, 13 and 14).

Investigating the dynamics of a single tip vortex generated in close vicinity to the ground, similar physical processes to those described for vortex dipoles (15) have been observed. The primary vortex generates the boundary layer on the ground, separation of which, leads to the creation of the secondary vortex (Fig. 3A,D). The secondary vortex rises up detaching itself from the vortex sheet shed from the ground (Fig. 3B,E). The vortex sheet, in turn, undergoes a strong Kelvin-Helmholtz instability breaking into a few concentrated vortices. The first vortex of the sheet can be absorbed by the secondary vortex increasing its strength. The remaining vortices involved in the pairing process create a tertiary vortex. The primary, secondary and tertiary vortices follow a complicated trajectory.

Breaking up of the vortex sheet and further interaction between vortices is an unstable process sensitive to perturbations. In Fig. 3 we present results of the calculation without (left) and with perturbations (right). Small perturbations in the velocity field were introduced at each 500th time step in form of a wind gust $\delta U_z = 0.02 \Delta z / \Delta t$. Due to perturbations the first vortex of the breaking sheet is not absorbed by the secondary vortex but follows its own looping trajectory. Because the secondary vortex absorbs the tertiary one, its circulation becomes stronger with perturbations than without.

Finally, we have stable vortex configurations consisting of three (without perturbations) or two (with perturbations) vortices (Fig. 3C and 3E) the intensities of

which remain nearly constant. The radii of the vortices increase due to physical and numerical diffusion. The new vortices generated on the ground are rather weak; either they diffuse due to viscosity, or they are absorbed by the vortex configurations mentioned above.

This phenomenon fully explains the differences between potential theory and practical experience (Fig. 4). The following conclusion can be made:

The trailing vortices behind a WIG craft don't follow the potential trajectory, but move in a corridor with a width not exceeding twelve vortex generation heights h_g plus the span of the WIG.

For the WIG craft Hydrowing VT01 flying in cruise (the height of flight is about 0.5-0.7 meter), the border of the corridor lies at about 6 m distance from the wing tip. Unfortunately, due to numerical viscosity, we cannot compute correct results for non-dimensional time > 360 . However, extrapolating the vortex trajectory to larger time, we can assume that the vortices remain in this corridor until they vanish due to various mechanisms of the vortex decay (4). Perhaps, the borders of the corridor will be determined more precisely in the future. Qualitatively the presence of a corridor of a limited width seems plausible. A similar tendency can be revealed from results obtained by Türk et al. (8) for shorter time intervals (see Fig. 4).

2.5 Turbulence Modelling

Turbulence models that are well validated in vortices do not exist today (4). To our opinion, the most serious effort has been done by Shur et al. (16) who used a modified version of the one-equation SA turbulence model proposed by Spalart and Allmaras. The authors modified the production term of the original SA model, multiplied it by the rotation function to take into account the weakening of turbulence in the vortices cores observed in experiments. We implemented this approach, called the SARC (Spalart-Allmaras Rotation/Curvature) model, within the framework of the two-dimensional vortex method.

The transport equation for the turbulent viscosity $\tilde{\nu}$ is

$$\begin{aligned} \tilde{\nu}(\vec{X}, t + \Delta t) = & \tilde{\nu}(\vec{X}, t) + \Delta t [f_{r1} c_{b1} (1 - f_{r2}) \tilde{S} \tilde{\nu} + \\ & 1 / \sigma (\nabla((\nu + \tilde{\nu}) \nabla \tilde{\nu}) + c_{b2} (\nabla \tilde{\nu})^2) - \\ & (c_{w1} f_w - c_{b1} / k^2 f_{r2}) [\tilde{\nu} / d]^2 + f_{r1} \Delta U^2]; \end{aligned}$$

for designations see in Ref. 16. The diffusion operator $\nabla[(\nu + \tilde{\nu}) \nabla \tilde{\nu}] + c_{b2} (\nabla \tilde{\nu})^2$ is resolved on the grid used for solving the Poisson equation (11). Results of our preliminary study which are similar to those presented in (16), show

- i) the altitude of turbulent vortex dipole rebound is about 0.52 times initial distance between vortices, whereas the corresponding value for laminar flow is 0.65,
- ii) the first loop of the vortex trajectory in the turbulent flow lies farther from the dipole symmetry axis than that in laminar flow,

iii) the SARC model predictions seem to be more realistic compared with original SA and shear stress transport models,

iiii) the SARC model allows to get a suppression of the turbulence inside of the vortex core (Compare Fig. 5B and 5C).

Unfortunately, we met significant difficulties arising from a strong numerical instability caused by the production term. Although, the modification proposed in the SARC model decreases the production term, that is not sufficient to prevent the amplification of the numerical instability at large time of simulation. Additional simulations will be conducted to improve the stability of the numerical scheme for turbulent flows.

2.6 Generalization to Three Dimensions

A special code was also developed to solve the present problem within a 3D formulation. For an inviscid flow we obtained promising results: the amplification rate of the 3D inviscid instability of a trailing vortex obtained numerically is very close to the analytical value, taken from (6). Unfortunately, calculation of 3D viscous flow requires excessive computer resources not available to us. Indeed, the length of the 3D instability wave, which is practically most interesting, is about $17.2h_g$. The necessary number of vortex elements, M is about $M \approx 17.2 h_g / \Delta$ times the number of vortex elements used when solving the corresponding 2D problem. Practically this means that a few million vortex elements are needed to resolve the flow. To avoid numerical instability one has to use a small time interval Δt , which together with estimates for M , makes the calculation on a PC impossible.

3 STUDY OF A WAKE VORTEX ENCOUNTER HAZARD BOUNDARY FOR WIG CRAFT HYDROWING

3.1 Formulation of Separated Problems and Their Scaling

Studying the influence of trailing vortices on the dynamics of a closely following small WIG craft can be separated into three partial problems:

1. Calculation of the circulations of the tip vortex generated by a foregoing WIG craft. This problem can be solved by using the commercial software package Autowing 3.0 (7). The circulation Γ_1 obtained from this calculation should be multiplied by $U_0 L$.
2. Calculation of trailing vortex dynamics near the ground. We determine dynamics of a two-dimensional Rankine vortex of unit strength ($\Gamma=1$) and altitude ($h_g=1$). The solution of this problem is described above.
3. Motion simulation for a WIG encountering the vortex wake of a foregoing WIG craft.

The trajectory of the primary and secondary vortices and their strengths (obtained from the solution of the second problem) are input data for the third problem.

The parameters determining the trajectory are dimensionalized as

$$t = h_g^2 T / (\Gamma_1 U_0 L); \quad x_3 = x_2 h_g; \quad y_3 = y_2 h_g,$$

$$\Gamma_{3i} = \Gamma_{2i} \Gamma_1 U_0 L$$

where h_g is the height of generation of the primary vortex, T, x_2, y_2 and Γ_{2i} are, respectively, the nondimensionless time, coordinates and circulations of vortices obtained from the second problem.

The mathematical model for simulation of WIG dynamics is based on the complex mathematical model developed for the WIG craft Hydrowing (17). The baseline simulation was modified to include the wake model and the calculation of the vortex-induced forces and moments using the Vortex Lattice Method. Neither a pilot model nor an automatic control system have been taken into consideration.

3.2 Wake Encounter Simulation

The simulation study was conducted to define the acceptable wake encounter region required for the Hydrowing VT01 to safely encounter a wake shed from the similar craft or from the Hydrowing 80.

In accordance with results obtained in the previous section, the wake model used in the simulation consists of six vortices. The remaining vortices were omitted because of their insignificant strengths. The vortices were modeled by potential vortex lines with a cross section in the form of a Rankine vortex. The core radius was set at 0.20 meter which corresponds to the worst case because the real radius estimated from (5) is larger. The simplified vortex model allows fast calculations of induced velocities anywhere. Due to increasing numerical diffusion we could perform simulations of vortex dynamics at distances $X < 800$ m behind the Hydrowing VT01 and only 170 m behind the Hydrowing 80. Actually, the problem of interaction between WIG craft and vortex wake should be analyzed at larger X . Bearing in mind, that at $T > 120$ the trajectory of vortices becomes nearly periodic, the vortex trajectories are extended to large X assuming the periodicity in the longitudinal direction.

The vortex circulation was decreased in time according to the PD model (6). Simulations of motion were performed using the Runge-Kutta-Verner fifth-order method. The WIG craft was initially positioned in equilibrium related to the cruise regime. The initial lateral distance between the WIG and the nearest tip vortex was about 1000 meters for course angles 45 and 90 degrees. For parallel encounter $\varphi=0^\circ$ the initial lateral distance was variable. The output data was recorded every 0.1s and analyzed to indicate the touch down and pitch-up tendency of the WIG. Limits for safe pitch angle and safe altitude were set at 6° and 3 m respectively. Violations of these limits is considered as an indication of the pitch-up tendency.

3.3 Summary of Calculations

For perpendicular encounter the appearance of the pitch-up tendency was the limiting criteria, whereas for the parallel encounter the limiting criteria was the touchdown due to large roll angle. For $\varphi = 45^\circ$ both touchdown and the pitch-up tendency are equally probable. The most hazardous is the parallel encounter $\varphi = 0^\circ$, because for this path the unacceptable wake encounter region is the largest. In reality, the WIG craft can not follow a course strictly perpendicular to the vortex wake. The initial course can be changed due to both pilot action and perturbations induced by the vortex wake. Therefore, the worst case $\varphi = 0$ should be used to determine the hazardous wake encounter region.

Fig.6 summarizes our results. The solid line limits the hazardous wake encounter region behind the WIG craft. The dashed lines result when taking into account the scattering data used for deriving (6). The results of the present study show, that the lateral distance between paths of small and large WIG craft, roughly estimated, should be not less than 28-30 meters, whereas in the longitudinal direction the spacing interval is about 2.5-3.5 kilometers.

ACKNOWLEDGEMENTS

The work was partly supported by the Russian Foundation for Basic Research, Grant 98-01-01098 and the German Academic Exchange Service (DAAD).

REFERENCES

- (1) Ebert, J., and Meyer, M. (1998), "Hydrowing - a new efficient wing-in-ground effect craft", Workshop proc. WISE up to ekranoplan GEMs, The University New South Wales, p. 267-272.
- (2) McCormick, B.W., Tangler, J.L., and Sherrieb, H.E. (1968), "Structure of trailing vortices", *Journal of Aircraft*, Vol. 5.
- (3) Cotel, A.J., and Breidenthal, R.E. (1999), "Turbulence inside a vortex", *Physics of Fluids*, Vol. 11, No. 10, p. 3026-3029.
- (4) Spalart, P.R. (1998), "Airplane trailing vortices", *Ann.Rev. of Fluid Mech.*, Vol. 30, p. 107-138.
- (5) Teske, M.E., and Bilanin, A.J. (1993), "Decay of aircraft vortices near the ground", *AIAA Journal*, Vol. 31, No. 8, p. 1531-1533.
- (6) Kornev, N.V., and Reichert, G. (1997), "Three-dimensional instability of a pair of trailing vortices near the ground", *AIAA Journal* Vol. 35, No.10, p. 1667-1669.
- (7) Kornev, N.V., and Taranov, A.E. (2001), *AutoWing3.0*, <http://www.cl.spb.ru/taranov/Index.htm>
- (8) Türk, L., Coors, D., and Jacob, D. (1999), "Behaviour of wake vortices near the ground over a large range of Reynolds numbers", *Aerospace Science and Technology*, No.2, p. 71-81.
- (9) Kornev, N.V., and Basin, M.A. (1998), "A way to split the Navier-Stokes equations in the context of vortex method", *Commun. Numer. Meth. in Eng.*, No.14, p. 313-319.
- (10) Koumoutsakos, P., and Leonard, A. (1995), "High resolution simulations of the flow around an impulsively started cylinder using vortex methods", *J.Fluid Mech.*, Vol. 296, p. 1-38.
- (11) Greengard, L., and Rokhlin, V. (1987), "A Fast algorithm for particle simulations", *J. Comput. Physics*, Vol. 73, p. 325-348.
- (12) Koumoutsakos, P., and Shiels, D. (1996), "Simulations of the viscous flow normal to an impulsively started and uniformly accelerated flat plate", *J.Fluid Mech.*, Vol. 328, p. 177-227.
- (13) Taranov, A.E., Kornev, N.V., and Leder, A. (2000), "Development of the computational vortex method for calculation of two-dimensional ship sections with flow separation", *Schiffbau Forschung*, Vol.39, No. 2, p. 95-105.
- (14) Kornev, N.V., and Taranov, A.E. (2000), "Behaviour and Potential Hazard of WIG Trailing Vortices", *Ship Technology Research*, Vol. 47, p. 115-125.
- (15) Orlandi, P. (1990), "Vortex dipole rebound from a wall", *Phys. Fluids A* 2(8), p. 1429-1436.
- (16) Shur M., Strelets M., Travin, A., and Spalart, P.R. (1998), "Two numerical studies of trailing vortices", *AIAA-98-0595*, 22p.
- (17) Benedict, K., Kornev, N., Meyer, M., and Ebert, J. (2001), "Complex mathematical model of the WIG motion including the take-off mode", to be published in the *Journal of Ocean Engineering*.

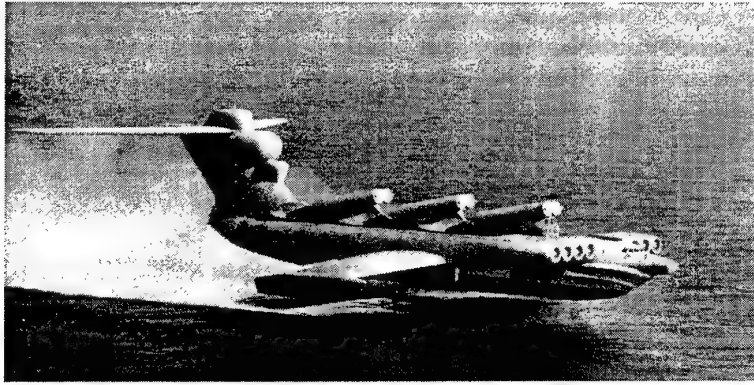


Fig 1. The large WIG craft Lun (360 t) generates strong tip vortices

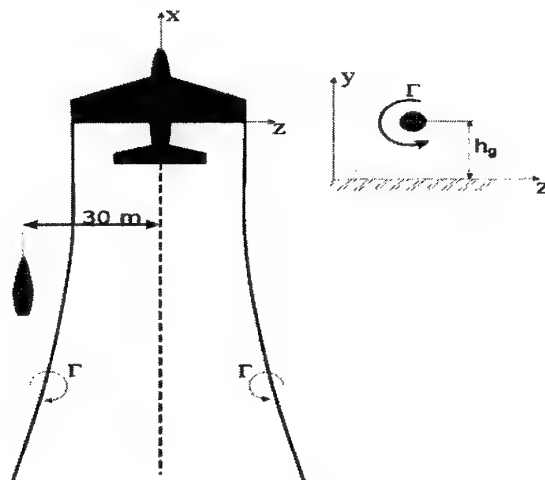


Fig. 2. Potential wake model for WIG craft.

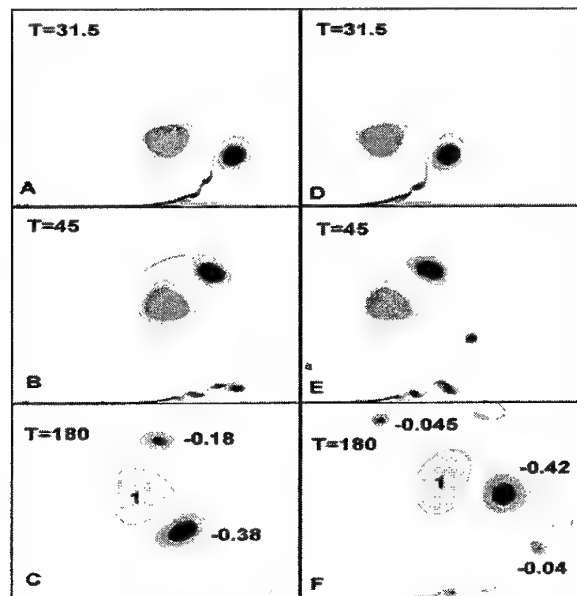


Fig. 3. Vorticity distribution without (left) and with (right) perturbations, $Re=10^5$, $T=\Gamma t/h_g^2$

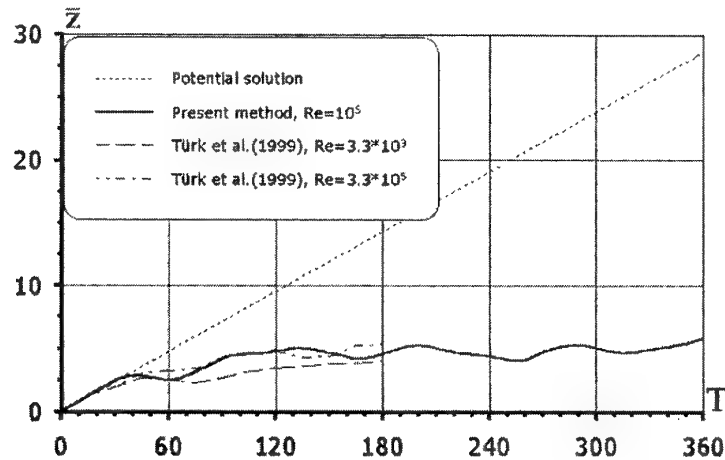


Fig. 4. Primary vortex lateral position versus time for different Reynolds numbers.



Fig.5. Fragments of vorticity and eddy viscosity fields for turbulent flow, $T=4$, $Re=3 \times 10^6$. A - vorticity field, SARC model, B - eddy viscosity field, SARC model, C - eddy viscosity field, SA model.

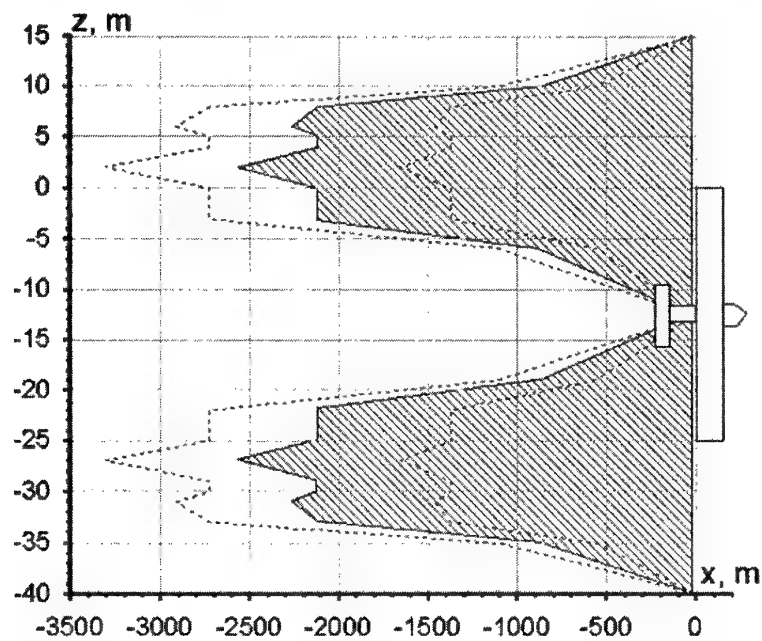


Fig. 6 Hazardous region for the Hydrowing VT01 (1 ton) operating close to the Hydrowing 80 (33 ton).

A STUDY OF THE BEHAVIOR OF CRITICAL LAYER IN DENSITY STRATIFIED SHEAR FLOWS BY LATTICE VORTEX METHOD

Michihisa TSUTAHARA* and Xiaofeng ZHANG

The Graduate School of Science and Technology, Kobe University
Rokko, Nada, Kobe 657-8501 Japan /Email: tutahara@mech.kobe-u.ac.jp

ABSTRACT

The lattice vortex method (LVM) is used to simulate density stratified fluid flows with a critical layer. From the viewpoint of vorticity generation mechanism, it is explained that a gravity wave approaching to a critical layer exhibits different properties depending on the Richardson number at the critical layer. When the Richardson number $R_i > 0.25$, the transported vorticity and generated vorticity near the critical layer are canceled out, and the critical layer acts as a absorber: the perturbation induced by an obstacle can not pass through the critical layer to propagate upward. For the Richardson number $R_i < 0.25$, the over reflection, predicted from the linear theory, is observed, and this mechanism is also explained by vortex dynamics.

1. INTRODUCTION

Density stratified flows are of importance in large-scale motions of fluid of atmosphere or oceans. One of the most interesting phenomena in the density-stratified flows is the internal gravity wave, which is generated by an obstacle in a flow. When the flow has shear with the velocity distribution of $U(z)$, where U is the horizontal velocity far upstream and z is

taken in the vertical upward direction, there will be a layer where the flow velocity and the phase velocity of the internal wave c coincide with each other $U = c$. This layer is called the critical layer. As to the interaction of the critical layer and the internal waves, the critical layer behaves like an absorber, or a amplifier. On the other hand, in a linear stability theory, the shear is stable when the Richardson number

$$R_i = \frac{N_0^2}{\left(\frac{dU(z)}{dz}\right)^2} \quad (1)$$

is larger than $1/4$, and vice versa[1][2], where

$$N_0 = \left(-\frac{g}{\rho_0} \frac{d\rho}{dz}\right)^{1/2} \quad (2)$$

is the buoyancy frequency and $\rho(z)$ is the density distribution without any disturbance, ρ_0 is the reference density, and g is the acceleration due to gravity. When the shear flow is stable the internal waves are absorbed at the critical layer[3]-[5]. On the other hand, when the shear is unstable the internal waves are sometimes over-reflected, that is, the waves are amplified and reflected [6][7].

These behavior of the critical layer is numerically studied by the lattice vortex

method. The lattice vortex method is one of the discrete vortex method, and the calculation domain is discretized by regular lattice and discrete vortices are located at the lattice sites. The vortices move with the induced velocity at each lattice site, and after the movements the vortices are re-distributed onto the lattice sites. The detail will be presented in the following section.

This paper shows that such complex phenomena like internal gravity waves and their absorption and/or reflections in density stratified fluids can be simulated just by the kinematics of vortex.

2. GOVERNING EQUATIONS AND METHOD OF CALCULATION

2.1 Formulation

The fluid is assumed incompressible, inviscid, and non-diffusive, and we consider a two-dimensional flow. The equation of continuity, the Euler equations and the equation of incompressibility are

$$\frac{\partial u}{\partial x} + \frac{\partial w}{\partial z} = 0 \quad (3)$$

$$\frac{\partial u}{\partial t} + u \frac{\partial u}{\partial x} + w \frac{\partial u}{\partial z} = -\frac{1}{\rho_0} \frac{\partial p}{\partial x} \quad (4)$$

$$\frac{\partial w}{\partial t} + u \frac{\partial w}{\partial x} + w \frac{\partial w}{\partial z} = -\frac{1}{\rho_0} \frac{\partial p}{\partial z} - \frac{\rho}{\rho_0} g \quad (5)$$

$$\frac{\partial \rho}{\partial t} + u \frac{\partial \rho}{\partial x} + w \frac{\partial \rho}{\partial z} = 0 \quad (6)$$

where u, w are the velocity components in x (horizontal) and z (vertical) directions, p is the pressure, g is the acceleration due to gravity, and ρ_0 is the reference density (say the density at the bottom).

From (4) and (5), we obtain an evolution equation for the vorticity $\xi = \frac{\partial w}{\partial x} - \frac{\partial u}{\partial z}$ as

$$\frac{\partial \xi}{\partial t} + u \frac{\partial \xi}{\partial x} + w \frac{\partial \xi}{\partial z} = \frac{D\xi}{Dt} = -\frac{g}{\rho_0} \frac{\partial \rho}{\partial x} \quad (7)$$

and RHS of (7), the density gradient, represents the source term of the

vorticity[8]. Equation (7) will be discretized in Lagrangean manner as

$$\xi(x + u\Delta t, z + w\Delta t, t + \Delta t) = \xi(x, z, t) - \frac{g}{\rho_0} \frac{\partial \rho}{\partial x} \Delta t \quad (8)$$

and u and w are calculated by the Biot-Svart law as

$$u_i = -\frac{1}{2\pi} \sum_{j=1}^M \frac{\Gamma_j (z_i - z_j)}{(x_i - x_j)^2 + (z_i - z_j)^2} \quad (9)$$

$$w_i = \frac{1}{2\pi} \sum_{j=1}^M \frac{\Gamma_j (x_i - x_j)}{(x_i - x_j)^2 + (z_i - z_j)^2} \quad (10)$$

In Eqs.(9) and (10), Γ represents the circulation of the vorticity which will be considered concentrate at the lattice site or that of the total vorticity spread over a finite area around the lattice site. Actually, (8) is solved by calculating the motion of the point vortices located at the lattice site. Calculation is performed in a semi-Lagrangean manner, that is, the point vortices at lattice sites move in a manner shown in (8) in which ξ should be replaced by Γ . At that time the value of the circulation must be renewed according to LHS of (8).

The point vortices usually move points different from the lattice sites. Then the vortices are re-distributed by the area rule shown as in Fig.1. Therefore the vortices are always defined at the lattice sites. In our method, the square lattice is used to discretize the flow domain. Since the lattice is very regular, the induced velocity can be calculated beforehand. These are points different from the ordinary Vortex-in-Cell method.

This method is also different from the so-called vorticity-streamline method in the finite difference calculation. In our method, the vortices are transferred in Lagrangian manner, so that this method is free from the so-called Courant-Friedrich-Lewy condition.

Equation (6) is calculated by the ordinary finite difference method.

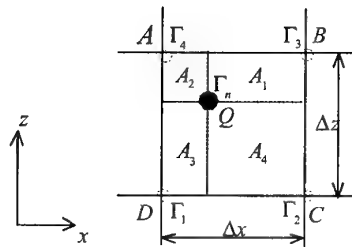


Fig.1 Area weighting scheme for the distribution of vorticity

Another point to be noted is that the velocity at any point is calculated by the Biot-Savart law (9) and (10), and the base flow velocity $U(z)$ is added. The shear layer may be represented as a layer of vorticity, but this layer is not treated as a vortical layer in this study. We also assume that the base shear layer is not affected by the vorticity generated in the flow field. In this sense, the treatment in this paper is linear approximation as for the shear layer.

2.2 Perturbation quantities

Some perturbation quantities will be introduced here, because they will be used to calculate the energy flow in the flow field.

The pressure and the density can be written as

$$p(x, z, t) = \bar{p}(z) + p'(x, z, t) \quad (11)$$

$$\rho(x, z, t) = \bar{\rho}(z) + \rho'(x, z, t) \quad (12)$$

$$\frac{d\bar{p}(z)}{dz} = -\bar{\rho}(z)g \quad (13)$$

where \bar{p} and $\bar{\rho}$ are the static hydraulic pressure and the density without the obstacle, and p' and ρ' represent the perturbation pressure and the density. Substituting (11) to (13) into (3) and (4), we obtain the following equations for the perturbation pressure.

$$\frac{\partial u}{\partial t} + u \frac{\partial u}{\partial x} + w \frac{\partial u}{\partial z} = -\frac{1}{\rho_0} \frac{\partial p'}{\partial x} \quad (14)$$

$$\frac{\partial w}{\partial t} + u \frac{\partial w}{\partial x} + w \frac{\partial w}{\partial z} = -\frac{1}{\rho_0} \frac{\partial p'}{\partial z} - \frac{\rho'}{\rho_0} g \quad (15)$$

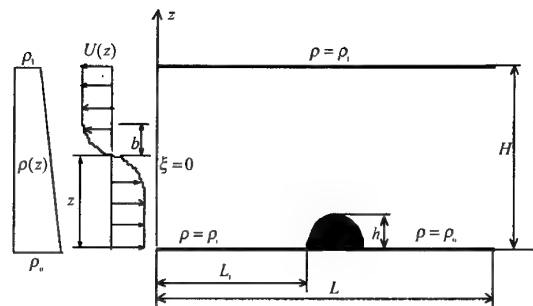


Fig.2 Schematic of critical layer problem

From (14) and (15), using the continuity equation (3), a Poisson equation for the perturbation pressure is given as

$$\Delta p' = -\rho_0 \left[\left(\frac{\partial u}{\partial x} \right)^2 + 2 \frac{\partial u}{\partial z} \frac{\partial w}{\partial x} + \left(\frac{\partial w}{\partial z} \right)^2 \right] - g \frac{\partial \rho'}{\partial z} \quad (16)$$

Equation (16) is solved by the ordinary SOR method.

3. MODEL OF SIMULATION

Two-dimensional incompressible density stratified flows past a semicircle obstacle in a channel of finite depth H as shown in Fig.2. The density distribution far upstream is expressed as

$$\rho(z) = \rho_0 - \left(1 - \frac{z}{H}\right) \rho_0 \quad (17)$$

and the velocity distribution there is assumed to have a form

$$U(z) = U_0 \tanh \left[\frac{z_c - z}{b} \right] \quad (18)$$

in which changing the value of b we can define any value of the Richardson number of the shear. In this case, the critical layer is at the level of zero velocity, that is at $z = z_c$, because the internal waves occur on the lee-side of the obstacle and their phase velocity is zero. Therefore the Richardson number of the shear flow is defined at $z = z_c$ as

$$R_i = b^2 \left(\frac{N_0}{U_0} \right)^2 \quad (19)$$

The square lattice is used and the width of the lattice is taken unity and all

the length scales are non-dimensionalized by the lattice width. The value of U_0 in (18) is taken as the standard velocity and the time is also non-dimensionalized by U_0 and the lattice width. The number of the lattice is 250×80 ($L \times H$), the position of the semicircle obstacle L_1 is 160, the height of the critical layer $z_c = 40$, the radius of the obstacle is 5 and the obstacle is represented by a block of the square lattices inside the semicircle.

4. RESULTS AND DISCUSSION

4.1 Case of stable critical layer

In Fig.3, the streamlines and the density contours near the obstacle at $t = 50$ for the Richardson number 5.0 are presented. In the linear theory, the critical layer is stable. These figures show that no internal waves appear above the critical layer, that is, all the internal waves generated by the obstacle are absorbed by the critical layer. The vorticity distributions at $t = 15$ and 50 are shown in Fig.4, and the density gradient distribution $\partial\rho/\partial x$ at the same instants in Fig.5. The patterns of internal

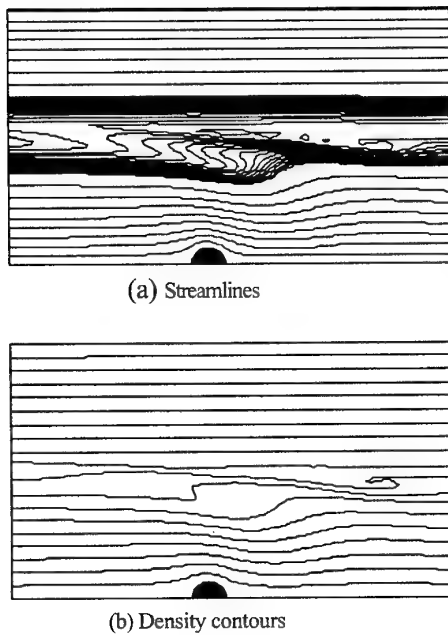


Fig.3 Flow patterns for $Ri=5.0$ at $t=50$

waves are clearly shown in these figures. In Fig.4, the symbols + and - represent the vorticity rotating, respectively, anti-clockwise and clockwise. In Fig.5, the same symbols represent the source producing the vorticity of the same

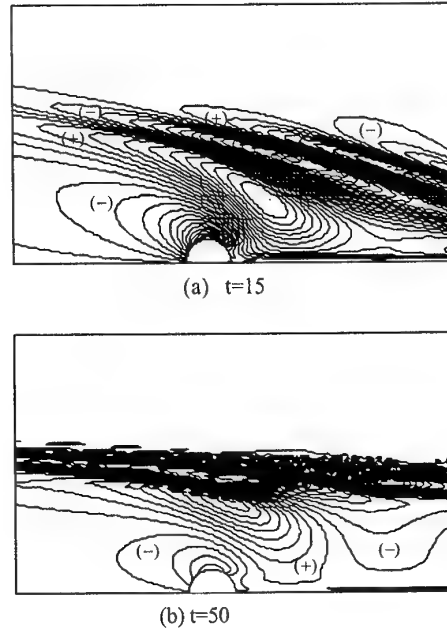


Fig.4. The contours of vorticity for $Ri=5.0$

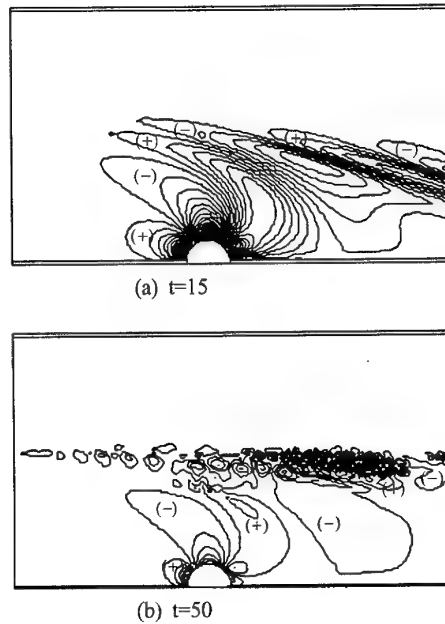


Fig.5 The contours of $\partial\rho/\partial x$ for $Ri=5.0$

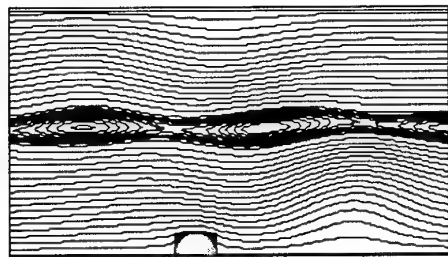
symbols. Looking at the two distributions, especially at $t=15$, the vorticity is canceled out by source term, that is the density gradient, near the critical layer.

At $t=50$, very strong vorticity layer appears near the critical layer, because the internal waves break down at the layer as shown in Fig. 3.

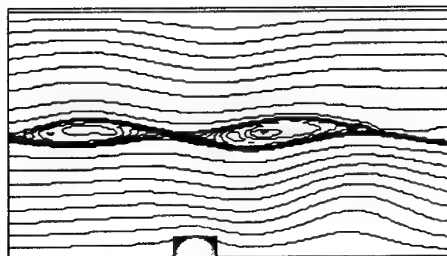
4.2 Case of unstable critical layer

Figure 6 shows the streamlines and the density contours at $t=50$ for the Richardson number 0.1, so that the critical layer is unstable according to the linear theory. It is seen that the internal waves propagate above the critical layer, and the cat's eye flow patterns appear in the critical layer [9].

In Fig.7, the vorticity distributions at $t=15$ and 50 are shown, and the density gradient distributions are shown in Fig.8. Different from the case of stable critical layer, density gradient distributes as to strengthen the vorticity. This means that the internal waves become stronger and reflect at the critical layer, that is called 'over reflection'.



(a) Streamlines



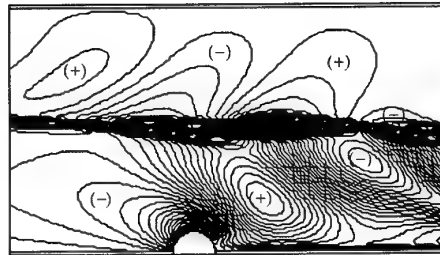
(b) Density contours

Fig.6 Flow patterns for $Ri=0.1$ at $t=50$

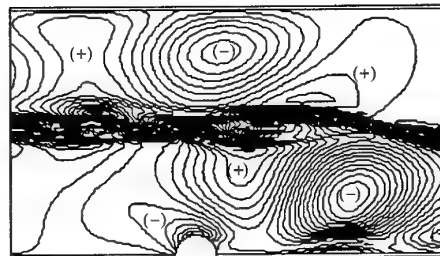
4.3 Perturbation energy

We consider the following perturbation energy equation

$$\frac{1}{2} \frac{\partial}{\partial t} \{ \overline{u'u'} + \overline{w'w'} \} = - \frac{dU}{dz} \overline{u'w'} - \frac{\partial}{\partial z} \overline{p'w'} \quad (19)$$

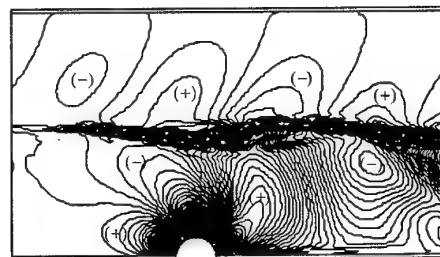


(a) $t=15$

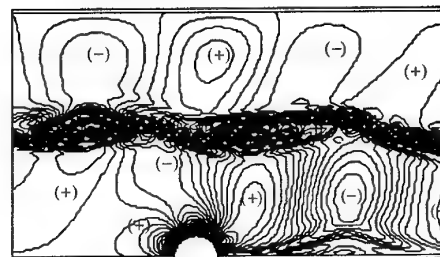


(b) $t=50$

Fig.7 The contours of vorticity for $Ri=0.1$



(a) $t=15$



(b) $t=50$

Fig.8 The contours of $\partial\rho/\partial x$ for $Ri=0.1$

where u' and w' are the perturbation velocity that are obtained by the Biot-Savart law, and p' is the perturbation pressure obtained by (16). The over bar represents the time average. The

perturbation kinetic energy $\frac{1}{2}(\overline{u'u'} + \overline{w'w'})$,

the Reynolds stress $\overline{u'w'}$, and the energy due to the pressure and the vertical component of the velocity $\overline{p'w'}$ is given as

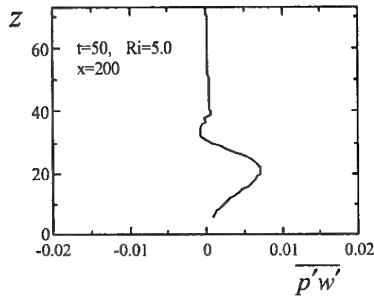
$$\frac{1}{2}(\overline{u'u'} + \overline{w'w'}) = \frac{\sum(u'u') + \sum(w'w')}{STEP} \quad (20)$$

$$\overline{u'w'} = \frac{\sum(u'w')}{STEP} \quad (21)$$

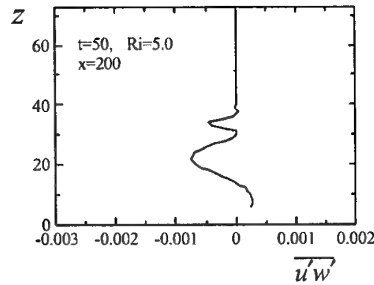
$$\overline{p'w'} = \frac{\sum(p'w')}{STEP} \quad (22)$$

where $STEP$ represents the number of time step to take time average and we chose $STEP=100$.

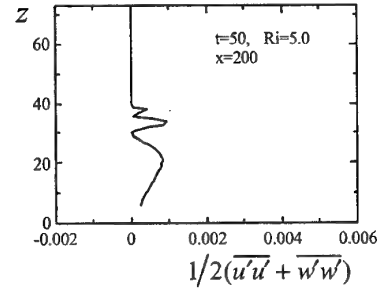
Figures 7 and 8 show the vertical distributions of $\overline{u'w'}$, $\overline{p'w'}$, $\frac{1}{2}(\overline{u'u'} + \overline{w'w'})$ on the cross-section at $x=200$ (lee-side of the obstacle) for $Ri=5.0$ and $Ri=0.1$ at time $t=50$.



(a) Distribution of $\overline{p'w'}$

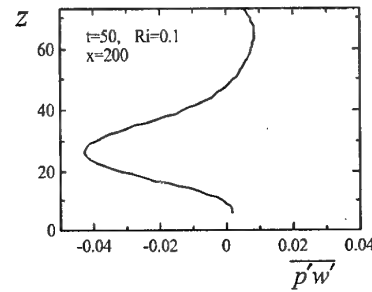


(b) Distribution of $\overline{u'w'}$

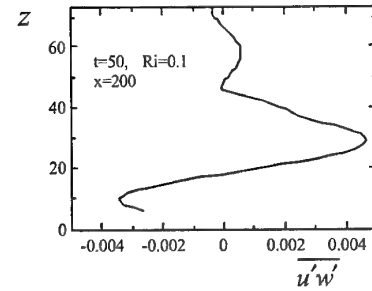


(c) Distribution of $\frac{1}{2}(\overline{u'u'} + \overline{w'w'})$

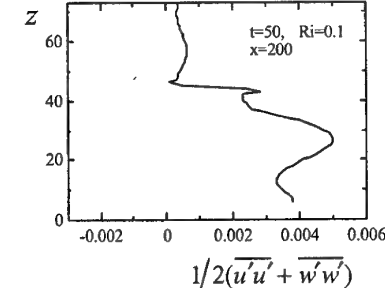
Fig.7 Distributions of perturbation valuables for $Ri=5.0$ at $t=50$



(a) Distribution of $\overline{p'w'}$



(b) Distribution of $\overline{u'w'}$



(c) Distribution of $\frac{1}{2}(\overline{u'u'} + \overline{w'w'})$

Fig.8 Distributions of perturbation valuables for $Ri=0.1$ at $t=50$

For the case of stable critical layer for $Ri=5.0$, the Reynolds stress is zero above the critical layer ($z>40$) and there is no exchange between the base flow and the waves. In the region below the critical layer ($z<40$), the perturbation energy is translated upward ($\overline{p'w'} > 0$), and the energy is fed to the base flow ($\overline{u'w'} < 0$) because $dU(z)/dz < 0$.

On the other hand, for the case of unstable critical layer for $Ri=0.1$, the perturbation energy is translated downward ($\overline{p'w'} < 0$) in the region below the critical layer ($z<40$). This shows that the internal waves occur the 'over-reflection' at the critical layer [10]. In the region above the critical layer ($z>40$), the perturbation energy is translated upward ($\overline{p'w'} > 0$), and the base flow feeds the energy to the internal waves ($\overline{u'w'} > 0$). It is also noted that the perturbation energy increases much in the region below the critical layer ($z<40$) as a result of the 'over-reflection'.

5. CONCLUSION

The internal gravity waves in stratified shear flows are studied by lattice vortex method employing the Boussinesque approximation. It is clarified by vortex dynamics that the behavior of the critical

layer to the internal waves generated by an obstacle changes with the shear strength.

REFERENCES

- (1) J. R. Booker and F.P. Bretherton, J. Fluid Mech., 27(1967), 513--539.
- (2) J.W. Miles, J. Fluid Mech., 10(1961), 496--508.
- (3) J. F. Scinocca and W.R. Peltier, J. Atmospheric Sci. 48(1991), 1560--1572.
- (4) D. R. Durran and J.B. Klemp, J. Atmospheric Sci. 44(1987), 3402--3412.
- (5) T. L. Clark and W.R. Peltier, J. Atmospheric Sci. 41(1984), 3122--3134.
- (6) M. G. Wurtele, etc., Annu. Rev. Fluid Mech. 28 (1996), 429--476.
- (7) P. G. Baines, Topographic effects in stratified flows, (1995), Cambridge University Press.
- (8) C.-S. Yih, Stratified Flows, Academic Press, (1980)
- (9) S.A. Maslowe, Ann. Rev. Fluid Mech. 18(1986), 803--814
- (10) R. S. Lindzen and K. K. Tung, J. Atmospheric Sci. 35(1978), 1627--1632.

ANALYSIS OF UNSTEADY HEAT TRANSFER IN THE WAKE BEHIND A CIRCULAR CYLINDER IN A UNIFORM FLOW BY A VORTEX AND HEAT ELEMENT METHOD

Hajime Nakamura

Department of Mechanical Engineering, National Defense Academy,
1-10-20 Hashirimizu, Yokosuka 239-8686, Japan / Email: nhajime@nda.ac.jp

Kyoji Kamemoto

Department of Mechanical Engineering and Materials Science, Yokohama National University,
79-5 Tokiwadai, Hodogaya-Ku, Yokohama 240-8501, Japan / Email: kame@post.me.ynu.ac.jp

Tamotsu Igarashi

Department of Mechanical Engineering, National Defense Academy,
1-10-20 Hashirimizu, Yokosuka 239-8686, Japan / Email: tigarash@nda.ac.jp

ABSTRACT

A vortex element method based on Biot-Savalt Law and the core spreading model was extended to an analysis for forced convection heat transfer. Discrete heat elements were introduced into the flow field close to a wall surface in addition to nascent vortex elements. In this study, unsteady flow and heat transfer were simulated around a circular cylinder in a uniform flow in the range of $Re = 200 - 1000$, and $Pr = 0.71$. From the result of the present simulation, the mechanism of unsteady heat transfer was clarified in the separated flow region behind the cylinder.

1. INTRODUCTION

Since the separated flow has an unsteady characteristic in nature, the heat transfer in the separated flow region is also unsteady. Boulos and Pei (1) and Kumada et al. (2) investigated the unsteady heat transfer around a circular cylinder in a uniform flow. However, its mechanism in the separated flow region was not satisfactorily clarified because of inadequate measurements technique, e.g., inadequate response time of a heat flux sensor, or the lack of simultaneous measurements of flow and heat transfer. Scholten and Murray (3) carried out the simultaneous measurements of heat transfer and velocity using a hot film and a LDV, respectively. However, the mechanism of the unsteady heat transfer in the separated flow region was still not clear. It is considered that an approach by a numerical simulation seems available to overcome this difficulty.

For the simulation of flow around bluff bodies, the vortex method based on Biot-Savalt Law has attractive features; its algorithm is easy to understand based on physics of flow, and the complex work of grid generation is not necessary for numerical treatment. In concern with

the expression of viscous diffusion of vorticity, the random walk method by Chorin (4,5), the core spreading method by Leonard (6), the surface element method by Lewis (7), and the diffusion velocity method by Ogami and Akamatsu (8) were proposed. It has been shown that an analysis for viscous flow is possible by the vortex method.

An application of the vortex method to the analysis for heat transfer was firstly considered by Smith and Stansby (9). Using the vortex in cell method incorporate with the random walk model, they introduced both vortex and temperature particles according to the similarity of equations of vorticity transport and forced convection heat transfer in a two-dimensional flow. The result of the surface and time-averaged Nusselt number of a circular cylinder at constant surface temperature showed reasonable agreement with experiment for moderate Reynolds number from $Re = 23$ to 289. Kamemoto and Miyasaka (10) used Biot-Savalt Law method incorporate with the core spreading model to simulate the forced convection heat transfer around a circular cylinder at constant surface temperature for the Reynolds number of $Re = 10^3$, 10^4 and 10^5 . Discrete heat elements with thermal core were introduced from the thin thermal layer along the body surface. Although they made an approximation that the temperature in the thermal layer was constant along the normal direction, the time-averaged Nusselt number distribution showed reasonable agreement with that of experiment.

The purpose of the present study is to clarify the mechanism of unsteady heat transfer in the separated flow region behind a circular cylinder. In order to simulate the velocity and thermal boundary layers around a body, we improved the method proposed by Kamemoto and Miyasaka (10). Each of vorticity and thermal layer was set to be much thinner than the boundary layer, and the temperature gradient along the normal direction was

considered in the thermal layer. The heat transport from the body surface to the thermal layer was determined by the temperature gradient at the surface. To reduce the computational time and to suppress the unnecessary fluctuation accompanied with discrete elements adjacent to the surface, the secondary vorticity and thermal layers were also introduced adjacent to each of first vorticity and thermal layers. In the present study, two-dimensional analysis around a circular cylinder was performed in the range of $Re = u_\infty d / \nu = 200 - 1000$ to clear the basic behavior of unsteady heat transfer in the separated flow region.

NOMENCLATURE

C_D, C_L	: Drag and lift coefficient
d	: diameter of a circular cylinder
h_i	: heat transfer coefficient $= \dot{q} / (T_w - T_\infty)$
L	: length of a flat plate
Nu	: Nusselt number $= h_i d / \lambda$
Nu_m	: overall Nusselt number
Nu_{rms}	: r.m.s. value of fluctuating Nusselt number
n	: normal direction to the surface
Pr	: Prandtl number $= \nu / \alpha$
p	: pressure
\dot{q}	: heat flux by convection
Re	: Reynolds number $= u_\infty d / \nu$
r	: position from the center of a circular cylinder
T	: temperature
T_∞, T_w	: free stream and wall temperature
t	: time
u	: velocity
u_0	: velocity at the outer edge of boundary layer
u_∞	: free stream velocity
u_d	: diffusion velocity
α	: thermal diffusivity
ϕ	: angle around a circular cylinder from front stagnation point
Γ	: circulation
λ	: thermal conductivity of fluid $= \rho c_p \alpha$
ν	: kinematic viscosity of fluid
ω	: vorticity

Subscripts

f, r	: front and rear stagnation point of a circular cylinder
h	: heat element
i, j	: i th surface element, and j th discrete element
n, t	: normal and tangential direction to surface

2. ALGORITHMS

2.1 Mathematical Basis

The governing equation of a viscous and incompressible flow is described by the vorticity transport equation derived from the Navier-Stokes equation and equation of flow continuity

$$\frac{\partial \bar{\omega}}{\partial t} + (\bar{u} \cdot \text{grad}) \bar{\omega} = (\bar{\omega} \cdot \text{grad}) \bar{u} + \nu \nabla^2 \bar{\omega}. \quad (1)$$

Here, the effect of buoyancy is not considered because the present study is focused on the forced convection heat transfer. The vorticity ω is defined as

$$\bar{\omega} = \text{rot } \bar{u}. \quad (2)$$

Lagrangian expression for the vorticity transport equation (1) is given by

$$\frac{d\bar{\omega}}{dt} = (\bar{\omega} \cdot \text{grad}) \bar{u} + \nu \nabla^2 \bar{\omega}. \quad (3)$$

In case of two-dimensional flow, the first term of the right hand side in Eq. (3) disappears and thus the vorticity transport equation is simply expressed as

$$\frac{d\bar{\omega}}{dt} = \nu \nabla^2 \bar{\omega}. \quad (4)$$

In the present study, viscous diffusion is taken into account by the core spreading method based on Eq. (4).

The energy equation is expressed as

$$\frac{\partial T}{\partial t} + (\bar{u} \cdot \text{grad}) T = \alpha \nabla^2 T. \quad (5)$$

Here, the effect of radiation is not considered. Lagrangian expression for Eq. (5) is given by

$$\frac{dT}{dt} = \alpha \nabla^2 T. \quad (6)$$

It is clear that the energy equation (6) has the similar form to the vorticity transport equation (4). This suggests that the energy equation (6) can be solved in an analogous way using the core spreading method.

2.2 Generalized Biot-Savart Law

As explained by Wu and Tompson (11), Biot-Savart Law can be derived from the definition equation of vorticity (2) as

$$\bar{u} = \int_V \bar{\omega}_0 \times \nabla_0 G dV + \int_S [(\bar{n}_0 \cdot \bar{u}_0) \cdot \nabla_0 G - (\bar{n}_0 \times \bar{u}_0) \times \nabla_0 G] dS, \quad (7)$$

where subscript '0' denotes variable, differentiation and integration at a location \bar{r}_0 , and \bar{n}_0 denotes the normal unit vector to a boundary surface S at \bar{r}_0 . And G is the fundamental solution of the scalar Laplace equation with the delta function $\delta(r - r_0)$ in the right hand side, which is written for the two-dimensional equation as

$$G = -\frac{1}{2\pi} \log R, \quad (8)$$

where $R = |\vec{R}| = |\vec{r} - \vec{r}_0|$. In Eq. (7), the first term of the right hand side expresses the induced velocity by the vorticity distribution in the flow field, and the second term expresses the velocity caused by source and vortex distributions around the body surface.

Each of vortex and heat elements distributed in the flow field moves according to the following equation,

$$\frac{d\vec{r}}{dt} = \vec{u}. \quad (9)$$

The position of each element at the next time step, $t + dt$, is determined by the 2nd order central difference equation, expressed as

$$\vec{r}(t + dt) = \vec{r}(t) + \frac{1}{2} \{ \vec{u}(t) + \vec{u}(t + dt)' \} dt, \quad (10)$$

where $\vec{u}(t + dt)'$ is the velocity predicted by a forward difference equation.

2.3 Calculation of Pressure

The pressure Poisson equation is expressed as

$$\nabla^2 p = -\text{div}(\vec{u} \cdot \text{grad } \vec{u}), \quad (11)$$

where p is the dimensionless pressure. The following integration equation was formulated by Uhlman (12) using the Bernoulli function $H = p + u^2/2$,

$$\begin{aligned} \beta H + \int_S H \frac{\partial G}{\partial n} dS = - \int_V \nabla G (\vec{u} \times \vec{\omega}) dV \\ - \nu \int_S \left\{ G \cdot \vec{n} \cdot \frac{\partial \vec{u}}{\partial t} + \vec{n} \cdot (\nabla G \times \vec{\omega}) \right\} dS. \end{aligned} \quad (12)$$

Here, $\beta = 1$ in the flow field and $\beta = 1/2$ on the boundary S . G is the fundamental solution given by Eq. (8).

2.4 Introduction of Nascent Vortex Elements

Figure 1 shows the model for thin vorticity layers and a nascent vortex element around a body surface. The height of each vortex sheet panel from the surface is $h = 1.136\sqrt{\nu dt}$, that is the displacement thickness of Rayleigh flow. We consider both the first and second vorticity layers. The thickness of the first layer, adjacent to the body surface, is set to $2h$ in order to coincident its center to h . The thickness of the second layer is set to h . Each layer is divided to a number of vortex elements in the tangential direction according to the segmentation of the vortex panels. The circulation on each vortex panel is assumed to distribute in each vortex element of the first layer with constant vorticity. If a linear distribution of the tangential velocity along the normal direction is assumed in the thin first layer, the normal velocity at the outer edge of the first layer is determined using the equation of

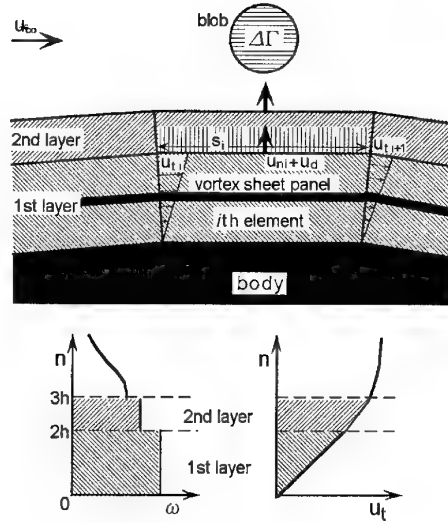


Fig. 1 Thin vorticity layer and nascent vortex element.

flow continuity and non-slip condition on the body surface,

$$u_{ni} = \frac{h}{s_i} (u_{ti} - u_{ti+1}), \quad (13)$$

where s_i is the outer length of the i th element, and u_{ti} is the tangential velocity at the outer left edge of the i th element. The circulation on each vortex panel at the next time step can be calculated from Eq. (7) and (13) by the boundary element method.

At the height of the vortex panel, the vorticity diffuses outward as $1.136 \{ \sqrt{\nu(2dt)} - \sqrt{\nu t} \}$ between dt and $2dt$. Taking account of the constant vorticity in each element, the diffusion velocity at the outer edge of the first layer is determined by

$$u_d = \frac{1.136 \{ \sqrt{\nu(2dt)} - \sqrt{\nu t} \} \times 2}{dt}. \quad (14)$$

If the sum of normal velocity, $u_{ni} + u_d$, is positive, a rectangular vortex element is introduced adjacent to the outer edge of the first layer. The thickness of the rectangular element is $h_{vor} = (u_{ni} + u_d) dt$, the length is s_i and the vorticity is $\omega_{vor} = \Gamma_i / (A_i + h_{vor} s_i)$. Here, Γ_i is the circulation originally involved in the i th panel, and A_i is the area of the i th element of the first layer.

For the second vorticity layer, each element has a constant vorticity and it diffuses outward based on Eq. (4). Each element of the second layer once moves together with the rectangular element according to Eq. (7) and (9), and then, the circulation that exists in the enclosed area of the second layer is redistributed to each element. This redistribution can suppress the unnecessary fluctuation accompanied with the discrete elements adjacent to the body surface. The circulation that moved out of the second layer is replaced with an equivalent vortex blob. A vorticity distribution in the blob is represented as a Gaussian distribution,

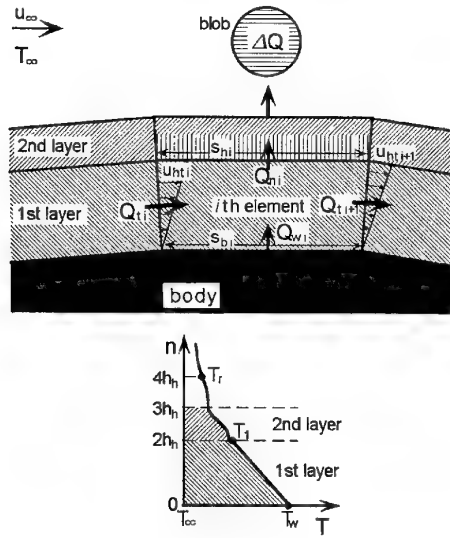


Fig. 2 Thin thermal layer and nascent heat element.

$$\omega(r) = \frac{\Delta\Gamma}{\pi \varepsilon_j^2} \exp\left\{-\left(\frac{r-r_j}{\varepsilon_j}\right)^2\right\}, \quad (15)$$

where r_j and ε_j are the center position and the core radius of j th blob, respectively. The core radius is given by

$$\varepsilon_j = 2\sqrt{\nu t}. \quad (16)$$

It diffuses by the following relation derived from the differentiation of Eq. (16),

$$\frac{d\varepsilon_j}{dt} = \frac{2\nu}{\varepsilon_j}. \quad (17)$$

2.5 Introduction of Nascent Heat Elements

Figure 2 shows the model for thin thermal layers and a nascent heat element around a body surface. The height h_h is defined by $h_h = 1.136\sqrt{\alpha dt}$, and the thickness of the first and second thermal layers are set to $2h_h$ and h_h , respectively. Each layer is divided to a number of heat elements in the tangential direction according to the segmentation of the vortex panels. A constant temperature gradient is assumed in the first layer along the normal direction, and a heat flux from the surface to the first layer is determined by Fourier's Law;

$$\dot{q} = -\lambda \frac{dT}{dn}, \quad (18)$$

where n denotes the normal direction to the surface. The dimensionless heat quantity transferred from the surface to the i th heat element of the first layer is given by

$$Q_{wi} = \dot{q}_i dt s_{bi} = \alpha \frac{T_{wi} - T_{l1}}{2h_h} dt s_{bi}, \quad (19)$$

where T_w and T_{l1} are dimensionless temperatures at the surface and the outer edge of the 1st layer, respectively, and s_{bi} is the length of the i th element on the body surface. If a linear distribution of the tangential velocity along the normal direction is assumed in the first thermal layer, the heat quantity transferred from the left edge of the i th element, Q_{li} , and that transferred to the right edge of the i th element, Q_{li+1} , are expressed as

$$\begin{aligned} Q_{li} &= \int_0^{2h_h} T u dt dn \\ &= T_{wi} u_{hi} h_h dt \left(1 - \frac{2}{3} \frac{T_{wi} - T_{l1}}{T_{wi}}\right) \end{aligned} \quad (20)$$

$$\begin{aligned} Q_{li+1} &= \int_0^{2h_h} T u dt dn \\ &= T_{wi+1} u_{hi+1} h_h dt \left(1 - \frac{2}{3} \frac{T_{wi+1} - T_{l1+1}}{T_{wi+1}}\right), \end{aligned} \quad (21)$$

where u_{hi} is the tangential velocity at the outer left edge of the i th element of the first layer. If Prandtl number $Pr = \nu/\alpha$ is much smaller than unity, the time step of the nascent heat element should be much smaller than that of nascent vortex element to satisfy the assumption of linear velocity distribution in the first thermal layer. Once the wall temperature, T_w , or the heat flux on the surface, \dot{q} , is given as a boundary condition, Eq. (19) – (21) can be solved by determining the temperature, T_{l1} , at the outer edge of the first layer. In the present study, T_{l1} is determined by extrapolating a complementary error function between the wall surface temperature, T_w , and a reference temperature, T_r , at the distance of $4h_h$ from the surface, where the heat blobs crowded.

The heat quantity transferred from the first layer to the second layer, Q_n , is determined by the energy conservation,

$$Q_{ni} = Q_{wi} + Q_{li} - Q_{li+1}. \quad (22)$$

A rectangular heat element, that has heat quantity of Q_n , is introduced adjacent to the outer edge of the first layer. The thickness of the rectangular element is $h_{heat} = (u_{hni} + u_{hd}) dt$, and the length is s_{hi} , where u_{hni} is the induced velocity in the normal direction at the outer edge of the first layer. By an analogy to Eq. (14), the thermal diffusion velocity at the outer edge of the first layer, u_{hd} , is given by

$$u_{hd} = \frac{1.136 \{ \sqrt{\alpha(2dt)} - \sqrt{\alpha dt} \} \times 2}{dt}. \quad (23)$$

For the second thermal layer, each heat element is assumed to have a Gaussian distribution of temperature in the normal direction. Although it is possible to assume the constant temperature in each heat element for simplicity, it increases the computing time because the smaller time step is necessary to calculate the thermal boundary layer with enough accuracy. Each heat element of the second layer diffuses outward based on Eq. (6),

and once moves together with the rectangular heat element according to Eq. (7) and (9). After that, the heat quantity in the enclosed area of the second layer is redistributed to each element. The heat quantity that moved out of the second layer is replaced with an equivalent heat blob. A temperature distribution in the blob is represented as a Gaussian distribution,

$$T(r) = \frac{\Delta Q}{\pi \varepsilon_{hj}^2} \exp\left\{-\left(\frac{r - r_{hj}}{\varepsilon_{hj}}\right)^2\right\}. \quad (24)$$

The core radius is given by

$$\varepsilon_{hj} = 2\sqrt{\alpha t}, \quad (25)$$

and it diffuses by the following relation, similar to Eq. (17),

$$\frac{d\varepsilon_{hj}}{dt} = \frac{2\alpha}{\varepsilon_{hj}}. \quad (26)$$

3. CALCULATION RESULTS

3.1 Calculation Conditions

Numerical simulation for flow and heat transfer was performed around a circular cylinder in the range of $Re = 200 - 1000$ and $Pr = 0.71$. The number of vortex sheet panels around a circular cylinder was $n = 100$, the dimensionless time step was $dt = 0.05$. A constant dimensionless temperature $T_w = 1$ was assumed on the body surface as a boundary condition, and the free stream temperature was set to $T_\infty = 0$. In order to reduce the computing time, the vortex blobs were combined and made an equivalent blob if they were apart more than $2d$ from the center of the cylinder and close to each other within one-tenth of their core radius. The positive and the negative vortex blobs were combined separately. The heat blobs were also combined if they were close to each other within one-fifth of their core radius. These merging process did not affect the basic behavior of flow and heat transfer adjacent to the body surface.

3.2 Flat Plate Boundary Layer

In order to verify the present method, the flow and heat transfer on a flat plate was simulated and the result was compared with theory. Since the present method is applicable for an arbitrary two-dimensional body, the vortex panels were set to the shape of a flat plate, as shown in Fig. 3, instead of a circular cylinder. Figure 3 shows a distribution of the vortex elements at $t = 5$ after the impulsive start of flow for $Re = 500$. A steady flow is formed symmetrically on the upward and downward faces of the flat plate. Figures 4 (a) and (b) show the velocity and temperature distributions, respectively, in the boundary layer at the center of the flat plate ($x/L = 0.5$) in the range of $Re = 200 - 1000$. Figure 5 shows the Nusselt number distributions on the plate for $Re = 200 -$

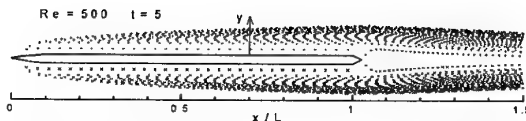
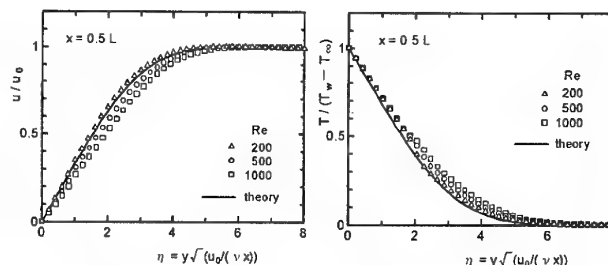


Fig. 3 Vortex element distribution around a flat plate for $Re = 500$ at $t = 5$.



(a) velocity distributions (b) temperature distributions
Fig. 4 Velocity and temperature distributions in the flat plate boundary layer for $Re = 200 - 1000$ at $x/L = 0.5$.

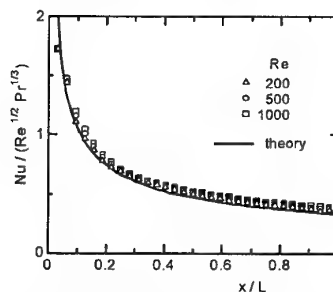
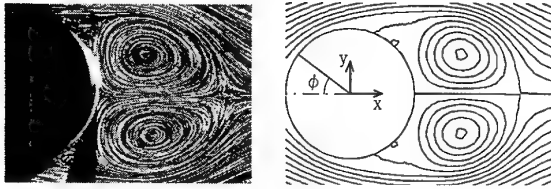


Fig. 5 Nusselt number distributions on a flat plate for $Re = 200 - 500$.

1000. It is shown that the present results agree well with the theory for the laminar boundary layer.

3.3 Recirculating Flow behind a Circular Cylinder

To confirm the applicability of the present method to the simulation in the separated flow region, the recirculating flow formed behind a circular cylinder at the early stage after the impulsive start is compared with the experiment. Figures 6 (a) shows a photograph of the flow obtained by Bouard and Coutanceau (13) and Fig. 6 (b) shows a stream line calculated by the present method for $Re = 550$ and at $t = 2.5$. Although there is a little discrepancy in the secondary vortex flow just behind the flow separating points, the stream line of the main vortex is almost correspond to the experiment. Figure 7 shows the velocity distribution behind the circular cylinder from $t = 0.5$ to 3.0 along the center line of $y = 0$. The present result agrees well with the experimental result by Bouard and Coutanceau (13).



(a) flow visualization by Bouard & Coutanceau⁽¹³⁾ (b) calculated stream line

Fig. 6 Flow structure behind a circular cylinder for $Re = 550$ at $t = 2.5$.

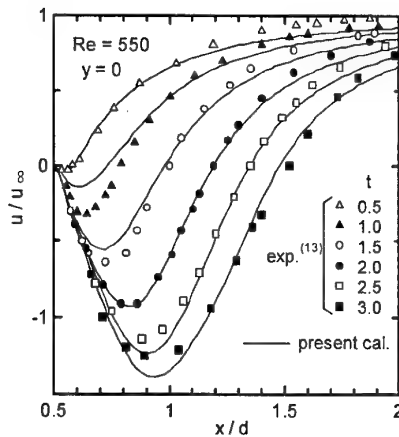


Fig. 7 Velocity distributions in the wake for $Re = 550$ at $y = 0$.

3.4 Flow and Heat Transfer around a Circular Cylinder

Figure 8 shows time histories of drag coefficient, C_D , lift coefficient, C_L , and overall Nusselt number, Nu_m , of the circular cylinder for $Re = 500$. Both values of C_D and C_L are defined by the sum of pressure and friction forces. Each property begins to fluctuate after $t = 10$, and the fluctuation becomes periodic after $t = 35$ according to the periodic vortex shedding. The fluctuations of C_D and Nu_m have double frequency that of C_L , because they fluctuate once for each of upper and lower shedding.

Figures 9 (a) – (c) show the distribution of vortex elements, stream line, and temperature distribution for $Re = 500$ at $t = 52.5$. A vortex street is formed behind the circular cylinder. It is shown that the higher temperature region is almost corresponds to the higher vorticity region because the heat elements are gathering by the induced velocity, as well as the vortex elements.

Figure 10 shows the Nusselt number distributions for $Re = 200$. The values of Nu and Nu_{rms} are the time-averaged Nusselt number and r.m.s. value of the fluctuating Nusselt number, respectively, during the periodic fluctuation of $30 \leq t \leq 60$. The distribution of Nu shows a maximum value at the front stagnation point, and shows a minimum value around the separation points of $\phi \approx \pm 120^\circ$. In the separated flow region, the value of Nu_{rms} increases because the temperature in this region fluctuates by the vortex shedding. The experimental result by Krall and Eckert (14) for $Re = 205$, the result of

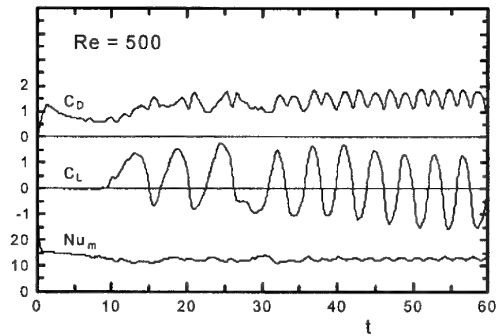
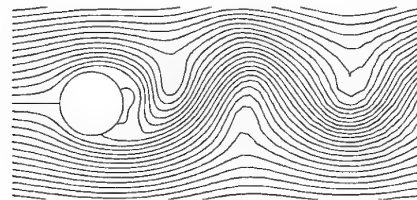


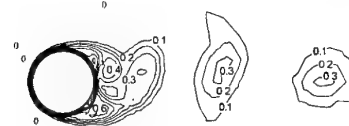
Fig. 8 Time histories of C_D , C_L and Nu_m of a circular cylinder for $Re = 500$.



(a) distribution of vortex elements



(b) stream line



(c) temperature distribution

Fig. 9 Flow pattern around a circular cylinder for $Re = 500$ at $t = 52.5$.

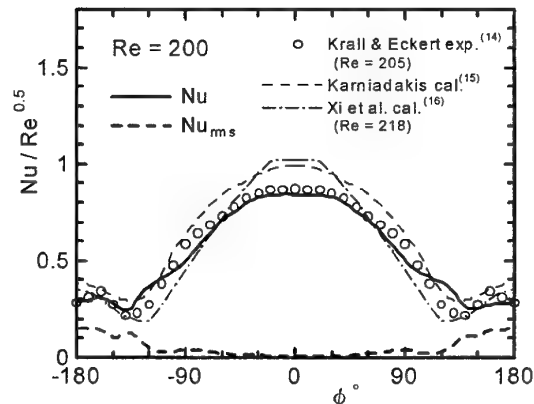


Fig. 10 Nusselt number distribution around a circular cylinder for $Re = 200$

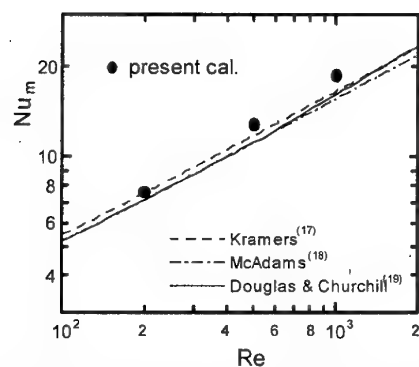


Fig. 11 Overall averaged Nusselt number of a circular cylinder

the spectral element method by Karniadakis (15) for $Re = 200$, and the result of differential method with compound grid system by Xi et al. (16) for $Re = 218$ are also shown in Fig. 10. These results, especially the result of the experiment, show the similar tendency to the present result. However the present result differs slightly from the experimental value around the separation point of $90^\circ \leq \phi \leq 130^\circ$. This error is probably due to the assumption of the constant vorticity and the constant temperature gradient in the first vorticity and thermal layers, respectively, or caused by extrapolating a complementary error function to determine the temperature at the outer edge of the first thermal layer.

Figure 11 shows the overall averaged Nusselt number of a circular cylinder compared with the experimental relations by Kramers (17), McAdams (18), Douglas and Churchill (19). The present result agrees well for the lower Reynolds number of $Re = 200$, however, for $Re = 1000$, it is about 15 % higher than experimental relations. The difference for the higher Reynolds number is considered to be the effect of three-dimensionality of the real flow. If we expect to simulate the heat transfer precisely for $Re \geq 1000$, it is necessary to perform a three-dimensional analysis.

4. MECHANISM OF UNSTEADY HEAT TRANSFER IN THE WAKE

Figures 12 show the time histories of Nusselt number, Nu , normal and tangential velocities, $-u_n$ and u_t , respectively, at the outer edge of the first vorticity layer. In the laminar flow region of $\phi = 92^\circ$, each value fluctuates regularly in the vortex shedding frequency. The value of Nu increases with the increase in u_t , because the colder fluid in the upstream region flows in this area with the tangential velocity u_t . At the rear stagnation point of $\phi = 180^\circ$, Nu and $-u_n$ fluctuate in the double frequency of the vortex shedding because each of upper and lower shear layers affects them alternatively. The maximum value of Nu appears together with that of $-u_n$, at the time when the colder fluid flows in this area from behind of the cylinder. The fluctuation of Nu is remarkably higher than that in the laminar region.

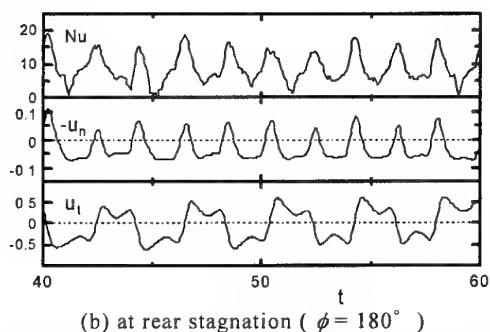
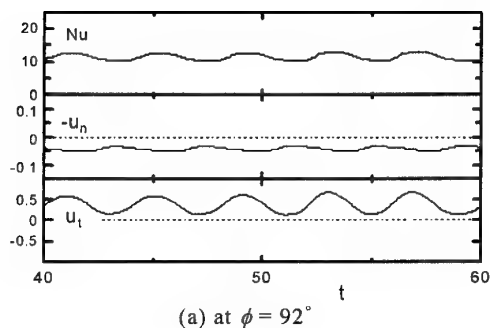


Fig. 12 Time histories of Nu , $-u_n$ and u_t for $Re = 500$.

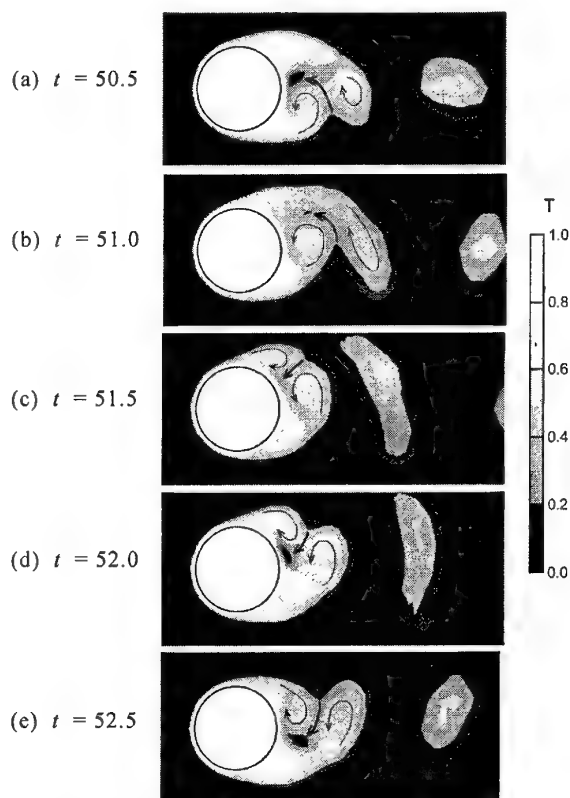


Fig. 13 Motion of temperature distribution around a circular cylinder for $Re = 500$.

In order to clarify the mechanism of the unsteady heat transfer in the separated flow region, the motion of the temperature distribution around the cylinder at the time interval of 0.5 is shown in Fig. 13. The thin and thick arrows just behind the cylinder denote the direction of the circulation and the induced velocity, respectively. At $t = 50.5$, a reverse flow is induced toward the rear stagnation point and thus the value of $-u_n$ shows maximum at $\phi = 180^\circ$, as shown in Fig. 12 (b). This causes the lower temperature just behind the rear stagnation and the higher value of Nu at $\phi = 180^\circ$. At $t = 51.5$, the position of the reverse flow shifts upward, resulting from the movement of a pair of circulation according to the vortex shedding. The Nusselt number increases at $\phi = 150^\circ$, however it decreases at $\phi = 180^\circ$. At $t = 52.5$, the position of the pair of circulation is almost upside-down to that of $t = 50.5$, and thus, the value of Nu increases again at $\phi = 180^\circ$. From the series of the temperature distributions, it is found that the fluctuation of the heat transfer in the separated flow region is caused by the motion of the pair of circulation just behind the cylinder. Figure 14 shows the time history of the Nusselt number distribution in the separated flow region for $Re = 500$. It is clear that the higher Nusselt number region, caused by the reverse flow, shows a zigzag trajectory around the rear stagnation point.

5. CONCLUSION

A vortex element method was extended to an analysis for forced convection heat transfer. Reynolds number ranged from 200 to 1000 and the Prandtl number was 0.71.

- (1) The result of the simulation for the laminar boundary layer on a flat plate agreed well with the theory. And the result for the flow and heat transfer around a circular cylinder agreed well with the experimental results. It is confirmed that the present method is applicable for the forced convection heat transfer around a two-dimensional bluff body including the separated flow region.
- (2) The mechanism of unsteady heat transfer was clarified in the separated flow region behind a circular cylinder. A pair of circulation formed just behind the cylinder induces the reverse flow that enhances the heat transfer. The movement of the pair of circulation causes the fluctuation of the heat transfer in the separated flow region.

REFERENCES

- (1) Boulos, M.I. and Pei, D.C.T., Dynamics of Heat transfer from Cylinders in a Turbulent Air Stream, *Int. J. Heat Mass Transfer*, **17**(1974), 767-783.
- (2) Kumada, M., Ishihara, K. and Kato, M., Unsteady Characteristics of Heat Transfer on a Separated Region of a Circular Cylinder, *Proc. 2nd JSME-KSME Thermal Eng. Conf.*, (1992), Vol.2, 37-42.
- (3) Scholten, J.W. and Murray, D.B., Unsteady Heat Transfer and Velocity of a Cylinder in Cross Flow - 1. Low Freestream Turbulence, *Int. J. Heat Mass Transf.*, **41**(1998), 1139-1148.

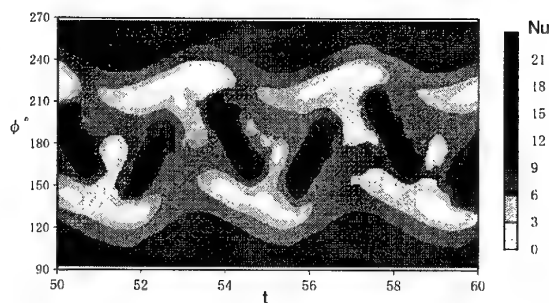


Fig. 14 Time history of Nu distribution in the separated flow region behind a circular cylinder for $Re = 500$.

- (4) Chorin, A.J., Numerical Study of Slightly Viscous Flow, *J. Fluid Mech.*, **57**-4(1973), 785-796.
- (5) Chorin, A.J., Vortex Sheet Approximation of Boundary Layers, *J. Computational Physics*, **27**(1978), 428-442.
- (6) Leonard, A., Vortex Methods for Flow Simulation, *J. Computational Physics*, **37**(1980), 289-335.
- (7) Lewis, R.I., Surface Vorticity Modeling of Separated Flows from Two-Dimensional Bluff Bodies of Arbitrary Shape, *J. Mech. Eng. Science*, **23**-1(1981), 1-12.
- (8) Ogami, Y. and Akamatsu, T., Viscous flow Simulation Using the Discrete Vortex Method - the Diffusion Velocity Method, *Computers & Fluids*, **19** (1991), pp. 433-441.
- (9) Smith, P.A. and Stansby, P.K., An Efficient Surface Algorithm for Random-Particle Simulation of Vorticity and Heat Transport, *J. Computational Physics*, **81**(1989), 349-371.
- (10) Kamemoto, K. and Miyasaka, T., Development of a Vortex and Heat Elements Method and Its Application to Analysis of Unsteady Heat Transfer around a Circular Cylinder in a Uniform Flow, *Proc. of 1st Int. Conf. on Vortex Methods*, Kobe Nov. 4-5, (1999), 191-203.
- (11) Wu, J.C. and Thompson, J.E., Numerical Solutions of Time-Dependent Incompressible Navier-Stokes Equations Using an Integro-Differential Formulation, *Computers & Fluids*, **1**(1973), 197-215.
- (12) Uhlman, J.S., An Integral Equation Formulation of the Equation of Motion of an Incompressible Fluid, *Naval Undersea Warfare Center T.R.*, (1992), 10, 086.
- (13) Bouard, R. and Coutanceau, M., The Early Stage of Development of the Wake Behind an Impulsively Started Cylinder for $40 < Re < 10^4$, *J. Fluid Mech.*, **101**-3(1980), 583-607.
- (14) Krall, K.M. and Eckert, E.R.G., Local Heat Transfer around a Cylinder at Low Reynolds Number, *Trans. ASME J. Heat Transfer*, **95**(1973), 273-275.
- (15) Karniadakis, G.E., Numerical Simulation of Forced Convection Heat Transfer from a Cylinder in Crossflow, *Int. J. Heat Mass Transfer*, **31**-1(1988), 107-118.
- (16) Xi, G., Torikoshi, K., Kawabata, K. and Suzuki, K., Numerical Analysis of Unsteady Flow and Heat Transfer around Bodies Using a Compound Grid System, *Trans. Jpn. Soc. Mech. Eng.*, (in Japanese), **61**-585(1995), 1796-1803.
- (17) Kramers, H.A., *Physics*, **12**(1946), 61.
- (18) McAdams, W.H., *Heat Transmission*, 3rd ed., (1954), McGraw-Hill, 259.
- (19) Douglas, M.J.M. and Churchill, S.W., Recorrelation of Data for Convective Heat Transfer between Gases and Single Cylinders with Large Temperature Difference, *Chemical Engineering Progress Symposium Series*, **52**-18(1956), 23-28.

VORTEX RING INTERACTING WITH SHEAR-LAYER VORTICES

Hitoshi Ishikawa and Osamu Mochizuki

Division of Mechanical Science, Graduate School of Engineering, Hokkaido University
N13W8, Kita-ku, Sapporo 060-8628, Japan/Email: ishi@eng.hokudai.ac.jp

Masaru Kiya

Kushiro National College of Technology
Kushiro, 084-0916, Japan

ABSTRACT

Interactions between shear layer vortices and a vortex ring are simulated by a vortex blob method. Active control of rolled-up vortices in a separated shear layer was made by introducing the self-propelling vortex ring from outside. The interaction is effective in enhancing the local growth of the shear layer. Parameter studies are made for the ratio of circulation of the vortex ring Γ_R to that of the shear layer vortices Γ_F , the initial position of introduction of the vortex ring. If the ratio $\Gamma_R/\Gamma_F = 1.0$, shear layer vortices and the vortex ring interact strongly, for example, the amalgamation between the shear layer vortices and the vortex ring occurs to generate large vortices. The vorticity thickness attains a maximum for $\Gamma_R/\Gamma_F = 1.0$. Although the ratio Γ_R/Γ_F exceeds about 1.5, the enhanced growth of the shear layer tends to saturate. This is because the vortex ring passes through the shear layer. The initial position of the vortex ring has a significant effect on the mode of interaction.

1. INTRODUCTION

Active control of separated shear layers usually employs sinusoidal disturbances, for example, acoustic wave, suction or blowing, oscillating flaps, etc (1). Kiya et al. and Sigurdson studied the effect of a sinusoidal disturbance on the separation bubble from the leading edge of a blunt cylinder

(2,3). Active control of turbulent mixing layers, having basically similar properties with a separated shear layer, was also made by means of the oscillating flap attached to the edge or acoustic wave (4). Inoue (5) numerically simulated a two-dimensional mixing layer perturbed by double-frequency forcing to control the amalgamation of vortices and the growth of the mixing layer. These methods enhanced the evolution of the vortical structures, automatically determined by a latent instability.

A novel method, in which external vortex rings were introduced into the separated shear layer of an inclined flat plate to reduce the separation zone, was proposed by Kiya et al. (6). The reduction was realized because a strong vortex ring interacts the shear layer vortices, successively transporting high-momentum fluid of the main flow into the separated zone.

Thus, if the interaction of the vortical structures could be directory controlled by local agents, more effective control is expected to be possible. Kiya et al. (7) studied by flow visualization the interaction between rolling-up vortices in the separated shear layer and a vortex ring. The interaction seems to be effective in enhancing the local growth of the separated shear layer. A vortex ring introduced into the middle of consecutive vortices is shown to experience an enormous stretching, yielding a rapid local growth of the shear layer. Maekawa and Nishioka (8) showed that the vortex ring deforms the mixing layer vortices to merge if

forced by the subharmonics instability modes. Numerical simulation demonstrated that the mode of interaction was affected by the ratio of circulation of the vortex ring to that of the shear layer vortices (9).

The purpose of this paper is to understand the interaction between shear layer vortices and a vortex ring to enhance the growth of the separated shear layer. Three-dimensional numerical simulations are performed for the rolling-up vortices in the shear layer affected by the vortex ring. The simulations are made by means of a vortex blob method. Parameter studies are made for the ratio of the circulation of the vortex ring to that of the shear layer vortices. A spatially evolving shear layer is investigated.

2. NUMERICAL SIMULATION

2.1. Vortex Method

In a vortex blob method, the evolution of a vortical region is represented by a summation of vortex blobs with overlapping cores. A vortex blob α is defined by the position \mathbf{x}^α , vorticity ω^α , volume $d^3\mathbf{x}^\alpha$. The strength of a vortex blob is denoted by $\gamma^\alpha = \omega^\alpha d^3\mathbf{x}^\alpha$. Vorticity field ω at a time t is given by

$$\omega^\alpha(\mathbf{x}, t) = \frac{1}{\sigma_\alpha^3} p\left(\frac{|\mathbf{x} - \mathbf{x}^\alpha(t)|}{\sigma_\alpha}\right) \gamma^\alpha \quad (1)$$

where $p(\cdot)$ is the smoothing function with the cut-off radius σ_α (10). To maintain the accuracy of the representation in Eq. (1), the value of σ_α should be larger than the distance between the centers of neighboring blobs. We apply the high-order algebraic smoothing, as follows

$$p(\xi) = \frac{15}{8\pi} \frac{1}{(\xi^2 + 1)^{7/2}} \quad (2)$$

The evolution of position \mathbf{x}^α is described by the Biot-Savart law and the vorticity equation in Lagrangian form, as follows

$$\frac{d\mathbf{x}^\alpha}{dt} = -\frac{1}{4\pi} \sum_\beta \frac{r_{\alpha\beta}^2 + (5/2)\sigma_\beta^2}{(r_{\alpha\beta}^2 + \sigma_\beta^2)} \mathbf{r}^{\alpha\beta} \times \gamma^\beta \quad (3)$$

where $\mathbf{r}^{\alpha\beta} = \mathbf{x}^\alpha - \mathbf{x}^\beta$, $r_{\alpha\beta} = |\mathbf{r}^{\alpha\beta}|$.

The evolution of vorticity ω^α is described by the vorticity equation without the viscous diffusion of vorticity.

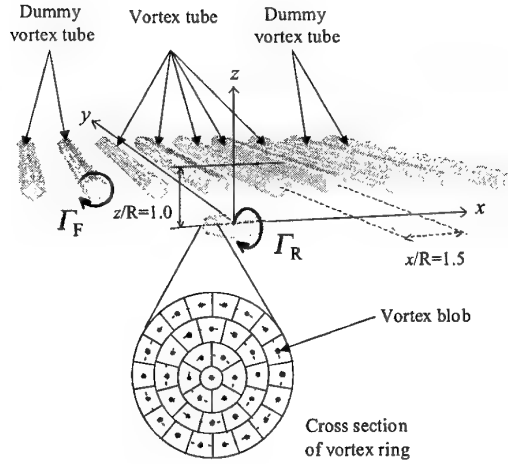


Fig.1 Flow configuration. Cross section of the vortex ring

$$\frac{d\gamma^\alpha}{dt} = (\gamma^\alpha \cdot \nabla) \mathbf{u}^\alpha \quad (4)$$

The molecular diffusion of viscosity is approximated by the core spreading $d\sigma_\alpha^2/dt = 4\nu$, where ν is the kinematic viscosity (11). The diffusion by small-scale turbulence is also modeled by $d\sigma_\alpha^2/dt = 4\nu_{SGS}$, where the subgrid eddy viscosity is approximated by $\nu_{SGS} = c^2 \sigma_\alpha^2 \omega^\alpha |d\omega/dt|$, where c is a numerical constant. $|\omega|$ is the magnitude of vorticity, on the basis of Smagorinsky eddy viscosity $\nu_{SGS} = c^2 \Delta^2 (s_{ij} s_{ij})^{-1/2}$, where Δ is the grid size and s_{ij} is the rate of strain tensor. The value of $c=0.17$, which is recommended for free turbulent shear flows, is employed. Thus, the combined model

$$\frac{d\sigma_\alpha^2}{dt} = 4(\nu + \nu_{SGS}) \quad (5)$$

was used, being interpreted as a Lagrangian turbulence model that includes Reynolds number effects (12).

2.2. Flow Configuration

Fig.1 shows the flow configuration and the cross section of the vortex ring. The vortex ring consists of 60 cross sections in the circumferential direction. Each cross section was divided into four layers. The first layer, the center part of the cross section, consists a single vortex blob. The second layer consists of six blobs. The third and fourth layer consists of 12 and 18 vortex blobs, respectively. Total

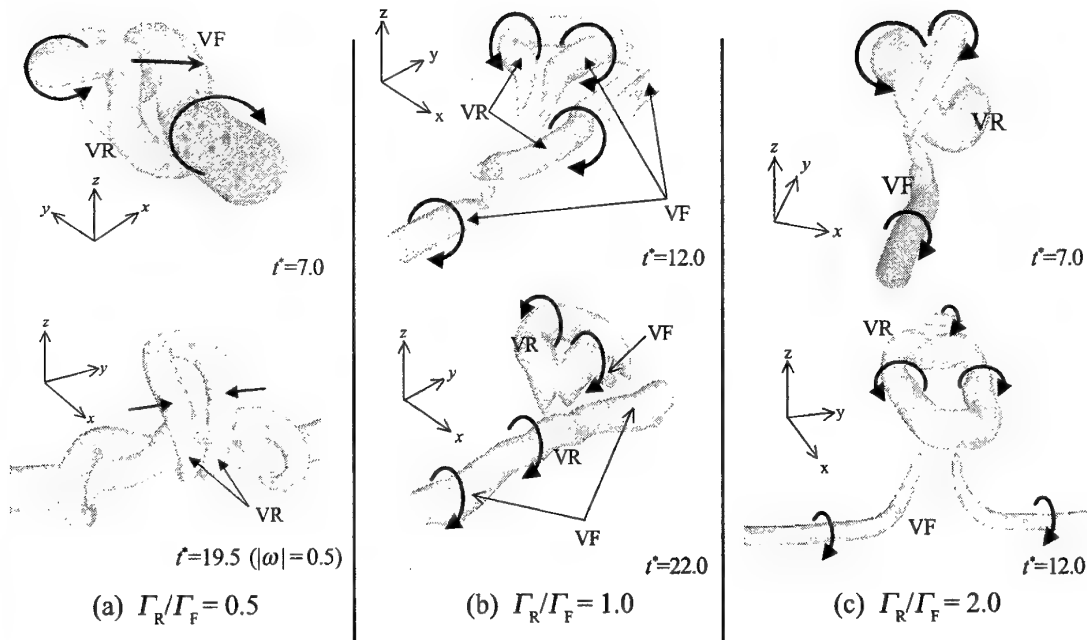


Fig.2 Isosurfaces of magnitude of vorticity $|\omega|$ for interacting the vortex ring and the single vortex tube

number of the vortex blobs is 37 in the cross section. The initial vorticity within the cross section is taken as a third-order Gaussian distribution (13).

$$\Omega(r) = \frac{1}{a\sigma_\alpha^2} \exp\left(-\frac{r^3}{\sigma_\alpha^3}\right) \quad (6)$$

where r is measured from the core center, numerical constant a is defined by the Gamma function. Radius of the vortex ring R is 1.0.

The shear layer is represented by a row of five vortex tubes for streamwise direction. Each vortex tube, having the same diameter as the vortex ring, consists of 37 vortex blobs in the cross section. The initial vorticity is also the same as that of the ring. However, the rotation of whole the shear layer occurred by self-induced velocity. In order to prevent this rotation, five dummy vortex tubes are arranged in the both side of shear layer. The cross section of dummy vortex tube consists of seven vortex blobs in two layers. The initial vorticity within the cross section is the same as vortex rings. The streamwise distance of neighboring vortex tubes is chosen as $1.5R$. The spanwise length of the vortex tube is chosen as $20R$.

The (x, y, z) coordinate system is defined such that x -, y - and z -axes are in the streamwise, spanwise and transverse direction. The initial position of the vortex ring is $(x, y, z) = (0, 0, 0)$. The distance of the shear layer vortices and vortex ring is $1.0R$.

3. INTERACTION BETWEEN VORTEX RING AND THE SINGLE VORTEX TUBE

As preliminary calculations, the interaction between a vortex ring and a single vortex tube was performed. The circulation ratio of the vortex ring to that of vortex tube Γ_R/Γ_F was varied in a range of 0.5 -2.0. Reynolds number is 300, based on the diameter and the initial convection velocity of the vortex ring. The time step of motion of vortex blobs Δt is chosen as 0.1.

Fig.2 shows the isosurfaces of magnitude of vorticity $|\omega| = 1.0$ at several non-dimensional times t^* ($=t\Gamma/R^2$). For the ratio $\Gamma_R/\Gamma_F = 0.5$ (Fig.2(a)), the vortex ring approaches to the vortex tube by the self-induced velocity, wrapping around in the vortex tube. The vortex tube is seen to deform such that "hairpin" shape by approaching of the vortex ring.

The vortex ring was split into two portions by the viscous diffusion of vorticity. The upper portion of the vortex ring splitting was folded into the middle by the deformed vortex tube. The lower part was further involved in the vortex tube. i.e. in this case $\Gamma_R/\Gamma_F = 0.5$, the vortex ring merged with the vortex tube because the circulation of the vortex ring is weaker than that of the vortex tube.

For $\Gamma_R/\Gamma_F = 1.0$ (Fig.2 (b)), the initial interaction is almost the same as the case $\Gamma_R/\Gamma_F = 0.5$. The vortex tube undergoes a large extension by approaching of the vortex ring, so that the vorticity was diffused by viscous effect. As a result, the cut and reconnection was occurred between the vortex ring and the vortex tubes. The reconnection in the pair vortex rotating in the same direction was occurred at the closest approach of the vortex ring and tube, a new vortex ring generating later. Such reconnection was observed in the interaction of two vortex rings (14).

The case $\Gamma_R/\Gamma_F = 2.0$ is shown in Fig.2 (c). The vortex ring was found to pass through the vortex tube. It noted that the vortex ring which Γ_R is approximately 1.5 times of Γ_F , pass through the vortex tube.

4. INTERACTION BETWEEN THE VORTEX RING AND THE SHEAR LAYER VORTICES

4.1. Evolution of Vortex Patterns

The profile of streamwise velocity u^* ($=uR/\Gamma_F$) in undisturbed shear layer is shown in Fig.3. The center of the shear layer vortex is at $y/R=1.0$.

Fig.4 show isosurfaces of the magnitude of the vorticity $|\omega|$ and contours of the y -components of the vorticity ω_y . In contour, the solid and broken lines show the positive and negative vorticity, respectively. For the case $\Gamma_R/\Gamma_F = 1.0$, the pair vortex rotating in the same direction as the shear layer vortices ($VR_+ + VF_4$), generate a large vortex in downstream side. On the other hand, another pair vortex rotating in the opposite direction ($VR_- + VF_3$) move in the upstream direction by self-induced velocity. The vortex ring is seen to experience an enormous stretch in the streamwise direction. In this case, the vortex ring directly interacts with five shear layer vortices at least.

Fig.4(b) shows the case $\Gamma_R/\Gamma_F = 1.5$. A comparison of this result with the case $\Gamma_R/\Gamma_F = 1.0$ reveals that amalgamating vortices ($VR_+ + VF_4$) on downstream side is of the greatest spatial extent.

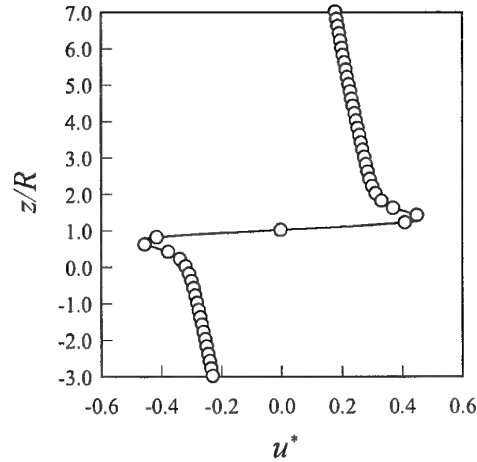


Fig.3 The velocity profile u^* in undisturbed shear layer

However, the case $\Gamma_R/\Gamma_F = 2.0$ (Fig.4(c)), the vortex ring pass through the shear layer vortices, almost keeping its identity. Because the circulation of the vortex ring is much larger than that of the shear layer vortices. It suggested the vortex ring of $\Gamma_R = 2.0$ could transport the high momentum fluid into the separated zone (6). The vortex ring of $\Gamma_R = 2.0$ interacts with only four vortices. The spatial extent during the interaction is least enhanced for $\Gamma_R/\Gamma_F = 2.0$.

4.2. Flow Properties

Fig.5 shows the time changes of the velocity profile of u^* at various circulation ratio. The velocity profiles experience a large fluctuation in the interaction region when the vortex ring meets the shear layer vortices $t^*=1.0$. Note that the advancing of the fluctuation of $\Gamma_R/\Gamma_F = 2.0$ is faster than other cases due to the high self-induced velocity.

The enhanced growth of the shear layer is shown in Fig.6, in terms of the vorticity thickness δ_ω plotted against time t^* for Γ_R/Γ_F . It is interesting that the vorticity thickness of $\Gamma_R/\Gamma_F = 1.0$ is larger than others at $t^*=2.5-3.5$. Experimental results (7) shows the same results that the interaction is strongly enhanced in the case $\Gamma_R/\Gamma_F = 1.0$.

The effect of interaction on the spanwise extent is shown in Fig.7. This is the time changes of the velocity profile v along the center of original vortex tube ($x=0$). The fluctuations during the interaction are not seen to propagate for the spanwise direction as time increases. The spanwise length of the interaction region does not have a significant

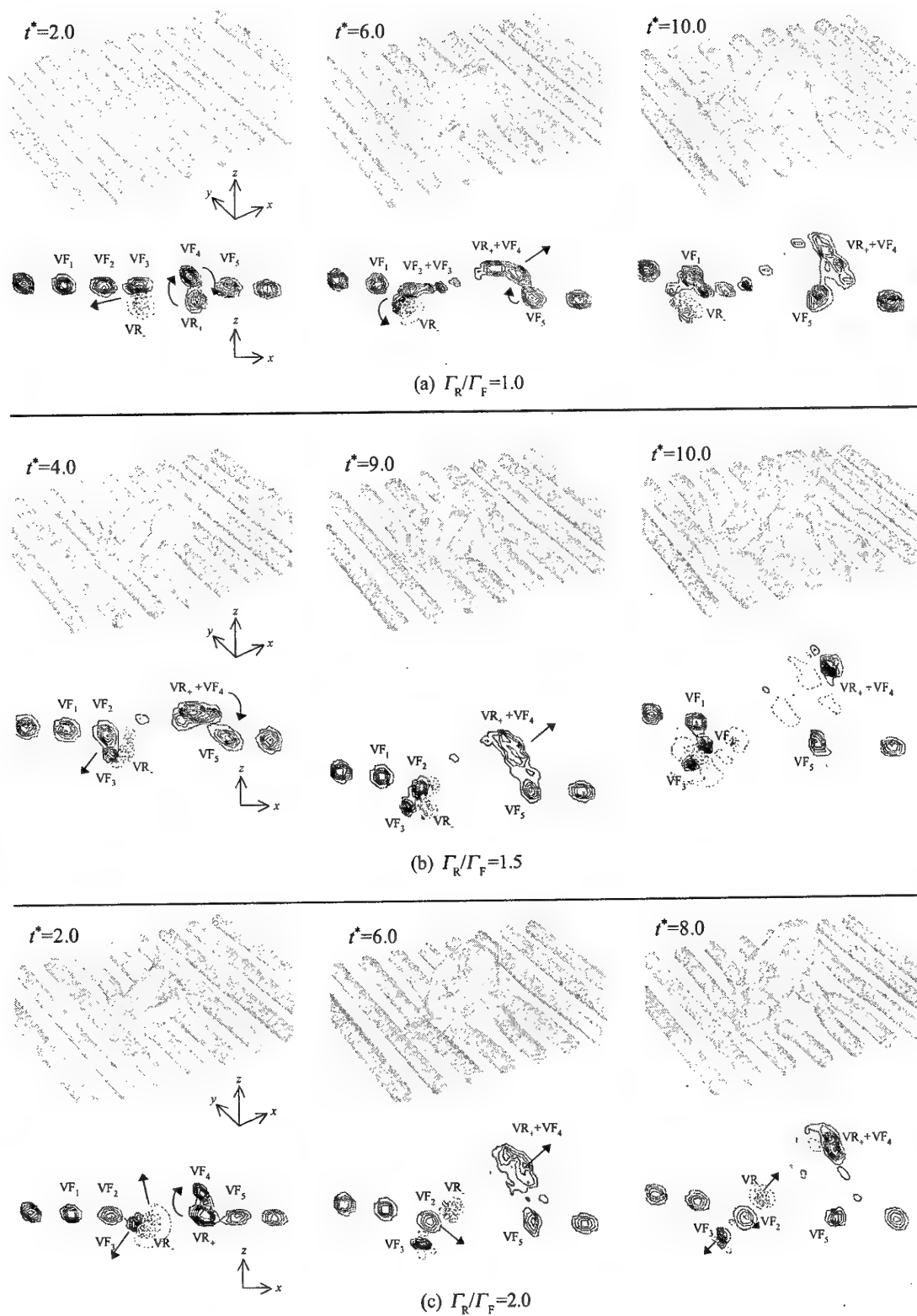
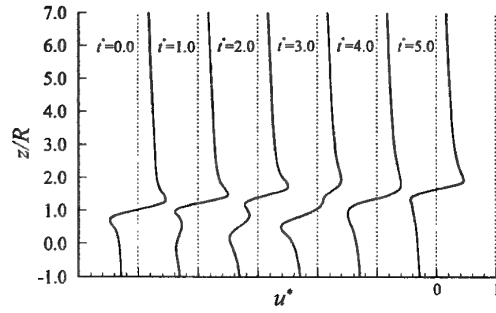
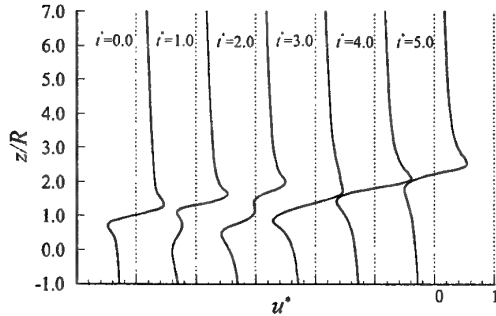


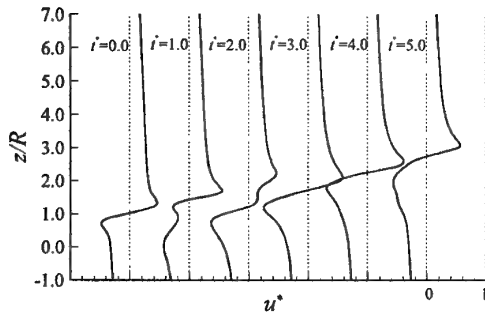
Fig. 4 Isosurfaces of magnitude of vorticity $|\omega|$ and contour of y -component of vorticity ω_y



(a) $\Gamma_R/\Gamma_F=1.0$

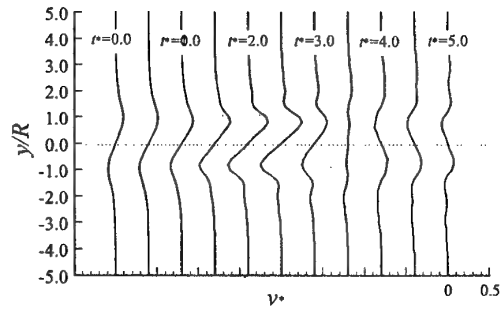


(b) $\Gamma_R/\Gamma_F=1.5$

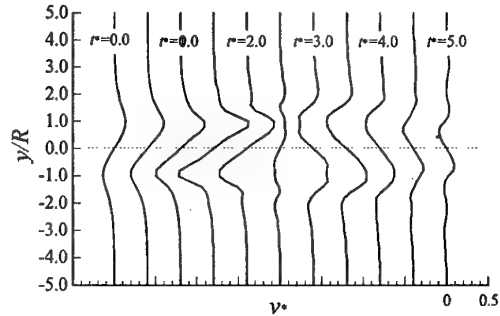


(c) $\Gamma_R/\Gamma_F=2.0$

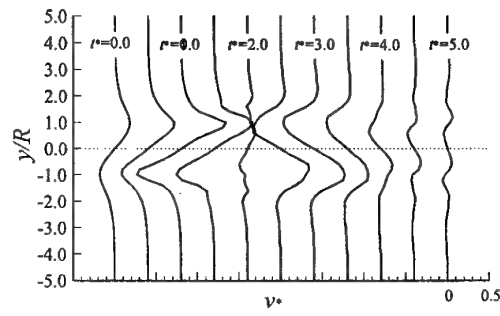
Fig.5 Time changes of velocity profile u^* at various circulation ratio



(a) $\Gamma_R/\Gamma_F=1.0$



(b) $\Gamma_R/\Gamma_F=1.5$



(c) $\Gamma_R/\Gamma_F=2.0$

Fig.7 Time changes of velocity profile v^* at various circulation ratio

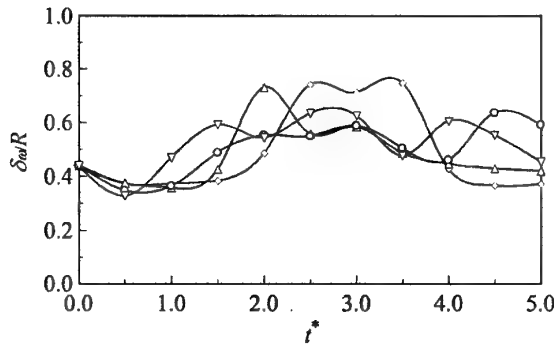


Fig.6 Time changes of the vorticity thickness δ_ω at various circulation ratio $\diamond, \Gamma_R/\Gamma_F=1.0$; $\triangle, 1.5$; $\circ, 2.0$; $\nabla, 2.5$

difference for the circulation ratio, almost saturating in the region of $y/R=-3.0-+3.0$.

5. EFFECT OF THE INITIAL POSITION OF THE VORTEXRING

Effect of the initial position of the vortex ring on the mode of interaction is shown in Fig.8. The center of the vortex ring is located at $(x,y,z)=(1,0,0)$, in the middle of two consecutive vortices. The circulation ratio Γ_R/Γ_F is 1.0. As compared with Fig.4(a), the vortex ring is seen to squeeze the shear layer vortex (VF_3). As a result, VF_3 vortex

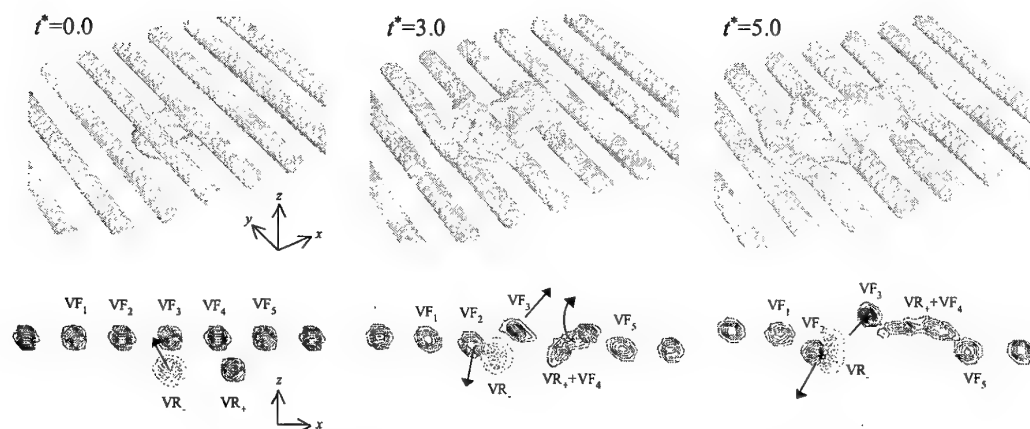


Fig. 8 Effect of the initial position of the vortex ring on the interaction mode. Isosurfaces of magnitude of vorticity $|\omega|$ and contours of y -component of vorticity ω_y

maintains its identity during the interaction. This shows that the interaction of vortices is depended on the initial position of the vortex ring and shear layer vortices.

6. CONCLUSIONS

The present paper has described results of numerical simulations of the interaction between separated shear layer vortices and a vortex ring. The purpose is to enhance the local growth of the shear layer, in the aim of active control by introducing external vortex ring. The simulations were made by means of a three dimensional vortex blob method.

The interaction between the shear layer vortices and the vortex ring is expected to include two major results: One is the enhanced growth of the separated shear layer has the most remarkable effect when the circulation ratio of the vortex ring to the shear layer vortices is 1.0. The vortex ring undergoes an enormous stretch in streamwise direction. Second, If the circulation ratio Γ_R/Γ_F is larger than 1.5-2.0, the spatial evolution of the interaction is weak this is because the vortex ring passes through the shear layer.

REFERENCES

- (1) Gad-el-Hak, M. and Bushnell, D.M. (1991), "Separation control: Review", Trans. ASME: J. Fluids Engng, 113, pp.5-30.
- (2) Kiya, M. et al. (1997), "Sinusoidal forcing of a turbulent separation bubble", J. Fluid Mech., 342, pp.119-139.
- (3) Sigurdson, L.W. (1995), "The structure and control of a turbulent reattaching flow", J. Fluid Mech., 298, pp.139-165.
- (4) Ho, C.-M. and Huerre, P. (1984), "Perturbed free shear layers", Annu. Rev. Fluid Mech., 16, pp.365-424.
- (5) Inoue, O., (1992) "Double-frequency forcing on spatially growing mixing layer", J. Fluid Mech., 234, pp.553-581.
- (6) Kiya, M., Mochizuki, O. and Ishikawa, H. (2001), "Interaction between vortex rings and a separated shear layer: Towards active control of separation zone", J. Fluids and Structures, 15, pp.399-413.
- (7) Kiya, M., Ohya, M. and Hunt, J.C.R. (1986), "Vortex pairs and rings interacting with shear-layer vortices", J. Fluid Mech., 172, pp.1-15.
- (8) Maekawa, H. and Nishioka, T. (1992), "Control of mixing layer developing structures using a vortex ring", Trans. JSME, 58, pp.2659-2666 (in Japanese).
- (9) Kiya, M., Takeo, H., Mochizuki, O. and Kudo, D. (1999), "Simulating vortex pairs interacting with mixing-layer vortices", Fluid Dyn. Res., 24, pp.61-79.
- (10) Winckelmans, G.S. and Leonard, A. (1993), "Contributions to vortex particle method for computation of three-dimensional incompressible

- unsteady flows", J.Comput.Phys., 109, pp.247-348.
- (11) Leonard, A. (1980), "Vortex methods for flow simulation", J.Comput. Phys, 37, pp.289-335
- (12) Seiichiro, I. and Kiya, M. (1999), "A turbulence model for the three-dimensional vortex blob method", Trans. JSME, 630, pp.581-589(in Japanese).
- (13) Knio, O.M. and Ghoniem, F. (1990), "Numerical study of a three-dimensional vortex method", J.Comput.Phys, 86, pp.75-106.
- (14) Kida, S., Takaoka, M. and Hussain, F. (1989) "Reconnection of two vortex rings", Phys. Fluids, 1(4), pp.630-632.

EFFECT OF PARTICLE PHASE ON VORTEX SHEDDING MECHANISM IN TWO-PHASE PLANAR JET FLOW

Mutlu Tunç^{*}, C. Ruhi Kaykayoglu^{**} and Orhan Gökçöl^{***}

^{*}Faculty of Engineering Department of Mechanical Engineering
Istanbul University
Istanbul, Turkey
e-mail: mtunc@istanbul.edu.tr

^{**}Faculty of Engineering
Bahçeşehir University
Istanbul, Turkey
e-mail: rkaykay@bahcesehir.edu.tr

^{***}Faculty of Engineering
Bahçeşehir University
Istanbul, Turkey
e-mail: gokcol@bahcesehir.edu.tr

ABSTRACT

In this study, the effect of particle size and particle concentration on the unsteady evolution of a two-phase planar jet flow is investigated by using a purely Lagrangian computational model. The flow field is modeled by the vortex elements so called Discrete Vortices. The solid sphere particles are injected into the upstream jet flow are acted as the second phase while the viscous effects are mimicked by using a Random Walk Approach, the Rankine Vortex Model is used to simulate the laboratory vortices. Both the passive (One-Way Coupling) and active (Two-Way Coupling) interactions between the particles and flow are studied. It was shown that the flow field characteristics are a strong function of both the particle diameter and particle concentration in the flow field. The instantaneous vortex distributions are investigated for ranges of different particle diameters. It is clear that the particles strongly control vortex shedding mechanisms. The flow Strouhal Number is also a function of particle diameter and concentration.

1. INTRODUCTION

Generally, there are two computational approaches to investigate the particle-fluid interactions in turbulent flows (1,2). The first approach uses the averaged equations by considering the motion as a two-phase flow. This mathematical model deals with some form of

averaged conservation equations. The second approach uses Eulerian frame formulation for the flow field while the particles are moved individually in Lagrangian coordinates.

Vortex Element Methods are being used to investigate the free shear flows such as jets, wakes and mixing layers. With the development of high speed computer technology, it is possible to use these methods more efficiently and precisely. In this investigation, a well known Vortex Element Method so called Discrete Vortex Method is used to simulate the two-phase turbulent jet flow. Hence a novel new particle-fluid interaction model is introduced.

On the other hand, a computational approach based on Lagrangian flow modeling should be considered as a third approach (1). Due to the known advantages of DVM, the authors of this paper has started a research program to simulate the particle motion in turbulent flows by using DVM.

In this investigation, a two-dimensional inviscid flow model is proposed for representing the two-phase planar jet flow. The model approximates the continuous jet flow by discrete vortices shed from the separation points at the nozzle exit. Solid particles act as a second phase.

2. MATHEMATICAL MODELING OF THE FLUID PHASE

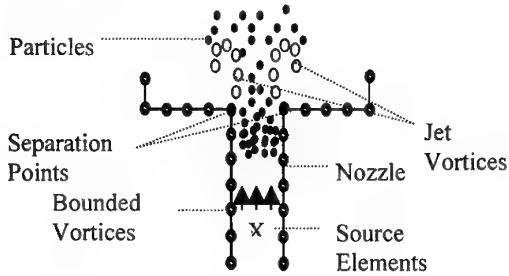


Figure 1. Research geometry

Figure 1 shows the corresponding research geometry. A planar jet is formed with the sudden expansion of the nozzle flow. The jet flow is generated by using source elements inside the nozzle. The strength distribution of sources is chosen to be parabolic so as to provide a correct initial velocity profile at the nozzle exit which can be adjusted easily to obtain the desired Reynolds numbers. Solid walls of the nozzle are modeled by using bounded surface vortex singularities. Control points which are chosen in the middle of the distance between each neighboring vortices are used to apply the necessary flow boundary conditions.

At high Reynolds numbers, it is known that jet flow causes periodic shedding of side vortices. In this study, the formation of these jet vortices are modeled by using an inviscid, two-dimensional Discrete Vortex model. According to the model, a couple of free vortices are shed to downstream at each time step from corner points of the nozzle. The time dependent flow field is then built up by tracing the vortex elements in space (3,4).

The traditional discrete vortex method combined with the surface singularity method consists of two main modeling steps:

Step 1:

Representation of solid surfaces of nozzle by 2-D vortex surface singularities ensuring that normal velocities on the solid surfaces are zero (5). Classical potential theory considers that the solid surfaces are actually "streamlines" so that no velocity component normal to it can exist. This condition can be utilized to study potential flows around or inside complex geometries. The strengths of the vortices are obtained using the boundary condition $\vec{V} \cdot \vec{n} = 0$ at the control points over the solid surface. Here \vec{V} is the velocity vector and \vec{n} is the normal vector to the surface.

Step 2:

Representation of the separated thin shear layers using the assumption that vorticity generated inside the boundary layers of the nozzle walls are shed to the downstream from the sharp edges of the nozzle. This task can easily be done by ejecting discrete vortices from

the known separation points to the flow field at each time step (5).

There are two components of velocity vector \vec{V} at any point inside the problem domain; velocity induced by the sources and the velocity induced by the vortices. The second component includes the two different components which are the velocity induced by the surface vortices of chamber walls and the velocity induced by the shed vortices. These components are mathematically provided below:

$$\vec{V} = \vec{V}_{\text{SOURCE}} + \vec{V}_{\text{VORTICES}} \quad (1)$$

$$\vec{V}_{\text{VORTICES}} = \vec{V}_{\text{BoundedVortices}} + \vec{V}_{\text{ShedVortices}} \quad (2)$$

$$\vec{V}_{\text{SOURCE}} = \frac{1}{2\pi} \left[\sum_{i=1}^{N_s} \sigma_i \left\{ \frac{(x-x_i)\vec{i} + (y-y_i)\vec{j}}{(x-x_i)^2 + (y-y_i)^2} \right\} \right] \quad (3)$$

where; N_s is the number of sources, σ_i is the strength of the i^{th} source and (x_i, y_i) are the coordinates of the i^{th} source.

Similarly, the velocity components from the wall vortices can be obtained by using the following formula;

$$\vec{V}_{\text{BV}} = \frac{1}{2\pi} \left[\sum_{i=1}^{N_v} \Gamma_i \left\{ \frac{(y-y_i)\vec{i} + (x-x_i)\vec{j}}{(x-x_i)^2 + (y-y_i)^2} \right\} \right] \quad (4)$$

where N_v is the number of vortices, Γ_i is the strength of the i^{th} vortex and (x_i, y_i) are the coordinates of the i^{th} vortex.

By substituting eqs. 3 and 4 into the boundary condition $\vec{V} \cdot \vec{n} = 0$, a set of algebraic equations are obtained where the vortex strengths are the unknowns. This system of equations are solved by using the Gauss Elimination approach yielding the unknown strengths of bounded vortices on the solid walls. Kelvin condition is also satisfied as an additional condition to solve this equation system (5).

As mentioned previously, time dependent vortex shedding is modelled by releasing the vortices from the separation points shown in Fig. 1 at each time step. The shed vortices are then followed within the period of interest. As the new vortices are shed downstream, the geometric representation by the bound vortices are reconsidered by appending the additional velocities induced by the shed vortices to the control points. If N_j is the number of shed vortices at the i^{th} time step then this additional velocity component at each (x,y) control point will be;

The separated shear layers are built continuously by releasing vortices from the separation edges. These vortices contribute to the overall velocity field. Hence;

$$\vec{V}_{SV} = \frac{1}{2\pi} \left[\sum_{j=1}^M \sum_{i=1}^{N_s} \Gamma_{i,j} \left\{ \frac{(y - y_{i,j})\vec{i} + (x - x_{i,j})\vec{j}}{(x - x_{i,j})^2 + (y - y_{i,j})^2} \right\} \right] \quad (5)$$

where N_s is the number of shed vortices, M is the number of shedding points, $\Gamma_{i,j}$ is the strength of the i^{th} vortex and the (x_i, y_i) are the coordinates of the i^{th} vortex shed from the j^{th} separation location. Hence, the present computational model allows the possible separations of the flow from M points. Two of these separation points belongs to the nozzle exit. The shear layers which separate from these points form the unsteady jet flow. An inviscid vortex element induces an infinite velocity at and near its center. In order to avoid this problem Rankine Vortex Core Model is applied in this study.

In this study, the relationship between vorticity diffusion and the random walk idea is used to mimic the viscous flow effects. The vorticity generated by diffusion generalizes a random motion of vortices. Random walk idea is first proposed by Chorin (6). The vortices are first moved by the Biot-Savart induction and then moved randomly in x - and y - directions. The new vortex positions are

$$\begin{aligned} x_i^{n+1} &= x_i^n + \eta_1 \\ y_i^{n+1} &= y_i^n + \eta_2 \end{aligned} \quad (6)$$

where η_1 and η_2 are random numbers generated by the procedure described by Chorin.

3. SOLID FLOW PHASE

A particle in a non-uniform time-dependent fluid flow responds to forces imposed by the fluid velocity and body forces. It is still a challenging task to model the nature of fluid-solid interaction (1,3,4).

The motion of particles in a fluid flow can be classified as being either dilute or dense. In dilute flow, it is assumed that the particle motion is controlled by the surface and body forces. In dense flow the main mechanism of particle motion is particle-particle collisions and interactions. In this study, dilute flow of particles in a two dimensional turbulent jet flow is considered.

Solid particles move under the effect of various number of force components in the flow field. These forces can be listed as; the contribution to the acceleration of the particle as a result of the drag force, nonuniformity in the far field gaseous stress tensor, virtual mass effect, Basset history terms, Saffman lift forces and gravity. In the present study only the drag force and gravity are included in the analysis and the other force terms are neglected due to their complexity and left for the future investigations.

In the present study, the drag force and the gravity are included in the analysis as the other force terms are considered to be negligible comparing to these forces. Hence, the acceleration of a solid particle then can be written as,

$$\frac{d\vec{U}_p}{dt} = F_1 (\vec{U}_g - \vec{U}_p) + \left(1 - \frac{\rho_g}{\rho_p} \right) \vec{g} \quad (7)$$

where \vec{U}_g is the fluid velocity, \vec{U}_p is the particle velocity, ρ_g is the fluid density, ρ_p is the particle density and F_1 is the drag coefficient. In two dimensional cartesian coordinate system Eqn.(7) has two components, which are;

$$\frac{du_p}{dt} = F_1 (u_g - u_p) \text{ on } x \text{ direction} \quad (8)$$

$$\frac{dv_p}{dt} = F_1 (v_g - v_p) - \left(1 - \frac{\rho_g}{\rho_p} \right) g \text{ on } y \text{ direction.} \quad (9)$$

The first term on the right-hand side of both equations represents the contribution to the acceleration of the particle as a result of the drag force and the second term in Eqn.(9) represents the gravity. F_1 is related to Reynolds Number, Re_p of a particle and defined as follows (9);

$$F_1 = \begin{cases} \frac{18\nu_g \rho_g}{D_p^2 \rho_p} \left(1 + \frac{3}{16} Re_p \right), & Re_p < 0.01 \\ \frac{18\nu_g \rho_g}{D_p^2 \rho_p} \left(1 + 0.1315 Re_p^{(0.82-0.05 \log Re_p)} \right), & 0.01 < Re_p < 20.0 \end{cases} \quad (10)$$

where Re_p is,

$$Re_p = \frac{\left((u_p^2 + v_p^2)^{1/2} - (u_g^2 + v_g^2)^{1/2} \right) D_p}{\nu_g} \quad (11)$$

At each time step, Re_p is calculated for each particle and then the drag coefficient F_1 is computed from Eqn. (10).

The particle velocity can accurately be calculated in Lagrangian coordinates using eq. 8. The initial velocity of each particle is assumed to be equal to the fluid velocity at the same location. After computing the particle velocities, the following equations are used to compute the particle positions at each time step;

$$\begin{aligned}\frac{dx_p}{dt} &= u_p \\ \frac{dy_p}{dt} &= v_p\end{aligned}\quad (12)$$

4. MODELS FOR FLUID-PARTICLE INTERACTION

Particle-fluid interaction can be studied using two types of models (1,2,7). The first model which is called "One Way Coupling", neglects the effect of solid phase on carrier flow phase. This kind of model is easier to apply since the particles are driven only by the flow field. If the particle-turbulence interactions relates to feed back of particle effects on the continuous phase flow field, this model is called "Two-way coupling" (1,4,6). In this work both models are applied to investigate the particle phase distribution inside the flow field.

The current research investigation considers both of the models. "One-way coupling" is a traditional and simple model approach since only the flow field drives the particles. On the other hand, "Two-way coupling" requires innovative models. One of these models treats the total force imposed on the fluid by particles as a body force which is apportioned to the grids in Eulerian type calculations (4). The body force can be obtained from the particle equations of motion. It could also be appropriate to couple the particle effect with the fluid in terms of a velocity disturbance. This last approach directly incorporates the local disturbance velocity field, due to each particle, into the undisturbed fluid velocity field. This is the approach used in this investigation.

Our model follows the similar approaches of the Vortex-In-Cell method (8). The flow field is divided into cells. At each instant of time, a disturbance velocity due to fluid-particle interaction is computed inside the cells. This flow component is mapped to the grids of the cells by area weighting. At each grid point the disturbance vorticity is computed. Then by using the inverse interpolation this vorticity value is converted into circulation which is added to the discrete vortex strengths inside the cell. Finally, the vortices are then advanced similar to the procedure followed in traditional VIC method (8).

5. RESULTS

5.1 Free Jet

The effect of particle density on free two-phase jet flow is investigated at the first phase of the investigation. Figures 2a-2c show the reference flow case where a single phase jet flow evolution is presented at nondimensional time $T = 98, 101.5$ and 105 . Flow Re

number is $Re = \frac{U_\infty D}{\nu} = 6.75 \times 10^4$. While the

downstream flow structures exhibit turbulent behavior, near field flow structures are typical of a turbulent jet vortices. Thin shear layers roll into coherent vortical structures on both sides of the jet forming the basic form of a Von Karman Street. Figure 4 shows a typical signal of axial velocity fluctuations at a downstream station

$Y = \frac{y}{D} = 6$. The flow Strouhal Number computed at

this station is $St = \frac{f_c D}{U_\infty} = 0.014$

5.2 Two-Phase Free Jet

5.2.1 Effect of Particle Density on Flow Structures (Particle diameter $D_p = 50\mu$)

Figures 3a-c show the instantaneous two-phase jet flow characteristics at three different time as a function of particle concentrations. It is clear that particles modify the upstream flow instabilities. As the particle concentration increases, the vortex formation frequency increases slightly (See Figure 4). The enhancement of vortex formation in the upstream flow field causes an increase in lateral flow characteristics at the downstream location. This observation is also seen in the instantaneous particle distributions which are depicted in Figure 5. As the particle density increases, the vortex formation occurs near the nozzle exit. The distance between the apparent centers of the side vortices also decreases. Moreover, jet system oscillates laterally as the particle density increases.

5.2.2 Effect of Particle Size on Two-Phase Jet Flow

The effect of particle size on jet flow characteristics is demonstrated in Figure 6a-d. Left column pictures show the instantaneous jet flow and particle distributions at $T=98$ with 750 particles inside the flow field. As the particle size increases both the vortex formation mechanisms and the coherent flow structures are modified. Particularly for the case $D_p = 75\mu$, the well organised jet flow evolution is very clear. On the other hand, well organised vortical structures can not carry themselves to downstream locations as the particle size increases.

The instantaneous particle distributions for the mentioned flow fields are exhibited in Figure 6. The particles with higher diameters, in other words heavier particles, settle near the nozzle exit while the lighter particles travel further downstream. As the particle size increases, the formation of coherent jet vortices are enhanced. Since all the pictures are shown at the same time, the effect of particle diameter on vortex spacing and phases between shed vortices are clearly highlighted. More detailed survey of the results are presented by Tunc (9).

6. CONCLUSION

A computational model based on DVM is used to simulate jet flow characteristics. It was shown that particle size and density effect near and far field characteristics. The vortex formation frequencies are strong functions of particle density. Furthermore, the phases of vortex formation differs as a function of particle diameter.

REFERENCES

- (1) Y. Pan, and S. Banerjee, (1996). "Numerical Simulation of Particle Interactions with Wall Turbulence", *Phys. Fluids*, 8, 2733-2755.
- (2) S. Elghobashi, and G.C. Truesdell, (1993). "On the Two Way Interaction Between Homogeneous Turbulence and Dispersed Solid Particles. I: Turbulence Modification", *Phys. Fluids A* 5.
- (3) S. Shimizu, (1986). "Discrete Vortex Simulation of Two-Dimensional Turbulent Jet", *Bulletin of JSME*, 29, 2440-2446.
- (4) R.R. Clements, (1973). "An Inviscid Model of Two-Dimensional Vortex Shedding", *Journal of Fluid Mechanics*, 57, 321-336.
- (5) R.I. Lewis, (1991). "Vortex Element Methods for Fluid Dynamics", *Analysis of Engineering Systems*, Cambridge University Press.
- (6) A.J. Chorin, (1994). "Vorticity and Turbulence", Springer Verlag, New York.
- (7) D. Drew, (1988). "Mathematical Modeling of Two-Phase Flow", *Annu. Rev. Fluid Mech.*, 15, 261.
- (8) J.P. Christiansen, (1973). "Numerical Simulation of Hydrodynamics by the Method of Point Vortices", *J. of Computational Physics*, 13, 253.
- (9) M. Tunç, (2000). "Simulation of Two-Phase Jet Flow by Using Discrete Vortex Method", PhD Thesis, *Istanbul University, Institute of Science and Technology*.

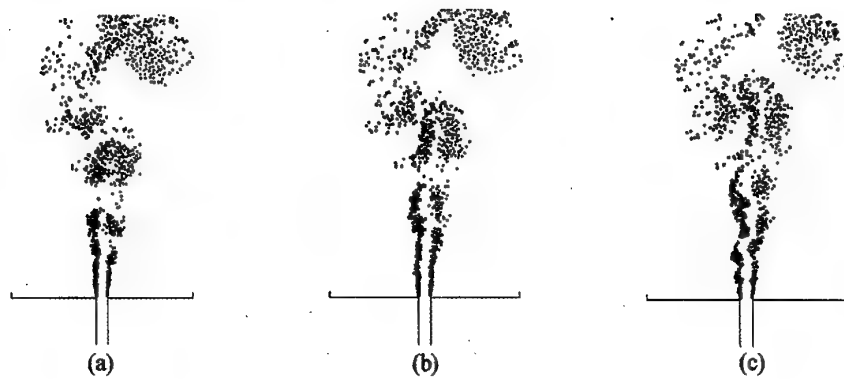


Figure 2. Flow field of single-phase jet

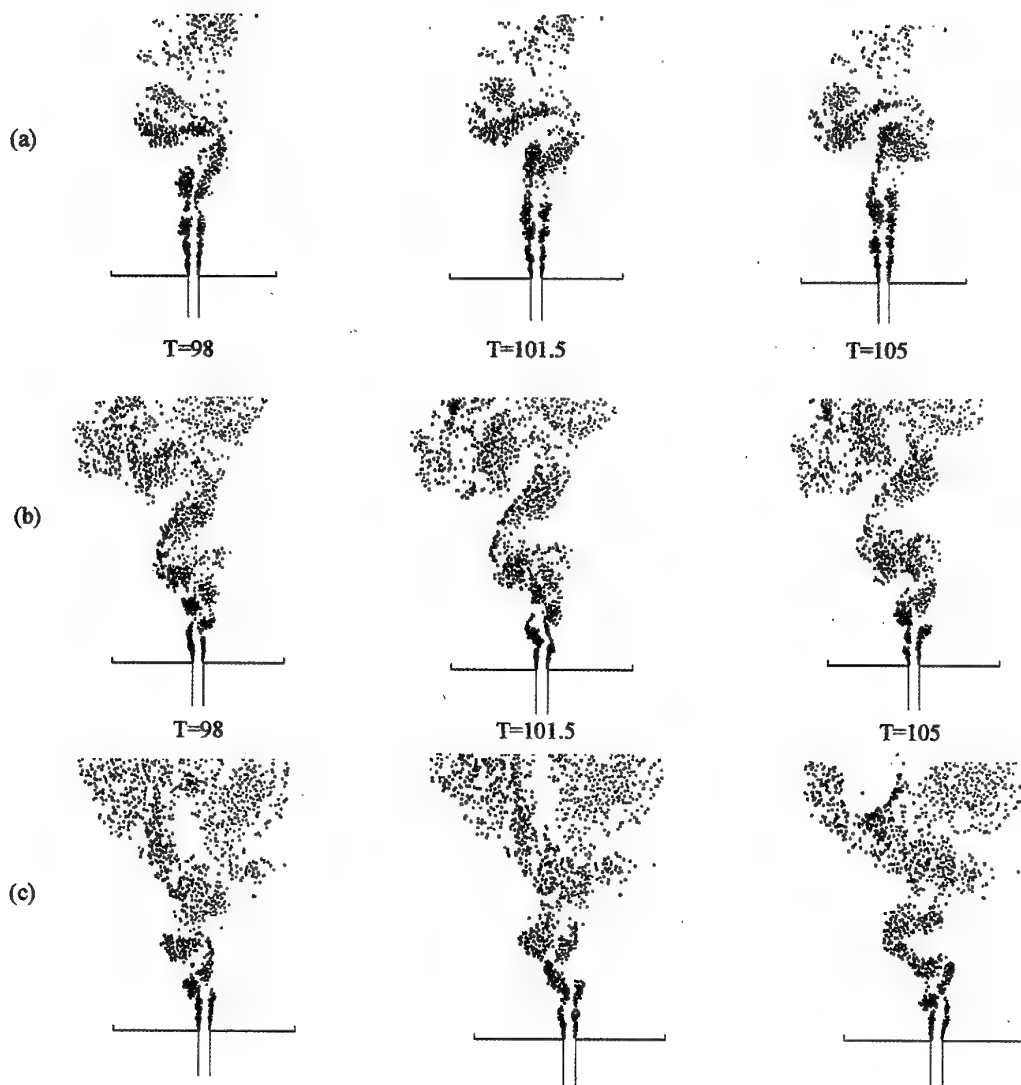


Figure 3. Flow field of two-phase jet, (a) 700 Particles, (b) 3500 Particles, (c) 7000 Particles

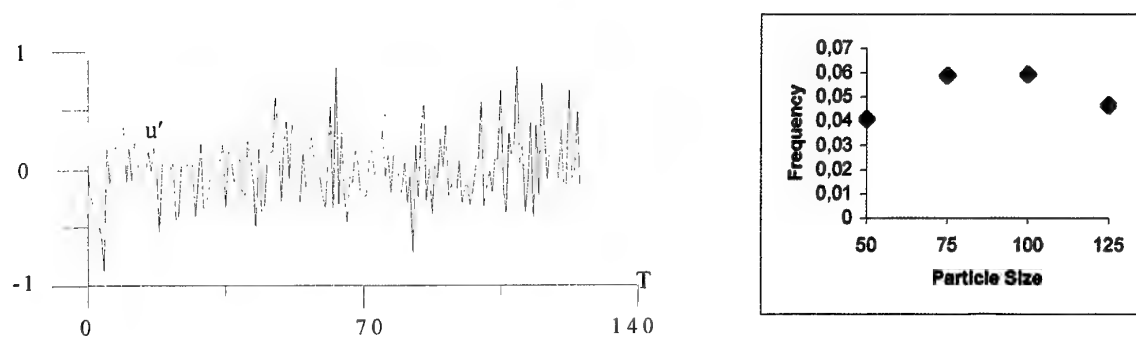


Figure 4. Axial velocity fluctuations at a station $Y=y/D=6$ and flow frequencies of cases for 50μ , 75μ , 100μ and 125μ particles with 7500 particles in the domain

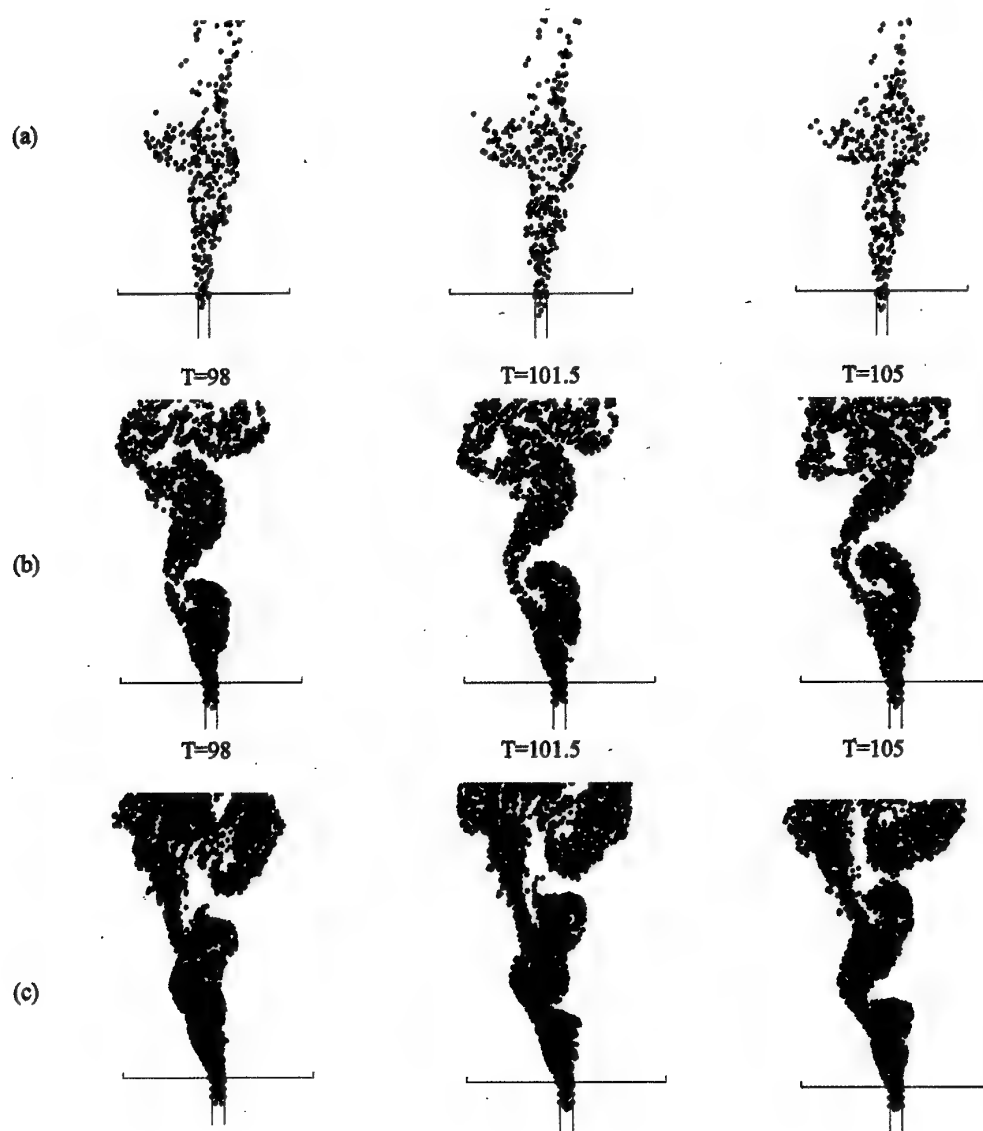


Figure 5. Particle distributions of two-phase jet , (a) 700 Particles, (b) 3500 Particles, (c) 7000 Particles

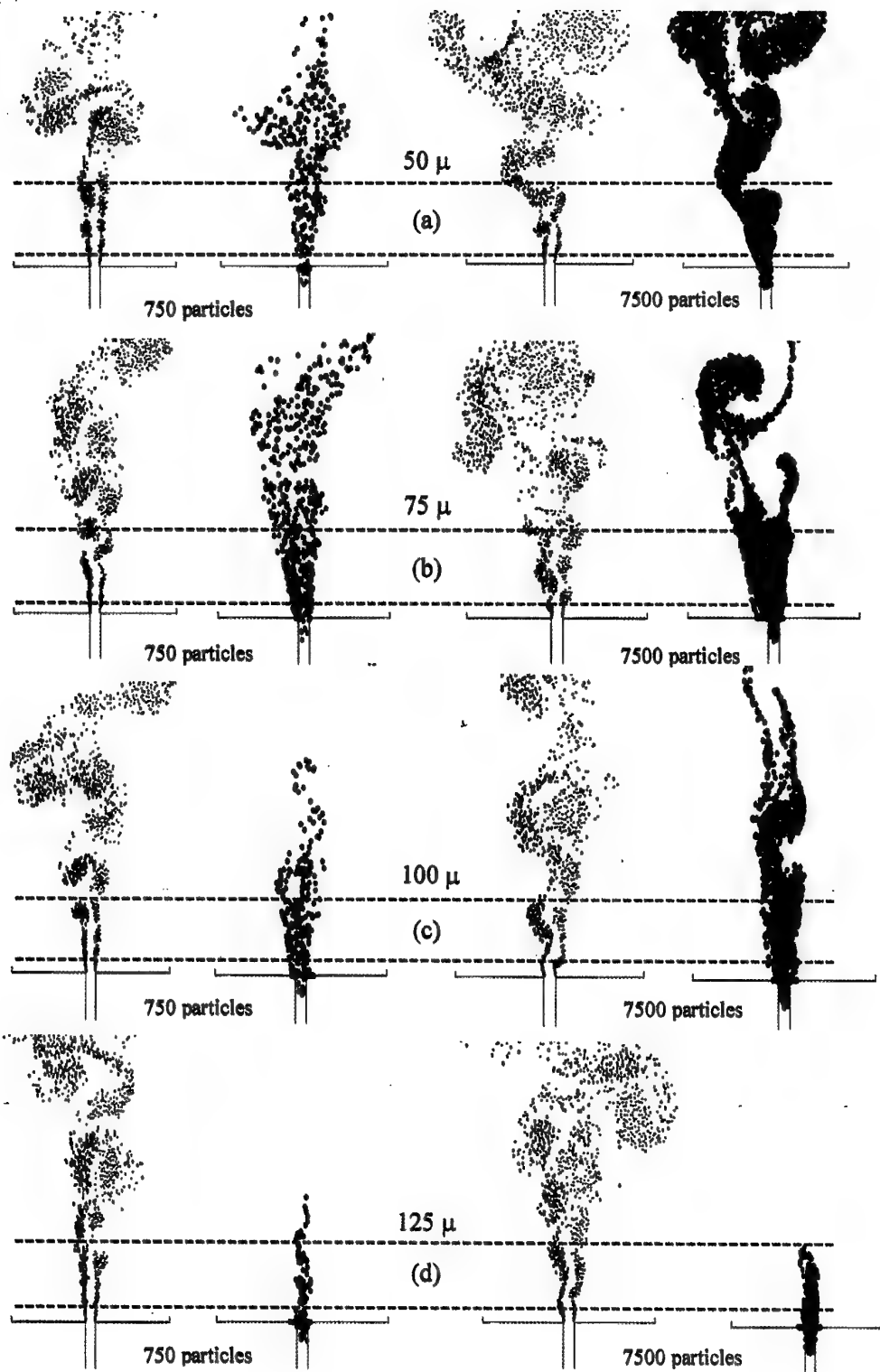


Figure 6. Flow fields and particle distributions of two-phase jets containing 50μ , 75μ , 100μ and 125μ particles with loading ratios 1 and 10 particles per computational time step

SMALL SCALE AURORAL VORTICES

G. Kandemir, M. Yilmaz, B. Ozugur

Faculty of Engineering, Kadir Has University, 80810 Gayrettepe, Istanbul, Turkey,
e-mail: kandemir@itu.edu.tr

Z. Kaymaz

Faculty of Aeronautics and Astronautics, Istanbul Technical University, 80626 Maslak, Istanbul, Turkey, e-mail:
zerefsan@itu.edu.tr

ABSTRACT

Auroral vortices are interesting natural features not only due to their interesting shape; but, due to their relation with MHD and chaotic dynamics. They cannot be described by the same mathematical models with similar looking natural phenomena; since, their physical parameters, duration, conditions in their surrounding medium are quite different. The origin of the small scale vortices is not certain and a complete model does not exist yet. Folds and curls are two periodic distortion types that are observed frequently. According to observations, these periodic folds repeat every 10-50 km while the curls repeat every 1-8 km. The sense of rotation reverses at the southern hemisphere. The curls move rapidly while the folds move much slower. Rapidly moving rays are observed to be curls while more stable rays are folds. Sometimes these forms are called "vortex streets" when they are viewed altogether.

The linear and non-linear effects resulting from the plasma instabilities in the auroral medium can be investigated by means of a simple one dimensional plasma simulation code (Birdsall and Langdon, 1995). Vlasov equations are employed and the fast Fourier transform is applied in the program. The input parameters are chosen to represent the medium surrounding the aurora.

In this study some auroral models are given, parameters to be used in the simulation of the auroral features are discussed and the result of a 1-D plasma simulation is given. Accumulation of microinstabilities leads to non-linear effects that are observed as vortices in the phase space. Among the simulation results in the phase space, the non-linear vortices in the configuration space display a strong resemblance to auroral vortices. Our model correlates the position of the auroral features with their velocity, *i.e.*, the model shows that ions and electrons with same velocity, arrive at the same point and only their velocity determines the position where the particles go. Thus, it gives a simple explanation for this resemblance and may indicate that this resemblance is not accidental. Thus, the images from the narrow-angle TV may be considered as a display of the phase space.

1. INTRODUCTION

Auroral vortices are less investigated natural vortices and are lacking a complete physical model. Pudovkin and Steen (1) reviewed theoretical and observational data on the vorticity of the magnetospheric plasma and classified the types of instabilities proposed for auroral vorticity. Properties of large scale and small scale auroral vortices differ (1, 2, 3).

The small-scale features are usually neglected in investigations by photography; they only give a

distorting effect on the large-scale aurora. But, the low-light-level television investigations near the local magnetic zenith reveal that the blurring is due to small-scale distortions. There are two periodic distortion types that are observed frequently: folds and curls. Folds and curls in auroral arcs seem to have axis of symmetry that are rotating from the normal to the arc. Folds rotate clockwise in the northern hemisphere while the curls rotate counterclockwise. The periodic folds repeat every 10-50 km while the curls usually repeat every 2-8 km. The sense of rotation reverses at the southern hemisphere. The curls move rapidly while the folds move much slower. Hallinan (3) suggests that rapidly moving rays are curls while more stable rays are folds. Sometimes these forms may be inferred as "vortex streets" when they are viewed altogether. These vortices at the first sight, remind turbulence in fluids. Therefore, most explanations depend on hydromagnetic calculations or gas-fluid code simulations. Auroral vortices are observed as rays as they are viewed from the side; this is an interesting and unexplained property.

Some auroral models are given in section 2 and parameters to be used in the simulation of the auroral features are discussed in 3. In Section 4, the results of a 1-D plasma code simulation are given.

2. AUROREAL MODELS

When additional energetic solar electrons and ions enter the magnetosphere, an electric field is produced in the region where electrons normally reflect. This field eliminates the reflection. Thus the electrons enter the atmosphere colliding with the atoms and molecules and causing the auroral lights.

An interesting numerical model has been proposed by Perreault and Akasofu (4). They established an auroral activity index, \mathcal{E} which was proposed as an alternative to the frequently used auroral index, AE. As the indices AE and \mathcal{E} give a quantitative account of the auroral activity, the behavior of the magnetosphere is resembled to a windsock. Variations of such models are discussed several times; a model adequate to describe the whole auroral phenomenon is not available yet.

The satellites reveal that the auroral substorms are related to the z component of the IMF. Following this idea, models are based on the magnetic reconnection (5) of the field lines on the day side of the earth with those in the interplanetary field. In all reconnection models, reconnection occurs while \mathbf{B}_{IMF} is southward and therefore opposes the magnetic field in the

dayside magnetopause that is northward. It is thought that on the night side, open field lines trap plasma from the solar wind into the geomagnetic field. These fields reconnect at a much farther distance on the night side. Reconnection mechanism for such a collisionless medium leads to several unanswered questions. The auroral electrons accelerate from low values as a few eV in the solar wind up to energies as a few tens of keV. This acceleration mechanism is not understood well. Electric fields parallel to the magnetic fields being produced during the large Birkeland currents are thought by several investigators to cause acceleration.

But, Bryant (6) approaches with caution, indicating that electric potentials produce closed contours that cannot lead to acceleration of particles outside these contours. Observations indicate that parallel electric fields occur only sporadically on discrete auroras. It has been proposed that there must be a perpendicular electric field in addition to the parallel electric field to produce shear in the sheet of precipitating electrons. This shear is thought to lead to Kelvin-Helmholtz instability that causes auroral vortices and curls. Hallinan proposes that electrostatic acceleration in discrete auroral arcs is a side effect that occurs only when appropriate instability criteria are satisfied (3).

There are three types of auroral currents. The simplified models neglect Birkeland currents at the arc boundaries. This gives an upper limit for the enhancement of the currents. Actually, Birkeland currents reduce the polarization charges and thus E_y . Pedersen current is perpendicular to the magnetic field, \mathbf{B} and is parallel to the electric field \mathbf{E} . The Hall current is perpendicular to both.

Different mechanisms may apply to the large and small scale structures of the auroral plasma. Models explaining the small scale structures in auroras are made only recently. Birk and Otto (7) try to explain extremely thin field-aligned layers of auroral luminosity by means of a simulation. They use a three-dimensional plasma-neutral gas-fluid code for the simulation of low energy electrons. They conclude that resistive instabilities result in localized plasma heating which may contribute to the formation of ionospheric plasma and neutral gas vortices. In another work, Otto (8) claims that a three-dimensional reconnection site is divided into filaments in the form of a multitude of reconnection patches.

Reconnection was criticized by Alfvén. During recent years concerns about the future of reconnection

models have been discussed (9). It may be concluded that although considerable theoretical work has been done for the reconnection process, the theory is far from being complete and needs caution to avoid confusion from time to time. There are several missing points and unexplained details in the models. Trying to link the solar events and the terrestrial magnetic effects sometimes fail. Eventually, a substorm is a complex event and a linear evaluation may lead to errors. The small-scale features in auroras are among hard to explain aspects.

Models based on assumptions departing from reconnection should be tried at least on the small scale structures. These features may display sporadic events of different origin. Evaluating the small-scale structures in terms of microinstabilities may help. It may be possible to evaluate them as an accumulation of microinstabilities that lead to non-linear effects. First application of one dimensional electrostatic simulation on aurora was made by Hudson and Potter (10). They studied conditions for formation of electrostatic shocks (double layers) in the auroral magnetosphere.

3. SIMULATION

In the present study, ES1, a simple one-dimensional (1-D) plasma simulation code has been used. It has been shown by Otto(8) that the 3-D simulations in the configuration space should be preferred to 2-D simulations and that 2-D simulations may lead to errors. Considering the fact that auroral vortices are observed only over a plane and assuming this plane as a manifestation of phase space, a 1-D simulation may be sufficient for the investigation of the small scale auroral features. For our study, a 1-D simulation in phase space is chosen. As models and theories become too much detailed and complicated treatments start to carry contradicting results, simple treatments may catch clarity.

ES1 is a vastly experienced and simple plasma simulation code (11). It has been applied in simulations of several astrophysical and space plasmas (e.g., 12). Vlasov equations are used and the fast Fourier transform is applied in the program. The input parameters are chosen to represent the plasma medium surrounding the aurora. This is also the medium where the small scale features take place.

Medium-energy (about 0.5-20 keV) particles produce the visual aurora. This may lead to a temperature below 100K. But, temperature enhancements may increase the temperature to 1000K for auroral and polar cap velocities much greater than 1 km/s (13).

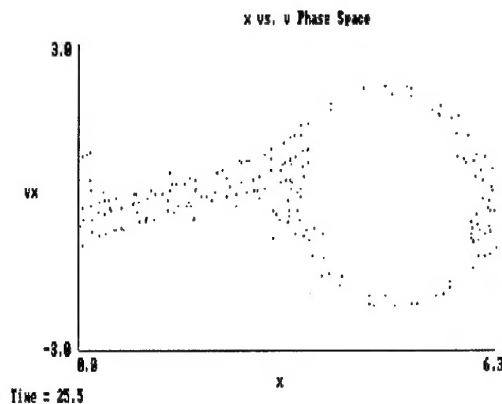


Figure 1. A sample vortex shape in phase space (two stream instability of electrons) as an application of the plasma simulation, ES1 (12).

Therefore, the auroral plasma can be treated as a cold plasma. At the nighttime auroral region, 10^7 m^{-3} is a reasonable value for the electron density. Therefore, $10^4 \text{ electrons m}^{-3}$ are adopted as the particle number in the 1-D simulation. The number of electrons may be considered equal to the number of ions. Molecular ions are known to dominate the E region while atomic ions dominate the F region. Electrons and ions are generally thought to move together in the electric field, \mathbf{E} , frozen to magnetic field lines, \mathbf{B} . They move with a velocity, \mathbf{v} which is perpendicular to both \mathbf{E} and \mathbf{B} ,

$$\mathbf{v}_e = \mathbf{v}_i = (\mathbf{E} \times \mathbf{B}) / B^2.$$

This equation applies to electrons down to about 100 km. It is known that at the auroral latitudes, strong auroral electric fields may move the ionospheric plasma with velocities as 1 km.s^{-1} (13).

Movement of energetic electrons relative to ions along the auroral magnetic field lines result in aurorae. In the present simulation, electrostatic instabilities in the auroral plasma are investigated. Electrostatic instabilities are the most destructive type among the plasma instabilities.

Considering electrons of energies 5-20 keV and using the auroral values ($10^4 \text{ electrons.m}^{-3}$), the thermal velocity, v_{th} can be calculated. It is about 200 km.s^{-1} for electrons of 5 keV, 400 km.s^{-1} for electrons of 10 keV, 850 km.s^{-1} for electrons of 20 keV. As the thermal velocity increases, the drift velocity, v_d decreases. The linear growth may be observed to decrease in the simulation. For cold electron beams, the threshold for growth is when the drift velocity is, $v_d = 1.3 v_{th}$. After this value, the exponential growth stops; but, nonlinearity features may be observed. The perturbed charge densities cause the particles to

bunch up or proceed before the neighboring particles. So that, they wrap into vortices in the phase space (11). Therefore, the drift velocity for the electrons starts with a value of about 350 km.s^{-1} during the growth of microinstability.

For the protons, the drift velocity is only of the order of 8 km.s^{-1} . It is even less for the molecular ions. The movement of auroral plasma that is attributed to auroral electric fields is reported to be about 1 km.s^{-1} . This value is comparable only with the drift velocity of the ions in the calculations. The non linear behavior of the auroral plasma resulted in vortices in the phase space. The origin of the small scale structures of 1-3 km width is not certain and a complete model does not exist yet.

Among the simulation results in the phase space, the non-linear vortices display a strong resemblance to the small scale auroral structures in the configuration space. The position of the auroral features due to their velocity may give a simple explanation for this resemblance and may indicate that this resemblance is not accidental. Such a model shows that ions or electrons with the same velocity, arrive at the same point and only their velocity determines the position where the particles go. Therefore, the aurora images from the narrow-angle TV may be considered as a display of the phase space.

4. CONCLUSION

1. The calculated drift velocity for the stability condition is much larger than the auroral plasma movement velocity. Linear behavior of small scale auroral plasma agrees with the previous simulations cited in literature. The large velocities in the microinstability region lead to non-linear behavior.
2. The simulation showed that small initial perturbations are sufficient to grow instabilities.
3. Non-linear behavior results in vortices in the phase space. These vortices display a strong
- (9) Otto, A., (1998), "Properties of 2-Dimensional and 3-Dimensional Magnetic Reconnection", *Phys. Scripta*, T74, 9.
- (10) Hudson, M.K. and Potter, D.W., (1981), in: *Physics of Aurora Arc Formation*, S. -I. Akasofu and J.R. Kan (eds.), Geophysical Monograph 25, American Geophysical Union, Wash. D.C.

resemblance with the small scale features in the configuration space. Therefore, these features may be interpreted as a result of velocity changes. It is possible to argue which parameters are important in representing the small-scale structures of auroras. Small-scale structures may be a manifestation of non-linear variations of the velocity. In this case, models made to represent these features should involve velocity differences correlating these with the positions of the particles.

References

- (1) Pudovkin, M.I. and Steen, A., (1995), "Plasma Motion Vorticity in the Magnetosphere-Ionosphere System" in: *The Solar Wind-Magnetosphere System 2*, Biernat, H.K., Landreiter, H.P., Bauer, S.J. and Farrugia, C.J. (eds.), pp.1-32, Austrian Academy of Sciences.
- (2) Kandemir, G., (2000), "Auroral Vortices", in: *The Solar Wind-Magnetosphere System 3*, (eds. H.K. Biernat, C.J. Farrugia and D.F. Vogl), pp.263-268, Austrian Academy of Sciences.
- (3) Hallinan, T.J., (1991), "Auroras" in: *Geomagnetism*, Vol.4, (ed.) Jacobs, J.A., Academic Press.
- (4) Perreault, P. and Akasofu, S.I. (1978), "A Study of Geomagnetic Storms", *Geophys. J. R. Astr. Soc.*, **54**, 547.
- (5) Biernat, H.K., (1993), "Reconnection at the Dayside Magnetopause: Theory and Comparison with Data", *Trends in Geophys. Res.*, **2**, pp. 535-651.
- (6) Bryant, D. A., (1989), "Auroral Electron Acceleration", *Phys. Scripta*, T30, 215.
- (7) Birk, G.T. and Otto, A., (1997), "On the Role of Macroscopic Resistive Instabilities in the Auroral Ionosphere-Thermosphere System", *Adv. Sp. Res.*, **20**, Iss 6, 1301.
- (8) Lundin, R., (1997) "Discussion 1: On Merging and Reconnection", *Phys. Chem. Earth*, **22**, 605.
- (11) Birdsall, C.K. and Langdon, A.B., (1985), *Plasma Physics via Computer Simulation*, McGraw-Hill.
- (12) Kandemir, G. and Boydag, S., (1997), *Astrophys. And Space Sci.*, **251**, 227.
- (13) Carlson, H.C. and Egeland A., (1996), in: *Introduction to Space Physics*, Kivelson, G.K. and Russell, C.T. (eds.), Cambridge Univ. Press.

Index of Authors

Author Page

Bearman, P.W.	131
Bernard, P.S.	41
Çetiner, O.	165
Chan, K.T.	107
Chung, K.H.	189
Dimas, A.A.	41
Fukuda, K.	63
Funakubo, Y.	9
Gökçöl, O.	251
Graham, J.M.R.	147
Hatano, J.	93
Igarashi, T.	235
Iida, A.	211
Ishikawa, H.	243
Izawa, S.	99
Kamemoto, K.	33, 63, 157, 173, 197, 211, 235
Kandemir, G.	259
Kaykayoglu, C.R.	251
Kaymaz, Z.	259
Keser, H.İ.	123, 131
Kida, T.	87
Kiya, M.	99, 243
Kornev, N.	219
Lam, K.	107, 115
Lee, D.J.	189
Lewis, R.I.	181
Li, J.Y.	107, 115
Maeda, T.	139
Mochizuki, O.	243
Nakamura, H.	235
Nakazawa, T.	139
Nishiwaki, K.	79

Author Page

Obi, S.	71
Ogami, Y.	79
Ogawa, K.	139
Ohtsuka, K.	55
Ojima, A.	173, 211
Ota, S.	33
Özugur, B.	259
Rockwell, D.	165
Ryu, K.W.	189
Sakajo, T.	17
So, R.M.C.	107, 115
Suzuki, M.	139
Takada, N.	139
Takaki, R.	55
Take, T.	87
Taranov, A.	219
Totsuka, Y.	71
Tsukamoto, H.	25
Tsutahara, M.	139, 227
Tunç, M.	251
Ünal, M.F.	123, 131, 165
Wang, H.	25
Watanabe, S.	9, 55, 93
Willden, R.H.J.	147
Yilmaz, M.	259
Ying, L-A.	1
Yoshihara, Y.	79
Zhang, X.	227
Zhu, B.	63, 157